

Development of a Spatially Multiplexed Ion Mobility Spectrometer and
Utilization of Ion Mobility-Mass Spectrometry for
Conformational Analyses of Lipids and Other Biomolecules

By

Katrina Lahoma Leaptrot

Dissertation

Submitted to the Faculty of the
Graduate School of Vanderbilt University
in partial fulfillment of the requirements
for the degree of

DOCTOR OF PHILOSOPHY

in

Chemistry

May 11, 2018

Nashville, Tennessee

Approved:

John A. McLean, Ph.D.

David E. Cliffler, Ph.D.

Brian O. Bachmann, Ph.D.

Erin C. Rericha, Ph.D.

To my family,
for years of love and encouragement.

ACKNOWLEDGMENTS

I have been extremely fortunate to enjoy years of support and direction from my advisor, Dr. John A. McLean, whom I would like to thank for providing the opportunity to study in a stimulating research environment at the forefront of our field. I would also like to thank Dr. Jody C. May for his mentorship in instrument development, both in the lab and over a thousand cups of coffee. I have appreciated guidance offered in the past by senior members of the McLean lab including Cody R. Goodwin, Kelly M. Hines, and Sarah M. Stow, and the members who joined with me in 2012, Nichole M. Lareau and J. Rafael Montenegro-Burke, all of whom have gone on to excel in their respective endeavors. Special thanks is extended to Caleb B. Morris and James N. Dodds, with whom I have shared many conversations, and who have always been happy to assist with my instrument building when I have asked. I wish the remaining members of the McLean lab the very best in their future undertakings.

My committee members, Dr. David E. Cliffler, Dr. Brian O. Bachmann, and Dr. Erin C. Rericha, were great sources of ideas and encouragement in the steps leading to my Ph.D. I appreciate the time and effort they expended to assist me along my way.

To the SyBBURE program and students, I would like to extend my gratitude for helping develop my mentorship capabilities and for making me become a more well-rounded scientist.

I would not have pursued a higher degree without the inspiration of West Virginia teachers including Ms. Pat Miller and Ms. Barbara Heckert, who imparted their passions for knowledge and science to me, and my undergraduate advisor, Dr. Xiaoping Sun, with whom I shared my first research experience and many, many Monday evenings of organic chemistry lab.

Of course, none of this would have been possible without my family. My mother and father, Donna M. and Kenneth H. Leaptrot II, have always believed in me; offering care, love, and encouragement. I thank my older brother, Brendon W. Leaptrot, who taught me long division two

years early, and my younger brother, Andrew J. Leaptrot, a great sponsor and friend. My grandfather and late grandmother, Kenneth I and Patsy Leaptrot, were always proud to see me pursuing a higher education without neglecting the humble West Virginia hollow in which I was raised. Finally, I would like to acknowledge my creative, talented, and loving husband, Seth K. Gregory. I would not have applied to Vanderbilt without his inspiration, and I would not have made it to where I am today without him. He is my favorite, and he is my only.

TABLE OF CONTENTS

	Page
DEDICATION	ii
ACKNOWLEDGMENTS	iii
LIST OF TABLES.....	ix
LIST OF FIGURES	x
LIST OF ABBREVIATIONS, ACRONYMS, AND VARIABLES	xii
 Chapter	
I. Temporally Dispersive Ion Mobility Techniques	1
I.I. Introduction and Historical Perspective	1
I.II. Ion Mobility Instrumental Considerations	5
I.II.I. Sample Preparation Strategies	5
I.II.II. Ionization Sources.....	8
I.II.II.I. Ionization by Radioactivity.....	8
I.II.II.II. Ionization by an Applied Electric Field.....	11
I.II.II.III. Ionization by Electromagnetic Radiation.....	16
I.II.III. Ion Mobility Analyzers: Space-Dispersion and Time-Dispersion.....	17
I.II.IV. Ion Mobility-Mass Spectrometry	21
I.III. Theory and Fundamentals of Time-Dispersive Ion Mobility Spectrometry	24
I.III.I. Transforming Drift Time to Collision Cross Section	24
I.III.II. Factors Affecting Separation in Ion Mobility.....	29
I.III.II.I. Influence of Gas Selection on Separations	29
I.III.II.II. Influence of Electrostatic Field-Strength on Separations	32
I.III.II.III. Influence of Temperature on Separations	33
I.IV. Multidimensional Separation Techniques.....	34
I.IV.I. Gas Chromatography-Ion Mobility Spectrometry	35
I.IV.II. Liquid Chromatography-Ion Mobility Spectrometry.....	36
I.IV.III. Supercritical Fluid Chromatography-Ion Mobility Spectrometry	36
I.IV.IV. Ion Mobility-Inductively Coupled Plasma Mass Spectrometry.....	38
I.V. Landscape of Ion Mobility Spectrometry Applications	41
I.VI. Conclusions and Prospects	43
I.VII. Acknowledgements	43
I.VIII. References	45

II.	Theoretical Considerations for Spatial Multiplexing in Ion Mobility Spectrometry	70
II.I.	Abstract	70
II.II.	Introduction	70
II.II.I.	History.....	70
II.II.II.	Theory.....	72
II.II.III.	Motivation.....	74
II.III.	Materials and Methods	77
II.IV.	Results and Discussion.....	78
II.IV.I.	Instrument Design Process.....	78
II.IV.II.	Modeling Electrode Geometries	81
II.IV.II.I.	Ion Mobility Drift Tube	82
II.IV.II.II.	Tandem Ion Funnels	85
II.IV.II.III.	Gating Apertures	91
II.IV.III.	Vacuum System Requirements.....	91
II.IV.IV.	Hardware and Infrastructure	97
II.IV.IV.I.	Ionization and Desolvation	99
II.IV.IV.II.	Tandem Ion Funnels	101
II.IV.IV.III.	Gated Aperture Array	104
II.IV.IV.IV.	Ion Mobility Drift Tube	105
II.IV.IV.V.	Faraday Detector	107
II.IV.IV.VI.	Infrastructure.....	108
II.IV.V.	Electronics.....	110
II.IV.V.I.	Power Supply Units	110
II.IV.V.II.	Tandem Ion Funnels	111
II.IV.V.III.	Aperture Array.....	114
II.IV.V.IV.	Drift Tube.....	114
II.IV.V.V.	Detector.....	114
II.IV.VI.	Control and Acquisition.....	115
II.V.	Conclusions	118
II.VI.	Supporting Information	118
II.VII.	Acknowledgements	119
II.VIII.	References	120

III.	Preliminary Results for an Eight-Channel Spatially Multiplexed Ion Mobility Spectrometer.....	125
III.I.	Introduction	125
III.II.	Preliminary Results	125
III.II.I.	Vacuum System	125
III.II.II.	Electronics.....	126
III.II.III.	Electrospray Ionization Characterization.....	129
III.II.IV.	Characterization of Ion Signal in Vacuum.....	134
III.III.	Current Obstacles	139
III.IV.	Conclusions and Future Directions	141
III.V.	References	144
IV.	Conformational Ordering of Biomolecules in the Gas Phase: Nitrogen Collision Cross Sections Measured on a Prototype High Resolution Drift Tube Ion Mobility-Mass Spectrometer	145
IV.I.	Abstract	145
IV.II.	Introduction	146
IV.III.	Experimental Methods	148
IV.III.I.	Preparation of Standards	148
IV.III.I.I.	Lipids	148
IV.III.I.II.	Carbohydrates	149
IV.III.I.III.	Peptides	149
IV.III.I.IV.	Quaternary Ammonium Salts	150
IV.III.II.	Instrumentation	150
IV.III.III.	Experimental Parameters	152
IV.III.IV.	Collision Cross Section Calculations.....	153
IV.IV.	Results and Discussion.....	154
IV.IV.I.	Database Description and General Cross Section Trends in Nitrogen	154
IV.IV.II.	Description of the Fits to the Empirical Data	157
IV.IV.III.	Extraction of Sub-Trend Information from the Data	159
IV.IV.IV.	Comparisons Between Helium and Nitrogen CCS Values.....	165
IV.V.	Conclusions	167
IV.VI.	Supporting Information	168
IV.VII.	Acknowledgements	169
IV.VIII.	References	170

V.	Structural Conformation Atlas for High Confidence Lipidomics	175
V.I.	Abstract	175
V.II.	Introduction	176
V.III.	Materials and Methods	176
V.III.I.	Preparation of Lipid Samples.....	178
V.III.II.	Instrumentation	178
V.III.III.	Experimental Parameters	179
V.III.IV.	Calibration Methods.....	179
V.IV.	Results and Discussion.....	180
V.IV.I.	Lipid Nomenclature	180
V.IV.II.	Lipid Population Observations	181
V.IV.III.	Category and Class IM-MS Correlation	181
V.IV.IV.	Cation Forms.....	186
V.IV.V.	Quantitative Mobility-Mass Correlations	188
V.IV.VI.	Identification by CCS	191
V.IV.VII.	Lipid Mixture Analysis	192
V.V.	Summary	194
V.VI.	Supporting Information	194
V.VII.	Acknowledgements	194
V.VIII.	References	196
VI.	Perspectives and Proposed Improvements for Ion Mobility Instrumentation.....	199
VI.I.	Introduction	199
VI.II.	A Highly Versatile Device for Mobility and Mass Analysis Based on a Printable Two-Dimensional Planar Array.....	199
VI.II.I.	Background and Significance	200
VI.II.II.	Preliminary Studies	205
VI.II.III.	Research Design and Methods.....	208
VI.II.IV.	Summary	214
VI.III.	Outlook for Spatially Multiplexing Ion Mobility Spectrometry	214
VI.IV.	Conclusions and Perspectives	215
VI.V.	References	216

Appendix

A.	References of Adaptations for Chapters	219
B.	Supporting Information for Chapter II.....	220
C.	Supporting Information for Chapter III	406
D.	Supporting Information for Chapter IV	408
E.	Supporting Information for Chapter V	440
F.	Curriculum Vitae	458

LIST OF TABLES

Table	Page
2.1 Improved Figures-of-Merit Summary.....	76
2.2 Tabulated Mobility Data.....	87
2.3 Tabulated Pumping Calculation Results.....	98
4.1 Summary of Statistics Related to the CCS Database.....	155
4.2 Measured CCS Values for TAA Salts Compared with Literature.....	156

LIST OF FIGURES

Figure	Page
1.1	Historical Developments in IM Technologies3
1.2	Geographical Distribution of IM Literature.....4
1.3	Primary IM and IM-MS Instrument Components6
1.4	Common Ionization Sources Utilized with IM.....9
1.5	DTIMS Instrument Layout and Selected Ionization Techniques13
1.6	Operational Principles of FAIMS19
1.7	Contemporary Time-Dispersive IM-MS Instrumentation22
1.8	Determination of Drift Time from Arrival Time in IM26
1.9	Chloroaniline and Iodoaniline Spectra in Four IM Drift Gases.....31
1.10	Schematic of HPLC Interface with ESI-IM-MS.....37
1.11	Experimental Arrangement of IM with ICP-MS40
2.1	IMS Separation Representation73
2.2	Spatially Multiplexed IM Schematic80
2.3	Theoretical Ion Trajectory Simulations and Arrival Time Distributions.....83
2.4	Conditional Resolving Power Plots86
2.5	Ion Trajectory Simulations to Determine RF Operational Parameters89
2.6	Selection of Aperture Orifice Inner Diameter92
2.7	Rendered Cutaway View of Assembled Instrument100
2.8	Electric Circuits for Tandem Ion Funnel.....112
2.9	Photograph of Select Electronic Components113
2.10	Block Diagram of Information Flow from User Interface to Electrodes.....116
3.1	Empirical Establishment of Corona and Discharge Limits.....130
3.2	Ion Signal Response to Solvent Type and Salt Concentration131
3.3	Ion Signal Response to Distance of ESI from Faraday Plate.....133
3.4	Ion Signal Transmitted Through RGC and High Pressure Ion Funnel.....135
3.5	Ion Signal Acquired by LabVIEW Software Written In-House.....138
3.6	Flow Diagram for the Design Process142
4.1	Details of the Prototype IM-MS Instrumentation151
4.2	Scatter Plots of CCS Values and Best Fit Lines of the Data158

4.3	Subclass Analysis of Carbohydrates	161
4.4	Subclass Analysis of Lipids	162
4.5	Comparison of Helium and Nitrogen-Derived CCS Values.....	164
5.1	Lipid Population Observations	182
5.2	Conformational Space Analysis of Singly Charged Lipids	184
5.3	Histogram Summarizing Change in CCS Across Adducts.....	187
5.4	Correlations Observed within PS and GlcCer Lipid Classes.....	189
5.5	IM-MS Spectrum of a Mixture of PE, PS, PC, SM, and GlcCer Lipids.....	193
6.1	Instrumental Design of a SLIM Device	202
6.2	Previously Demonstrated Alternative Quadrupole Designs	203
6.3	Box Diagram of Instrument Layout.....	207
6.4	Results for Operation as an IM Separation Device.....	209
6.5	Results for Operation as a Quadrupole Mass Filter	210
6.6	Timeline for Proposed Research.....	212

LIST OF ABBREVIATIONS, ACRONYMS, AND VARIABLES

α	Correction factor for choked flow
α_d	Dipole polarizability of neutral gas
β	Correction factor for ratio of thickness to inner diameter for an orifice
γ	Isentropic exponent
η	Gas viscosity
θ	Fractional contribution of molecular flow
λ	Mean free path length of ion in direction of electrostatic field
μ	Reduced mass of ion-neutral collision pair
π	Pi
ψ	Dimensionless flow function
Ω	Ion-neutral collision cross section
\bar{C}	Mean particle speed
A	Cross sectional area of an aperture
ACCESSR	Adaptable Circuit Configuration to Effect Sample Selection and Reaction
ADH	Alcohol Dehydrogenase
AIMS	Aspirator Ion Mobility Spectrometry
APCI	Atmospheric Pressure Chemical Ionization
BNC	Bayonet Neill-Concelman
BNG	Bradbury-Nielsen Gate
BSA	Serum Albumin
C	Conductance
CAD	Computer Aided Design
CCS	Collision Cross Section
CD	Corona Discharge
CE	Capillary Electrophoresis
Cer	Ceramide
CFD	Computational Fluid Dynamics
CID	Collision Induced Dissociation
CLA	Conjugated Linoleic Acid
CPC	Condensation Particle Counter
C_{TV}	Conductance for viscous flow through a tube

CV	Compensation Voltage
d	Molecular diameter
DART	Direct Analysis in Real Time
DC	Direct Current
DESI	Desorption Electrospray Ionization
DLLME	Dispersive Liquid-Liquid Microextraction
DMA	Differential Mobility Analysis
DMS	Differential Mobility Spectrometry
d_p	Diameter of path connective two pressure regions
DTIMS	Drift Tube Ion Mobility Spectrometry
E	Electric field
EI	Electron Impact
ESI	Electrospray Ionization
ETD	Electron Transfer Dissociation
ExPASy	Expert Protein Analysis System
FAIMS	Asymmetric High-Field Ion Mobility Spectrometry
FPGA	Field-Programmable Gate Array
FR	Flame Retardant
GC	Gas Chromatography
GlcCer	Glycosphingolipids, or cerebroside
HPLC	High Performance Liquid Chromatography
ICP	Inductively Coupled Plasma
IM, IMS	Ion Mobility Spectrometry
IM-MS	Ion Mobility-Mass Spectrometry
IMR	Ion-Molecule Reactions
IMS-IMS	Tandem Ion Mobility Spectrometry
K	Ion mobility coefficient, or proportionality constant
k_B	Boltzmann constant
K_n	Knudsen number
K_o	Reduced mobility
K_{pol}	Polarization limit, or contribution of ion-induced dipole interaction to reduced mobility
L	Length, either of drift cell or of tube connecting two pressure regions

LA	Laser Ablation
LC	Liquid Chromatography
LLE	Liquid-Liquid Extraction
LPME	Liquid Phase Microextraction
LTP	Low Temperature Plasma
m	Molecular weight
m/z	Mass-to-Charge Ratio
MALDI	Matrix Assisted Laser Desorption/Ionization
MCC	Multi-Capillary Column
ME	Membrane Extraction
MEPS	Microextraction in Packed Syringe
m_i	Ion mass
MIP	Molecularly Imprinted Polymers
m_n	Neutral mass
MNP	Magnetic Nanoparticle
MS/MS	Tandem Mass Spectrometry
N, n	Drift gas or molecular number density
N_A	Avogadro's number
P^*	Critical pressure
P, p	Pressure
P_1	Greater inlet pressure
P_2	Lesser outlet pressure
PA	Phosphatidic Acid
PC	Phosphatidylcholine
PCB	Printed Circuit Board
PE	Phosphatidylethanolamine
PI	Photoionization
P_R	Reference pressure where molecular and viscous flow contributions are similar
PR1	Pressure Region 1
PR2	Pressure Region 2
PR3	Pressure Region 3
PR4	Pressure Region 4

PS	Phosphatidylserine
PTM	Post-Translational Modifications
q	Ionic charge
Q	Throughput, or flow rate
Q_{OM}	Throughput for molecular flow through an orifice
Q_{OT}	Throughput for transition flow through an orifice
Q_{OV}	Throughput for viscous flow through an orifice
Q_T	Total throughput
Q_{TH}	Total throughput for the high pressure funnel
Q_{TL}	Total throughput of low pressure funnel
QTOF	Quadrupole Time-of-Flight
Q_{TV}	Total throughput for viscous flow through a tube
r	Radius of the tube
R	Universal gas constant
R ²	Coefficient of determination
RC	Resistor-capacitor
RF	Radio Frequency
RGC	Resistive Glass Capillary
RIF	Rectilinear Ion Funnel
RIO	Reconfigurable Input/Output
S	Pumping speed at pump entrance
SBSE	Stir-Bar Sorptive Extraction
SCX	Strong Cation Exchange
SDME	Single Drop Microextraction
SESI	Secondary Electrospray Ionization
SFC	Supercritical Fluid Chromatography
SHV	Safe High Voltage
SLIM	Structures for Lossless Ion Manipulation
SM	Sphingomyelin
SPE	Solid Phase Extraction
SPME	Solid Phase Microextraction
T	Temperature
TAA	Tetraalkylammonium

t_{ATD}	Arrival time distribution of ion packet at the detector
t_d	Drift time of ion packet through ion mobility cell
$t_{d1/2}$	Width of mobility peak at half maximum
$t_{drift\ time\ correction}$	Time the ion packet resides in regions of the instrument outside of the drift cell
TLC	Thin-Layer Chromatography
TOF	Time-of-Flight
TTL	Transistor-Transistor Logic
TWIM, TWIMS	Traveling Wave Ion Mobility Spectrometry
V	Potential across the length of the drift cell
v_d	Drift velocity
VI	Virtual Instrument
v_{mean}	Mean thermal velocity of a gas
V_{pp}	Volts peak to peak
ze	Ion charge

CHAPTER I

TEMPORALLY DISPERSIVE ION MOBILITY TECHNIQUES

I.I. Introduction and Historical Perspective

Ion mobility spectrometry (IMS) is an analytical technique based on measurement of the electrophoretic mobility of ions through a neutral gas. As will be discussed in Section I.V, the application of IMS was traditionally limited to analysis of vapors or gaseous samples mainly of chemical warfare agents, drugs of abuse, and explosives. Contemporary IMS research has expanded enormously to the analysis of gaseous, liquid, and solid samples in many fields including biology, medicine, environmental studies, forensics, pharmaceuticals, and food research. The ability of IMS in separating ions is based on collision cross section (CCS) or ion surface area. This is directly related to ion shape or structure. Presently, this information is used for structural and conformational studies in biomedical research, structural biology, and for separation of many types of isomer species.

The popularity of IMS as an analytical technique is due to its excellent figures-of-merit including low limits of detection (amol to pmol), fast separation times (μs to ms), low cost for handheld or standalone devices (20k to 100k USD), and high throughput (seconds per sample). Simple standalone IMS devices can be hand-held instruments utilized in the field and high performance IMS-mass spectrometer (IM-MS) platforms embody footprints dictated by the MS. Operation is feasible at low, ambient, or high pressures, making it amendable to field monitoring. Several excellent monographs address fundamental characteristics of ion mobility and its applications.¹⁻⁷

In Section I.IV, we will discuss how the IMS platform can be used as a stand-alone instrument or as a detector for orthogonal separation techniques such as gas chromatography (GC), high performance liquid chromatography (HPLC), and supercritical fluid chromatography (SFC). The integration of IM-MS is considered one of the most significant developments in the field and is a key feature for advances in biological and biomedical research.

There are five common types of IMS analyzers, based on temporal-dispersion or spatial-dispersion of analyte ions. Analogous to analyses by MS, temporally-dispersive IMS instrumentation provides near-simultaneous readout of all analytes in the sample. It is most applicable for characterizing samples via untargeted analyses. Spatially-dispersive instruments provide high selectivity for specific targeted analyses. The most common temporally-dispersive devices differ in how electromigration of ions is achieved. The first type is electrostatic as utilized in drift tube IMS (DTIMS), for which this chapter is primarily focused.⁸ The second type is based on electrodynamics, as in traveling wave IMS (TWIMS). Among the spatially-dispersive devices, the most common are field asymmetric IMS (FAIMS) or differential mobility spectrometry (DMS),^{9,10} differential mobility analysis (DMA),¹¹ and aspirator IMS (AIMS). These devices are discussed in Section I.II.III.¹²

In the late 1990s, research using various types of IMS and IM-MS rapidly increased as shown by the annual number of peer-reviewed publications (Figure 1.1).¹³ This growth coincides with the commercial release of field-portable IMS platforms in the 1990s. The progress further accelerates with the release of commercial IM-MS platforms beginning in the mid-2000s. Figure 1.2 illustrates the regional provenance of research publications for the top ten contributing countries: United States, United Kingdom, Germany, Canada, China, Iran, France, Spain, Russian Federation, and Finland, clearly underscoring the global adoption of IMS technologies.

Historical Developments in Ion Mobility (IM) Technologies

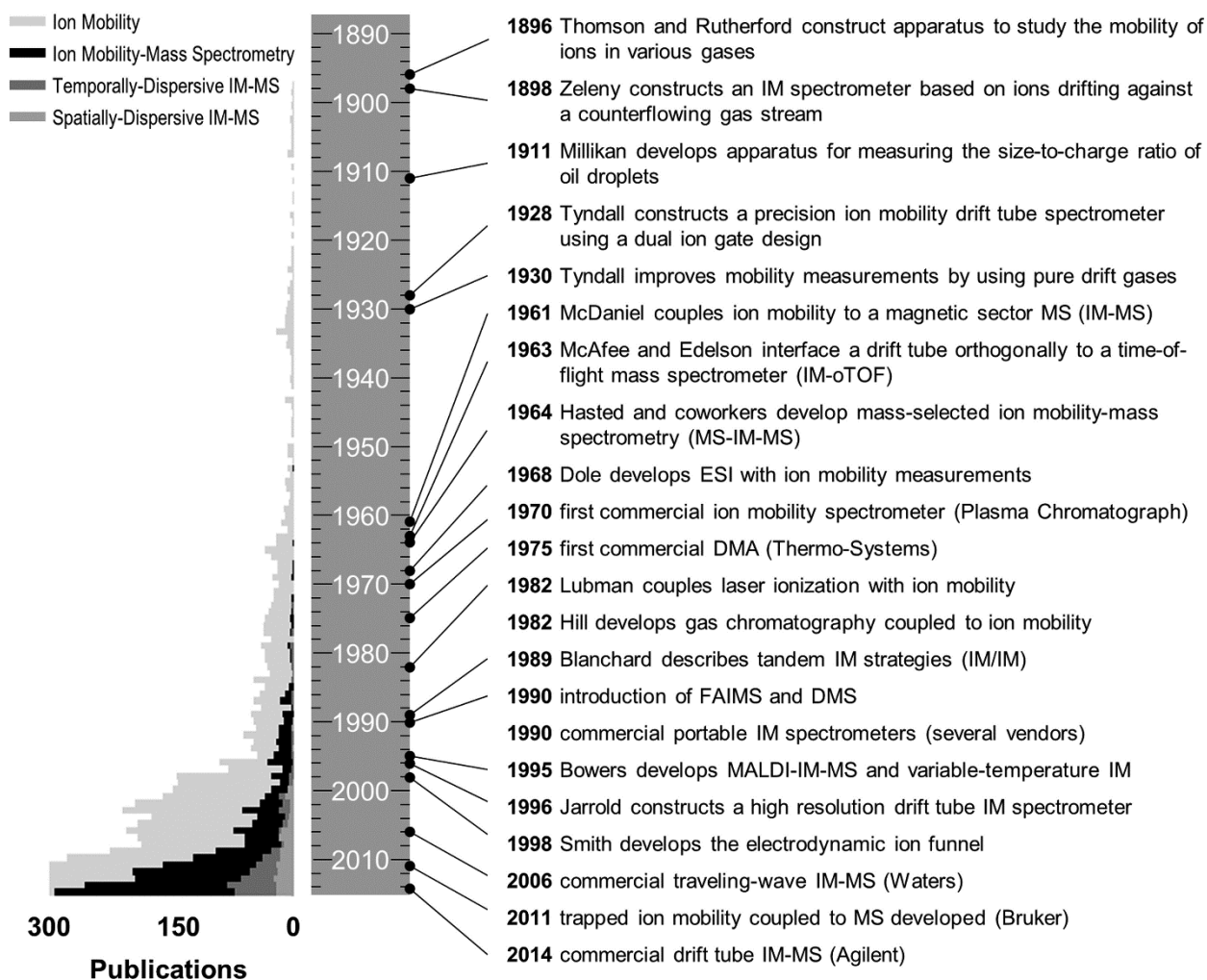


Figure 1.1: (Left) Histogram of the number of publications published per year in ion mobility and ion mobility-mass spectrometry. Note that the scale is truncated at 300 to highlight the number of publications specifically utilizing IM-MS. Further distinction is made to discriminate the frequency of publication for both time and space-dispersive IM-MS publications. (Right) Historical milestones in the development of ion mobility and IM-MS instrumentation. Reprinted with permission from J. C. May and J. A. McLean, *Analytical Chemistry*, 87, 1422-1436 (2015). Copyright 2015 American Chemical Society.

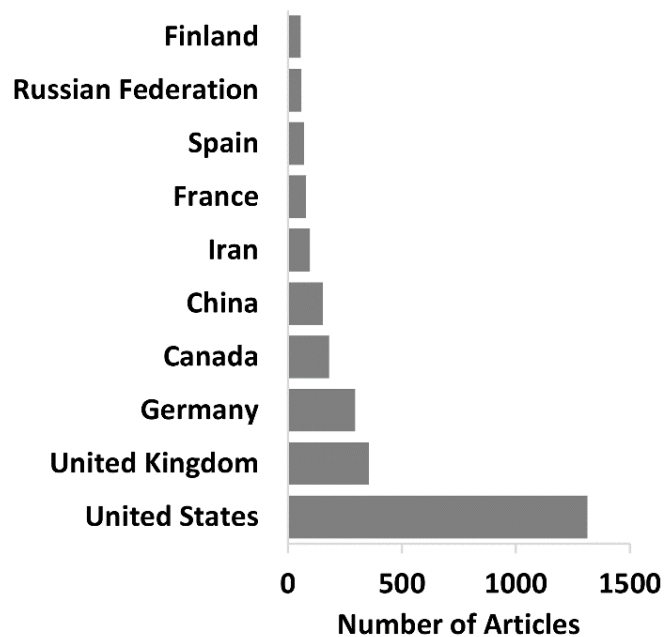


Figure 1.2: The number of peer-reviewed papers published through January 2015 using ion mobility spectrometry as a function of country of origin. The top-ten countries contributing to these papers. Data generated using Scopus between 1970 and 2015, search terms ‘ion mobility spectrometry’ and ‘plasma chromatography’.

I.II. Ion Mobility Instrumental Considerations

To frame the following discussion, the general components of IMS and IM-MS are shown schematically in Figure 1.3. In Section I.II.I, we provide a description of common strategies used for sample preparation prior to ionization into the IMS. Many methods of ionization have been used to convert solid, liquid, or gaseous samples into gas-phase ions. The most common standalone IMS instruments are presented in Section I.II.II. A survey of strategies for performing IMS separations, on the basis of ion mobility, is then presented in Section I.II.III. In Section I.III.I, we present in greater details the fundamental footing of DTIMS technique for determining ion structure via CCS measurement. Strategies for tailoring the separations are outlined in Section I.III.II. The approaches rely on altering the conditions using gas phase kinetic theory and prevailing physical chemical forces. In Section I.IV, a survey is presented on combining chromatographic separations with the IMS. In the final section (I.V), applications of cited techniques are presented.

I.II.I. Sample Preparation Strategies

All sample forms, gaseous, liquid, and solid, can be analyzed by IMS. In principle, all sample ionization methods can be used for IMS or IM-MS as the separation only relies on ionized analytes. In both IMS and IM-MS gaseous samples are directly introduced, liquids are nebulized, and solids are evaporated, dispersed, or desorbed into the vapor phase for subsequent ionization.¹⁴⁻
¹⁶ Examples of ion sources for direct coupling with IMS are electrospray ionization (ESI),¹⁷ corona spray,¹⁸ desorption electrospray ionization (DESI),¹⁹ matrix assisted laser desorption/ionization (MALDI),²⁰ direct analysis in real time (DART),²¹ and low-temperature plasma (LTP).^{22,23}

As a detector for chromatographic methods, such as GC, LC, or SFC, the column effluent is directly introduced into the IMS using suitable manifolds to match the pressure of the IMS.

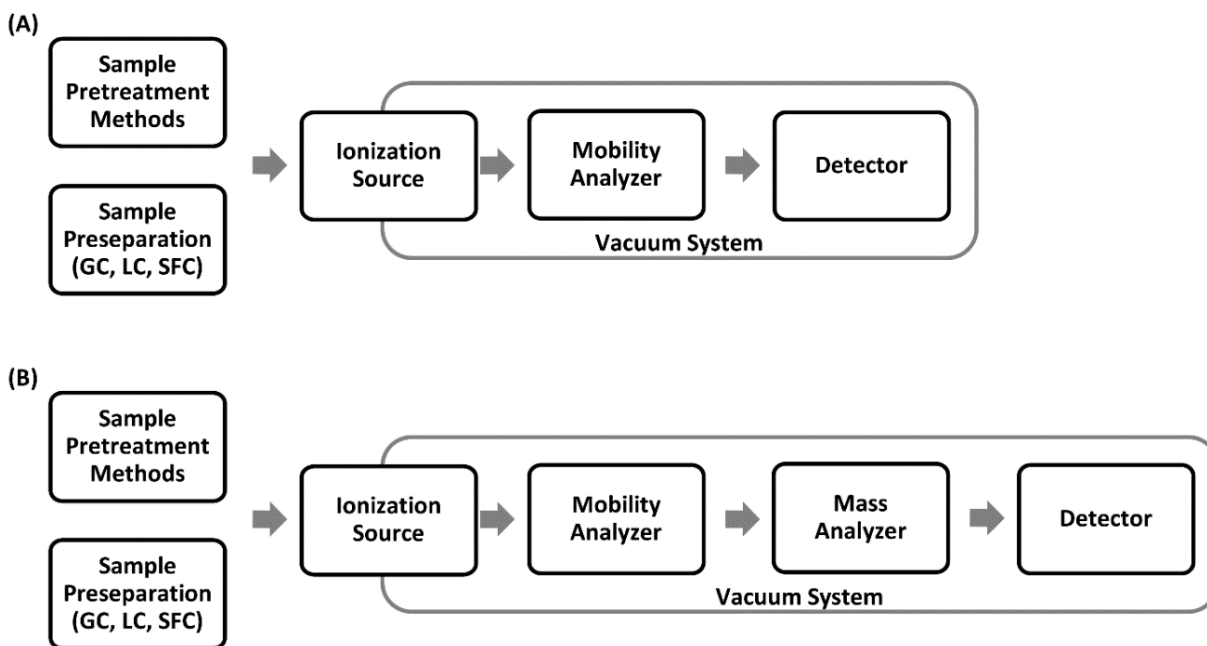


Figure 1.3: A conceptual diagram highlighting the primary components of (A) ion mobility spectrometry and (B) ion mobility-mass spectrometry instrumentation, respectively.

Often, this involves flow splitting to match the solvent flow rates to the optimal pressure of the IMS. For the analysis of complex samples such as those in biology, medicine, and materials science, sample pretreatment may be required to separate the compounds of interest from concomitant interferences to simplify the complex IMS analysis. The high peak capacity of the MS as the detector, that is, following IMS-MS or LC-IMS-MS, offers the ability to deconvolute complex IMS and LC-IMS spectra.²⁴⁻²⁷

The significance of sample pretreatment in IMS analyses is addressed in several recent reviews.²⁸⁻³⁰ The IMS sample preparation techniques include extractions by liquid–liquid (LLE),³¹ solid phase (SPE),^{32,33} molecularly imprinted polymers (MIP),³⁴⁻³⁶ stir–bar sorptive (SBSE),^{37,38} magnetic nanoparticle (MNP),³⁹ and membrane (ME).^{40,41} Miniaturized sample pretreatment techniques are currently used to reduce the amount of sample and solvent. Several microextraction techniques have been developed, such as solid phase microextraction (SPME),⁴²⁻⁴⁶ aptamer-based sorbent extraction,⁴⁷ microextraction in a packed syringe (MEPS),⁴⁸ and several types of liquid phase microextraction (LPME) including single-drop microextraction (SDME),^{49,50} hollow fiber liquid phase microextraction (HF-LPME)⁵¹⁻⁵⁴ and dispersive liquid-liquid microextraction (DLLME).⁵⁵ The SPME approach is solvent free, simple, and rapid showing potential to overcome several difficulties associated with conventional extraction methods.⁵⁶ Aptamer-based extraction exhibits high selectivity and recovery efficiency, making its combination with IMS ideal for analysis of compounds like tetracycline in biological fluids.⁴⁷ To avoid sample carry-over and fiber degradation associated with SPME, single-drop SDME approaches were developed.⁵⁷ Extraction of the analyte from an aqueous sample can be performed by LPME, in either a two-phase mode or a three-phase mode. In two-phase LPME, the analyte is extracted into a water-immiscible organic solvent that has been immobilized in the pores and lumen of the hollow fiber.⁵⁸ In three-phase

LPME, the analyte is extracted through the water-immiscible organic solvent into another aqueous phase, present in the lumen of the hollow fiber. To combine sample extraction and pre-concentration in a single step, DLLME can be used.⁵⁹ In each of these strategies the main aim is to simplify the complexity of the sample to enhance selectivity and/or quantitation capabilities for the species of interest.

I.II.II. Ionization Sources

Several ionization sources have been developed for IMS analysis (Figure 1.4). They are generally classified by the initial phase of the sample presented to the source. These sources date back to the discovery of x-rays in 1895 and their subsequent utilization as an ionization source described by Thompson and Rutherford starting in 1896 (Figure 1.1). Recent research in ion source technology parallels that with MS based on applications such as in defense/security and biology/medicine.⁶⁰⁻⁶³ Each source offers unique advantages and limitations for specific types of compounds. In the following section, we only focus on common contemporary and emerging ion sources for IMS: radioactive decay, electric fields, and light radiation.

I.II.II.I. Ionization by Radioactivity

Several radioactive elements have been used to ionize molecules for IMS analysis including tritium (^3H), americium (^{241}Am), and nickel (^{63}Ni).⁶⁴⁻⁷⁰ Tritium has lower radiation hazards than ^{63}Ni sources and a high ionization efficiency.⁷¹ In 2015, a ^3H source was utilized with IMS to monitor undesirable flavors in food samples where temperature and light are the most influential factors in degrading species such as lipids in linseed oil and milk samples.⁷² Americium is present in small amounts in many smoke detectors as an alpha particle source.⁷³ It has been used for detection of various chemical agents.^{74,75} Radioactive ^{63}Ni produces beta particles and used to

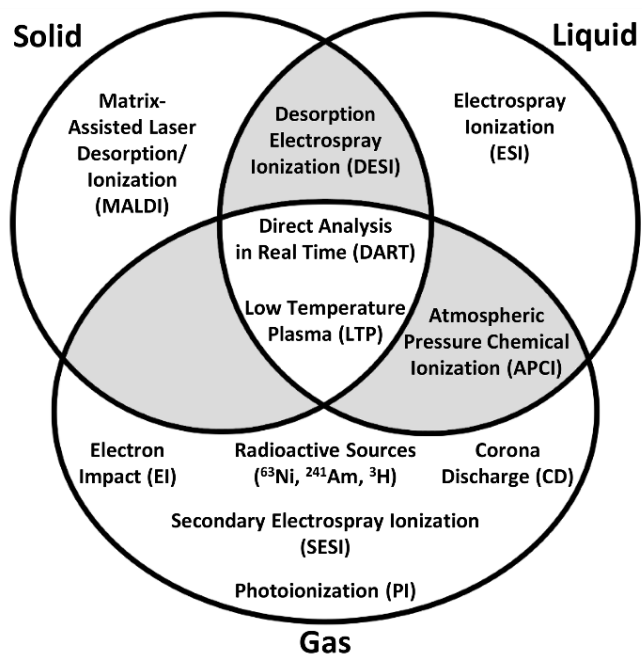
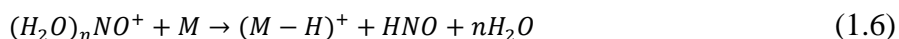
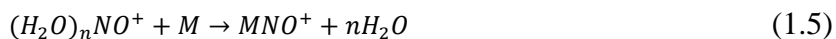
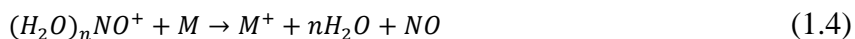
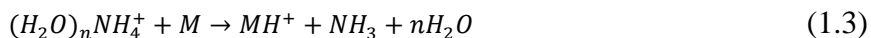


Figure 1.4: A Venn-diagram of common ionization sources utilized in conjunction with IMS, grouped by the phase of the sample typically utilized for ionization.

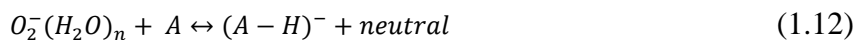
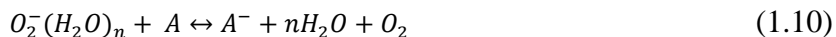
be the preferred ionization source for most IMS experiments,⁶⁸ particularly for studies of aromatic compounds, chlorocarbons, and chemical warfare agents, among others.⁷⁶⁻⁸¹ One of the main advantages of these sources is that they do not require an external power supply. They provide a stable, continuous source of ionization for years, easing portability and utilization in the field. The drawbacks of radioactive ion sources are the necessity of regulatory leak tests for safety purposes and low ion currents relative to other sources.⁸² These inherent limitations have led to nonradioactive ionization devices. Yet, one of the most common sources in stand-alone or field portable IMS devices is the ⁶³Ni foil source. When nitrogen or air is used as the IMS drift gas, the following reactions prevail:⁶⁴



Here, β represents the beta particles emitted from the ⁶³Ni source. The primary N_2^+ ion initiates a series of ion-molecule reactions with trace amounts of H_2O , NH_3 , and NO . These secondary ion clusters, or reactant ions, are $(H_2O)_nNH_4^+$, $(H_2O)_nNO^+$, and $(H_2O)_nH^+$. When the gas-phase sample containing the analyte is introduced into a region preceding the IMS drift cell, its components are ionized via ion molecule reactions with the reactant ions. The dominant reaction pathway of analyte ionization is through proton transfer which occurs when the analyte, M , has a greater proton affinity than that of the reactant ions. Reactions (1.2)-(1.6) show processes that occur to produce the various analyte ions observed in positive ionization mode.



In negative ionization mode, the formation of reactant ions is much more complicated. If the drift gas is pure nitrogen, thermalized electrons are produced. Electronegative analytes can capture these electrons, becoming negatively charged ions. Yet, when the drift gas is air instead of pure nitrogen, very diverse reactant ions are produced. Two groups identified reactant ions mainly as O_2^- and $(H_2O)O_2^-$, with less prominent reactant ions including Cl^- , $(H_2O)OH^-$ and NO_2^- .^{83,84} Also in some of these studies, hydrated oxygen ions, O_2^- and $O_2^- \cdot O_2$, were found to be the most abundant ionic species. Moreover, significant quantities of CO_3^- and $O_2^- \cdot CO_2$ ions and trace amount of NO_2^- were observed. In the presence of oxygen, the following reactions can occur, producing negative analyte ions via ion molecule reactions.



Importantly, it is possible to change reactant ions or ion molecule reactions by introducing a dopant gas into the drift tube in either positive or negative ionization mode. This method can enhance sensitivity and selectivity of IMS. Using reagent or dopant gas in IMS can suppress background interferences, simplify IMS spectrum, and enhance resolution by controlling the reactant ion composition.⁸⁵⁻⁸⁶

I.II.II.II. Ionization by an Applied Electric Field

Electric fields and currents can be applied in different ways to ionize molecules. This has led to development of a wide variety of electric field-based ionization methods for IMS. A few

common sources for operation at atmospheric pressure are corona discharge (CD), low temperature plasma (LTP), and electrospray ionization (ESI). The reader is directed to several excellent references for details on other common sources, including electron impact (EI),^{87,88} secondary electrospray ionization (SESI),^{89,90} desorption electrospray ionization (DESI),^{19,91,92} atmospheric pressure chemical ionization (APCI),⁹³⁻⁹⁵ and direct analysis in real time (DART).^{21,92,96,97} Schematic diagrams for a selection of source arrangements operated at atmospheric pressure are depicted in Figure 1.5. The characteristics of these techniques are dramatically different. For instance, three approaches (i.e. CD, LTP, and ESI) are described here to illustrate the extent of strategies where electric fields are utilized to achieve different functions in desorption/ionization of samples: electrical breakdown, plasma formation (CD and LTP), charge separation (ESI).

Compared to radioactive ion sources, CD ionization provides better sensitivity, higher signal-to-noise ratio, and a wider linear dynamic range.⁹⁸ Yet, CD exhibits a time-dependence on signal quality due to erosion at the discharge point.⁹⁹ In negative ion mode, CD ionization is challenging to use due to formation of NO_x negative ions, which in particular instrumental arrangements can be difficult for four reasons.

First, the NO_x cluster ions have very high electron affinities (ca. 3.9 eV) that can quench the formation of product ions for samples of halogenated compounds. In contrast, when ⁶³Ni is used in negative mode, an ion peak corresponding to [(H₂O)_nO₂]⁻ (electron affinity ca. 0.45 eV) is the reactant ion peak that can mitigate this problem. Second, the high background of extrinsic NO_x ions arising from the ionization source precludes the analysis of NO_x should these species be those desired for analysis. Third, the high background of NO_x species can result in spectral overlap of other analytes of interest in the mobility spectrum. Finally, NO_x ions can in some cases form coordination complexes with analytes of interest resulting in complex spectra. To overcome these

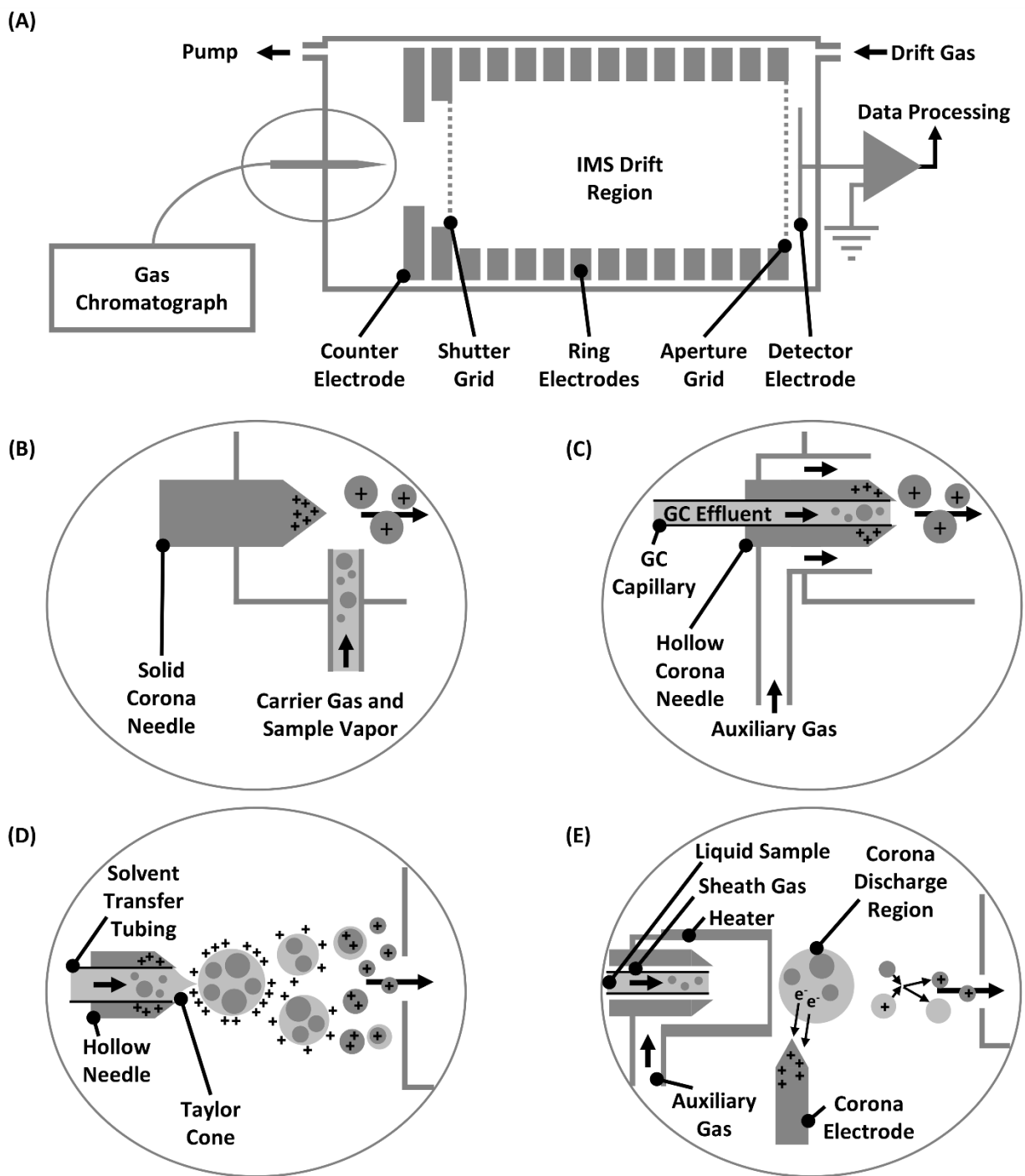


Figure 1.5: A schematic diagram of the conventional arrangement for DTIMS and selected interfaces combining electric field-based ionization techniques. (A) Schematic diagram of gas chromatography interfaced with DTIMS. The counter electrode helps establish the electric field to

draw ions toward the drift region. A shutter grid is used to gate discrete ion packets to initialize each separation event. The ring electrodes are connected via a resistor network, and an electric potential is applied across the stack of ring electrodes. An aperture grid helps prevent bias of the detector electrode, at which ions are terminated. (B) Corona discharge ionization source where sample gas is introduced orthogonally to the discharge needle. (C) Corona discharge ionization source where sample gas is introduced coaxially to the discharge needle. (D) Electrospray ionization source in which a liquid sample flows through a charged needle. Coulombic repulsion draws the liquid sample into a Taylor cone which then disintegrates into a highly charged aerosol. (E) Atmospheric pressure chemical ionization source where a liquid sample is nebulized with auxiliary gases and passed through a heater. In the corona discharge region, electrons are transferred from solvent molecules to the corona electrode and undergo further secondary reactions to ionize the neutral analyte species.

challenges, a pulsed CD is used to coordinate the ion generation with the entrance shutter pulse to the drift tube.¹⁰⁰ Alternatively, a more recent point-in-cylinder geometry may be utilized to establish a continuous CD, while suppressing the formation of NO_x ions.¹⁰¹

As discussed earlier, an LTP may be modified for use as an ionization source for IMS.²² The LTP method utilizes dielectric barrier discharge to create a cooled plasma. It operates through numerous microdischarges, which generate chemically active species such as high-energy electrons, metastable neutrals, and radical ions.¹⁰² The temperature of the surface area in contact with the plasma plume is nearly 30°C, resulting in no surface damage due to heating. In addition, the high voltage electrode is electrically isolated from the direct discharge region and therefore, the sample is isolated from discharge arising from electrical breakdown. These features make the LTP suitable for the analysis of surfaces, such as biological tissues, that would be negatively impacted by heating or discharge. In one such application, an LTP was described for forensic applications in characterizing illicit chemicals directly from skin.¹⁰³

As a soft ionization method, ESI is able to ionize large molecules without fragmentation.^{89,104-106} In 2007, a design was developed for ESI-IMS in which a desolvating gas was introduced as a means of solvent evaporation where the ESI needle was relocated outside of the desolvation region, allowing for increased heating without causing clogging of the electrospray needle in the analysis of environmental pollutants and drugs.¹⁰⁷ Collectively, these approaches have been useful for environmental monitoring, biomedical diagnostics, and drug discovery. Electrospray ionization is well suited for online integration of sample effluent from condensed phase pre-separation methods such as LC, SFC, and capillary electrophoresis (CE) with IMS or IM-MS. In ESI, samples are perfused through a conductive capillary where an aerosol is generated through coulombic repulsion in a strong electric field. Ultimately, as the droplets evaporate, under

ambient conditions or using a heated gas, intact ionized species are directed into the IMS or IM-MS.

I.II.II.III. Ionization by Electromagnetic Radiation

The two most common means for desorption and/or ionization of analytes by electromagnetic radiation are matrix assisted laser desorption/ionization (MALDI)¹⁰⁸⁻¹¹³ and photoionization (PI).¹¹⁴⁻¹¹⁷ The former is a soft ionization technique for the analysis of large intact molecules. In this respect, MALDI is similar to ESI. While ESI generates ions from the solution phase, MALDI creates ions from the solid phase.

In MALDI, the analyte is co-crystallized with a matrix that serves to absorb the radiation from a pulsed laser to heat the matrix. Importantly, the laser energy is not absorbed by the analyte, thus avoiding analyte fragmentation. Following irradiation at a suitable wavelength, the heated matrix rapidly expands from the surface carrying with it the analytes to create ions from the ejected plume of material.

Since the first reports on the combination of MALDI with IM-MS, MALDI has been a key source for biomolecular analysis using IMS.^{20,118-123} In contrast with ESI, MALDI produces ions of lower charges exhibiting narrower distribution. Importantly, MALDI-based strategies are highly applicable to imaging intact biomolecules,¹²⁴⁻¹²⁷ similar to laser ablation-inductively coupled plasma MS (LA-ICP-MS) techniques. In more recent applications, datasets for both LA-ICP-MS and MALDI-IM-MS have been integrated for a mouse model of Parkinson's disease, providing both quantitative maps of elemental distribution across brain slices with LA-ICP-MS with intact biomolecular distribution across adjacent slices using MALDI-IM-MS.¹²⁷

Photoionization is less commonly used than MALDI, but this type of source has shown utility in various studies of gaseous analytes over past decades.^{114-117,128} Using lasers and/or

discharge lamps, ion excitation at resonant wavelengths, corresponding with the ionization potential of the molecules, provides excellent selectivity for the analyte directly in the ion source itself. In one ambient pressure IMS study, several organic compounds were studied via multiphoton ionization, with two photons absorbed per ionization event and a resulting spectrum that included one-photon absorption information that could be used to uniquely identify molecules.¹¹⁴ Dopants such as toluene, acetone, and benzene, among others, have been used to improve sensitivity in IM studies through a combination of photoionization and subsequent chemical reactions.^{115,117}

I.II.III. Ion Mobility Analyzers: Space-Dispersion and Time-Dispersion

There is a key difference between pressure regimes essential for IMS versus MS analyzers. The MS analyzers often require mean free path lengths corresponding to collision-free-environments (e.g. 10^{-3} to $< 10^{-6}$ Torr). In contrast, short mean free path lengths and high collision frequencies are essential to promote analyte separation in IMS (e.g. several Torr to atmospheric pressure). Yet, IMS analyzer analogs exist now for virtually all MS analyzers.¹³ As noted in Section I.I, similar to MS techniques, IMS devices utilize space-dispersion (e.g. ion filtering in quadrupoles) and time-dispersion (e.g. near-simultaneous detection in TOFMS). A brief overview of space-dispersive techniques is presented here. A theoretical treatment for time-dispersive approaches is presented in Section I.III.

Spatially-dispersive IMS separation techniques include FAIMS, DMA, and AIMS. In FAIMS, an asymmetric electric field is applied between two electrodes, typically at electric field strengths of 10-30 kV/cm and frequencies of 0.2-2 MHz. The periodic asymmetric field is perpendicular to the direction of ion travel and ions are separated based on the difference between

their inherent mobility values at high and low electric field strengths.^{9,129,130} Atmospheric pressure FAIMS devices have generated considerable interest in combination with a variety of MS instruments, because they offer both higher sensitivity, by focusing ions at the MS interface, and increased structural selectivity. An excellent review article presents the historical development, fundamentals, and applications of FAIMS-MS.¹³¹ Still there is extensive research to identify the central physical processes of ion separations in FAIMS.^{5,132,133} Consequently, it is not presently possible to write a closed equation to predict the separation in FAIMS, as will be developed below in Section I.III for electrostatic-field DTIMS. CCS measurements using FAIMS devices are currently derived by calibration against literature values for the CCS obtained on uniform-field DTIMS instruments.¹³⁴

In addition to the asymmetric field in FAIMS, a direct current (DC) potential, termed the DC compensation voltage (CV), is present between the electrodes. The DC voltage magnitude is scanned during the experiment to obtain a CV spectrum. The operational principles of FAIMS are illustrated in Figure 1.6, which shows CV spectra acquired from a CD-FAIMS-MS instrument.¹³⁵ A recent development in FAIMS technology is a new manifestation of the technique, the ultra FAIMS microchip spectrometer, which forms an array of parallel channels (35 μm x 300 μm) across which an asymmetric dispersion field is applied.¹³⁶ The ions are transmitted through the chip by applying a CV. The separation of ions in FAIMS is orthogonal to LC or MS, therefore this pre-separation gives the option of selecting ions of interest, allowing them to pass through the chip while blocking unwanted interference ions.

In DMA, the electric field is applied perpendicular to the gas flow. At a condition specific for a particular analyte mobility, the ion will travel a specific distance dependent on the gas flow and mobility such that it will be transmitted through a slit. By scanning the gas flow rate or the

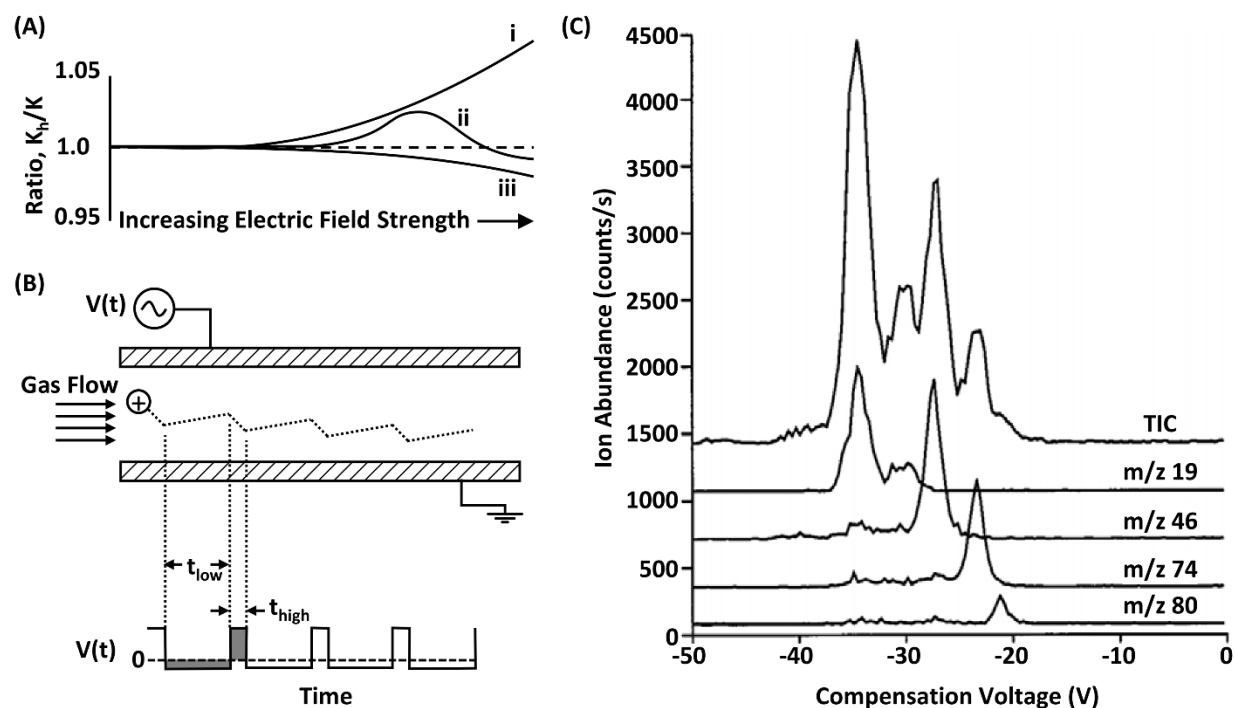


Figure 1.6: (A) Shows the dependence on electric field strength for three ions of differing mobility. As the electric field increases the (i) ions' mobility also increases, the (ii) ions' mobility increases to a maximum then decreases at higher fields, and the (iii) ions' mobility decreases. K_h is the ion mobility at high voltage. (B) Shows a diagram of a FAIMS separation and an example ion trajectory through the mobility region. A stream of gas carries an ion between two parallel plates, where the lower plate is grounded and the upper plate has an asymmetric waveform applied, $V(t)$. The time at low voltage is greater than the time at high voltage ($t_{low} > t_{high}$). The trajectory shown is that for an (i) ion from (A), for which $K_h > K$. The (ii) and (iii) ions will have different trajectories, thus the FAIMS instrument functions as an ion filter. (C) A single ion monitoring, corona discharge-FAIMS-MS compensation voltage spectrum of ethylamine, diethylamine, and pyridine. The four primary peaks in the TIC are interpreted to be $(H_2O)_nH^+$, $N_2(H_2O)H^+$,

$C_2H_7NH^+$, and $C_4H_{11}NH^+$. (A) and (B) Adapted with permission from R. W. Purves and R. Guevremont, *Analytical Chemistry*, 71, 2346-2357 (1999). Copyright 1999 American Chemical Society. (C) Adapted with permission from R. W. Purves, R. Guevremont, S. Day, C. W. Pipich, M. S. Matyjaszczyk, *Rev. Sci. Inst.* 69, 4094-4105 (1998). Copyright 1998, AIP Publishing LLC.

electric field, different species can be brought to the entrance of the slit. In AIMS, an electric field perpendicular to gas flow is applied on two series of parallel electrodes. These electrodes can simultaneously detect positive and negative ions. An AIMS does not use a shutter grid and the neutral gas flow rate is about 1-2 L/min.⁶⁶ The ions are separated based on their mobility. High mobility ions hit the first electrodes, ions with low mobility collide with the latter electrodes, and the current in each electrode is measured to determine the abundance of each type of ions. The limitations of AIMS are low resolution and limited dynamic range.

Temporally-dispersive methods of IMS include DTIMS and TWIMS.¹³ The key difference between the two techniques is that electrostatic and electrodynamic fields are utilized for DTIMS and TWIMS, respectively. Schematic diagrams of both DTIMS-MS and TWIMS-MS are provided in Figure 1.7, which share many similarities in their instrumental implementation. While further details on DTIMS are provided in Section I.III., a recent review of time-dispersive instrumentation offers a treatment of TWIMS and future developments in instrumental architecture.¹³

I.II.IV. Ion Mobility-Mass Spectrometry

Although determination of mobility with IMS alone can be helpful in identifying well-characterized compounds, definitive identification of complex sample components is enabled by combining IMS with MS. Among the IMS hyphenated techniques, IM-MS, which was first commercialized as plasma chromatography, is becoming a popular analytical technique in many research fields, as seen in Figure 1.1.^{8,13,222,235,137-139}

Since the mid-90s, several improvements and developments in IM-MS instrumentation have resulted in extensive adoption of the technology in three key research areas, (i) structural biology through interpreting ion structure (IM) and identification (MS) with computational

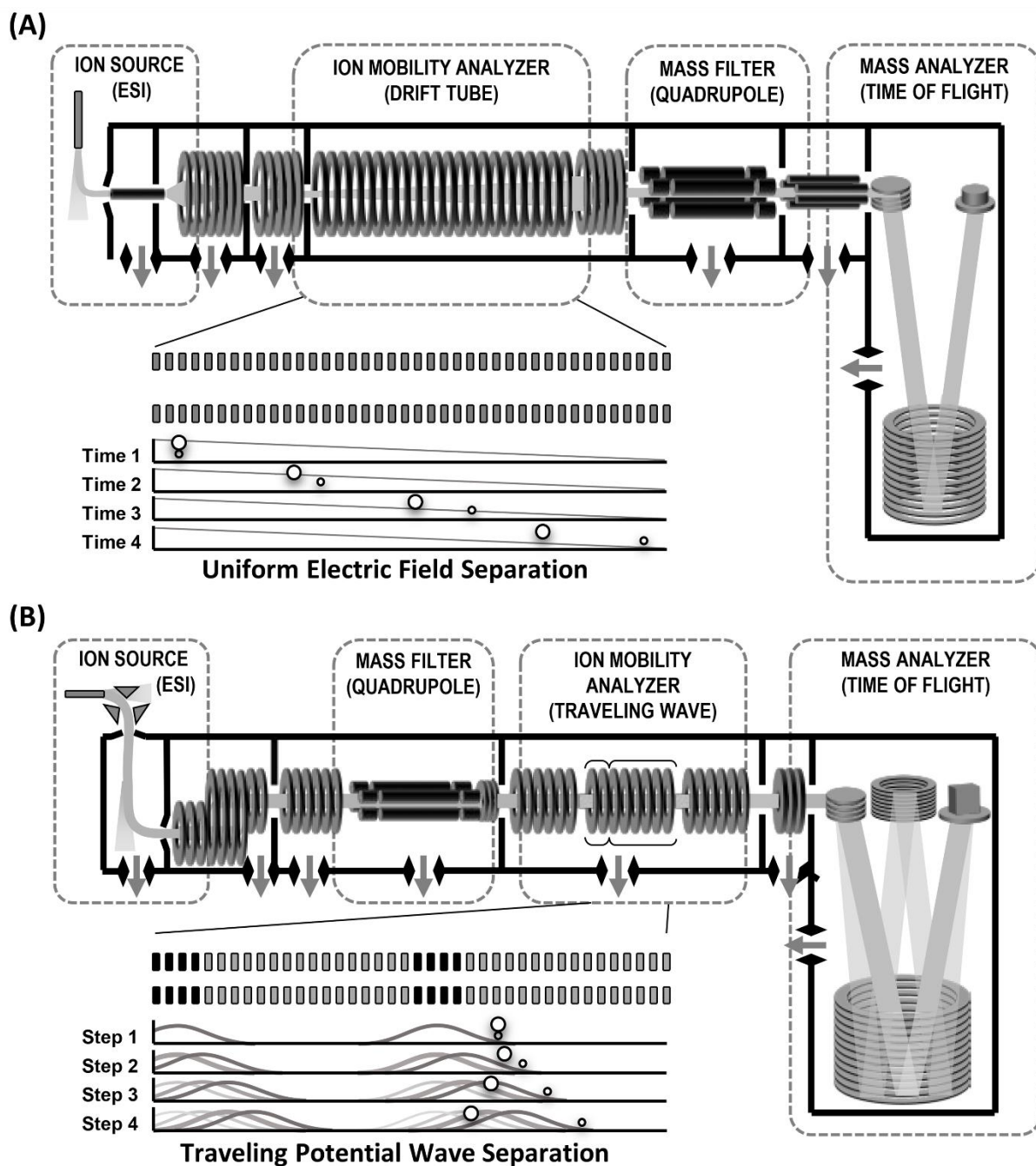


Figure 1.7: Two representative schematic diagrams for contemporary time-dispersive IM-MS instrumentation. (A) An electrostatic drift tube (DTIMS) arrangement. (B) An electrodynamic drift tube (TWIMS) arrangement. In both arrangements, hypothetical time courses are shown to

illustrate the temporal separation of smaller and larger collision cross section ions. Adapted with permission from J. C. May and J. A. McLean, *Analytical Chemistry*, 87, 1422-1436 (2015).
Copyright 2015 American Chemical Society.

approaches, (ii) rapid separations for complex sample analysis, and (iii) integrating broad scale omics analyses.^{24-26,123,137,139-160} Though for decades IM-MS has been used mainly in academic institutions for research, several commercial versions have become available in recent years, including TWIMS-MS in 2006, trapped IM-MS in 2011, and DTIMS-MS in 2014.¹³⁷

The aim of this chapter is to highlight the potential avenues primarily for stand-alone IMS platforms with broad applicability for ICP-related research, while IM-MS is discussed as it directly pertains to the subject matter described. Throughout the chapter, the reader is referred to recent manuscripts, reviews, and books to highlight advances in IM-MS.

I.III. Theory and Fundamentals of Time-Dispersive Ion Mobility Spectrometry.

Several excellent books and reviews outline the theory of IMS and the derivation of ion-neutral CCS measurements from IMS profiles using the kinetic theory of gases.^{1-3,4-7,161,162} This section summarizes several key equations and practical considerations for determining ion-neutral CCS values, or ion surface areas, in uniform electrostatic-field DTIMS experiments. This treatment is based on a previous description utilizing the kinetic theory of gases for determining and understanding DTIMS CCS measurements.¹⁶³

I.III.I. Transforming Drift Time to Collision Cross Section

The movement of ions in a weak electrostatic-field (E) is measured as the ion drift velocity (v_d) and is related by the proportionality constant, K , which is the mobility of the ion in a particular neutral gas:

$$v_d = KE \tag{1.13}$$

The drift cell is of a fixed length (L), and therefore the velocity of the ion packet is found by measuring the drift time (t_d) of the ions across the drift cell. In practice, the parameter that is physically measured is the arrival time distribution (t_{ATD}) of the ion packet at the detector, which is the sum of both the drift time (t_d) of the ion packet through the IM cell and the time the ion packet resides in other regions of the instrument (i.e. in the ion source, ion optics, and MS regions, etc.). For example, the measured time in IM-MS typically constitutes both the time in the IM and MS analyzers and is measured as a single time following both analyzer regions. In stand-alone IMS instruments, a correction may not be necessary when grids are used at the entrance and exit of the drift region, usually of Bradbury-Nielsen gate (BNG) design.¹⁶⁴

For IM-MS instruments, the evaluation of the amount of time the ion packet spends outside of the drift cell is critical, and is usually empirically determined by performing the IM separation at several electrostatic-field strengths by changing the potential (V) applied across the length of the drift cell. As illustrated in Figure 1.8, the t_{ATD} for each of the separations is determined and plotted as a function of the inverse of the IM electric field strength. Provided the separations are performed using sufficiently weak electrostatic-fields (where K remains constant), the points can be fitted by a linear regression where the y-intercept corresponds to the residence time that ions spend outside the drift cell, that is, the limit of infinitely fast ion velocities across the IM cell or $t_d = 0$. By subtracting this time from t_{ATD} , the measured times represent t_d across the IM cell. For the most accurate results, the drift time correction should be evaluated for each component in the IM profile. The motivation for evaluating individual drift time corrections arises from additional ion-neutral collisions in the differential pumping regions at the entrance and/or exit of the IM drift cell, especially when additional gating such as BNG gates are not utilized in the IMS region. In the extra-drift cell regions of IM-MS the gas dynamics typically transition from viscous to molecular

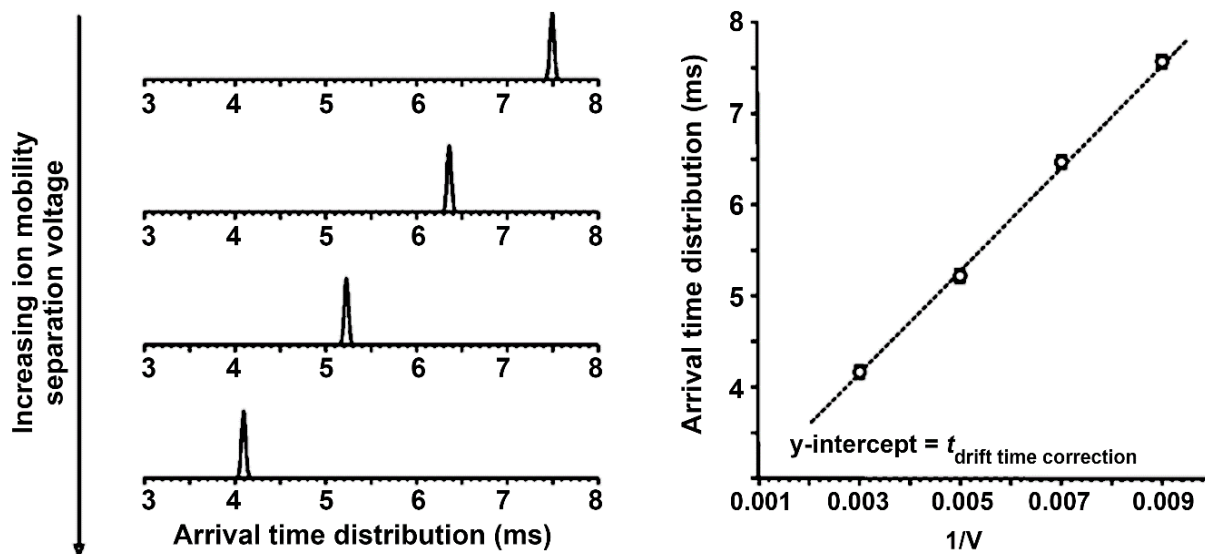


Figure 1.8. Procedure for transforming t_{ATD} for ion mobility signals to t_d . (left) The arrival time distribution is measured sequentially at several increasing electric field strengths. By selecting the time at the apex of the IMS profile, the t_{ATDS} are plotted as a function of $1/V$, where V is the strength of the electric field applied across the drift cell (right). A linear best fit to these points indicates that the separation is performed under low-field conditions, where the y-intercept represents the time the ion packet resides in regions of the instrument outside of the drift cell ($t_{\text{drift time correction}}$). Adapted with permission from J. A. McLean, J. A. Shultz and A. S. Woods, Richard B. Cole, Ed. John Wiley & Sons, 411-439 (2010). Copyright 2010, John Wiley & Sons.

flow, e.g. at the exit aperture of the drift cell at 2-10 Torr to the high vacuum (ca. 10^{-8} Torr) of the mass spectrometer.

In evaluating K , the drift velocity of the ion packet also depends on the pressure (p , Torr) of the neutral drift gas and the temperature (T , Kelvin) of separation. The latter dictates the mean free velocity of the drift gas, which influences the ion mean free path and hence collision frequency of the ion-neutral pair. Thus, K is conventionally reported as the standard or reduced mobility (K_0), which normalizes the measured mobility to standard temperature and pressure conditions (i.e. 0 °C and 760 Torr):

$$K_0 = K \frac{p}{760} \frac{273}{T} \quad (1.14)$$

When IMS is used to obtain structural information about the ion, separations are performed using low electrostatic-field conditions (relative to the ratio of electrostatic-field to neutral gas density). If a Maxwellian distribution function of velocities in thermodynamic equilibrium is assumed, then the mean thermal velocity (v_{mean}) of a gas is:

$$v_{mean} = \left(\frac{8kT}{\pi M_r} \right)^{\frac{1}{2}} \quad (1.15)$$

If the electrostatic-field is sufficiently low, the ion velocity in the gas will be the random motion of ions at the temperature of the gas, over which a small velocity component in the direction of the electrostatic-field is superimposed. Provided these conditions are met, the mobility separation is achieved under so-called “low-field” conditions. At higher electrostatic fields, the ion velocity distribution depends less strongly on the temperature of the separation, and the mean ion energy increases as ions traverse the drift region. Consequently, K is no longer constant, i.e. the plot in Figure 1.8(B) is no longer linear and is better modeled by the curves in Figure 1.6(A),

and depends on the specific ratio of the electrostatic-field to the gas number density (E/N). This forms the basis for FAIMS.

When the mobility separations are performed in low-field conditions, i.e. constant K , and the collisions can be assumed to be purely elastic (e.g. billiard balls), then the mobility is related to the CCS of the ion-neutral pair:

$$K_0 = \frac{(18\pi)^{1/2}}{16} \frac{ze}{(k_B T)^{1/2}} \left[\frac{1}{m_i} + \frac{1}{m_n} \right]^{1/2} \frac{760}{p} \frac{T}{273} \frac{1}{N_0} \frac{1}{\Omega} \quad (1.16)$$

Where these parameters include the ion charge (ze), the number density of the drift gas at STP (N_0 , $2.69 \times 10^{19} \text{ cm}^{-3}$), the reduced mass of the ion-neutral collision pair (ion and neutral masses of m_i and m_n , respectively), Boltzmann's constant (k_b), and the ion-neutral CCS (Ω). Inspection of Equation 1.16 shows that the mobility of an ion is inversely related to its CCS, or apparent surface area/size, which provides the ability to interpret analyte ion structure. Substituting for K_0 in Equation 1.16 and rearranging to solve for the CCS yields:

$$\Omega = \frac{(18\pi)^{1/2}}{16} \frac{ze}{(k_B T)^{1/2}} \left[\frac{1}{m_i} + \frac{1}{m_n} \right]^{1/2} \frac{t_d E}{L} \frac{760}{p} \frac{T}{273} \frac{1}{N_0} \quad (1.17)$$

This is the typical functional form of the equation to solve for CCS. These equations are derived from classical electrodynamics, and as such, great care should be exercised in the dimensionality of the units used. Specifically, the units for E are expressed in cgs Gaussian units (i.e. statvolts cm^{-1} , where 1 statvolt equals 299.79 V). Note that statvolts cm^{-1} is equivalent to statcoulombs cm^{-2} and that elementary charge, e , is 4.80×10^{-10} statcoulombs.

In both Equations 1.16 and 1.17, ion-neutral collisions are considered completely elastic processes. Under these conditions, the CCS obtained is termed the “hard sphere” CCS. Only momentum is transferred between the two collision partners, conserving kinetic energy.

Comparison of empirically-determined cross sections with computationally-obtained theoretical results has shown the hard sphere approximation is best suited for analytes larger than ca. 1000 Da.^{159,165-168} However, as the size of the analyte approaches the size scale of the drift gases used for separation, long-range interaction potential between the ion and neutral must be considered for accurate results.¹⁶⁸⁻¹⁷⁰

I.III.II. Factors Affecting Separation in Ion Mobility

I.III.II.I. Influence of Gas Selection on Separations

As discussed above, for structural studies using the hard sphere approximation, the long-range interaction between the ion and neutral should be minimized. Accordingly, helium gas is typically used, when possible, for two primary reasons: (i) reduction of long-range interaction potential from low polarizability (ca. $0.21 \times 10^{-24} \text{ cm}^3$), and (ii) enhancement of ion transmission efficiency from relatively low mass (ca. 4 Da), i.e. lessening scattering losses. Nevertheless the selection of the neutral drift gas composition in IMS can alter the ion separation selectivity and absolute drift times, which is conceptually similar to the selection and tuning of mobile-phase composition in HPLC separations. Alternatively, reactive gases can be used as a complementary probe of analyte ion structure, or as reagents for probing the structural effects of ion-molecule reactions.

As a separations tool, the drift gas composition used in an unreactive mode can be tuned to serve several purposes including (i) changing the mobility of the analyte (i.e. for faster or slower drift times), and (ii) altering selectivity for specific analytes on the basis of ion-induced dipole interactions. Based on Equation 1.16, the mobility of an analyte decreases with increasing drift gas mass, yielding larger drift times for more massive neutrals ($t_d, \text{Ar} > \text{N}_2 > \text{He}$, etc.). Markedly, this

is beneficial at the limit of increasing analyte ion mass, as the reduced mass term more closely approximates the mass of the neutral gas. For high throughput separations, faster drift times are advantageous. However, for accurate determination of CCS measurements, slower drift times are desirable because this minimizes the relative contribution of ion residence times outside of the drift cell to the t_{ATD} . A further instrumental motive for changing the rate at which analytes elute from the drift cell is to increase the number of time points sampled across each IM peak to enhance the accuracy of the profiles.

In the separation of small molecules, the utility of tuning the selectivity of mobility separations (elution order of analytes) has been explored on the basis of drift gas polarizability.¹⁷¹⁻
¹⁷⁴ By utilizing more polarizable drift gases, the long-range potential between the analyte ion and drift gas is promoted in the form of ion-induced dipole interactions. The contribution of ion-induced dipole interaction to K_0 is defined as the polarization limit, or K_{pol} , which represents the mobility of an ion, in a gas of particular polarizability, in the limit of diminishing energy and temperature:^{161,175}

$$K_{pol} \equiv K_0(E/N \rightarrow 0, T \rightarrow 0) = \frac{13.853}{(\alpha_d \mu)^{1/2}} \quad (1.18)$$

Here, α_d is the dipole polarizability of the neutral gas and μ is the reduced mass of the ion-neutral collision pair. For smaller analyte ions (e.g. < ~500 Da) ion-induced dipole interactions can exhibit a marked effect on analyte elution order. For example, the IM-profiles in Figure 1.9, for the separation of chloroaniline ($M_r = 128$ Da) and iodoaniline ($M_r = 220$) in increasing polarizable gases (He, Ar, N₂, and CO₂), have gas-phase polarizabilities of 0.21, 1.64, 1.74, and 2.91×10^{-24} cm³, respectively.¹⁷¹ Although iodoaniline is nearly twice the mass of chloroaniline, its mobility serially increases with drift gas polarizability as indicated by the inversion of the IM-

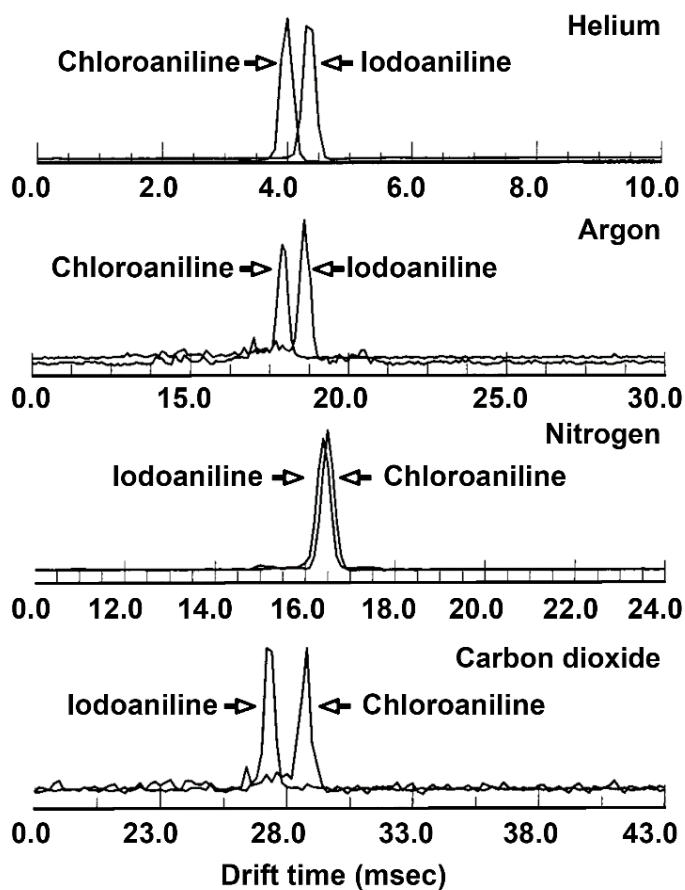


Figure 1.9. Ion mobility spectra of chloroaniline and iodoaniline in each of the four drift gases. As the polarizability increases, the velocity of the chloroaniline ion decreases relative to the iodoaniline ion. This change allows one to use drift gas polarizability to change the long-range interaction potential and hence separation order in IMS. Adapted with permission from G. R. Asbury and H. H. Hill Jr., *Anal. Chem.* 72, 580-584 (2000). Copyright 2000 American Chemical Society.

profiles. Likewise, there is extensive value in modifying the drift gas to enhance reactive ion-neutral collisions for tailoring the separation parameters.

Studies of reactions between gas-phase ions and neutrals are important in many areas such as atmospheric, inorganic, and physical organic chemistry. Typically, such reactions occur by adding a small amount of a reactive gas to an excess of inert drift gas. Assuming the collision frequency with the reactive gas, or conjugate product species is sufficiently low, the reverse reactions are considered to be negligible. Though there are many studies on atomic and small molecule ions with reactive gases,^{1,2,7} few studies utilize reactive collisions for the study of biomolecules. The utility of H/D exchange in the drift cell has been used to explore the effect of protein structure on the number of exchangeable hydrogen atoms.^{176,177} Importantly, H/D exchange can provide complementary information regarding the analyte structure by changing the partial pressure of D₂O in the He drift gas. Measurements of H/D exchange following drift cell elution or complementary to CCS determination have shown great utility in structural interpretation.¹⁷⁸⁻¹⁸⁰

I.III.II.II. Influence of Electrostatic Field-Strength on Separations

Independent of the gas type selected for ion mobility separations, the electrostatic-field strength applied across the drift cell can be used to tailor: (i) ion drift velocity, (ii) IMS resolution, and (iii) analyte selectivity. For a given K , the drift velocity is proportional to E as indicated by Equation 1.13.

Typically the resolution in ion mobility separations ($t_d/\Delta t_{d1/2}$) is limited by longitudinal diffusion in the drift cell. For separations under low-field conditions, the diffusion-limited resolution is described by Equation 1.19 for an initially narrow pulse of ions injected into the drift tube:¹⁶¹

$$\frac{t_d}{\Delta t_{d1/2}} = \frac{1}{4} \left(\frac{zeV}{k_B T \ln 2} \right)^{1/2} \quad (1.19)$$

Where, as above, the parameters are ion drift time (t_d), width of the mobility peak at half maximum ($\Delta t_{d1/2}$), ion charge (ze), potential voltage drop across the drift cell (V), Boltzmann's constant (k_b), and drift gas temperature (T). This indicates IMS resolution can be improved by increasing the voltage applied across the drift cell, independent of E . Practically, one may increase the drift cell length or use higher drift cell pressures to avoid breakdown of the gas at high voltages. High resolution (ca. $R \sim 100$ -200) IM-MS instruments have been developed for operation at high pressure and high drift voltage.^{105,181} If the ion injection pulse width is not sufficiently short, relative to the resolution predicted at the diffusion limit, additional terms are incorporated to account for it.^{182,183}

As stated in Section I.III.I for Equation 1.17, we assume ion separations are achieved in the low-field limit. This means the imparted energy to the ions by the electrostatic field is small compared with the thermal energy of the system. This is qualitatively described by:²

$$\left(\frac{m_n}{m_i} + \frac{m_i}{m_n} \right) zeE\lambda \ll k_B T \quad (20)$$

Here, λ represents the mean free path of the ion in the direction of the electrostatic-field. Furthermore, λ is inversely proportional to the product of CCS and pressure. Therefore, specific E/p ratios for maintaining ion separation increase in the low-field regime with Ω . In the separation of atomic ions, the E/p ratio should be maintained at $< 2 \text{ V cm}^{-1} \text{ Torr}^{-1}$.² Larger ions exhibit low-field behavior even at E/p ratios up to $70 \text{ V cm}^{-1} \text{ Torr}^{-1}$ or greater.¹⁸⁴

I.III.II.III. Influence of Temperature on Separations

Structural features of mass-selected analyte ions can be studied by measuring CCS at

varying temperatures to acquire structurally-resolved thermodynamic and kinetic information.¹⁸⁵⁻
²²¹ Although gas composition and electrostatics are in principle tailorable on all instruments, ion mobility separations at reduced or elevated temperatures require specialized instrumental platforms that are not currently commercially available. The reader is directed to several studies that demonstrate the potential of utilizing variable temperature separations to elucidate structurally-resolved information, expressly in four areas: (i) effects of desolvation and stepwise hydration on molecular structure,¹⁸⁵⁻¹⁹¹ (ii) small molecule structure and reaction chemistry,¹⁹²⁻²⁰⁸ (iii) biomolecular structural investigation,²⁰⁹⁻²¹⁵ and (iv) electronic-state elucidation.^{201,216-221} The concepts developed in the preceding sections are generally applicable for IMS and IM-MS separations in uniform electrostatic-fields, i.e. for separations performed at constant K and in low E -fields or at variable temperatures using DTIMS.

I.IV. Multidimensional Separation Techniques

In hyphenated techniques, an IMS can be used as a detection system after a chromatographic separation or as a tool for pre-separation of ions before a mass spectrometer. To date, various chromatographic systems such as LC, GC, and SFC have been combined with IMS. One of the early challenges of stand-alone IMS instruments was matrix interference. Importantly, the pre-separation of compounds achieved in chromatographic techniques decreases the number of components present in the reaction region at a given time, simplifying the ion molecule reactions in the ion source. Many chromatographic detectors do not offer additional analyte information, beyond retention times, and can only separate compounds with certain properties. An IMS detection system adds a dimension of separation (drift time) and can improve identification of species.

I.IV.I. Gas Chromatography-Ion Mobility Spectrometry

Since its inception in the late-70s, IMS has also been considered as a potentially unique detector for GC.^{137,222} Unlike MS, no vacuum system is required in IMS, which offers the benefits of simplicity, portability and reduction in size, weight, power, and cost. Consequently, IMS may occupy a significant position as a sophisticated detector for portable gas chromatographs in field analysis. These advantages have resulted in GC-IMS to be an acceptable analytical tool for the analysis of samples in complex matrices and for use in the international space station.²²³⁻²²⁶ Many GC-IMS systems utilize ⁶³Ni as the preferred ion source, likely owing to the commensurate low power and ease of use of the source. Since the early 1980s, the physical coupling of capillary columns to ⁶³Ni-IMS systems has been developed to correct for design complications and improve system performance.^{7,227, 228,229-231} More recently, a CD-IMS with a novel sample inlet system, similar to that shown in Figure 1.5(C), was introduced as a detector for capillary GC.²³² Instead of the commonly used solid needle for CD generation, a hollow needle was used, providing direct axial interfacing for GC-IMS. The capillary column was passed through the needle, resulting in reaction of effluents with reactant ions on the upstream side of the CD ionization source. This scheme offered higher ionization efficiency. Additionally, the volume of the ionization region was reduced to minimize the residence time of compounds in the ionization source for enhanced chromatographic resolution.

In the multi-capillary column (MCC) technology, up to 1000 capillary columns with a diameter of 40 μm are bundled into a single column of ~ 2 mm diameter. This arrangement offers relatively high flow rate and sample capacity which are useful for GC-IMS. The combination

MCC-GC-IMS offers higher resolution, faster separation, and lower detection limits (down to the ng/L and pg/L range) relative to conventional capillary GC-IMS.^{233,234}

I.IV.II. Liquid Chromatography-Ion Mobility Spectrometry

The LC-IMS technique was first introduced in the early-70s,²³⁵ but its use was complicated by requirements of excessive volumes of effluent solvent. It was not until 1998 that HPLC-IMS was first reported.²³⁶ In that design, the transfer line was connected between a split tee and a waste bottle, directing only 10% of the effluent to the IMS. Reduced mobility constants were reported for 21 carbohydrates including simple sugars, sugar alcohols, and amino sugars. The quantification limits were 5.8×10^{-14} and 8.2×10^{-11} mol for D (+)-cellobiose and L-iditol, respectively. Two years later, coronaspray IMS was used following reverse-phase liquid chromatographic separation to obtain ion mobility spectra and chromatographic responses for para-hydroxy benzoic acid, isomers of nitroaniline, and a mixture of acetaminophen, caffeine, and phenacetin.²³⁷ Ultra-high pressure liquid chromatography coupled with high-resolution nano-ESI-IMS has offered composite peak capacities of 39 and 33 for benzodiazepine and triazine herbicide mixtures, respectively, in less than 75 s.²³⁸

Currently, the most common interface is ESI-IMS combined with MS detection, first reported in 2001.²³⁹ An LC-ESI-IM-MS schematic is shown in Figure 1.10. This system has become a workhorse for multidimensional separations of complex peptide mixtures in many laboratories for the broad scale analysis of complex biological samples.²⁴⁰⁻²⁴²

I.IV.III. Supercritical Fluid Chromatography-Ion Mobility Spectrometry

IMS has also been developed as a detector for SFC.²⁴³ Capillary SFC coupled to IMS has

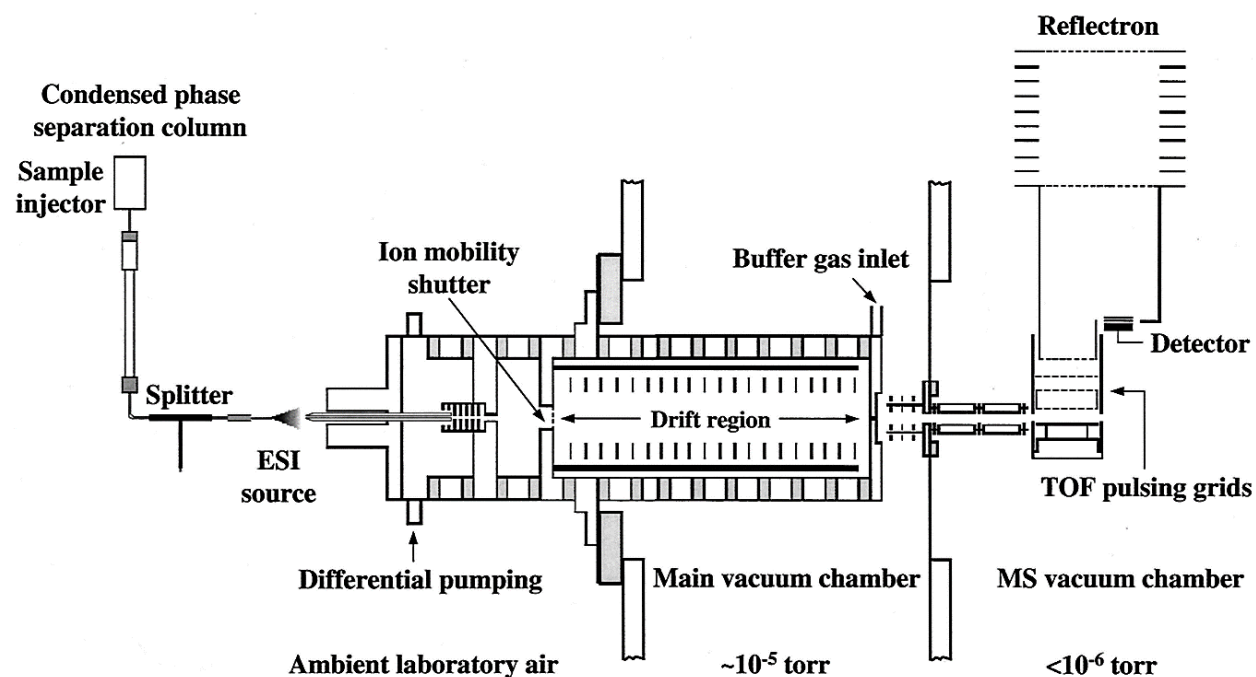


Figure 1.10: A schematic diagram illustrating the interfacing of HPLC with ESI-IM-MS. Reprinted with permission from S. J. Valentine, M. Kulchania, C. A. S. Barnes, and D. E. Clemmer, *Inter. J. Mass Spectro.* 212, 97–109 (2001). Copyright 2001, with permission from Elsevier.

been used for the qualitative and quantitative detection of organic compounds.²⁴⁴⁻²⁴⁶ In these studies, a ⁶³Ni ionization source was utilized without any modifier, CO₂ functioned as both the chromatographic mobile phase and the IMS drift gas and the amount of sample input was reduced via a split restrictor.

The use of packed column SFC combined with IMS was proposed in 1991.²⁴⁷ It was found that CO₂ up to 40 mL min⁻¹ did not change the detector response. At higher flow rates, the intensity of the reactant ions decreased, disappearing by 100 mL min⁻¹. Conventional chromatographic packed columns of 2-4 mm inner diameter are used at flow rates of several hundred milliliters per minute, with only a small, split portion of effluent directed to the IMS. In 2013, a packed column SFC was directly coupled to a continuous CD-IMS and used to determine testosterone, medroxyprogesterone, caffeine, and theophylline.²⁴⁸ This system incorporated design modifications that offered the capability of introducing up to 2000 mL min⁻¹ CO₂ gas directly into the IMS.

I.IV.IV. Ion Mobility-Inductively Coupled Plasma-Mass Spectrometry

Recent years have seen an intense research effort focused on nanotechnology and, in particular, the development of noble metal nanoparticles for a broad array of applications in medicine, diagnostics, and drug delivery. In the synthesis of nanoparticles (NP), three critical metrics define the efficacy of the NP constructs: (i) the core size of the NP, (ii) the surface derivatization of the NP, and (iii) the concentration of NPs that are synthesized. IMS, IM-MS, and ICP-MS each potentially play critical roles in evaluating these metrics, namely size and surface characterization by IMS and IM-MS, and concentration of total metal in solution by ICP-MS. Through characterization of size distribution and total metal concentration, the total NP

concentration in solution can be calculated assuming a bonding configuration of the metal atoms in the core of the particle and hence an average density.

Two strategies have incorporated IMS and IM-MS to provide detailed characterization of NPs. These differ in whether ICP and IMS measurements are decoupled or are performed online.²⁴⁸⁻²⁶⁰ In a series of manuscripts, McLean and colleagues have described the use of IM-MS for characterizing the surface derivatization of AuNPs through the selective use of MALDI-IM-MS to probe the composition of thiolate-ligands decorating the surface of the particles.²⁵³⁻²⁵⁸ Using this decoupled method, multivalent mixed-ligand AuNPs could be characterized on the extent to which the ligand distribution on the surface was phase-segregated (e.g. Janus-like or presenting two distinct faces), exhibited ligand domains, or was randomly distributed.²⁵⁶

Pergantis and Coworkers have described online ESI-DMA-ICP-MS experiments, see Figure 1.11, to analyze NP sizes.^{259,260} A condensation particle counter (CPC) determines the number of each size NP. ICP-MS is used to assess the NP elemental composition. Using this arrangement, online characterization of metals, metalloids, and halogens was performed for NPs and for sizing proteins, DNA, and other inorganic NPs.²⁵⁹ One of the technical challenges in the online coupling of atmospheric pressure DMA was air introduction into the Ar ICP-MS. To detect and size proteins and DNA using this approach, CsI was utilized to create molecular-Cs adducts, yielding a linear response between protein concentration and Cs levels monitored by ICP-MS. Importantly, this method offered a means for the quantitative analysis of large biomolecules.²⁶⁰ Hackley and colleagues extended these strategies by investigating loading of the chemotherapeutic drug cisplatin on AuNP, where the IMS and ICP-MS approach provided both surface loading information of the drug on the AuNPs and the stability of the drug-AuNP conjugate.²⁵⁰

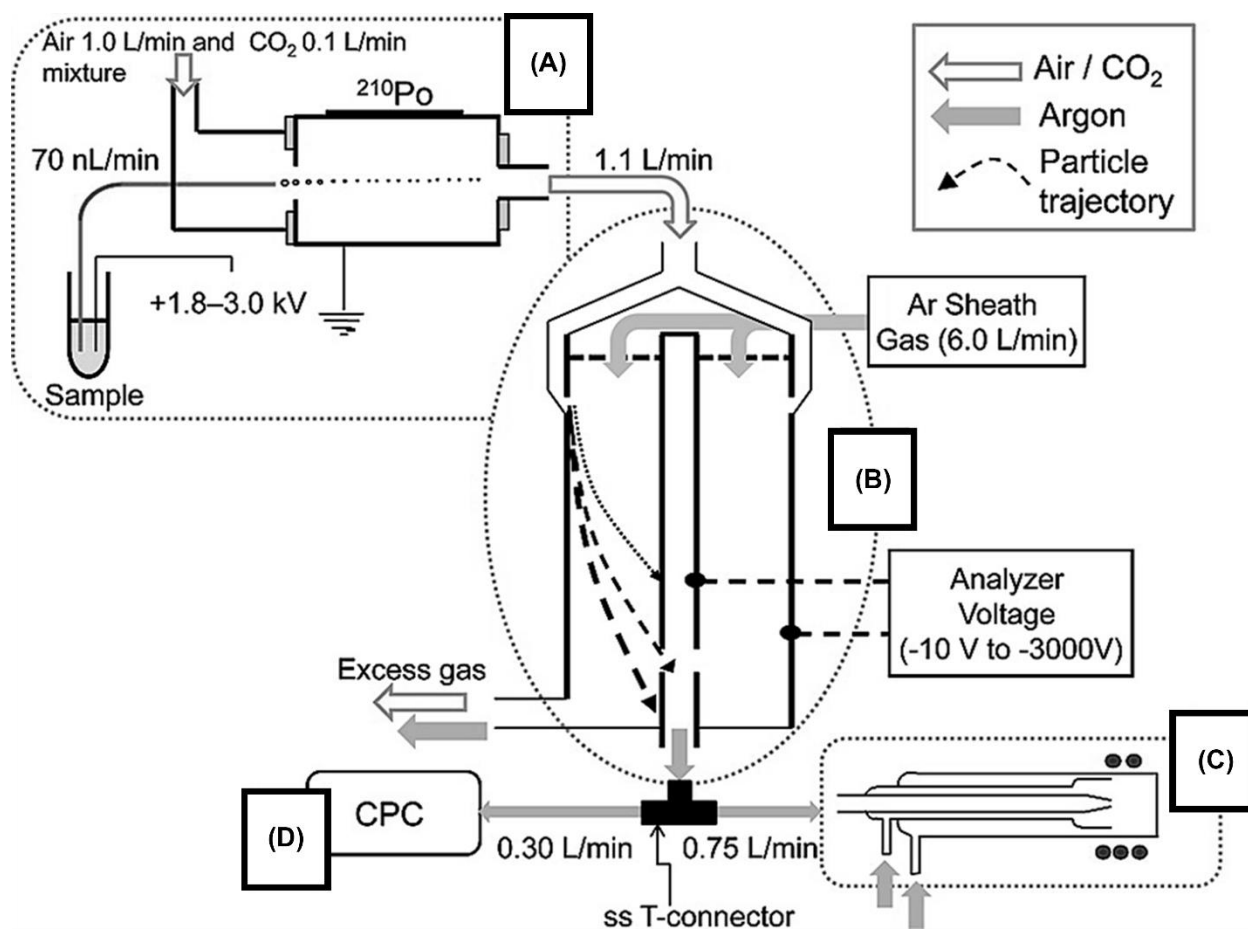


Figure 1.11: Experimental arrangement integrating IMS with ICP-MS. Configuration of the (a) nanoelectrospray, (b) differential mobility analyzer, (c) inductively coupled plasma mass spectrometer, and (d) condensation particle counting. Adapted with permission from C. Carazzone, R. Raml, S. A. Pergantis, *Analytical Chemistry* 80, 5812-5818, 2008. Copyright 2008 American Chemical Society.

I.V. Landscape of Ion Mobility Spectrometry Applications

In the 1970s, IMS was introduced by Karasek under the name of “plasma chromatography” for the trace detection of organic compounds.¹³⁷ The technique was further developed by utilizing a variety of sample preparation methods, chromatographic methods, and ionization sources in combination with IMS. The coupling of IMS with MS has expanded the applications for analysis of compounds in complex matrices in a variety of fields such as security, environmental monitoring, biology, and medicine.^{7,85,261-265}

Currently, IMS is a common tool for detecting trace levels of explosives and chemical warfare agents at airports, high security buildings, and other security check points.^{266,267} IMS is one of the most widely used methods in military preparedness and commercial aviation security.²⁶⁸ As of 2004, over 50,000 handheld IMS analyzers had been distributed for chemical-weapons monitoring within the armed forces of several nations, and more than 10,000 bench-top analyzers were being utilized as explosives detectors in airports worldwide.²⁶⁸ IMS is a powerful tool for analysis, storage, processing, quality control, and characterization of foodstuffs.²⁶⁹ This technique has also been used for the determination of a broad range of chemical compounds in environmental and industrial analysis.³⁰ The combination of IMS with the different sample preparation techniques provides suitable conditions for monitoring the chemical quality of water.²⁹ A variety of aliphatic and aromatic hydrocarbons, halocarbons, and oxygenated hydrocarbons in environmental and industrial samples have been measured with IMS analyzers.³⁰ Moreover, IMS is a widely used diagnostic tool in analysis of drugs and volatile biomarkers.²⁷⁰⁻²⁷⁴ For example, acetone is a potential biomarker for identifying fat metabolism-related diseases using human and cow urine samples.²⁷⁵ Also, the combination of IMS and multi-capillary GC can be used for metabolic profiling of human breath.²⁷⁶

Ion mobility spectrometry is applied for diagnostic purposes and determination of drugs by utilizing biological samples such as urine and serum.^{275,277} In IMS, it is possible to enhance the selectivity with dopant gases.⁸⁶ Enzyme activity inhibition can be explored by IMS in cases such as acetylcholinesterase inhibition by neostigmine and galanthamine.²⁷⁸ In addition, IMS is an efficient tool for studying enzyme reactions in drug screening and/or indirectly performing enzymological studies.²⁷⁸ This technique has been utilized for detecting and separating ribonucleotides, ribonucleosides,²⁷⁹ and analysis of bio-processes.²⁸⁰ High resolution IM-MS is used to determine metabolites in blood with the aim of gaining insight into many human diseases and identifying diagnostic biomarkers.²⁸¹ With ESI-IMS, biomolecules having high molecular mass and low volatility (such as amino acids, peptides, and proteins) can be separated and identified.²⁸² Separation and sequencing of proteins after digestion to peptides has also been accomplished using IMS.²⁸³ Hill's group has studied a number of peptides using atmospheric pressure IM-MS.²⁸⁴ Clemmer's group has made notable advances in LC-IM-MS instrumentation including the development of *tandem* ion mobility spectrometry (IMS-IMS) for the analysis of proteins and peptides in complex mixtures.²⁸⁵⁻²⁸⁷ Russell has designed and implemented MALDI-IM-MS instrumentation for the analysis of peptide mixtures and protein digests.^{121,288} Smith and coworkers have also applied IM-MS for the analysis of complex proteomic mixtures,¹⁴⁶ and made a considerable improvement in the application of this technique.²⁸⁹ Ion mobility has also been used to resolve many different structural isomers widely ranging in size such as leucine and isoleucine,²⁹⁰ as well as branching patterns in carbohydrates.^{291,292}

The coupling of LC-IM-MS offers an attractive approach for the rapid profiling of hundreds of plasma proteins. A total of 731 unique peptide ions have been analyzed corresponding to 438 unique proteins in plasma.²⁹³ Using two dimensional LC separation, with strong cation

exchange (SCX) and reverse phase LC, the protein profiling was achieved without separating high abundant proteins in the plasma.²⁹³ In a related study, plasma samples of five healthy humans were analyzed with a preliminary identification of over 9000 proteins from more than 37000 unique peptide assignments.²⁹⁴ In this study, nearly 3000 proteins were identified with high confidence, and, importantly, many were unique.^{240,295-301}

I.VI. Conclusions and Prospects

All of the main components of IMS instrumentation, including the ionization source, analyzer, detector, and data processing, have been vastly improved upon in the past decades. The combination of a variety of sample preparation techniques with stand-alone IMS instruments has improved the selectivity of IMS for the analysis of complex samples. In addition, the coupling of IMS with MS, and/or chromatographic techniques provides enhanced separation selectivity for qualitative and quantitative analyses forever increasing sample complexity. We also envision that the development of robust CCS databases would unite the community and increase confidence in chemical identifications for users around the world. Furthermore, the ability of IMS to separate isobaric analytes of differing mobilities empowers MS for broad scale analyses in biology, medicine, and nanotechnology.

I.VII. Acknowledgements

This chapter contains the invited book chapter for Mass Spectrometry with Inductively Coupled Plasmas Fundamental, Instrumentation, and Novel Applications: “Ion Mobility and Ion Mobility-Mass Spectrometry,” by Katrina L. Leaptrot, T. Khayamian, M. T. Jafari, and John A. McLean. Akbar Montaser, Ed. John Wiley and Sons, submitted 2017.

Financial support for K.L.L. and J.A.M. is gratefully acknowledged from the National Science Foundation (MRI CHE-1229341), the Center for Innovative Technology, the Vanderbilt Institute of Chemical Biology, the Vanderbilt Institute for Integrative Biosystems Research and Education, and Vanderbilt University.

I.VIII. References

1. E. W. McDaniel, *Collision Phenomena in Ionized Gases*. John Wiley & Sons Inc.: New York, pp 775 (1964).
2. E. W. McDaniel; E. A. Mason, *The Mobility and Diffusion of Ions in Gases*. John Wiley & Sons Inc.: New York, pp 372 (1973).
3. T. W. Carr, *Plasma Chromatography*, Ed.; Plenum Press: New York, pp 259 (1984).
4. E. A. Mason; E. W. McDaniel, *Transport Properties of Ions in Gases*; John Wiley & Sons Inc.: New York, pp 560 (1988).
5. A. A. Shvartsburg; *Differential Ion Mobility Spectrometry: Nonlinear Ion Transport and Fundamentals of FAIMS*; CRC Press Taylor & Francis Group: Boca Raton, pp 322 (2008).
6. C. L. Wilkins; S. Trimpin, *Ion Mobility Spectrometry-Mass Spectrometry Theory and Applications*, CRC Press Taylor & Francis Group: Boca Raton, pp 357 (2011).
7. G. A. Eiceman; Z. Karpas; H. H. Hill, Jr., *Ion Mobility Spectrometry*, 3rd Ed.; CRC Press Taylor & Francis Group: Boca Raton, pp 444 (2013).
8. F. W. Karasek, *Plasma Chromatography*, *Anal. Chem.*, 46, 710 A-720 A (1974).
9. R. Guevremont and R. W. Purves, *Atmospheric pressure ion focusing in a high-field asymmetric waveform ion mobility spectrometer*, *Rev. Sci. Instrum.*, 70, 1370 (1999).
10. R. Guevremont, R. W. Purves, D. A. Barnett, and L. Ding, *Ion trapping at atmospheric pressure (760 Torr) and room temperature with a high-field asymmetric waveform ion mobility spectrometer*, *Int. J. Mass Spectrom.*, 193, 45–56 (1999).
11. A. A. Solis and E. Sacristan, *Designing the measurement cell of a swept-field differential aspiration condenser*, *Rev. Mex. Fis.*, 52, 322–328 (2006).
12. E. Sacristan and A. A. Solis, *A Swept-Field Aspiration Condenser as an Ion-Mobility Spectrometer*, *IEEE T. Instrum. Meas.*, 47, 769-775 (1998).
13. J. C. May and J. A. McLean, *Ion Mobility-Mass Spectrometry: Time-Dispersive Instrumentation*. *Analytical Chemistry*, 87, 1422-1436 (2015).
14. Z. Hashemian, A. Mardihallaj, and T. Khayamian, *Analysis of biogenic amines using corona discharge ion mobility spectrometry*, *Talanta*, 81, 1081–1087 (2010).
15. K. Tuovinen , H. Paakkanen and O. Hänninen, *Detection of pesticides from liquid matrices by ion mobility spectrometry*, *Anal. Chim. Acta*, 404, 7–17 (2000).

16. M. Menendez, R. Garrido-Delgado, L. Arce, and M. Valcarcel, Direct determination of volatile analytes from solid samples by UV-ion mobility spectrometry, *J. Chromatogr. A* 1215, 8–14 (2008).
17. Y. H. Chen, W. K. Luckenbll, and H. H. Hill Jr., Electrospray Ionization Ion Mobility Spectrometry, *Anal. Chem.* 66, 2348-2355 (1994).
18. C. B. Shumate and H. H. Hill Jr., Coronaspray Nebulization and Ionization of Liquid Samples for Ion Mobility Spectrometry, *Anal. Chem.*, 61, 601-606 (1909).
19. K. M. Roscioli, J. A. Tufariello, X. Zhang, S. X. Li, G. H. Goetz, G. Cheng, W. F. Siems and H. H. Hill Jr., Desorption electrospray ionization (DESI) with atmospheric pressure ion mobility spectrometry for drug detection, *Analyst*, 139, 1740–1750 (2014).
20. K. J. Gillig, B. Ruotolo, E. G. Stone, and D. H. Russell, Coupling High-Pressure MALDI with Ion Mobility/Orthogonal Time-of-Flight Mass Spectrometry, *Anal. Chem.* 72, 3965-3971 (2000).
21. J. D. Keelor, P. Dwivedi, and F. M. Fernandez, An Effective Approach for Coupling Direct Analysis in Real Time with Atmospheric Pressure Drift Tube Ion Mobility Spectrometry, *J. Am. Soc. Mass Spectrom.* 25, 1538-1548 (2014).
22. M. T. Jafari, Low-Temperature Plasma Ionization Ion Mobility Spectrometry, *Anal. Chem.*, 83, 797–803 (2011).
23. W. Vautz, A. Michels, and J. Franzke, Micro-plasma: a novel ionisation source for ion mobility spectrometry, *Anal. Bioanal. Chem.*, 391, 2609–2615 (2008).
24. L. S. Fenn and J. A. McLean, Biomolecular Structural Separations by Ion Mobility-Mass Spectrometry, *Anal. Bioanal. Chem.*, 391, 905-909 (2008).
25. J. A. McLean, The mass-mobility correlation redux: the conformational landscape of anhydrous biomolecules, *J. Am. Soc. Mass Spectrom.*, 20, 1775-1781 (2009).
26. L. S. Fenn, M. Kliman, A. Mahsut, S. R. Zhao and J. A. McLean, Characterizing ion mobility-mass spectrometry conformation space for the analysis of complex biological samples, *Anal. Bioanal. Chem.*, 394, 235-244 (2009).
27. M. Kliman, J. C. May, and J. A. McLean, Lipid analysis and lipidomics by structurally selective ion mobility-mass spectrometry, *Biochimica et Biophysica Acta*, 1811, 935-945 (2011).
28. L. Arce, M. Menendez, R. Garrido-Delgado, and M. Valcarcel, Sample-introduction systems coupled to ion-mobility spectrometry equipment for determining compounds present in gaseous, liquid and solid samples, *Trends Anal. Chem.*, 27,139-150 (2008).

29. S. Holopainen, M. Nousiainen, O. Anttalainen, and M. E. T. Sillanpaa, Sample-extraction methods for ion-mobility spectrometry in water analysis, *Trends Anal. Chem.*, 37, 124-134 (2012).
30. I. Marquez-Sillero, E. Aguilera-Herrador, S. Cardenas, and M. Valcarcel, Ion-mobility spectrometry for environmental analysis, *Trends Anal. Chem.*, 30, 677-690 (2011).
31. A. Ashori and A. Sheibani, Homogeneous Liquid-Liquid Extraction Coupled to Ion Mobility Spectrometry for the Determination of p-Toluidine in Water Samples. *Bull. Environ. Contam. Toxicol.*, 94, 474-478 (2015).
32. Y. Lu, R. M. Odonnell, and P. B. Harrington, Detection of cocaine and its metabolites in urine using solid phase extraction-ion mobility spectrometry with alternating least squares, *Forensic Sci. Int.*, 189, 54–59 (2009).
33. S. Mirmahdieh, and T. Khayamian, Electrospun Nanofibers of Poly(methylmethacrylate)/Polystyrene Blend as a Microcolumn Extraction Sorbent Followed by Corona Discharge Ion Mobility Spectrometry for Analysis of Tramadol in Biological Fluids, *Chromatographia* 76, 541–548 (2013).
34. M. T. Jafari, B. Rezaei, and B. Zaker, Ion Mobility Spectrometry as a Detector for Molecular Imprinted Polymer Separation and Metronidazole Determination in Pharmaceutical and Human Serum Samples, *Anal. Chem.*, 81, 3585–3591 (2009).
35. W. Lu, H. Li, Z. Meng, X. Liang, M. Xue, Q. Wang, and X. Dong, Detection of nitrobenzene compounds in surface water by ion mobility spectrometry coupled with molecularly imprinted polymers, *J. Hazard. Mater.*, 280 588–594 (2014).
36. B. Rezaei, M.T. Jafari, and R. Khademi, Selective separation and determination of primidone in pharmaceutical and human serum samples using molecular imprinted polymer-electrospray ionization ion mobility spectrometry (MIP-ESI-IMS), *Talanta*, 79, 669–675 (2009).
37. C. Zscheppank, U. Telgheder, and K. Molt, Stir-bar sorptive extraction and TDS-IMS for the detection of pesticides in aqueous samples, *Int. J. Ion Mobil. Spec.*, 15, 257–264 (2012).
38. J. K. Lokhnauth, and N. H. Snow, Stir-bar sorptive extraction and thermal desorption-ion mobility spectrometry for the determination of trinitrotoluene and 1,3,5-trinitro-1,3,5-triazine in water samples, *J. Chromatogr. A*, 1105, 33–38 (2006).
39. M. Saraji, T. Khayamian, and Z. Hashemian, Extraction of methocarbamol from human plasma with a polypyrrole/multiwalled carbon nanotubes composite decorated with magnetic nanoparticles as an adsorbent followed by electrospray ionization ion mobility spectrometry detection, *J. Sep. Sci.* 37, 3518–3525 (2014).
40. Y. Du, W. Zhang, W. Whitten, H. Li, D. B. Watson, and J. Xu, Membrane-Extraction Ion Mobility Spectrometry for in Situ Detection of Chlorinated Hydrocarbons in Water, *Anal. Chem.*, 82, 4089–4096 (2010).

41. S. Holopainen, M. Nousiainen, and M. Sillanpaa, Determination of fuel ethers in water by membrane extraction ion mobility spectrometry, *Talanta* 106, 448–453 (2013).
42. J. K. Lokhnauth, and N. H. Snow, Solid phase micro-extraction coupled with ion mobility spectrometry for the analysis of ephedrine in urine, *J. Sep. Sci.*, 28, 612–618 (2005).
43. X. Liu , S. Nacson , A. Grigoriev , P. Lynds , and J. Pawliszyn, A new thermal desorption solid-phase microextraction system for hand-held ion mobility spectrometry, *Anal. Chim. Acta*, 559 159–165 (2006).
44. J. R. Enders, C. C. Marasco, J. P. Wikswo and J. A. McLean, A Dual-Column Solid Phase Extraction Strategy for Online Collection and Preparation of Continuously Flowing Effluent Streams for Mass Spectrometry, *Anal. Chem.*, 84, 8467-8474 (2012).
45. M. T. Jafari, M. Saraji, and H. Sherafatmand, Polypyrrole/montmorillonite nanocomposite as a new solid phase microextraction fiber combined with gas chromatography–corona discharge ion mobility spectrometry for the simultaneous determination of diazinon and fenthion organophosphorus pesticides, *Anal. Chim. Acta*, 814, 69–78 (2014).
46. H. Kalhor and N. Alizadeh, Determining urea levels in dialysis human serum by means of headspace solid phase microextraction coupled with ion mobility spectrometry and on the basis of nanostructured polypyrrole film, *Anal. Bioanal. Chem.*, 405, 5333–5339 (2013).
47. S. N. Aslipashaki, T. Khayamian, and Z. Hashemian, Aptamer based extraction followed by electrospray ionization-ion mobility spectrometry for analysis of tetracycline in biological fluids, *J. Chromatogr. B*, 925, 26–32 (2013).
48. M. T. Jafari , M. Saraji, and S. Yousefi, Negative electrospray ionization ion mobility spectrometry combined with microextraction in packed syringe for direct analysis of phenoxyacid herbicides in environmental waters, *J. Chromatogr. A*, 1249, 41– 47 (2012).
49. I. Marquez-Sillero, S. Cardenas, and M. Valcarcel, Direct determination of 2,4,6 trichloroanisole in wines by single-drop ionic liquid microextraction coupled with multicapillary column separation and ion mobility spectrometry detection, *J. Chromatogr. A*, 1218, 7574–7580 (2011).
50. E. Aguilera-Herrador, R. Lucena, S. Cardenas, and M. Valcarcel, Ionic liquid-based single drop microextraction and room-temperature gas chromatography for on-site ion mobility spectrometric analysis, *J. Chromatogr. A*, 1216, 5580–5587 (2009).
51. M. Saraji, A. A. H. Bidgoli, T. Khayamian, and A. Moradmand, Combination of corona discharge ion mobility spectrometry with a novel reagent gas and two immiscible organic solvent liquid–liquid–liquid microextraction for analysis of clomipramine in biological samples, *J. Chromatogr. A*, 1218, 8600– 8607 (2011).
52. M. Saraji, M. T. Jafari, and H. Sherafatmand, Hollow fiber-based liquid–liquid–liquid microextraction combined with electrospray ionization-ion mobility spectrometry for the

- determination of pentazocine in biological samples, *J. Chromatogr. A* 1217, 5173–5178 (2010).
53. M. T. Jafari, M. Saraji, and H. Sherafatmand, Electrospray ionization-ion mobility spectrometry as a detection system for three-phase hollow fiber microextraction technique and simultaneous determination of trimipramine and desipramine in urine and plasma samples, *Anal. Bioanal. Chem.*, 399, 3555–3564 (2011).
 54. M. Saraji, T. Khayamian, Z. Hashemian, S. N. Aslipashakia and M. Talebi, Determination of artemisinin in *Artemisia* species by hollow fiber-based liquid-phase microextraction and electrospray ionization-ion mobility spectrometry, *Anal. Methods*, 5, 4190–4195 (2013).
 55. M. T. Jafari, and F. Riahi, Feasibility of corona discharge ion mobility spectrometry for direct analysis of samples extracted by dispersive liquid–liquid microextraction, *J. Chromatogr. A*, 1343 63–68 (2014).
 56. S. Risticvic, V. H. Niri, D. Vuckovic, and J. Pawliszyn, Recent developments in solid-phase microextraction, *Anal. Bioanal. Chem.*, 393, 781–795 (2009).
 57. M. A. Jeannota, A. Przyjazny, and J. M. Kokosa, Single drop microextraction—Development, applications and future trends, *J. Chromatogr. A*, 1217, 2326–2336 (2010).
 58. L. Chimuka, M. Michel, E. Cukrowska, and B. Buszewski, Advances in sample preparation using membrane-based liquid-phase microextraction techniques, *Trend. Anal. Chem.*, 30, 1781-1792 (2011).
 59. M. Saraji, and M. K. Boroujeni, Recent developments in dispersive liquid–liquid microextraction, *Anal. Bioanal. Chem.*, 406, 2027–2066 (2014).
 60. S. K. Guharay, P. Dwivedi, and H. H. Hill Jr., Ion Mobility Spectrometry: Ion Source Development and Applications in Physical and Biological Sciences, *IEEE T. Plasma Sci.*, 36, 1458-1470 (2008).
 61. W. E. Steiner, B. H. Clowers, P. E. Haigh and H. H. Hill, Secondary Ionization of Chemical Warfare Agent Simulants: Atmospheric Pressure Ion Mobility Time-of-Flight Mass Spectrometry. *Anal. Chem.*, 75, 6068-6076 (2003).
 62. C. Bhardwaj and L. Hanley, Ion sources for mass spectrometric identification and imaging of molecular species, *Nat. Prod. Rep.*, 31, 756-767 (2014).
 63. J. D. Watrous and P. C. Dorrestein, Imaging mass spectrometry in microbiology, *Nat. Rev. Microbiol.*, 9, 683-694 (2011).
 64. H. H. Hill, Jr.; M. A. Baim, Ambient pressure ionization detectors for gas chromatography. Part II. Radioactive source ionization detectors. *TrAC, Trends Anal. Chem. (Pers. Ed.)*, 1, 232-6 (1982).

65. V. Matsaev, M. Gumerov, L. Krasnobaev, V. Pershenkov, V. Belyakov, A. Chistyakov, V. Boudovitch, IMS spectrometers with radioactive, X-ray, UV and laser ionization. *Int. J. Ion Mobility Spectrom.*, 5, 112-114 (2002).
66. M. A. Makinen, O. A. Anttalainen, M. E.T. Sillanpaa, Ion Mobility Spectrometry and Its Applications in Detection of Chemical Warfare Agents, *Anal. Chem.*, 82, 9594-9600 (2010).
67. A. Adamov, T. Mauriala, V. Teplov, J. Laakia, C. S. Pedersen, T. Kotiaho, A. A. Sysoev, Characterization of a high resolution drift tube ion mobility spectrometer with a multi-ion source platform. *Int. J. Mass Spectrom.*, 298, 24-29 (2010).
68. C. L. Crawford, H. H. Hill, Comparison of reactant and analyte ions for ⁶³Nickel, corona discharge, and secondary electrospray ionization sources with ion mobility-mass spectrometry. *Talanta* 2013, 107, 225-232 (2013).
69. Z. Karpas, A. V. Guaman, A. Pardo, S. Marco, Comparison of the performance of three ion mobility spectrometers for measurement of biogenic amines. *Anal. Chim. Acta*, 758, 122-129 (2013).
70. J. Zheng, T. Shu, J. Jin, Ion mobility spectrometry for monitoring chemical warfare agents. *Appl. Mech. Mater.*, 241-244, 980-983 (2013).
71. J. W. Leonhardt, New detectors in environmental monitoring using tritium sources. *J. Radioanal. Nucl. Chem.*, 206, 333-339 (1996).
72. I. Marquez-Sillero, S. Cardenas, S. Sielemann and M. Valcarcel, On-line headspace-multicapillary column-ion mobility spectrometry hyphenation as a tool for the determination of off-flavours in foods. *J. Chromatogr. A*, 1333, 99-105 (2014).
73. R. S. Pepling, Americium, *Chem. Eng. News*, 81, 170 (2003).
74. M. Salehkoutahi, F. Payervand and A. Tavassoli, Ionization increase in a miniaturized ion mobility spectrometer (IMS) cell using a thin layer on an Am-241 ionization source. *Maj. Ulum va Funun-i Hastah-i*, 34, 7-13 (2005).
75. S. Kishi, R. Sekioka, M. Sodeyama, M. Shiga and Y. Seto, Evaluation of detection performance of portable aspiration-type ion mobility spectrometer with seven detection cells for chemical warfare agents. *Bunseki Kagaku*, 59, 65-76 (2010).
76. A. Kuklya, F. Uteschil, K. Kerpen, R. Marks and U. Telgheder, Non-polar modifier assisted analysis of aromatic compounds by means of planar differential ion mobility spectrometry with a ⁶³Ni ionization source. *Anal. Methods*, 7, 2100-2107 (2015).
77. G. A. Eiceman, E. V. Krylov, B. Tadjikov, R. G. Ewing, E. G. Nazarov and R. A. Miller, Differential mobility spectrometry of chlorocarbons with a micro-fabricated drift tube. *Analyst (Cambridge, U. K.)*, 129, 297-304 (2004).

78. W. E. Steiner, S. J. Klopsch, W. A. English, B. H. Clowers and H. H. Hill, Detection of a Chemical Warfare Agent Simulant in Various Aerosol Matrixes by Ion Mobility Time-of-Flight Mass Spectrometry. *Anal. Chem.*, 77, 4792-4799 (2005).
79. S. Yamaguchi, R. Asada, S. Kishi, R. Sekioka, N. Kitagawa, K. Tokita, S. Yamamoto and Y. Seto, Detection performance of a portable ion mobility spectrometer with ^{63}Ni radioactive ionization for chemical warfare agents. *Forensic Toxicol.*, 28, 84-95 (2010).
80. V. Bocos-Bintintan, A. Brittain and C. L. P. Thomas, Characterisation of the phosgene response of a membrane inlet ^{63}Ni ion mobility spectrometer. *Analyst (Cambridge, U. K.)*, 127, 1211-1217 (2002).
81. A. Kuklya, F. Uteschil, K. Kerpen, R. Marks and U. Telgheder, Development of an electrospray- ^{63}Ni -differential ion mobility spectrometer for the analysis of aqueous samples. *Talanta*, 120, 173-180 (2014).
82. M. Tabrizchi, T. Khayamian, and N. Taj, Design and optimization of a corona discharge ionization source for ion mobility spectrometry, *Rev. Sci. Instrum.* 71, 2321-2328 (2000).
83. G. E. Spangler, C. I. Collins, Reactant ions in negative ion plasma chromatograph, *Anal. Chem.* 47, 393-402 (1975).
84. H. H. Hill, Jr, W. F. Siems, R. H. St. Louis, and D. G. McMinn, Ion mobility spectrometry, *Anal Chem.* 62, 1201A-1209A (1990).
85. G. A. Eiceman, and Z. Karpas, *Z. Ion Mobility Spectrometry*, 2nd ed.; CRC Press: Boca Raton, FL, (2005).
86. J. Puton, M. Nousiainen, and M. Sillanp, Ion mobility spectrometers with doped gases, *Talanta*, 76, 978-987 (2008).
87. M. J. Rusyniak, Y. M. Ibrahim, D. L. Wright, S. N. Khanna and M. S. El-Shall, Gas-Phase Ion Mobilities and Structures of Benzene Cluster Cations $(\text{C}_6\text{H}_6)_n^+$, $n = 2-6$. *J. Am. Chem. Soc.*, 125, 12001-12013 (2003).
88. G. Zschornack, M. Schmidt and A. Thorn, Electron beam ion sources. University of Technology Dresden: 2013; pp 165-201.
89. C. Wu, W. F. Siems, J. Klasmeier, and H. H. Hill Jr., Separation of Isomeric Peptides Using Electrospray Ionization/High-Resolution Ion Mobility Spectrometry, *Anal. Chem.*, 72, 391-395 (2000).
90. M. Tam and H. H. Hill, Jr., Secondary electrospray ionization-ion mobility spectrometry for explosive vapor detection. *Anal. Chem.*, 76, 2741-2747 (2004).
91. S. Myung, J. M. Wiseman, S. J. Valentine, Z. Takats, R. G. Cooks and D. E. Clemmer, Coupling Desorption Electrospray Ionization with Ion Mobility/Mass Spectrometry for

- Analysis of Protein Structure: Evidence for Desorption of Folded and Denatured States. *J. Phys. Chem. B*, 110, 5045-5051 (2006).
92. R. G. Cooks, Z. Ouyang, Z. Takats and J. M. Wiseman, *Ambient Mass Spectrometry. Science* (Washington, DC, U. S.), 311, 1566-1570 (2006).
 93. R. G. Ewing, D. A. Atkinson, G. A. Eiceman and G. J. Ewing, A critical review of ion mobility spectrometry for the detection of explosives and explosive related compounds. *Talanta*, 54, 515-529 (2001).
 94. R. G. Ewing, M. J. Waltman and D. A. Atkinson, Characterization of Triacetone Triperoxide by Ion Mobility Spectrometry and Mass Spectrometry Following Atmospheric Pressure Chemical Ionization. *Anal. Chem.* (Washington, DC, U. S.), 83, 4838-4844 (2011).
 95. W. C. Byrdwell, Atmospheric pressure chemical ionization mass spectrometry for analysis of lipids. *Lipids*, 36, 327-346 (2001).
 96. G. A. Harris, M. Kwasnik and F. M. Fernandez, Direct analysis in real time coupled to multiplexed drift tube ion mobility spectrometry for detecting toxic chemicals. *Anal Chem*, 83, 1908-15 (2011).
 97. R.-M. Raesaenen, P. Dwivedi, F. M. Fernandez and T. J. Kauppila, Desorption atmospheric pressure photoionization and direct analysis in real time coupled with travelling wave ion mobility mass spectrometry. *Rapid Commun. Mass Spectrom.*, 28, 2325-2336 (2014).
 98. M. Tabrizchi and E. Jazan, Inverse Ion Mobility Spectrometry, *Anal. Chem.*, 82, 746-750 (2010).
 99. M. J. Waltman, P. Dwivedi, H. H. Hill Jr., W. C. Blanchard, and R. G. Ewing, Characterization of a distributed plasma ionization source (DPIS) for ion mobility spectrometry and mass spectrometry, *Talanta*, 77, 249-255 (2008).
 100. C. A. Hill and C. L. P. Thomas, A pulsed corona discharge switchable high resolution ion mobility spectrometer-mass spectrometer, *Analyst*, 128, 55-60 (2003).
 101. M. T. Jafari, Design of corona discharge ionization source in negative mode without interference of NO_x ions, Patent # 79253, Iran, Nov 26, 2012.
 102. A. Michels, S. Tombrink, W. Vautz, M. Miclea, and J. Franzke, Spectroscopic characterization of a microplasma used as ionization source for ion mobility spectrometry, *Spectrochim. Acta B*, 62, 1208-1215 (2007).
 103. J. D. Harper, N. A. Charipar, C. C. Mulligan, X. Zhang, R. G. Cooks, and Z. Ouyang, Low-Temperature Plasma Probe for Ambient Desorption Ionization, *Anal. Chem.*, 80, 9097-9104 (2008).

104. M. L. Gieniec, J. Cox, D. Teer, and M. Dole, Proceedings of the 20th Annual Conference on Mass Spectrometry and Allied Topics, Dallas, TX, June 4-9, (1972).
105. C. Wu, W. F. Siems, G. R. Asbury, and H. H. Hill Jr., Electrospray Ionization High-Resolution Ion Mobility Spectrometry-Mass Spectrometry, *Anal. Chem.*, 70, 4929-4938 (1998).
106. C. Wu, W. F. Siems, and H. H. Hill Jr., Secondary Electrospray Ionization Ion Mobility Spectrometry/Mass Spectrometry of Illicit Drugs, *Anal. Chem.*, 72, 396-403 (2000).
107. T. Khayamian and M. T. Jafari, Design for Electrospray Ionization-Ion Mobility Spectrometry, *Anal. Chem.*, 79, 3199-3205 (2007).
108. K. Tanaka, H. Waki, Y. Ido, S. Akita, Y. Yoshida and T. Yohida, Protein and polymer analyses up to m/z 100,000 by laser ionization time-of-flight mass spectrometry. *Rapid Commun. Mass Spectrom.*, 2, 151-153 (1988).
109. M. Karas, U. Bahr and U. Giessmann, Matrix-assisted laser desorption ionization mass spectrometry. *Mass Spectrom. Rev.*, 10, 335-357 (1991).
110. K. D. Cook, ASMS members John Fenn and Koichi Tanaka share Nobel: the world learns our "secret". American Society for Mass Spectrometry. *J Am Soc Mass Spectrom*, 13, 1359 (2002).
111. K. Dreisewerd, The desorption process in MALDI. *Chem. Rev.* (Washington, DC, U. S.), 103, 395-425 (2003).
112. R. Knochenmuss, Ion formation mechanisms in UV-MALDI. *Analyst* (Cambridge, U. K.), 131, 966-986 (2006).
113. F. Hillenkamp, M. Karas, R. C. Beavis and B. T. Chait, Matrix-assisted laser desorption/ionization mass spectrometry of biopolymers. *Anal. Chem.*, 63, 1193A-1203A (1991).
114. D. M. Lubman and M. N. Kronlck, Resonance-Enhanced Two-Photon Ionization Spectroscopy in Plasma Chromatography, *Anal. Chem.*, 55, 1486-1492 (1983).
115. M. Tabrizchi and H. Bahrami, Improved Design for the Atmospheric Pressure Photoionization Source, *Anal. Chem.* 83, 9017-9023 (2011).
116. C. S. Leasure, M. E. Fleischer, G. K. Anderson and G. A. Eiceman, Photoionization in air with ion mobility spectrometry using a hydrogen discharge lamp. *Anal. Chem.*, 58, 2142-2147 (1986).
117. S. Cheng, J. Dou, W. Wang, C. Chen, L. Hua, Q. Zhou, K. Hou, J. Li and H. Li, Dopant-Assisted Negative Photoionization Ion Mobility Spectrometry for Sensitive Detection of Explosives. *Anal. Chem.* (Washington, DC, U. S.), 85, 319-326 (2013).

118. G. von Helden, T. Wytttenbach, and M. T. Bowers, Conformation of Macromolecules in the Gas Phase: Use of Matrix-Assisted Laser Desorption Methods in Ion Chromatography, *Science* 267, 1483-1485 (1995).
119. T. Wytttenbach, G. von Helden, and M. T. Bowers, Gas-Phase Conformation of Biological Molecules: Bradykinin, *J. Am. Chem. Soc.* 118, 8355-8364 (1996).
120. A. S. Woods, A Study of Peptide–Peptide Interactions Using MALDI Ion Mobility o-TOF and ESI Mass Spectrometry, *J. Am. Soc. Mass Spectrom.*, 13, 166–169 (2002).
121. J. A. McLean and D. H. Russell, Sub-Femtomole Peptide Detection in Ion-Mobility-Time-of-Flight Mass Spectrometry Measurements, *J. Proteome Res.*, 2, 427-430 (2003).
122. W. E. Steiner, B. H. Clowers, W. A. English and H. H. Hill Jr., Atmospheric pressure matrix-assisted laser desorption/ionization with analysis by ion mobility time-of-flight mass spectrometry, *Rapid Commun. Mass Spectrom.*, 18, 882–888 (2004).
123. S. Sevugarajan, J. C. May, J. A. McLean, A dual source ion mobility-mass spectrometer for direct comparison of ESI and MALDI collision cross section measurements, *Anal. Chem.* 82, 3247-3254 (2010).
124. J. A. McLean, W. B. Ridenour and R. M. Caprioli, Profiling and imaging of tissues by imaging ion mobility-mass spectrometry. *J. Mass Spectrom.*, 42, 1099-1105 (2007).
125. S. N. Jackson, M. Ugarov, T. Egan, J. D. Post, D. Langlais, J. A. Schultz and A. S. Woods, MALDI-ion mobility-TOFMS imaging of lipids in rat brain tissue, *J. Mass Spectrom.*, 42, 1093–1098 (2007).
126. S. D. Sherrod, E. T. Castellana, J. A. McLean and D. H. Russell, Spatially dynamic laser patterning using advanced optics for imaging matrix assisted laser desorption/ionization (MALDI) mass spectrometry. *International Journal of Mass Spectrometry*, 262, 256-262 (2007).
127. A. Matusch, L. S. Fenn, C. Depboylu, M. Kliezt, S. Strohmer, J. A. McLean and J. S. Becker, Combined elemental and biomolecular mass spectrometry imaging (MSI) for probing the inventory of tissue at a micrometer scale, *Anal. Chem.*, 84, 3170-3178 (2012).
128. J. Laakia, A. Adamov, M. Jussila, C. S. Pedersen, A. A. Sysoev and T. Kotiaho, Separation of different ion structures in atmospheric pressure photoionization-ion mobility spectrometry-mass spectrometry (APPI-IMS-MS). *J. Am. Soc. Mass Spectrom.*, 21, 1565-1572 (2010).
129. I. A. Buryakov, E. V. Krylov, E. G. Nazarov, U. Kh. Rasulev, A New Method of Separation of Multi-Atomic Ions by Mobility at Atmospheric Pressure Using a High-Frequency Amplitude-Asymmetric Strong Electric Field, *Int. J. Mass Spectrom. Ion Proc.* 128, 143-148 (1993).

130. R. W. Purves, R. Guevremont, S. Day, C. W. Pipich, M. S. Matyjaszczyk, Mass Spectrometric Characterization of a High-Field Asymmetric Waveform Ion Mobility Spectrometer, *Rev. Sci. Instr.* **69**, 4094-4105 (1998).
131. R. Guevremont, High-Field Asymmetric Waveform Ion Mobility Spectrometry: A New Tool for Mass Spectrometry, *J. Chrom. A* **1058**, 3-19 (2004).
132. N. Krylova, E. Krylov, G.A. Eiceman and J.A. Stone, Effect of Moisture on the Field Dependence of Mobility for Gas-phase ions of Organophosphorus Compounds at Atmospheric Pressure with Field Asymmetric Ion Mobility Spectrometry, *J. Phys. Chem. A* **107**, 3648-3654 (2003).
133. A. A. Shvartsburg, K. Tang, and R. D. Smith, Optimization of the Design and Operation of FAIMS Analyzers, *J. Am. Soc. Mass Spectrom.* **16**, 2-12 (2005).
134. R. W. Purves, D. A. Barnett, B. Ells and R. Guevremont, Investigation of Bovine Ubiquitin Conformers Separated by High-Field Asymmetric Waveform Ion Mobility Spectrometry: Cross Section Measurements Using Energy-Loss Experiments with a Triple Quadrupole Mass Spectrometer. *J. Am. Soc. Mass Spectrom.* **11**, 738–745 (2000).
135. R. W. Purves and R. Guevremont, Electrospray Ionization High-Field Asymmetric Waveform Ion Mobility Spectrometry–Mass Spectrometry. *Analytical Chemistry*, **71**, 2346-2357 (1999).
136. M. R. Menlyadiev, A. Tarassov, A. M. Kielnecker and G. A. Eiceman, Tandem differential mobility spectrometry with ion dissociation in air at ambient pressure and temperature. *Analyst*, **140**, 2995-3002 (2015).
137. M. J. Cohen, and F. W. Karasek, Plasma Chromatography™—A New Dimension for Gas Chromatography and Mass Spectrometry, *J. Chromatogr. Sci.*, **8**, 330-337 (1970).
138. G. M. Bird and R. A. Keller, Vapor concentration dependence of plasmagrams. *Journal of Chromatographic Science*, **14**, 574-577 (1976).
139. F. Lanucara, S. W. Holman, C. J. Gray and C. E. Eyers, The power of ion mobility-mass spectrometry for structural characterization and the study of conformational dynamics, *Nature Chem.*, **6**, 281-294 (2014).
140. H. Li, B. Bendiak, W. F. Siems, D. R. Gang, and H. H. Hill, Jr., Carbohydrate structure characterization by tandem ion mobility mass spectrometry (IMMS)², *Anal. Chem.* **85**, 2760–2769 (2014).
141. S. R. Harvey, C. E. Macphée and P. E. Barran, Ion mobility mass spectrometry for peptide analysis. *Methods*, **54**, 454-61 (2011).
142. A. Konijnenberg, A. Butterer, and F. Sobott, Native ion mobility-mass spectrometry and related methods in structural biology, *Biochimica. Et. Biophysica, Acta*, **1834**, 1239–1256 (2013).

143. C. Laphorn, F. Pullen, and B. Z. Chowdhry, Ion mobility spectrometry-mass spectrometry (IMS-MS) of small molecules: separating and assigning structures to ions, *mass Spectrom. Rev.*, 32, 43–71 (2013).
144. L. A. Woods, S. E. Radford, and A. E. Ashcroft, Advances in ion mobility spectrometry–mass spectrometry reveal key insights into amyloid assembly, *Biochimica. Et. Biophysica. Acta*, 1834, 1257–1268 (2013).
145. Y. Zhong, S. J. Hyung, B. T. Ruotolo, Ion mobility-mass spectrometry for structural proteomics, *Inf. Healthc.* 9, 47–58 (2012).
146. S. J. Valentine, M. D. Plasencia, X. Liu, M. Krishnan, S. Naylor, H. R. Udseth, R. D. Smith, D. E. Clemmer, Toward Plasma Proteome Profiling with Ion Mobility-Mass Spectrometry, *Journal of Proteome Research*, 5, 2977 (2006).
147. S. Kim and G. Spangler, Ion Mobility Spectrometry/Mass Spectrometry of Two Structurally Different Ions Having Identical Ion Mass. *Analytical Chemistry*, 57, 567-569 (1985).
148. Z. Karpas, R. M. Stimac and Z. Rappoport, Differentiating between large isomers and derivation of structural information by ion mobility spectrometry/mass spectrometry techniques. *International journal of mass spectrometry and ion processes*, 83, 163-175 (1988).
149. P. R. Kemper and M. T. Bowers, Electronic-state chromatography: application to first-row transition-metal ions. *The Journal of Physical Chemistry*, 95, 5134-5146 (1991).
150. D. P. Smith, T. W. Knapman, and A. E. Ashcroft, Deciphering drift time measurements from travelling wave ion mobility spectrometry– mass spectrometry studies. *Eur. J. Mass Spectrom.*, (Chichester, Eng.). 15, 113–130 (2009).
151. L. Tao, J. R. McLean, J. A. McLean, and D. H. Russell, A Collision Cross-Section Database of Singly-Charged Peptide Ions, *J. Am. Soc. Mass Spectrom.*, 18, 1232–1238 (2007).
152. S. J. Valentine, A. E. Counterman, and D. E. Clemmer, A Database of 660 Peptide Ion Cross Sections: Use of Intrinsic Size Parameters for Bona Fide Predictions of Cross Sections, *J. Am. Soc. Mass Spectrom.*, 10, 1188–1211 (1999).
153. F. A. Fernandez-Lima, R. C. Blase, and D. H. Russell, A study of ion-neutral collision cross-section values for low charge states of peptides, proteins, and peptide/protein complexes, *Int. J. Mass Spectrom.*, 298,111–118 (2010).
154. Y. Guo, Y. Ling, B. A. Thomson, and K. W. M. Siu., Combined Ion-Mobility and Mass-Spectrometry Investigations of Metallothionein Complexes Using a Tandem Mass Spectrometer with a Segmented Second Quadrupole, *J. Am. Soc. Mass Spectrom.*, 16, 1787–1794 (2005).

155. L. Chen, Q. Shao, Y. Gao, and D. H. Russell, Molecular Dynamics and Ion Mobility Spectrometry Study of Model β -Hairpin Peptide, Trpzip1, *J. Phys. Chem. A*, 115, 4427–4435 (2011).
156. F. A. Fernandez-Lima, H. Wei, Y. Q. Gao, and D. H. Russell, On the Structure Elucidation Using Ion Mobility Spectrometry and Molecular Dynamics, *J. Phys. Chem. A*, 113, 8221–8234 (2009).
157. D. E. Clemmer, R. R. Hudgins, and M. F. Jarrold, Naked Protein Conformations: Cytochrome c in the Gas Phase, *J. Am. Chem. Soc.* 117, 10141-10142 (1995).
158. J. C. May, C. R. Goodwin, N. M. Lareau, K. L. Leaptrot, C. B. Morris, R. T. Kurulugama, A. Mordehai, C. Klein, W. Barry, E. Darland, G. Overney, K. Imatani, G. C. Stafford, J. C. Fjeldsted and J. A. McLean, Conformational Ordering of Biomolecules in the Gas Phase: Nitrogen Collision Cross Sections Measured on a Prototype High Resolution Drift Tube Ion Mobility-Mass Spectrometer, *Anal. Chem.*, 86, 2107–2116 (2014).
159. S. M. Stow, C. R. Goodwin, M. Kliman, B. O. Bachmann, J. A. McLean, and T. P. Lybrand, Distance Geometry Protocol to Generate Conformations of Natural Products to Structurally Interpret Ion Mobility-Mass Spectrometry Collision Cross Sections, *J. Phys. Chem. B*, 118, 13812–13820 (2014).
160. E. R. Badman, S. Myung, and D. E. Clemmer, Evidence for Unfolding and Refolding of Gas-Phase Cytochrome c Ions in a Paul Trap, *J Am Soc Mass Spectrom*, 16, 1493–1497 (2005).
161. E. A. Mason, and H. W. Schamp, Mobility of gaseous ions in weak electric fields, *Ann. Phys.*, 4, 233–270 (1958).
162. H. E. Revercomb and E. A. Mason, Theory of Plasma Chromatography/ Gaseous Electrophoresis- A Review, *Anal. Chem.*, 47, 970-983 (1975).
163. J. A. McLean, J. A. Shultz and A. S. Woods, “Ion Mobility-Mass Spectrometry for Biological and Structural Mass Spectrometry.” In *Electrospray and MALDI Mass Spectrometry: Fundamentals, Instrumentation, Practicabilities, and Biological Applications*, Richard B. Cole, Ed. John Wiley & Sons, 411-439 (2010).
164. I. A. Zuleta, G. K. Barbula, M. D. Robbins, O. K. Yoon and R. N. Zare, Micromachined Bradbury–Nielsen Gates. *Analytical Chemistry*, 79, 9160-9165 (2007).
165. A. A. Shvartsburg, G. C. Schatz, and M. F. Jarrold, Mobilities of Carbon Cluster Ions: Critical Importance of the Molecular Attractive Potential, *J. Chem. Phys.* 108, 2416-2423 (1998).
166. R. R. Hudgins and M. F. Jarrold, Conformations of Unsolvated Glycine-Based Peptides, *J. Phys. Chem. B* 104, 2154-2158 (2000).

167. S. L. Bernstein, T. Wytttenbach, A. Baumketner, J.-E. Shea, G. Bitan, D. B. Teplow, and M. T. Bowers, Amyloid β -Protein: Monomer Structure and Early Aggregation States of A β 42 and Its Pro¹⁹ Alloform, *J. Am. Chem. Soc.* 127, 2075-2084 (2005).
168. M. F. Mesleh, J. M. Hunter, A. A. Shvartsburg, G. C. Schatz, and M. F. Jarrold, Structural Information from Ion Mobility Measurements: Effects of the Long-Range Potential *J. Phys. Chem.* 100, 16082-16086 (1996).
169. T. Wytttenbach, G. von Helden, J. J. Batka Jr., D. Carlat, and M. T. Bowers, Effect of the Long-range Interaction Potential on Ion Mobility Measurements, *J. Am. Soc. Mass Spectrom.* 8, 275-282 (1997).
170. T. Wytttenbach, M. Witt, M. T. Bowers, On the Stability of Amino Acid Zwitterions in the Gas Phase: The Influence of Derivatization, Proton Affinity, and Alkali Ion Addition, *J. Am. Chem. Soc.* 122, 3458-3464 (2000).
171. G. R. Asbury and H. H. Hill Jr., Using Different Drift Gases To Change Separation Factors (α) in Ion Mobility Spectrometry, *Anal. Chem.* 72, 580-584 (2000).
172. G. R. Asbury and H. H. Hill Jr., Evaluation of Ultrahigh Resolution Ion Mobility Spectrometry as an Analytical Separation Device in Chromatographic Terms, *J. Microcolumn Sep.* 12, 172-178 (2000).
173. L. M. Matz, H. H. Hill, L. W. Beegle, and I. Kanik, Investigation of Drift Gas Selectivity in High Resolution Ion Mobility Spectrometry with Mass Spectrometry Detection, *J. Am. Soc. Mass Spectrom.* 13, 300-307 (2002).
174. L. W. Beegle, I. Kanik, L. Matz, and H. H. Hill, Effects of Drift-Gas Polarizability on Glycine Peptides in Ion Mobility Spectrometry, *Int. J. Mass Spectrom.* 216, 257-268 (2002).
175. E. A. Mason and E. W. McDaniel, "Some Accurate Theoretical Results", Chapter 6 in *Transport Properties of Ions in Gases*, John Wiley & Sons, New York (1988) pp. 225-381.
176. S. J. Valentine and D. E. Clemmer, H / D Exchange Levels of Shape-Resolved Cytochrome c Conformers in the Gas Phase, *J. Am. Chem. Soc.* 119, 3558-3566 (1997).
177. S. J. Valentine and D. E. Clemmer, Temperature-Dependent H/D Exchange of Compact and Elongated Cytochrome c Ions in the Gas Phase, *J. Am. Soc. Mass Spectrom.* 13, 506-517 (2002).
178. T. Wytttenbach, B. Paizs, P. Barran, L. Brechi, D. Liu, S. Suhai, V. H. Wysocki, and M. T. Bowers, The Effect of the Initial Water of Hydration on the Energetics, Structures, and H/D Exchange Mechanism of a Family of Pentapeptides: An Experimental and Theoretical Study, *J. Am. Chem. Soc.* 125, 13768-13775 (2003).

179. B. T. Ruotolo and D. H. Russell, Gas-Phase Conformations of Proteolytically Derived Protein Fragments: Influence of Solvent on Peptide Conformation, *J. Phys. Chem. B* 108, 15321-15331 (2004).
180. H. A. Sawyer, J. T. Marini, E. G. Stone, B. T. Ruotolo, K. J. Gillig, and D. H. Russell, The Structure of Gas-Phase Bradykinin Fragment 1-5 (RPPGF) Ions: An Ion Mobility Spectrometry and H/D Exchange Ion-Molecule Reaction Chemistry Study, *J. Am. Soc. Mass Spectrom.* 16, 893-905 (2005).
181. Ph. Dugourd, R. R. Hudgins, D. E. Clemmer, M. F. Jarrold, High-Resolution Ion Mobility Measurements, *Rev. Sci. Instr.* 68, 1122-1129 (1997).
182. S. Rokushika, H. Hatano, M. A. Baim, and H. H. Hill Jr., Resolution Measurement for Ion Mobility Spectrometry, *Anal. Chem.* 57, 1902-1907 (1985).
183. W. F. Siems, C. Wu, E. E. Tarver, H. H. Hill Jr., P. R. Larsen, and D. G. McMinn, Measuring the Resolving Power of Ion Mobility Spectrometers, *Anal. Chem.* 66, 4195-4201 (1994).
184. B. T. Ruotolo, J. A. McLean, K. J. Gillig, and D. H. Russell, The Influence and Utility of Varying Field Strength for the Separation of Tryptic Peptides by Ion Mobility-Mass Spectrometry, *J. Am. Soc. Mass Spectrom.* 16, 158-165 (2005).
185. M. Kohtani and M. F. Jarrold, The initial steps in the hydration of unsolvated peptides: water molecule adsorption on alanine-based helices and globules. *J. Am. Chem. Soc.*, 124, 11148-11158 (2002).
186. Y. M. Ibrahim, M. Meot-Ner, E. H. Alshraeh, M. S. El-Shall and S. Scheiner, Stepwise Hydration of Ionized Aromatics. Energies, Structures of the Hydrated Benzene Cation, and the Mechanism of Deprotonation Reactions. *J. Am. Chem. Soc.*, 127, 7053-7064 (2005).
187. P. O. Momoh, E. Xie, S. A. Abrash, M. Meot-Ner and M. S. El-Shall, Gas Phase Reactions between Acetylene Radical Cation and Water. Energies, Structures and Formation Mechanism of $C_2H_3O^+$ and $C_2H_4O^+$ Ions. *J. Phys. Chem. A*, 112, 6066-6073 (2008).
188. B. Gao, T. Wyttenbach, and M. T. Bowers, Hydration of Protonated Aromatic Amino Acids: Phenylalanine, Tryptophan, and Tyrosine, *J. Am. Chem. Soc.*, 131, 4695-4701 (2009).
189. P. O. Momoh, A. M. Hamid, S. A. Abrash and M. S. El-Shall, Structure and hydration of the $C_4H_4^+$ ion formed by electron impact ionization of acetylene clusters. *J. Chem. Phys.*, 134, 204315/1-204315/13 (2011).
190. A. M. Hamid, P. Sharma, M. S. El-Shall, R. Hilal, S. Elroby, S. G. Aziz and A. O. Alyoubi, Hydration of the pyrimidine radical cation and stepwise solvation of protonated pyrimidine with water, methanol, and acetonitrile. *J. Chem. Phys.*, 139, 084304/1-084304/11 (2013).

191. I. K. Attah, S. P. Platt, M. Meot-Ner, M. S. El-Shall, S. G. Aziz and A. O. Alyoubi, Hydrogen bonding of the naphthalene radical cation to water and methanol and attachment of the naphthalene ion to extended hydrogen bonding chains. *Chem. Phys. Lett.*, 613, 45-53 (2014).
192. G. Von Helden, P. R. Kemper, N. G. Gotts and M. T. Bowers, Isomers of small carbon cluster anions: linear chains with up to 20 atoms. *Science (Washington, D. C., 1883-)*, 259, 1300-2 (1993).
193. J. M. Hunter and M. F. Jarrold, Drift Tube Studies of Large Carbon Clusters: New Isomers and the Mechanism of Giant Fullerene Formation. *J. Am. Chem. Soc.*, 117, 10317-24 (1995).
194. S. Lee, N. Gotts, G. von Helden and M. T. Bowers, Structures of $C_nH_x^+$ Molecules for $n \leq 22$ and $x \leq 5$: Emergence of PAHs and Effects of Dangling Bonds on Conformation. *J. Phys. Chem. A*, 101, 2096-2102 (1997).
195. A. A. Shvartsburg, R. R. Hudgins, P. Dugourd and M. F. Jarrold, Structural Elucidation of Fullerene Dimers by High-Resolution Ion Mobility Measurements and Trajectory Calculation Simulations. *J. Phys. Chem. A*, 101, 1684-1688 (1997).
196. E. H. Alsharaeh, Y. M. Ibrahim and M. S. El-Shall, Direct Evidence for the Gas Phase Thermal Polymerization of Styrene. Determination of the Initiation Mechanism and Structures of the Early Oligomers by Ion Mobility. *J. Am. Chem. Soc.*, 127, 6164-6165 (2005).
197. P. O. Momoh, S. A. Abrash, R. Mabrouki and M. S. El-Shall, Polymerization of Ionized Acetylene Clusters into Covalent Bonded Ions: Evidence for the Formation of Benzene Radical Cation. *J. Am. Chem. Soc.*, 128, 12408-12409 (2006).
198. P. O. Momoh, A.-R. Soliman, M. Meot-Ner, A. Ricca and M. S. El-Shall, Formation of Complex Organics from Acetylene Catalyzed by Ionized Benzene. *J. Am. Chem. Soc.*, 130, 12848-12849 (2008).
199. P. O. Momoh, A. M. Hamid, A.-R. Soliman, S. A. Abrash and M. S. El-Shall, Structure of the $C_8H_8^+$ Radical Cation Formed by Electron Impact Ionization of Acetylene Clusters. Evidence for a (Benzene $\cdot+$ Acetylene) Complex. *J. Phys. Chem. Lett.*, 2, 2412-2419 (2011).
200. E. H. Alsharaeh and M. S. El-Shall, Ion mobility study of the mechanism of the gas phase thermal polymerization of styrene and the structures of the early oligomers. *Polymer*, 52, 5551-5559 (2011).
201. J. C. May and D. H. Russell, A mass-selective variable-temperature drift tube ion mobility-mass spectrometer for temperature dependent ion mobility studies. *J. Am. Soc. Mass Spectrom.*, 22, 1134-1145 (2011).

202. A.-R. Soliman, A. M. Hamid, P. O. Momoh, M. S. El-Shall, D. Taylor, L. Gallagher and S. A. Abrash, Formation of Complex Organics in the Gas Phase by Sequential Reactions of Acetylene with the Phenylum Ion. *J. Phys. Chem. A*, 116, 8925-8933 (2012).
203. A.-R. Soliman, A. M. Hamid, I. Attah, P. Momoh and M. S. El-Shall, Formation of Nitrogen-Containing Polycyclic Cations by Gas-Phase and Intracluster Reactions of Acetylene with the Pyridinium and Pyrimidinium Ions. *J. Am. Chem. Soc.*, 135, 155-166 (2013).
204. A. M. Hamid, A.-R. Soliman and M. S. El-Shall, Stepwise Association of Hydrogen Cyanide and Acetonitrile with the Benzene Radical Cation: Structures and Binding Energies of $(C_6H_6^{\bullet+})(HCN)_n$, $n = 1-6$, and $(C_6H_6^{\bullet+})(CH_3CN)_n$, $n = 1-4$, Clusters. *J. Phys. Chem. A*, 117, 1069-1078 (2013).
205. I. K. Attah, S. P. Platt, M. Meot-Ner, M. S. El-Shall, S. G. Aziz and A. O. Alyoubi, Proton-bound dimers of nitrogen heterocyclic molecules: Substituent effects on the structures and binding energies of homodimers of diazine, triazine, and fluoropyridine. *J. Chem. Phys.*, 140, 114313/1-114313/11 (2014).
206. P. O. Momoh, I. K. Attah, M. S. El-Shall, R. P. F. Kanters, J. M. Pinski and S. A. Abrash, Formation of Covalently Bonded Polycyclic Hydrocarbon Ions by Intracluster Polymerization of Ionized Ethynylbenzene Clusters. *J. Phys. Chem. A*, 118, 8251-8263 (2014).
207. A. M. Hamid, M. S. El-Shall, R. Hilal, S. Elroby and S. G. Aziz, Unconventional hydrogen bonding to organic ions in the gas phase: Stepwise association of hydrogen cyanide with the pyridine and pyrimidine radical cations and protonated pyridine. *J. Chem. Phys.*, 141, 054305/1-054305/11 (2014).
208. A.-R. Soliman, I. K. Attah, A. M. Hamid and M. S. El-Shall, Growth kinetics and formation mechanisms of complex organics by sequential reactions of acetylene with ionized aromatics. *Int. J. Mass Spectrom.*, 377, 139-151 (2015).
209. K. B. Shelimov and M. F. Jarrold, Conformations, Unfolding, and Refolding of Apomyoglobin in Vacuum: An Activation Barrier for Gas-Phase Protein Folding. *J. Am. Chem. Soc.*, 119, 2987-2994 (1997).
210. Y. Mao, J. Woenckhaus, J. Kolafa, M. A. Ratner, and M. F. Jarrold, Thermal Unfolding of Unsolvated Cytochrome c: Experiment and Molecular Dynamics Simulations, *J. Am. Chem. Soc.*, 121, 2712-2721 (1999).
211. B. Mészáros, I. Simon, and Z. Dosztány, The Expanding View of Protein-Protein Interactions: Complexes Involving Intrinsically Disordered Proteins, *Phys. Bio.*, 8, 035003 (2011).
212. C. Bleiholder, N. F. Dupuis, T. Wyttenbach and M. T. Bowers, Ion mobility-mass spectrometry reveals a conformational conversion from random assembly to β -sheet in amyloid fibril formation. *Nat. Chem.*, 3, 172-177 (2011).

213. Y. Berezovskaya, M. Porrini and P. E. Barran, The effect of salt on the conformations of three model proteins is revealed by variable temperature ion mobility mass spectrometry. *Int. J. Mass Spectrom.*, 345-347, 8-18 (2013).
214. E. R. Dickinson, E. Jurneczko, K. J. Pacholarz, D. J. Clarke, M. Reeves, K. L. Ball, T. Hupp, D. Campopiano, P. V. Nikolova and P. E. Barran, Insights into the Conformations of Three Structurally Diverse Proteins: Cytochrome c, p53, and MDM2, Provided by Variable-Temperature Ion Mobility Mass Spectrometry. *Anal. Chem.* (Washington, DC, U. S.), 87, 3231-3238 (2015).
215. K. J. Pacholarz and P. E. Barran, Distinguishing Loss of Structure from Subunit Dissociation for Protein Complexes with Variable Temperature Ion Mobility Mass Spectrometry. *Anal. Chem.* (Washington, DC, U. S.), Ahead of Print (2015).
216. P. R. Kemper and M. T. Bowers, Electronic-state chromatography: application to first-row transition-metal ions. *J. Phys. Chem.*, 95, 5134-46 (1991).
217. P. A. M. Van Koppen, P. R. Kemper and M. T. Bowers, Electronic state-selected reactivity of transition metal ions: cobalt(+) and iron(+) with propane. *J. Am. Chem. Soc.*, 114, 10941-50 (1992).
218. M. T. Bowers, P. R. Kemper, G. von Helden and P. A. M. van Koppen, Gas-phase ion chromatography: transition metal state selection and carbon cluster formation. *Science*, 260, 1446-51 (1993).
219. G. F. Verbeck, K. J. Gillig and D. H. Russell, Variable-temperature ion mobility time-of-flight mass spectrometry studies of electronic isomers of Kr_2^+ and CH_3OH^+ radical cations. *Eur. J. Mass Spectrom.*, 9, 579-587 (2003).
220. Y. Ibrahim, E. Alsharaeh, R. Mabrouki, P. Momoh, E. Xie and M. S. El-Shall, Ion Mobility of Ground and Excited States of Laser-Generated Transition Metal Cations. *J. Phys. Chem. A*, 112, 1112-1124 (2008).
221. J. C. May and D. H. Russell, A Cryogenic Temperature Ion Mobility-Mass Spectrometer for Improved Ion Mobility Resolution, in *Ion Mobility-Mass Spectrometry: Theory and Applications*, C.L. Wilkins and S. Trimpin, Eds.; CRC Press: Boca Raton, FL, pp 137-151 (2010).
222. F. W. Karasek, H. H. Hill Jr., and S. H. Kim, Gas chromatographic detection modes for the plasma chromatograph, *J. Chromatogram.*, 135, 329-339 (1977).
223. A. B. Kanu, and H. H. Hill Jr., Ion mobility spectrometry detection for gas chromatography, *J. Chromatogr. A*, 1177, 12-27 (2008).
224. G. A. Eiceman, Y. Wang, L. Garcia-Gonzalez, C. S. Harden, and D. B. Shoff, Enhanced selectivity in ion mobility spectrometry analysis of complex mixtures by alternate reagent gas chemistry, *Anal. Chim. Acta*, 306, 21-33 (1995).

225. A. P. Snyder, W. M. Maswadeh, A. Tripathi, J. Eversole, J. Ho, and M. Spence, Orthogonal analysis of mass and spectral based technologies for the field detection of bioaerosols, *Anal. Chim. Acta*, 513, 365–377 (2004).
226. P. T. Palmer, and T. F. Limero, Mass Spectrometry in the U.S. Space Program: Past, Present, and Future, *J. Am. Soc. Mass Spectrom.*, 12, 656–675 (2001).
227. M. A. Baim and H. H. Hill Jr., Tunable Selective Detection for Capillary Gas Chromatography by Ion Mobility Monitoring, *Anal. Chem.*, 54, 38-43 (1982).
228. R. H. St. Louis, W. F. Siems and H. H. Hill Jr., Evaluation of direct axial sample introduction for ion mobility detection after capillary gas chromatography, *J. Chromatogr.*, 479, 221-231 (1989).
229. Z. Karpas, Y. Wang and G. A. Eiceman, Qualitative and quantitative response characteristics of a capillary gas chromatograph/ion mobility spectrometer to halogenated compounds, *Anal. Chim. Acta*, 282, 19-31 (1993).
230. D. Young, C. L. P. Thomas, J. Breach, A. H. Brittain, and G. A. Eiceman, Extending the concentration and linear dynamic range of ion mobility spectrometry with a sheath flow inlet, *Anal. Chim. Acta*, 381, 69-83 (1999).
231. D. Young, G. A. Eiceman, J. Breach, A. H. Brittain, and C. L. P. Thomas, Automated control and optimisation of ion mobility spectrometry responses using a sheath-flow inlet, *Anal. Chim. Acta*, 463, 143–154 (2002).
232. M. T. Jafari, M. Saraji, and H. Sherafatmand, Design for gas chromatography–corona discharge–ion mobility spectrometry, *Anal. Chem.*, 84, 10077–10084 (2012).
233. T. Perl, B. Bödeker, M. Jünger, J. Nolte, and W. Vautz, Alignment of retention time obtained from multicapillary column gas chromatography used for VOC analysis with ion mobility spectrometry, *Anal. Bioanal. Chem.*, 397, 2385–2394 (2010).
234. S. t. Sielemann, J. I. Baumbach, H. Schmidt, and P. Pilzecker, Quantitative analysis of benzene, toluene, and m-xylene with the use of a UV–ion mobility spectrometer, *Field Anal. Chem. Tech.*, 4, 157–169 (2000).
235. F.W. Karasek and O. W. Denney, Evaluation of the plasma chromatograph as a qualitative detector for liquid chromatography, *Anal. Lett.*, 6, 993-1004 (1973).
236. D. Lee, C. Wu, and H. H. Hill Jr., Detection of carbohydrates by electrospray ionization-ion mobility spectrometry following microbore high-performance liquid chromatography, *J. Chromatogr. A*, 822, 1-9 (1998).
237. D. G. McMinn, J. A. Kinzer, C. B. Shumate, W. F. Siems, and H. H. Hill Jr., Ion Mobility Detection Following Liquid Chromatographic Separation, *J. Microcol. Sep.* 2, 188-192 (1990).

238. D. C. Collins, Y. Xiang and M. L. Lee, *Comprehensive Ultra-high Pressure Capillary Liquid Chromatography/Ion Mobility Spectrometry*, *Chromatographia*, 55, 123-128 (2002).
239. S. J. Valentine, M. Kulchania, C. A. S. Barnes, and D. E. Clemmer, Multidimensional separations of complex peptide mixtures: a combined high-performance liquid chromatography/ion mobility/time-of-flight mass spectrometry approach, *Inter. J. Mass Spectro.* 212, 97–109 (2001).
240. C. R. Goodwin, S. D. Sherrod, C. C. Marasco, B. O. Bachmann, N. L. Schramm-Sapyta, J. P. Wikswo and J. A. McLean, Phenotypic mapping of metabolic profiles using self-organizing maps of high-dimensional mass spectrometry data, *Anal. Chem.* 86, 6563-6571 (2014).
241. K. M. Hines, B. R. Ballard, D. R. Marshall and J. A. McLean, Structural mass spectrometry of tissue extracts to distinguish cancerous and non-cancerous breast diseases, *Molecular BioSystems* 10, 2827-2837 (2014).
242. J. C. May, C. R. Goodwin and J. A. McLean, Ion mobility-mass spectrometry strategies for untargeted systems, synthetic, and chemical biology, *Curr. Opin. Biotechnol.* 31, 117-121 (2015).
243. H. H. Hill Jr., R. H. S. Louis, M. A. Morrissey, C. B. Shumate, and W. F. Siems, and D. G. McMinn, A Detection Method for Unified Chromatography: Ion Mobility Monitoring, *J. high resol. Chro.* 15, 417-422 (1992).
244. R. L. Eatherton, M. A. Morrissey, W. F. Siems, and H. H. Hill Jr., Ion Mobility Detection after Supercritical Fluid Chromatography, *J. High Res. Chromatog.*, 9, 154-160 (1986).
245. S. Rokushika, H. Hatano, and H. H. Hill Jr., Ion Mobility Spectrometry after Supercritical Fluid Chromatography, *Anal. Chem.*, 59, 8-12 (1987).
246. R. L. Eatherton, M. A. Morrissey, and H. H. Hill Jr., Comparison of Ion Mobility Constants of Selected Drugs after Capillary Gas Chromatography and Capillary Supercritical Fluid Chromatography, *Anal. Chem.*, 60, 2240-2243 (1988).
247. M. A. Morrissey and H. M. Widmer, Ion-mobility spectrometry as a detection method for packed column supercritical fluid chromatography, *J. Chromatogr.*, 552, 551-561 (1991).
248. J. Gigault, and V. A. Hackley, Differentiation and characterization of isotopically modified silver nanoparticles in aqueous media using asymmetric-flow field flow fractionation coupled to optical detection and mass spectrometry, *Anal. Chim. Acta* 763, 57–66 (2013).
249. S. Elzey, D. Tsai, L. L. Yu, M. R. Winchester, M. E. Kelley and V. A. Hackley, Real-time size discrimination and elemental analysis of gold nanoparticles using ES-DMA coupled to ICP-MS, *Anal. Bioanal. Chem.* 405, 2279–2288 (2013).

250. D. Tsai, T. J. Cho, S. R. Elzey, J. C. Gigault and V. A. Hackley, Quantitative analysis of dendron-conjugated cisplatin-complexed gold nanoparticles using scanning particle mobility mass spectrometry, *Nanoscale* 5, 5390-5395 (2013).
251. J. M. Pettibone, J. Gigault, and V. A. Hackley, Discriminating the States of Matter in Metallic Nanoparticle Transformations: What Are We Missing?, *ACS Nano* ,7, 2491–2499 (2013).
252. D. Tsai, F. W. DelRio, J. M. Pettibone, P. Lin, J. Tan, M. R. Zachariah and V. A. Hackley, Temperature-programmed electrospray–differential mobility analysis for characterization of ligated nanoparticles in complex media, *Langmuir*, 29, 11267–11274 (2013).
253. K. M. Harkness, D. E. Cliffel and J. A. McLean, Characterization of thiolate-protected gold nanoparticles by mass spectrometry. *Analyst* (Cambridge, U. K.), 135, 868-874 (2010).
254. K. M. Harkness, L. S. Fenn, D. E. Cliffel and J. A. McLean, Surface Fragmentation of Complexes from Thiolate Protected Gold Nanoparticles by Ion Mobility-Mass Spectrometry. *Anal. Chem.* (Washington, DC, U. S.), 82, 3061-3066 (2010).
255. K. M. Harkness, B. C. Hixson, L. S. Fenn, B. N. Turner, A. C. Rape, C. A. Simpson, B. J. Huffman, T. C. Okoli, J. A. McLean and D. E. Cliffel, A Structural Mass Spectrometry Strategy for the Relative Quantitation of Ligands on Mixed Monolayer-Protected Gold Nanoparticles. *Anal. Chem.* (Washington, DC, U. S.), 82, 9268-9274 (2010).
256. K. M. Harkness, A. Balinski, J. A. McLean and D. E. Cliffel, Nanoscale Phase Segregation of Mixed Thiolates on Gold Nanoparticles. *Angew. Chem., Int. Ed.*, 50, 10554-10559 (2011).
257. K. M. Harkness, Y. Tang, A. Dass, J. Pan, N. Kothalawala, V. J. Reddy, D. E. Cliffel, B. Demeler, F. Stellacci, O. M. Bakr and J. A. McLean, Ag₄₄(SR)₃₀₄-: a silver-thiolate superatom complex. *Nanoscale*, 4, 4269-4274 (2012).
258. K. M. Harkness, B. N. Turner, A. C. Agrawal, Y. Zhang, J. A. McLean and D. E. Cliffel, Biomimetic monolayer-protected gold nanoparticles for immunorecognition. *Nanoscale*, 4, 3843-3851 (2012).
259. C. Carazzone, R. Raml, and S. A. Pergantis, Nanoelectrospray Ion Mobility Spectrometry Online with Inductively Coupled Plasma-Mass Spectrometry for Sizing Large Proteins, DNA, and Nanoparticles, *Anal. Chem.*, 80, 5812–5818 (2008).
260. E. A. Kapellios and S. A. Pergantis, Size and elemental composition of nanoparticles using ion mobility spectrometry with inductively coupled plasma mass spectrometry, *J. Anal. At. Spectrom.*, 27, 21-24 (2012).
261. H. Borsdorf, and G. A. Eiceman, Ion Mobility Spectrometry: Principles and Applications, *Appl. Spectrosc. Rev.*, 41, 323–375 (2006).

262. C. S. Creaser, J. R. Griffiths, C. J. Bramwell, S. Noreen, C. A. Hill and C. L. P. Thomas, Ion mobility spectrometry: a review. Part 1. Structural analysis by mobility measurement, *Analyst*, 129, 984–994, (2004).
263. H. Borsdorf, T. Mayer, M. Zarejousheghani, and G. A. Eiceman, Recent Developments in Ion Mobility Spectrometry, *Appl. Spectrosc. Rev.*, 46, 472–521 (2011).
264. T. Fink, J. I. Baumbach and S. Kreuer, Ion mobility spectrometry in breath, *J. Breath Res.* 8, 027104-027115 (2014).
265. S. Armenta, M. Alcala, and M. Blanco, A review of recent, unconventional applications of ion mobility spectrometry (IMS), *Anal. Chim. Acta*, 703, 114–123 (2011).
266. I. A. Buryakov, Detection of Explosives by Ion Mobility Spectrometry, *J. Anal. Chem.*, 66, 674–694 (2011).
267. L. Yang, Q. Han, S. Cao, J. Yang, J. Yang and M. Ding, Portable Solid Phase Micro-Extraction Coupled with Ion Mobility Spectrometry System for On-Site Analysis of Chemical Warfare Agents and Simulants in Water Samples, *Sensors*, 14, 20963-20974 (2014).
268. G. A. Eiceman and J. A. Stone, Ion Mobility Spectrometers in National Defense. *Analytical Chemistry*, 76, 390 A-397 A (2004).
269. Z. Karpas, Applications of ion mobility spectrometry (IMS) in the field of foodomics, *Food Res. Int.*, 54, 1146–1151 (2013).
270. Y. Wang, S. Nacson, and J. Pawliszyn, The coupling of solid-phase microextraction/surface enhanced laser desorption/ionization to ion mobility spectrometry for drug analysis, *Anal. Chim. Acta*, 582, 50–54 (2007).
271. M. Saraji, T. Khayamian, S. Mirmahdieh, and A. A. H. Bidgoli, Analysis of amantadine in biological fluids using hollow fiber-based liquid–liquid–liquid microextraction followed by corona discharge ion mobility spectrometry, *J. Chromatogr. B*, 879, 3065–3070 (2011).
272. M. T. Jafari, M. Kamfirozi, E. Jazan, and S. M. Ghoreishi, Selective extraction and analysis of pioglitazone in cow plasma using a molecularly imprinted polymer combined with ESI ion mobility spectrometry, *J. Sep. Sci.* 37, 573–579 (2014).
273. S. Mirmahdieh, T. Khayamian and M. Saraji, Analysis of dextromethorphan and pseudoephedrine in human plasma and urine samples using hollow fiber-based liquid–liquid–liquid microextraction and corona discharge ion mobility spectrometry, *Microchim. Acta*, 176, 471–478 (2012).
274. D. Isailovic, R. T. Kurulugama, M. D. Plasencia, S. T. Stokes, Z. Kyselova, R. Goldman, Y. Mechref, M. V. Novotny, and D. E. Clemmer, Profiling of Human Serum Glycans Associated with Liver Cancer and Cirrhosis by IMS-MS, *J. Proteome Res.* 7, 1109–1117 (2008).

275. R. Garrido-Delgadoa, L. Arcea, C. C. Perez-Marinb, and M. Valcarcel, Use of ion mobility spectroscopy with an ultraviolet ionization source as a vanguard screening system for the detection and determination of acetone in urine as a biomarker for cow and human diseases, *Talanta*, 78, 863–868 (2009).
276. J. I. Baumbach, Ion mobility spectrometry coupled with multi-capillary columns for metabolic profiling of human breath, *J. Breath Res.*, 3, 036004/1-036004/8 (2009).
277. R. M. Odonnell, X. Sun, and P. d. B. Harrington, Pharmaceutical applications of ion mobility spectrometry, *Trends Anal. Chem.*, 27, 44-53 (2008).
278. S. Armenta, and M. Blanco, Ion mobility spectrometry: A valuable tool for kinetic studies in enzymology, *Anal. Chim. Acta*, 685, 1–8 (2011).
279. A. B. Kanua, G. Hampikianb, S. D. Brandtc, and H. H. Hill Jr., Ribonucleotide and ribonucleoside determination by ambient pressure ion mobility spectrometry, *Anal. Chim. Acta*, 658 91–97 (2010).
280. W. Vautz, and J. I. Baumbach, Analysis of Bio-Processes using Ion Mobility Spectrometry, *Eng. Life Sci.*, 8,19–25 (2008).
281. P. Dwivedia, A. J. Schultzb, and H. H. Hill Jr., Metabolic profiling of human blood by high-resolution ion mobility mass spectrometry (IM-MS), *Int. J. Mass Spectrom.*, 298, 78–90 (2010).
282. N. Arabzadeh, and T. Khayamian, Pneumatically assisted electrospray-ion mobility spectrometry for quantitative analysis of intact proteins, *Talanta*, 99, 29–35 (2012).
283. S. I. Merenbloom, S. L. Koeniger, S. J. Valentine, M. D. Plasencia, and D. E. Clemmer, IMS-IMS and IMS-IMS-IMS/MS for Separating Peptide and Protein Fragment Ions, *Anal. Chem.*, 78, 2802-2809 (2006).
284. C. Wu, J. Klasmeier and H. H. Hill Jr., Atmospheric Pressure Ion Mobility Spectrometry of Protonated and Sodiated Peptides, *Rapid Commun. Mass Spectrom.*, 13, 1138–1142 (1999).
285. J. A. Taraszka, R. Kurulugama, R. A. Sowell, S. J. Valentine, S. L. Koeniger, R. J. Arnold, D. F. Miller, T. C. Kaufman, and D. E. Clemmer, Mapping the Proteome of *Drosophila melanogaster*: Analysis of Embryos and Adult Heads by LC-IMS-MS Methods, *J. Proteome Res.*, 4, 1223-1237 (2005).
286. S. I. Merenbloom, B. C. Bohrer, S. L. Koeniger, and D. E. Clemmer, Assessing the Peak Capacity of IMS-IMS Separations of Tryptic Peptide Ions in He at 300 K, *Anal. Chem.*, 79, 515-522 (2007).
287. S. J. Valentine, R. T. Kurulugama, B. C. Bohrer, S. I. Merenbloom, R. A. Sowell, Y. Mechref, and D. E. Clemmer, Developing IMS–IMS–MS for rapid characterization of abundant proteins in human plasma, *Int. J. Mass Spectrom.*, 283, 149–160 (2009).

288. J. A. McLean, B. T. Ruotolo, K. J. Gillig, and D. H. Russell, Ion mobility–mass spectrometry: a new paradigm for proteomics, *Int. J. Mass Spectrom.*, 240, 301–315 (2005).
289. Y. M. Ibrahim, D. C. Prior, E. S. Baker, R. D. Smith, and M. E. Belov, Characterization of an ion mobility-multiplexed collision-induced dissociation-tandem time-of-flight mass spectrometry approach, *Int. J. Mass Spectrom.*, 293, 34–44 (2010).
290. D. A. Barnett, B. Ells, R. Guevremont, and R. W. Purves, Separation of Leucine and Isoleucine by Electrospray Ionization–High Field Asymmetric Waveform Ion Mobility Spectrometry–Mass Spectrometry, *J. Am. Soc. Mass Spectrom.*, 10, 1279–1284 (1999).
291. L.S. Fenn and J.A. McLean, Structural resolution of carbohydrate positional and structural isomers based on gas-phase ion mobility-mass spectrometry, *Phys. Chem. Chem. Phys.*, 13, 2196-2205 (2011).
292. D. M. Williams, and T. L. Pukala, Novel insights into protein misfolding diseases revealed by ion mobility-mass spectrometry, *Mass Spectrom. Rev.*, 32, 169–187 (2013).
293. X. Liu, S. J. Valentine, M. D. Plasencia, S. Trimpin, S. Naylor, D. E. Clemmer, Mapping the Human Plasma Proteome by SCX-LC-IMS-MS, *J Am Soc Mass Spectrom.*, 18, 1249 (2007).
294. L. S. Fenn and J. A. McLean, Enhanced carbohydrate structural selectivity in ion mobility-mass spectrometry analyses by boronic acid derivatization, *Chem. Commun.*, 5505–5507 (2008).
295. P. Chen, and P. B. Harrington, SIMPLISMA applied to two-dimensional wavelet compressed ion mobility spectrometry data, *Anal. Chim. Acta*, 484, 75–91 (2003).
296. V. Pomareda, D. Calvo, A. Pardo, and S. Marco, Hard modeling Multivariate Curve Resolution using LASSO: Application to Ion Mobility Spectra, *Chemometr. Intell. Lab. Sys.*, 104, 318–332 (2010).
297. T. Khayamian, S. M. Sajjadi, S. Mirmahdieh, A. Mardihallaj, and Z. Hashemian, Simultaneous analysis of bifenthrin and tetramethrin using corona discharge ion mobility spectrometry and Tucker 3 model, *Chemometr. Intell. Lab. Sys.*, 118, 88–96 (2012).
298. P. Chen, and P. d. B. Harrington, Discriminant Analysis of Fused Positive and Negative Ion Mobility Spectra Using Multivariate Self-Modeling Mixture Analysis and Neural Networks, *Appl. Spectrosc.*, 62, 133-141 (2008).
299. S. Prasad, K. M. Pierce, H. Schmidt, J. V. Rao, R. Guth, R. E. Synovec, G. B. Smith and G. A. Eiceman, Constituents with independence from growth temperature for bacteria using pyrolysis-gas chromatography/differential mobility spectrometry with analysis of variance and principal component analysis, *Analyst*, 133, 760–767 (2008).

300. C. G. Fraga, D. R. Kerr and D. A. Atkinson, Improved quantitative analysis of ion mobility spectrometry by chemometric multivariate calibration, *Analyst*, 134, 2329–2337 (2009).
301. Z. Boger and Z. Karpas, Use of Neural Networks for Quantitative Measurements in Ion Mobility Spectrometry (IMS), *J. Chem. Ins. Comput. Sci.*, 34, 576-580 (1994).

CHAPTER II

THEORETICAL CONSIDERATIONS FOR SPATIAL MULTIPLEXING IN ION MOBILITY SPECTROMETRY

II.I. Abstract

Multiplexed strategies have been employed in genomics research and high-throughput screening. Many studies, including *in-situ* analysis of environmental contaminants¹ and studies of biological systems,² have recognized a need for improved figures-of-merit in ion mobility-mass spectrometry (IM-MS). Temporally multiplexed IM-MS has been reported previously, but a spatially multiplexed IM instrument has yet to be described.^{3,4} A multi-channel IM-MS could provide benefits in throughput, sensitivity, versatility, and temporal sampling resolution (for on-line analyses), among others. The development of a novel multiplexed IM, which can be interfaced with MS in the future, is therefore described to satisfy these needs. The spatially multiplexed IM consists of arrays of eight ESI sources, resistive glass capillaries (RGC), tandem ion funnels, gated apertures, drift tubes, and detectors, with all components housed in a single vacuum system, utilizing one set of electronics, and supported by shared hardware, with analytical figures-of-merit comparable with conventional single channel instruments in regards to IM resolving power, sensitivity, and spectral reproducibility across each discrete channel.

II.II. Introduction

II.II.I. History

Ion mobility (IM) is a developing technique, though its roots go back to J. J. Thomson's work in 1895, when he observed the decomposition of neutral gases to ions, and the subsequent migration of those charged molecules in an electric field.⁵ In 1948, James Lovelock described a device used to measure air currents, the ionization anemometer, which ionizes gas molecules by irradiating a region of air between two electrodes with alpha particles.⁶ Lovelock observed that current between the electrodes decreased proportionately to the velocity of the atmospheric gas and that the mobility of ions was influenced by gas impurities, an early example of the possibility of gas composition analysis via IM.

The development of the drift tube for IM measurements was pioneered by McDaniel and coworkers in the 1960s.⁷ Their drift tube apparatus consisted of 11 stainless steel electrodes separated by Pyrex insulators and electrically connected via a resistor network, over which a direct current (DC) voltage was applied. It was constructed primarily to study ion-molecule reactions, but McDaniel recognized its potential for simultaneous IM and mass analyses. Before the close of the decade, McDaniel redesigned his drift tube apparatus to mass-identify H_3^+ and H^+ ions and measure their drift velocities in hydrogen gas.⁸ In 1969, the method of measuring mobility was commercialized as plasma chromatography,^{9,10} but this instrumentation somewhat discredited the IM technique with poor performance and studies suggesting concentration-dependent results.¹¹ Research and development in IM faded in the following years with no refereed journal articles on this technique published in 1980, but, fortunately for today's IM community, this technology would be revived.¹² While the military found utility in developing handheld IM analyzers for detection of drugs and explosives,¹³ the advent of novel ionization sources such as electrospray ionization (ESI) and matrix assisted laser desorption/ionization (MALDI) enabled generation of macromolecular ions unprecedented in size, encouraging use of IM in studies of biomolecules.^{14,15}

II.II.II. Theory

Uniform field IM is a separation technique used to characterize a packet of gas-phase ions, known as an ion swarm, based on their velocities under the influence of an electric field (E , $V \cdot \text{cm}^{-1}$) and in the presence of neutral gas molecules. Sample molecules are vaporized, ionized, and pulsed into the analysis region, or drift tube. The drift tube consists of a stack of ring electrodes electrically connected via a chain of resistors with a uniform DC electric field gradient applied longitudinally. The drift tube is pressurized with a neutral buffer gas (i.e. helium, nitrogen, carbon dioxide, etc.) to induce ion-neutral collisions as the sample ions traverse the tube. As shown in Figure 2.1, larger ions experience more collisions, causing them to exit the drift tube later than the smaller ions.

The velocity achieved by sample ions in the drift tube is termed the drift velocity (v_d) and is proportional to the magnitude of the electric field (E) via the ion mobility coefficient (K , $\text{cm}^2 \cdot \text{V}^{-1} \cdot \text{s}^{-1}$) as shown in Equation 2.1.^{12,16}

$$v_d = KE \quad (2.1)$$

This equation is a first approximation, applicable to the swarm but not to individual ions. The ion mobility coefficient is constant at low electric fields where ions and buffer gas molecules possess approximately equivalent thermal energies.¹⁷ High electric fields are not commonly used because ions in them have significant energy between collisions, making K variable and the relationship between v_d and E nonlinear.

The v_d of an ion is affected by both the temperature, T , and number density, n , of the drift gas, so it is common to normalize the mobility coefficient to ambient temperature and pressure via the following equation.^{12,16}

$$K_o = K \left(\frac{273 \text{ }^\circ\text{K}}{T} \right) \left(\frac{P}{760 \text{ Torr}} \right) \quad (2.2)$$

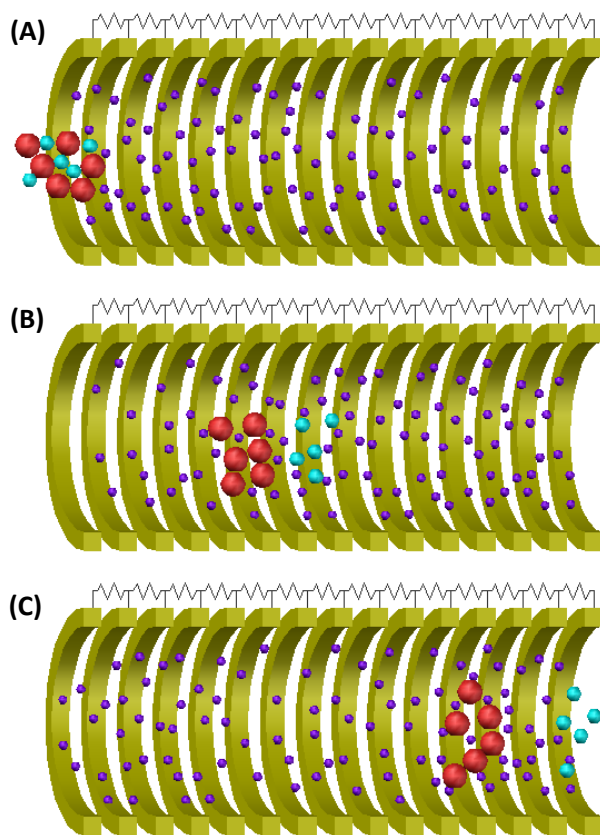


Figure 2.1: Representation of an IMS separation. A) A packet of large (red spheres) and small (blue spheres) ions is pulsed into the drift tube (brass cut rings), which is filled with a neutral buffer gas (purple spheres). B) As the ions drift through the buffer gas, they are separated by their mobility coefficients. C) The smaller ions will reach the end of the drift tube first, followed by the larger ions.

Pressure, P , describes the drift tube buffer gas, and the reduced mobility, K_o , shares the same units as K . The average gas-phase collision cross section of the swarm (CCS, Ω , \AA^2), can also be determined from measurement of the IM coefficient. This relation is described in Equation 2.3, from Chapman-Enskog kinetic theory, where q is ionic charge, μ is the reduced mass based on the ions and neutrals, and k_B is the Boltzmann constant.¹⁷

$$K = \frac{3}{8} \frac{q}{N} \left(\frac{\pi}{2\mu k_B} \right)^{\frac{1}{2}} \frac{1}{\Omega} \quad (2.3)$$

II.II.III. Motivation

In recent years, IM-MS has been applied across an increasingly broad range of technologies and applications. High sensitivity, resolving power, and throughput have helped establish this instrumentation in the analytical laboratory, and its popularity has been further bolstered by technological advances that have enhanced its practicality for studying a wide range of biological and medical samples. There is always demand for improvement, however, and one way to further enhance the figures-of-merit for IM-MS instrumentation is via multiplexing strategies for IM.

Multiplexing can be performed temporally or spatially, with either technique increasing the instrument throughput, or quantity of mobility separations performed within a single acquisition cycle. Temporal multiplexing is a form of oversampling where overlapping, time-dispersive ion pulses are introduced to the IMS, increasing sensitivity and throughput.^{18,19,20,21,22,23} One of the fundamental limitations of temporal multiplexing is that the acquired signal must be deconvoluted in post-processing, with data transformation introducing signal artifacts, though algorithms are being developed to assist in detection and removal of these artifacts.^{24,25,26} Spatial multiplexing involves multiple physically disparate analysis channels utilized in parallel. This type of analysis has been demonstrated with spatially dispersive IM including differential mobility

spectrometry (DMS) and asymmetric high-field IM (FAIMS),^{27,28} and the first implementation of spatial multiplexing with drift tube IM (DTIMS) is the subject of this work.

There are numerous benefits of spatially multiplexing IM instrumentation, as summarized in Table 2.1. (1) The throughput of a spatially multiplexed IM is theoretically a multiple of the throughput of a single channel instrument and the number of channels in the multiplexed IM, thus a spatially multiplexed instrument would exhibit higher throughput. (2) The sensitivity is ideally increased with the square root of the number of measurements. Therefore, if the same sample is analyzed in each channel, the multiplexed instrument's sensitivity would be higher than a single channel instrument by a multiple of the square root of the number of channels. (3) Multiple channels on one instrument platform offers greater versatility, enabling multiple experiments to be performed simultaneously on that platform. (4) While there are new imprecisions introduced by multiplexing an IM, calibrations can be made to correct for channel-to-channel variations decreasing precision. Factors that would decrease precision in a single-channel instrument can also be mitigated. For example, drift time deviation can occur over time for IM instrumentation due to variations in experimental parameters (i.e. pressure, temperature, and voltage) inherent to laboratory environments where temperature fluctuations occur. These temperature fluctuations induce an instrumental response to alter certain variables (i.e. buffer gas' number density) in order to maintain constant pressure and voltage. Because IM separation depends on the number of ion-neutral collisions in the drift tube, variation of the number density in the drift tube will alter drift times. Performing multiple experiments simultaneously on one IM platform avoids variations in laboratory parameters that can occur with time, such as temperature fluctuations or sample degradation. (5) Spatially multiplexing an IM allows a sample and control to be run simultaneously and, with channel-to-channel variation accounted for, higher accuracy can be attained by using the

Improved Figure-of-Merit	Explanation
Throughput	Multiple of the number of operating channel, $N = 8$
Sensitivity	Signal-to-noise ratio improved by signal averaging, $\sqrt{8} \approx 3.1$
Accuracy	Analyze control and sample concurrently
Precision	Average of larger number of measurements
Versatility	Analyze various samples for comparison

Table 2.1: Summary of the improved figures-of-merit expected for spatially multiplexed IM compared to single channel instrumentation.

control data to compensate for variation caused by fluctuations in experimental parameters. (6) Shared electronics and vacuum systems offer lower production costs and occupy less space than multiple instruments.

II.III. Materials and Methods

Unless otherwise noted, raw materials and components were purchased from McMaster-Carr (GA, USA). Custom parts were fabricated from raw materials in the Vanderbilt Physics Department Machine Shop. Machine drawings for custom components, assembly diagrams, and a complete list of the commercial components used in this research, along with identifying information and suppliers, can be found in Appendix B. Components related to the infrastructure and vacuum system include: vented or coated nuts and bolts (UC Components, CA, USA), RGCs for ion transfer (Photonis, MA, USA), electronics racks and micrometer translation stages (Thorlabs Inc., NJ, USA), high capacity dry scroll pumps (Edwards, West Sussex, UK), vacuum hardware (Duniway Stockroom Corp., CA, USA), stainless steel laser-drilled apertures, (Lenox Laser, MD, USA), borosilicate glass viewing panes (Gray Glass, NY, USA), and extruded aluminum framing, brackets, and linear bearings for the primary supporting infrastructure (GatorJaw, CA, USA; and Futura Industries, UT, USA).

High voltage DC power supplies (Applied Kilovolts, UK) are controlled with a high resolution analog output board (National Instruments, TX, USA). Radio frequency (RF) signals of identical amplitude, 180 degrees out of phase, are generated, amplified, and manipulated by a custom power supply with two remote RF oscillator high Q-heads (Ardara Technologies, PA, USA). Ion gating is accomplished by a transistor-transistor logic (TTL) signal sent from a multifunction reconfigurable input/output (RIO) board (National Instruments) through a voltage

pulsar (IonWerks, TX, USA). Electric circuit components include 5 kV and 10 kV resistors (Caddock Electronics, CA, USA), 100 pF ceramic capacitors (Vishay Intertechnology, PA, USA), Kapton coated wire (Kurt J. Lesker Company, PA, USA), high voltage feedthroughs (Accu-Glass Products, CA, USA), and printed circuit boards (PCB; Amitron, IL, USA). A PCB 8-channel Faraday plate detector array, used for IMS signal acquisition, is connected to the multifunction RIO board via a home-built amplifier, modeled after Intra and Tippayawong,²⁹ assembled on a custom PCB (Advanced Circuits, CO, USA) from operational amplifiers (Analog Devices Inc., MA, USA; Texas Instruments, TX, USA) and passive components (Bourns Inc., CA, USA; TE Connectivity, Switzerland; Vishay Intertechnology, PA, USA).

Ion trajectory simulations are performed with SIMION, Version 8.1 (Scientific Instrument Services, NJ, USA).³⁰ User programs designed in-house are coded with Lua programming language into SIMION to model the effects of RF fields, neutral gas flows, and ion collisions with neutral gas molecules.^{31,32,33} Computational fluid dynamics (CFD) modeling was done with COMSOL Multiphysics® software (COMSOL AB, Sweden)³⁴ and Simulation CFD software (AutoDESK, CA, USA)³⁵ for analysis of neutral gas flow dynamics. AutoCAD 3D-modeling software (AutoDESK, CA, USA)³⁶ is utilized to design custom instrument components. PCB schematics are designed with KiCad (open source software). LabVIEW software (National Instruments)³⁷ is used to control power supplies, gate ions, acquire signal, and visualize data.

II.IV. Results and Discussion

II.IV.I. Instrument Design Process

As with engineering, the design process for scientific instrument development relies on a

complex feedback system where multiple parameters including simulation results, material availability and cost, fabrication techniques, and laboratory conditions, among others, are juggled simultaneously to optimize instrument figures-of-merit. Numerous iterations of performance simulation and element design are executed in software before physical components are commissioned for fabrication. Here, software for simulation of ion trajectories helps determine appropriate electrode geometries to guide, focus, trap, or otherwise manipulate ions. Simulation conditions are varied within real world boundaries for theoretical parameters including electric field strength, gas pressure, channel dimensions, temperature, etc., to optimize various performance parameters including, for example, transmission in funnels, trapping efficiency in gating regions, and resolution in the drift tube. Preliminary geometries are evaluated with CFD modeling, specifically at the entrance capillaries and ion funnels where differential pumping causes significant neutral gas velocities that can impact ion transmission. Computer aided design (CAD) modeling software is used to develop and visualize custom parts in three-dimensions for fabrication. Consideration of first principles conductance calculations, machining capabilities, commercially available components and raw materials, etc., influence subsequent design iterations.

The 8-channel IMS instrument, shown in Figure 2.2A,³⁸ consists of an 8-array ESI source; RGCs (500 μm inner diameter, 140 mm length) mounted in a heated, stainless steel block; tandem, differentially pumped, stacked PCB ion funnels; gated 500 μm stainless steel aperture array; electrostatic, stacked brass ring electrode drift tube; and a Faraday plate array detector. The instrument is mounted on a custom table designed to facilitate assembly, kinematic stability, and routine maintenance within a compact design. Ion channel electrodes are fixed in-line on threaded rods shielded by high purity, precision cut ceramic tubes and are contained within custom-welded

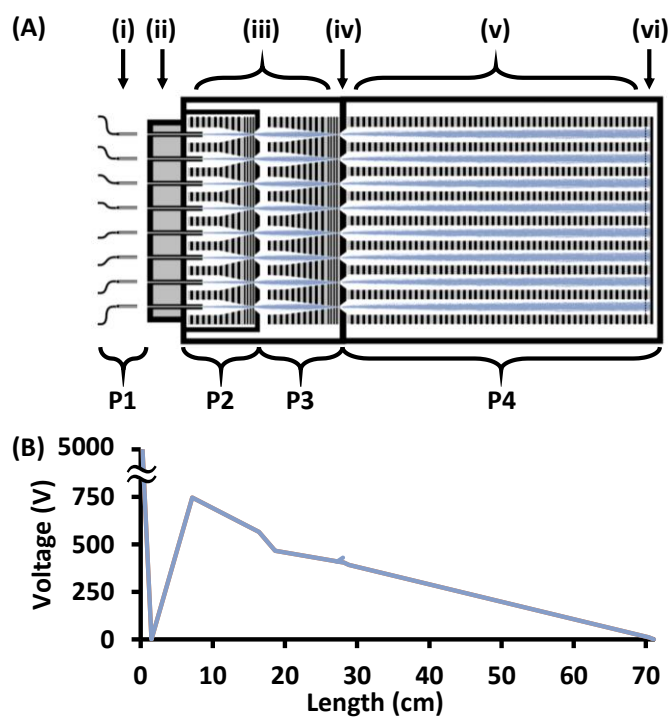


Figure 2.2: (A) Spatially multiplexed IM schematic consisting of (i) ESI source, (ii) RGCs mounted in a heated desolvation block, (iii) tandem, differentially pumped ion funnels, (iv) gated stainless steel aperture array, (v) electrostatic drift tube array, and (vi) Faraday plate array detector. Instrument components are shown in black, simulated ion trajectories are shown in blue. (B) Graph of operational DC voltage settings, predicted from ion trajectory simulation results, length scaled to the schematic in (A). Ordinate axis is broken to show high voltage application to ESI needles. RGCs' atmospheric end and Faraday detector are held at ground voltage, and apertures at ca. 28 cm are pulsed between voltages for gating.

stainless steel vacuum chambers which are mounted on extruded aluminum cradles, galvanized steel turntables, and a case-hardened steel rail system to facilitate multi-axis adjustment of the first vacuum chamber (linear motion along x and z, and y-axis rotation) relative to the second chamber for alignment and ease of maintenance.

II.IV.II. Modeling Electrode Geometries

While it can be tempting to first design and fabricate the vacuum chamber, the most visible of the instrument components, it is advantageous to develop from the inside outward, i.e. taking a bottom-up approach, relative to an ion's perspective. This method of form following function ensures a final structure best suited for preparation and measurement of ions. In addition, it prevents circumstances of designing around or within previously fabricated components, which can require compromise of function to save time and funds.

The innermost physical components, from an ion's perspective, are the electrode surfaces composing the ion channel and generating the electric fields used for ion manipulation. These electric potentials are modeled in SIMION 8.1, which solves the Laplace equation with finite difference methods and approximates ion behavior in the calculated electric fields. Simulation CFD was used to model gas flow in regions of significant velocity, including the RGCs and transition between the high pressure funnel and low pressure funnel. CFD results were coded into in-house user programs for application in SIMION to investigate effects of neutral gas flow velocity and direction on ion trajectories. For the multiplexed instrument, this combination of simulations was performed both to aid in design of the electrodes and to evaluate the instrument's theoretical performance. Successful electrode geometries were reconstructed in AutoCAD with added functionality for mounting and alignment within the vacuum system.

II.IV.III.I. Ion Mobility Drift Tube

Initial simulations focused on the portion of the device crucial to the experimental measurement, i.e. the IM drift tube. Performance parameters including sensitivity, resolution, and mass bias were assessed for ions spanning a wide range of mobilities and masses. Several iterations of simulations were performed and analyzed to optimize design variables of both longitudinal and radial dimensions: electrode thickness and spacing, channel length and diameter, and applied RF and DC voltages.

Figure 2.3 shows a summary of the drift tube ion trajectory simulations, which were modeled with SIMION HS1, hard sphere, collision model.³⁹ This collision model was selected for the drift tube without the incorporation of external CFD modeling results because HS1 default conditions approximate the expected experimental conditions; in HS1, elastic ion-neutral collisions are simulated in an environment where gas velocities follow the Maxwell-Boltzmann distribution and there is no net flow of the neutral gas. Simulation settings were comparable to conditions in existing IM instrumentation, with nitrogen buffer gas modeled at 4.0 Torr (533 Pa) and 298 K, and an ion gate pulse-width of 100 μ sec. Electric field strength is reported here as a ratio of the electric field intensity (E , V/cm) to the drift gas number density (n , cm^{-3}) in Townsends (E/n , Td), where 1 Td is equivalent to 10^{-17} V \cdot cm². In Figure 2.3(A), for methane and C₆₀ fullerene at low electric field conditions (5 Td), it is qualitatively shown that smaller ions (methane) experience greater radial diffusion as they traverse the IM drift tube. In addition, low field conditions are qualitatively shown to cause greater radial diffusion, as is observed when comparing trajectories of C₆₀ fullerene at low field (5 Td) and high field (60 Td) conditions. Because of the simulation results, mitigation of the worst-case scenario for diffusive ion loss (small ions at low electric field strength) was found to require a ratio of drift length to internal diameter of less than

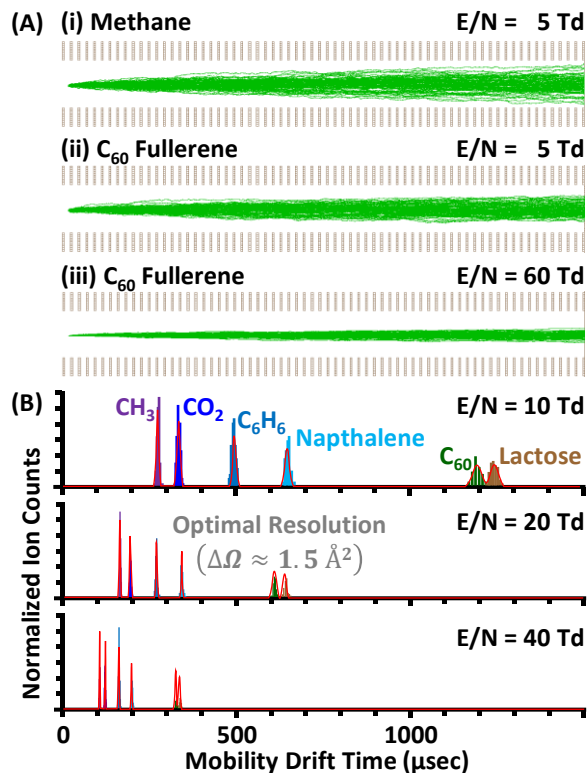


Figure 2.3: (A) Ion simulations direct the geometric design of the IM electrodes. Small ions at low field (i) represent the worst case for radially diffusive ion losses. Mitigating ion losses under these conditions requires a ratio of drift length to internal diameter to be less than ca. 50. (B) Theoretical IM spectra based on histograms of the arrival time distributions for the simulation data. Experimental parameters include drift tube length of 19.0 in (48.3 cm), pressure 4.0 Torr (533.3 Pa), temperature 298 K, and gate pulse width 100 μsec .

ca. 50. Simulated arrival time distributions for various molecules, representing a wide range of mobilities, are shown in Figure 2.3(B) to approximate what actual spectra from the multichannel instrument should look like.

Ion simulations indicate that avoidance of destructive radial ion diffusion for highly diffuse ions (mass-to-charge, $m/z < 200$) requires the drift tube inner diameter to be approximately 1.00 in (2.54 cm) for the chosen drift length at low electric field strength (< 5 Td). Thickness and spacing of electrodes were found to exhibit optimal performance when equivalent, though these parameters were much less influential on IM performance than the ratio of the drift length to internal diameter. Thus, electrode thickness and spacing were set at 0.080 in (2.0 mm) and 0.0625 in (1.59 mm) to accommodate use of commonly available thicknesses for the raw materials from which the brass electrodes and Delrin spacers were manufactured. These dimensions balance thinness for establishing uniformity of the electric field with thickness for maintaining structural rigidity, while keeping the electrode number (133) and corresponding electronic circuitry within a manageable order of magnitude. A drift length of 19.0 in (48.3 cm) was modeled based on desired resolution and voltage constraints for helium breakdown. The final internal diameter of the drift tube was selected to be 1.00 in (2.54 cm), and its length was shortened to 14.62 in (37.13 cm, 103 electrodes) for practical reasons with regard to installation in the existing vacuum chamber. The drift region was later extended, however, by addition of a narrow drift tube (0.500 in (12.7 mm) diameter ion channel) between the gating apertures and the full size drift tube, as described in Section II.IV.IV.IV, with ion trajectory simulations indicating ion loss due to radial diffusion would not increase due to the use of this narrower ion channel at the front of the drift tube.

Theoretical calculations suggest the drift tube array will perform with resolving powers ranging from 30 to 90 for a broad range of ions (m/z 100-10,000), comparable to the performance

of commercial instrumentation, with the capacity to resolve the protonated leucine/isoleucine (m/z 132) system. Figure 2.4 shows predicted conditional resolving power, calculated from the equations presented by Kanu, et al., plotted as a function of drift voltage and reduced mobility for various analytes, listed in Table 2.2, representing a wide range of sizes and chemical classes.⁴⁰ Simulations also predict near-lossless ion transmission across a wide range of mobilities and masses.

II.IV.II.II. Tandem Ion Funnels

Although the mobility measurement occurs solely in the drift tube, analyte preparation is another important process that includes manipulation within the vacuum system with as little loss as possible. Prior to introduction of the ion funnel in 1997, skimmer cones were commonly used to transfer ions from high to low pressure regions.⁴¹ Ion funnels have been increasingly utilized to focus charged molecules into a narrow beam for transfer through a small, gas conductance-limiting aperture, allowing much greater sensitivity than was previously attainable with skimmers.^{42,43,44} For the multichannel instrument, tandem ion funnels were utilized with differential pumping to accommodate the increased gas load inherent to operating multiple atmospheric inlets (see Section II.IV.III). This tandem ion funnel design was demonstrated previously by Richard Smith and coworkers and has also been incorporated into commercial instrumentation.^{45,46}

Simulations for the ion funnels were modeled with SIMION statistical diffusion simulation (SDS), high pressure, collision model.^{31,33} The hard-sphere model, HS1, is also appropriate for the given conditions, and was used for simulations in which the pressure was modeled at less than 1 Torr.³⁹ Both the SDS and HS1 models are user programs that simulate collisions of ions with neutral gas molecules, but where the hard-sphere model calculates every collision for every ion, the high pressure model applies an adjustment to ion motion at each time step to account for a

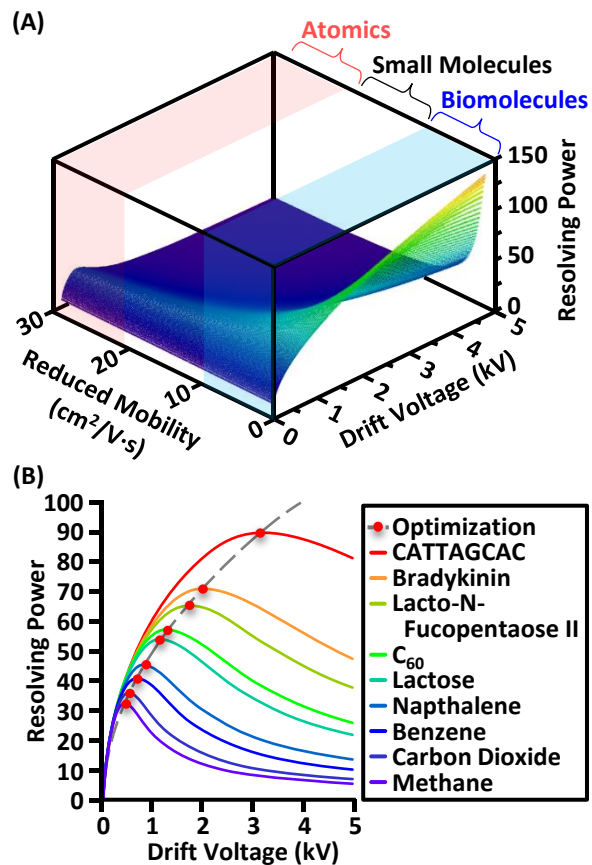


Figure 2.4: (A) Conditional resolving power 3D surface plot for positive, singly-charged ions as a function of reduced mobility and drift voltage for a single channel of the spatially multiplexed IM with parameters: 4.0 Torr nitrogen, 298 K, 19.0 in (48.3 cm) drift tube length, 1.0 in (2.54 cm) drift tube inner diameter, and 100 μ sec ion gate width. (B) Select resolving power curves taken from the 3D plot in (A) for the analytes in Table 2.2.

Analyte	Mass [Da]	K_0 [cm^2/Vs]	Ω^* [\AA^2]	Maximum Resolving Power (Theoretical)
CATTAGCAC Nucleic Acid	2723.28	1.10	486.2	90
Bradykinin Cardiac Peptide	1060.21	2.21	242.0	70
Lacto-N-Fucopentoase II Glycan	860.77	2.88	201.3	65
C_{60} Fullerene	720.64	4.32	122.6	56
Lactose Disaccharide Sugar	365.30	5.15	121.1	53
Napthalene	128.17	8.80	61.9	44
Benzene	78.11	11.80	46.6	40
Carbon Dioxide	44.01	18.40	30.5	35
Methane	15.03	24.00	25.1	32

* Calculated from the Mason-Schamp equation. Small mass ion CCS values are largely governed by the ion-helium interaction potential.

Table 2.2: Tabulated mobility data (reduced mobility, K_0 and collision cross sections, Ω) for various analytes representing a wide range of gas-phase mobilities and chemical classes.

Conversion from K_0 to CCS is described in Section I.III.I, Equation 2.16.

statistically predicted set of collisions, which is a less computationally expensive method. Previous research has found the SDS model to be applicable at least as low as 6 Torr,³¹ and preliminary studies for the multichannel instrument tandem ion funnels indicated that either collision model could be used effectively to predict ion transmission efficiency at least as low as 1 Torr. Simulations were utilized to determine the operational voltage settings that optimize ion transmission. Figure 2.5(A) shows example ion trajectories for 101 bradykinin [M]⁺ ions through the tandem ion funnels with near-lossless (~96%) ion transmission.

Fluid dynamics simulations were performed to investigate the behavior of neutral gas in the ion funnels, and the results were incorporated into SIMION simulations to determine the effect of neutral gas flow on ion transmission. Figure B.1.1 shows a three-dimensional perspective of the results for the neutral gas velocity in the tandem ion funnel geometry with differential pumping. The ion funnels had a keyhole geometry (Figure B.1.2) before the tandem ion funnel design (Figure B.1.3), and CFD models were compared (Figure B.1.4) to evaluate each design. Isosurfaces for velocity (Figure B.1.5(A)) and pressure (Figure B.1.5(B)) found from CFD modeling of the keyhole design were approximated by equations for ellipsoids and paraboloids in the three-dimensional Cartesian coordinate system (Figure B.1.5(C)). These equations, determined for multiple velocity and pressure magnitudes, were written into a SIMION user program (Figure B.1.6) for incorporation in the ion trajectory simulations. As described in Figure B.1.7, throughout the stages of development for the ion funnels of the spatially multiplexed instrument, experimental settings have been found such that the predicted ion transmission has always been near-lossless (> 96%), and the pressure and velocity magnitudes calculated by CFD modeling did not significantly impact ion transmission, supporting implementation of the tandem ion funnel geometry.

After establishing the tandem ion funnel geometry, experimental parameters were

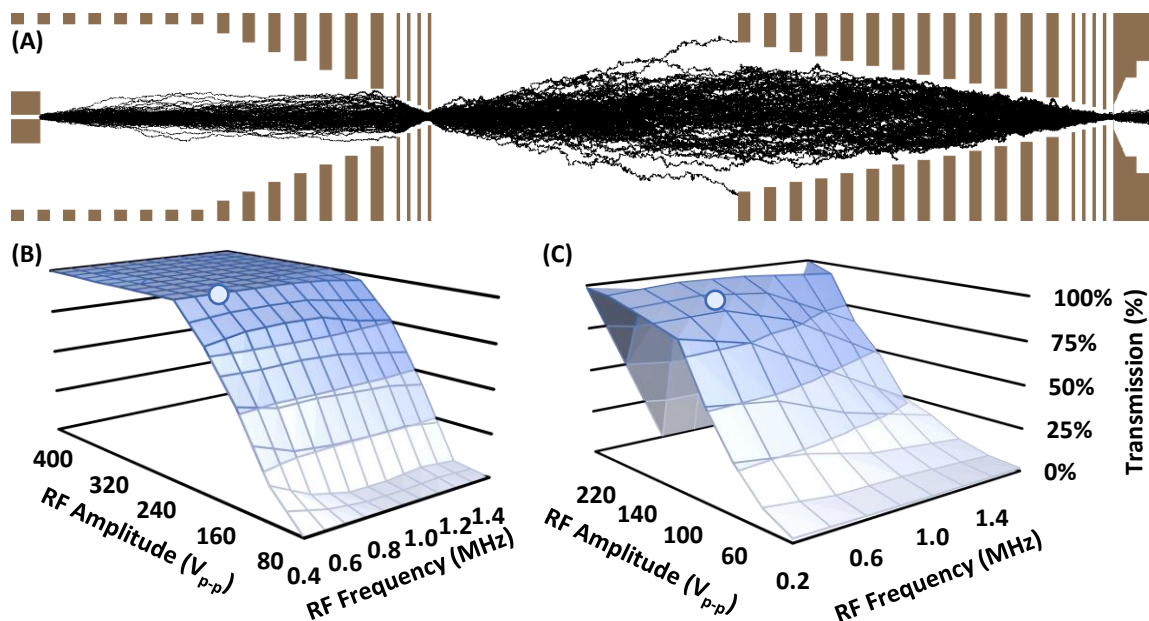


Figure 2.5: (A) Ion trajectory simulation for 101 bradykinin $[M]^+$ ions through tandem ion funnels. Electrodes are shown in brown and ion trajectories in black. High pressure funnel is held at 10 Torr and 300 V_{pp} RF, and low pressure funnel is operated at 4 Torr and 130 V_{pp} . Through both funnels, electric fields are low at ~ 5 Td, there is no neutral gas flow, and calculated transmission efficiency is $96.4 \pm 0.01\%$. (B) Simulation results for high pressure funnel at frequencies ranging from 0.4-1.4 MHz and amplitudes ranging from 60-400 V_{pp} at 10 Torr and 20 Td. Maximum transmission settings indicated by marker at 600 kHz and 200 V_{pp} for bradykinin $[M]^+$ ions. (C) Simulation results for low pressure funnel at frequencies ranging from 0.2-1.6 MHz and amplitudes ranging from 40-220 V_{pp} at 4 Torr. Maximum transmission settings indicated by marker at 600 kHz and 120 V_{pp} for bradykinin $[M]^+$ ions. Higher amplitudes resulted in ion trapping by the fields at the last low pressure funnel electrode, of the smallest channel diameter.

optimized to determine appropriate RF power supply settings. As shown in Figure 2.5(B), although changes in RF frequency were seen to have much less effect than changes in amplitude over the range of simulated values, 600 MHz resulted in the highest transmission efficiency, and has shown success previously in the literature, so this was the frequency selected for operation of both funnels.⁴⁵ The high pressure funnel was observed to transmit ions most efficiently at 200 V_{pp}, and the low pressure funnel at 120 V_{pp}. Higher RF amplitudes in the low pressure funnel were observed to collapse the field, meaning the proportion of time that the voltage is favorable for ion transmission in each RF cycle is decreased to the point that ions no longer have time to react to the field and pass through the aperture, and they are trapped at the narrowest electrode of the funnel. As a result of these simulations, a custom dual RF power supply was commissioned with two remote RF oscillator high Q-heads, both operating at 600 kHz with amplitude variable to 400 V_{pp}.

Funnel electrodes were fabricated from PCBS, rather than brass, because of their relatively lower electrical conductance (beneficial in the funnels where an RF voltage is applied in conjunction with the DC gradient) in addition to lower manufacturing costs and faster fabrication times. Like the raw materials for the drift tube, PCBs are available in common, predetermined dimensions that dictate the possible thicknesses for the electrode geometries. The standard PCB thickness of 0.063 in (1.6 mm) is the most cost-effective, but constructing the funnel solely of this PCB thickness was observed to reduce ion transmission. A thinner PCB of 0.02 in (0.5 mm) could be employed to keep the funnel transmission near 100%, but the cost for a funnel of this construction was exorbitant. According to ion trajectory simulations, the most crucial point of funneling occurs at the narrowest portion of the funnel, across the last few electrodes (exact number depends on various parameters), and the main function of the wider portion of the funnel

is to entrain the ions in the field and allow the neutral gas jet to dissipate. As a compromise, by constructing just the last few electrodes (four for the multichannel instrument) of each funnel from thinner PCBs, and the remainder of the funnel from standard thicker PCBs minimizes cost without sacrificing ion transmission.

II.IV.II.III. Gating Apertures

Simulations aided in determination of the orifice diameter of the apertures used to gate ions into the IM drift tube from the low pressure ion funnel. As shown in Figure 2.6, ion transmission was modeled for several commercially available aperture orifice sizes ranging from 200 μm to 1000 μm . As a result of these simulations, the aperture size was chosen to be 600 microns, a balance between the increased gas flow from the drift tube and transmission increases observed with larger orifices. The stainless steel apertures were adhered with conductive silver epoxy to a stainless steel plate that serves as part of the hermetic seal between the low pressure ion funnel and the IM drift tube.

II.IV.III. Vacuum System Requirements

Because of the eight ambient sampling inlets that impose a significant gas load, the spatially multiplexed IM instrument has vacuum system requirements that are greater than those of traditional instrumentation, although to increase analyte sensitivity, some single channel instruments utilize multi-capillary inlets that also exhibit increased neutral gas conductance.^{47,48} Unlike those multi-capillary, single channel instruments, gas flow in the multichannel instrument is also increased between subsequent pressure regions due to additional apertures accommodating extra ion channels. Exploring first-principles calculations of conductance between vacuum chambers assists in determination of which commercial pumps are capable of achieving desired

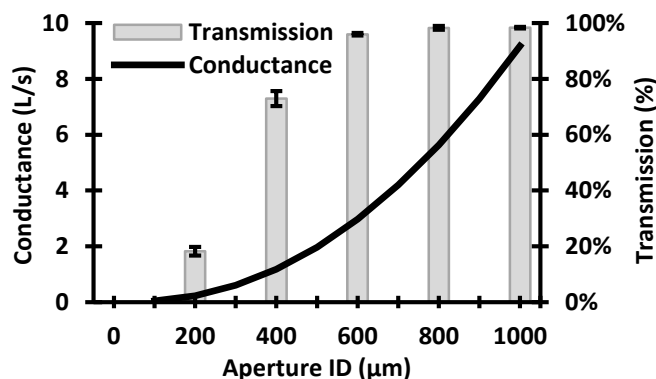


Figure 2.6: Simulated ion transmission versus theoretically calculated conductance for various aperture orifice inner diameters. Conductance was calculated at 100 μm aperture inner diameter intervals from the equations outlined in Section II.IV.III for eight apertures with the drift tube operating at 4.0 Torr nitrogen and the first vacuum chamber held at 3.8 Torr nitrogen. Only aperture inner diameter (200 μm , 400 μm , 600 μm , 800 μm , and 1000 μm) was varied in the simulations. For each inner diameter, 5000 bradykinin $[\text{M}]^+$ ions were simulated in five groups of 1000 particles at optimized RF voltages (determined from Figure 2.5) and at DC voltages of moderate field strength (20 Td). Ions were generated 1.5" (38 mm) outside the second ion funnel at 3.8 Torr with no neutral gas flow. The percentage of ions transmitted through each simulated aperture inner diameter is plotted. The aperture inner diameter chosen for the instrument was 500 μm , because this size balances the benefit of high ion transmission with the detriment of increased neutral gas conductance.

operational pressures.

The eight-channel instrument has four defined pressure regions, as indicated in Figure 2.2(A), including the atmospheric ESI source (PR1), high pressure ion funnel (PR2), low pressure ion funnel (PR3), and drift tube (PR4). In order to calculate the pumping speeds required to achieve desired pressures in each region, appropriate equations must be chosen based on the type of flow between those regions. The flow regime is defined by the ratio of the mean free path length (λ) to the diameter (d_p) of the path connecting two pressure regions.⁴⁹ This ratio is calculated as the Knudsen number (K_n , Equation 2.4), where $K_n \leq 0.01$ represents continuum (i.e. viscous) flow, $0.01 < K_n < 0.1$ represents slip flow, $0.1 < K_n < 10$ is considered transitional flow, and $K_n \geq 10$ denotes molecular flow.⁵⁰

$$K_n = \frac{\lambda}{d_p} \quad (2.4)$$

The equation for mean free path (Equation 2.7) can be derived from Equations 2.5 and 2.6.⁵¹

$$\lambda = \frac{1}{\sqrt{2}\pi d^2 n} \quad (2.5)$$

$$P = nk_B T \quad (2.6)$$

Here, d is molecular diameter, n signifies molecular number density, P is pressure, k_B is Boltzmann's constant, and T is temperature. Recommended values for Van der Waals hard sphere radii are available.⁵² By treating the molecules as hard spheres and implementing the ideal gas law (Equation 2.6), Equation 2.7 can be derived.

$$\lambda = \frac{k_B T}{\sqrt{2}\pi d^2 P} \quad (2.7)$$

For the multichannel instrument, the calculated values of K_n indicate all flows between pressure regions to be continuum except for gas movement between the drift tube and low pressure funnel (PR4→PR3), which is in the slip flow regime.

Neutral gas at atmospheric pressure near the ESI source is pulled into the vacuum system

(PR1→PR2) via an RGC of 7.09 in (180 mm) length and 0.01 in (250 μm) inner radius. Calculating the conductance here requires an equation for viscous flow through a long tube, for which the length is approximately 20 or more times longer than the diameter.⁵³

$$C_{TV} = \frac{0.1962(P_1+P_2)r^4}{\eta L} \quad (2.8)$$

where C_{TV} is the conductance for viscous flow through the tube, P_1 is the greater inlet pressure, P_2 is the lesser outlet pressure, r is the radius of the tube, η is the gas viscosity which can be found at multiple references ($1.8 \cdot 10^{-4}$ poise for nitrogen),^{54,55} and L is the length of the tube. The original reference requires specific units for each variable to correct for pressure in Torr, but here the multiplicative factor (0.1962) is unitless, and an approach by dimensional analysis is appropriate. An alternate method, based on a parameterization of the Knudsen equation to fit metal capillary data, yields a similar result.^{56,57}

$$C_{TV} = \frac{4r^3}{3L} \sqrt{\frac{2\pi k_B T}{m}} \left(\frac{0.1472r}{\lambda} + \frac{1 + \frac{3.50r}{\lambda}}{1 + \frac{5.17r}{\lambda}} \right) \quad (2.9)$$

In this equation, m represents the molecular weight of the neutral gas. Conductance (C) is converted to throughput, or flow rate, (Q) via Equation 2.10.⁵³

$$Q = C(P_1 - P_2) \quad (2.10)$$

The required pumping speed from the high pressure funnel is also dependent on the channel outlets to the low pressure funnel (PR2→PR3), for which a calculation of viscous flow through an orifice (or aperture, where the thickness is approximately 20 or more times smaller than the diameter) is appropriate. This flow rate can be approximated with Equation 2.13 after calculating the mean particle speed (\bar{c}) and finding the dimensionless flow function (ψ), as determined by the ratio of inlet and outlet pressures.⁵⁸ For gas passing through an orifice, the abrupt change in the diameter of the path causes the flow to be unguided, and the effective cross section of the opening

behaves as if it was contracted, to a degree, based on the pressure differential.⁵⁹ Due to this behavior, Equation 2.13 has also been posited to describe viscous flow through a nozzle, with a correction factor applied to the cross sectional area of the aperture (A) to account for the lessened flow rate resulting from unguided flow.⁵⁹

$$\bar{c} = \sqrt{\frac{8RT}{\pi m N_A}} \quad (2.11)$$

$$\psi = \sqrt{\frac{\gamma}{\gamma-1} \left[\left(\frac{P_2}{P_1}\right)^{2/\gamma} - \left(\frac{P_2}{P_1}\right)^{(\gamma+1)/\gamma} \right]} \quad (2.12)$$

$$Q_{OV} = \alpha A \sqrt{\frac{\pi}{4}} P_1 \bar{c} \psi \quad (2.13)$$

$$\alpha = \begin{cases} 0.60 & \text{if } P_2 \approx P_1 \\ 0.86 & \text{if } P_2 < P^* \end{cases} \quad (2.14)$$

Here, R is the universal gas constant, N_A is Avogadro's number, γ is the ratio of the specific heat of a gas at constant pressure to that at constant volume (i.e. isentropic exponent, 1.400 for diatomic gases including nitrogen), Q_{OV} represents the flow rate for viscous flow through an orifice, (α) is the correction factor (in Roth's work, α is omitted)⁵⁸ and P^* is the critical pressure ($P^* = 0.528 \cdot P_1$ for nitrogen).^{59,60}

In parallel, throughput is additive, so to account for the multiple channels and calculate the required pumping speed (S) at the pump entrance of the high pressure funnel, the results of the above equations are combined to total throughput (Q_T) as shown in Equation 2.15, and then converted to S via Equation 2.16.^{53,61,62}

$$Q_{TH} = 8Q_{TV} - 8Q_{OV} \quad (2.15)$$

$$S = \frac{Q_T}{P_{pump}} \quad (2.16)$$

Here, Q_{TH} specifically represents the total throughput for the high pressure funnel and can be substituted for Q_T , Q_{TV} has been converted from C_{TV} via Equation 2.10, and P_{pump} is the desired

pressure at the pump entrance. Although the flow rate from the high pressure funnel to the low pressure funnel (PR2→PR3) has already been discussed ($8 \cdot Q_{OV}$), neutral gas from the pressurized drift tube also contributes to the total throughput of the low pressure funnel (Q_{TL}). Gas moving through the apertures separating the drift tube and the low pressure funnel (PR4→PR3) is in the slip flow regime. Santeler provides an equation applicable to transition flow (defined there as flows between viscous and molecular, and thus applicable to slip flow) through an aperture that identifies the empirical contribution to the total throughput from the viscous and molecular flow regimes.^{61,63}

$$Q_{OT} = \theta Q_{OM} + (1 - \theta)Q_{OV} \quad (2.17)$$

$$\theta = \frac{P_R}{P_R + P_1} \quad (2.18)$$

The variables Q_{OT} and Q_{OM} represent throughput through an orifice for transition and molecular flow, respectively, θ is the fractional contribution of molecular flow, and P_R is a reference pressure close to the point at which effects of molecular and viscous flow are equivalent. Because in the molecular flow regime there are little to no collisions between molecules, they pass through an orifice without influencing each other, and their movement in both directions must be considered, as is done in Equation 2.19.^{53,58,64}

$$Q_{OM} = \beta A(P_1 - P_2) \sqrt{\frac{RT}{2\pi m N_A}} \quad (2.19)$$

Hablanian employs the correction factor, β , (in Roth's and Lafferty's works, β is omitted) to correct for the ratio of the thickness of the orifice (0.00197 in, 50.0 μm) to its inner diameter (0.0197 in, 500. μm).⁵³ The value of β (0.922 for the apertures used in this work) can be determined from a lookup graph⁶⁵ or by Equation 2.20, which empirically approximates the data and is applicable within the bounds of length-to-diameter ratios of 10^{-2} to 10^3 with an R^2 value of 0.99998.

$$\log\beta = -0.00228\log\left(\frac{L}{2r}\right)^5 + 0.01399\log\left(\frac{L}{2r}\right)^4 + 0.00686\log\left(\frac{L}{2r}\right)^3 - 0.21676\log\left(\frac{L}{2r}\right)^2 - 0.45050\log\left(\frac{L}{2r}\right) - 0.28254 \quad (2.20)$$

Equation 2.13 has already been introduced to approximate viscous flow through an orifice and can be used to calculate Q_{OV} for PR4→PR3. Applying the throughputs calculated from Equations 2.13 and 2.19 in Equation 2.17 gives the throughput for transition flow from the drift tube to the low pressure funnel through a single aperture. Combining the calculated throughputs as shown in Equation 2.21 yields Q_{TL} , which is converted to S via Equation 2.16.

$$Q_{TL} = 8Q_{OV} + 8Q_{OT} \quad (2.21)$$

To operate the spatially multiplexed instrument at pressures common to commercially available mobility instrumentation, as detailed in Figure 2.2(A), calculations indicated a required pumping speed in the high pressure funnel of approximately 24-32 L/s, and a required pumping speed in the low pressure funnel of approximately 5-7 L/s. Calculation results are listed in Table 2.3. These speeds are accomplished via two high-capacity dry scroll pumps, listed in Table B.16.

II.IV.IV. Hardware and Infrastructure

As discussed in Section II.IV.II, electrode geometries can be optimized through simulations, but those models aid only in determining the shapes and sizes of conductive surfaces. Design of additional infrastructure is necessary to mount and align electrodes in the real world, and physical properties of available raw materials must be considered concerning performance at operational pressure, temperature, and electrical conditions. Furthermore, vacuum chambers need to be designed to maintain proper operating conditions, and the entire instrument needs to be supported and stabilized on a structure, or table, with storage for electronics and adequate surface area from which the user can work. The discussion of such hardware and infrastructure can

	P1		P2		P3		P4
Pressure (Torr)	760	Flow→	5.0	Flow→	3.8	←Flow	3.95
Conductance Limit Diameter (mm)		0.50		2.0		0.50	
Conductance (C, L/s)		0.19-0.24		18-21		0.25-0.26	
Throughput (Q, Torr·L/s)		150-180	120-160	22-25	22-25	0.31-0.31	
Required Pumping Speed (S, L/s)	Gas Inlet		24-32		5.7-6.7		Gas Inlet

Table 2.3: Tabulated results from calculations of vacuum system requirements, finding a required pumping speed of 24-32 L/s at the inner vacuum chamber and 5.7-6.7 L/s at the first vacuum chamber.

logically be organized by following the path of the analyte from the ionization source to the detector. While most items are described here, further detail can be found in Appendix B, which contains the machine drawings for custom pieces designed for this instrument and the list of commercial components utilized in this research. Figure 2.7 displays a detailed, rendered cutaway of the assembled instrument, which will be referenced throughout this section to provide clarity.

II.IV.IV.I. Ionization and Desolvation

The prepared sample is first loaded into a glass syringe and dispensed, for a single channel, through a polyimide-coated, silica capillary (length 25 cm) by a single-syringe infusion pump that rests on the instrument table. PEEK fluidic fittings are used to couple the syringe to the silica capillary, and a PEEK tee fitting joins the silica capillary, ESI capillary needle (length 30 mm), and a 25 mm length of platinum wire, which is used to introduce high DC voltage to the liquid sample. The eight needle ESI source indicated in Figure 2.7(A) (assembly and component drawings in Figure B.2.1 through Figure B.2.10) was designed to mount on the same rail system as the first vacuum chamber and allows grouped and individual multi-point adjustment (linearly and rotationally) for ESI optimization of each channel by the use of slots, springs, XYZ micrometer, and goniometer. A strong electric field (ca. 3 kV/cm) exists between the stainless steel ESI capillary needle and the desolvation block (Figure 2.7(B) and Figure B.3.1), which is heated to ca. 100°C and thermally isolated from the first chamber by a custom thermoplastic (Delrin) flange (Figure B.3.2) and washers (Figure B.3.3). The heated desolvation block and atmospheric ends of the RGCs are thermally and electrically linked via metal-to-metal connection and held at earth ground with the instrument chassis, for safety. This connection also aligns the RGCs in the center of each ion channel, with the desolvation block mounting directly to the top hat flange (Figure B.3.4), fittingly named for its protruding shape.

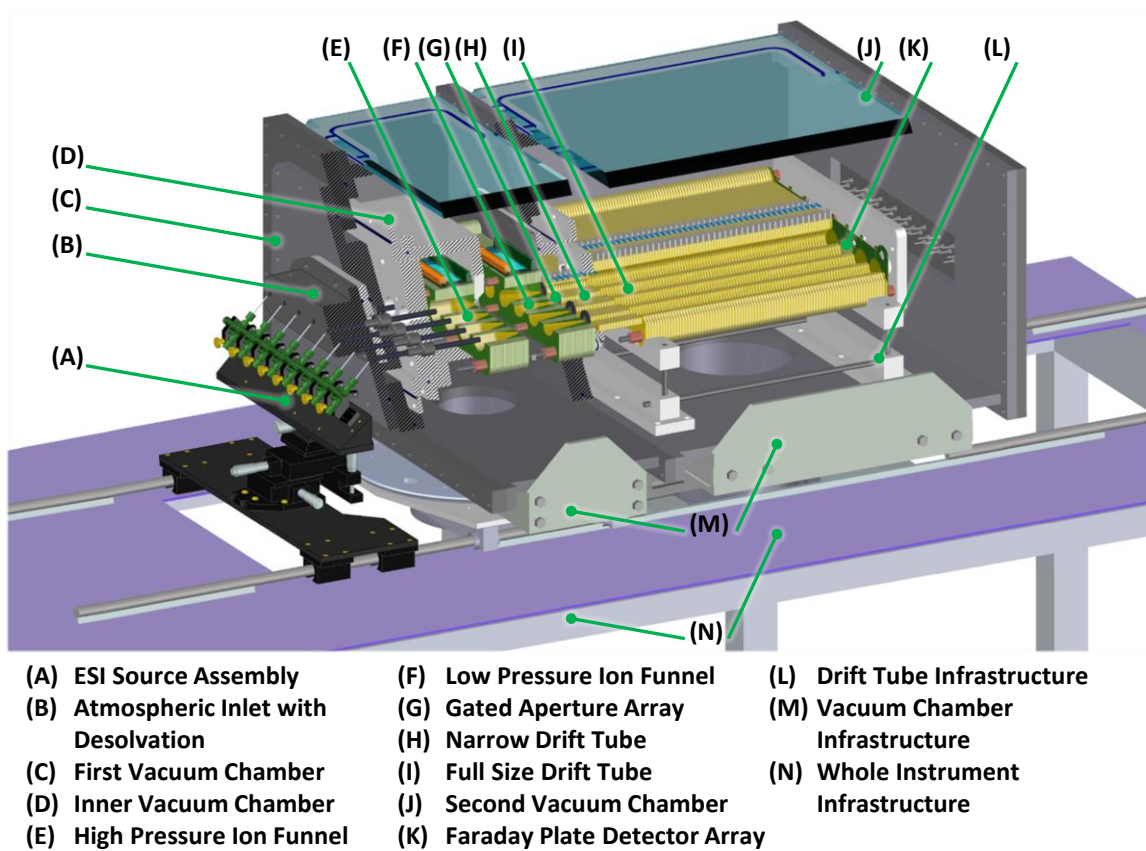


Figure 2.7: Rendered cutaway view of the assembled instrument.

The opposite ends of the RGCs, situated inside the vacuum system, are held at the same DC voltage as the first electrode of the high pressure funnel. The RGCs provide $1\text{ G}\Omega$ of resistance across 180 mm, and ions, drawn by the pressure differential, climb the electric potential gradient as they enter the vacuum system. A hermetically sealed electrical feedthrough (Figure B.3.6) is used to apply the DC voltage to the vacuum side of the RGCs, with the connecting wire being held in place by both by grooves cut in the funnel 1 mount block (Figure B.6.1) as well as to the nichrome-coated surface of the RGC by a steel spring of similar inner diameter to the outer diameter of the RGC. The feedthrough is mounted orthogonally to the axis of ion motion via a piston seal on the extension collar (Figure B.3.5, 1.5" (3.8 cm) thick), which is of a thickness that positions the ion exit of the RGC at the appropriate depth, just within the high pressure funnel.

An additional flange ($\frac{3}{4}$ " flange, Figure B.3.7) serves as an intermediate, sealing to the first vacuum chamber (Figure 2.7(C), assembly and component drawings in Figure B.4.1 through Figure B.4.8) with the assistance of a custom floating nut (Figure B.4.10) and supporting the contents of that chamber. An assembly support structure (assembly and component drawings in Figure B.14.1 through Figure B.14.4) was designed to move those contents out of the first vacuum chamber by 20 in (0.5 m) for easy installation and maintenance of the ion funnels, aperture array, and narrow drift tube. The assembly support structure consists of a braced, extruded aluminum frame set on a carriage-rail system with brackets on which to mount the four corners of the $\frac{3}{4}$ " flange.

II.IV.IV.II. Tandem Ion Funnels

Figure 2.7(D) indicates the inner vacuum chamber (component drawings in Figure B.5.1 through Figure B.5.3) that establishes the pressure differential between the tandem ion funnels. The inner vacuum chamber was fabricated from two blocks of Delrin thermoplastic, hermetically

joined via compression of a Viton O-ring. Although fabrication of this component from a single block of Delrin would have been a simpler design and easier to assemble, raw material of sufficient magnitude was not commercially available. No gas leak has been detected at the junction of the two sections of the inner vacuum chamber, indicating no compromise in function. Two ports were designed on the larger section of the inner chamber, with a dedicated electrical feedthrough at the top to supply RF and DC voltages to the funnel electrodes (described in Section II.IV.V), and a system of commercial vacuum bellows and flanges leading from the bottom port to a custom-welded pumpout flange (Figure B.4.9). While space was incorporated above the funnel electrodes to accommodate the resistor-capacitor (RC) circuit and electrical connections inside the inner vacuum chamber, the wall below the funnel electrodes was raised to accommodate the vacuum flanges by which the inner vacuum chamber is evacuated. Because the tapped mounting holes for the inner vacuum chamber are blind, compression of its face seal to the $\frac{3}{4}$ " flange (Figure B.3.7) represents one of several sites where vented bolts are required.

A set of ten threaded rods (Figure B.6.2) are used to mount and align the PCB electrodes of both funnels. These rods attach to the aforementioned top hat flange, via the funnel 1 mount block (Figure B.6.1), for consistent alignment with the RGCs. Each threaded rod is locked from rotation by tightening a nut down against each tapped hole in the funnel 1 mount block, similar to the two-nut locking method.⁶⁶ Locking rotation of the threaded rods allows for tightening of additional nuts further along the rods (after the inner vacuum chamber and after the aperture panel), as described below. Delrin standoffs (Figure B.6.3 and Figure B.6.4) with counterbore holes to house the locking nuts are used to position the high pressure funnel along the threaded rods, opening the area near the vacuum end of the RGCs to assist pumpout of neutral molecules. The opposite ends of the standoffs are counterbored to a depth of 0.500 in (1.27 cm) to center them on

the ceramic tubes (Figure B.6.5 and Figure B.6.6) which are used to align the PCB funnel electrodes precisely and shield the threaded rods electrically from the conductive PCB surfaces. The inner vacuum chamber, previously described, also mounts along the ten threaded rods and has counterbore holes (2 mm depth) to align the ion exits of the inner vacuum chamber (conically shaped to prevent loss due to increased radial ion diffusion across the pressure decrease) with the ion channels on the ion funnel electrodes and to tolerate compression of the stack of PCBs and Delrin spacers (described below) without shattering the alumina ceramic tubes. Compression and sealing of the high pressure funnel are achieved with polymer-coated washers and self-sealing nuts on the ten threaded rods (at the low pressure side of the inner vacuum chamber). A modified dog bone spacer (Figure B.5.4) is used to level progression across the ten threaded rods before mounting the low pressure ion funnel. A second set of Delrin standoffs (Figure B.6.10 and Figure B.6.11) and ceramic tubes (Figure B.6.12 and Figure B.6.13), similar to those previously described for the high pressure funnel, are used to electrically isolate the threaded rods and incorporate space before the low pressure funnel to assist pumpout of neutral molecules.

The dog-bone shaped PCB electrodes of the tandem ion funnels indicated in Figure 2.7(E) and Figure 2.7(F) (component drawing in Figure B.6.7) differ only by the silkscreen label, board thickness, and inner diameter of an array of eight vias that form the ion channels. The vias decrease from 23.0 mm to 2.00 mm inner diameter across the electrodes of the high pressure funnel, and from 18.5 mm to 2.00 mm across the low pressure funnel, as detailed in Figure B.6.8. Ion channel vias are linked by 1 oz copper traces of 0.0500 in (1.27 mm) width and are connected to smaller vias on two tabs, located at the top and bottom of each electrode, where wires are soldered to introduce the overlaid RF and DC voltages. Turns in traces are made at 45°, following the rule of thumb for PCB development that persists despite reports claiming no detriment comes from

sharper, right angle turns.⁶⁷⁻⁶⁹ While the majority of the funnel electrodes are 0.063 in (1.6 mm) thick, a standard measurement for flame retardant-4 (FR-4), two-layer PCBs, the last four electrodes of each funnel are 0.02 in (0.5 mm) thick to balance performance and cost, as described in Section II.IV.II.II. Delrin spacers (0.031 in (0.79 mm), Figure B.6.9) of similar, dog-bone shape are used to electrically isolate adjacent PCBs, with two spacers separating thicker boards and one spacer following thinner PCBs. The strength of the electric field is maintained by matching resistor value with the electrode spacing, as described in Section II.IV.V. The funnel electrodes each have ten mounting holes (four corners 12.7 mm diameter, six inset 9.53 mm diameter) for the ceramic tubes described above. An array of o-rings (Figure B.5.4) prevents the copper surface of the ion channel vias of electrode 19 (smallest inner diameter of high pressure funnel) from pressing directly against the back wall of the inner vacuum chamber.

II.IV.IV.III. Gated Aperture Array

An array of eight stainless steel apertures (Figure 2.7(G)) serve as the conductance limit between the low pressure funnel in the first vacuum chamber and the drift tube in the second vacuum chamber (assembly and component drawings in Figure B.7.1 through Figure B.7.8), establishing the pressure differential. An aperture panel (assembly drawing in Figure B.8.1, component drawing in Figure B.8.2) was designed with eight discrete holders (Figure B.8.3) to allow replacement of individual faulty apertures, as needed. The aperture panel mounts in line with the ion funnels along the set of ten threaded rods, and a hermetic seal, as well as compression of the low pressure funnel, is achieved with self-sealing nuts on the drift tube side of the aperture panel. Custom insulating washers (Figure B.8.4) with o-rings are used to isolate the aperture panel electrically from the threaded rods and self-sealing nuts. The front of each stainless steel holder has a shallow countersunk hole where an aperture is adhered, flush to the aperture panel surface,

with conductive silver epoxy. Adhered apertures cover an opening on the aperture holders with nearly eight times greater inner diameter that widens conically to the ion exit: designed to avoid ion collisions with the channel edges. Each aperture holder has four countersunk mounting holes, and because the complementary tapped holes in the aperture panel could not be made blind due to thinness of the material, o-rings (1/32 in width) are used around the threads of the #2-56 mount screws to seal the holes. A third set of o-rings are employed to seal the aperture panel, with compression achieved against the outer edge of each aperture holder when mount screws are installed. To seal the aperture panel with the walls separating the first and second vacuum chambers while maintaining electrical isolation, a Delrin flange (aperture panel piston seal, Figure B.8.5) is used with two o-rings to create a face seal to the aperture panel, mounting with a set of 16 tapped holes, and a piston seal to the back flange of the first chamber (Figure B.4.7). Seating of the piston seal occurs during installation of the front assembly, when the 3/4" flange is mounted to the first vacuum chamber.

II.IV.IV.IV. Ion Mobility Drift Tube

The ion mobility drift tube of the spatially multiplexed instrument consists of two portions: the narrow drift tube (Figure 2.7(H), component drawings in Figure B.9.1 through Figure B.9.6) and the full size drift tube (Figure 2.7(I), component drawings in Figure B.10.1 through Figure B.10.9). The narrow drift tube was incorporated after fabrication of the vacuum chambers, and it was designed to connect the gated aperture array to the full size drift tube by protruding through the narrow openings in the adjacent walls of the first and second vacuum chamber. A set of PEEK columns (Figure B.9.1) with blind tapped holes at each end, vented to negate a need for vented hardware, are used to align the electrodes and spacers of the narrow drift tube. A Delrin spacer (Figure B.9.2), large relative to other spacers of the narrow drift tube, is used to shield the drift

tube electrodes from the stainless steel aperture panel, and this spacer is the last component designed to accommodate the set of ten threaded rods on which the tandem ion funnels are mounted. The narrow drift tube is mounted to the aperture panel, rather than the full size drift tube, by a set of four vented bolts and blind tapped holes that align with holes on the mounting tabs of the narrow drift tube tabbed electrode (Figure B.9.3). The tabbed electrode also has five countersunk holes for the screws that thread into the PEEK columns, along which custom spacers (Figure B.9.4) are alternated with narrow drift tube middle electrodes (Figure B.9.5), terminating with a final narrow drift tube electrode (Figure B.9.6) that has countersunk holes, similar to the tabbed electrode, but no mounting tabs. All three variations of the narrow drift tube electrodes have an array of eight holes, forming the ion channels that are 0.500 in (12.7 mm) inner diameter, as discussed in Section II.IV.II.I. These ion channels are half the diameter of the full size drift tube to be accommodated on the smaller electrodes, designed to fit in the narrow opening between the first and second vacuum chambers. All narrow drift tube electrode variations also have asymmetric electrical tabs on the top and bottom, which are staggered across the top of the drift tube in assembly, to which the DC voltage is applied. All spacers and electrodes of the narrow drift tube have circular cutouts along the top and bottom edges permitting juxtaposition with the mounting materials of the full size drift tube, described below.

The full size drift tube is mounted on the front mount block (Figure B.10.1), which has counterbore holes to recess the nuts and washers used to compress the drift tube, and a central cavity that accommodates the narrow drift tube and the line of resistors that chain together its electrical tabs, with a tight tolerance that assures ion channel alignment upon installation. A second set of ten threaded rods (Figure B.10.2), similar to those used in the first vacuum chamber, are used to mount and align the full size drift tube, with electrodes being positioned by Delrin standoffs

(Figure B.10.3 and Figure B.10.4) and electrically isolated by ceramic tubes (Figure B.10.5 and Figure B.10.6). The electrodes and spacers of the full size drift tube (Figure B.10.7 and Figure B.10.8), although thicker, share the dog-bone shape of the ion funnel electrodes, with an array of eight 1.00 in (25.4 mm) holes forming the ion channels. Resistors are attached to the electrical tabs, connecting adjacent electrodes as depicted in Figure 2.7. The back mount block (Figure B.10.9) has through holes for mounting the ten threaded rods.

The support structure indicated in Figure 2.7(L) was built to cradle the full size drift tube (assembly diagram in Figure B.11.1). The support cradle (Figure B.11.2) rests on a carriage and rail system to allow the full size drift tube to slide along the axis of ion movement and to facilitate installation. A system of bolts, shaft collars, and tapped holes (Figure B.11.3 through Figure B.11.5) allow alignment and leveling of the drift tube.

II.IV.IV.V. Faraday Detector

The Faraday detector (Figure 2.7(K), Figure B.10.12) is manufactured on a PCB with the same dog-bone shape of the other instrument electrodes. Traces that encircle the detector pads and connect to a tab at the bottom of the board are held at a higher DC voltage to reduce noise and prevent crosstalk between ion channels at the detector. The detector board mounts on the same ten threaded rods of the full size drift tube, between the last drift tube electrode and the back mount block. Each exposed copper pad in the array of eight has a discrete connection to a tab at the top of the board, at which a Kapton coated wire is soldered to transmit electrical current, originating from the termination of ions, via the the Faraday feedthrough flange (Figure B.7.9) to the signal acquisition system, as described in more detail in Section II.IV.V. The feedthrough flange seals to the back wall of the second vacuum chamber with a Viton o-ring, and an array of eight holes and

blind, tapped bolt circles for bulkhead clamps facilitate the attachment and sealing of eight electrical feedthroughs.

II.IV.IV.VI. Infrastructure

The first vacuum chamber, which was mentioned briefly in Section II.IV.IV.I, houses the tandem ion funnels, gating apertures, and a portion of the narrow drift tube. As shown in Figure 2.7, the inner vacuum chamber, which was thoroughly discussed in Section II.IV.IV.II, is housed within the first vacuum chamber and contains the high pressure ion funnel. The second vacuum chamber (Figure 2.7(J)), mentioned in Section II.IV.IV.III, contains the ion mobility drift tube and Faraday detector. The design of these vacuum chambers and supporting infrastructure is described here.

The first and second vacuum chambers are similar in design. Both chambers consist of six flanges (Figure B.4.2 through Figure B.4.7, and Figure B.7.2 through Figure B.7.8) and a glass viewport (Figure B.4.8 and Figure B.7.8). The individual flanges were tack welded at the exterior surface, and then the inner joints were fully welded to provide a gas-tight seal. After assembly, each chamber was tested under vacuum to ascertain its ultimate pressure. Detection of leaks was performed by monitoring the chamber pressure during localized application of methanol, and discovered leaks were labelled, so that the welds could be improved. The borosilicate viewports were designed for each chamber to display the contents for teaching purposes, even when the instrument is in operation. When the instrument is pumped down, negative pressure inside the chambers pulls on the borosilicate panes, compressing o-rings for a robust seal. The glass tops can also be easily removed, when the instrument is vented to atmospheric pressure, for easy access and maintenance in either chamber. The bottom flange of each chamber has a large port for pumping,

although the port to the second chamber is closed with a valve after initial pump-down, and remains closed during operation. The scroll pumps for the spatially multiplexed instrument rest on a separate, shock-absorbing surface to isolate vibrational noise from the detection system.

Assembly diagrams for the support structures of the first and second vacuum chambers are shown in Figure B.12.1 and Figure B.12.5 (Figure 2.7(M)). Both chambers rest on extruded aluminum cradles (Figure B.12.2 and Figure B.12.3, Figure B.12.6 and Figure B.12.7) which are designed to allow linear adjustment along a plane parallel to the table surface. The first vacuum chamber is fixed, via an intermediate plate (Figure B.12.4), to a galvanized steel turntable and a case-hardened steel rail system (Figure B.12.11 and Figure B.12.12) that facilitates multi-axis adjustment (linear motion along x and z, and y-axis rotation), relative to the second chamber, for alignment and ease of maintenance. The second vacuum chamber is securely mounted to the instrument table via a set of low-profile, angled support beams and modified commercial brackets (Figure B.12.8 through Figure B.12.10).

A custom table (Figure 2.7(N), assembly diagram in Figure B.13.1) was designed to support the instrument hardware and electronics. A large cutout in the table top (Figure B.13.2) allows for the lower pumping flanges of the first and second vacuum chambers. Two lines of mount holes in the table top allow attachment of the rail support shafts, and holes along the perimeter allow the aluminum surface to be secured to the table frame. The table's sturdy, extruded aluminum frame (component drawings in Figure B.13.3 through Figure B.13.7) is designed to accommodate standard rack-mounted supplies, permitting installation of shelves, drawers, and control and read-back units. Adapter plates (Figure B.13.8) are used to attach caster wheels that allow the instrument to be relocated easily, which proved especially useful during multiple laboratory expansions and renovations.

II.IV.V. Electronics

II.IV.V.I. Power Supply Units

Details of the power supply units of the spatially multiplexed instrument are listed in Table B.16. The ESI source is supplied by a 6 kV, 20 mA unit, with options to limit voltage or current, as required. The ESI source supply is rack-mounted to the instrument chassis, and high voltage from its output cable is introduced to the liquid sample by means of an alligator clip, which is soldered to the cable and clamped on the platinum wire described in Section II.IV.IV.I. Additional DC voltages are supplied by nine high voltage modules. Each unit has reversible polarity through zero and less than 65 mV (peak to peak) ripple at full load. Two linear AC to DC transformers, rated to 4.8 A each, convert 120 V wall power to 24 VDC, required by the DC modules to amplify a voltage control input of ± 10 V. The DC units are able to source or sink current up to 400 μ A or 1 mA for the 2.5 kV or 1 kV supplies, respectively. Two 2.5 kV units supply DC to the vacuum end of the RGC and the first and last electrodes of the high pressure ion funnel. Seven 1 kV units supply DC to the low pressure ion funnel, gated aperture array, drift tube, and Faraday detector. The nine DC modules are secured with custom brackets (Figure B.15.6 and Figure B.15.7) in rack-mounted drawers. Output cables carry the DC voltages through safe high voltage (SHV) connectors, mounted on panels at the back of each drawer, to the appropriate breakout box where they are bundled in nine-conductor cables prior to crossing into the vacuum system (shown in Figure 2.9). A dual RF power supply controller with two remote RF oscillator heads accepts wall power and provides two 180° out of phase signals for each ion funnel circuit. Both heads are manufactured to output 600 kHz, with one matched to the 750 pF load of the high pressure funnel, and the other matched to the 660 pF load of the low pressure funnel. The dual RF supply is rack-mounted to the instrument chassis, and bayonet Neill-Concelman (BNC) connectors carry RF

signals to the breakout boxes to be bundled in the nine-conductor cables that lead into the vacuum system. Wiring diagrams for power supplies are shown in Figure B.17.1 and Figure B.17.2.

II.IV.V.II. Tandem Ion Funnels

Theory and implementation of the ion funnel will not be discussed at length here, as they have been previously described.^{42,44,46} Diagrams for the RC circuits of the spatially multiplexed instrument tandem ion funnels can be found in Figure 2.8. The DC gradient is established by applying a DC voltage to the first and last electrode in each funnel and connecting each PCB electrode via a chain of resistors. The chosen resistance magnitude of each ion funnel circuit keeps current and power low (~ 1 mA and ~ 0.1 W) in weak electric fields (~ 10 Td), with 10 k Ω resistors across 1.6 mm spacing and 5 k Ω resistors across 0.80 mm spacing (to maintain consistent electric field), as indicated in Figure 2.8. Calculating power and current across each circuit with Ohm's Law⁷⁰ determined the minimum rating required for each resistor to be less than 0.5 W. Additional DC inputs are optional and offer versatility that can be incorporated in later experiments. RF voltage applied to adjacent electrodes is 180° out of phase. Capacitance magnitude was chosen such that the RF cycle would be greater than one time constant (a measure of capacitor discharge),⁷⁰ making 100 pF capacitors suitable to the 600 kHz frequency used in each ion funnel.

On the PCB circuit boards detailed in Figure B.15.1 and Figure B.15.2, passive components are soldered along with terminal blocks that provide a means of connection to 15 cm Kapton coated wires. Those Kapton-coated wires are soldered to the upper electrical tabs of the ion funnel PCB electrodes, as shown in Figure 2.9(A). DC voltage inputs to the PCB circuit boards are carried to the atmospheric side of the instrument by Kapton coated wires through 9 -pin subminiature-C connectors and feedthroughs on the first vacuum chamber feedthrough flange. As shown in Figure 2.9(B), the individual wires of the two nine-conductor cables are matched with appropriate RF and

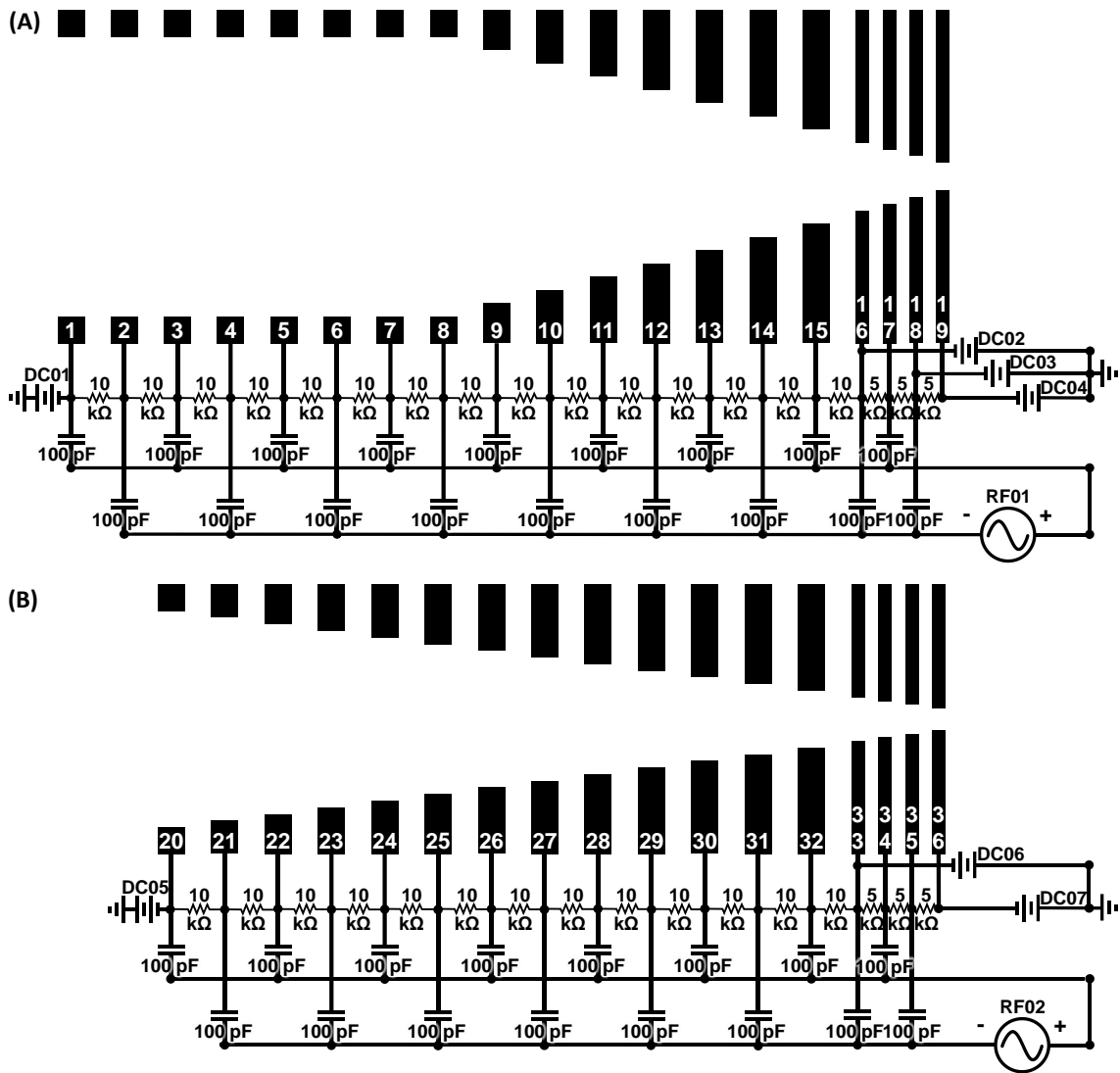


Figure 2.8: Electric circuits for tandem ion funnels. Funnel electrodes are represented by two-dimensional cross sections, with ion motion proceeding from left to right within each funnel. (A) Schematic for high pressure ion funnel. (B) Schematic for low pressure ion funnel.

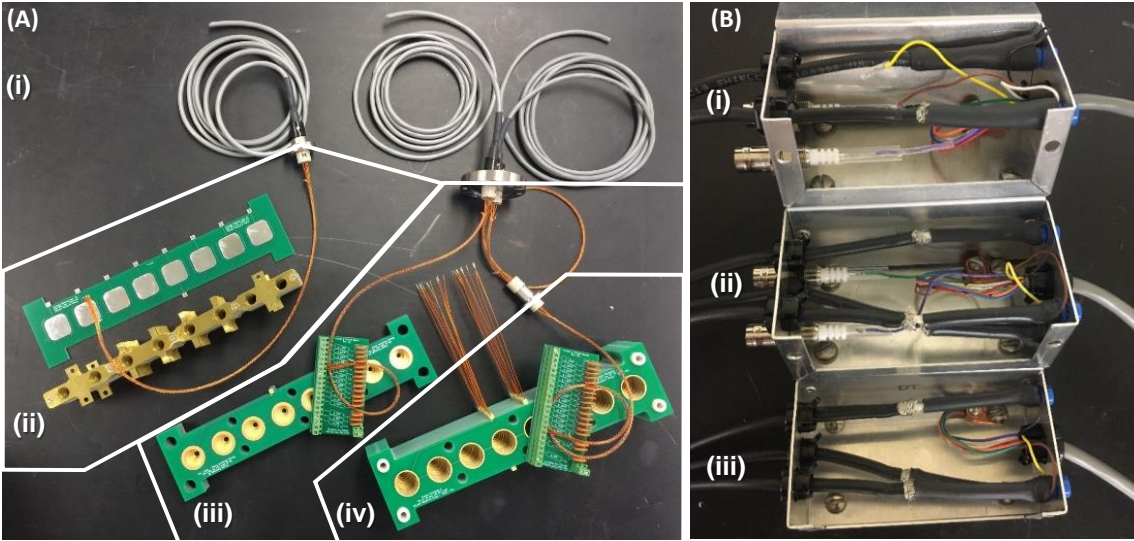


Figure 2.9: Pictures of some electronic components and cables, displayed for clarity. (A) PCB electrodes and circuit boards for the tandem ion funnels, brass electrodes for the narrow drift tube, and a prototype PCB Faraday detector. (i) Atmospheric-side cables are shown with nine-pin subminiature-C connectors on feedthrough flanges. (ii) A bundle of Kapton coated wires connects to the detector and drift tube. (iii) The low pressure ion funnel is shown with its RC circuit board and a bundle of Kapton coated wires. (iv) The first funnel is shown with Kapton coated wires soldered to the electrical tabs that connect to terminal blocks on the RC circuit board. A bundle of Kapton coated wires connects to the same feedthrough flange as the low pressure funnel via an intermediate feedthrough mounted at the top of the inner vacuum chamber. (B) Breakout boxes for (i) high pressure funnel, (ii) low pressure funnel, and (iii) drift tube. The gray cables at the right are the same seen in (A) (i). More detail on cable connections can be found in Appendix B.17.

DC voltages at custom breakout boxes (component drawings in Figure B.15.3 and Figure B.15.4). Figure B.17.3 and Figure B.17.4 show details of the electronic connection for the tandem ion funnels.

II.IV.V.III. Aperture Array

The aperture array is mounted on a conductive stainless steel plate, and apertures are adhered to the plate with conductive silver epoxy. One of the Kapton coated wires is attached to the aperture panel to apply the DC voltage to all apertures simultaneously. Currently, gating is not employed, but means of incorporating this feature, necessary for initializing each ion packet, is discussed in Chapter III.

II.IV.V.IV. Drift Tube

The drift tube electronics are much simpler than those of the tandem ion funnels. The DC gradient is established by applying a DC voltage to the first electrode of the narrow drift tube and the last electrode of the full size drift tube and connecting each brass electrode via a chain of resistors. DC voltage inputs are carried to the brass electrodes by Kapton coated wires from a nine-pin subminiature-C connector on the feedthrough flange of the second vacuum chamber. The nine-pin subminiature-C feedthrough connects to atmospheric-side nine-conductor cables that are matched with appropriate DC voltages at a custom breakout box (component drawing in Figure B.15.5), as shown in Figure 2.9. Figure B.17.5 shows details of the electronic connections for the drift tube.

II.IV.V.V. Detector

The Faraday plate detector array consists of eight copper pads on a PCB. A track connects each detector pad to a discrete electronics tab at the top of the board. Kapton coated and shielded wires are soldered to a via on each tab with vacuum-compatible silver solder. These wires pass

through the Faraday feedthrough flange via safe high voltage (SHV) shielded feedthroughs to be amplified and acquired by software. One DC voltage is applied to an electrical tab at the bottom of the Faraday plate detector, with connecting traces encircling each pad to serve as barriers to reduce noise and prevent cross talk between ion channels. At the time of this work, signal gathered by one detector is fed to a single-channel picoammeter operational amplifier, built in-house, and the voltage output can be read either by oscilloscope or software developed in LabVIEW, described in Section II.IV.VI. Circuit diagrams and calculations for the picoammeter (Figure B.15.8), which models that described by Intra and Tippayawong, are shown in Figure B.17.6.^{29,71}

II.IV.VI. Control and Acquisition

National Instruments LabVIEW was selected as the development test bed for the control and acquisition software of the spatially multiplexed instrument because of efficient development times, compatibility across a broad range of hardware, data acquisition capabilities, and previous deployment in IM-MS.^{72,73} Programs in LabVIEW are produced via a graphical programming technique, which can make software design accessible to more researchers.⁷⁴ LabVIEW programming incorporates sub programs termed virtual instruments (VIs), each of which consist of a front panel and block diagram. The executable program is built in the block diagram, and the front panel serves as a user interface, communicating with the block diagram, with the user supplying inputs via controls and the software displaying outputs via indicators.

Images of the front panel and block diagrams of the software developed for the spatially multiplexed instrumentation can be found in Appendix B.18. A flow chart of movement of information from the software to the instrument is shown in Figure 2.10. As shown in Figure B.18.1, the front panel design is kept simple to make the software easier to use. The device status

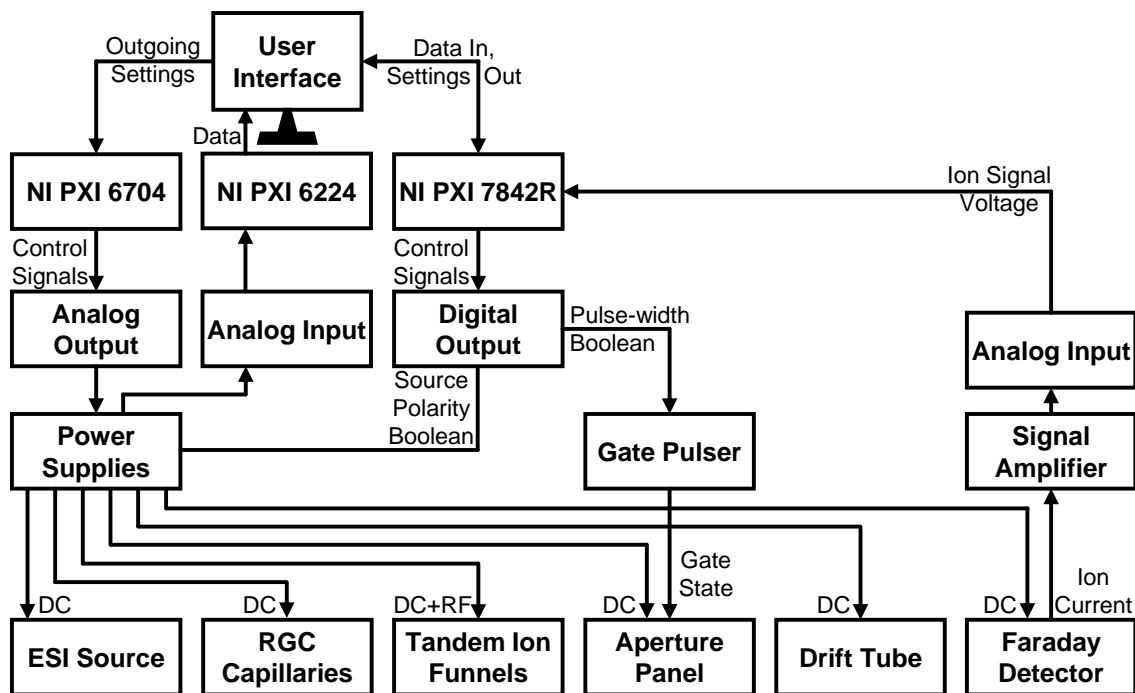


Figure 2.10: System block diagram showing flow of information. Control settings programmed from the LabVIEW user interface go through analog and digital outputs to power supplies, and DC and RF voltages are applied to appropriate instrument components. Voltage and current monitors on power supply units are read back at the user interface via analog input. Ion current at the Faraday detector is amplified and read as voltage via an analog input.

is indicated at the top of the screen, along with any error notifications. Graphs at the top show signal acquisition and monitor instrument voltages during operation. The elapsed time is displayed to notify the user of how long the program has been running. Controls to set voltages are aligned across the top of an instrument schematic, with labels that identify where various voltage controls are applied in the instrument. A list of optional operational voltages is shown to prompt the user with possible starting inputs. Cases of the program behind the front panel are shown in Figure B.18.2 through Figure B.18.4. Running the main program in LabVIEW will initialize the plots on the front panel, according to the block diagram shown in Figure B.18.5, but the program will not attempt to enter the running state until the user presses the start button from the front panel. Pressing the stop button will terminate execution of the software at any time (Figure B.18.2). When the start button is pressed, the voltage settings from the front panel are checked against safe operational voltage values (Figure B.18.6). As Figure B.18.3 shows, if the set voltages exceed safe values, an error message is displayed for the user and the device stays in the idle state. When the voltages are found to be within safe limits, the device enters the running state (Figure B.18.4) and sends the voltages, which are scaled down and offset to correct for variability in individual power supply units, to PXI-6704 for communication with power supplies (Figure B.18.7). In addition, while running, voltage monitors are retrieved from PXI-6224, scaled, and displayed to show the user the actual voltage applied to the instrument (Figure B.18.8). Time is kept to show the user how long the program has been executing (Figure B.18.9). A field-programmable gate array (FPGA) is used to collect ion signal as voltage (Figure B.18.11). The collected ion signal is averaged and normalized for display on the front panel plot (Figure B.18.10).

II.V. Conclusions

This work describes the theoretical considerations and development of a spatially multiplexed ion mobility spectrometer that offers advances in throughput, sensitivity, and versatility, among other benefits. The instrument consists of arrays of eight ESI sources, RGCs, tandem ion funnels, gated apertures, drift tubes, and detectors, with all components housed in a single vacuum system, utilizing one set of electronics, and supported by shared hardware. The ESI source was designed allowing grouped and individual multi-point adjustment (linearly and rotationally) for optimization of each channel. Electric potentials were modeled to determine optimal electrode geometries based on simulated ion trajectories. Vacuum chambers were developed and vacuum pumps were chosen based on first-principles pumping calculations and CFD modeling results. Infrastructure was developed from suitable materials to provide proper alignment and support of electrodes while isolating pressure regions and facilitating ease of maintenance and assembly. Electronics were designed to safely deliver the appropriate electric potentials modeled in initial simulations. Software was developed to provide a link between the user and the instrument for control, feedback, and signal acquisition. Results from preliminary testing, plans to incorporate gating electronics, and approaches to troubleshoot existing obstacles are described in Chapter III.

II.VI. Supporting Information

Simulation results from CFD and ion trajectories, machine drawings of all custom components, a table of components purchased commercially, electronic schematics, diagrams showing logic for control and acquisition software, and photographs taken during the development of the instrument described here can be found in Appendix B.

II.VI. Acknowledgements

The author would like to thank Jody C. May, especially, for his preliminary work on this project and years of mentorship in instrument development. The author acknowledges the initial research and development of this instrument conducted by Sevugarajan Sundarapandian. The author is also grateful to the undergraduate students under her mentorship, including Alexa M. Zytneck for her contributions to the electronics and breakout boxes and Babatunde H. Bello for his foundational work on the instrument control and acquisition software. Gratitude is extended further to graduate students including Andrew D. La Croix, Caleb B. Morris, and James N. Dodds, who were once mentees and always willing to lend mind or muscle to the development of the described instrument. Additional appreciation is extended to a few particularly helpful representatives from various companies including Jim Edwards of Applied Kilovolts, Ltd., Kristen Kannen of National Instruments, and David Robinson of Pfeiffer Vacuum, Inc.

Financial support for this work was provided by the National Science Foundation (CHE1229341), the US Defense Threat Reduction Agency (HDTRA1-09-1-0013), a Vanderbilt Institute of Chemical Biology Fellowship and Pilot Grant, Vanderbilt Institute for Integrative Biosystems Research and Education, a Vanderbilt College of Arts and Sciences Discovery Grant, and the Mitchum C. Warren Endowment Fund.

II.VII. References

1. I. Marquez-Sillero, E. Aguilera-Herrador, S. Cardenas and M. Valcarcel, Ion-mobility spectrometry for environmental analysis, *TrAC, Trends Anal. Chem.*, 2011, **30**, 677-690.
2. J. Enders, C. Marasco, A. Kole, B. Nguyen, S. Sevugarajan, K. Seale, J. Wikswo and J. McLean, Towards monitoring real-time cellular response using an integrated microfluidics-matrix assisted laser desorption ionisation/nanoelectrospray ionisation-ion mobility-mass spectrometry platform, *IET systems biology*, 2010, **4**, 416-427.
3. W. Sun, J. C. May and D. H. Russell, A novel surface-induced dissociation instrument for ion mobility-time-of-flight mass spectrometry, *International Journal of Mass Spectrometry*, 2007, **259**, 79-86.
4. W. Sun, J. C. May, K. J. Gillig and D. H. Russell, A dual time-of-flight apparatus for an ion mobility-surface-induced dissociation-mass spectrometer for high-throughput peptide sequencing, *International Journal of Mass Spectrometry*, 2009, **287**, 39-45.
5. J. J. Thomson, On the Electrolysis of Gases, *Proceedings of the Royal Society of London*, 1895, **58**, 244-257.
6. J. E. Lovelock and E. M. Wasilewska, An Ionization Anemometer, *Journal of Scientific Instruments*, 1949, **26**, 367.
7. E. McDaniel, D. Martin and W. Barnes, Drift tube-mass spectrometer for studies of low-energy ion-molecule reactions, *Review of Scientific Instruments*, 1962, **33**, 2-7.
8. D. L. Albritton, T. Miller, D. Martin and E. McDaniel, Mobilities of mass-identified H³⁺ and H⁺ ions in hydrogen, *Physical Review*, 1968, **171**, 94.
9. M. J. Cohen and F. Karasek, Plasma chromatographyTM—a new dimension for gas chromatography and mass spectrometry, *Journal of Chromatographic Science*, 1970, **8**, 330-337.
10. F. W. Karasek, Plasma chromatography, *Analytical Chemistry*, 1974, **46**, 710A-720a.
11. G. M. Bird and R. A. Keller, Vapor concentration dependence of plasmagrams, *Journal of Chromatographic Science*, 1976, **14**, 574-577.
12. G. A. Eiceman and Z. Karpas, *Ion mobility spectrometry*, CRC press, Boca Raton, 2nd edn., 2005.
13. G. A. Eiceman and J. A. Stone, Ion Mobility Spectrometers in National Defense, *Analytical Chemistry*, 2004, **76**, 390 A-397 A.
14. J. B. Fenn, M. Mann, C. K. Meng, S. F. Wong and C. M. Whitehouse, Electrospray ionization for mass spectrometry of large biomolecules, *Science*, 1989, **246**, 64-71.

15. K. Tanaka, H. Waki, Y. Ido, S. Akita, Y. Yoshida and T. Yohida, Protein and polymer analyses up to m/z 100,000 by laser ionization time-of-flight mass spectrometry, *Rapid Communications in Mass Spectrometry*, 1988, **2**, 151-153.
16. P. R. Kemper and M. T. Bowers, Electronic-state chromatography: application to first-row transition-metal ions, *Journal of Physical Chemistry*, 1991, **95**, 5134-5146.
17. E. W. McDaniel and L. Viehland, The transport of slow ions in gases: Experiment, theory, and applications, *Physics Reports*, 1984, **110**, 333-367.
18. F. J. Knorr, R. L. Eatherton, W. F. Siems and H. H. Hill, Jr., Fourier transform ion mobility spectrometry, *Analytical Chemistry*, 1985, **57**, 402-406.
19. M. E. Belov, B. H. Clowers, D. C. Prior, W. F. Danielson, 3rd, A. V. Liyu, B. O. Petritis and R. D. Smith, Dynamically multiplexed ion mobility time-of-flight mass spectrometry, *Analytical Chemistry*, 2008, **80**, 5873-5883.
20. B. H. Clowers, M. E. Belov, D. C. Prior, W. F. Danielson, Y. Ibrahim and R. D. Smith, Pseudorandom Sequence Modifications for Ion Mobility Orthogonal Time-of-Flight Mass Spectrometry, *Analytical Chemistry*, 2008, **80**, 2464-2473.
21. B. H. Clowers, Y. M. Ibrahim, D. C. Prior, W. F. Danielson, M. E. Belov and R. D. Smith, Enhanced Ion Utilization Efficiency Using an Electrodynamic Ion Funnel Trap as an Injection Mechanism for Ion Mobility Spectrometry, *Analytical Chemistry*, 2008, **80**, 612-623.
22. M. Kwasnik, J. Caramore and F. M. Fernández, Digitally-Multiplexed Nanoelectrospray Ionization Atmospheric Pressure Drift Tube Ion Mobility Spectrometry, *Analytical Chemistry*, 2009, **81**, 1587-1594.
23. G. A. Harris, M. Kwasnik and F. M. Fernández, Direct Analysis in Real Time Coupled to Multiplexed Drift Tube Ion Mobility Spectrometry for Detecting Toxic Chemicals, *Analytical Chemistry*, 2011, **83**, 1908-1915.
24. S. A. Prost, K. L. Crowell, E. S. Baker, Y. M. Ibrahim, B. H. Clowers, M. E. Monroe, G. A. Anderson, R. D. Smith and S. H. Payne, Detecting and removing data artifacts in Hadamard transform ion mobility-mass spectrometry measurements, *Journal of the American Society for Mass Spectrometry*, 2014, **25**, 2020-2027.
25. R. H. St. Louis, W. F. Siems and H. H. Hill, Apodization functions in Fourier transform ion mobility spectrometry, *Analytical Chemistry*, 1992, **64**, 171-177.
26. X. Zhang, R. Knochenmuss, W. F. Siems, W. Liu, S. Graf and H. H. Hill, Evaluation of Hadamard Transform Atmospheric Pressure Ion Mobility Time-of-Flight Mass Spectrometry for Complex Mixture Analysis, *Analytical Chemistry*, 2014, **86**, 1661-1670.
27. S. Zimmermann, N. Abel, W. Baether and S. Barth, An ion-focusing aspiration condenser as an ion mobility spectrometer, *Sensors and Actuators B: Chemical*, 2007, **125**, 428-434.

28. F. Tang, X. Wang, L. Zhang and Z. Yan, Study on simulation and experiment of array micro Faraday cup ion detector for FAIMS, *Science China Technological Sciences*, 2010, **53**, 3225-3231.
29. P. Intra and N. Tippayawong, Development of a fast-response, high-resolution electrical mobility spectrometer, *Korean Journal of Chemical Engineering*, 2011, **28**, 279-286.
30. D. Manura and D. A. Dahl, *SIMION (R) 8.0 User Manual*, Scientific Instrument Services, Inc., Ringoes, NJ, 2008.
31. A. D. Appelhans and D. A. Dahl, SIMION ion optics simulations at atmospheric pressure, *International Journal of Mass Spectrometry*, 2005, **244**, 1-14.
32. D. A. Dahl, T. R. McJunkin and J. R. Scott, Comparison of ion trajectories in vacuum and viscous environments using SIMION: Insights for instrument design, *International Journal of Mass Spectrometry*, 2007, **266**, 156-165.
33. H. Lai, T. R. McJunkin, C. J. Miller, J. R. Scott and J. R. Almirall, The predictive power of SIMION/SDS simulation software for modeling ion mobility spectrometry instruments, *International Journal of Mass Spectrometry*, 2008, **276**, 1-8.
34. COMSOL Multiphysics® v.5.2. www.comsol.com, COMSOL AB, Stockholm, Sweden.
35. Simulation CFD v.2013. www.autodesk.com, AutoDESK, California.
36. AutoCAD v.2015. www.autodesk.com, AutoDESK, California.
37. LabVIEW v.2015. www.ni.com/labview, National Instruments Corporation (U.K.) Ltd., Berkshire.
38. J. C. May and J. A. McLean, Ion Mobility-Mass Spectrometry: Time-Dispersive Instrumentation, *Analytical Chemistry*, 2015, **87**, 1422-1436.
39. D. Manura, Collision Model HS1, http://simion.com/info/collision_model_hs1.html, (accessed March, 2011).
40. A. B. Kanu, M. M. Gribb and H. H. Hill, Jr., Predicting Optimal Resolving Power for Ambient Pressure Ion Mobility Spectrometry, *Analytical Chemistry*, 2008, **80**, 6610-6619.
41. R. D. Smith, K. Tang and G. A. Anderson, *U.S. Pat.*, WO9749111A1, 1997.
42. S. A. Shaffer, K. Tang, G. A. Anderson, D. C. Prior, H. R. Udseth and R. D. Smith, A novel ion funnel for focusing ions at elevated pressure using electrospray ionization mass spectrometry, *Rapid Communications in Mass Spectrometry*, 1997, **11**, 1813-1817.
43. S. A. Shaffer, D. C. Prior, G. A. Anderson, H. R. Udseth and R. D. Smith, An ion funnel interface for improved ion focusing and sensitivity using electrospray ionization mass spectrometry, *Analytical Chemistry*, 1998, **70**, 4111-4119.

44. T. Kim, A. V. Tolmachev, R. Harkewicz, D. C. Prior, G. Anderson, H. R. Udseth, R. D. Smith, T. H. Bailey, S. Rakov and J. H. Futrell, Design and Implementation of a New Electrodynamic Ion Funnel, *Analytical Chemistry*, 2000, **72**, 2247-2255.
45. Y. Ibrahim, K. Tang, A. V. Tolmachev, A. A. Shvartsburg and R. D. Smith, Improving Mass Spectrometer Sensitivity Using a High-Pressure Electrodynamic Ion Funnel Interface, *Journal of the American Society for Mass Spectrometry*, 2006, **17**, 1299-1305.
46. R. T. Kelly, A. V. Tolmachev, J. S. Page, K. Tang and R. D. Smith, The ion funnel: theory, implementations, and applications, *Mass Spectrometry Reviews*, 2010, **29**, 294-312.
47. T. Kim, H. R. Udseth and R. D. Smith, Improved Ion Transmission from Atmospheric Pressure to High Vacuum Using a Multicapillary Inlet and Electrodynamic Ion Funnel Interface, *Analytical Chemistry*, 2000, **72**, 5014-5019.
48. T. Kim, K. Tang, H. R. Udseth and R. D. Smith, A Multicapillary Inlet Jet Disruption Electrodynamic Ion Funnel Interface for Improved Sensitivity Using Atmospheric Pressure Ion Sources, *Analytical Chemistry*, 2001, **73**, 4162-4170.
49. M. Barisik and A. Beskok, Molecular free paths in nanoscale gas flows, *Microfluidics and Nanofluidics*, 2015, **18**, 1365-1371.
50. G. Karniadakis, A. Beşkök and N. R. Aluru, *Microflows and Nanoflows : Fundamentals and Simulation*, Springer, New York, NY, 2005.
51. G. A. Bird, *Molecular Gas Dynamics and the Direct Simulation of Gas Flows*, Oxford University Press, 1994.
52. A. Bondi, van der Waals Volumes and Radii, *Journal of Physical Chemistry*, 1964, **68**, 441-451.
53. M. H. Hablanian, *High-vacuum technology: a practical guide*, CRC Press, 1997.
54. G. P. Flynn, R. V. Hanks, N. A. Lemaire and J. Ross, Viscosity of Nitrogen, Helium, Neon, and Argon from -78.5° to 100°C below 200 Atmospheres, *The Journal of Chemical Physics*, 1963, **38**, 154-162.
55. J. Kestin, S. T. Ro and W. A. Wakeham, Viscosity of the Noble Gases in the Temperature Range $25-700^{\circ}\text{C}$, *The Journal of Chemical Physics*, 1972, **56**, 4119-4124.
56. M. Knudsen, The Law of the Molecular Flow and Viscosity of Gases Moving through Tubes, *Annals of Physics*, 1909, **28**, 75-130.
57. S. A. Tison, Experimental data and theoretical modeling of gas flows through metal capillary leaks, *Vacuum*, 1993, **44**, 1171-1175.
58. A. Roth, *Vacuum Technology*, Elsevier, Amsterdam, 2nd edn., 1982.

59. K. Jousten, *Handbook of vacuum technology*, Wiley-VCH, Weinheim, 2008.
60. B. W. Andersen, *The Analysis and Design of Pneumatic Systems*, John Wiley & Sons, New York, 1967.
61. D. J. Santeler, Gas-flow experiments in the transition region, *Journal of Vacuum Science & Technology A*, 1994, **12**, 1744-1749.
62. P. J. Biltoft and M. A. Benapfl, Vacuum Technology, *Theory and Laboratory Exercises*, Las Positas College, 2002, 126.
63. S. Demuth and J. S. Watson, *Prediction of flow rates through an orifice at pressures corresponding to the transition between molecular and isentropic flow*, 1986.
64. J. M. Lafferty, *Foundations of Vacuum Science and Technology*, John Wiley & Sons, Inc. [US], New York, 1998.
65. M. Deserno, Linear and Logarithmic Interpolation, https://www.cmu.edu/biolphys/deserno/pdf/log_interpol.pdf, (accessed Nov 01, 2017).
66. B. Eccles, *Fastener & Fixing*, 2008, (54), 106-107.
67. M. I. Montrose, *Time and frequency domain analysis for right angle corners on printed circuit board traces*, Denver, Colorado, 1998.
68. D. G. Brooks, *Printed Circuit Design*, 1998, 1-5.
69. D. G. Brooks, N. Codreanu and J. Adam, *Printed Circuit Design & Fab/Circuits Assembly*, 2017, (1), 22-27.
70. H. V. Malmstadt, C. G. Enke and E. C. Toren, Jr., *Electronics for scientists: Principles and experiments for those who use instruments*, W. A. Benjamin, Inc., New York, 1963.
71. A. P. D. P. Intra and N. Tippayawong, *An electrostatic sensor for nanometer-sized aerosol particles detection*, 2009.
72. E. J. Davis, B. H. Clowers, W. F. Siems and H. H. Hill, Comprehensive software suite for the operation, maintenance, and evaluation of an ion mobility spectrometer, *International Journal for Ion Mobility Spectrometry*, 2011, **14**, 117.
73. D. C. Howse, Ph.D. Thesis, University of Birmingham, 2015.
74. J. Travis and J. Kring, *LabVIEW for Everyone: Graphical Programming Made Easy and Fun (3rd Edition) (National Instruments Virtual Instrumentation Series)*, Prentice Hall PTR, 2006.

CHAPTER III

PRELIMINARY RESULTS FOR AN EIGHT-CHANNEL SPATIALLY MULTIPLEXED ION MOBILITY SPECTROMETER

III.I. Introduction

Chapter II describes the motivation, simulates the performance, and establishes operational parameters for a spatially multiplexed IM spectrometer. Details of the simulations and calculations that went into the theoretical design of the spatially multiplexed instrument, considerations of software, geometries, and electronics contributing to its development, and explanations of fabrication and assembly concerning materials, manufacturers, methods, and more are also included in Chapter II. The eight-channel IM is currently undergoing iterations of testing, troubleshooting, modification, and optimization. This section expresses the current state of the instrument, covering preliminary data, existing obstacles, and forthcoming endeavors.

III.II. Preliminary Results

III.II.I. Vacuum System

Prior to complete fabrication and assembly, initial testing was conducted on individual instrument components and systems including investigation of vacuum chamber seals and scroll pump gas displacement performance. The welded stainless steel vacuum chambers were individually leak tested, with blank flanges installed to reduce the number of possible leak sources. The scroll pump used in testing could achieve a minimum pressure of 0.020 Torr with no load. In

initially testing, a leak was found in the first vacuum chamber, specifically at the junction of the top flange and feedthrough flange, which limited the base pressure to above 3.0 Torr. Leak testing involved monitoring the base pressure for an abrupt increase, while small aliquots of methanol were sprayed along each seal to isolate the location of the leak, and the offending weld of the first vacuum chamber was located and subsequently remade. After modification, the first vacuum chamber achieved a pressure of 0.025 Torr after 30 minutes of pumping, and 0.018 Torr after two hours. Testing the second vacuum chamber revealed robust welds, with a base pressure of 0.032 Torr measured after 30 minutes of pumping. These pressures are sufficiently low relative to the operational pressures, which are greater by two orders of magnitude.

Results of another vacuum system test, evaluating the pumping speed of the Edwards XDS35i scroll pump, are shown in Figure C.1. Pressure measurements were taken during pump down of the first vacuum chamber, which has a calculated internal volume of 25 L. These results indicated that pump down of the instrument from atmosphere should take at least six minutes, and that the empirically tested pumping speed is comparable to that reported by the manufacturer.

III.II.II. Electronics

Testing of electronic components and circuits was also performed to confirm safe operational limits, diagnose faulty components, identify assembly errors, etc. Assessment of cables, connectors, printed circuits, and soldered components involved measuring resistance between conductors to ensure robust connections as desired and adequate insulation where required. The linearity, gain, and drift of the DC power supply modules were evaluated by comparing measurements of the input control voltages to measurements of the high voltage outputs. With the instrument at atmospheric pressure, output voltages were measured at the

electrodes comprising the ion channels. Results from these experiments (listed in Table C.1) are subsequently programmed into the LabVIEW instrument control software to calibrate each individual power supply to match the supply and readback voltages. Because the empirically-measured voltage offsets are linear (R^2 values of 1.000), the calibration factors can be derived from the slope-intercept equation, where the high voltage output (ordinate, y-axis) is plotted against the input control voltage (abscissa, x-axis), with the slope and intercept representing the true gain and the voltage drift from zero, respectively.

Confidence in safe bounds for passive electronic components was established by applying voltage approximately 20% greater than operational values. Though useful in detecting errors, testing can be destructive; for example, during high voltage testing, the high pressure ion funnel's resistor-capacitor (RC) circuit was found to have been wired incorrectly, so that an atypically high voltage and current were applied across DC02 and DC03 (as labeled in Figure B.15.1). This test revealed the wiring error, but destroyed two 5 k Ω resistors, as shown in Figure B.19.5, which had to be replaced and retested. In proper operation, two DC supplies are linked by the RC circuit, and the two supplies source and sink current up to 1 mA, which, over the full resistance of each funnel, is well below the rated power maximums for the passive components used in the assembly.

In measuring the DC voltages applied to electrodes while the instrument was under vacuum, erratic behavior was observed at higher voltages representing the upper voltage limits of instrument operation as determined through ion simulations. This behavior, which manifested as an abrupt voltage drop and subsequent fluctuation of the readback potential, was found to correlate with the initiation of corona streamers and glow discharges within the vacuum chambers. By inspecting the ion optics assembly through the upper borosilicate plate of each vacuum chamber, these electrical discharges can be observed with the naked eye as purple glows and sparks of light.

Photographs of these discharges occurring in the spatially multiplexed instrument are included in Figure B.19.25. Investigation of the Paschen breakdown curve equation¹ indicates the minimum breakdown voltage occurs near the operational pressures of the instrument.

$$V_B = \frac{B_{N_2} \cdot P \cdot d_e}{\ln(A_{N_2} \cdot P \cdot d_e) - \ln\left(\ln\left(1 + \frac{1}{\gamma_{se}}\right)\right)} \quad (3.1)$$

Here, V_B is the breakdown voltage, A_{N_2} and B_{N_2} are experimentally determined coefficients that are constants over a restricted range of E/P (E is electric field) for a given gas, P is pressure, d_e is the distance between electrodes or conductive surfaces, and γ_{se} is the experimentally measured secondary electron emission coefficient, which varies for different materials and gases. Values for A_{N_2} ($11.8 \text{ cm}^{-1} \cdot \text{Torr}^{-1}$) and B_{N_2} ($325 \text{ V} \cdot \text{cm}^{-1} \cdot \text{Torr}^{-1}$) are constant in the E/P range of $100 \text{ V} \cdot \text{cm}^{-1} \cdot \text{Torr}^{-1}$ to $600 \text{ V} \cdot \text{cm}^{-1} \cdot \text{Torr}^{-1}$.¹ Values for γ_{se} , available from various sources, are specific to the conductor material and gas, among other measurement-specific parameters, and range from 0.1 to 0.47 for N_2 with Cu, stainless steel 304, or Al¹⁻³ and from 0.81 to 1.65 for N_2 with brass⁴ (metals common to the multiplexed instrument). Solving Equation 3.1 over these variable ranges yields many solutions, and thus it is difficult to theoretically determine one specific breakdown voltage for the instrument. However, the compilation of results indicate that lowest magnitude of the breakdown voltage occurs in a pressure range of 1.4 to 7.0 Torr (assuming a value of 0.79 mm for d_e , which is the minimum known spacing between conductive, unconnected surfaces). Unfortunately, this range of pressures in which electrical breakdown is likely to occur corresponds to the operational pressure range of the instrument. To mitigate this issue, coronas and discharges within the instrument can be prevented by coating conductive surfaces at points of high E in insulating material. In the multiplexed instrumentation, Super Corona Dope 4226 (MG Chemicals) and Kapton sheets have been incorporated in multiple locations, with some applications shown in Figure B.19.5, Figure B.19.6, Figure B.19.8, and Figure B.19.26. Although coronas and discharges

are no longer visible during instrument operation, monitoring operational voltages for the abrupt, erratic behavior previously seen indicates that they are still occurring at the upper range of operational voltages, which are initially determined through ion simulation results. Another way to prevent coronas and discharges is to operate the instrument parameters (i.e., pressures and voltages) within limits of their occurrence. Figure 3.1 shows the results of the experiments to empirically establish the limits of corona and/or discharge initiation, where the voltage was increased until the phenomena were observed (corona initiating) and then decreased until the behavior ceased (corona quenching). Note that once a discharge is initiated, a significantly lower voltage is required to quench that discharge, since gaseous electron propagation is a self-sustaining process. These results suggest that, for the expected operational voltages, the high pressure ion funnel (750 V) should be operated at 10 Torr or higher, and the low pressure ion funnel (475 V) should be operated at 3.9 Torr or higher to prevent coronas and/or discharges.

III.II.III. Electrospray Ionization Characterization

Sodium iodide (NaI) was chosen for initial tests evaluating the ESI source because it has been shown to form clusters over a wide range of masses, providing a good case for ion transmission even if the ion funnels were to exhibit an extreme mass bias.⁵ The prepared solution was first diluted to ca. 50 μM and analyzed with commercial instrumentation (Agilent 6560 IM-MS), confirming ion generation and cluster formation. After exhaustive troubleshooting of the detector circuit and source power supply (the discussion of which has been omitted for the sake of brevity), ion signal was detected on the home-built Faraday plate and amplifier circuit. Using the experimental setup shown in Figure 3.2(A), initial experiments were conducted to characterize and optimize the ESI source in a stand-alone configuration. Figure 3.2(B) shows results from an

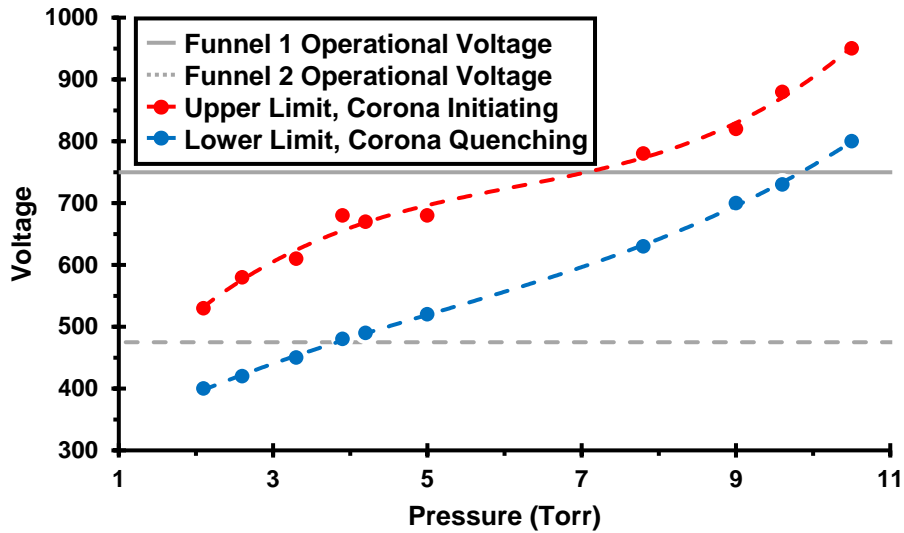


Figure 3.1: Empirical testing of initiation and quenching of coronas and/or discharges in the tandem ion funnels of the spatially multiplexed IM. These tests were performed after super corona dope was applied to the RC circuit boards of each funnel, and after Kapton sheets were installed to prevent coronas and/or discharge in locations they had previously been observed. Coronas and/or discharges were not observed at the RC circuit boards in this experiment, but they were observed at the inner via surfaces that comprise the ion channels. The high pressure ion funnel (Funnel 1) is expected to operate near 750 V, at which the pressure must remain greater than 10 Torr to prevent coronas and/or discharges. The low pressure ion funnel (Funnel 2) is expected to operate near 475 V, at which the pressure must remain greater than 3.9 Torr to prevent coronas and/or discharges. Trendlines are third order polynomial equations and serve to visually connect the data points for the reader.

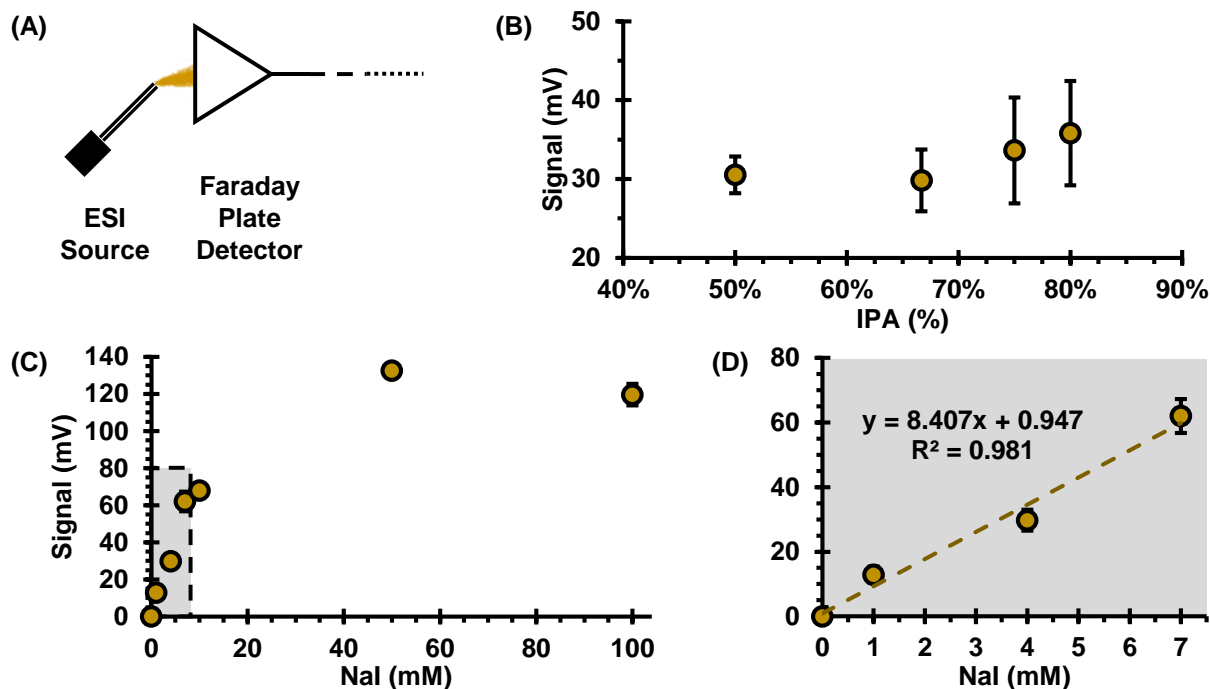


Figure 3.2: Tests of solvent ratios and sample concentration to optimize signal strength. (A) Diagram of system setup, where Faraday plate is positioned approximately 5 mm from the ESI needle. (B) Empirical data comparing 1:1, 2:1, 3:1, and 4:1 IPA:H₂O. Mean difference of 1 mM NaI and a blank for each solvent system is plotted. Flow rate is 0.5 mL/hr. Error bars represent ± 1 standard deviation from the mean of six measurements. No significant solvent bias was observed, and 80% IPA was chosen for subsequent experiments. (C) Investigation of signal response with respect to concentration of NaI. Mean difference of sample and blank at each concentration is plotted. Flow rate is 0.5 mL/hr. Linear range extending to 7 mM is boxed and shown closer in (D). Ionization efficiency is decreased above 7 mM, and ion suppression may cause decrease at higher concentrations. (D) Linear region of signal response to NaI concentration. Above this concentration, no increase in ionization efficiency was observed. Subsequent experiments were performed with 1 mM NaI. Error bars in (C) and (D) represent ± 1 standard deviation from the mean of nine measurements.

investigation of the effect of IPA:H₂O solvent ratio on detected ion signal with the detector positioned 5 mm from the ESI needle using a 1 mM NaI solution at a flow rate of 0.5 mL/hr. Although this study was by no means an exhaustive investigation of solvents, no significant bias between solvent composition and detector response was observed in this experiment, indicating that if a stable spray is observed as in Figure B.19.2, solvent composition should have no significant effect. A ratio of 4:1 IPA:H₂O was chosen for use in subsequent experiments. Figure 3.2(C) shows results from an investigation of signal response with respect to NaI concentration in 4:1 IPA:H₂O at 0.5 mL/hr flow rate. A linear response in signal was observed up to 7 mM NaI (Figure 3.2(D)), above which ionization efficiency was observed to decrease. Specifically, the signal decreased between 50 mM NaI and 100 mM NaI, which may indicate the occurrence of ion suppression at these high analyte concentrations. Because of the findings from this study, combined with the observation of mineral deposits on the detector at high salt concentrations (Figure B.19.14), a concentration of 1 mM NaI, corresponding to the lower end of the linear range, was chosen for subsequent experiments. Figure 3.3(A) shows the experimental setup utilized in characterization and optimization of the ESI source. Figure 3.3(B) displays findings of the effect of E on ion generation, where the ESI voltage was held constant at 1500 V and the distance between the needle and Faraday plate was varied between 1 mm and 7 mm. The flow rate for this experiment was 0.2 mL/hr, a current limit of 120 μ A was imposed on the SC power supply, and the sample was prepared in 4:1 IPA:H₂O, as used in previous experiments. The sample was a mixture of 1 mM NaI, chosen after previous concentration-dependent experiments, and 1 mM CsI, which was added to expand mass coverage.⁶ Ion detection in these studies was achieved using a digital oscilloscope, with an in-line variable resistor adjusted to 82.1 Ω resistance. When the needle was too far from the Faraday plate, at E values less than 4 kV/cm, the spray was unstable and the

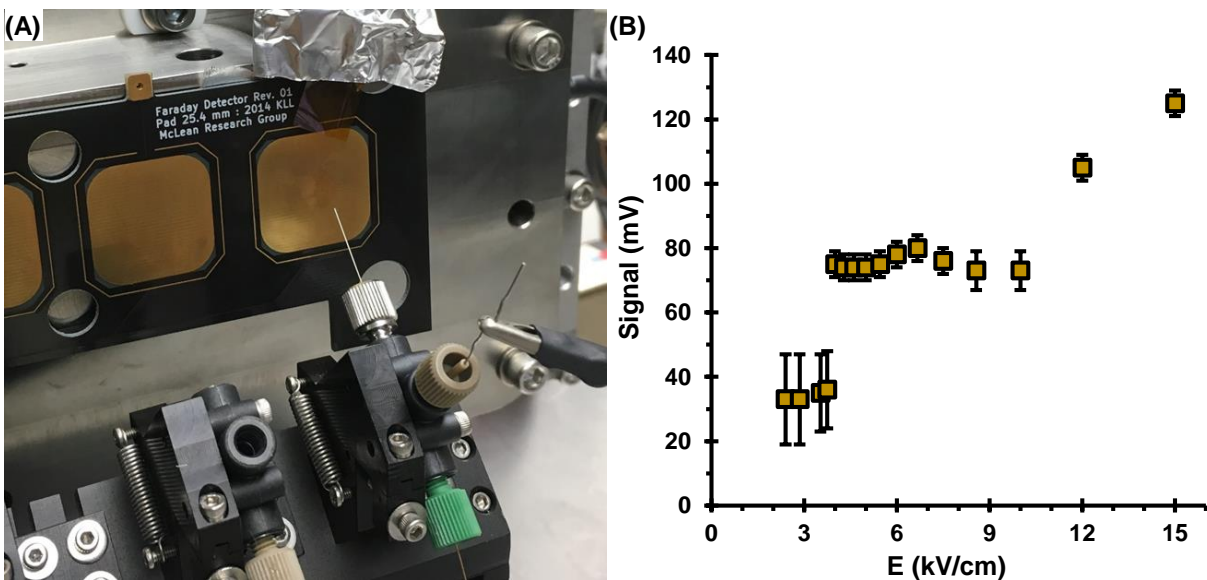


Figure 3.3: Empirical test evaluating signal at the detector for various electric field strength, E , between the tip of the ESI needle and the Faraday plate. (A) Experimental setup with Faraday plate in atmosphere, fixed in front of the ESI source. (B) Data showing dependence of E on ESI initialization from 1 mm to 7 mm distance from needle to detector at 1500 V, a current limit of $120 \mu\text{A}$ on the SC power supply, and 82.1Ω resistance between the detector and voltage measurement. Error bars indicate peak to peak noise corresponding to each measurement. Sample was 1 mM NaI and 1 mM CsI in 4:1 IPA:H₂O at a flow rate of 0.2 mL/hr. Under 4 kV/cm, the field was not strong enough and the spray was unstable. Between 4 kV/cm and 10 kV/cm, ESI was stable. Over 10 kV/cm, the needle was within 1.5 mm of the Faraday plate and the solvent droplet closed the circuit.

signal was low. Between 4 kV/cm and 10 kV/cm, a stable spray was observed and signal was steady, increasing with E until the strength of the field destabilized the spray, causing sputtering and a decrease in signal. Above 10 kV/cm, when the needle was within 1.5 mm of the Faraday plate, the solvent droplet was close enough to touch the surface of the detector, closing the electric circuit and corresponding to a large increase in the detected ion signal. These experiments indicate that, at this voltage, the ESI is stable around $3 \text{ mm} \pm 1 \text{ mm}$ distance from the counter electrode, which represents the Faraday plate in these experiments.

III.II.IV. Characterization of Ion Signal in Vacuum

After the ESI parameters were characterized, the Faraday plate was repositioned and installed ca. 25 mm from the vacuum end of the RGC to test ion transmission through the RGC into vacuum. Although the noise observed on the oscilloscope was greatly decreased by moving the detector into the vacuum system (shielded by the vacuum chamber), ion signal was undetectably low when using the in-line variable resistor as the amplifier in the detector circuit. A low-noise, dual operational amplifier (described in Chapter II and multiple revisions depicted in Figure B.19.17), was subsequently constructed based on a previously reported design,^{7,8} and incorporated into the detector circuit in order to detect picoamperes of current, enabling collection of the data shown in Figure 3.4. The experimental setup is shown in Figure 3.4(A), where the Faraday detector is situated in one of two locations: positioned immediately after the RGC or positioned at the exit of the high pressure ion funnel. In testing ion transmission through the RGC, the change in signal was observed when the ESI was either initialized or blocked. To block the ESI, a Kapton sheet was physically placed between the ESI needle and the atmospheric end of the RGC, destabilizing spray and preventing ion formation or entry into vacuum, but neutral gas

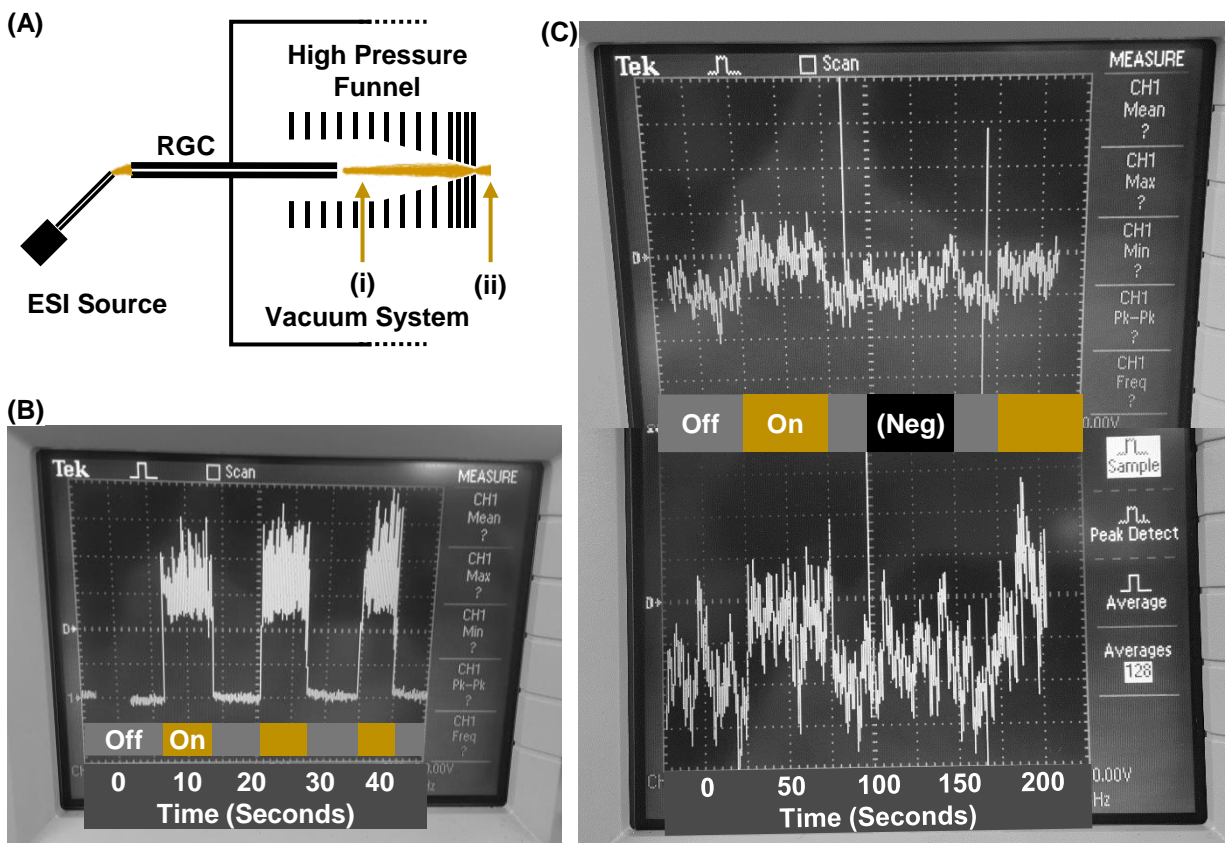


Figure 3.4: (A) Diagram showing position of Faraday plate detector during testing with (i) representing testing of ion transmission through the RGC and (ii) representing testing of ion transmission through the high pressure ion funnel. (B) and (C) show photographs of the oscilloscope screen during ESI initialization experiments. (B) Results for test of ion transmission through RGC, with Faraday plate detector in ((A), position (i)). ESI was initialized, “On,” and quenched, “Off,” by physically blocking the needle from the RGC with a sheet of Kapton. Neutrals were transmitted throughout the experiment, however, because the Kapton sheet did not prohibit gas flow through the RGC, thus the pressure was unaffected. Voltage increase indicates approximately 1.8 nA of ion current. (C) Results for two trials testing of ion transmission through RGC and high pressure ion funnel, with Faraday plate detector in ((A), position (ii)). DC ramp

across ion funnel was positive for regions marked “On,” DC ramp was negative for regions marked “Negative,” and ESI was quenched in regions marked “Off.” Neutrals were transmitted throughout the experiment, however, because the Kapton sheet did not prohibit gas flow through the RGC, thus the pressure was unaffected. Voltage increase during ESI for this experiment was difficult to determine, either quantitatively or qualitatively, but approximately 330 pA was measured for the same setup in later experiments (not pictured). Pressure in vacuum was 11 Torr throughout.

molecules were still permitted to enter the vacuum system, as the RGC entrance was not sealed by the Kapton sheet, and the corresponding pressure remained stable at 11 Torr throughout the experiment. The voltage increase seen in Figure 3.4(B) is indicative of approximately 1.8 nA of ion current, calculated from the equations discussed in Chapter II and shown in B.17.6, with a 100 k Ω bridge resistor in the amplifier circuit and a signal to noise ratio of ca. 10:1. Evaluation of ion transmission through the high pressure ion funnel yielded the results shown in Figure 3.4(C), where the same Kapton sheet blocking method used in the previous experiment was employed. Here, the DC gradient across the high pressure ion funnel was established either to transmit ions (“On”) or to discourage ion transmission (“Neg”) as a null experiment in case ions were finding their way through the RGC despite the Kapton blocking sheet. A voltage increase during initialization of the ESI was difficult to determine, either quantitatively or qualitatively, for the results shown. A subsequent reproduction of this experiment yielded a measured ion current of approximately 330 pA.

Before further experiments were conducted, the LabVIEW control and acquisition software was developed. Various roadblocks and troubleshooting methods led to the experiment depicted in Figure 3.5(A), where a piece of aluminum foil molded to a piece of plastic (photograph in Figure B.19.14) was substituted for the PCB Faraday array. Figure 3.5(B) shows successful transmission of ions through the RGC, high pressure funnel, and conductance limit of the Delrin wall of the inner vacuum chamber with detection by the NI PXI-7842R card and visualization in the LabVIEW program written in-house. Because only one RGC is open to atmosphere, a pressure differential between the inner vacuum chamber and first vacuum chamber is not established, and pressure in both chambers was measured at 11 Torr. Here, 1 mM NaI and 1 mM CsI in 4:1 IPA:H₂O were directly infused at 0.3 mL/hr with 1850 V on the ESI needle. The RGC and first electrode of

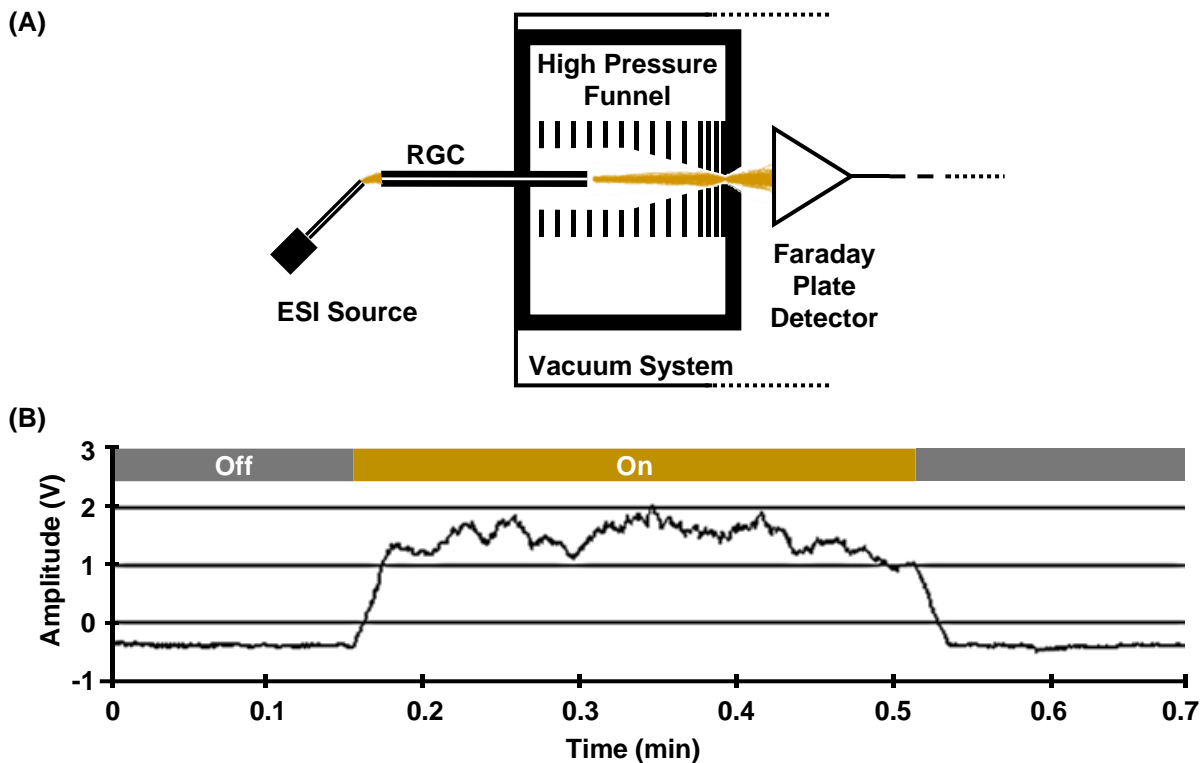


Figure 3.5: ESI initialization experiment with signal acquisition by NI LabVIEW software. Experimental setup of foil Faraday plate suspended after inner vacuum chamber, with ions transmitted through RGC and high pressure funnel at 11 Torr. ESI was initialized, “On,” and quenched, “Off,” by physically blocking the needle from the RGC with a sheet of Kapton. Neutrals were transmitted throughout the experiment, however, because the Kapton sheet did not prohibit gas flow through the RGC, thus the pressure was unaffected. Flow rate was 0.3 mL/hr for 1 mM NaI and 1 mM CsI and ESI needle was held at 1850 V. For high pressure ion funnel, 180 VDC was applied to the RGC and first electrode, 5 VDC was applied to the last electrode, and 100 V_{pp} RF was applied across the funnel. Software loop duration was set at 25 ms and 40 iterations. Voltage increase indicates approximately 110 pA of ion current ($6.8 \cdot 10^4$ counts per 0.1 ms).

the high pressure funnel are at 180 V, the last electrode of the high pressure funnel is at 5 V, and 100 V_{pp} RF is applied across the funnel as described in Chapter II. Acquisition software was set to acquire 40 iterations of 25 ms between screen updates, with signal averaging occurring every 32 samples. The voltage increase observed when ESI is initialized corresponds to 110 pA of ion current without a bridge resistor in the picoammeter, or $6.8 \cdot 10^4$ ion counts per 0.1 ms.

III.III. Current Obstacles

During the testing of the spatially multiplexed instrument, many obstacles have been encountered. Troubleshooting has helped to overcome some of these, as described above. Others, however, are persistent, and it is expected that many obstacles to commissioning the spatially multiplexed IM have yet to be identified. For example, Chapter II describes two source power supplies, when only one is utilized, because of issues concerning the originally intended module. Tests conducted in-house indicate the power supply unit is faulty, and interpretation of those results (some of which were eventually attributed to a faulty multimeter) were corroborated by a technician at the manufacturer, but when the unit was returned for repair, problems persisted with the performance of the supply. Additionally, when this unit is in use, current flows to instrument ground, causing the ESI micrometer stage and the table surface to be electrified, resulting in an unsafe operational situation in which these surfaces conducted unwanted current to the user. Thus, for reliability and safety, an alternate supply was utilized, which tests and performs as expected. . Another issue of note involves electronic noise, detected by the Faraday plate, originating from ESI auxiliary appliances including a television, video camera, heater, and lamp. Noise from these units was observed most when the Faraday plate was positioned outside of vacuum (Figure 3.3(A)), and it is hoped that this noise will diminish as the detector is moved further from the ESI

source to the end of the drift tube where the stainless steel vacuum system will act as a Faraday cage.

Figure B.19.12 depicts the aperture panel, which is fabricated from a stainless steel plate. There is a concern that the panel's electrical capacitance is high enough to slow the response to voltage changes, which will later be incorporated for ion gating. If the response is slow, the shape of the initial ion packet will be affected, which will adversely affect the ion mobility resolution, and redesign of the aperture panel may need to be considered.

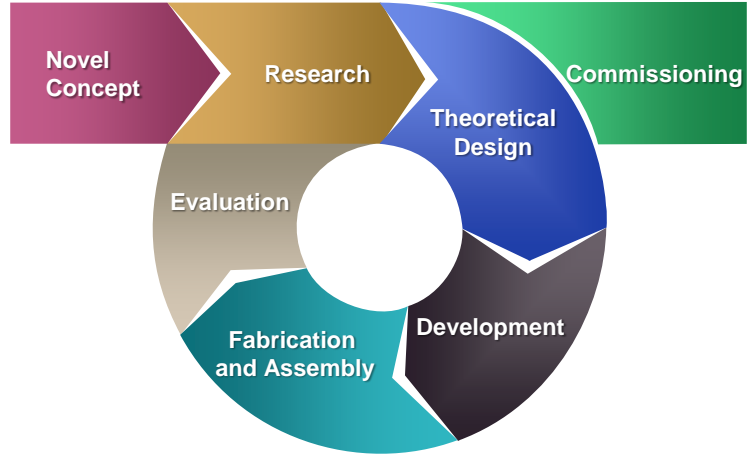
Another obstacle was realized after preliminary testing with both ion funnels installed, which has not yet successfully demonstrated detectable ion transmission. One suspicion is that electric charge is accumulating on the surface of the Delrin that forms the conical ion exits of the inner vacuum chamber (Figure B.19.7). Although ions have passed through this exit and been detected within ca. 10 mm, the electric field may be deformed by the charged Delrin to an extent that prevents them from traversing the 25 mm distance to the first electrode of the low pressure ion funnel. Note that ion simulations do not account for these dielectric components, which may contribute significantly to the electric fields that the ions ultimately experience. Attempts to circumvent this suspected obstacle were made by first suspending a metal ring just outside the inner vacuum chamber to serve as an intermediate electrode and second fabricating a conical metal electrode to shield the Delrin surface, but neither of these efforts yielded detectable ion signal at the exit of the low pressure ion funnel. Further attempted mitigation strategies included removal of the inner vacuum chamber such that only the ESI, RGC, and high pressure ion funnel were being tested, but signal in this configuration resulted only from neutral gas flow (tested by alternately opening and sealing the RGC atmospheric end), with no significant detection of ions. These results indicate an additional, undetermined obstacle exists preventing ion transmission

through both ion funnel stages and into the drift tube region.

III.IV. Conclusions and Future Directions

The flow chart in Figure 3.6 represents the design process for the spatially multiplexed IM instrument. This project started with a novel concept of spatially multiplexing IM with the motivation of increasing throughput, sensitivity, accuracy, precision, and versatility, as discussed in Chapter II. Research in the field was conducted to determine novelty, ascertain demand, and discover state-of-the-art methods and designs after which to model the new instrument. This was the first step in the first iteration of the cyclical design process depicted in Figure 3.6(A). Development of the spatially multiplexed IM is still undergoing iterations of this cycle of research followed by theoretical design, development, fabrication, assembly, and evaluation leading to more research. To date, the elements indicated in Figure 3.6(B) as “Complete” are considered well-established facets in the development of this instrument, though aspects of these subjects may be revisited to optimize instrument performance. Topics indicated as “In Progress” regard evaluation of the instrument, with some topics included in the above discussion. Ions have been successfully generated at the ESI source, transferred into vacuum via a resistive glass capillary (RGC), transmitted through the high pressure ion funnel, transported from the inner vacuum chamber to the first vacuum chamber, and neutralized at a Faraday plate detector. Current generated by the ion neutralization event has been effectively amplified, converted to a voltage measurement by a home-built picoammeter, and displayed to a user via both an oscilloscope and the LabVIEW software interface. Future work within the iteration loop of the design process includes further testing, incorporation of ion gating, and benchmarking of performance. When the instrument has been thoroughly evaluated and optimized, it will be commissioned for use.

(A)



(B)

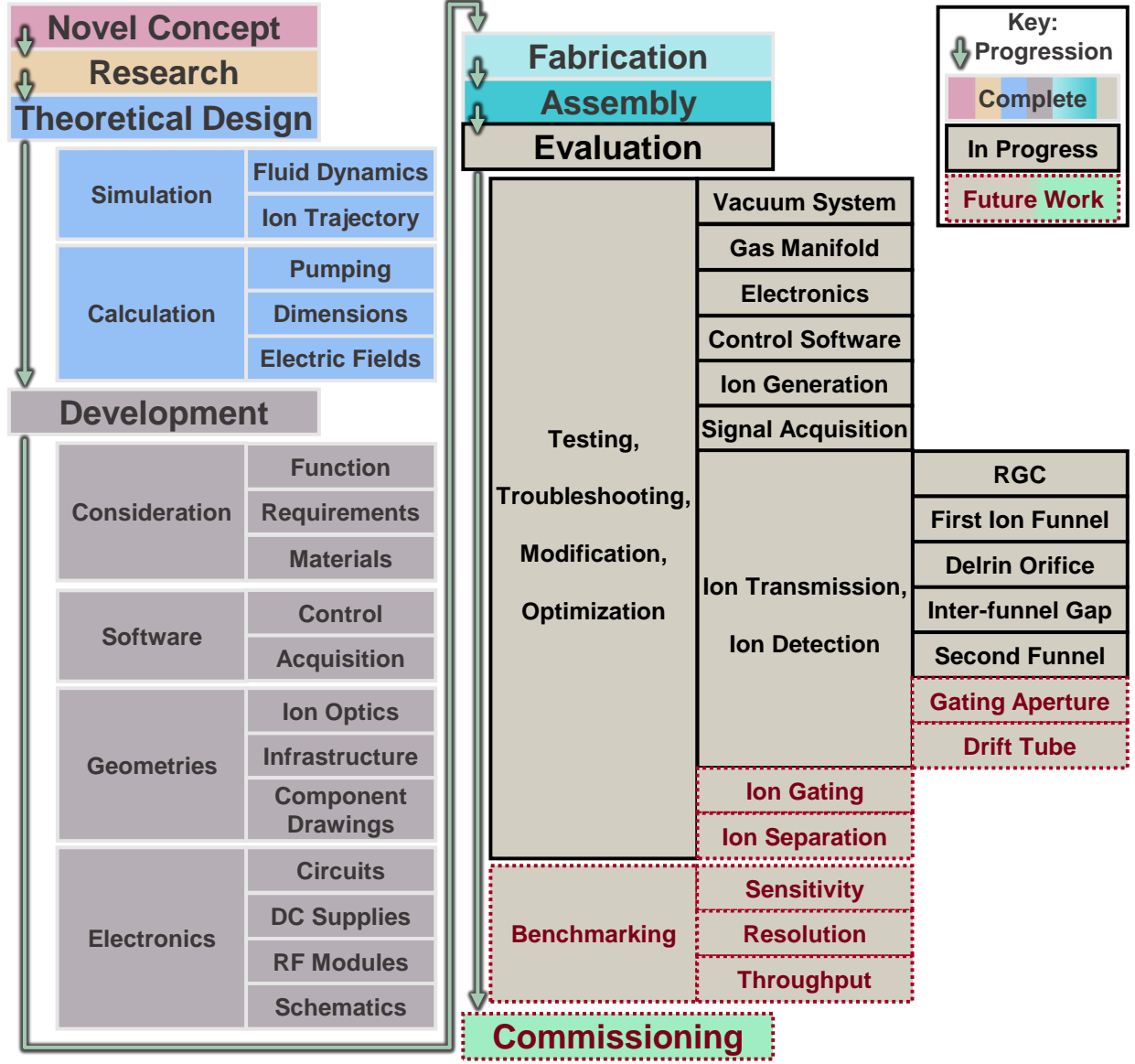


Figure 3.6: (A) Flow diagram for the design process. Note the cyclical process, representing multiple design iterations prior to commissioning, in which current efforts are being focused. (B) Details of the design process specific to the spatially multiplexed ion mobility spectrometer described in Chapter II. Note that work has been completed through assembly, and the instrument is currently being evaluated. Future work includes further testing, incorporation of ion gating, benchmarking of performance, and commissioning of the instrument.

III.V. References

1. M. A. Lieberman and A. J. Lichtenberg, *Principles of plasma discharges and materials processing*, John Wiley & Sons, 2nd edn., 2005.
2. S. Arumugam, P. Alex and S. K. Sinha, Effective secondary electron emission coefficient in DC abnormal glow discharge plasmas, *Physics of Plasmas*, 2017, **24**, 112106.
3. K. Akio, S. Takashi and S. Hideo, Secondary Electron Emission from Al, Cu, Ag and Au Metal Targets under Proton Bombardment, *Japanese Journal of Applied Physics*, 1981, **20**, 65.
4. S. Arumugam, P. Alex and S. K. Sinha, *Effective Secondary Electron Emission Coefficient of Brass*, 2016.
5. J. F. Anacleto, S. Pleasance and R. K. Boyd, Calibration of ion spray mass spectra using cluster ions, *Organic Mass Spectrometry*, 1992, **27**, 660-666.
6. S. König and H. M. Fales, Calibration of mass ranges up to m/z 10,000 in electrospray mass spectrometers, *Journal of the American Society for Mass Spectrometry*, 1999, **10**, 273-276.
7. A. P. D. P. Intra and N. Tippayawong, *An electrostatic sensor for nanometer-sized aerosol particles detection*, 2009.
8. P. Intra and N. Tippayawong, Development of a fast-response, high-resolution electrical mobility spectrometer, *Korean Journal of Chemical Engineering*, 2011, **28**, 279-286.

Chapter IV

CONFORMATIONAL ORDERING OF BIOMOLECULES IN THE GAS PHASE: NITROGEN COLLISION CROSS SECTIONS MEASURED ON A PROTOTYPE HIGH RESOLUTION DRIFT TUBE ION MOBILITY-MASS SPECTROMETER

IV.I. Abstract

Ion mobility-mass spectrometry measurements which describe the gas-phase scaling of molecular size and mass are of both fundamental and pragmatic utility. Fundamentally, such measurements expand our understanding of intrinsic intramolecular folding forces in the absence of solvent. Practically, reproducible transport properties, such as gas-phase collision cross-section (CCS), are analytically useful metrics for identification and characterization purposes. Here, we report 594 CCS values obtained in nitrogen drift gas on an electrostatic drift tube ion mobility-mass spectrometry (IM-MS) instrument. The instrument platform is a newly developed prototype incorporating a uniform-field drift tube bracketed by electrodynamic ion funnels and coupled to a high resolution quadrupole time-of-flight mass spectrometer. The CCS values reported here are of high experimental precision ($\pm 0.5\%$ or better) and represent four chemically distinct classes of molecules (quaternary ammonium salts, lipids, peptides, and carbohydrates), which enables structural comparisons to be made between molecules of different chemical compositions for the rapid “omni-omic” characterization of complex biological samples. Comparisons made between helium and nitrogen-derived CCS measurements demonstrate that nitrogen CCS values are systematically larger than helium values; however, general separation trends between chemical classes are retained regardless of the drift gas. These results underscore that, for the highest CCS

accuracy, care must be exercised when utilizing helium-derived CCS values to calibrate measurements obtained in nitrogen, as is the common practice in the field.

IV.II. Introduction

With the rising demand for high-throughput analyses of increasingly complex samples, ion mobility-mass spectrometry (IM-MS) has found broad application in the analysis of biological systems, as this rapid 2D separation (ms and μ s, respectively) provides comprehensive molecular information regarding analyte size, mass, and relative abundance. In ion mobility, separation is achieved by low-energy interactions of charged analytes with an inert buffer gas (conventionally helium or nitrogen), where analyte size-to-charge ratio is measured as a function of the time required to traverse the mobility region.¹ As a means of comparison with other laboratory measurements, drift time values are either normalized to standard temperature and pressure as a reduced mobility (K_0) or converted to a collision cross-section (CCS) value, the latter of which is a size parameter related to the averaged momentum transfer impact area of the molecule.² Structural information in the form of CCS values assists in the characterization of analytes by biomolecular class, as these classes are known to separate in IM-MS space and adopt conformational correlations due to prevailing class-specific structural folding in the gas-phase.^{3,4} These class-specific mobility-mass correlations can be used as a predictor for molecule class, demonstrating the potential value of IM-MS structural separations for life sciences research which seek systems biology level information. Expanding upon this concept, CCS-based molecular prediction has previously been explored for peptides, utilizing intrinsic size parameter calculations⁵⁻⁷ and machine learning algorithms⁸ for sequence prediction, but no detailed study of other biochemical classes has yet been undertaken.

The separation and characterization of biological samples by IM-MS has been achieved using both commercial and laboratory built instrumentation. Virtually all contemporary commercial IM-MS instruments utilize nitrogen as the buffer gas for IM separations, motivated by practical considerations of cost, availability, and technical considerations for pumping requirements and electrical discharge. The most common commercial IM-MS platform utilizes an electrodynamic field (i.e., a traveling wave potential) for mobility separation,^{9,10} and drift time measurements must be calibrated against electrostatic drift tube data in order to convert these measurements to CCS values.^{11,12} Conversely, many independently constructed instruments incorporate uniform electrostatic field mobility regions utilizing helium as the buffer gas. Uniform field measurements serve as the benchmark for electrodynamic CCS value determination, as the CCS obtained from a uniform field drift tube can be determined empirically through kinetic theory.^{13,14}

One common practice among researchers utilizing IM-MS is calibration of nitrogen-based traveling wave ion mobility measurements against helium-based CCS values reported in the literature.¹⁵⁻¹⁸ The use of helium-based CCS values to calibrate nitrogen-based drift time measurements results in calibrated “helium-equivalent” CCS values, which can be useful for comparing with literature values and correlating measurements to theory.¹⁹⁻²² There is, however, concern that this practice introduces added experimental error, as nitrogen vs. helium mobility measurements differ substantially in magnitude, and the success of calibration strategies relies heavily on careful selection of calibrants that accurately describe the sample conditions, charge state, mass range and chemical class of the system of interest.^{11,17,23} Differences in CCS values in helium versus nitrogen arise due to several factors including intrinsic size differences between the buffer gases, mass effects which factor into the momentum transfer cross-section (the experimental

CCS), and the over eight-fold difference in gas polarizability between helium and nitrogen (0.21×10^{-24} and $1.74 \times 10^{-24} \text{ cm}^3$, respectively).^{14,24}

Recently, a prototype IM-MS instrument utilizing nitrogen drift gas was developed (Agilent Technologies, Santa Clara, CA). This instrument incorporates a uniform electrostatic field ion mobility separator bracketed by electrodynamic focusing devices (ion funnels), which allows for high sensitivity and direct measurements of CCS values in nitrogen.^{8,25} Presented in this report is an extensive and diverse database of empirically-derived nitrogen CCS measurements (594 values), which comprises four molecular classes and expands upon several previous databases for the structural characterization of biological molecules.^{5,7,8,11,26-29} This affords the opportunity to explore the fundamental considerations of buffer gas composition and the subsequent effects on ion mobility parameters (reduced mobility and CCS) across different molecular classes.

IV.III. Experimental Methods

IV.III.I. Preparation of Standards

IV.III.I.I. Lipids

All solvents and buffers were purchased as HPLC grade from Sigma-Aldrich (St. Louis, MO, USA). Dry lipid extracts were purchased from Avanti Lipids (Birmingham, AL, USA) and constituted in chloroform prior to analysis. Lipid extracts include sphingomyelins (SM, porcine brain), glycosphingolipids (GlcCer, porcine brain), phosphatidylcholines (PC, chicken egg), phosphatidylserines (PS, porcine brain), and phosphatidylethanolamines (PE, chicken egg). For analysis, lipid standards were diluted in 90% chloroform/10% methanol (v/v) with 10 mM sodium acetate to a final concentration of 10 $\mu\text{g/mL}$. Putative identification of lipids was performed using

the exact mass measurement through the Lipid Metabolites and Pathways Strategy (LIPID MAPS) Structural Database (LMSD).³⁰ A full list of identified lipids can be found in Section IV.VI.

IV.III.I.II. Carbohydrates

Carbohydrate dextrans (linear and cyclic) and sugar alcohol standards were purchased from Sigma-Aldrich. Lacto-*N*-difucohexaose I and II and lacto-*N*-fucopentaose I and II were purchased from Dextra Laboratories (Reading, UK). All carbohydrate standards were prepared as received and reconstituted in water with 10 mM ammonium acetate to final concentrations of 10 µg/mL. For cationization, 10 mM NaCl, 10 mM LiCl, 10 mM CsCl, 10 mM KCl, and 10 mM RbCl solutions were prepared in water to a final concentration of ca. 10 µM. A full list of identified carbohydrates can be found in Section IV.VI.

IV.III.I.III. Peptides

Predigested peptide standards (MassPREP) were purchased from Waters (Milford, MA, USA). Peptide standards (SDGRG and GRGDS) were purchased from Sigma-Aldrich. All peptide standards were received as a lyophilized powder and reconstituted in 10 mM ammonium acetate in water to a final concentration of 10 µg/mL. The MassPREP digestion standard mix contained approximately equimolar concentrations of four tryptically digested proteins: Alcohol Dehydrogenase (ADH, yeast), Serum Albumin (BSA, bovine), Phosphorylase B (PHOSPH, Rabbit) and Enolase (ENOLASE, yeast). Peptide identifications were assigned on the basis of exact mass of all possible tryptic peptides (no missed cleavages) produced by the Expert Protein Analysis System (ExPASy) PeptideMass proteomics tool³¹ (Swiss Institute of Bioinformatics, Lausanne, Switzerland) using the SWISS-PROT database entry number for each intact protein (P00330, P02769, P00924, and P00489, respectively). A full list of identified peptides can be found in Section IV.VI.

IV.III.IV. Quaternary Ammonium Salts

Tetraalkylammonium (TAA) salts with alkyl chain lengths between 3 and 18 carbons (TAA3 to TAA18) were purchased from the following sources: TAA4, TAA6, TAA7, TAA10, TAA12, and TAA16 from Sigma-Aldrich; TAA3, TAA5, and TAA8 from Acros Organics; and TAA18 from Alfa Aesar. All TAA salts were supplied with a stated purity of greater than 98% and were prepared as received. TAA3 to TAA8 were prepared in 50% methanol/50% water, while TAA10, TAA12, TAA16, and TAA18 were prepared in 50% methanol/50% isopropanol. Final concentrations were ca. 1 $\mu\text{g/mL}$. A full list of primary TAA salt standards and concomitant ions identified in the samples can be found in Section IV.VI.

IV.III.II. Instrumentation

A schematic of the instrumentation used to obtain the cross-section measurements is shown in Figure 4.1. The instrument used in this work is a commercial prototype IM-MS which incorporates a drift tube coupled to a quadrupole time-of-flight mass spectrometer (IM-Q-TOFMS, Agilent Technologies, Santa Clara, CA). For this work, an orthogonal electrospray ionization (ESI) source (Agilent Jet Stream) was utilized which incorporates a heated sheath gas nebulizer to aerodynamically focus and desolvate ions prior to introduction into the vacuum system. Ions from the ESI are introduced to a single-bore glass capillary tube which is resistively coated across its length, allowing the nebulizer to be maintained at ground potential, while the exit end of the capillary can be biased to around 2100 V.³² Ions exiting the capillary are introduced into a tandem ion funnel interface consisting of a high-pressure transmission ion funnel in the first stage,³³ followed by a second stage trapping ion funnel which incorporates a dual-grid ion gate.³⁴ The second stage ion funnel trap operates as an ion focusing and accumulation region whereby

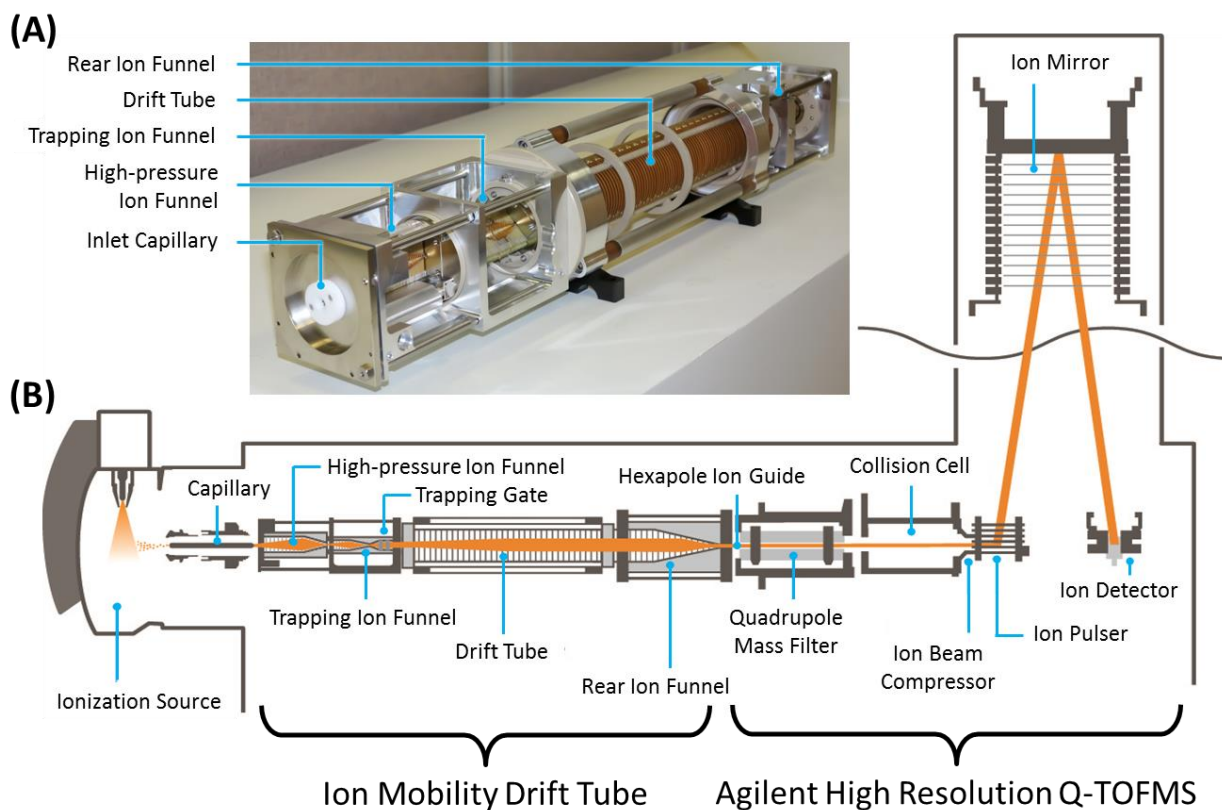


Figure 4.1: Details of the prototype IM-MS instrumentation used in this study. (A) A picture of the ion optical elements of the ion mobility component. (B) A representative schematic of the instrumentation used with significant components annotated.

temporally narrow (typically 100 to 150 μs) ion pulses are gated into the IM spectrometer. Mobility separation occurs in a 78 cm uniform field drift tube comprised of a series (ca. 150) of 50 mm internal diameter gold-plated ring electrodes. The buffer gas is high purity nitrogen. Ions traverse the drift tube under the influence of a weak electric field (10 to 20 $\text{V}\cdot\text{cm}^{-1}$) and consequently drift under low-field conditions. The combination of extended drift length, precision electronics, and high drift voltages enables high resolution ion mobility separations in excess of 60 resolving power ($t/\Delta t$, observed for a +1 ion, m/z 294). Ions exiting the drift region are refocused axially using an ion funnel and traverse a differential pressure interface region by means of a resistively-coated hexapole ion guide. Following the hexapole, ions are introduced into a modified Q-TOFMS (Agilent 6550), which incorporates a quadrupole mass filter and collision cell to enable mass-selective ion fragmentation experiments. The TOFMS is capable of greater than 40,000 mass resolving power and can acquire MS spectra at a rate of up to 8.3 kHz (120 μs transients at m/z 1700). Additional instrumentation details are provided in Figure 4.1.

IV.III.III. Experimental Parameters

All 2D IM-MS spectra were acquired via direct infusion using positive mode electrospray ionization (Agilent Jet Stream Source) with a flow rate of ca. 10 $\mu\text{L}/\text{min}$. The Jet Stream source was operated with a nitrogen sheath gas temperature between 400 and 600 K (solvent dependent) at a flow rate of 12 L/min. Nitrogen drying gas applied at the source entrance was heated to ca. 570 K at a flow rate of 10 L/min. The source was operated in positive mode with the following voltages: ground potential emitter, -4.5 kV capillary entrance, and -1.8 kV nozzle. The three ion funnels were operated as follows: high-pressure funnel RF 100 V_{pp} (peak-to-peak) at 1.5 MHz, 150 V DC; trapping funnel RF 100 V_{pp} at 1.2 MHz, 180 V DC; rear funnel RF 100 V_{pp} at 1.2 MHz,

200 V DC. The IM drift gas pressure (nitrogen) was maintained at ca. 4 Torr and ca. 300 K, while the drift potential varied from 750 to 1450 V, which represents an E/N ratio of 7 to 15 Td. In this E/N range, the mobility operates under low field conditions as all analytes investigated exhibited a linear change in drift times with respect to the electric field. Data was acquired with a modified version of the MassHunter software (Agilent Technologies). The mass measurement was calibrated externally using a series of homogeneously substituted fluorinated triazatriphosphorines (Agilent tuning mixture, ca. 100 to 3000 m/z), which are characterized as being amphoteric and nonreactive. Additionally, a mixture of tetraalkylammonium salts (TAA3 to TAA18) was added to all samples as an internal mass and mobility calibration standard for positive mode analysis.

IV.III.IV. Collision Cross-Section Calculations

Uncorrected drift times are extracted as centroid values using a beta version of the IM-MS Browser (Agilent Technologies). This uncorrected drift time represents the total transit time of the ions, including the mobility drift time and the flight time through the interfacing IM-MS ion optics and MS. Because the non-mobility flight time component (the transit time of ions outside the drift region) is independent of the drift voltage, this value can be determined from a plot of the measured drift time versus the inverse drift voltage,^{35,36} where a linear fit to the data will indicate the non-mobility time component (y-intercept) in the limit of infinite electric field ($1/V$ of zero). Time measurements are obtained from a minimum of six different drift voltages, ranging from 750 V to 1450 V. The determined non-mobility time is subtracted from the uncorrected drift times in order to obtain the corrected ion mobility drift time. Corrected drift times are used to determine the gas-phase momentum transfer collision cross-section (CCS) using the Mason-Schamp relationship,³⁷ incorporating the scaling terms for standard temperature and pressure. Based on a propagation-of-

error analysis incorporating the limits of precision for individual experimental parameters, we estimate the accuracy of all CCS values to be better than 2% (see Section IV.VI).

IV.IV. Results and Discussion

IV.IV.I. Database Description and General Cross-Section Trends in Nitrogen

A total of 594 nitrogen collision cross-section values were measured empirically in this study, representing three biomolecular classes (lipids, carbohydrates, and peptides), and TAA salts. This includes 92 peptides, 125 carbohydrates, 314 lipids, and 63 TAA salts and TAA salt derivatives. The range of CCS values measured spans from 140-460 Å², covering a mass range of 130-2150 Da. Summary statistics regarding the CCS database are provided in Table 4.1. The average RSD of all database values was 0.3% ($\pm 0.1\%$), with each CCS value representing an average of 11 (± 4) measurements. A complete list of all analytes and respective CCS measurements is provided as supplemental material.

TAA salts ranging from tetraethylammonium (TAA2) to tetraoctadecylammonium (TAA18) were analyzed and their subsequent CCS values were compared with literature values in order to estimate the CCS measurement accuracy.²¹ Results of this comparison are summarized in Table 4.2. Where CCS literature values existed for nitrogen, the absolute differences were found to be less than 2% and, in most cases, less than 1% deviation was observed. All TAA salts investigated exhibited excellent CCS measurement reproducibility (less than 0.5% RSD). TAA2 was included in the sample, but ultimately did not appear in significant abundance in the IM-MS spectra.

A scatter plot of CCS versus m/z for all database values is presented in Figure 4.2(A),

	collision cross-section statistics				fits to empirical data			
	number of CCS values	mass range [Da]	CCS range [Å ²]	average CCS precision ^a	average <i>N</i> for each value	fit equation coefficients ($y = Ax^b$)	coefficient of determination ^b	amount of data included within ±5% of fit ^c
peptides	92	430–1760	200–450	0.2% (±0.1%)	7 (±2)	A = 6.8440 B = 0.5547	$R^2 = 0.975$	91%
carbohydrates	125	190–2150	140–410	0.3% (±0.1%)	12 (±3)	A = 11.553 B = 0.4656	$R^2 = 0.983$	89%
lipids	314	500–1600	220–460	0.2% (±0.1%)	10 (±2)	A = 5.2469 B = 0.6000	$R^2 = 0.949$	96%
tetraalkyl-ammonium salts	63	130–1030	140–400	0.4% (±0.1%)	18 (±8)	A = 8.2631 B = 0.5561	$R^2 = 0.991$	98%

^aThe precision reported here represents the reproducibility across replicate measurements. The total precision due to propagation of uncertainty in experimental parameters is estimated to be less than 2%. ^bThe observed R^2 value for the nonlinear power fit. ^cThe data inclusion band chosen is based on the smallest sized band which incorporates the most amount of data (refer to Figure 2B, inset).

Table 4.1: Summary of statistics related to the CCS database.

name		exact mass [Da]	CCS (this work ^a) [Å ²]	CCS (literature ^b) [Å ²]	abs. percent difference ^c [%]
tetramethylammonium	TAA1	74.14		107.40	
tetraethylammonium	TAA2	130.25		122.20	
tetrapropylammonium	TAA3	186.36	144.1 ± 0.7 (23)	143.80	0.22
tetrabutylammonium	TAA4	242.46	166.6 ± 0.9 (16)	166.00	0.36
tetrapentylammonium	TAA5	298.57	190.1 ± 1.0 (28)	190.10	0.02
tetrahexylammonium	TAA6	354.68	213.5 ± 1.0 (31)	214.00	0.23
tetraheptylammonium	TAA7	410.78	236.4 ± 0.4 (31)	236.80	0.17
tetraoctylammonium	TAA8	466.54	256.6 ± 0.7 (31)	258.30	0.64
tetradecylammonium	TAA10	579.11	293.5 ± 0.7 (24)		
tetradodecylammonium	TAA12	691.32	319.0 ± 0.9 (24)		
tetrahexadecylammonium	TAA16	915.04	361.5 ± 0.9 (24)		
tetraoctadecylammonium	TAA18	1027.16	379.0 ± 1.7 (21)		

^aThe number of measurements is reported in parentheses. The error due to experimental uncertainty is reported next to each value and is less than 0.5% for all measurements. The total error based on propagating the limits of precision in experimental parameters is estimated to be less than 2%.

^bLiterature values from ref 16. ^cThe absolute percent difference is the difference in CCS compared to the average of both values.

Table 4.2: Measured CCS values for the TAA salts compared with literature values.

separated into chemical classes. We refer to this type of 2D IM-MS projection as conformational space analysis,^{4,38} as the differential scaling of mass (m/z) and size (CCS) between molecular classes is indicative of differences in gas-phase packing efficiency.²⁶

IV.IV.II. Description of the Fits to the Empirical Data

Several different equation functional forms were evaluated in order to determine which expression best described molecular class correlations between CCS and m/z values, and, it was found that the datasets were adequately described by a power-law relationship ($y=Ax^B$), based upon the coefficient of determination (R^2). Conceptually, power-law equations are descriptors for several phenomena related to mass-size scaling, including allometric scaling laws in biology,³⁹ stellar velocity dispersion relative to black hole mass (M-sigma relation),⁴⁰ and the well-known square-cube law, first described by Galileo,⁴¹ which universally relates any shape's increase in volume relative to its surface area. Additionally, power-law relationships are scale-invariant such that different power-law functions can be related by a simple scaling factor, which has implications for describing universal relationships independent of the specific details of the measurement.

The resulting power-law fits to the empirical data are presented in Figure 4.2(B). Coefficients and associated R^2 values are summarized in Table 4.1. The data inclusion bands projected in Figure 4.2(B) representing $\pm 5\%$ deviation from the line of best fit. Other inclusion band sizes are summarized in Figure 4.2(B), inset, averaged across the four datasets. For all datasets, a $\pm 5\%$ inclusion band incorporated an average of 94% ($\pm 4\%$) of data. Decreasing the band to $\pm 4\%$ results in an average of 86% ($\pm 3\%$) of data being included (a decrease of ca. 8% data inclusion), whereas increasing the band to $\pm 6\%$ only incorporated an additional 3% ($\pm 2\%$) of data on average. Thus, the $\pm 5\%$ data inclusion band represents an optimal balance between specificity

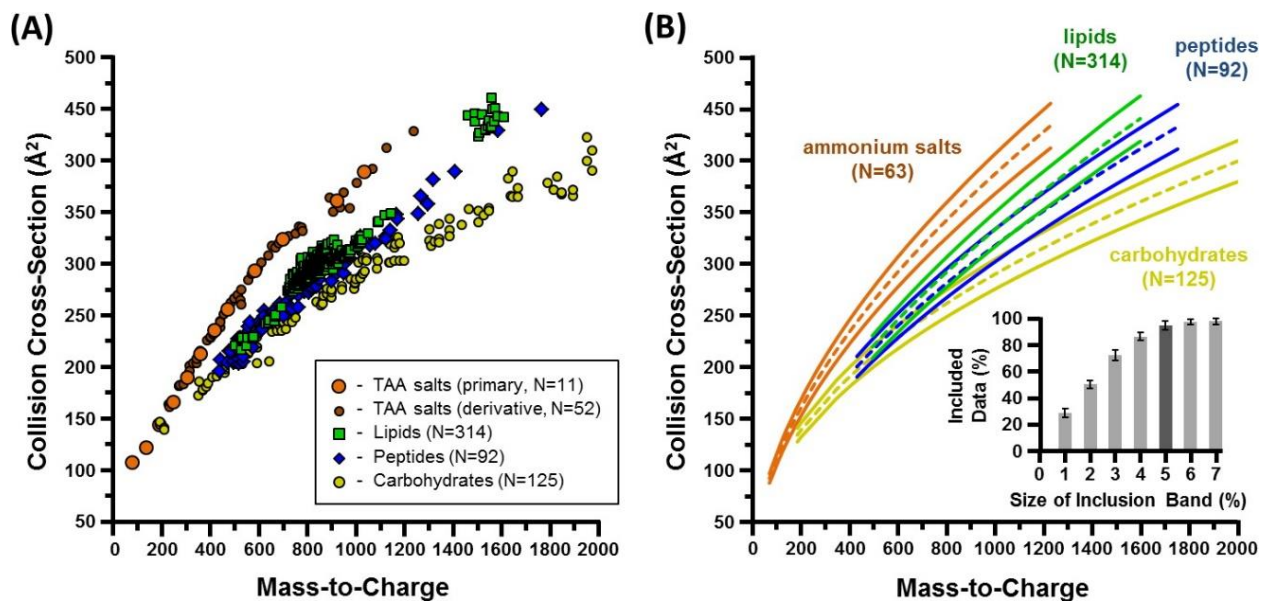


Figure 4.2: (A) A scatter plot of the CCS values measured in this study, separated by chemical class. (B) Best fit lines of the data, separated into class and fit to a power-law function. Also shown are data inclusion bands representing $\pm 5\%$ deviation from the best fit line. The inset bar graph represents the amount of data included within different sized inclusion bands. Fit equations and their corresponding coefficients of determination (R^2) can be found in Table 4.1.

and data incorporation. Interestingly, the $\pm 5\%$ band describes all datasets similarly, regardless of chemical class.

Several observations can be made from the data contained in Figure 4.2. The TAA salts were found to exhibit the highest CCS values relative to m/z , and were located in a region of 2D IM-MS space, which was disparate from the biomolecules. Previously, TAA salts were recommended as an ion mobility calibrant due to their low propensity for forming clusters, which otherwise complicates the interpretation of mobility data.⁴² Here, it is found that in addition to the lack of clustering, the TAA salts are useful mobility-mass calibrants as the complete series (1 to 18 carbons) span a wide range of CCS values (107 to 400 Å²), m/z values (75 to 1027 Da), and occupy a region of 2D IM-MS space where biomolecules are not predicted to occur. Carbohydrates were observed to have the lowest CCS values relative to their mass, while peptides and lipids occupy similar regions of conformational space. In general, all of the biochemical classes surveyed were readily separated above a mass of ca. 1200 Da, indicating that differences in relative gas-phase packing scale with molecular size and mass.

IV.IV.III. Extraction of Sub-Trend Information from the Data

From a cursory analysis of the CCS database described in this report, it is evident that the general chemical class information is retained through the specific mobility-mass correlation trends in the 2D IM-MS projection. Such trends hold promise for conducting comprehensive omics experiments whereby unknown analytes originating from a complex sample (e.g., blood, tissue, whole cell lysate) can be prioritized based upon their likely chemical class. This biomolecular filtering would allow for the sorting of unknown analytes into distinct identification workflows, as lipid, peptide, metabolite, and glycan identification methods often warrant searching of specific

databases. In order to determine the detail of class-specific information obtained from the conformational space analysis, select coarse biomolecular classes were further categorized into finer specific sub-classes. Figure 4.3 contains a detailed analysis of carbohydrates, which were further delineated into glycans (human milk oligosaccharides), cyclic dextrans (cyclodextrins), and linear dextrans (maltose polysaccharides). Figure 4.3(A) and Figure 4.3(B) illustrates the relative location of each carbohydrate sub-class in conformational space, while Figure 4.3(C) describes the data as a histogram relative to the best fit line. In general, there is no strong correlation between the carbohydrate sub-classes, with all signals distributed in relatively the same locations with respect to the power-law fit. This suggests that the carbohydrates surveyed do not adopt strong structural differences which can be easily differentiated in the 2D analysis. On the other hand, the sub-classes chosen here represent broad descriptors for carbohydrate structure, and as such are not structurally-descriptive sub-classifications. For example, glycans can represent both linear and branched oligosaccharides and thus occupy a broad region of the total carbohydrate conformational trend. Interestingly, the cyclization of sugars (cyclodextrins) does not seem to enhance gas-phase packing efficiency as compared with their linear analogues. A more comprehensive carbohydrate dataset may engender sub-class differentiation, or differences may bear out for more limited situations such as positional and structural isomers or various metal-coordinated species.⁴³

Application of a similar sub-class analysis to the lipid dataset is illustrated in Figure 4.4. In this case, the lipid dataset is substantially larger than the carbohydrate dataset (N=314 vs. N=125, respectively), and measurements were obtained from five distinct lipid structural classes. These lipid sub-classes can be broadly categorized into two structural classes as sphingolipids (SM, GlcCer) and glycerophospholipids (PE, PC, PS). It is qualitatively evident in Figure 4.4(A)

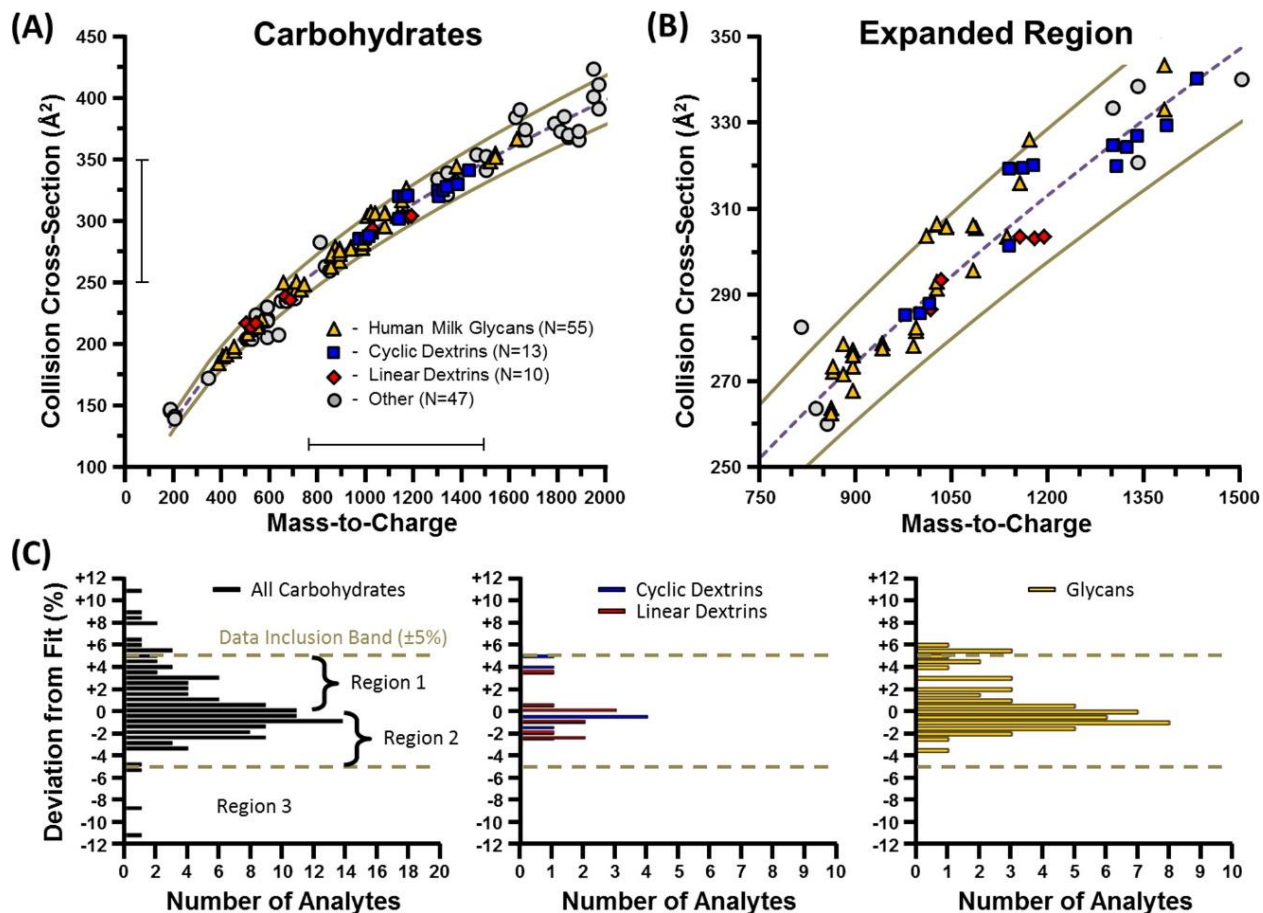


Figure 4.3: A subclass analysis of carbohydrates, with subclasses comprised of human mild derived glycans, cyclic, and linear dextrins. (A) A scatter plot of the relative location of carbohydrate subclasses in 2D IM-MS conformational space. (B) An expanded region of the scatter plot where all three subclasses of carbohydrates are observed. (C) A histogram analysis for carbohydrate subclass deviation in 2D IM-MS space relative to the best fit line. In general, the carbohydrate subclasses do not differentiate into distinct regions of conformational space.

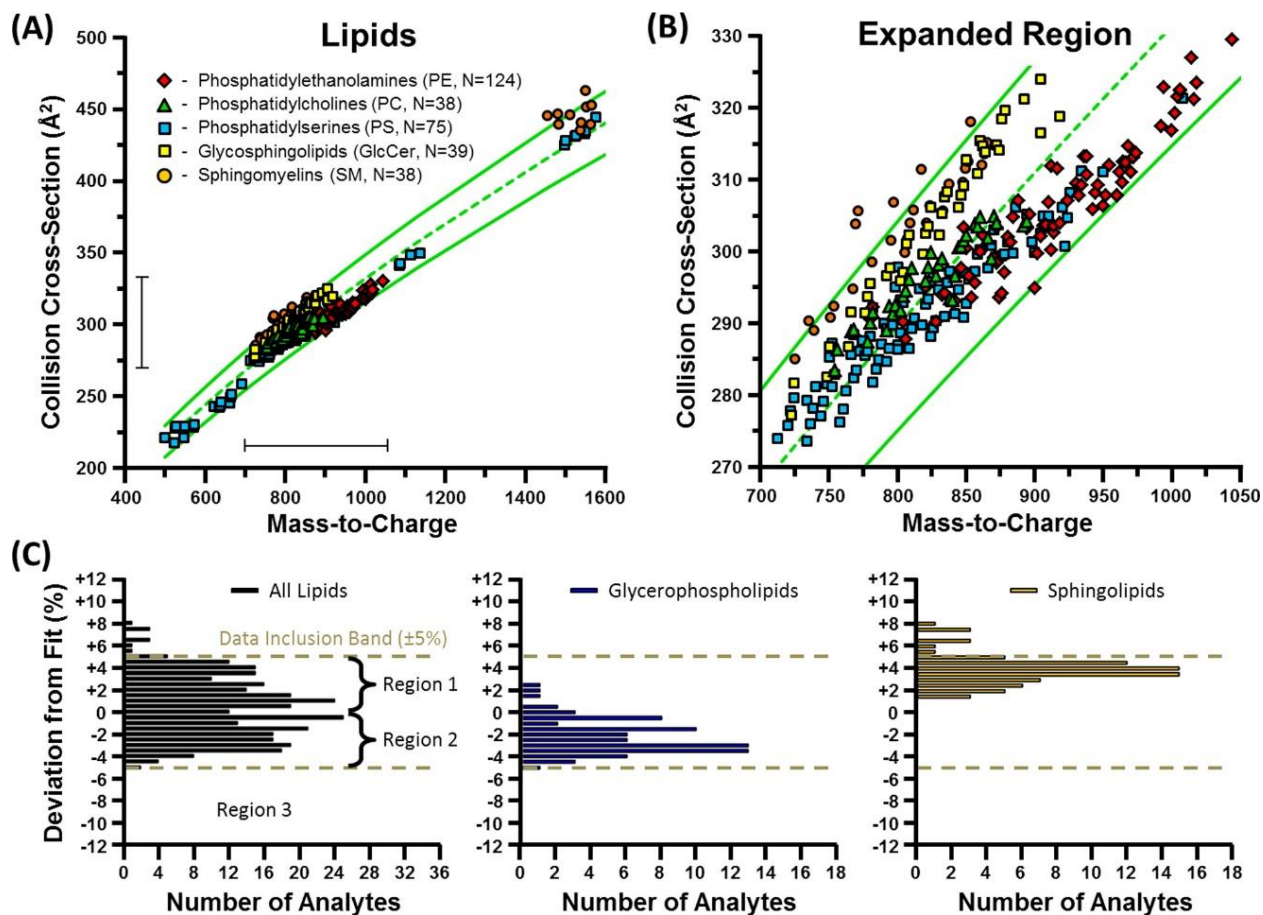


Figure 4.4: (A) A subclass analysis of lipids comprised of PE, PC, PS, GlcCer, and SM lipids. These lipids are further categorized into two general structural groups: glycerophospholipids (PE, PC, PS) and sphingolipids (GlcCer, SM). (A) A scatter plot of the conformational ordering of each subclass of lipid. (B) An expanded region of the scatter plot detailing a preferential ordering of the different lipid subclasses in conformational space. (C) A histogram analysis and locations of general lipid structural groups relative to the best fit line. Unlike carbohydrates, individual lipid subclasses partition into distinct regions of 2D IM-MS space, allowing finer structural information to be extracted from the conformational space analysis.

and Figure 4.4(B) that each class of lipid exists in a distinct region of conformational space. The histogram distribution analysis in Figure 4.4(C) (right panel) indicates that sphingolipids fall predominantly above the best fit line (97% in region 1), whereas glycerophospholipids (Figure 4.4(C), middle panel) are more broadly dispersed around the mobility-mass correlation (33% in region 1, 65% in region 2), and adopt denser gas phase conformations than sphingolipids. These results suggest that, with proper structural sub-class descriptors, conformational space analysis is capable of differentiating finer structural detail beyond general biomolecular class.

IV.IV.IV. Comparisons between Helium and Nitrogen CCS Values

The diverse compilation of CCS values described in this report allows for direct comparisons against helium-derived CCS values reported in the literature. Of the over 3000 singly-charged helium CCS values surveyed from the literature, overlapping measurements exist for 121 nitrogen CCS values in the current database (8 TAA salts, 49 lipids, 40 peptides, and 24 carbohydrates; refer to IV.VI. Supporting Information). Differences between helium and nitrogen-derived CCS measurements have been previously noted for atomic species,⁴⁴⁻⁴⁷ small molecules and peptides,⁴⁸ and, more recently, proteins and large protein complexes.^{11,29} Here, we add the differences observed for TAA salts, lipids, and carbohydrates, in addition to corroborating previous peptide observations.

A scatter plot of the overlapping helium and nitrogen CCS values is provided in Figure 4.5(A). Vertical error bars representing $\pm 2\%$ are also included, although this error is sufficiently small such that most of the error bars are obscured within the scale of individual data points. Figure 4.5(B) contains the power fits to the data, which are useful in visualizing differences between datasets. In general, gross separation trends between chemical classes are retained within the

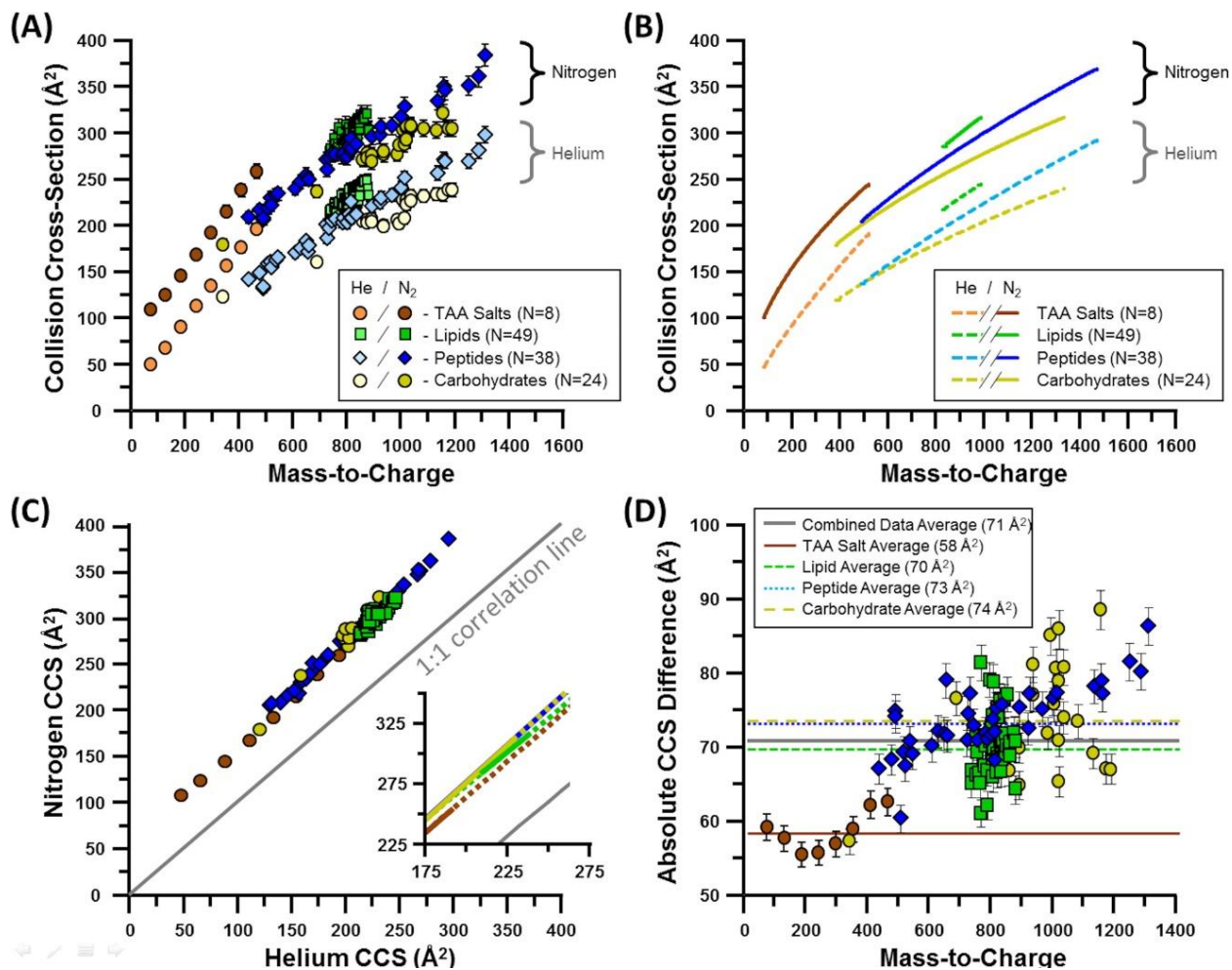


Figure 4.5: Comparisons between helium and nitrogen-derived CCS values. (A) A scatter plot of class-specific subsets of CCS data measured in both helium and nitrogen. (B) Power fits to the data projected in panel A. (C) Correlation plot of helium vs nitrogen CCS values. (D) Absolute differences in CCS between helium and nitrogen measurements, plotted as a function of mass-to-charge. In general, nitrogen CCS values are significantly larger than helium, with subtle differences being observed between different chemical classes.

helium and nitrogen-based datasets, with qualitatively similar conformational space ordering being exhibited regardless of the drift gas (i.e. carbohydrate density > peptide density > lipid density > TAA salt density). However, subtle differences exist with respect to the amount of average separation observed between class-specific fits. For example, the lipids and peptides exhibit slightly better average separation as a group in helium than in nitrogen, whereas the peptides and carbohydrate are better separated in nitrogen than in helium. These trends can also be observed in Figure 4.5(C), which contains the same overlap data as projected on a plot of nitrogen versus helium CCS values. In Figure 4.5(C), all of the class-specific data reside within the same region of the projection, indicating that overall differences between helium and nitrogen CCS are systematic within this range, and thus can be accounted for to allow conversion of one dataset to another, with some loss in precision associated with error propagation. This possibility of generating effective helium-based CCS values from nitrogen measurements was previously noted by Bush et al. for peptides and proteins.^{11,28} Recently, Pagel and Harvey noted good correlation (less than 1.5% error) between helium and nitrogen CCS measurements for singly-charged carbohydrates, though significant error was introduced when multiply-charged values were incorporated into the calibration.²³ Here we confirm a strong correlation between singly-charged helium and nitrogen CCS values for lipids, peptides, carbohydrates and TAA salts. It should be cautioned, however, that the relationship between helium and nitrogen-based CCS values are both charge-state and mass-dependent,⁴⁹ and it is expected that any correlation between the two measurements would deviate at the extremes of low and high mass. In fact, Bush et al. previously noted that cross-calibration error from nitrogen to helium CCS is higher at lower masses (up to 15% error) where the magnitude of the CCS value is small, while at higher masses, the error can be reduced to as low as 2.2% for predicting helium CCS from nitrogen measurements.¹¹ It was

also noted in this study and elsewhere that calibration across different chemical classes (e.g., using literature peptide values to calibrate lipids¹⁷) introduces additional and significant error (ca. 7%), further underscoring the importance of compiling a chemically diverse set of empirical drift tube CCS values. Figure 4.5(C), inset contains the linear best fits to the data, with the axes rescaled to a region where data exists for all four chemical classes. Linear fits are extrapolated (dotted lines) for visualization purposes. Here, the small but notable differences between chemical classes can be observed as offset correlation lines, which corroborate with the absolute CCS differences between helium and nitrogen noted previously for each chemical class. Specifically, peptides, carbohydrates, and lipids fall along a similar helium-nitrogen CCS correlation trend, while the TAA salts exhibit a slightly lower correlation. Interestingly, all class correlations exhibit similar slopes (ca. 1), suggesting that the factors which give rise to the cross-sectional differences between helium and nitrogen (buffer gas size, mass and polarizability) affect different chemical classes in a similar manner across a broad range of both size and mass.

Absolute CCS differences between the helium and nitrogen datasets are plotted as a function of mass in Figure 4.5(D), with error bars representing $\pm 2\%$ CCS uncertainty. Average absolute CCS differences are projected as a horizontal line through each class distribution, with the following values: TAA salts, $58 (\pm 3) \text{ \AA}^2$; lipids, $70 (\pm 4) \text{ \AA}^2$; carbohydrates, $74 (\pm 8) \text{ \AA}^2$; and peptides, $73 (\pm 5) \text{ \AA}^2$. Cross-sectional differences are lowest for the TAA salts, while lipids, carbohydrates and peptides differ by approximately the same amount. Overall, there is a small but notable increase in the helium-nitrogen CCS difference with increasing mass for all classes except lipids where a limited mass range is surveyed. This suggests that the nitrogen and helium CCS are not increasing at the same rate relative to the mass of the analyte, with the greater CCS increase occurring in nitrogen. Wytenbach et al. recently noted that ion systems up to ca. 760 Da (sodiated

PEG₁₇) still exhibit strong contributions from the ion-neutral interaction potential in their measured CCS.^{50,51} From their atomic superposition argument, it would be expected that with nitrogen buffer gas, the combined effect of each atomic potential for large polyatomic systems would give rise to a steeper increase in CCS than with helium buffer gas, since the atom-nitrogen interaction potential is stronger than the atom-helium interaction potential. In other words, the stronger interaction potential of nitrogen would be expected to scale with the number of atoms in the ionic system being measured, at least to a first approximation. Ion systems with different heteroatom compositions (e.g., lipids vs. peptides) would also be expected to exhibit different scaling of mass to CCS between helium and nitrogen; this effect cannot be definitively observed in the relatively narrow mass range surveyed in this work, though cursory effects of gas polarization seem to be present in the enhanced high-mass separation of lipids and peptides in nitrogen vs. helium. Such class-specific CCS differences may bear out as more overlapping measurements are obtained in future studies.

IV.V. Conclusions

The large database of nitrogen-derived CCS values presented here offers a glimpse at the intrinsic intermolecular packing forces of four chemically different molecular classes across a relatively wide range of both size (ca. 150 to 450 Å²) and mass (ca. 150 to 2200 Da). Four molecular classes were investigated in this study, with relative gas-phase densities observed as follows, from least to most efficient packing: TAA salts, lipids, peptides, and carbohydrates. The biopolymers (carbohydrates and peptides) demonstrated the highest efficiency for gas-phase packing, and among these, carbohydrates tend to adopt the most compact gas-phase CCS values. This observation is somewhat intuitive in that carbohydrates have considerable degrees of freedom

and can adopt both linear and branched primary structures. In contrast, lipids exhibit the largest CCS values among the biomolecules investigated, and this observation appears to be intrinsic to the inability of lipids for forming compact, self-solvated structures in the gas phase. Noteworthy among these findings is that despite the significant differences between helium and nitrogen in terms of mass, degrees-of-freedom (atomic vs diatomic), and polarization, the biomolecular class trends observed here for the nitrogen-based ion mobility are qualitatively the same as those previously observed in helium.^{3,26} We do observe evidence that these qualitative trends between the two drift gases are not retained at low mass, and a more detailed investigation of helium and nitrogen-based ion mobility studies for low mass analytes (less than 200 Da) will be the subject of future studies.

We emphasize that these studies are only possible by the remarkable advances made over the past decade in the development of biological IM-MS instrumentation. The IM-MS described in this report can achieve high resolving powers with high sensitivity, making it possible to observe and characterize low abundance isomeric species in highly complex samples with unprecedented scale and throughput. While we have purposely chosen to report only the highest abundant species, we note that the observation of multiple ion mobility peak features (i.e., structural and positional isomers) is routine with this instrumentation. As the analytical capabilities of distinguishing low-abundance isomeric species become widely accessible, we begin to move toward a new paradigm whereby it no longer becomes the question of if a particular isomer exists but rather how much of it is present and in what context.

IV.VI. Supporting Information

Empirically measured transport properties for the analytes evaluated in this work (Tables

D.1–D.4). A summary of the overlapping helium and nitrogen CCS measurements compared in this study (Table D.5). This material is available in Appendix D.

IV.VII. Acknowledgements

This chapter contains the published research article: Jody C. May, Cody R. Goodwin, Nichole M. Lareau, Katrina L. Leaprot, Caleb B. Morris, Ruwan T. Kurulugama, Alex Mordehai, Christian Klein, William Barry, Ed Darland, Gregor Overney, Kenneth Imatani, George C. Stafford, John C. Fjeldsted, and John A. McLean, “Conformational Ordering of Biomolecules in the Gas Phase: Nitrogen Collision Cross Sections Measured on a Prototype High Resolution Drift Tube Ion Mobility-Mass Spectrometer,” *Analytical Chemistry*, **2014**, 84, 2107-2116.

Financial support for this research to Vanderbilt University authors was in part from the NIH National Center for Advancing Translational Sciences (UH2TR000491); the Defense Threat Reduction Agency (HDTRA1-09-1-00-13 and DTRA100271 A-5196); the Defense Advanced Research Projects Agency (W911NF-12-2-0036); the Vanderbilt Institute of Chemical Biology; and the Vanderbilt Institute for Integrative Biosystems Research and Education. N.M.L. acknowledges a Vanderbilt Chemical Biology Interface training grant (T32GM065086). The content is solely the responsibility of the authors and does not necessarily represent the official views of the funding agencies and organizations.

IV.VIII. References

1. E. W. McDaniel, *Collision phenomena in ionized gases*, Wiley, New York, 1964.
2. E. W. McDaniel and E. A. Mason, *Mobility and diffusion of ions in gases*, John Wiley and Sons, Inc., New York, 1973.
3. L. S. Fenn and J. A. McLean, Biomolecular structural separations by ion mobility-mass spectrometry, *Analytical and Bioanalytical Chemistry*, 2008, **391**, 905-909.
4. J. A. McLean, The Mass-Mobility Correlation Redux: The Conformational Landscape of Anhydrous Biomolecules, *Journal of the American Society for Mass Spectrometry*, 2009, **20**, 1775-1781.
5. S. J. Valentine, A. E. Counterman and D. E. Clemmer, A database of 660 peptide ion cross sections: use of intrinsic size parameters for bona fide predictions of cross sections, *Journal of the American Society for Mass Spectrometry*, 1999, **10**, 1188-1211.
6. A. A. Shvartsburg, K. W. M. Siu and D. E. Clemmer, Prediction of peptide ion mobilities via a priori calculations from intrinsic size parameters of amino acid residues, *Journal of the American Society for Mass Spectrometry*, 2001, **12**, 885-888.
7. S. J. Valentine, A. E. Counterman, C. S. Hoaglund-Hyzer and D. E. Clemmer, Intrinsic Amino Acid Size Parameters from a Series of 113 Lysine-Terminated Tryptic Digest Peptide Ions, *The Journal of Physical Chemistry B*, 1999, **103**, 1203-1207.
8. A. R. Shah, K. Agarwal, E. S. Baker, M. Singhal, A. M. Mayampurath, Y. M. Ibrahim, L. J. Kangas, M. E. Monroe, R. Zhao, M. E. Belov, G. A. Anderson and R. D. Smith, Machine learning based prediction for peptide drift times in ion mobility spectrometry, *Bioinformatics*, 2010, **26**, 1601-1607.
9. K. Giles, S. D. Pringle, K. R. Worthington, D. Little, J. L. Wildgoose and R. H. Bateman, Applications of a travelling wave-based radio-frequency-only stacked ring ion guide, *Rapid Communications in Mass Spectrometry*, 2004, **18**, 2401-2414.
10. S. D. Pringle, K. Giles, J. L. Wildgoose, J. P. Williams, S. E. Slade, K. Thalassinou, R. H. Bateman, M. T. Bowers and J. H. Scrivens, An investigation of the mobility separation of some peptide and protein ions using a new hybrid quadrupole/travelling wave IMS/oa-ToF instrument, *International Journal of Mass Spectrometry*, 2007, **261**, 1-12.
11. M. F. Bush, Z. Hall, K. Giles, J. Hoyes, C. V. Robinson and B. T. Ruotolo, Collision Cross Sections of Proteins and Their Complexes: A Calibration Framework and Database for Gas-Phase Structural Biology, *Analytical Chemistry*, 2010, **82**, 9557-9565.
12. J. P. Williams, M. Grabenauer, R. J. Holland, C. J. Carpenter, M. R. Wormald, K. Giles, D. J. Harvey, R. H. Bateman, J. H. Scrivens and M. T. Bowers, Characterization of simple isomeric oligosaccharides and the rapid separation of glycan mixtures by ion mobility mass spectrometry, *International Journal of Mass Spectrometry*, 2010, **298**, 119-127.

13. H. E. Revercomb and E. A. Mason, Theory of Plasma Chromatography/Gaseous Electrophoresis: A Review, *Analytical Chemistry*, 1975, **47**, 970-983.
14. E. A. Mason and E. W. McDaniel, *Transport Properties of Ions in Gases*, John Wiley & Sons, New York, 1988.
15. B. T. Ruotolo, K. Giles, I. Campuzano, A. M. Sandercock, R. H. Bateman and C. V. Robinson, Evidence for Macromolecular Protein Rings in the Absence of Bulk Water, *Science*, 2005, **310**, 1658-1661.
16. B. T. Ruotolo, J. L. P. Benesch, A. M. Sandercock, S.-J. Hyung and C. V. Robinson, Ion mobility-mass spectrometry analysis of large protein complexes, *Nature Protocols*, 2008, **3**, 1139-1152.
17. W. B. Ridenour, M. Kliman, J. A. McLean and R. M. Caprioli, Structural Characterization of Phospholipids and Peptides Directly from Tissue Sections by MALDI Traveling-Wave Ion Mobility-Mass Spectrometry, *Analytical Chemistry*, 2010, **82**, 1881-1889.
18. T. W. Knapman, J. T. Berryman, I. Campuzano, S. A. Harris and A. E. Ashcroft, Considerations in experimental and theoretical collision cross-section measurements of small molecules using travelling wave ion mobility spectrometry-mass spectrometry, *International Journal of Mass Spectrometry*, 2010, **298**, 17-23.
19. A. A. Shvartsburg, S. V. Mashkevich and K. W. M. Siu, Incorporation of Thermal Rotation of Drifting Ions into Mobility Calculations: Drastic Effect for Heavier Buffer Gases, *The Journal of Physical Chemistry A*, 2000, **104**, 9448-9453.
20. A. A. Shvartsburg, R. R. Hudgins, P. Dugourd and M. F. Jarrold, Structural information from ion mobility measurements: applications to semiconductor clusters, *Chemical Society Reviews*, 2001, **30**, 26-35.
21. I. Campuzano, M. F. Bush, C. V. Robinson, C. Beaumont, K. Richardson, H. Kim and H. I. Kim, Structural Characterization of Drug-like Compounds by Ion Mobility Mass Spectrometry: Comparison of Theoretical and Experimentally Derived Nitrogen Collision Cross Sections, *Analytical Chemistry*, 2011, **84**, 1026-1033.
22. C. Larriba and C. J. Hogan, Ion Mobilities in Diatomic Gases: Measurement versus Prediction with Non-Specular Scattering Models, *The Journal of Physical Chemistry A*, 2013, **117**, 3887-3901.
23. K. Pagel and D. J. Harvey, Ion Mobility–Mass Spectrometry of Complex Carbohydrates: Collision Cross Sections of Sodiated N-linked Glycans, *Analytical Chemistry*, 2013, **85**, 5138-5145.
24. W. M. Haynes, D. R. Lide and T. J. Bruno, *CRC Handbook of Chemistry and Physics 2012-2013*, CRC press, 93 edn., 2012.
25. E. S. Baker, B. H. Clowers, F. Li, K. Tang, A. V. Tolmachev, D. C. Prior, M. E. Belov and

- R. D. Smith, Ion Mobility Spectrometry-Mass Spectrometry Performance Using Electrodynamic Ion Funnel and Elevated Drift Gas Pressures, *Journal of the American Society for Mass Spectrometry*, 2007, **18**, 1176-1187.
26. L. Fenn, M. Kliman, A. Mahsut, S. Zhao and J. McLean, Characterizing ion mobility-mass spectrometry conformation space for the analysis of complex biological samples, *Anal. Bioanal. Chem.*, 2009, **394**, 235-244.
 27. L. Tao, J. R. McLean, J. A. McLean and D. H. Russell, A collision cross-section database of singly-charged peptide ions, *Journal of the American Society for Mass Spectrometry*, 2007, **18**, 1232-1238.
 28. M. F. Bush, I. D. G. Campuzano and C. V. Robinson, Ion Mobility Mass Spectrometry of Peptide Ions: Effects of Drift Gas and Calibration Strategies, *Analytical Chemistry*, 2012, **84**, 7124-7130.
 29. R. Salbo, M. F. Bush, H. Naver, I. Campuzano, C. V. Robinson, I. Pettersson, T. J. D. Jørgensen and K. F. Haselmann, Traveling-wave ion mobility mass spectrometry of protein complexes: accurate calibrated collision cross-sections of human insulin oligomers, *Rapid Communications in Mass Spectrometry*, 2012, **26**, 1181-1193.
 30. M. Sud, E. Fahy, D. Cotter, A. Brown, E. A. Dennis, C. K. Glass, A. H. Merrill, Jr., R. C. Murphy, C. R. H. Raetz, D. W. Russell and S. Subramaniam, LMSD: LIPID MAPS structure database, *Nucleic Acids Res.*, 2007, **35**, D527-D532.
 31. M. R. Wilkins, I. Lindskog, E. Gasteiger, A. Bairoch, J.-C. Sanchez, D. F. Hochstrasser and R. D. Appel, Detailed peptide characterization using PEPTIDEMASS - a World-Wide-Web-accessible tool, *Electrophoresis*, 1997, **18**, 403-408.
 32. J. Fenn, M. Mann, C. Meng, S. Wong and C. Whitehouse, Electrospray ionization for mass spectrometry of large biomolecules, *Science*, 1989, **246**, 64-71.
 33. Y. Ibrahim, K. Tang, A. V. Tolmachev, A. A. Shvartsburg and R. D. Smith, Improving Mass Spectrometer Sensitivity Using a High-Pressure Electrodynamic Ion Funnel Interface, *Journal of the American Society for Mass Spectrometry*, 2006, **17**, 1299-1305.
 34. Y. Ibrahim, M. E. Belov, A. V. Tolmachev, D. C. Prior and R. D. Smith, Ion Funnel Trap Interface for Orthogonal Time-of-Flight Mass Spectrometry, *Analytical Chemistry*, 2007, **79**, 7845-7852.
 35. P. R. Kemper and M. T. Bowers, A hybrid double-focusing mass spectrometer--high-pressure drift reaction cell to study thermal energy reactions of mass-selected ions, *Journal of the American Society for Mass Spectrometry*, 1990, **1**, 197-207.
 36. G. von Helden, M.-T. Hsu, P. R. Kemper and M. T. Bowers, Structures of carbon cluster ions from 3 to 60 atoms: Linears to rings to fullerenes, *The Journal of Chemical Physics*, 1991, **95**, 3835-3837.

37. E. A. Mason and H. W. Schamp, Mobility of gaseous ions in weak electric fields, *Annals of Physics*, 1958, **4**, 233-270.
38. J. A. McLean, B. T. Ruotolo, K. J. Gillig and D. H. Russell, Ion mobility-mass spectrometry: a new paradigm for proteomics, *International Journal of Mass Spectrometry*, 2005, **240**, 301-315.
39. G. B. West, J. H. Brown and B. J. Enquist, A General Model for the Origin of Allometric Scaling Laws in Biology, *Science*, 1997, **276**, 122-126.
40. Y. Shen, J. E. Greene, M. A. Strauss, G. T. Richards and D. P. Schneider, Biases in virial black hole masses: An SDSS perspective, *The Astrophysical Journal*, 2008, **680**, 169.
41. G. Galilei, Discourses and Mathematical Demonstrations Relating to Two New Sciences, *Leiden*, 1638.
42. J. Viidanoja, A. Sysoev, A. Adamov and T. Kotiaho, Tetraalkylammonium halides as chemical standards for positive electrospray ionization with ion mobility spectrometry/mass spectrometry, *Rapid Communications in Mass Spectrometry*, 2005, **19**, 3051-3055.
43. L. S. Fenn and J. A. McLean, Structural resolution of carbohydrate positional and structural isomers based on gas-phase ion mobility-mass spectrometry, *Physical Chemistry and Chemical Physics*, 2011, **13**, 2196-2205.
44. H. W. Ellis, R. Y. Pai, E. W. McDaniel, E. A. Mason and L. A. Viehland, Transport Properties of Gaseous Ions Over a Wide Energy Range, *Atomic Data and Nuclear Data Tables*, 1976, **17**, 177-210.
45. H. W. Ellis, E. W. McDaniel, D. L. Albritton, L. A. Viehland, S. L. Lin and E. A. Mason, Transport Properties of Gaseous Ions Over a Wide Energy Range. Part II, *Atomic Data and Nuclear Data Tables*, 1978, **22**, 179-217.
46. H. W. Ellis, M. G. Thackston, E. W. McDaniel and E. A. Mason, Transport Properties of Gaseous Ions Over a Wide Energy Range. Part III, *Atomic Data and Nuclear Data Tables*, 1984, **31**, 113-151.
47. L. A. Viehland and E. A. Mason, Transport Properties of Gaseous Ions Over a Wide Energy Range, IV, *Atomic Data and Nuclear Data Tables*, 1995, **60**, 37-95.
48. L. M. Matz, H. H. Hill Jr, L. W. Beegle and I. Kanik, Investigation of drift gas selectivity in high resolution ion mobility spectrometry with mass spectrometry detection, *Journal of the American Society for Mass Spectrometry*, 2002, **13**, 300-307.
49. Z. Berant and Z. Karpas, Mass-mobility correlation of ions in view of new mobility data, *Journal of the American Chemical Society*, 1989, **111**, 3819-3824.
50. T. Wyttenbach, C. Bleiholder and M. T. Bowers, Factors Contributing to the Collision

Cross Section of Polyatomic Ions in the Kilodalton to Gigadalton Range: Application to Ion Mobility Measurements, *Analytical Chemistry*, 2013, **85**, 2191-2199.

51. G. von Helden, T. Wyttenbach and M. T. Bowers, Inclusion of a MALDI ion source in the ion chromatography technique: conformational information on polymer and biomolecular ions, *International Journal of Mass Spectrometry and Ion Processes*, 1995, **146-147**, 349-364.

CHAPTER V

STRUCTURAL CONFORMATION ATLAS FOR HIGH CONFIDENCE LIPIDOMICS

V.I. Abstract

Lipids represent a wide array of diverse molecules, with structural dissimilarities determining their biological function. Several analytical techniques including ion mobility-mass spectrometry (IM-MS) have emerged over the past decade to elucidate these structural details. In this study, measurements obtained from high precision IM-MS were used to compile a structural database of 354 mass-resolved collision cross section (CCS) values within the sphingolipid and glycerophospholipid categories, including sphingomyelin (SM), cerebroside (GlcCer), ceramide (Cer) phosphatidylethanolamine (PE), phosphatidylcholine (PC), phosphatidylserine (PS), and phosphatidic acid (PA) classes. Despite primary structural differences in head groups, all of the lipids from the two lipid categories exhibited near equivalent increases in CCS (ca. 0.15 \AA^2) per mass unit, suggesting these lipids adopt general and predictable gas-phase conformations governed by bond differences within the acyl tails. Primary differences observed were between the broad lipid classes, with sphingolipids possessing a 4 to 5% larger CCS than glycerophospholipids of similar mass, interpreted to be a result of the sphingosine backbone's restriction of the sn1 tail length which in turn limits the gas-phase packing efficiency of this lipid class. Conformational broadening of 0.19 to 0.20 \AA^2 per mass was collectively observed for the sphingolipids, whereas less CCS broadening (0.14 to 0.17 \AA^2 per mass) was observed for glycerophospholipids. Within each of the seven lipid classes investigated, total acyl tail length and degree of unsaturation were found to be primary structural descriptors that determined the magnitude of the CCS. In addition

to the empirical CCS values supporting future lipid identification workflows, the quantitative trends mapped in this study have broad utility for predicting the CCS of lipids not explicitly observed.

V.II. Introduction

Lipids are an essential class of biomolecules, performing functions such as contributing to cell membrane structure, regulating cell activities, and storing concentrated energy.¹ Lipids represent a wide array of structurally diverse, often isomeric, molecules because each lipid can vary in headgroup type, acyl chain length, position of attachment, degree of unsaturation, and stereochemistry.² The position of double bonds in lipids is important in the determination of their biological function; for example, naturally occurring conjugated linoleic acid (CLA) isomers have been revealed to play varied biological roles based on the positions of the double bonds. Specifically, the effects of *trans*-10,*cis*-12 CLA on body composition and *cis*-9,*trans*-11 CLA on growth/feed efficiency appear to be a result of separate biochemical mechanisms,³ and only the *trans*-10,*cis*-12 CLA isomer regulates human stearoyl-CoA desaturase in HepG2 cells.⁴

Lipid research from the 1960s and 70s contributed much of our current knowledge of lipid biochemistry and metabolism,⁵ though, in the past few decades, several new analytical techniques have emerged to elucidate lipid structural details, specifically in the field of mass spectrometry (MS). For example, structures of brain gangliosides have been investigated by tandem MS/MS utilizing low-energy collision induced dissociation (CID) in both positive and negative ion mode nano-electrospray ionization (nano-ESI),⁶ as well as by a combination of nano-ESI, with Fourier-transform MS, and chip-based nano-ESI with thin-layer chromatography (TLC).⁷ Seamless post-source decay fragment ion analysis has been utilized to assign the position and identity of fatty

acid residues on the glycerol backbones of glycerophospholipids,⁸ and gas-phase ozonolysis reactions with MS detection have been developed to identify lipid double bond position.^{2,9-11}

Another emerging analytical technique that has found utility in lipid structural analysis is ion mobility coupled to MS (IM-MS).¹²⁻¹⁸ The structural measurement in IM-MS is in the form of a 2-dimensional collision cross section (CCS), which is an averaged measurement of the cross sectional area of the analyte. Comprehensive reviews of developments with respect to lipid analysis by IM-MS have been published.^{19,20} Interfacing IM with MS results in a comprehensive 2D separation capable of differentiating isomers and delineating molecules into respective biomolecular classes.^{21,22} IM-MS has been coupled with dual stage CID fragmentation to localize sites of unsaturation in phosphatidylcholines.²³ Detailed IM-MS analyses have previously revealed specific and reproducible mobility-mass correlations within each biomolecular class, related to molecular structures and packing efficiencies.²⁴⁻²⁶ The majority of lipid IM-MS work has been conducted using drift time measurements which are difficult to reproduce and compare across different laboratories and instrumentation.

In this study we focus on the relationship between lipid structure and gas-phase conformation via IM-MS analysis. Newly developed high precision IM-MS instrumentation based on uniform field measurements has enabled the quantitation of trends which have been previously observed in smaller data sets.^{12,13,19,27,28} These trends manifest in each lipid class and relate to varying conformational changes due to the degree of unsaturation or the acyl chain lengths. While similar observations have been made using other IM-MS methods,²⁹ this work represents the first large scale study which quantifies trends directly between mass and empirical CCS values obtained with uniform field ion mobility.

V.III. Materials and Methods

V.III.I. Preparation of Lipid Samples

HPLC grade solvents and buffers were obtained from Sigma-Aldrich (St. Louis, MO, USA). Lipid standards including phosphatidylethanolamine (PE, chicken egg), phosphatidylcholine (PC, chicken egg), phosphatidylserine (PS, porcine brain), sphingomyelin (SM, porcine brain), and cerebroside (GlcCer, porcine brain), were purchased as purified TLC fractions from Avanti Polar Lipids (Birmingham, AL, USA) and the dry extracts were reconstituted in chloroform prior to analysis. Lipid standards were diluted in 90% chloroform/10% methanol (v/v) to a final concentration of 10 µg/mL for analysis. Identification of lipids was based on exact mass measurements and the Lipid Metabolites and Pathways Strategy (LIPID MAPS) Structural Database (LMSD) and the Scripps Center for Metabolomics Metabolite Database (METLIN).

V.III.II. Instrumentation

Two independent high resolution IM-MS instruments (Model 6560) from Agilent Technologies, Inc. were utilized to acquire accurate mass and CCS measurements from lipid samples. Instrumentation has been described in more detail in a previous work.²⁴ Briefly, the instrument consists of an orthogonal electrospray ionization (ESI) source and a tandem ion funnel interface to create and direct ions into the uniform field IMS drift tube. An additional rear ion funnel refocuses ions as they exit the drift tube, and ions pass through a quadrupole and collision cell before mass measurement is performed in an orthogonal time-of-flight mass spectrometer (TOFMS).

V.III.III. Experimental Parameters

All 2D IM-MS spectra was obtained with direct infusion in positive mode ESI (Agilent Jet Stream Source) at 10 μ L/min flow rate. Nitrogen sheath gas at 12 L/min and 400-600 K and nitrogen drying gas at 10 L/min and 570 K were used in the Jet Stream source. The source potential emitter was held at ground voltage, the capillary entrance was biased to -4.5 kV, and the nozzle was biased to -1.8 kV. The high-pressure ion funnel was operated at ca. 4.8 Torr with RF 100 Vpp at 1.5 MHz and 150 V DC, the trapping ion funnel was operated at 3.8 Torr with RF 100 Vpp at 1.2 MHz and 180 V DC, and the rear funnel was operated at ca. 4.0 Torr with RF 100 Vpp at 1.2 MHz and 200 V DC. The IM was pressurized to ca. 4.0 Torr and ca. 300 K with ultrahigh purity nitrogen, and the voltage was varied between 750 to 1450 V (E/N range of 7 to 15 Td). Data was acquired and processed using modified MassHunter software (Data Acquisition and IMS Browser, Agilent Technologies).

V.III.IV. Calibration Methods

Mobility and mass calibration was applied externally using homogenously substituted fluorinated triazatriphosphorines (Agilent tune mix, ca. 100 to 3000 mass). In addition, tetraalkylammonium (TAA) salts, which fall outside the IM and MS range of lipids, were added to all samples as internal standards for positive mode analysis. TAA salts of 98% purity or greater and varying alkyl chain lengths were obtained from several sources: TAA4, TAA6, TAA7, TAA10, TAA12, and TAA16 were purchased from Sigma Aldrich, TAA3, TAA5, and TAA8 were purchased from Acros Organics (Morris Plains, New Jersey, USA), and TAA18 was purchased from Alfa Aesar (Ward Hill, MA, USA). TAA3 to TAA8 were prepared in 50% methanol/50%

water. TAA10, TAA12, TAA16, and TAA18 were prepared in 50% methanol/50% isopropanol. Final concentrations for analyses were ca. 1 $\mu\text{g/mL}$.

V.IV. Results and Discussion

V.IV.I. Lipid Nomenclature

Lipid nomenclature in this study follows the classification system used in LIPIDMAPS (<http://www.lipidmaps.org>) and developed by Fahy, et al.,^{30,31} where the first set of letters represents the lipid class (head group), modifications are denoted by any following letters (h or HETE for hydroxyl group presence and O for loss of a carboxyl group from one of the fatty acyl chains), the number preceding the colon denotes the summed carbon chain lengths, and the number following the colon refers to the total number of double bonds in the carbon chains. Although IM-MS analysis for glycerophospholipids is often performed in negative ionization mode, this work was done in positive ionization mode in order to explore lipid features of complex mixtures in the more commonly used analysis mode for biological samples. Only singly-charged cations are reported, and there is no evidence in the spectra of lipid monomers adopting higher charge states. Although multiply charged multimers are observed in low abundance, the majority of these are heteromultimers arising from combination of different lipids, which are difficult to assign an identity to with single-stage IM-MS alone.

Lipids were analyzed from class-specific TLC fractions and identifications were assigned primarily based on exact mass measurements. The CCS measurements were utilized when mass data alone was inconclusive, i.e., when mass resolution is low the additional separation dimension provided by IM can aid in lipid identification.

V.IV.II. Lipid Population Observations

This work presents CCS values for 354 uniquely identified lipid monomer features representing 7 lipid classes (Figure 5.1(A), Table E.2) analyzed by uniform field, positive mode IM-MS. 74 of these CCS values have been previously published.²⁴ Lipid categories included glycerophospholipid (PA, PE, PC, and PS) and sphingolipid (Cer, GlcCer, and SM) extracts from chicken egg and porcine brain. The resulting lipid identification distributions are presented in Figure 5.1(B). For glycerophospholipids, longer alkyl chain lengths allowed accommodation of more sites of unsaturation, with PA and PC species containing as many as 6 sites of unsaturation, and PE and PS including as many as 9 and 10 sites of unsaturation, respectively. Observed sphingolipids had less sites of unsaturation, as is common in biological samples, with 5, 4, and 3 or less doubly bonded carbons for GlcCer, SM, and Cer, respectively. Maximum alkyl chain lengths increased with the head group size for glycerophospholipids, with PA lipids found with 35-40 carbons, PE 32-42, PC 32-40, and PS 34-44. The sphingolipids exhibited a slightly wider range of chain lengths than the glycerophospholipids, with GlcCer having 34-50 carbon atoms, SM 34-44, and Cer 36-44. These observations are summarized in the histograms of Figure 5.1(D).

V.IV.III. Category and Class IM-MS Correlation

Previous IM-MS studies have demonstrated that biomolecules separate into distinctive class-based trends in plots of CCS vs. mass,²² and that different lipid categories, e.g., glycerophospholipids and sphingolipids, occupy unique space within these correlations.²⁴ In this work, all primary lipid classes exhibit a positive mobility-mass correlation in conformational space analyses. Within the combined lipid trendline, unique lipid categories (sphingolipids and glycerophospholipids) could be further differentiated, with little overlap, by their respective CCS

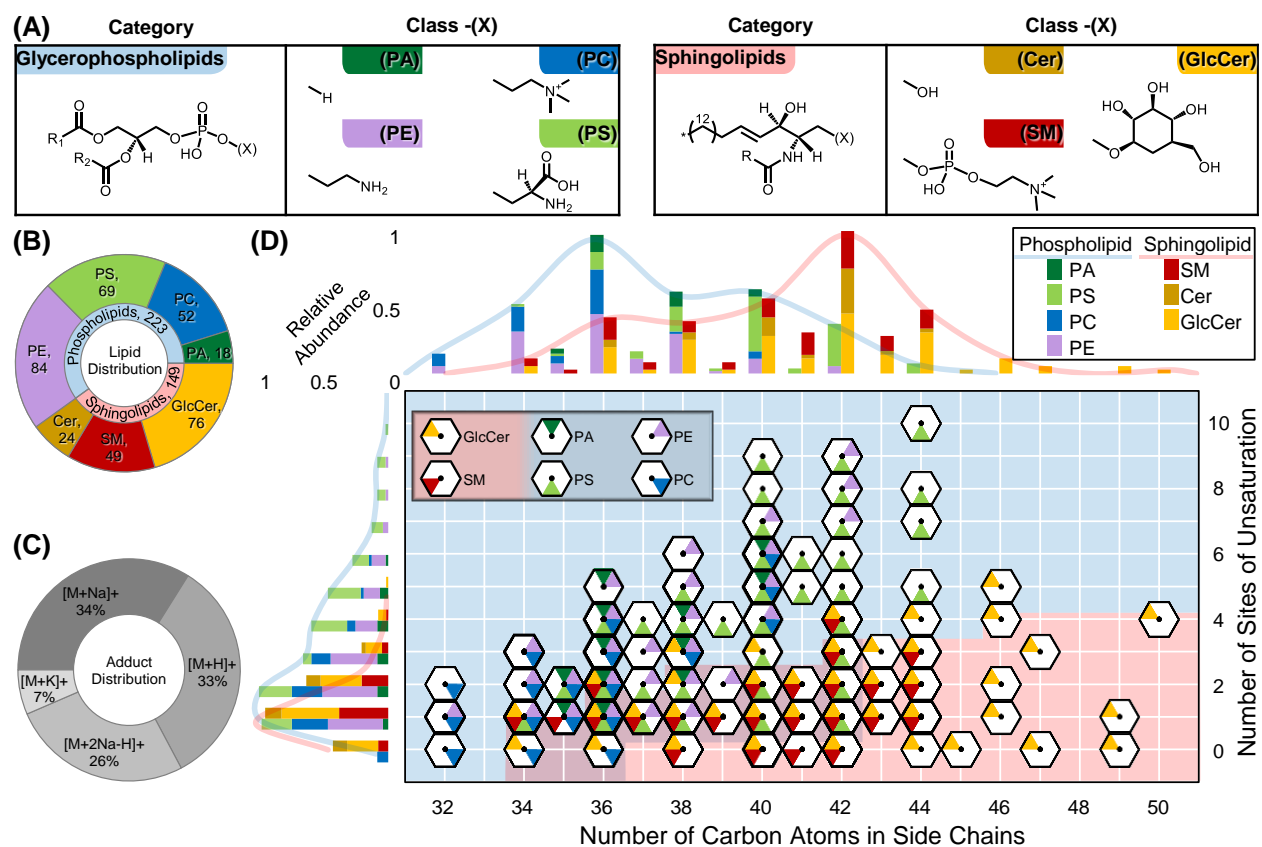


Figure 5.1: (A) Lipids investigated in this work are classified by head group. Expected and observed species are listed by the total number of carbons or double bonds in the fatty acid tails. (B) The distribution of lipids observed in this work. The inner ring denotes lipid categories whereas the outer ring details features observed in each lipid class. (C) The distribution of adducts observed in this work. (D) Central graph represents population of lipid summed chain lengths (x-axis) and degrees of unsaturation (y-axis) identified in this work, separated by class and excluding adduct and modification information. Cer class lipids are included with GlcCer. Background shading delineates lipid categories, with sphingolipids in red and glycerophospholipids in blue. Left histogram displays distribution of degree of unsaturation, normalized to each category. Top histogram shows summed chain length distribution, normalized to each category.

information, as each category exhibited an average CCS increase of 0.15 \AA^2 per mass unit, with glycerophospholipids having CCS values 13 \AA^2 (4-5%) less than sphingolipids of equivalent mass in the investigated mass range of 500 to 1000 Da (Figure 5.2(A)). This finding suggests that lipids originating from complex mixtures can be readily classified into one of these two primary lipid categories using CCS and mass information.

A closer examination of the IM-MS data (Figure 5.2(B)), shows a regular increase in size (linear slopes) for individual lipid classes within the glycerophospholipid category with corresponding slopes (CCS vs. mass) ranging from 0.14 to 0.17 \AA^2 per mass unit. Classes within the sphingolipid category exhibit a slightly larger increase in size with mass, with an empirically observed range in slope, from 0.19 to 0.20 \AA^2 per mass unit. The larger conformations observed for sphingolipids are likely related to the limited degrees of unsaturation due to the constraint of the sphingosine backbone. Lipid class trends within each category are very similar, indicating that while the acyl chain governs the change in CCS, the lipid head group dominates the overall magnitude of the ion cross section. This observation is discussed later in the manuscript.

Although sphingomyelin is categorized as a sphingolipid due to the sphingosine backbone, as a ceramide with phosphatidylcholine in the head group, it shares structural aspects with the PC lipid class, whereas other lipid classes investigated in this work fall strictly into a single lipid category by conventional definitions. Interestingly, though sphingomyelin contains structural attributes of both the sphingolipid and glycerophospholipid categories, instead of falling between PC and GlcCer, it exhibits larger than expected CCS values, being similar in size to GlcCer (Figure 5.2(B)). This is likely due to a combination of the sphingosine backbone constraining the sn1 tail length and the choline head group conformation, which packs less efficiently than the GlcCer monosacharride headgroup.

V.IV.IV. Cation Forms

In positive ionization mode, multiple adducts are commonly formed for each lipid species. Adduction of protons and sodium ions were predominantly observed in this study (Figure 5.1(C)). Positive identifications with these common adducts prompted subsequent searches for the same lipids with other adducts to deconvolute the spectra. For example, SM 36:01 was subsequently found in the spectra as $[M+H]^+$, $[M+Na-H_2O]^+$, $[M+Na]^+$, and $[M+K]^+$, and both PC 34:01 and PE 34:01 were found as $[M+H]^+$, $[M+Na]^+$, $[M+K]^+$, and $[M+2Na-H]^+$.

Commonly observed charged adducts varied slightly between the different lipid classes with $[M+Na]^+$ being most common, followed by $[M+H]^+$ which was observed in all classes except PA. $[M+2Na-H]^+$ adducts were identified in SM and all four glycerophospholipid classes, and $[M+K]^+$ features were identified in SM, PC, PE, and PS. The lack of appearance of the $[M+K]^+$ adduct in PA is likely due to the lower abundance of this class. Neutral water loss, though common in the hydroxyl abundant sphingolipids, was not observed in glycerophospholipids: $[M+H-H_2O]^+$ occurred in Cer, GlcCer, and SM, and $[M+H-2H_2O]^+$ was observed in Cer and GlcCer. Whether water loss occurs in solution or during ionization is unknown.

The nature of the charge carrier was found to influence the overall CCS of all lipids (Figure 5.3). In general, $[M+Na]^+$, $[M+K]^+$, and $[M+2Na-H]^+$ features increased CCS over $[M+H]^+$ by $2.5 \pm 2.0 \text{ \AA}^2$, $4.7 \pm 1.2 \text{ \AA}^2$, and $5.6 \pm 1.4 \text{ \AA}^2$ in 43, 15, and 26 cases, respectively. Sphingomyelin data is omitted from this analysis, as it exhibited significantly different behavior, with 15 cases of $[M+H]^+$ all being larger than $[M+Na]^+$ by $1.9 \pm 1.1 \text{ \AA}^2$. This unusual trend of smaller CCS values for sodiated species compared to potassiated species is likely related to the larger gas-phase conformations observed for sphingolipids, where the adduction of a metal does not add significantly to the CCS.

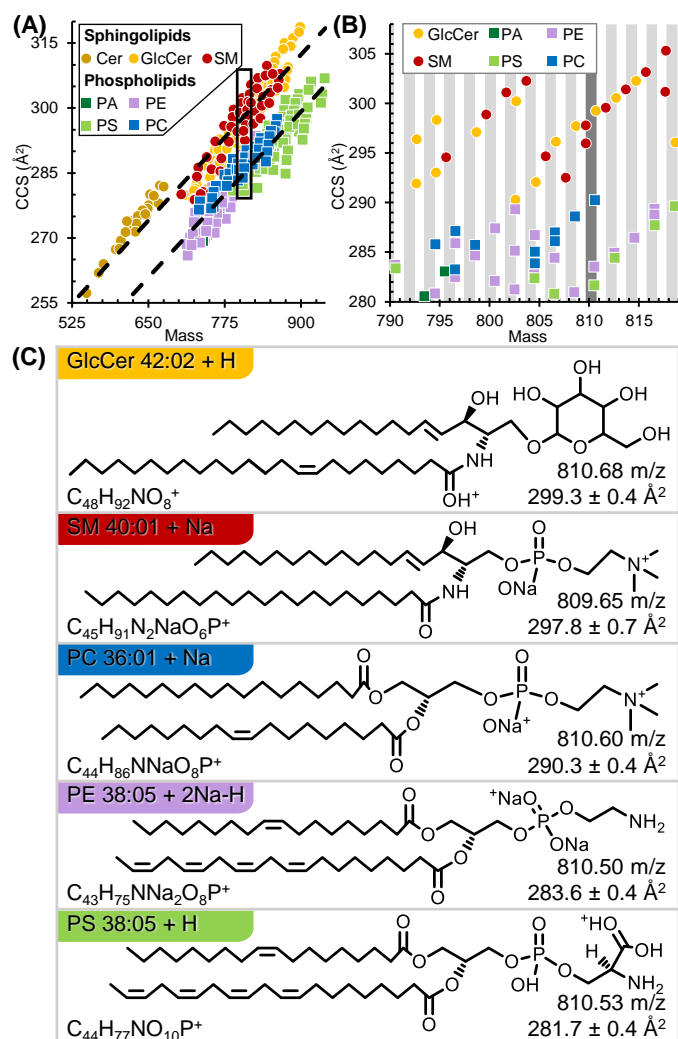


Figure 5.2: (A) Conformational space analysis of singly charged lipids including 7 classes from 2 lipid categories. (B) Expanded region from (A) highlighting occupancy of each lipid class by mass and CCS. The gray bars highlight series of nominal mass isomers (± 1 Da). Note the largest CCS difference for peaks of similar mass is between glycerophospholipids and spingolipids. (C) Primary structures of the five nominal mass isomeric lipids (809.6 to 810.7 Da) highlighted in panel B. CCS values are all statistically different and largest for spingolipids. Note structural information is inferred from rules described by Voet, et al. with (i) lipids assembled as concatenations of C_2 units making even-numbered chains prevalent, (ii) the first unsaturation site

preferably located between C9 and C10, (iii) subsequent unsaturation sites occurring every third bond, and (iv) double bonds existing primarily in the cis- configuration.³³ Adducts are shown at likely basic sites. Additionally, sphingolipids contain a sphingosine backbone.

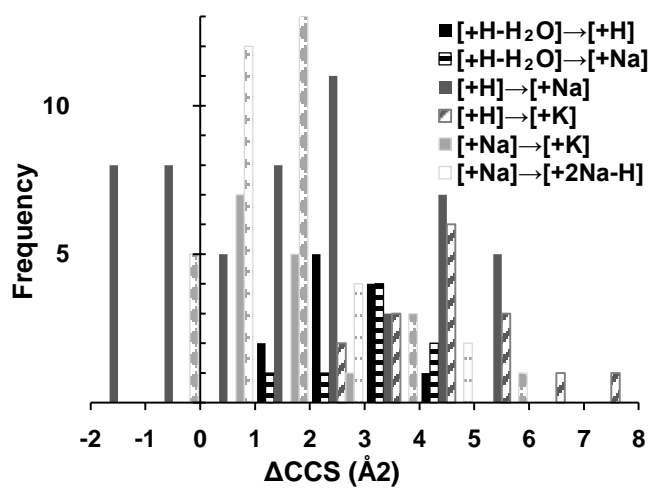


Figure 5.3: Histogram summarizing observed change in collision cross section (CCS) across the different adducts.

V.IV.V. Quantitative Mobility-Mass Correlations

Within each individual lipid class, highly linear mobility-mass correlations were observed (Figure 5.4, and Figure E.1). With either the degree of unsaturation or the chain length held constant, no secondary dependence on the modification type or adduct was found to influence these mobility-mass correlation trends. For example, the correlation of protonated PE lipids with a single acyl double bond is nearly identical to correlations observed for lipids with either a sodium adduct, hydroxylated beta carbon, or different number of double bonds. Thus, the lipid trends are predominately a result of two primary structural features: the number of carbons in the acyl tail and the degree of unsaturation.

For each lipid class, lipid features were grouped based on either the same numbers of double bonds or acyl chain carbons, and linear functions were fitted to three or more lipid features within each category. Across the 7 lipid classes investigated, this yielded linear fits for 56 sets of lipids with varying degrees of unsaturation (Figure 5.4(A), Figure 5.4(C), and Figure E.1), and 44 sets of lipids with varying number of acyl chain carbons (Figure 5.4(B), Figure 5.4(D), and Figure E.1). In agreement with findings from Zhang et al., a linear equation was found to best describe the correlation between CCS and mass.³² Here, average R^2 values of 0.98 (0.89 minimum) for common alkyl chain length and 0.99 (0.94 minimum) for common degree of unsaturation were observed. Though size is inherently expected to increase with mass, structural changes affect molecular density, and changes in the degree of unsaturation were found to be four times as influential on CCS as changes in alkyl chain length across all lipid classes (Table E.1) with slopes of $0.95 \pm 0.16 \text{ \AA}^2$ per mass unit and $0.23 \pm 0.03 \text{ \AA}^2$ per mass unit, respectively.

The larger deviation in slopes observed for lipids with a common degree of unsaturation is

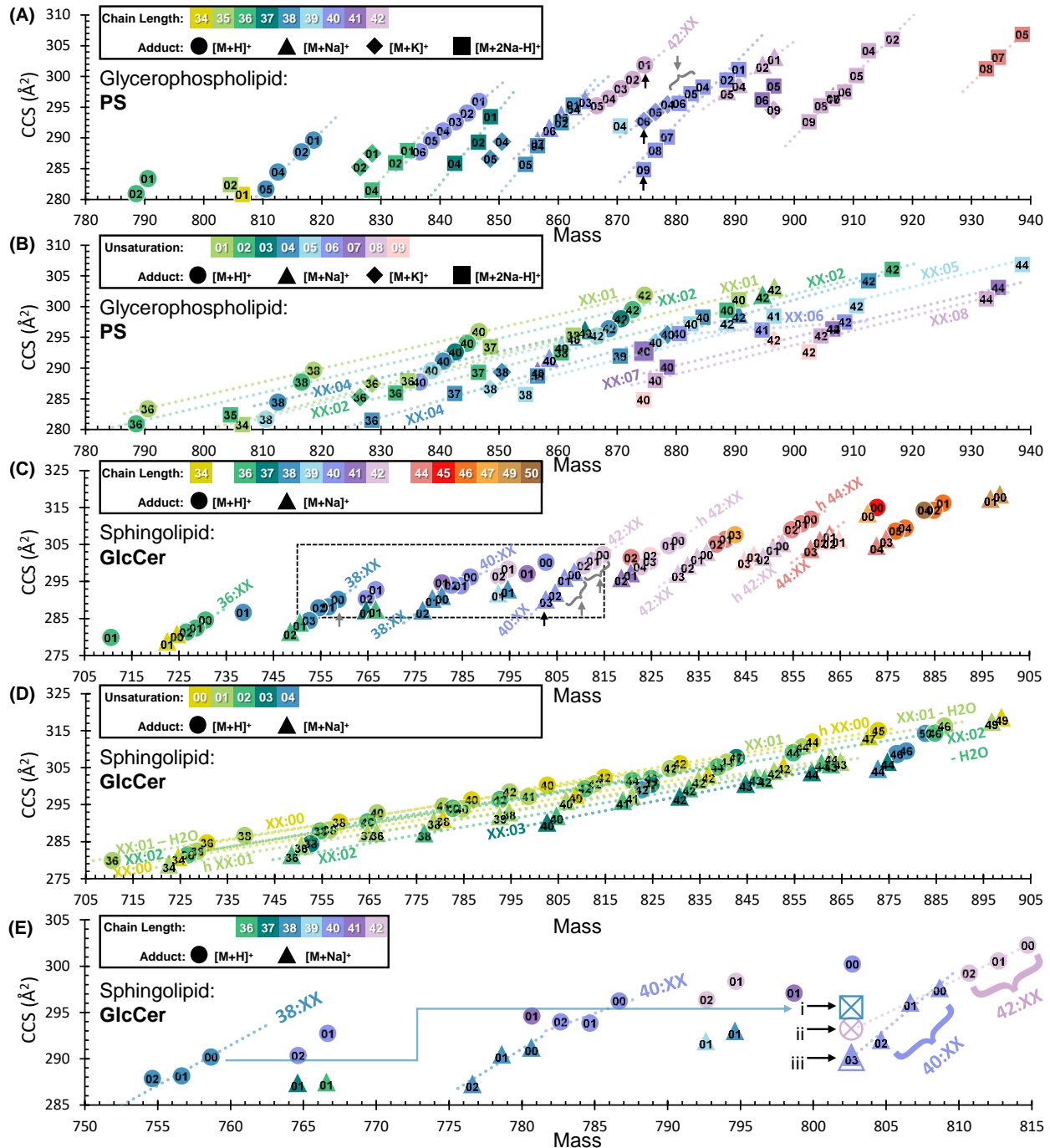


Figure 5.4: Select plots of quantitative correlations observed within the PS and GlcCer lipid classes. Colors correspond to either summed chain length or degree of unsaturation whereas shapes correspond to cation type, as specified in the corresponding panel legends. Numerical annotations within symbols correspond either to degree of unsaturation or carbon length, depending on the

panel. Error bars for the CCS measurements are all within the size of the markers. (A) For the same carbon chain length, GS lipids increase linearly in CCS with each loss of unsaturation. (B) A regular increase in CCS is also observed as the GS acyl chain length increases, with linear trends observed for the same degree of unsaturation. (C) GlcCer lipids exhibit longer chain lengths than PS, however, the same linear trends are observed for both number of double bonds, and (D) for carbon chain length within the same double bond category. (E) A closer inspection of the boxed region highlighted in (C) demonstrates identification of the initially unknown lipid feature at 802.616 Da, 290.3 Å². (i) Based on the quantitative CCS trends, the lipid feature is lower in CCS than the 295.8 Å² predicted for GlcCer 38:00 + 2Na-H, while (ii) the predicted value of 293.1 Å² for GlcCer 42:06 + H is higher than the measured CCS of this feature. (iii) However, the CCS predicted for GlcCer 40:03 + Na, 290.1 Å², aligns with the unknown feature, which provides high confidence identification of this lipid based on the CCS information of neighboring species.

attributed to a combination of mass overlap and poorly resolved drift times. Lipids of common chain length tend to occur with multiple degrees of unsaturation, and the loss of one double bond (equivalent to an addition of 2 hydrogen atoms, or 2.02 Da) overlaps the third isotope of the smaller, more unsaturated lipid in mass, decreasing the measured CCS of the heavier species. In addition to isotopic interference, mass overlap also occurs for lipids of varied structure and adduct. For example, at nominal mass 874 corresponding to PS 40:09 + 2Na-H, PS 40:06 + K, and PS 42:01 + H (Figure 5.4(A); 874.46, 874.50, and 874.65, respectively), the latter nominal mass isomer, PS 42:01 + H, has a larger CCS and is also more abundant in the spectra, which results in PS 40:06 + K to be calculated at a CCS higher than predicted from trends in the data. In another example, PS 42:09 + Na, PS 42:08 + Na, and PS 42:07 + Na have CCS values which are higher than expected (Figure 5.4(A)) and which is attributed to spectral overlap with PS 40:03 + K, PS 40:02 + K, and PS 40:01 + K, respectively, although these potassium adducted species were not able to be resolved as unique features. We present these examples to demonstrate the level of complexity which is present even for class-purified lipid standards.

V.IV.VI. Identification by CCS

The quantitative trends which describe lipid chain length and number of unsaturation sites can be used as an aid in identifying unknown lipids. For example, the peak at 802.62 Da, 290.3 Å² (Figure 5.4(C)) could be confidently mass-identified within 5 ppm as either GlcCer 42:06 + H, GlcCer 40:03 + Na, or GlcCer 38:00 + 2Na-H, but addition of sub-trend information adds confidence to the identification of the feature. In this case an [M+2Na-H]⁺ lipid would be expected to fall ~5.6 Å² higher in CCS than the corresponding [M+H]⁺ peak, but GlcCer 38:00 + H had a CCS of 290.2 Å², and, although this lipid's mass is closest to the measured mass, the predicted

CCS, 295.8 \AA^2 , is significantly higher than the measured CCS. Likewise, the $[M+H]^+$ candidate, aside from its uncommonly high degree of unsaturation for a sphingolipid, would be expected to fall on the linear trend with GlcCer 42:00 + H, GlcCer 42:01 + H, and GlcCer 42:02 + H, but this trend predicts a CCS of 293.1 \AA^2 for a peak at this mass, also significantly higher than the observed CCS. The $[M+Na]^+$ peak, on the other hand, aligns well with the trend corresponding to GlcCer 40:00 + Na, GlcCer 40:01 + Na, and GlcCer 40:02 + Na, which predicts a CCS of 290.1 \AA^2 , in close agreement with the measured value (Figure 5.4(E)).

V.IV.VII. Lipid Mixture Analysis

Figure 5.5 contains the 2D IM-MS spectrum of a mixture of PE, PS, PC, SM, and GlcCer lipids. While high resolution mass measurement is oftentimes enough to resolve and confidently identify lipids by accurate mass, in cases where significant feature overlap is observed, mass information alone is insufficient (Figure E.2). For example, three features are found at nominal mass 834 within a 0.3 Da window (Figure 5.5(B)) and correspond to the first isotopes of GlcCer 42:01 + Na, PC 38:03 + Na, and PS 38:04 + Na. The two phospholipids are present in very low relative abundance, which results in their peak features being challenging to resolve in either the IM or MS dimension alone, with the integrated spectrum (black line) for each dimension exhibiting only a single distribution. With the combined IM-MS information, however, three features are readily observed and can be extracted to resolve each of the three lipids in both IM and MS space. This in turn allows accurate mass and CCS information to be obtained. Using the CCS information, more confident identifications of the components in this narrow mass window can be made by correlating the two lower CCS features to PS and PC lipids, and the high CCS feature to GlcCer.

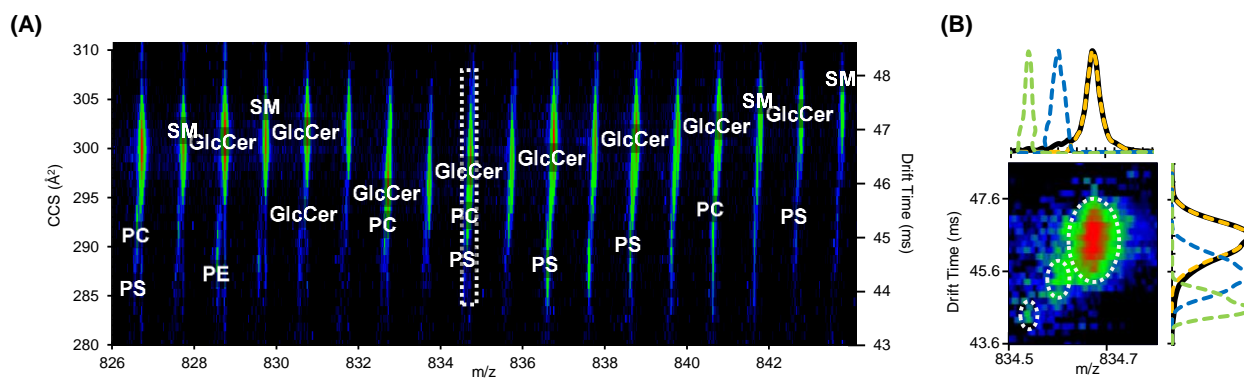


Figure 5.5: (A) A 2D IM-MS spectrum for a mixture of lipid extracts, with individual lipid classes annotated. (B) Selected region demonstrated multiple lipid features fall within a narrow mass and CCS range. Dotted lines represent extracted mobility and mass spectra for circled features which include GlcCer (orange), PC (blue), and PS (green) lipids.

V.V. Summary

In this work, 354 CCS measurements are presented for 4 classes of glycerophospholipids (PA, PC, PE, PS) and 3 classes of sphingolipids (Cer, SM, GlcCer). In complex IM-MS spectra, lipids can be observed in a region separate from other biomolecular classes and discerned within this region by lipid category, trending uniquely relative to head group size. Multiple adducts of each lipid species were observed in positive ionization mode, with, in general, relative CCS values being commensurate with the relative size of the adducts, that is, $[M+2Na-H]^+ > [M+K]^+ > [M+Na]^+ > [M+H]^+$. For lipids of common head group, changes in the degree of unsaturation were found to be four times as influential on conformational broadening, as were changes in alkyl chain length. We believe the trends determined from this data and the knowledge of their generalizability to other lipid classes will aid in identifications of lipid features in future analyses, when mass information alone is found to be insufficient.

V.VI. Supporting Information

Supporting information for this chapter including CCS vs. mass plots for PA, PE, PC, SM, and GlcCer, a table of variables describing the linear fits, a sample mobility separation for a set of lipid isomers, and a table of all CCS data obtained in this study is available in Appendix E.

V.VII. Acknowledgements

This chapter contains the research article by Katrina L. Leaptrot, Jody C. May, James N. Dodds, and John A. McLean, “Structural Conformation Atlas for High Confidence Lipidomics,” in preparation for submission in 2018.

Financial support for this work was provided by the National Institutes of Health (R01GM092218 and NCATS 3UH3TR000491-0451), the Warren Endowment Fund, and the Vanderbilt Institute for Integrative Biosystems Research and Education. The content is solely the responsibility of the authors and does not necessarily represent the official views of the funding agencies and organizations.

V.VIII. References

1. M. I. Gurr, J. L. Harwood and K. N. Frayn, *Lipid Biochemistry, 5th Edition*, Blackwell Science Ltd., Oxford, UK, 2002.
2. S. H. J. Brown, T. W. Mitchell and S. J. Blanksby, Analysis of unsaturated lipids by ozone-induced dissociation, *Biochimica et Biophysica Acta (BBA)-Molecular and Cell Biology of Lipids*, 2011, **1811**, 807-817.
3. M. W. Pariza, Y. Park and M. E. Cook, The biologically active isomers of conjugated linoleic acid, *Progress in Lipid Research*, 2001, **40**, 283-298.
4. Y. Choi, Y. Park, M. W. Pariza and J. M. Ntambi, Regulation of Stearoyl-CoA Desaturase Activity by the *trans*-10, *cis*-12 Isomer of Conjugated Linoleic Acid in HepG2 Cells, *Biochemical and Biophysical Research Communications*, 2001, **284**, 689-693.
5. M. Orešič, Informatics and computational strategies for the study of lipids, *Biochimica et Biophysica Acta (BBA)-Molecular and Cell Biology of Lipids*, 2011, **1811**, 991-999.
6. W. Metelmann, Z. Vukelic and J. Peter-Katalinic, Nano-electrospray ionization time-of-flight mass spectrometry of gangliosides from human brain tissue, *Journal of Mass Spectrometry*, 2001, **36**, 21-29.
7. Ž. Vukelić, S. Kalanj-Bognar, M. Froesch, L. Bîndilă, B. Radić, M. Allen, J. Peter-Katalinić and A. D. Zamfir, Human gliosarcoma-associated ganglioside composition is complex and distinctive as evidenced by high-performance mass spectrometric determination and structural characterization, *Glycobiology*, 2007, **17**, 504-515.
8. G. Stübiger, E. Pittenauer and G. Allmaier, MALDI seamless postsource decay fragment ion analysis of sodiated and lithiated phospholipids, *Analytical Chemistry*, 2008, **80**, 1664-1678.
9. R. L. Grimm, R. Hodyss and J. L. Beauchamp, Probing interfacial chemistry of single droplets with field-induced droplet ionization mass spectrometry: Physical adsorption of polycyclic aromatic hydrocarbons and ozonolysis of oleic acid and related compounds, *Analytical Chemistry*, 2006, **78**, 3800-3806.
10. M. C. Thomas, T. W. Mitchell and S. J. Blanksby, Ozonolysis of phospholipid double bonds during electrospray ionization: A new tool for structure determination, *Journal of the American Chemical Society*, 2006, **128**, 58-59.
11. M. C. Thomas, T. W. Mitchell, D. G. Harman, J. M. Deeley, R. C. Murphy and S. J. Blanksby, Elucidation of double bond position in unsaturated lipids by ozone electrospray ionization mass spectrometry, *Analytical Chemistry*, 2007, **79**, 5013-5022.
12. S. N. Jackson, M. Ugarov, J. D. Post, T. Egan, D. Langlais, J. A. Schultz and A. S. Woods, A study of phospholipids by ion mobility TOFMS, *Journal of the American Society for Mass Spectrometry*, 2008, **19**, 1655-1662.

13. H. I. Kim, H. Kim, E. S. Pang, E. K. Ryu, L. W. Beegle, J. A. Loo, W. A. Goddard and I. Kanik, Structural Characterization of Unsaturated Phosphatidylcholines Using Traveling Wave Ion Mobility Spectrometry, *Analytical Chemistry*, 2009, **81**, 8289-8297.
14. M. Groessl, S. Graf and R. Knochenmuss, High resolution ion mobility-mass spectrometry for separation and identification of isomeric lipids, *Analyst*, 2015, **140**, 6904-6911.
15. G. Astarita and G. Paglia, Ion-mobility mass spectrometry in metabolomics and lipidomics, *LC GC Europe*, 2015, **33**, 702-709.
16. S. E. Hancock, B. L. J. Poad, A. Batarseh, S. K. Abbott and T. W. Mitchell, Advances and unresolved challenges in the structural characterization of isomeric lipids, *Analytical Biochemistry*, 2016, DOI: 10.1016/j.ab.2016.09.014, Ahead of Print.
17. K. M. Hines, J. C. May, J. A. McLean and L. Xu, Evaluation of Collision Cross Section Calibrants for Structural Analysis of Lipids by Traveling Wave Ion Mobility-Mass Spectrometry, *Analytical Chemistry*, 2016, **88**, 7329-7336.
18. S. N. Jackson, H.-Y. J. Wang, A. S. Woods, M. Ugarov, T. Egan and J. A. Schultz, Direct tissue analysis of phospholipids in rat brain using MALDI-TOFMS and MALDI-ion mobility-TOFMS, *Journal of the American Society for Mass Spectrometry*, 2005, **16**, 133-138.
19. M. Kliman, J. C. May and J. A. McLean, Lipid analysis and lipidomics by structurally selective ion mobility-mass spectrometry, *Biochimica et Biophysica Acta (BBA)-Molecular and Cell Biology of Lipids*, 2011, **1811**, 935-945.
20. G. Paglia, M. Kliman, E. Claude, S. Geromanos and G. Astarita, Applications of ion-mobility mass spectrometry for lipid analysis, *Analytical and Bioanalytical Chemistry*, 2015, **407**, 4995-5007.
21. L. Tao, J. R. McLean, J. A. McLean and D. H. Russell, A collision cross-section database of singly-charged peptide ions, *Journal of the American Society for Mass Spectrometry*, 2007, **18**, 1232-1238.
22. L. Fenn and J. McLean, Biomolecular structural separations by ion mobility-mass spectrometry, *Analytical and Bioanalytical Chemistry*, 2008, **391**, 905-909.
23. J. Castro-Perez, T. P. Roddy, N. M. Nibbering, V. Shah, D. G. McLaren, S. Previs, A. B. Attygalle, K. Herath, Z. Chen and S.-P. Wang, Localization of fatty acyl and double bond positions in phosphatidylcholines using a dual stage CID fragmentation coupled with ion mobility mass spectrometry, *Journal of the American Society for Mass Spectrometry*, 2011, **22**, 1552-1567.
24. J. C. May, C. R. Goodwin, N. M. Lareau, K. L. Leaptrot, C. B. Morris, R. T. Kurulugama, A. Mordehai, C. Klein, W. Barry, E. Darland, G. Overney, K. Imatani, G. C. Stafford, J. C. Fjeldsted and J. A. McLean, Conformational Ordering of Biomolecules in the Gas

- Phase: Nitrogen Collision Cross Sections Measured on a Prototype High Resolution Drift Tube Ion Mobility-Mass Spectrometer, *Analytical Chemistry*, 2014, **86**, 2107-2116.
25. J. E. Kyle, X. Zhang, K. K. Weitz, M. E. Monroe, Y. M. Ibrahim, R. J. Moore, J. Cha, X. Sun, E. S. Lovelace, J. Wagoner, S. J. Polyak, T. O. Metz, S. K. Dey, R. D. Smith, K. E. Burnum-Johnson and E. S. Baker, Uncovering biologically significant lipid isomers with liquid chromatography, ion mobility spectrometry and mass spectrometry, *Analyst*, 2016.
 26. C. L. Wilkins and S. Trimpin, *Ion mobility spectrometry-mass spectrometry: theory and applications*, CRC press, 2010.
 27. S. Trimpin, B. Tan, B. C. Bohrer, D. K. O'Dell, S. I. Merenbloom, M. X. Pazos, D. E. Clemmer and J. M. Walker, Profiling of phospholipids and related lipid structures using multidimensional ion mobility spectrometry-mass spectrometry, *International Journal of Mass Spectrometry*, 2009, **287**, 58-69.
 28. S. N. Jackson, D. Barbacci, T. Egan, E. K. Lewis, J. A. Schultz and A. S. Woods, MALDI-ion mobility mass spectrometry of lipids in negative ion mode, *Analytical Methods*, 2014, **6**, 5001-5007.
 29. G. Paglia, P. Angel, J. P. Williams, K. Richardson, H. J. Olivos, J. W. Thompson, L. Menikarachchi, S. Lai, C. Walsh, A. Moseley, R. S. Plumb, D. F. Grant, B. O. Palsson, J. Langridge, S. Geromanos and G. Astarita, Ion Mobility-Derived Collision Cross Section As an Additional Measure for Lipid Fingerprinting and Identification, *Analytical Chemistry*, 2015, **87**, 1137-1144.
 30. E. Fahy, S. Subramaniam, H. A. Brown, C. K. Glass, A. H. Merrill, R. C. Murphy, C. R. H. Raetz, D. W. Russell, Y. Seyama and W. Shaw, A comprehensive classification system for lipids, *Journal of Lipid Research*, 2005, **46**, 839-862.
 31. E. Fahy, S. Subramaniam, R. C. Murphy, M. Nishijima, C. R. Raetz, T. Shimizu, F. Spener, G. van Meer, M. J. Wakelam and E. A. Dennis, Update of the LIPID MAPS comprehensive classification system for lipids, *Journal of Lipid Research*, 2009, **50**, S9-S14.
 32. F. Zhang, S. Guo, M. Zhang, Z. Zhang and Y. Guo, Characterizing ion mobility and collision cross section of fatty acids using electrospray ion mobility mass spectrometry, *Journal of Mass Spectrometry*, 2015, **50**, 906-913.
 33. D. Voet, J. G. Voet and C. W. Pratt, *Fundamentals of Biochemistry: Life at the Molecular Level*, John Wiley & Sons, Hoboken, NJ, 4th ed. edn., 2013.

CHAPTER VI

PERSPECTIVES AND PROPOSED IMPROVEMENTS FOR ION MOBILITY

INSTRUMENTATION

VI.I. Introduction

The following points of discussion are meaningful endeavors that have the potential to advance IM studies. The first topic of discussion concerns an adaptable instrument platform built on interfacing printed circuit boards (PCBs) that will enable novel studies of numerous molecules in both simple and complex samples with a design allowing modularity of the analytical platform to be customized to best suit the system of interest. The second topic of discussion concerns the outlook for future spatial multiplexing IM strategies. Pursuit of the described advancements will facilitate versatility in future applications with improved figures-of-merit including high throughput, sensitivity, and resolution.

VI.II. A Highly Versatile Device for Mobility and Mass Analysis Based on a Printable Two-Dimensional Planar Array

The first area of proposed research involves development of a highly versatile device on two interfacing PCBs with three stages including one for mobility or mass selection, a second for reaction or collision of selected ions, and a third stage for high resolution mobility and mass analyses of products or fragments. In the past five years, two-dimensional ion conveyors, termed “structures for lossless ion manipulation” (SLIM), and planar geometry ion optical devices such as the rectilinear ion funnel (RIF) have been developed to facilitate complex sequences of gas-

phase ion analyses. SLIM in particular is modular, low-cost, and forecast to comprise the next generation of mass spectrometry instrumentation. This novel technology has demonstrated potential for increasing analyses versatility by conducting IM separations within a small footprint.

The proposed research seeks to integrate prior research in PCB, quadrupole, collision induced dissociation (CID), ion-molecule reactions (IMR), and IM designs in the development of a single electrode geometry supporting variable electric fields, background gases, and pressures. The proposed device is of a novel electrode geometry, consisting of two separation/reaction regions, and will be interfaced with commercially available IM quadrupole time-of-flight (IM-QTOF) instrumentation for highly dimensional ($N \geq 5$) chemical analyses. Although commercial instrumentation can perform CID post-mobility, supporting gas-phase collisions or reactions prior to mobility analysis would allow collision cross section information to be collected on the products or fragments, rather than the reactants. The proposed instrument configuration would facilitate high versatility for analytical analyses, allowing pre-separation of ions by either mass or mobility in the first region, followed by CID or IMR in the second region, and concluding with high-resolution IM-QTOF analyses where additional mass-selected fragmentation (MS/MS) experiments can be conducted.

VI.II.I. Background and Significance

Over the last five years, developments have been made toward a class of novel ion optical devices based on two-dimensional electrode arrays, fabricated on PCBs. These new PCB devices typically have a smaller footprint, lower manufacturing costs, and are faster to prototype compared to conventional stacked ring (radially symmetric) ion optics. Because of their modularity, PCB devices facilitate complex sequences of single-platform, gas-phase ion analyses. Among the most

significant PCB-based ion optics developed in the past few years are SLIM developed by Smith and coworkers at Pacific Northwest National Labs.¹⁻⁵ Transport, trapping, focusing, and mobility separation geometries in SLIM have been demonstrated successfully as interfaced with a commercial time-of-flight (TOF) instrument (Figure 6.1). PCB ion optics afford a great advantage over traditional stacked ring electrodes because designs can be rapidly fabricated and tested at low production cost, permitting a large variety of geometries to be investigated. Intricate combinations of radio frequency (RF) confinement and direct current (DC) electric fields have enabled near-lossless ion transmission, even through multiple ion manipulations.^{3,6}

A key feature of interfacing, two-dimensional array, PCB technology is their ready assembly into alternative geometries, with analogous arrangements to the ion funnel, IM drift tube, gates, switches, traps, and turns having been demonstrated in previous studies, though further development analogous to other traditional ion manipulation techniques has not yet been reported. One geometry yet to be explored with printable two-dimensional arrays is the quadrupole, classically used as both a dynamic mass analyzer and ion transfer device, with the latter supporting additional ion-molecule experiments including CID and IMR.⁷ A PCB-based quadrupole has been previously designed using a flexible substrate that encircles the ion channel by being precisely wrapped on a cylindrical mount. The prototype quadrupole, which was used to manipulate a low-energy electron beam, has not been utilized for ion manipulations (Figure 6.2(A)).^{8,9} In a separate study, a segmented quadrupole was developed in a single, highly-adaptable device for utilization as either a high pressure quadrupole or an IM drift tube from an assembly of over 80 electrically-isolated stacked metal cylinders forming the quadrupole rods (Figure 6.2(B)).¹⁰ Collectively, these approaches to the quadrupole offer novel alternatives to traditional parallel rod geometry, and combining their desirable attributes on a single, PCB-based platform has great potential to benefit

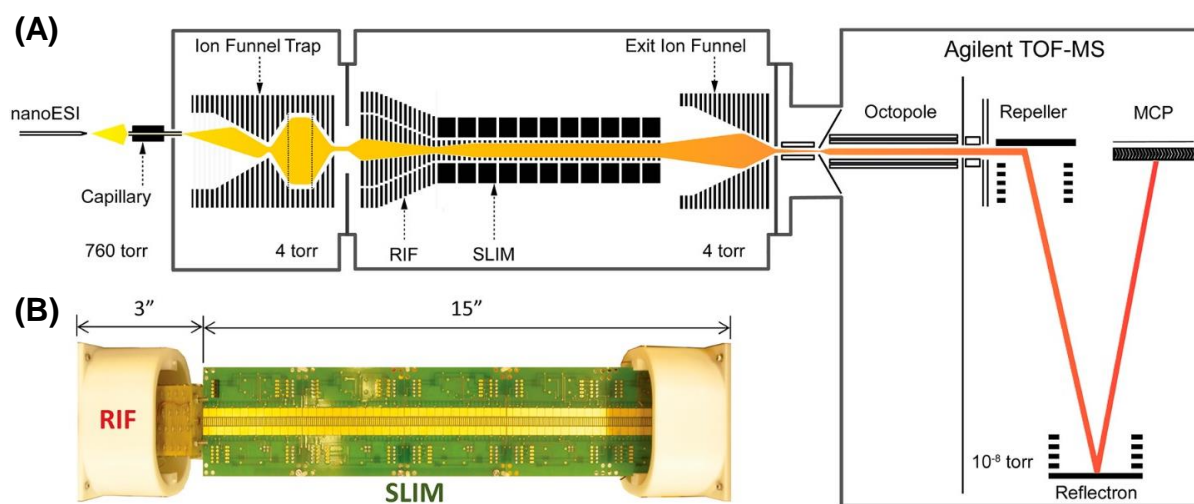


Figure 6.1: Instrumental design of SLIM device with a rectilinear ion funnel (RIF). A commercial TOF-MS is interfaced as a detector, as is also proposed here. (A) Representative schematic of instrument used for overall system performance evaluation of RIF. (B) Photo showing RIF and SLIM module. Figure reproduced from Chen et al., *Analytical Chemistry* 2015, 716-722.

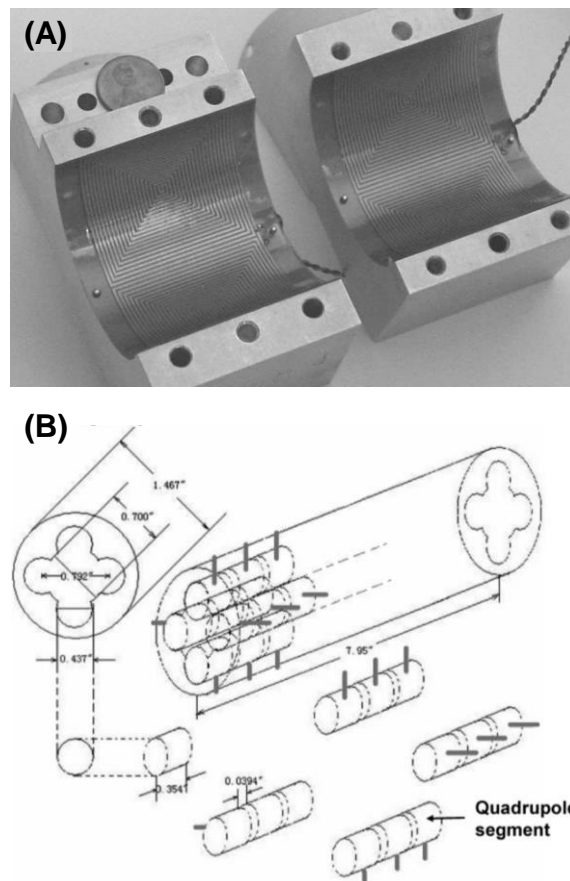


Figure 6.2: Previously demonstrated alternative quadrupole designs. (A) Photograph of flexible PCB prototype quadrupole adhered onto the inner surface of a cylindrical mount. Figure reproduced from Zhang et al., *Phys. Rev. ST Accel. Beams* 2000, 122401. (B) Diagram of a 20-segment quadrupole/IMS cell, which allows precise tailoring of the electric field. Figure adapted from Guo et al., *Analytical Chemistry* 2001, 266-275.

analytical sciences.

The research proposed here seeks to integrate prior endeavors in PCB, IM, quadrupole, ion activation, and ion reaction designs in the development of a singular electrode geometry supporting variable electric fields, background gases, and pressures. Variation of these experimental parameters across a single geometry provides a wide range of flexibility to adapt the instrument configuration and perform the experiment(s) most needed for sample characterization. The proposed instrument would consist of an ionization source, ion funnel, two selection/reaction regions, and an interface to a commercially available IM-QTOF. Integrating the commercial IM-QTOF will enable mass- or mobility-selected experiments to be conducted. Additionally, because interfacing PCB technologies have previously been demonstrated successfully to trap ions, and linear ion traps have previously been utilized for ion/ion reactions, the proposed device could also be used for electron transfer dissociation (ETD).^{4,11} Thus, this proposed instrument would facilitate high versatility for analytical analyses, allowing for pre-selection of ions in the first region by either mass or mobility followed by CID, IMR, or ETD in the second region, and concluding with high-resolution IM-QTOF analyses, where additional mass-selected fragmentation experiments can be conducted.

One specific and potentially transformative application for the proposed device involves the study of peptide post-translational modifications (PTMs). PTMs are important to cellular processes of proteins including localization, function regulation, and complex formation, but these numerous ubiquitous modifications complicate the study of these molecules and of their biological function.¹² It is challenging to isolate the site of modification using MS alone, due to low abundance, instability, and decreased ionization efficiency. IM approaches have previously been shown to benefit PTM studies due to modified peptides exhibiting different gas-phase packing

efficiencies observable with IM.^{13,14} A direct fragmentation method such as ETD, which fragments peptides at each residue of the backbone without abstracting PTMs, is necessary for comprehensive analyses.^{15,16} Peptide studies of PTMs could benefit further from analysis with the proposed device in MS-ETD mode, where peptides could be mass-selected, dissociated with the modification intact, and then characterized with a high-resolution IM-QTOF.

A second specific and potentially transformative application for the proposed device involves the study of lipids structure. Lipids represent a wide array of structurally diverse, often isomeric, molecules as each lipid can vary in headgroup type, acyl chain length, position of attachment, degree of unsaturation, and stereochemistry.¹⁷ The position of double bonds in lipids is crucial in the regards to their biological function; for example, naturally occurring conjugated linoleic acid (18:2) isomers have been found to play varied biological roles based on the positions of the double bonds.^{18,19} While lipids have been studied by many methods, there is an ongoing need for techniques to identify lipid molecules quickly and accurately. Performing comprehensive lipid analyses in the gas phase would greatly increase the throughput of lipid identification studies. For example, recent gas-phase ozonolysis reactions with MS detection have been developed to identify lipid double bond position, even for polyunsaturated lipids.^{17,20-23} By using the proposed device in IM-IMR mode, lipid isomers could first be isolated from other components in a complex sample, and subsequent ozonolysis reaction chemistry could be performed within the PCB device prior to high resolution IM-MS to better define the molecular structures responsible for targeted biological studies.

VI.II.II. Preliminary Studies

The proposed adaptable circuit configuration to effect sample selection and reaction

(ACCESSR), patent pending, will be composed of an electrospray ionization (ESI) source, ion funnels for focusing ions at low pressure, and tandem segmented quadrupoles interfaced to a commercial IM-QTOF for high-resolution CCS and m/z analyses (Figure 6.3). Preliminary simulations have been conducted to investigate the efficacy of a segmented PCB electrode geometry for the experiments described here. Each unit of the proposed ACCESSR platform is approximately 200 mm in length with an inscribed electrode radius of 4.25 mm consisting of 42 sets of four electrodes. In the final configuration, each region will be capable of operation in multiple modes including quadrupole mass selection, IM selection, trapping for ETD, and full transmission to accommodate CID or IMR. The first, selection, region of the tandem segmented devices will be held either in the 10^{-3} Torr or 10^0 Torr range with nitrogen or another background gas, depending on the selected mode of operation. The second, reaction, region will be operated in the 10^{-3} Torr range with the background gas chosen to facilitate the mode of operation. For example, electron transfer and collision studies can be performed in an inert gas, such as nitrogen or argon, while ion molecule reactions require a reactive background gas, such as ozone. The vacuum chamber for the selection and reaction regions will be built to accommodate these pressures and gas types.

Due to the desire for a small instrument footprint, mobility experiments will be conducted via traveling wave IM (TWIM),^{24,25} allowing separation to occur within a shorter distance, relative to the drift tube length required for a comparable separation using uniform field IM. This assessment is supported by simulations of the ACCESSR operating under a uniform field, where observed separations were insignificant over 200 mm. TWIM, however, showed greater potential as a mobility separation mechanism for this device. As shown in Figure 6.4, ions are radially confined by an RF field and separated by traveling DC potential energy waves applied along the

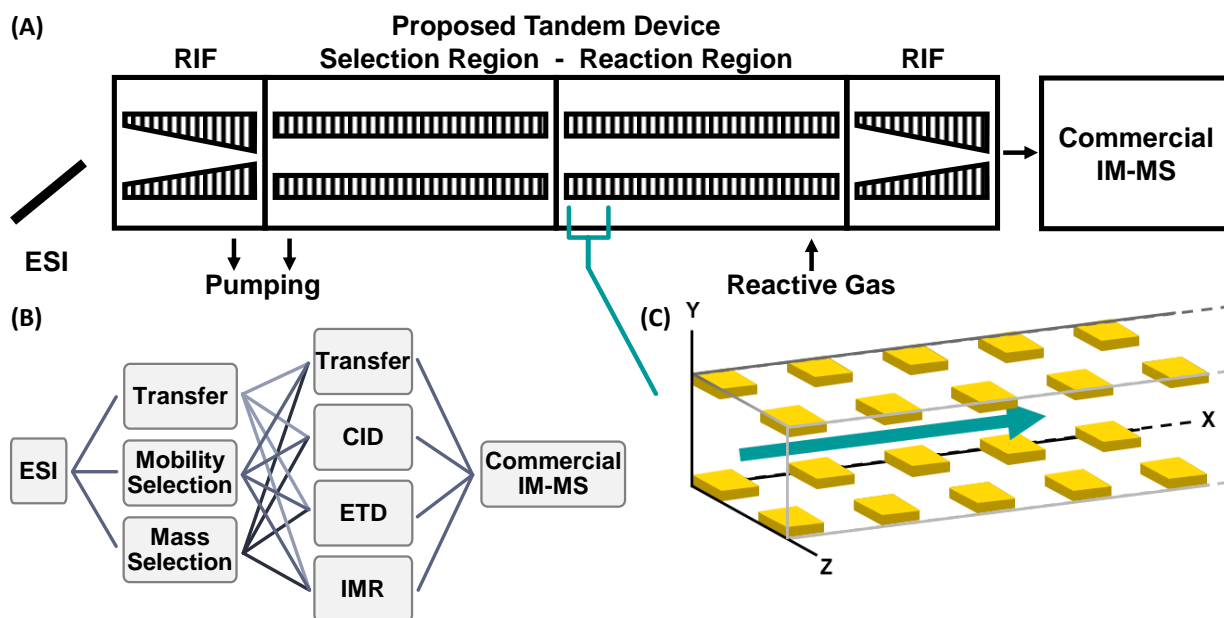


Figure 6.3: (A) Box diagram of general instrument layout in final configuration, with electrospray introduction of ions, beam narrowing with an ion funnel (RIF), tandem segmented quadrupoles capable of multiple combinations of modes of operation, and high resolution IM-QTOF analysis via a commercially available instrument. (B) Diagram of possible modes of operation for the proposed device. (C) Representation of first five sets of four pads for one of the regions. Teal arrow designates direction of ion movement in the device.

main axis. In these experiments, 9000 ions of 500 Da, varying in CCS (200, 300, and 400 Å²) were simulated, and the arrival times at the far side of the device were recorded. Simulation results demonstrated over 75% transmission efficiency across all ions. Ions resided in a diamond-shaped region, as was observed when viewing ion trajectories down the main axis (Figure 6.4(A)), which is a result of the electric field generated with PCB pads rather than the stacked ring electrodes used in traditional TWIM devices. Resolution in these proof-of-concept simulations is rather low, but separation is observed for same-mass ions (e.g., isomers) and improvement in resolution is expected to transpire through exploration of alternative geometries, pressures, and electric field settings in future developments that fell outside the scope of these preliminary studies.

Simulation results for the ACCESSR in operation as a mass selective quadrupole are shown in Figure 6.5. Electrodes are paired cross-wise about the main axis, as in a traditional quadrupole, with RF voltages 180° out of phase and superimposed upon an applied DC bias. When filtering for a single mass, selected ions are confined along the main axis (green trajectories in Figure 6.5), whereas low mass ions are rejected along the RF-dominated plane (blue trajectories in Figure 6.5), and high mass ions are rejected along the orthogonal DC-dominated plane (red trajectories in Figure 6.5). A wide-ranging combination of settings results in 100% ion transmission for multiple masses (Figure 6.5(B)), but masses can also be filtered by using settings exclusive to transmission of the desired mass (Figure 6.5(C)). While the modest resolution seen in these preliminary studies can be improved with design modifications and changes to instrumental parameters including pressure and electric fields, for the purposes of this proposal these preliminary results show great promise for utilization of the proposed geometry as a quadrupole mass filter.

VI.II.III. Research Design and Methods

The proposed instrument development is projected to span three years, and the timeline is

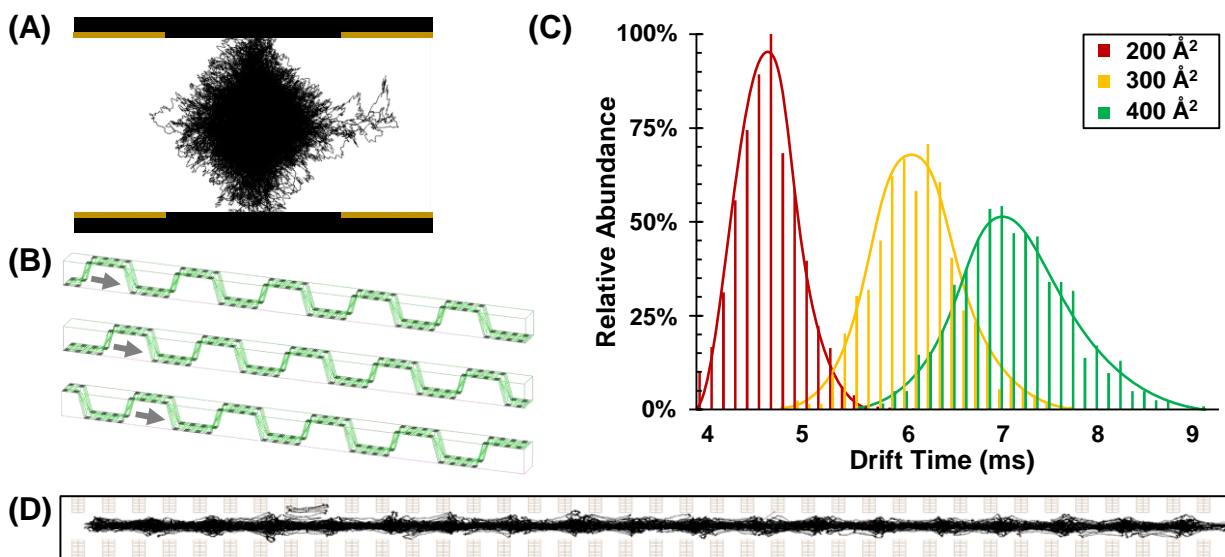


Figure 6.4: Summary of proof-of-concept simulation results for the proposed PCB electrode geometry operating as an IM separation device. (A) Example ion trajectories simulated in the proposed instrument. Note the diamond-shaped trajectory profile resultant from operating with four electrode pads, rather than conventional concentric ring electrodes. (B) Potential energy diagrams for three sequential phases of the traveling wave, with arrows indicating the direction of the voltage wave. RF fields have been omitted for clarity. (C) Three groups of 500 Da ions were generated, differing only in CCS, and the arrival time distributions are shown for separation simulated at 1.5 Torr. (D) Example trajectories for 500 Da, 200 Å² ions displaying periodic radial broadening as a result of the traveling waves and high percent transmission resultant of the confining RF field.

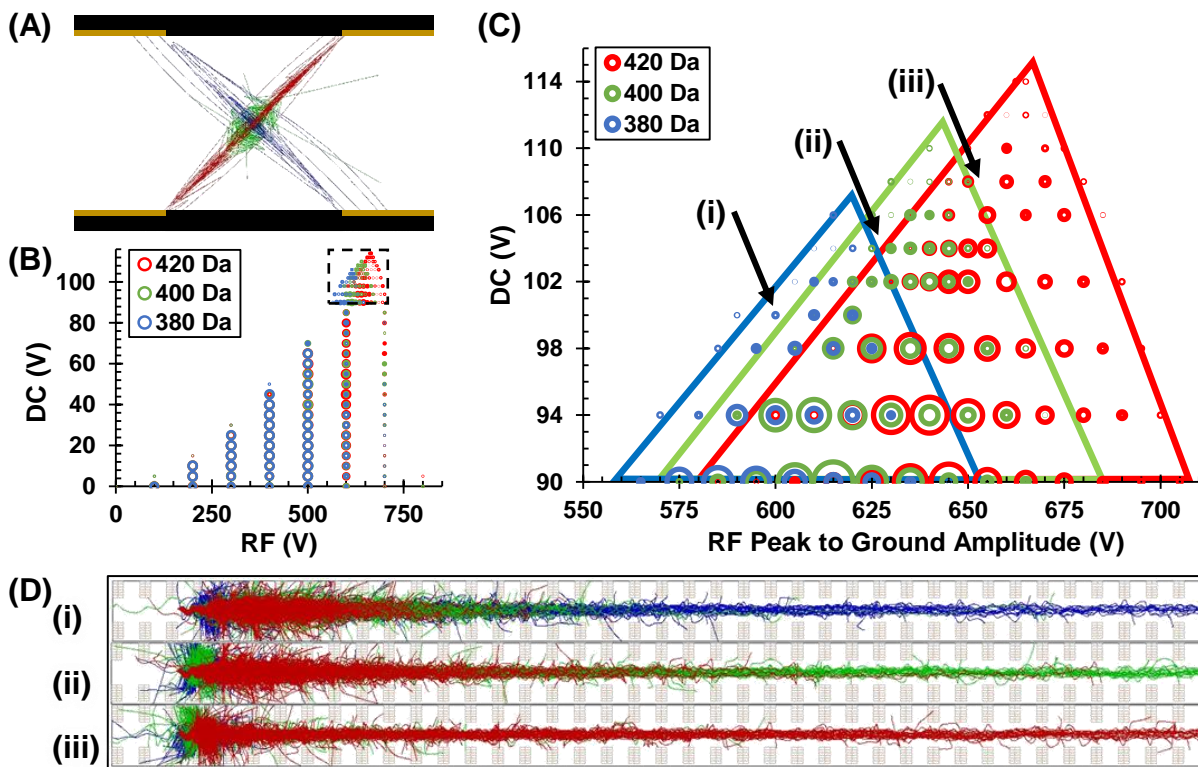


Figure 6.5: Summary of simulation results for the proposed device operating as a quadrupole mass filter. (A) Example simulated ion trajectories, projected down the main axis of the device. Note low mass ions (blue trajectories) are filtered orthogonally to high mass ions (red trajectories), as in a traditional quadrupole. (B) Preliminary, proof-of-concept data from simulations of the segmented PCB-based device functioning as a quadrupole mass selector. Marker size indicates relative transmission for each mass. (C) Close-up of boxed region in (B), with triangular boundaries indicating predicted transmission windows for each mass. Arrows and Roman numerals refer to RF and DC settings used in the simulations shown in (D). (D) Example ion trajectories for settings that filter for (i) 380 Da, (ii) 400 Da, and (iii) 420 Da ions.

displayed in Figure 6.6. Initial simulations of electrode geometries and fluid dynamics would take place in the first year, along with design of instrument infrastructure and electronics. In the second year, most instrument components including PCBs, vacuum infrastructure, and electronics would be fabricated and assembled. Work in the third year would focus first on testing of electronics, vacuum system, and ion transmission, and then testing the multiple operational iterations of the ACCESSR would occur.

The first aim is to theoretically evaluate the ACCESSR, a segmented quadrupole/IM device, with the capability of varying operational pressures and voltages for mass selection or IM separation within a single electrode geometry. Preliminary and proposed ion trajectory simulation studies are performed with a gas collisional model (SIMION software with hard-sphere user program), modified with custom in-house programming to account for variable electrode voltages and ion-gas collisions, to computationally model electrodes and electric fields and predict ion trajectories, in order to evaluate possible electrode geometries and optimize figures-of-merit including transmission, selectivity, and resolution, among others. Preliminary progress has been made toward rapid development of new simulation geometries. Foundational scripts have been written in-house to allow large electrode geometries, which would have taken hours to generate using the default user interface, to be defined by the user in minutes and generated by the software in fractions of a second. This custom programming interface will allow more geometries to be rapidly tested in the future, providing a greater opportunity for discovering a highly functioning final geometry with improved transmission and ion selectivity. Computational fluid dynamics (CFD) will be utilized to investigate gas flow within the vacuum chamber, and resultant velocity and pressure gradients will be incorporated into the ion simulations with custom user programs to

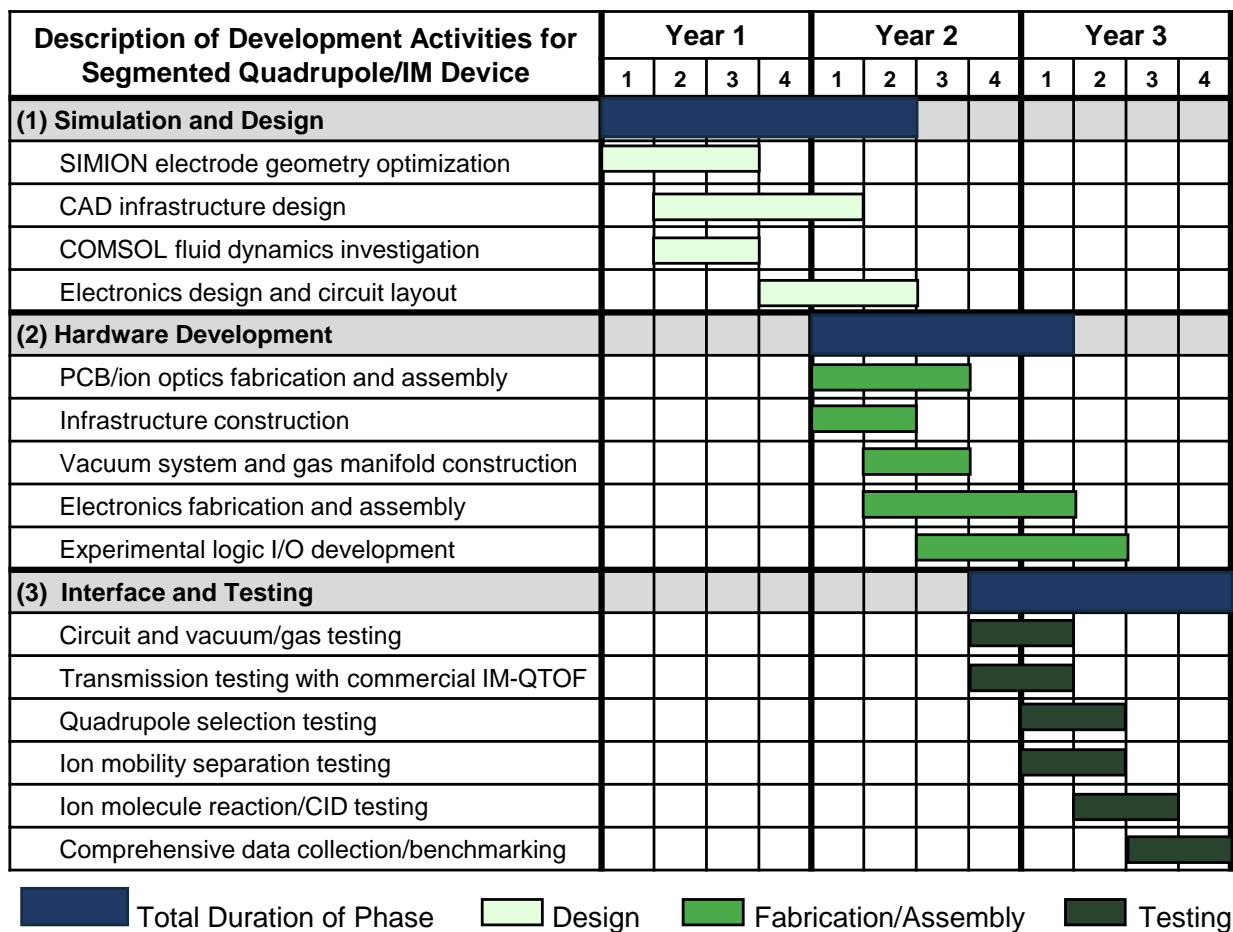


Figure 6.6: The timeline for the proposed research is shown here. Initial simulation and design work will be completed prior to fabrication of components. Following assembly, testing of the device and benchmarking of figures-of-merit will be performed.

observe effects on ion trajectories, directing further development of the electrode geometries and vacuum system.

The second aim is to develop hardware, electronics, vacuum system, and control software for the ACCESSR compatible with interfacing to a commercial IM-QTOF. Electrode geometry and component layouts will be developed in response to ion simulation results and optimized for efficiency of size, cost, and maintenance. Instrument components will be computationally designed (AutoCAD) in order to visualize the 3D instrument assembly and facilitate rapid prototyping. Circuit boards will be developed in PCB-design software, commissioned for production off-site, and assembled with high-quality electrical components in-house. Vacuum system hardware will be conceptualized with CAD software to conform to CFD results and will be assembled in-house from commercially available and custom pieces. Instrument control software will be written in-house with the LabVIEW graphical programming language for compatibility with all operational modes.

The third aim is to interface the ACCESSR on a commercial IM-QTOF platform and benchmark analytical performance. An existing collaboration with Agilent Technologies will assist the process of interfacing the proposed design with their commercial IM-QTOF (model 6560). Testing will include evaluation of the electronics, vacuum system, and ion source. Auxiliary test equipment including pressure gauges, voltage read-back, and temperature monitors will be installed to comprehensively evaluate important experimental parameters in response to specific operational modes. Studied analyte systems will include isomers (leucine/isoleucine), fatty acids, saccharide standards, peptides, etc. Benchmarking of instrument performance in each mode of operation, including combinations of IM, CID, IMR, ETD, and quadrupole mass selection, will include analyses of calibration in both the mass and mobility dimensions with biological standards

for comparison to existing commercial instrumentation, with evaluation of important analytical figures-of-merit including resolution, sensitivity, dynamic range, and selectivity.

VI.II.IV. Summary

The proposed research described here seeks to integrate printed two-dimensional ion optics technology with prior research in quadrupole, CID, IMR, and IM designs in the development of a single electrode geometry supporting all of these experiments using a combination of variable electric fields, background gases, and pressures. Because two-dimensional devices are fabricated from PCBs rather than stacked metal electrodes, they typically have a smaller footprint, lower manufacturing costs, are developed faster, and are highly customizable compared to traditional scientific instruments. Preliminary ion simulations have successfully shown proof-of-concept data for operation of the proposed instrument as an IM separation device and as a quadrupole mass filter with a single electrode geometry. The proposed research should provide a highly versatile instrument platform, the ACCESSR, which will enable novel studies of numerous molecules in both simple and complex samples, and the modularity of the design will allow the analytical platform to be customized to best suit the system of interest.

VI.III. Outlook for Spatial Multiplexing in Ion Mobility Spectrometry

As discussed in Section VI.II, it is expected the next generation of ion manipulation devices will be built on two-dimensional planar arrays. Modular PCB designs are highly versatile and are quick and inexpensive to manufacture in comparison to conventional designs. Additionally, because of their small footprint relative to traditional stacked-ring modules, PCBs are an excellent candidate for higher orders of multiplexing in IM-MS devices. Higher channel numbers would

offer increased throughput and versatility, which would benefit high throughput screening for early stage drug discovery, condensed phase separations integrated with IM-MS, integrated microfluidic devices coupled with IM-MS, and imaging mode IM-MS applications, among others. The eight-channel IM described in Chapter II is the first step toward a 96-channel instrument, which could analyze every sample in a 96-well plate simultaneously. As we progress toward this end, the amount of data acquired gets bigger and bigger, illuminating a corresponding need for advanced computational methods capable of handling the big data from these experiments and comparing it to reveal patterns and variants.

VI.IV. Conclusions and Perspectives

Throughout this work, the authors sought to make advances in the field of ion mobility (IM), both through instrument development and via analytical studies. Chapter I laid the foundation for this work by detailing previous applications and developments of IM. Chapter II described the development of a novel, spatially multiplexed IM instrument designed for high throughput, sensitivity, and versatility, among other figures-of-merit. Chapter III examined preliminary data from the spatially multiplexed IM. Chapter IV explored the difference in gas-phase packing efficiencies of various biological classes, making them occupy dissimilar regions conformational space in ion mobility-mass spectrometry (IM-MS) analyses. Chapter V investigated sub-trends within the lipid biological class to enhance identification techniques with the application of IM-MS. Chapter VI proposes a new, high versatility platform built on interfacing PCBs. This work has significantly advanced the fields of IM instrument development via the development and optimization of new instrument components, and biomolecule analyses, especially of lipids, via the evaluation of mobility-mass correlations for identification strategies.

VI.V. References

1. A. V. Tolmachev, I. K. Webb, Y. M. Ibrahim, S. V. B. Garimella, X. Zhang, G. A. Anderson and R. D. Smith, Characterization of Ion Dynamics in Structures for Lossless Ion Manipulations, *Analytical Chemistry*, 2014, **86**, 9162-9168.
2. T.-C. Chen, I. K. Webb, S. A. Prost, M. B. Harrer, R. V. Norheim, K. Tang, Y. M. Ibrahim and R. D. Smith, Rectangular ion funnel: a new ion funnel interface for structures for lossless ion manipulations, *Analytical Chemistry*, 2015, **87**, 716-722.
3. I. K. Webb, S. V. B. Garimella, A. V. Tolmachev, T.-C. Chen, X. Zhang, R. V. Norheim, S. A. Prost, B. LaMarche, G. A. Anderson, Y. M. Ibrahim and R. D. Smith, Experimental Evaluation and Optimization of Structures for Lossless Ion Manipulations for Ion Mobility Spectrometry with Time-of-Flight Mass Spectrometry, *Analytical Chemistry*, 2014, **86**, 9169-9176.
4. X. Zhang, S. V. B. Garimella, S. A. Prost, I. K. Webb, T.-C. Chen, K. Tang, A. V. Tolmachev, R. V. Norheim, E. S. Baker, G. A. Anderson, Y. M. Ibrahim and R. D. Smith, Ion Trapping, Storage, and Ejection in Structures for Lossless Ion Manipulations, *Analytical Chemistry*, 2015, **87**, 6010-6016.
5. I. K. Webb, S. V. B. Garimella, A. V. Tolmachev, T.-C. Chen, X. Zhang, J. T. Cox, R. V. Norheim, S. A. Prost, B. LaMarche, G. A. Anderson, Y. M. Ibrahim and R. D. Smith, Mobility-resolved ion selection in uniform drift field ion mobility spectrometry/mass spectrometry: dynamic switching in structures for lossless ion manipulations, *Analytical Chemistry*, 2014, **86**, 9632-9637.
6. L. Deng, I. K. Webb, S. V. B. Garimella, A. M. Hamid, X. Zheng, R. V. Norheim, S. A. Prost, G. A. Anderson, J. A. Sandoval, E. S. Baker, Y. M. Ibrahim and R. D. Smith, Serpentine Ultralong Path with Extended Routing (SUPER) High Resolution Traveling Wave Ion Mobility-MS using Structures for Lossless Ion Manipulations, *Analytical Chemistry*, 2017, **89**, 4628-4634.
7. P. H. Dawson, *Quadrupole Mass Spectrometry and Its Applications*, American Institute of Physics, 1995.
8. T. F. Godlove, S. Bernal and M. Reiser, *Printed-circuit quadrupole design*, Dallas, TX, 1995.
9. W. Zhang, S. Bernal, H. Li, T. Godlove, R. Kishek, P. O'Shea, M. Reiser, V. Yun and M. Venturini, Design and field measurements of printed-circuit quadrupoles and dipoles, *Physical Review Special Topics-Accelerators and Beams*, 2000, **3**, 122401.
10. Y. Guo, J. Wang, G. Javahery, B. A. Thomson and K. W. M. Siu, Ion Mobility Spectrometer with Radial Collisional Focusing, *Analytical Chemistry*, 2005, **77**, 266-275.

11. Y. Xia, J. Wu, S. A. McLuckey, F. A. Londry and J. W. Hager, Mutual storage mode ion/ion reactions in a hybrid linear ion trap, *Journal of the American Society for Mass Spectrometry*, 2005, **16**, 71-81.
12. O. Alzate, *Neuroproteomics*, CRC Press, 2009.
13. B. T. Ruotolo, G. F. Verbeck IV, L. M. Thomson, A. S. Woods, K. J. Gillig and D. H. Russell, Distinguishing between phosphorylated and nonphosphorylated peptides with ion mobility– mass spectrometry, *Journal of Proteome Research*, 2002, **1**, 303-306.
14. J. A. McLean, B. T. Ruotolo, K. J. Gillig and D. H. Russell, Ion mobility-mass spectrometry: a new paradigm for proteomics, *International Journal of Mass Spectrometry*, 2005, **240**, 301-315.
15. M. A. Baird and A. A. Shvartsburg, Localization of Post-Translational Modifications in Peptide Mixtures via High-Resolution Differential Ion Mobility Separations Followed by Electron Transfer Dissociation, *Journal of The American Society for Mass Spectrometry*, 2016, **27**, 2064-2070.
16. H. Molina, D. M. Horn, N. Tang, S. Mathivanan and A. Pandey, Global proteomic profiling of phosphopeptides using electron transfer dissociation tandem mass spectrometry, *Proceedings of the National Academy of Sciences*, 2007, **104**, 2199-2204.
17. S. H. J. Brown, T. W. Mitchell and S. J. Blanksby, Analysis of unsaturated lipids by ozone-induced dissociation, *Biochimica et Biophysica Acta (BBA)-Molecular and Cell Biology of Lipids*, 2011, **1811**, 807-817.
18. Y. Choi, Y. Park, M. W. Pariza and J. M. Ntambi, Regulation of Stearoyl-CoA Desaturase Activity by the *trans*-10, *cis*-12 Isomer of Conjugated Linoleic Acid in HepG2 Cells, *Biochemical and Biophysical Research Communications*, 2001, **284**, 689-693.
19. M. W. Pariza, Y. Park and M. E. Cook, The biologically active isomers of conjugated linoleic acid, *Progress in Lipid Research*, 2001, **40**, 283-298.
20. R. L. Grimm, R. Hodyss and J. L. Beauchamp, Probing interfacial chemistry of single droplets with field-induced droplet ionization mass spectrometry: Physical adsorption of polycyclic aromatic hydrocarbons and ozonolysis of oleic acid and related compounds, *Analytical Chemistry*, 2006, **78**, 3800-3806.
21. M. C. Thomas, T. W. Mitchell and S. J. Blanksby, Ozonolysis of phospholipid double bonds during electrospray ionization: A new tool for structure determination, *Journal of the American Chemical Society*, 2006, **128**, 58-59.
22. M. C. Thomas, T. W. Mitchell, D. G. Harman, J. M. Deeley, R. C. Murphy and S. J. Blanksby, Elucidation of double bond position in unsaturated lipids by ozone electrospray ionization mass spectrometry, *Analytical Chemistry*, 2007, **79**, 5013-5022.

23. J. Castro-Perez, T. P. Roddy, N. M. Nibbering, V. Shah, D. G. McLaren, S. Previs, A. B. Attygalle, K. Herath, Z. Chen and S.-P. Wang, Localization of fatty acyl and double bond positions in phosphatidylcholines using a dual stage CID fragmentation coupled with ion mobility mass spectrometry, *Journal of the American Society for Mass Spectrometry*, 2011, **22**, 1552-1567.
24. K. Giles, S. D. Pringle, K. R. Worthington, D. Little, J. L. Wildgoose and R. H. Bateman, Applications of a travelling wave-based radio-frequency-only stacked ring ion guide, *Rapid Communications in Mass Spectrometry*, 2004, **18**, 2401-2414.
25. K. Giles, J. P. Williams and I. Campuzano, Enhancements in travelling wave ion mobility resolution, *Rapid Communications in Mass Spectrometry*, 2011, **25**, 1559-1566.

APPENDIX A

REFERENCES OF ADAPTATIONS FOR CHAPTERS

- Chapter I. Katrina L. Leaptrot, T. Khayamian, M. T. Jafari, and John A. McLean, “Ion Mobility and Ion Mobility-Mass Spectrometry,” invited chapter for inclusion in “Mass Spectrometry with Inductively Coupled Plasmas Fundamental, Instrumentation, and Novel Applications,” Akbar Montaser, Ed. John Wiley and Sons, submitted 2017.
- Chapter IV. Jody C. May, Cody R. Goodwin, Nichole M. Lareau, Katrina L. Leaptrot, Caleb B. Morris, Ruwan T. Kurulugama, Alex Mordehai, Christian Klein, William Barry, Ed Darland, Gregor Overney, Kenneth Imatani, George C. Stafford, John C. Fjeldsted, and John A. McLean, “Conformational Ordering of Biomolecules in the Gas Phase: Nitrogen Collision Cross Sections Measured on a Prototype High Resolution Drift Tube Ion Mobility-Mass Spectrometer,” *Analytical Chemistry*, 2014, 84, 2107-2116.
- Chapter V. Katrina L. Leaptrot, Jody C. May, James N. Dodds, and John A. McLean, “Structural Conformation Atlas for High Confidence Lipidomics,” in preparation for submission in 2018.
- Chapter VI. Katrina L. Leaptrot, Jody C. May, John A. McLean, “Methods and Systems for Mass Analysis,” U.S. Provisional Patent Application No. 62623762, 2018.

APPENDIX B

SUPPORTING INFORMATION FOR CHAPTER II

B.1: Simulations.....225

- Figure B.1.1:** Tandem Funnel 3D CFD Velocity
- Figure B.1.2:** Keyhole Funnel CFD Velocity
- Figure B.1.3:** Tandem Funnel CFD Velocity
- Figure B.1.4:** Pressure and Velocity Comparison for Two Funnel Geometries
- Figure B.1.5:** Pressure and Velocity Isosurfaces
- Figure B.1.6:** SIMION User Program Incorporating CFD Data (4 pages)
- Figure B.1.7:** Funnel Geometry Ion Transmission Comparison

B.2: Electrospray Ionization Source235

- Figure B.2.1:** ESI Source Assembly
- Figure B.2.2:** ESI Brass Floating Nut
- Figure B.2.3:** ESI Base Plate
- Figure B.2.4:** ESI XYZ to Goniometer Adapter
- Figure B.2.5:** ESI Holster Base
- Figure B.2.6:** ESI Holster Wedge
- Figure B.2.7:** ESI Holster Top
- Figure B.2.8:** ESI Spring-Loaded Floating Nut
- Figure B.2.9:** ESI Spring-Loaded Bottom
- Figure B.2.10:** ESI Spring-Loaded Top

B.3: Atmospheric Inlet and Desolvation.....245

- Figure B.3.1:** Heated Desolvation Block
- Figure B.3.2:** Insulating Flange for Desolvation Block
- Figure B.3.3:** Desolvation Bolt Spacer
- Figure B.3.4:** Chamber 1 Top Hat Flange
- Figure B.3.5:** Extension Collar
- Figure B.3.6:** RGC Electrical Feedthrough Piston Seal
- Figure B.3.7:** Chamber 1, 3/4" Flange

B.4: First Vacuum Chamber252

- Figure B.4.1:** Chamber 1 Assembly
- Figure B.4.2:** Chamber 1 Front Flange
- Figure B.4.3:** Chamber 1 Bottom Flange
- Figure B.4.4:** Chamber 1 Feedthrough Flange
- Figure B.4.5:** Chamber 1 Blank Flange

Figure B.4.6:	Chamber 1 Top Flange	
Figure B.4.7:	Chamber 1 Back Flange	
Figure B.4.8:	Chamber 1 Glass Top	
Figure B.4.9:	Inner Chamber Pumpout Flange	
Figure B.4.10:	Chamber-Joining Floating Nut	
B.5:	Inner Vacuum Chamber	262
Figure B.5.1:	Inner Chamber Smaller, Face seal	
Figure B.5.2:	Floating Nut, Cut	
Figure B.5.3:	Inner Chamber (2 pages)	
Figure B.5.4:	Inner Chamber Exit Spacer	
B.6:	Ion Funnels	267
Figure B.6.1:	Funnel 1 Mount Block	
Figure B.6.2:	Funnel Mount Rods	
Figure B.6.3:	Funnel 1 Delrin Standoff Type 1	
Figure B.6.4:	Funnel 1 Delrin Standoff Type 2	
Figure B.6.5:	Funnel 1 Ceramic Tubes Type 1	
Figure B.6.6:	Funnel 1 Ceramic Tubes Type 2	
Figure B.6.7:	Funnel Electrode Template	
Figure B.6.8:	Table of Funnel Electrode Dimensions	
Figure B.6.9:	Funnel Spacer	
Figure B.6.10:	Funnel 2 Standoff	
Figure B.6.11:	Funnel 2 Finishing Washer for Standoffs	
Figure B.6.12:	Funnel 2 Ceramic Tubes Type 1	
Figure B.6.13:	Funnel 2 Ceramic Tubes Type 2	
B.7:	Second Vacuum Chamber	280
Figure B.7.1:	Chamber 2 Assembly	
Figure B.7.2:	Chamber 2 Front Flange	
Figure B.7.3:	Chamber 2 Bottom Flange	
Figure B.7.4:	Chamber 2 Feedthrough Flange	
Figure B.7.5:	Chamber 2 Blank Flange	
Figure B.7.6:	Chamber 2 Top Flange	
Figure B.7.7:	Chamber 2 Back Flange	
Figure B.7.8:	Chamber 2 Glass Top	
Figure B.7.9:	Faraday Feedthrough Flange	
B.8:	Apertures	289
Figure B.8.1:	Aperture Panel Assembly	
Figure B.8.2:	Aperture Panel	
Figure B.8.3:	Aperture Holder	
Figure B.8.4:	Insulating Washers	
Figure B.8.5:	Aperture Panel Piston Seal	

B.9: Narrow Drift Tube.....	294
Figure B.9.1: PEEK Column	
Figure B.9.2: Narrow DT Spacer Large	
Figure B.9.3: Narrow DT Tabbed Electrode	
Figure B.9.4: Narrow DT Spacer	
Figure B.9.5: Narrow DT Middle Electrode	
Figure B.9.6: Narrow DT Electrode	
B.10: Full Size Drift Tube.....	300
Figure B.10.1: DT Mount Block Front	
Figure B.10.2: Drift Tube Threaded Rods	
Figure B.10.3: Drift Tube Standoffs Type 1	
Figure B.10.4: Drift Tube Standoffs Type 2	
Figure B.10.5: Drift Tube Ceramic Tubes Type 1	
Figure B.10.6: Drift Tube Ceramic Tubes Type 2	
Figure B.10.7: Drift Tube Electrode	
Figure B.10.8: Drift Tube Spacer	
Figure B.10.9: Drift Tube Mount Block Back	
Figure B.10.10: Faraday Detector	
B.11: Drift Tube Infrastructure	310
Figure B.11.1: IMS Support Assembly Diagram	
Figure B.11.2: IMS Delrin Support Cradle	
Figure B.11.3: IMS Support Aluminum Block	
Figure B.11.4: IMS Support T-Slot	
Figure B.11.5: IMS Support Aluminum Plate	
B.12: Vacuum Chamber Infrastructure	315
Figure B.12.1: Chamber 1 Support Assembly Diagram	
Figure B.12.2: Chamber 1 Cradle Clamp Plate	
Figure B.12.3: Chamber 1 Cradle Long Beam	
Figure B.12.4: Chamber 1 Pivot Table Intermediate	
Figure B.12.5: Chamber 2 and Rail Support Assembly Diagram	
Figure B.12.6: Chamber 2 Cradle Clamp Plate	
Figure B.12.7: Chamber 2 Cradle Long Beam	
Figure B.12.8: Chamber 2 Angled Support Beam	
Figure B.12.9: Modified GJ Bracket Type 1	
Figure B.12.10: Modified GJ Bracket Type 2	
Figure B.12.11: Vacuum Chamber Support Rails	
Figure B.12.12: Vacuum Chamber Support Shafts	
B.13: Whole Instrument Infrastructure	327
Figure B.13.1: Table Assembly Diagram	
Figure B.13.2: Table Top	

Figure B.13.3:	Table Base Beam Type 1, 2, & 3	
Figure B.13.4:	Table Base Beam Type 4 & 5	
Figure B.13.5:	Table Base Panel Type 1	
Figure B.13.6:	Table Base Panel Type 2	
Figure B.13.7:	Table Base Panel Type 3	
Figure B.13.8:	Caster Adapter Plate	
B.14:	Assembly Support Structure for Front End and Chamber 1 Contents	335
Figure B.14.1:	Assembly Support Structure Assembly diagram	
Figure B.14.2:	Assembly Support Structure Frame Sides and Frame Top	
Figure B.14.3:	Assembly Support Structure Frame Base, Brace Base, and Slide Rails	
Figure B.14.4:	Assembly Support Structure Brace Angled Beam	
B.15:	Electronics	339
Figure B.15.1:	Funnel 1 RC Circuit Board	
Figure B.15.2:	Funnel 2 RC Circuit Board	
Figure B.15.3:	Funnel 1 Breakout Box	
Figure B.15.4:	Funnel 2 Breakout Box	
Figure B.15.5:	Drift Tube Breakout Box	
Figure B.15.6:	Flat Power Supply Mounting Bracket	
Figure B.15.7:	Lofted Power Supply Mounting Bracket	
Figure B.15.8:	Op Amp Circuit Board	
B.16:	Commercial Components	347
Table B.16:	Commercial Components (13 pages)	
B.17:	Electronic Schematics and Wiring Diagrams	360
Figure B.17.1:	DC PSU Wiring	
Figure B.17.2:	SC and RF PSU Wiring	
Figure B.17.3:	ESI, RGC, and High Pressure Funnel PSUs	
Figure B.17.4:	Low Pressure Funnel PSUs	
Figure B.17.5:	Drift Tube PSUs	
Figure B.17.6:	Diagram and Calculations for Amplifier Circuit	
Table B.17.1:	PXI-6704 Connector Block Terminals	
Table B.17.2:	PXI-6224 Connector Block Terminals, Connector 0	
Table B.17.3:	PXI-7842R Connector Block Terminals, MIO Connector 0	
B.18:	LabVIEW Software Development	369
Figure B.18.1:	Front Panel	
Figure B.18.2:	Block Diagram Before Initialization	
Figure B.18.3:	Block Diagram After Start	
Figure B.18.4:	Block Diagram Running	
Figure B.18.5:	Startup Sub.vi	
Figure B.18.6:	Safety Sub.vi	
Figure B.18.7:	Control Sub.vi	

Figure B.18.8:	Readback Sub.vi	
Figure B.18.9:	Timer Sub.vi	
Figure B.18.10:	Acquire Sub.vi	
Figure B.18.11:	Simple FPGA.vi	
B.19: Photographs		380
Figure B.19.1:	ESI Source	
Figure B.19.2:	ESI Source in Operation	
Figure B.19.3:	RGC and Home-Built Capillary	
Figure B.19.4:	Heated Desolvation Block and Insulating Flange	
Figure B.19.5:	High Pressure Ion Funnel and Blown Resistors	
Figure B.19.6:	RC Circuit and High Pressure Ion Funnel Assembly	
Figure B.19.7:	Inner Vacuum Chamber	
Figure B.19.8:	Vacuum Flange Connection, Low Pressure Funnel RC Board	
Figure B.19.9:	Extension Collar and RGC Feedthrough	
Figure B.19.10:	Top Hat Flange Assembly and Funnel 1 Mount Block	
Figure B.19.11:	Narrow Drift Tube	
Figure B.19.12:	Aperture Panel Assembly	
Figure B.19.13:	Drift Tube Electrodes Disassembled for Detector Installation	
Figure B.19.14:	Faraday Plate Detector	
Figure B.19.15:	Ion Funnel Electrode Comparison	
Figure B.19.16:	Multiple Electrode Components Displayed	
Figure B.19.17:	Picoammeter Revisions	
Figure B.19.18:	Power Supplies, 24 VDC	
Figure B.19.19:	Breakout Boxes	
Figure B.19.20:	Organization of Cables	
Figure B.19.21:	Assembly Support Structure Method and Table Frame	
Figure B.19.22:	Full Instrument Assembly Prior to Electronics Wiring	
Figure B.19.23:	User Work Area and First Vacuum Chamber Pumping Port	
Figure B.19.24:	Back of Instrument Showing Pump Connections	
Figure B.19.25:	Coronas and/or Discharges	
Figure B.19.26:	Super Corona Dope Application	

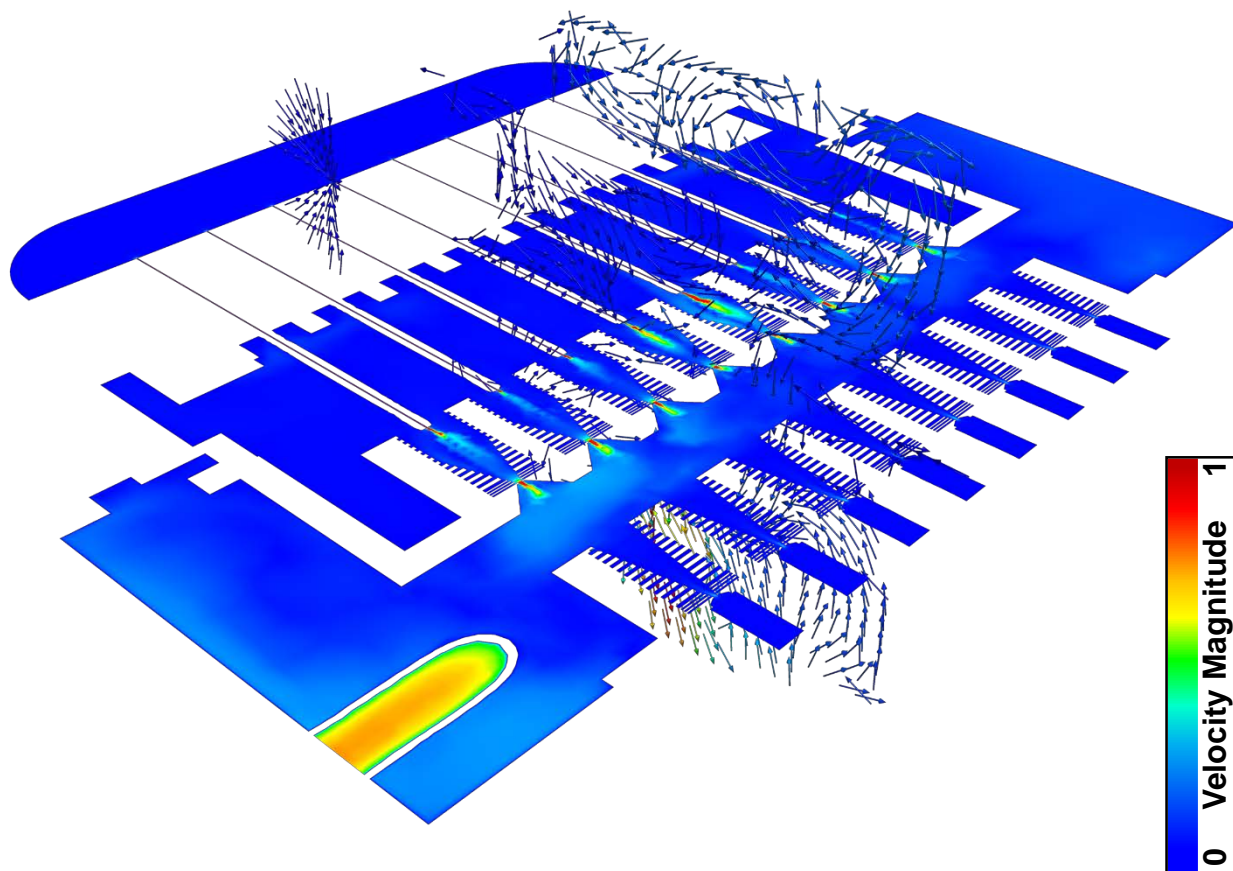


Figure B.1.1: Velocity magnitude results for 3D CFD modeling for tandem ion funnel geometry with differential pumping. Normalized arrows indicate direction of gas flow along the cut XY-plane, which bisects the fourth ion channel. The XZ-plane is also projected, as a heat map, intersecting all eight ion channels and a portion of the 90° elbow of the vacuum tubing originating from the inner chamber and exiting at the edge of the first chamber. In this particular solution, results vary between channels, with some RGC entrance jets being of higher magnitude than others, but this is just one possible case predicted by the model.

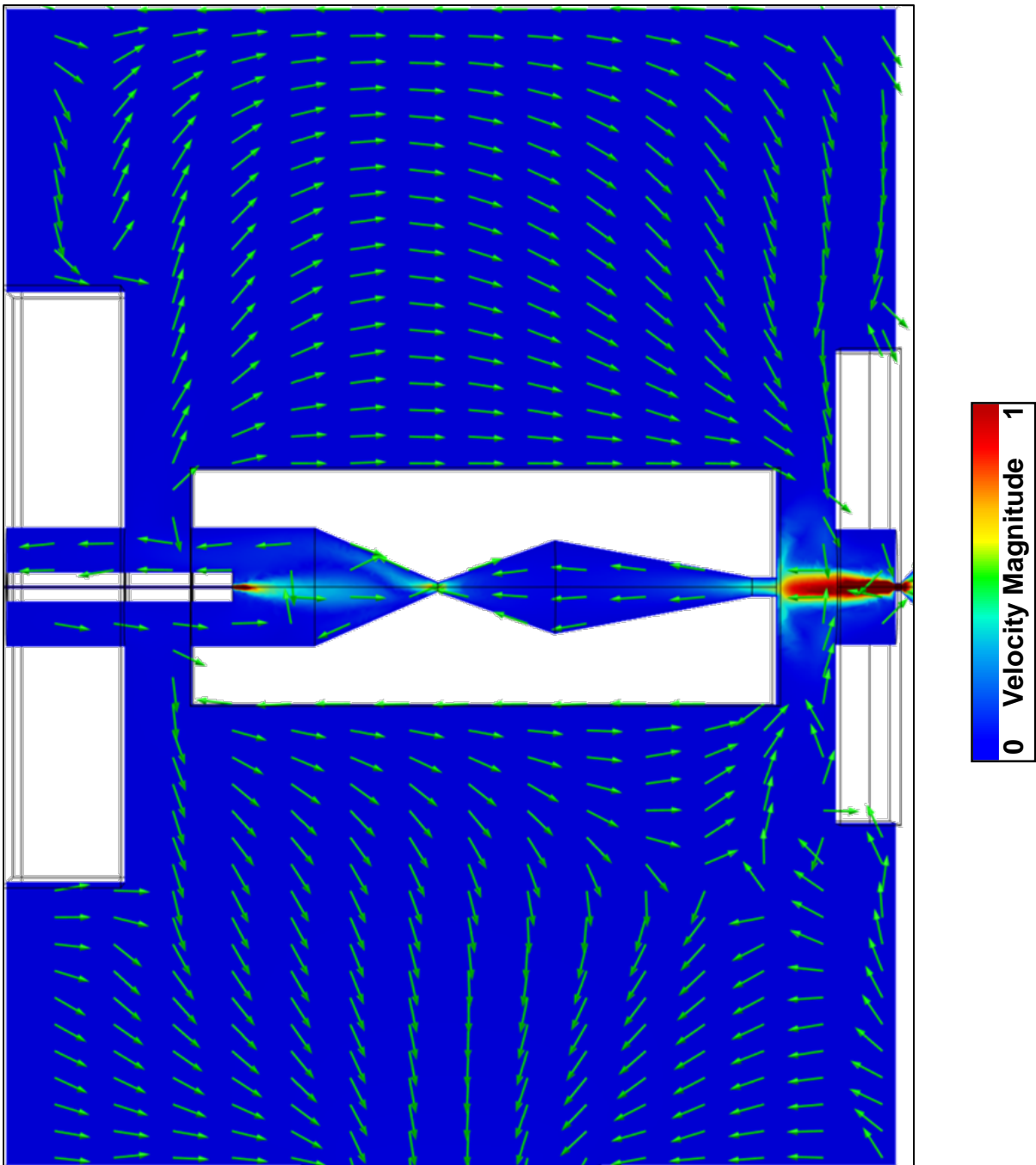


Figure B.1.2: Velocity magnitude results for 3D CFD modeling for a preliminary ion funnel geometry (keyhole) with countering gas jets emitted from the capillary exit and drift tube entrance. Normalized arrows indicate direction of gas flow along the cut plane.

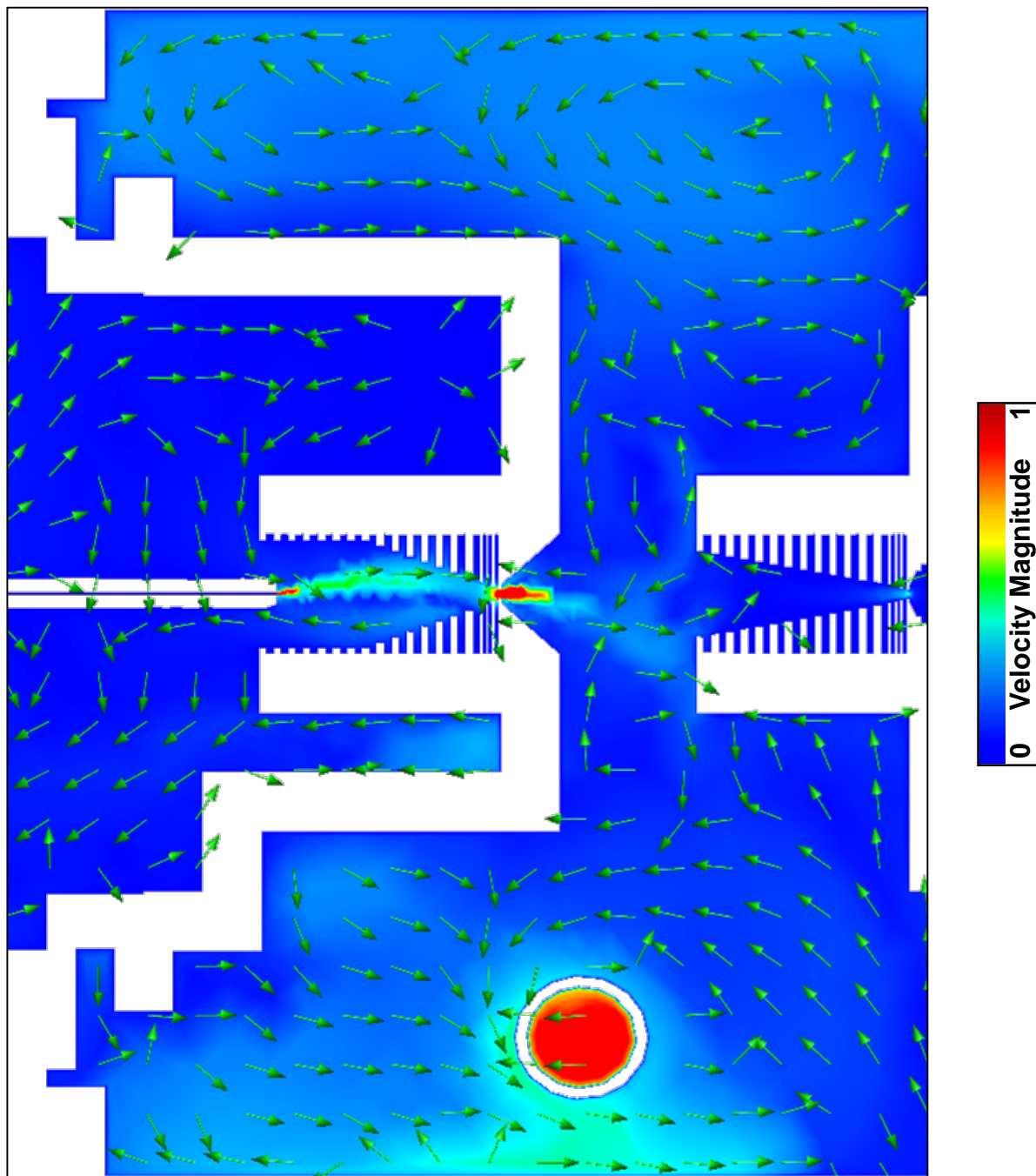


Figure B.1.3: Velocity magnitude results for 3D CFD modeling for tandem ion funnel geometry with differential pumping. Normalized arrows indicate direction of gas flow along the cut plane. High magnitude circle in lower portion of the chamber is where the plane intersects the pumping tubing originating from inner chamber.

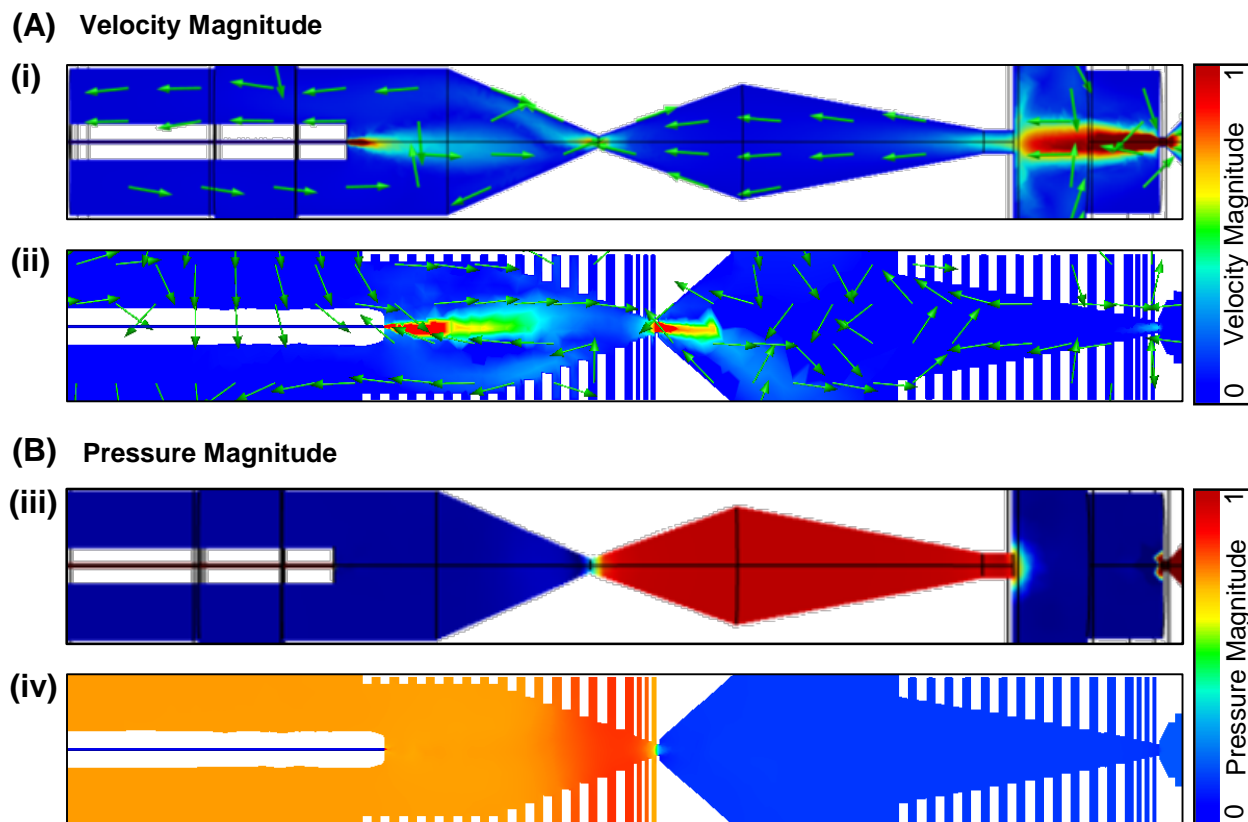


Figure B.1.4: Simulation results showing cross-sections of a single ion channel from the ion funnel array. Velocity and pressure magnitudes are shown on relative scales for qualitative comparison. Normalized arrows in (A) indicate direction of gas flow along the cut plane. (i) Velocity magnitude for a preliminary ion funnel geometry (keyhole) with countering gas jets emitted from the capillary exit and drift tube entrance. (ii) Velocity magnitude for tandem ion funnel geometry with differential pumping. (iii) Pressure magnitude for a preliminary ion funnel geometry (keyhole) showing pressurized trapping region. (iv) Pressure magnitude for tandem ion funnel geometry with delineated high and low pressure regions.

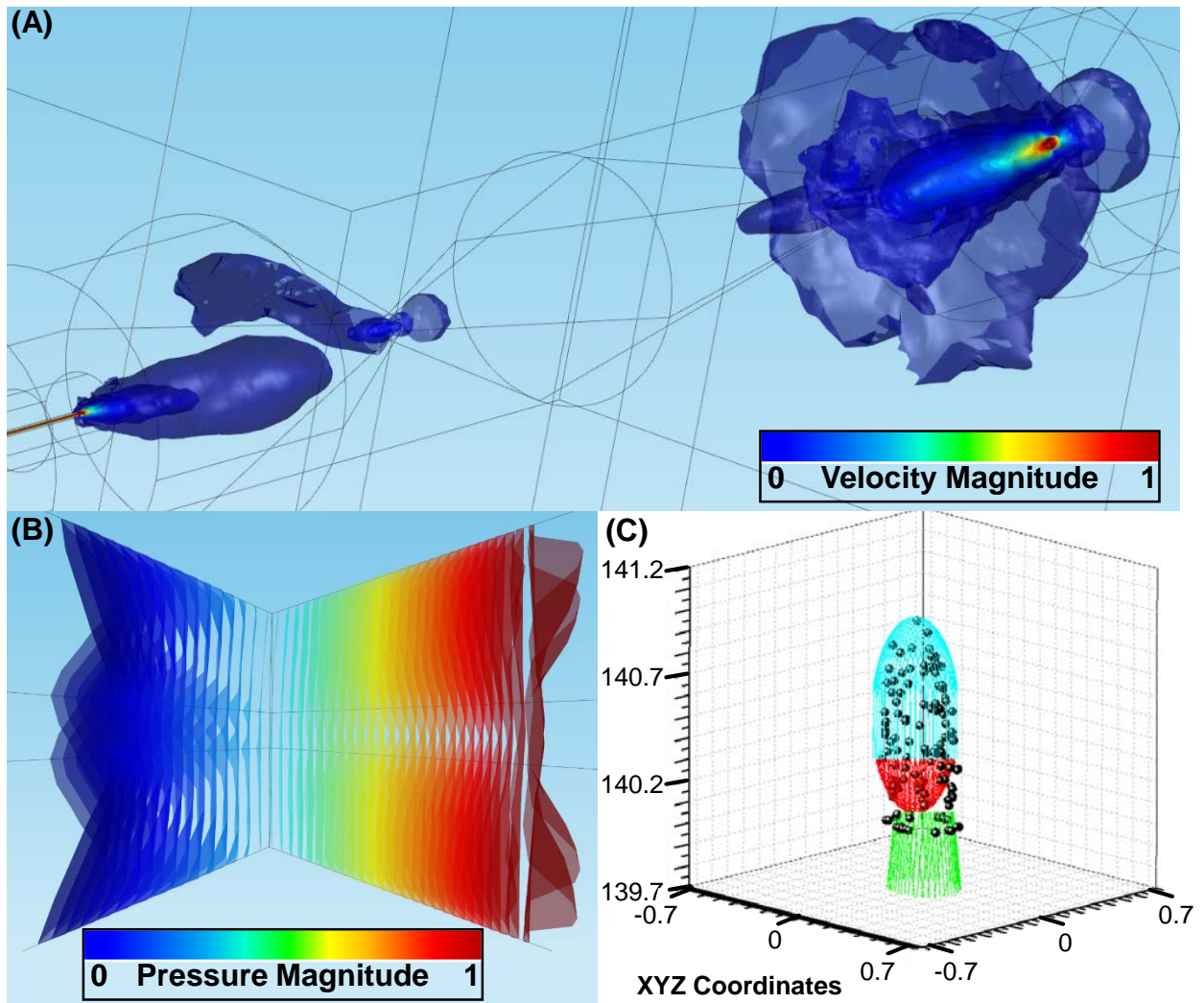


Figure B.1.5: CFD modeling results for a preliminary ion funnel geometry (keyhole). (A) Near-isometric 3D view of velocity isosurfaces ranging from 1 m/s to 42 m/s in steps of 2 m/s. Note the jets issuing from the RGC at the bottom left and the drift tube at the upper right. (B) Close-up view of junction between two keyhole geometry funnel regions, oriented perpendicular to the XZ-plane, with pressure isobars ranging from 1.000 Torr to 1.040 Torr in steps of 0.001 Torr. (C) Example isosurface at 26 m/s X-component velocity where three equations for ellipsoids and paraboloids (colored mesh) approximate the data points. Note ions would move along the vertical axis. These equations, determined for multiple velocity and pressure magnitudes, are written into a SIMION user program for incorporation in the ion trajectory simulations.

```

1  -- CFD Results Applied -KLL 2012
2  -- funnel3.lua - SIMION Lua workbench user program for ion funnel.
3  --
4  -- This is similar to funnel2.lua but uses additional electrode
5  -- solution arrays to allow adjustable variables (_RF_amplitude,
6  -- _DC_offset_1, _DC_offset_96, and _DC_offset_97) to be adjusted
7  -- during the Fly'm (without editing the .pa+ file and re-refining
8  -- the array).
9  --
10 -- D.Manura, 2009-08, based on funnel2.lua.
11 -- Modified by K. Leaptrot, 2012-11
12
13 simion.workbench_program()
14
15 -- import standard Hs1 collision model from this directory.IMPORTING COLLISION SDS!
16 simion.import("collision_sds.lua")
17
18 function SDS.pressure(x,y,z) -- Torr
19     local p
20     if x < (0.42-y^2-(z-0.2)^2)^0.5+139.74-131.2 then
21         p = 1.2
22     else
23         if x < (0.522-(y-0.05)^2-(z-0.2)^2)^0.5+139.69-131.2 then
24             p = 1.15
25         else
26             if x < (0.8752-(y-0.25)^2-(z+0.125)^2)^0.5+139.575-131.2 then
27                 p = 1.10
28             else
29                 if x < (1-y^2-z^2)^0.5+139.6-131.2 then
30                     p = 1.05
31                 else
32                     if x < 182 or x < (2.22-y^2-z^2)^0.5+181.1-131.2 then
33                         p = 1
34                     else
35                         if x < 256.9 or x < (8.22-(y+1.3)^2-(z+0.125)^2)^0.5+254.6-131.2 then
36                             p = 1.05
37                         else
38                             p = 1
39                         end
40                     end
41                 end
42             end
43         end
44     end
45     --print(('DEBUG:x=%g,y=%g,z=%g,P=%g'):format(ion_px_mm,ion_py_mm,ion_pz_mm,p))
46     return p
47 end

```

Figure B.1.6: SIMION user program in lua programming language incorporating equations for functions approximating pressure and velocity isosurfaces for ion funnel simulations. pg 1 of 4

```

48 function SDS.temperature(x,y,z) -- K
49     return 298.15
50 end
51 function SDS.velocity(x,y,z) -- (m/s) vx,vy,vz in workbench coordinates
52     local vx
53     if x < 140.2-131.2-(y+0.01)^2/(0.1^2)-(z-0.01)^2/(0.2^2) and x > 8.0 then
54         vx = 51
55     else
56         if x < 140.325-131.2-(y+0.01)^2/(0.13^2)-(z-0.01)^2/(0.2^2) and x > 8.4 then
57             vx = 46
58         else
59             if x < 140.5-131.2-(y+0.02)^2/(0.14^2)-(z-0.01)^2/(0.2^2) and x > 8.8 then
60                 vx = 41
61             else
62                 if x < 140.67-131.2-(y+0.02)^2/(0.16^2)-(z-0.01)^2/(0.18^2) and x > 8.8 then
63                     vx = 36
64                 else
65                     if x < 140.85-131.2-(y+0.02)^2/(0.2^2)-(z-0.01)^2/(0.21^2) and x > 8.8 then
66                         vx = 31
67                     else
68                         if x < ((1-(y+0.05)^2/(0.2^2)-(z-0)^2/(0.2^2))*(0.46^2))^0.5+140.52-131.2 or x <
69                             140.67-131.2-y^2/(0.16^2)-(z-0.01)^2/(0.18^2) and x > 8.8 then
70                             vx = 26
71                         else
72                             if x < 140.7-131.2-y^2/(0.23^2)-(z-0.01)^2/(0.275^2) or x < ((1-(y+0.025)^2/(0.2^2
73                                 )-z^2/(0.25^2))*(0.7^2))^0.5+140.8-131.2 and x > 8.8 then
74                                 vx = 21
75                             else
76                                 if x < ((1-(y+0.025)^2/(0.3^2)-(z-0)^2/(0.35^2))*(1^2))^0.5+141-131.2 and x >
77                                     8.8 then
78                                     vx = 16
79                                 else
80                                 if x < ((1-(y+0.025)^2/(0.45^2)-(z+0.075)^2/(0.5^2))*(1.75^2))^0.5+141.75-
81                                     131.2 or x < 140.8-131.2-(y-0.01)^2/(0.3^2)-(z+0.01)^2/(0.25^2) and x > 8.8 then
82                                     vx = 11
83                                 else
84                                 if x < ((1-(y+0.15)^2/(0.8^2)-(z+0.075)^2/(0.75^2))*(3.75^2))^0.5+142.5-
85                                     131.2 and x > 8.8 then
86                                     vx = 6
87                                 else
88                                 if x < ((1-(y+0.75)^2/(4^2)-(z+1)^2/(4^2))*(17.5^2))^0.5+157-131.2 and x
89                                     > 8.8 then
90                                     vx = 1
91                                 else
92                                 if x > 179-131.2+(y)^2/(0.5^2)+(z+0.01)^2/(0.45^2) and x < ((1-y^2-z^2)*(
93                                     3.2^2))^0.5+183-131.2 then
94                                     vx = -4
95                                 else
96                                 if x > 253.7-131.2+((y^2+(z+0.1)^2)/(0.45^2))^0.5 then
97                                     vx = -4
98                                 else
99                                     vx = 0
100                                end

```

Figure B.1.6: SIMION user program in lua programming language incorporating equations for functions approximating pressure and velocity isosurfaces for ion funnel simulations. pg 2 of 4


```

94 |         end
95 |     end
96 | end
97 | end
98 | end
99 | end
100 | end
101 | end
102 | end
103 | end
104 | end
105 | end
106 | local vy = 0
107 | local vz = 0
108 | return vx,vy,vz
109 | end
110 |
111 | function SDS.init()
112 |     -- Plot gas flow.
113 |     local CON = simion.import 'contourlib81.lua' -- [3][4]
114 |     CON.plot{func=SDS.velocity, npoints=30, z=0, mark=false, color=2} --[2]
115 |     CON.plot{func=SDS.velocity, npoints=30, y=0, mark=false}
116 |     CON.plot{func=SDS.velocity, npoints=30, x=0, mark=false}
117 | end
118 |
119 | -- adjustable during flight
120 |
121 | adjustable _temperature_k      = 298.0      -- Background gas temperature (K)
122 |
123 |                                 -- [OVERRIDE HS1]
124 | adjustable _sigma_m2          = 2.27E-18    -- Collision-cross section (m^2),
125 |                                 -- from experiment
126 |                                 -- [OVERRIDE HS1]
127 | adjustable _gas_mass_amu      = 28.0        -- Mass of background gas particle
128 |                                 -- (u), (N2 gas)
129 |                                 -- [OVERRIDE HS1]
130 | adjustable _mark_collisions   = 0           -- Mark collisions (1=yes,0=no).
131 |                                 -- [OVERRIDE HS1]
132 | adjustable pe_update_each_usec = 0.05      -- PE display update period (in usec)
133 |
134 | -- adjustable at beginning of flight
135 |
136 | adjustable _frequency_hz      = 5E5        -- RF frequency of funnel (in Hz)
137 |                                 -- CAREFUL: time-step sizes should
138 |                                 -- be some fraction below period.
139 | adjustable phase_angle_deg    = 0.0        -- entry phase angle of ion (deg)
140 | adjustable _RF_amplitude      = 20         -- RF peak-to-ground voltage (in V)
141 | adjustable _DC_offset_1       = 0.00      -- DC offset of electrode 1 (in V)
142 | adjustable _DC_offset_96      = -33        -- DC offset of electrode 96 (in V)
143 | adjustable _DC_offset_97      = -36.0     -- DC offset of electrode 97 (in V),
144 |                                 -- DC only electrode

```

Figure B.1.6: SIMION user program in lua programming language incorporating equations for functions approximating pressure and velocity isosurfaces for ion funnel simulations. pg 3 of 4

```

145 adjustable _pressure_pa      = 1.0*133.28 -- Pressure (in Pa)
146                               -- Note: 1 Torr = 133.28 Pa.
147                               -- [OVERRIDE HS1]
148
149 -- internal variables
150 local omega                   -- frequency in radians / usec
151 local theta                   -- phase offset in radians
152 local last_pe_update = 0.0    -- last potential energy surface update time (usec)
153
154 function segment.fast_adjust()
155     -- NOTE: This segment is the only code that differs from funnel2.lua.
156
157     -- Initialize constants once.
158     if not theta then
159         theta = phase_angle_deg * (3.141592 / 180)
160         omega = _frequency_hz * 6.28318E-6
161     end
162
163     -- Apply RF+DC to each electrode (see README file for explanation).
164     adj_elect01 = _RF_amplitude * sin(ion_time_of_flight * omega + theta)
165     adj_elect02 = _DC_offset_1
166     adj_elect03 = _DC_offset_96 - _DC_offset_1
167     adj_elect04 = _DC_offset_97
168 end
169
170
171 -- This trick first runs the other_actions segment defined previously
172 -- by the HS1 collision model and then runs our own code.
173 local previous_other_actions = segment.other_actions
174                               -- copy previously defined segment.
175 function segment.other_actions()
176     -- Run previously defined segment.
177     previous_other_actions()
178     -- Now run our own code...
179
180     -- Update PE surface display.
181     if abs(ion_time_of_flight - last_pe_update) >= pe_update_each_usec then
182         last_pe_update = ion_time_of_flight
183         sim_update_pe_surface = 1    -- Request a PE surface display update.
184     end
185 end

```

Figure B.1.6: SIMION user program in lua programming language incorporating equations for functions approximating pressure and velocity isosurfaces for ion funnel simulations. pg 4 of 4

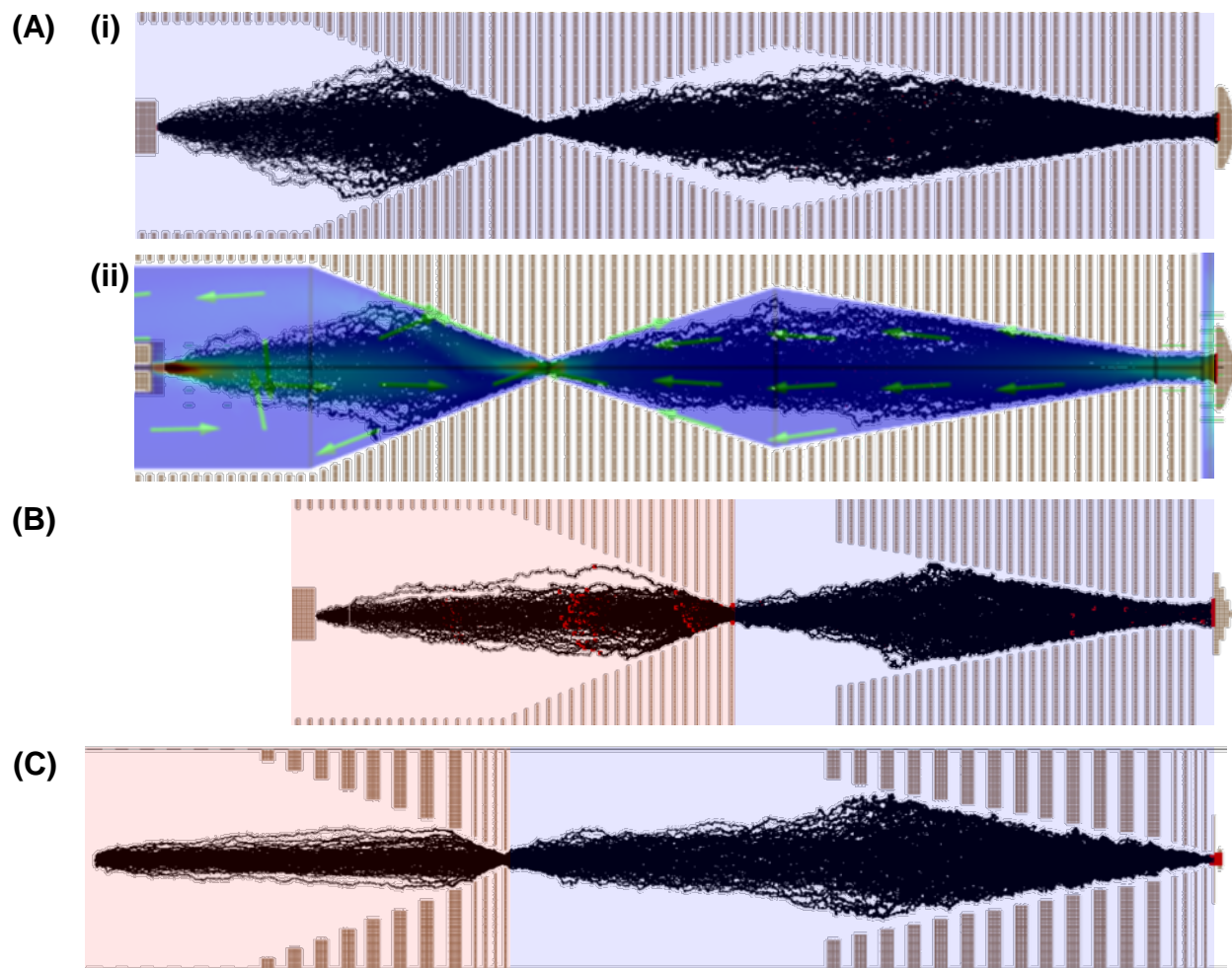
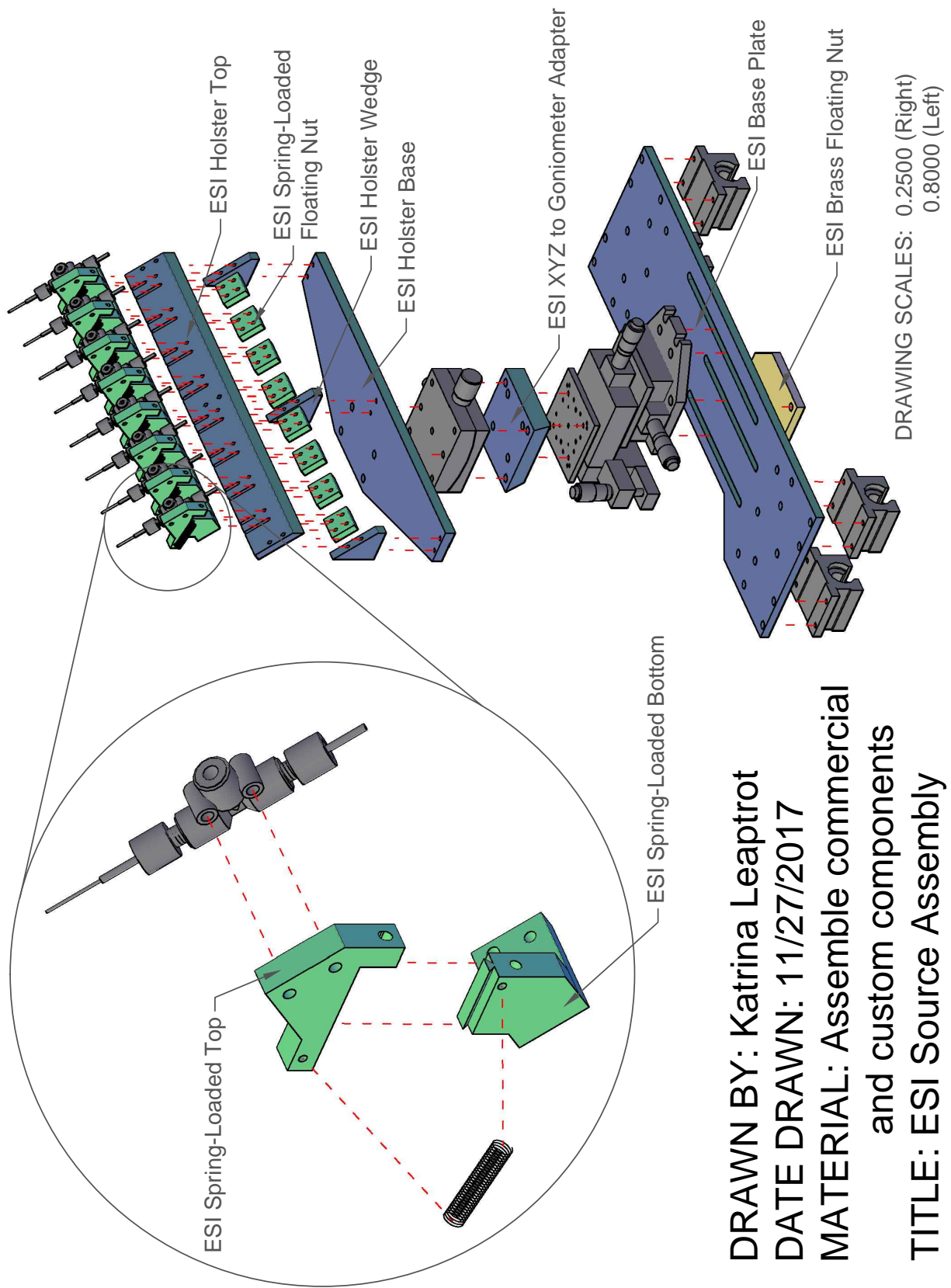
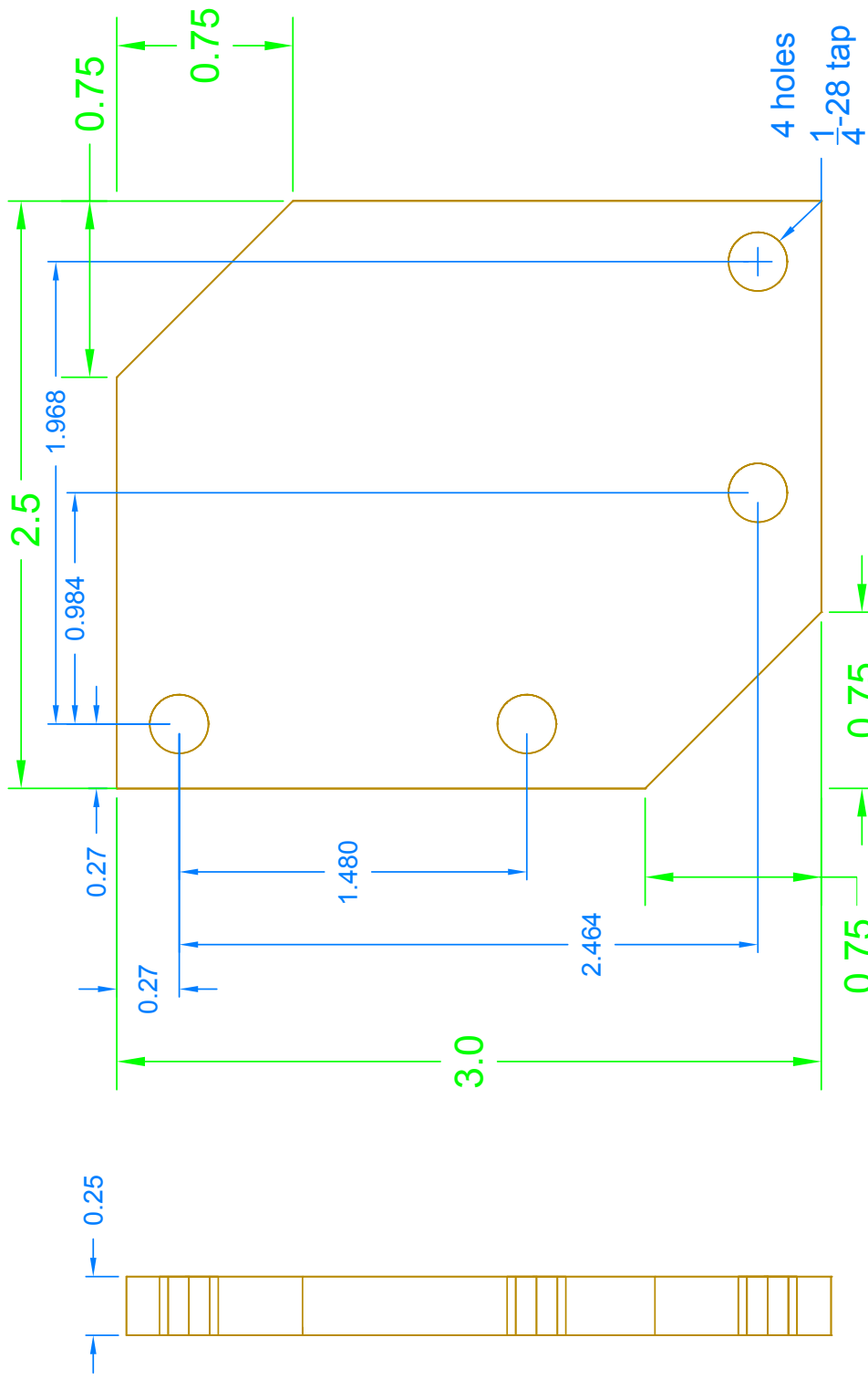
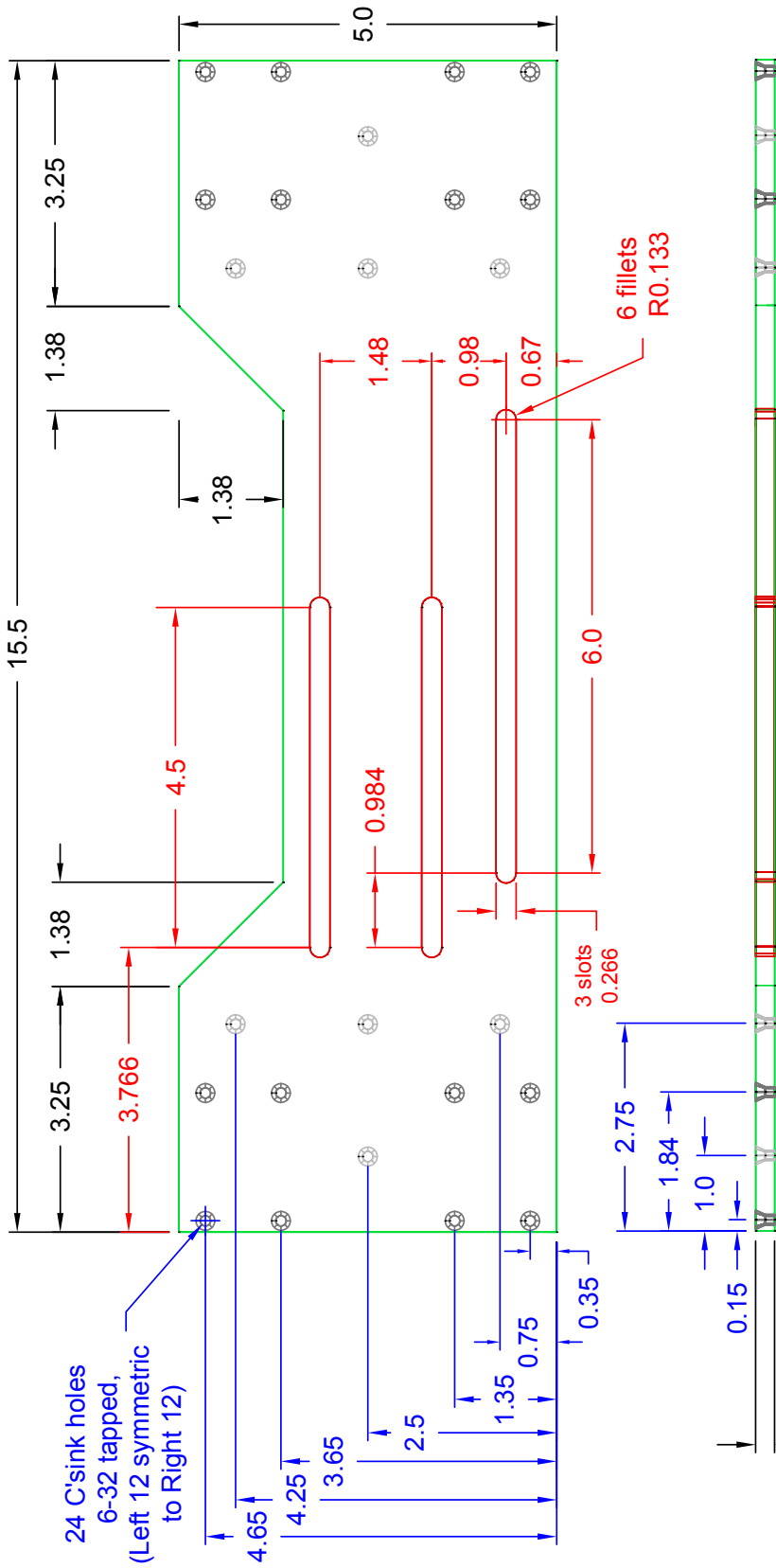


Figure B.1.7: SIMION ion trajectory simulations for four stages of development of the spatially multiplexed instrument ion funnels. Background colors indicate pressure regions as described below. (A) Previous keyhole geometry with brass electrodes where (i) is at 1 Torr and transmission was estimated at $99.8\% \pm 0.0\%$ and (ii) has pressures ranging from 1 Torr to 1.2 Torr, neutral gas velocity from -4 m/s to 51 m/s along the axis of ion movement, and transmission estimated at $99.6\% \pm 0.0\%$. (B) Tandem geometry with brass electrodes, 0.5 in gap between funnels, 10 Torr in first funnel, 3 Torr in second funnel, and transmission estimated at $96.4\% \pm 0.0\%$. (C) Final PCB tandem geometry at 10 Torr in the first funnel and 3 Torr in the second funnel with transmission estimated at $96.0\% \pm 2.0\%$.





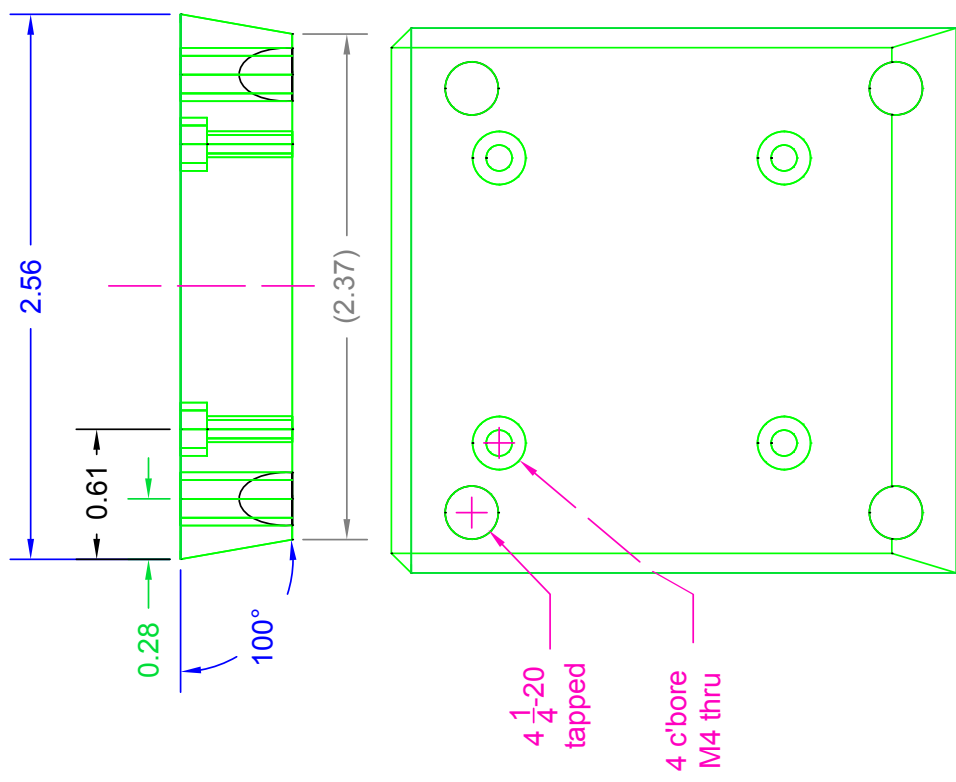
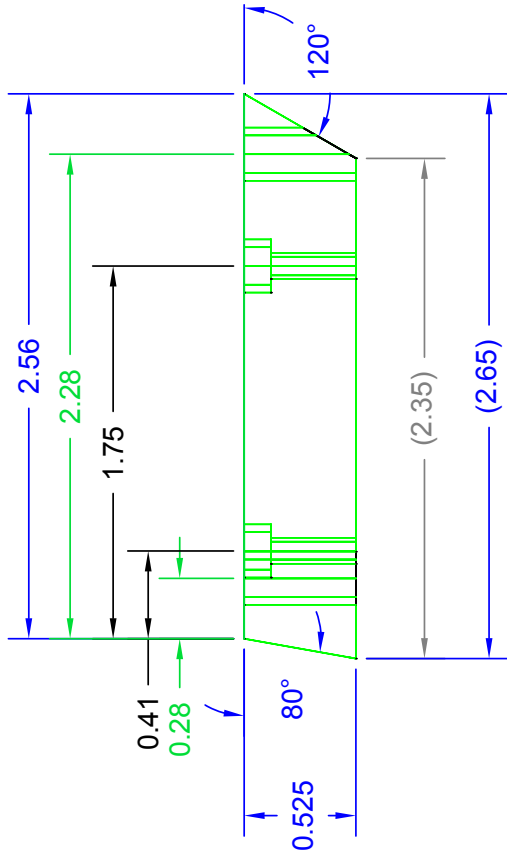
DRAWN BY: Katrina Leaptrot
 DATE DRAWN: 04/25/12
 MATERIAL: Brass
 QUANTITY: 1
 TITLE: ESI Brass Floating Nut



DRAWN BY: Katrina Leaptrot
DATE DRAWN: 04/24/12
MATERIAL: Aluminum
QUANTITY: 1
TITLE: ESI Base Plate

TOLERANCES:
 X.X ±0.030
 X.XX ±0.010
 X.XXX ±0.005

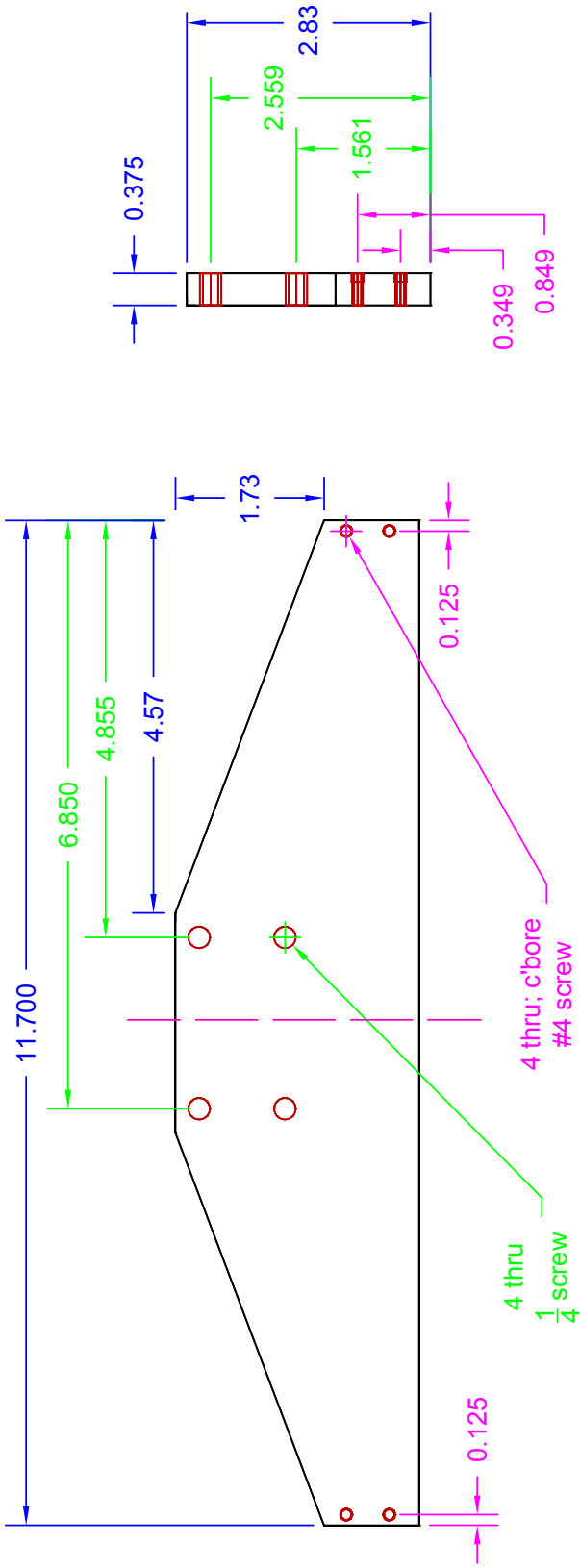
DRAWING SCALE: 0.600
DIMENSIONS ARE IN INCHES



DRAWN BY: Katrina Leaprot
 DATE DRAWN: 05/15/12
 MATERIAL: Aluminum
 QUANTITY: 1
 TITLE: ESI XYZ to Goniometer Adapter

TOLERANCES:
 X.XX ±0.010
 X.XXX ±0.005
 Angles ±1°

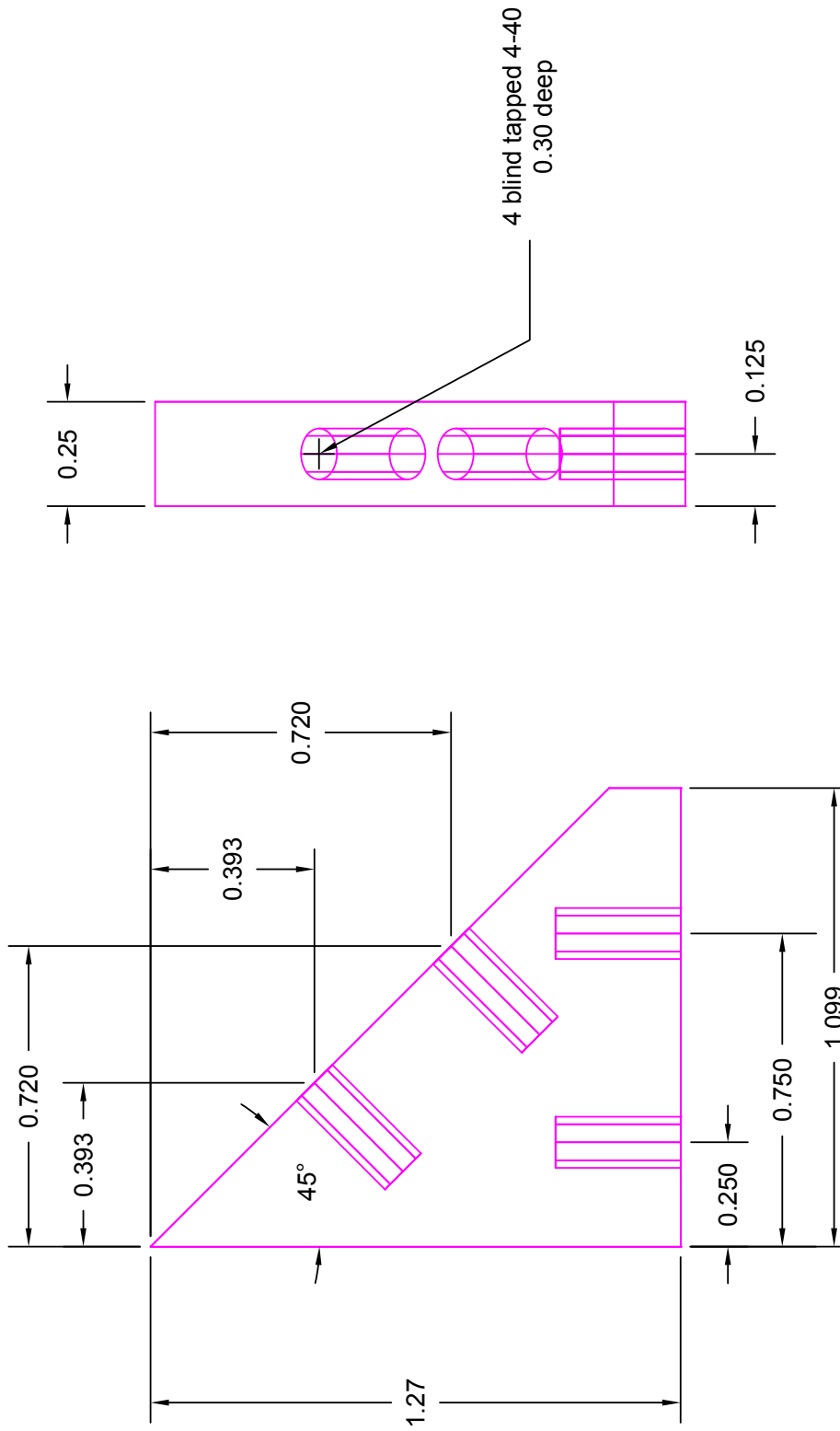
DRAWING SCALE: 1.250
 DIMENSIONS ARE IN INCHES



DRAWN BY: Katrina Leaptrot
 DATE DRAWN: 05/15/12
 MATERIAL: Aluminum
 QUANTITY: 1
 TITLE: ESI Holster Base

TOLERANCES:
 X.XX ±0.010
 X.XXX ±0.005

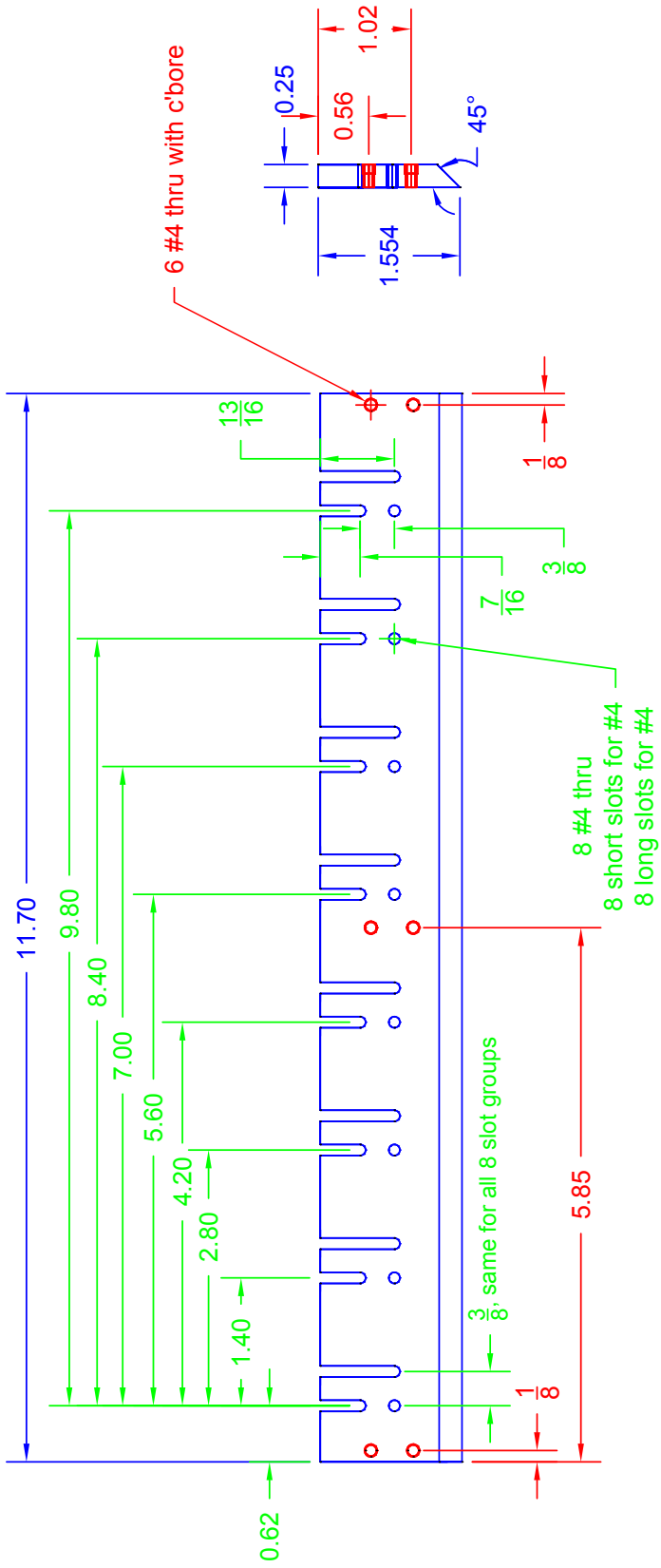
DRAWING SCALE: 0.500
 DIMENSIONS ARE IN INCHES



TOLERANCES:
 X.XX ±0.010
 X.XXX ±0.005

DRAWING SCALE: 2.500
 DIMENSIONS ARE IN INCHES

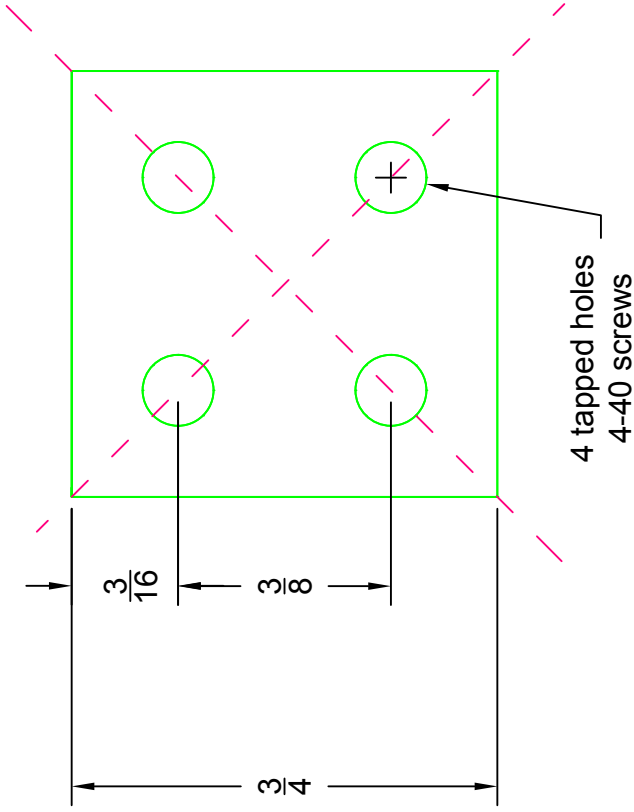
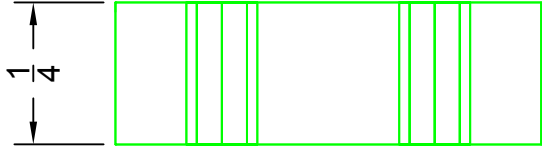
DRAWN BY: Katrina Leaptrot
DATE DRAWN: 05/15/12
MATERIAL: Aluminum
QUANTITY: 3
TITLE: ESI Holster Wedge



DRAWN BY: Katrina Leaptrot
 DATE DRAWN: 05/15/12
 MATERIAL: Aluminum
 QUANTITY: 1
 TITLE: ESI Holster Top

TOLERANCES:
 X.XX ±0.010
 X.XXX ±0.005
 Fractions ±1/32

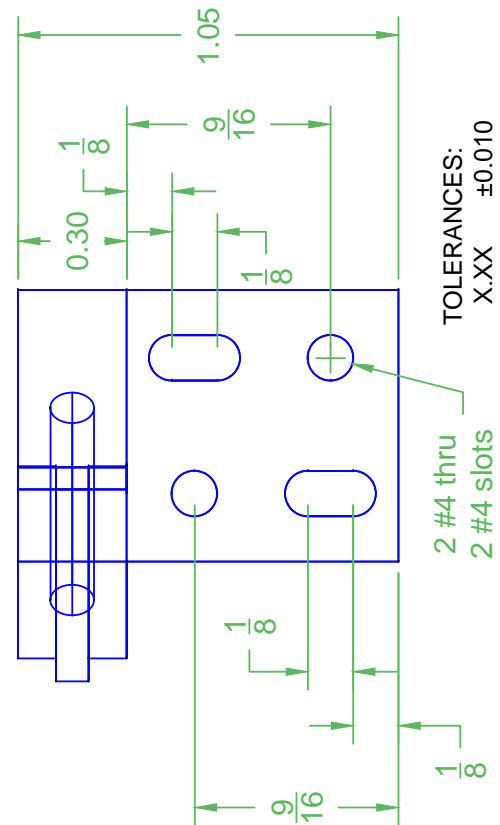
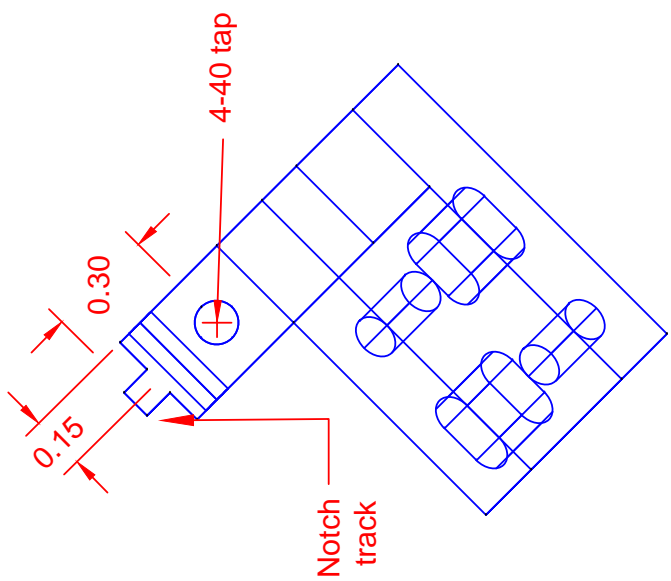
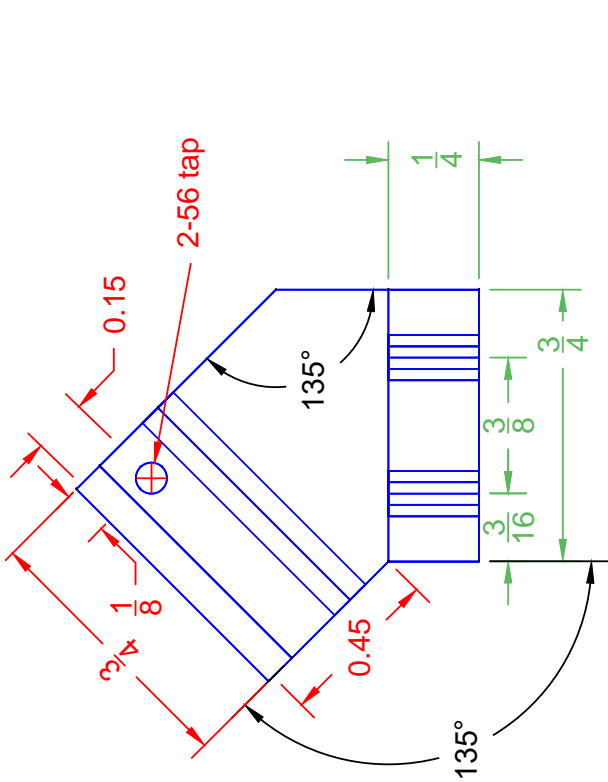
DRAWING SCALE: 0.550
 DIMENSIONS ARE IN INCHES



DRAWN BY: Katrina Leaptrot
DATE DRAWN: 05/08/12
MATERIAL: Aluminum
QUANTITY: 8
TITLE: ESI Spring-Loaded Floating Nut

TOLERANCES:
 Fraction $\pm 1/32$

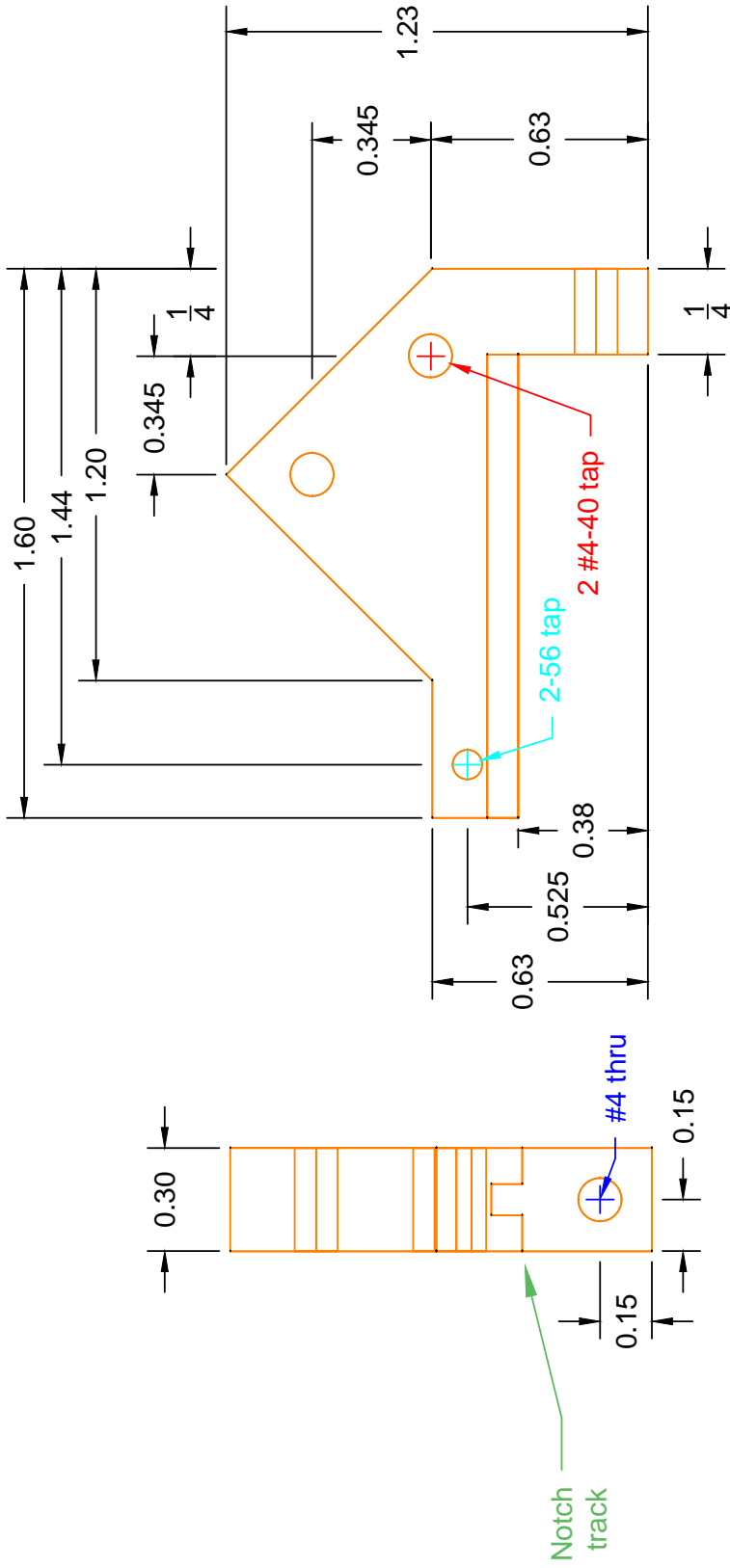
DRAWING SCALE: 3.000
DIMENSIONS ARE IN INCHES



DRAWN BY: Katrina Leaptrot
 DATE DRAWN: 05/08/12
 MATERIAL: Aluminum
 QUANTITY: 8
 TITLE: ESI Spring-Loaded Bottom

TOLERANCES:
 X.XX ±0.010
 Fractions ±1/32
 Angles ±1°

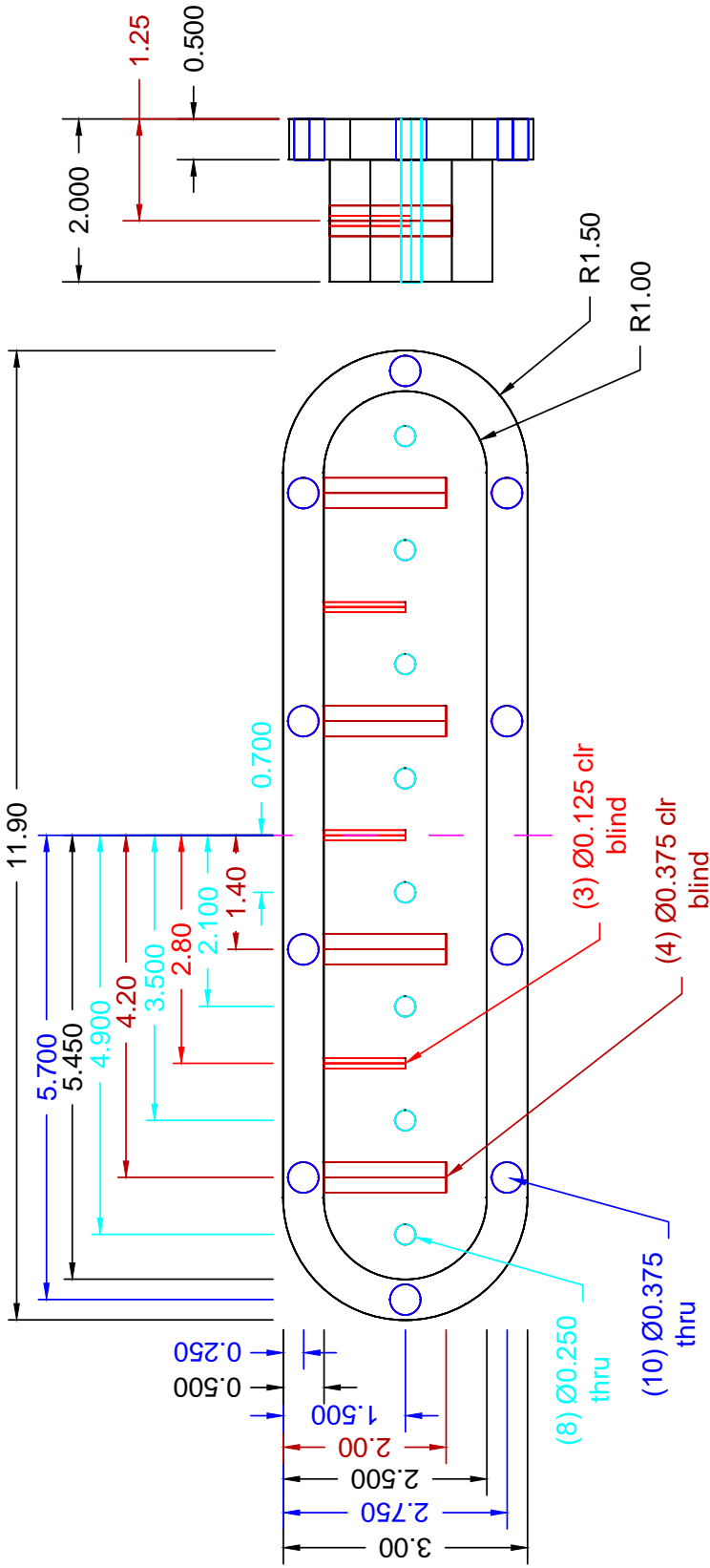
DRAWING SCALE: 2.000
 DIMENSIONS ARE IN INCHES



DRAWN BY: Katrina Leaptrot
 DATE DRAWN: 05/08/12
 MATERIAL: Aluminum
 QUANTITY: 8
 TITLE: ESI Spring-Loaded Top

TOLERANCES:
 X.XX ±0.010
 X.XXX ±0.005
 Fractions ±1/32

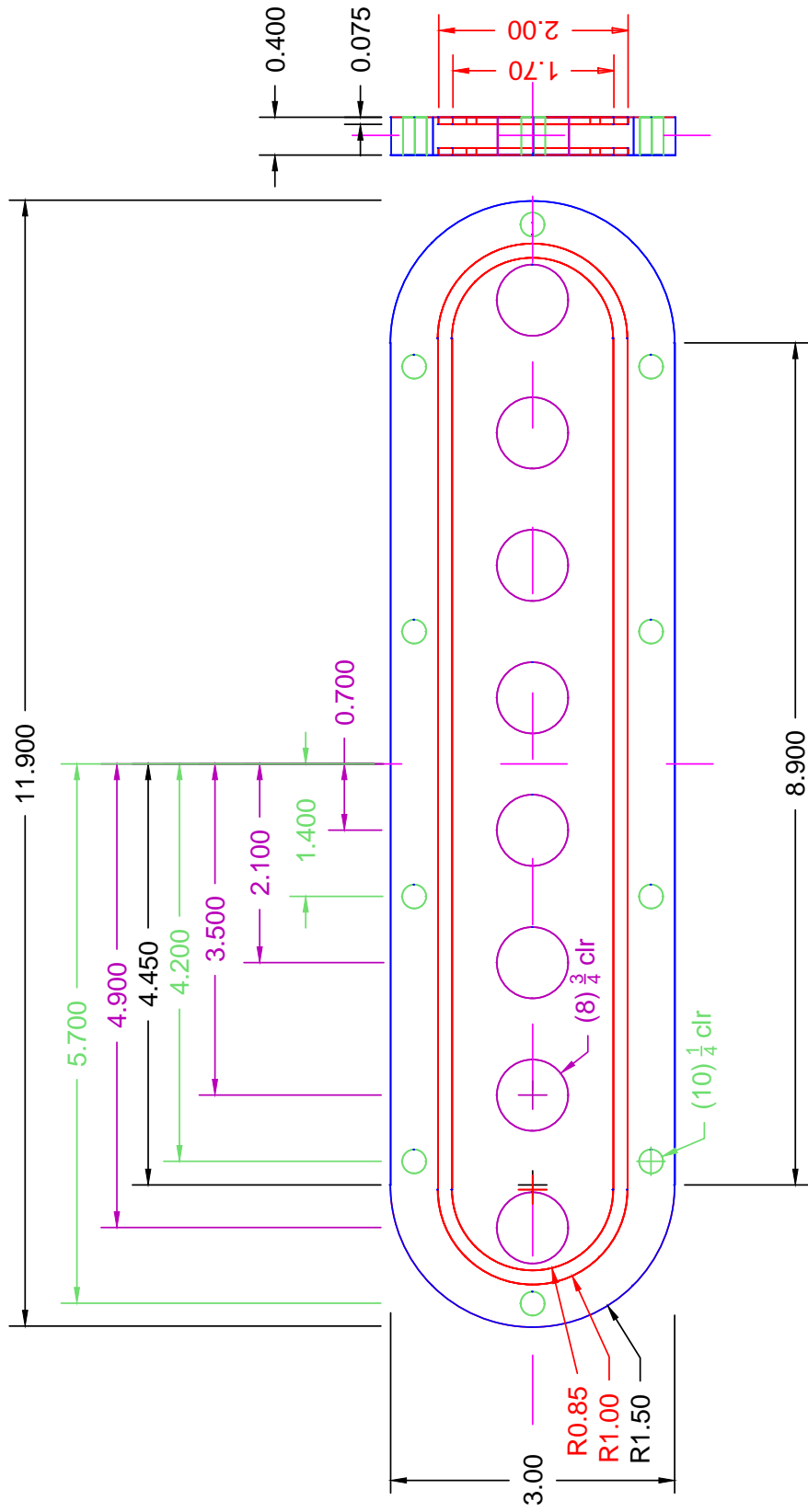
DRAWING SCALE: 2.000
 DIMENSIONS ARE IN INCHES



TOLERANCES:
 X.XX ± 0.030
 X.XXX ± 0.020

DRAWING SCALE: 0.5000
 DIMENSIONS IN INCHES

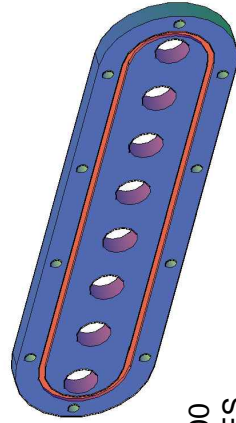
DRAWN BY: Katrina Leaprot
 DATE DRAWN: 11/27/2017
 MATERIAL: Stainless Steel
 QUANTITY: 1
 TITLE: Heated Desolvation Block

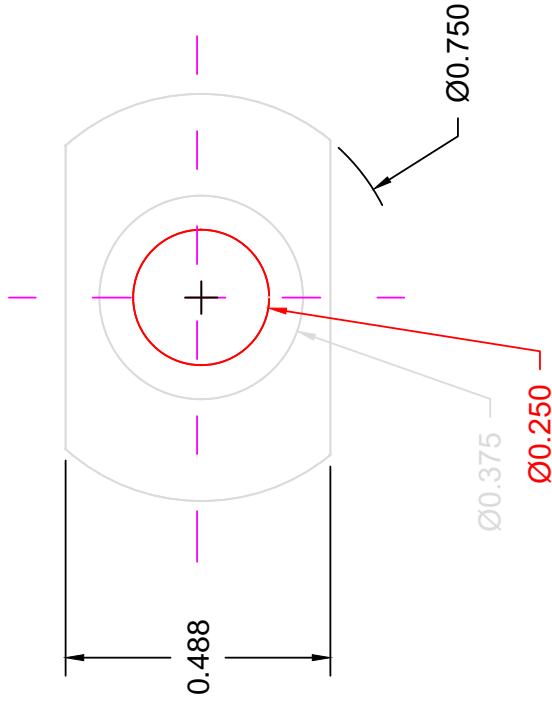
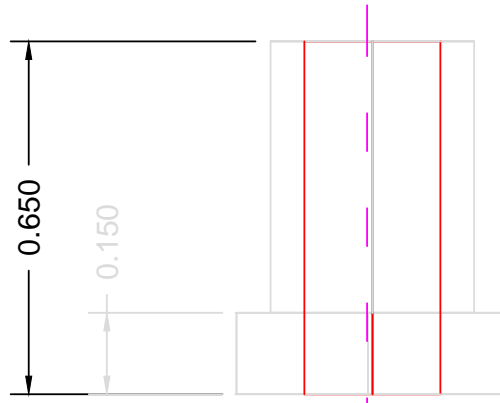


DRAWN BY: Katrina Leaptrot
 DATE DRAWN: 01/12/15
 MATERIAL: Black Delrin
 QUANTITY: 1
 TITLE: Insulator Flange for Desolvation Block

TOLERANCES:
 X.XX ±0.030
 X.XXX ±0.020
 Fractions ±1/32

DRAWING SCALE: 0.700
 DIMENSIONS IN INCHES

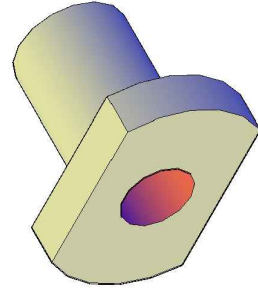


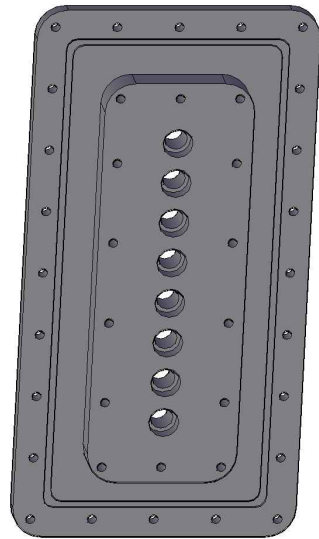
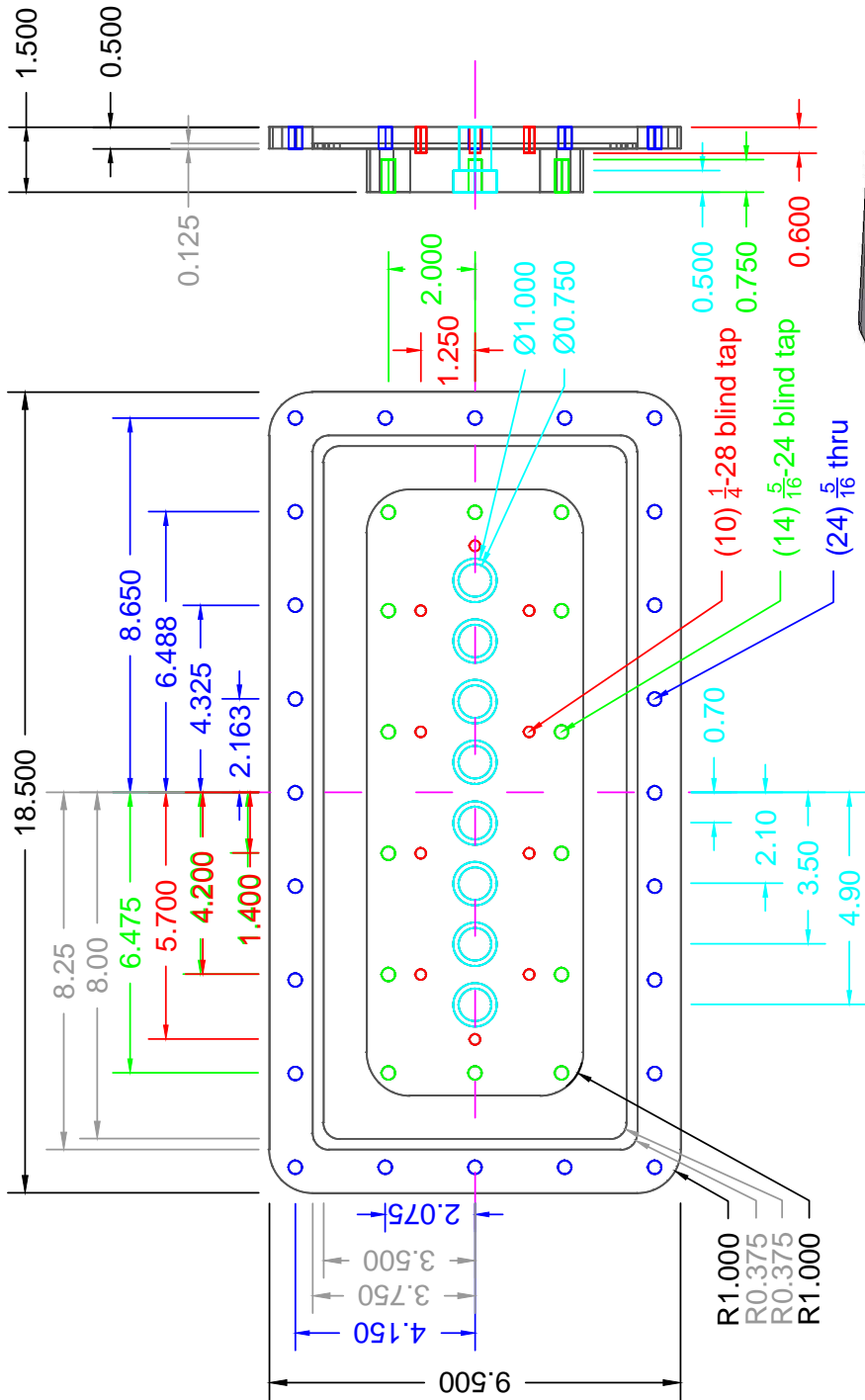


DRAWN BY: Katrina Leaprot
DATE DRAWN: 11/27/2017
MATERIAL: Delrin
QUANTITY: 10
TITLE: Desolvation Bolt Spacer

TOLERANCES:
 X.XX ±0.030
 X.XXX ±0.020

DRAWING SCALE: 3.0000
DIMENSIONS IN INCHES

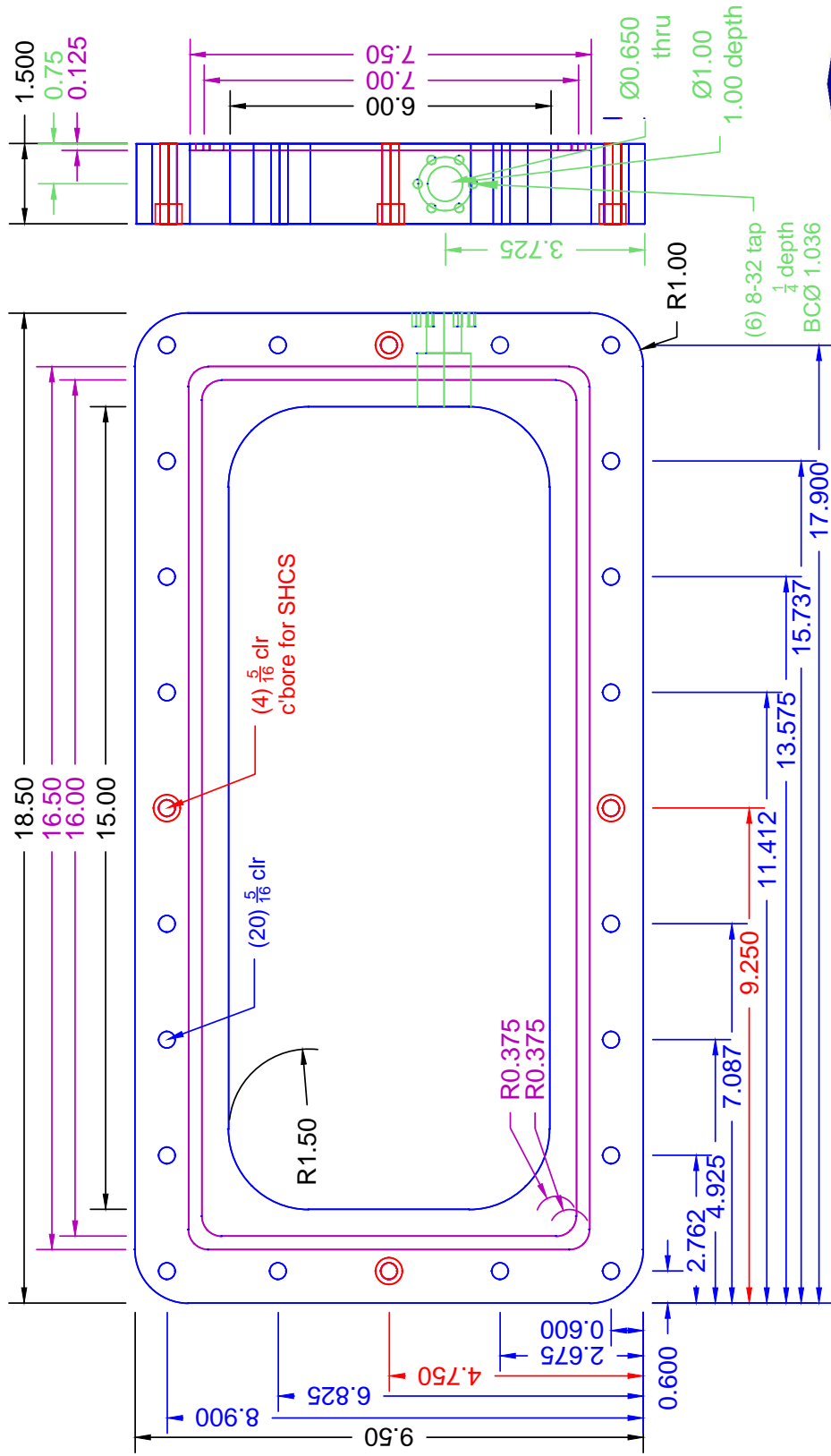




TOLERANCES:
 X.X ±0.030
 X.XX ±0.020
 X.XXX ±0.010
 Fractions ±1/32

DRAWING SCALE: 0.2500
 DIMENSIONS IN INCHES

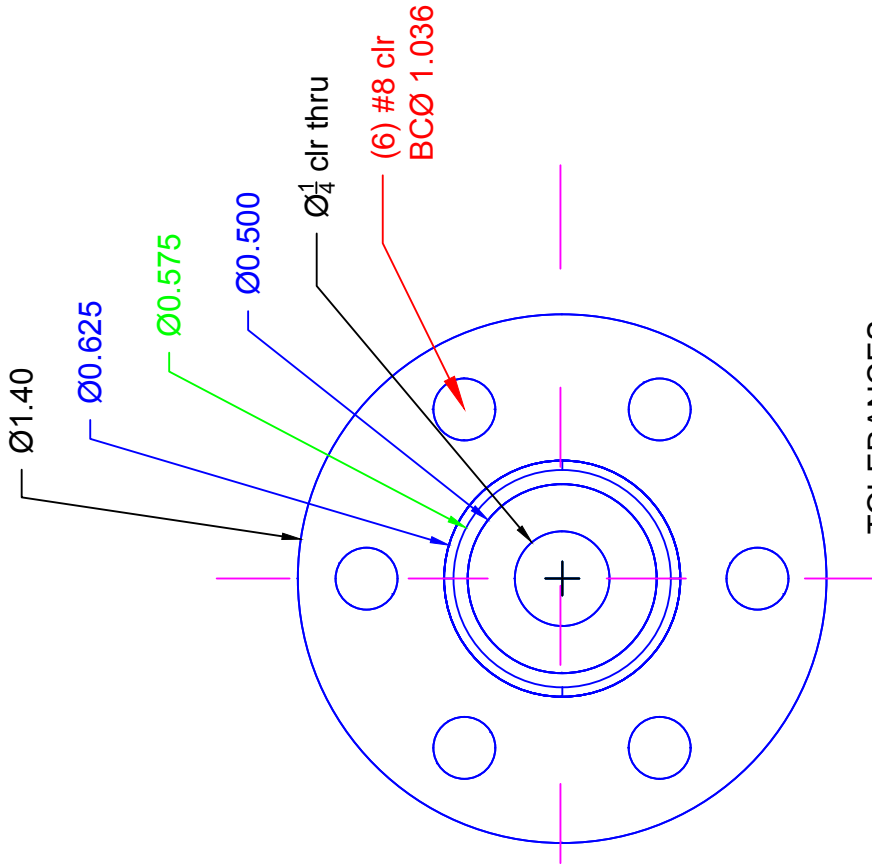
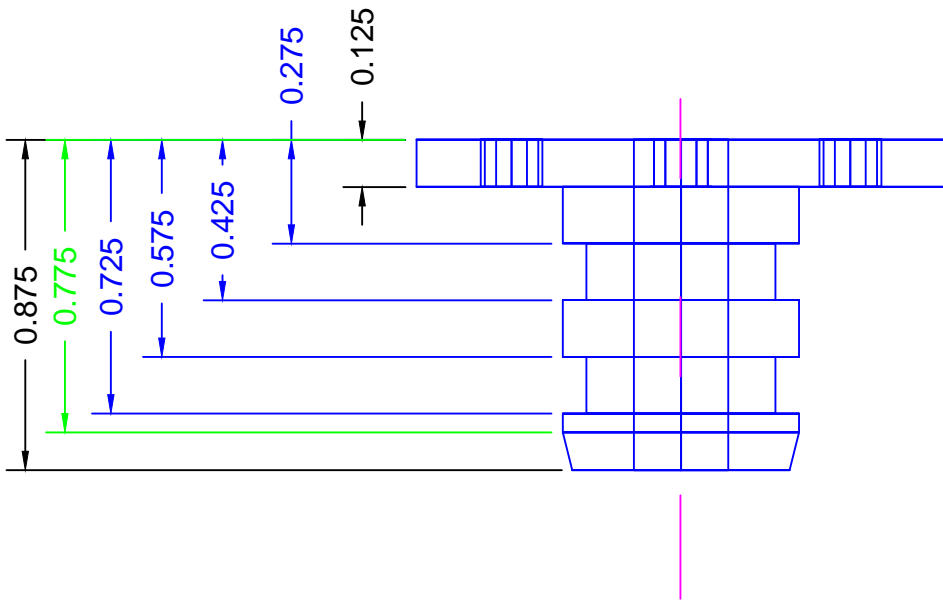
DRAWN BY: Katrina Leaprot
DATE DRAWN: 11/21/2017
MATERIAL: Stainless Steel
QUANTITY: 1
TITLE: Chamber 1 Top Hat Flange



DRAWN BY: Katrina Leaptrot
DATE DRAWN: 01/09/15
MATERIAL: Black Delrin
QUANTITY: 1
TITLE: Extension Collar (R3)

TOLERANCES:
 X.XX ±0.030
 X.XXX ±0.020
 Fractions ±1/32

DRAWING SCALE: 0.350
DIMENSIONS IN INCHES



DRAWN BY: Katrina Leaprot

DATE DRAWN: 01/09/15

MATERIAL: Delrin

QUANTITY: 1

TITLE: RGC Electrical Feedthrough
Piston Seal (R3)

TOLERANCES:

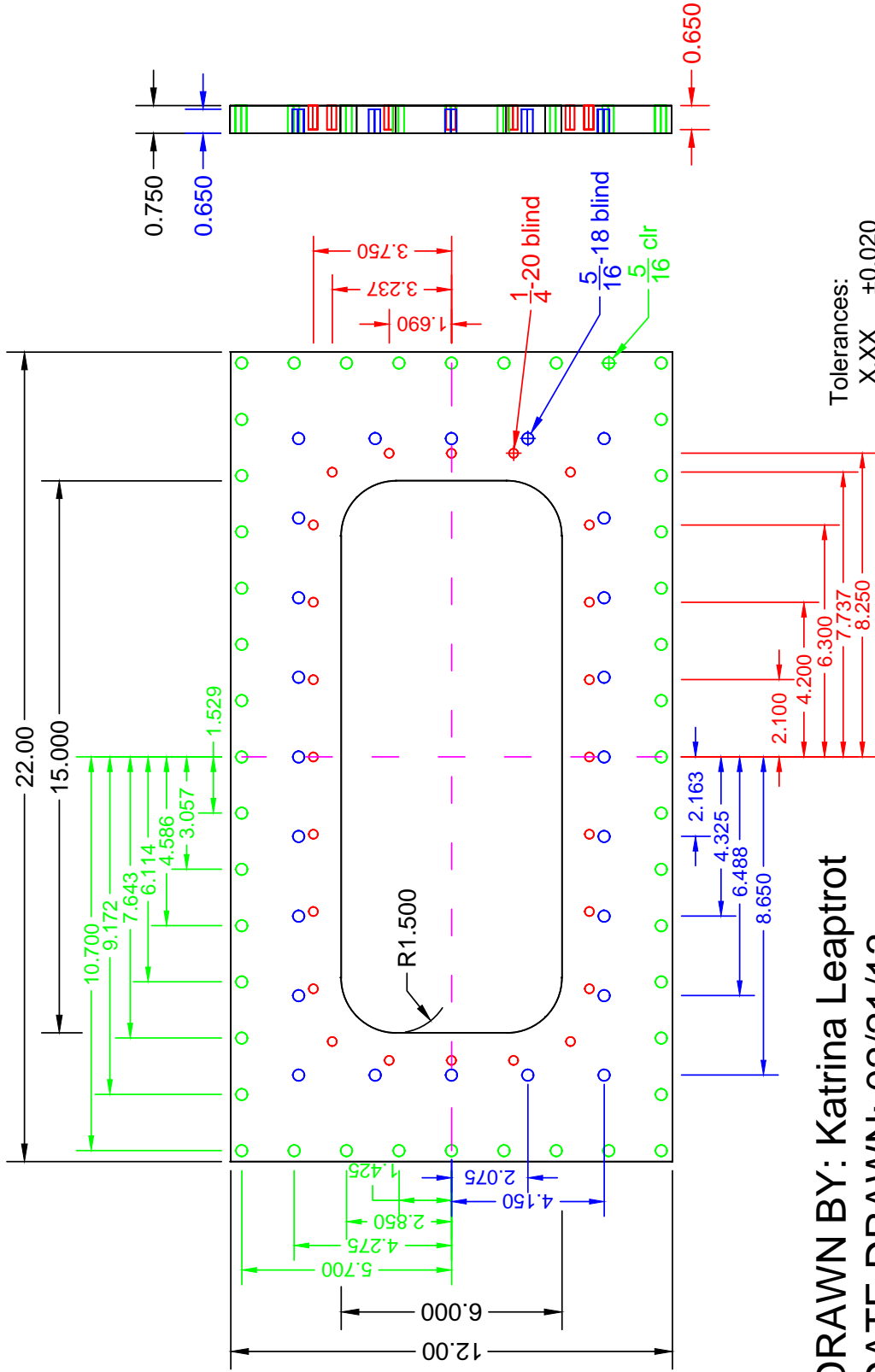
X.XX ±0.030

X.XXX ±0.010

Fractions ±1/32

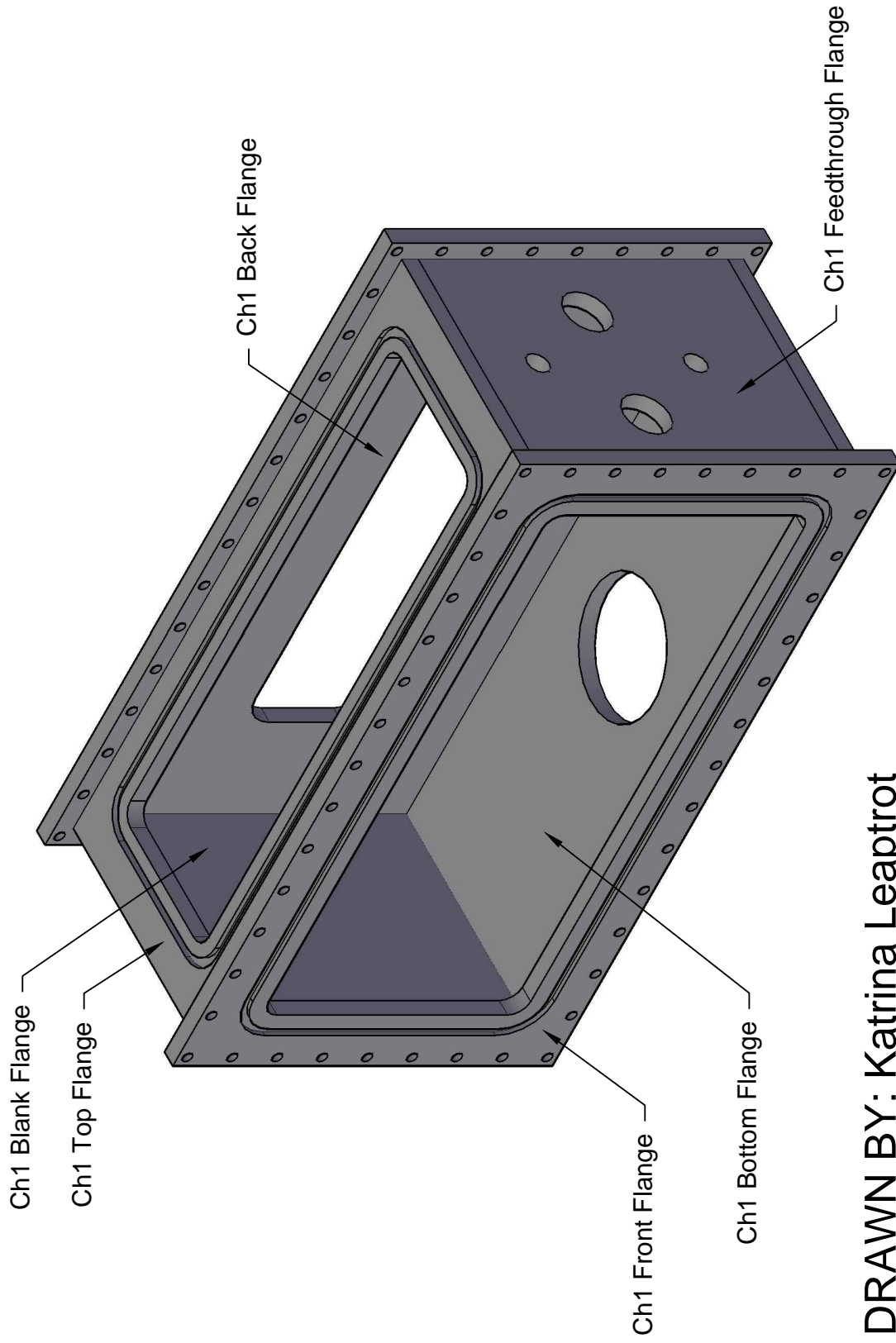
DRAWING SCALE: 2.000
DIMENSIONS IN INCHES

Use with -112 Viton O-rings



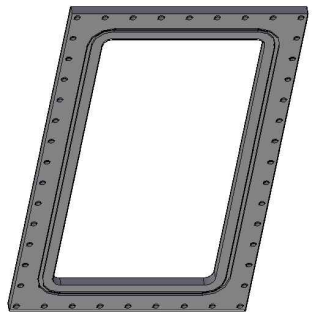
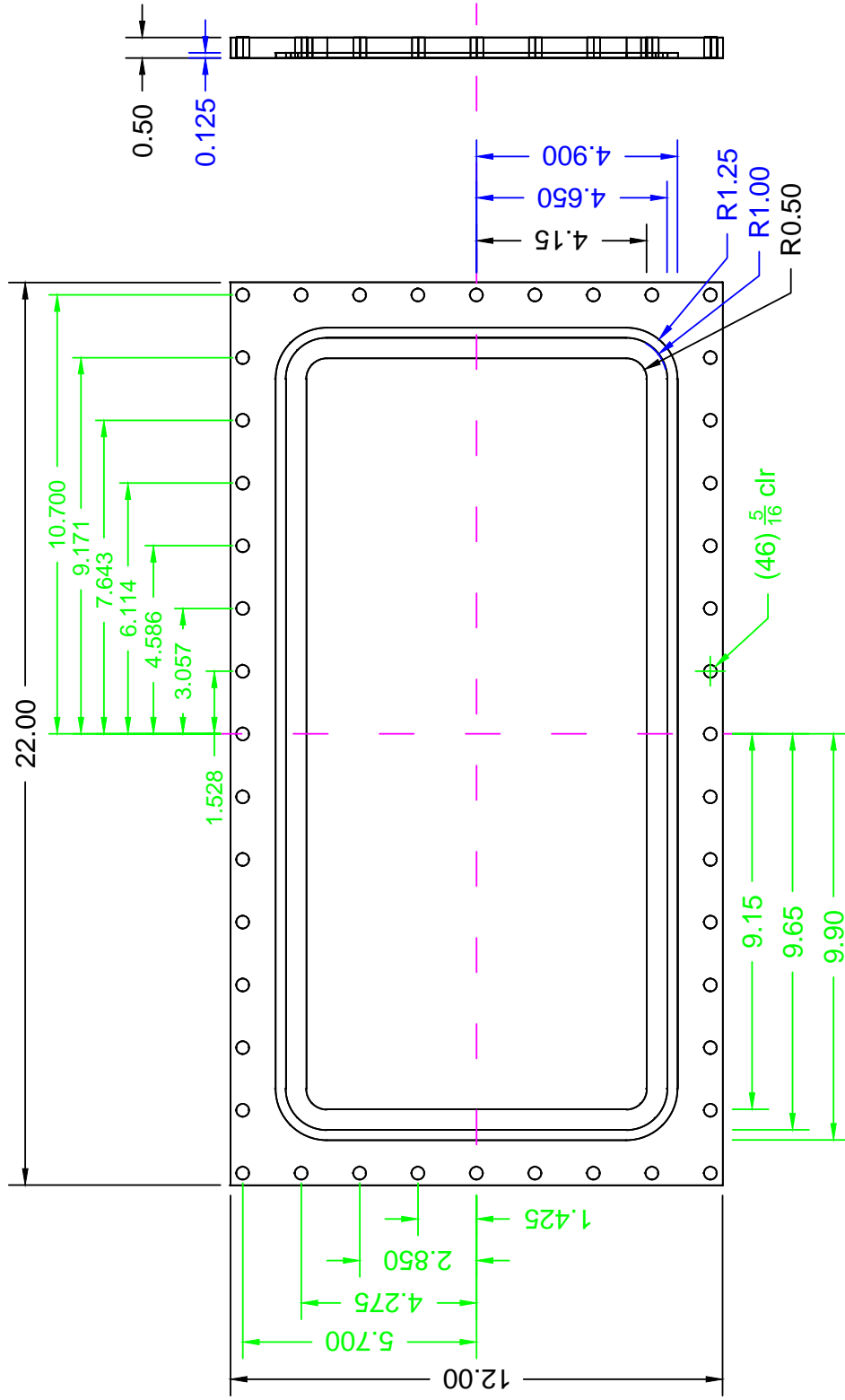
Tolerances:
 X.XX ±0.020
 X.XXX ±0.010
 DRAWING SCALE: 0.2500
 DIMENSIONS IN INCHES

DRAWN BY: Katrina Leaptrot
DATE DRAWN: 02/21/13
MATERIAL: Aluminum
QUANTITY: 1
TITLE: Chamber 1, 3/4" Flange



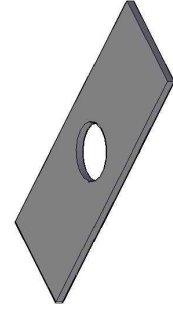
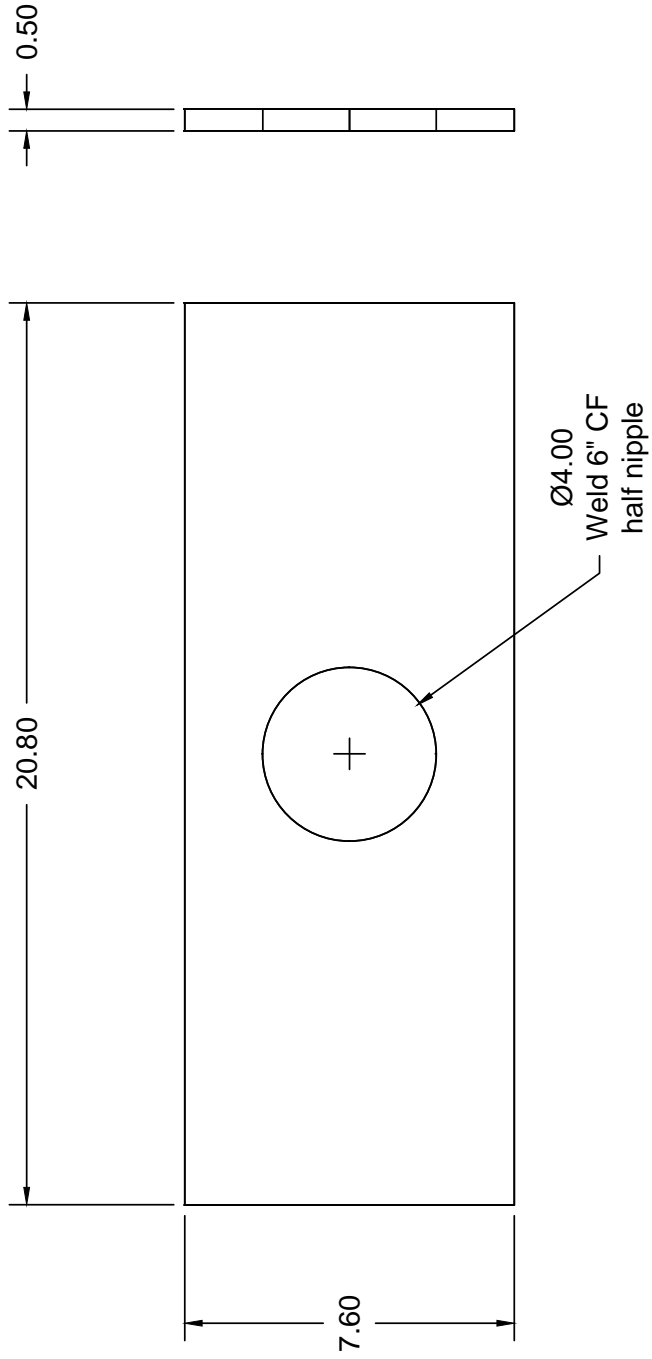
DRAWN BY: Katrina Leaprot
DATE DRAWN: 11/27/2017
MATERIAL: Weld Existing
TITLE: Chamber 1 Assembly

DRAWING SCALE: 0.2500



DRAWN BY: Katrina Leaptrot
DATE DRAWN: 11/21/2017
MATERIAL: Stainless Steel
QUANTITY: 1
TITLE: Chamber 1 Front Flange

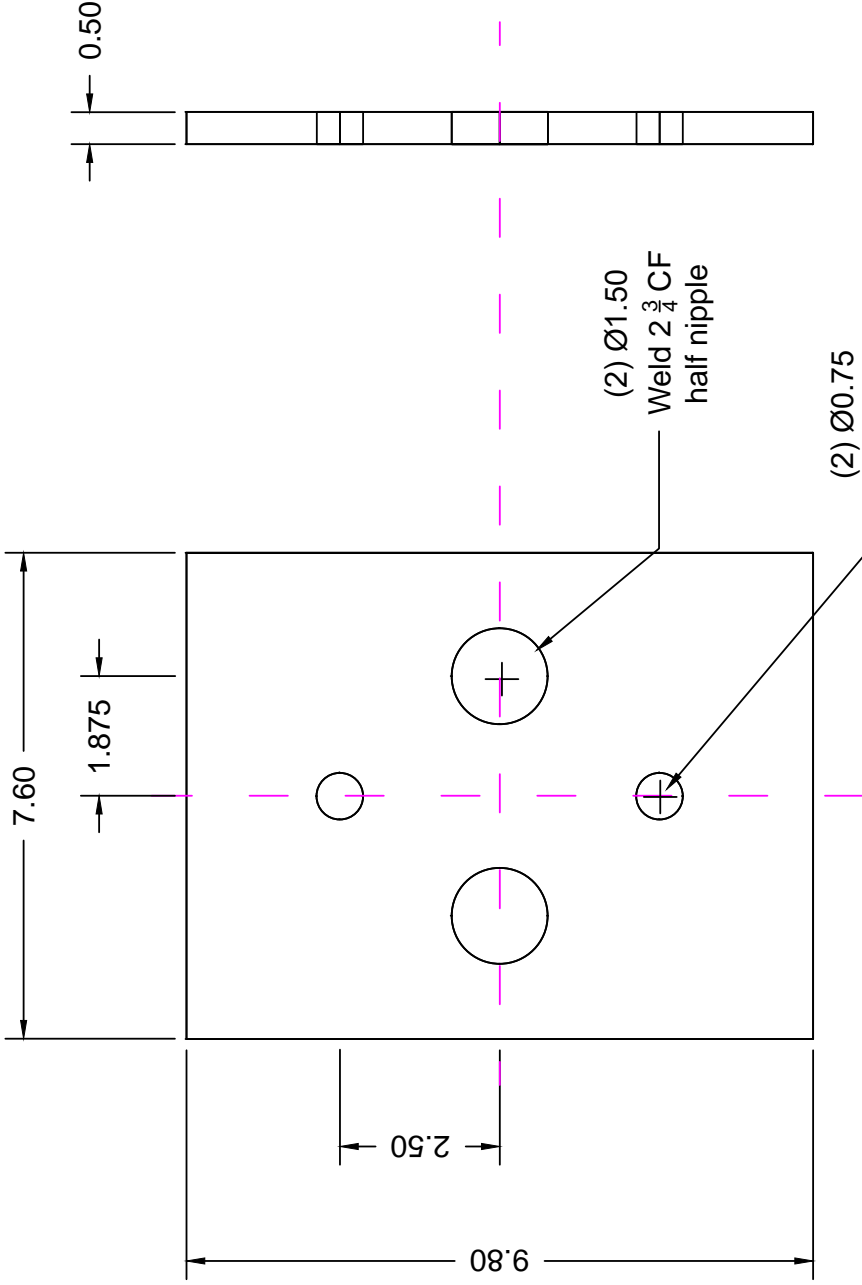
TOLERANCES:
 X.XX ±0.020
 X.XXX ±0.010
 Fractions ±1/32
DRAWING SCALE: 0.2500
DIMENSIONS IN INCHES



DRAWN BY: Katrina Leaptrot
DATE DRAWN: 11/21/2017
MATERIAL: Stainless Steel
QUANTITY: 1

TOLERANCES:
 X.XX ±0.020
DRAWING SCALE: 0.2500
 DIMENSIONS IN INCHES

TITLE: Chamber 1 Bottom Flange



DRAWN BY: Katrina Leaprot

DATE DRAWN: 11/21/2017

MATERIAL: Stainless Steel

QUANTITY: 1

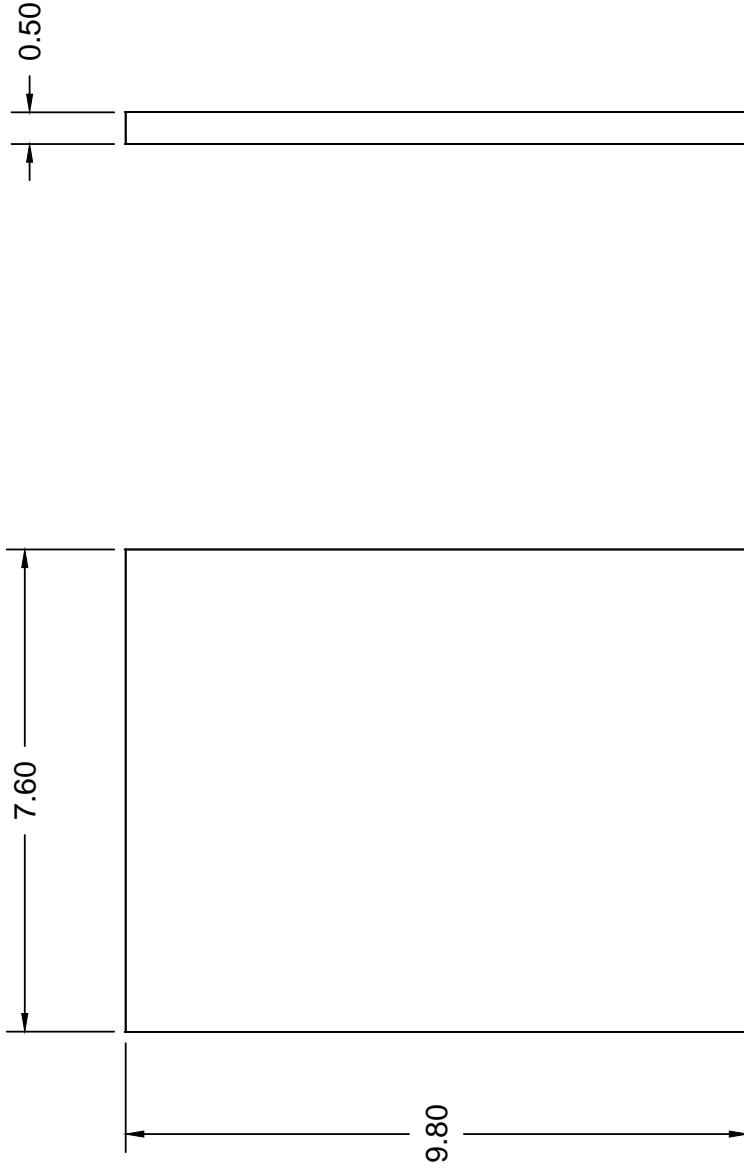
TITLE: Chamber 1 Feedthrough
Flange

TOLERANCES:

X.XX ±0.020

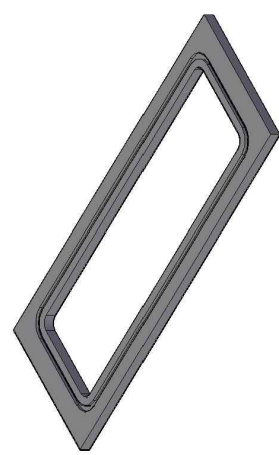
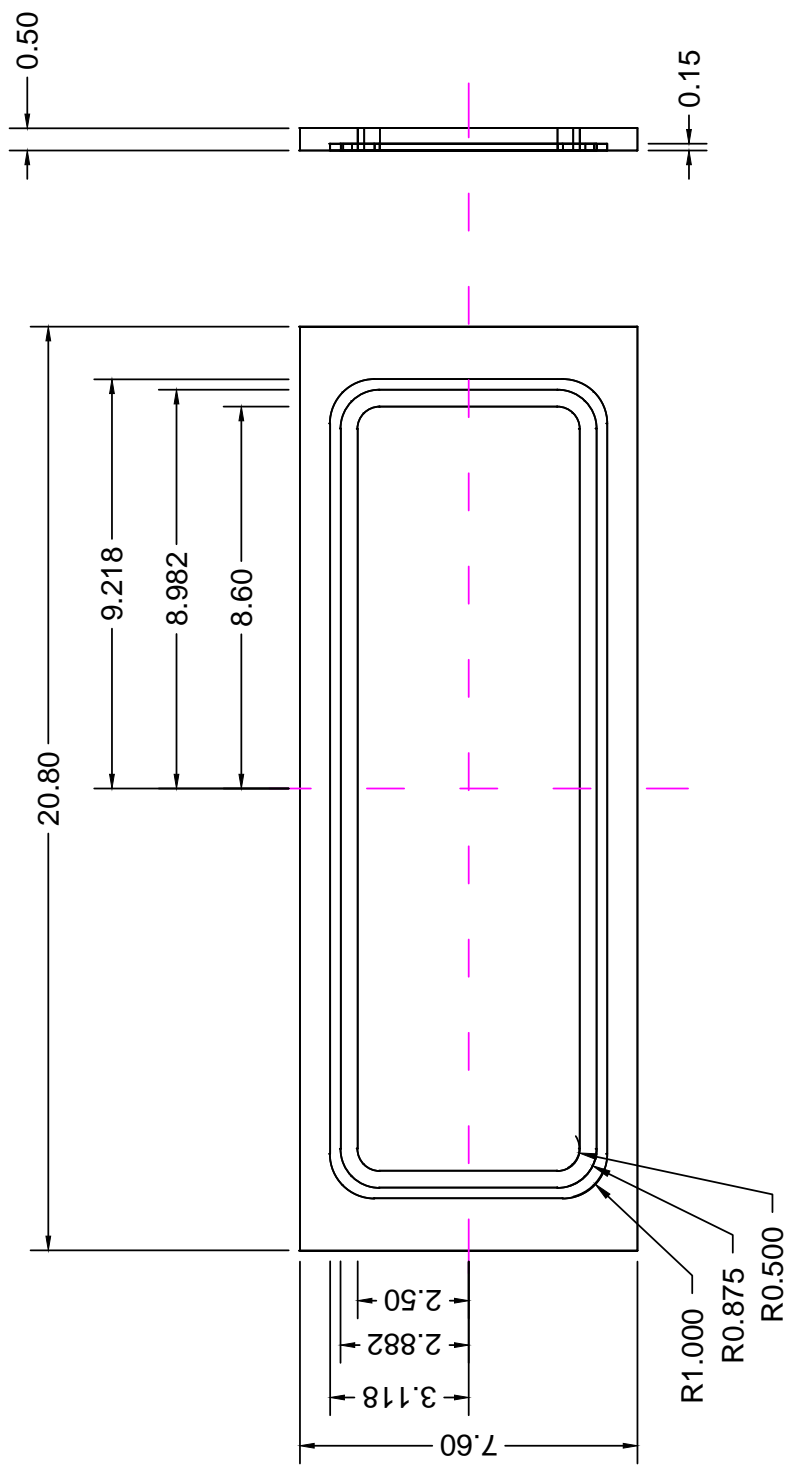
X.XXX ±0.020

DRAWING SCALE: 0.3500
DIMENSIONS IN INCHES



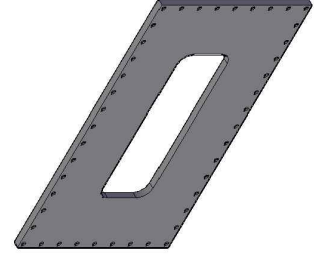
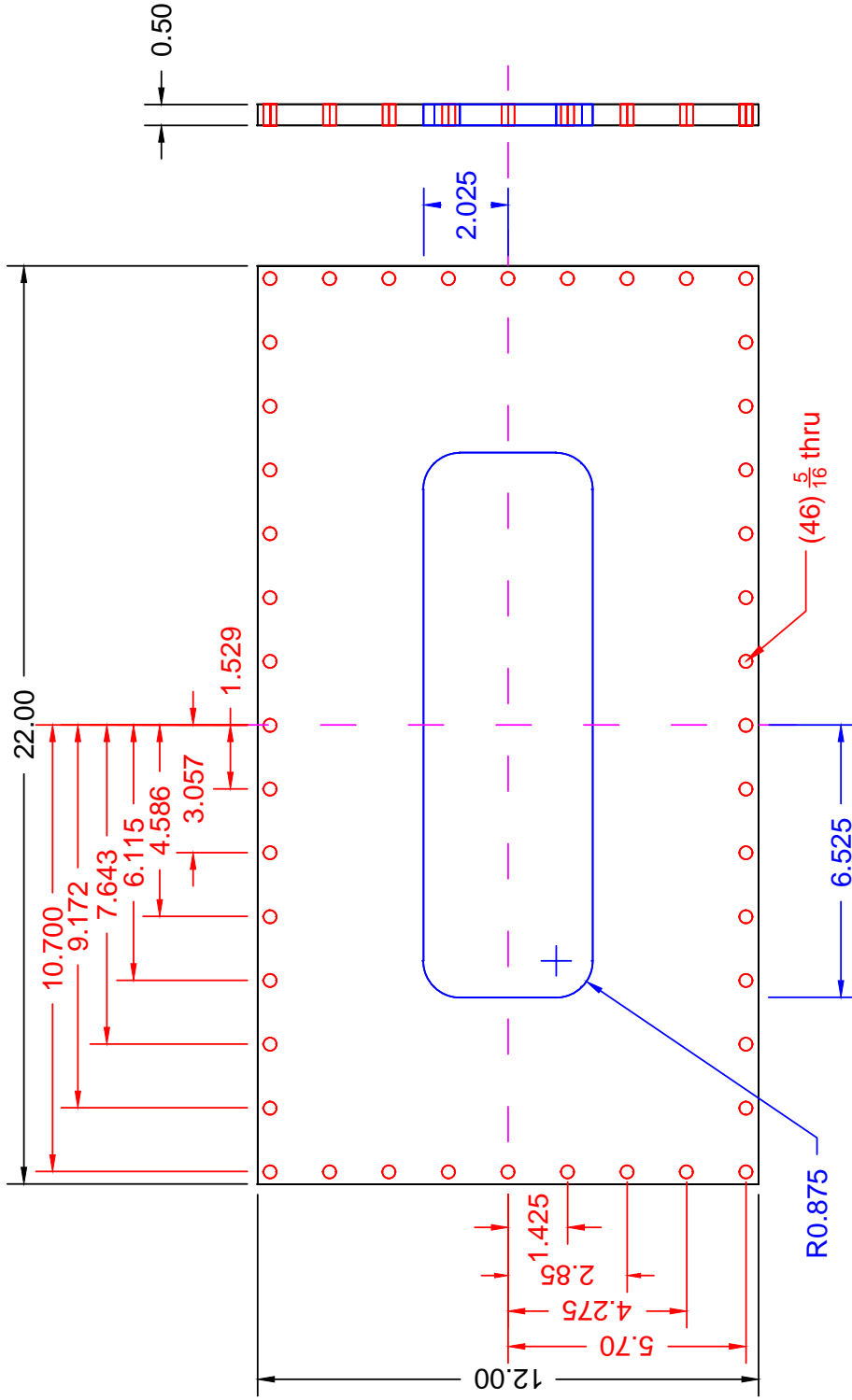
DRAWN BY: Katrina Leaptrot
DATE DRAWN: 11/21/2017
MATERIAL: Stainless Steel
QUANTITY: 1
TITLE: Chamber 1 Blank Flange

TOLERANCES:
X.XX ±0.020
DRAWING SCALE: 0.3500
DIMENSIONS IN INCHES



DRAWN BY: Katrina Leaptrot
DATE DRAWN: 11/21/2017
MATERIAL: Stainless Steel
QUANTITY: 1
TITLE: Chamber 1 Top Flange

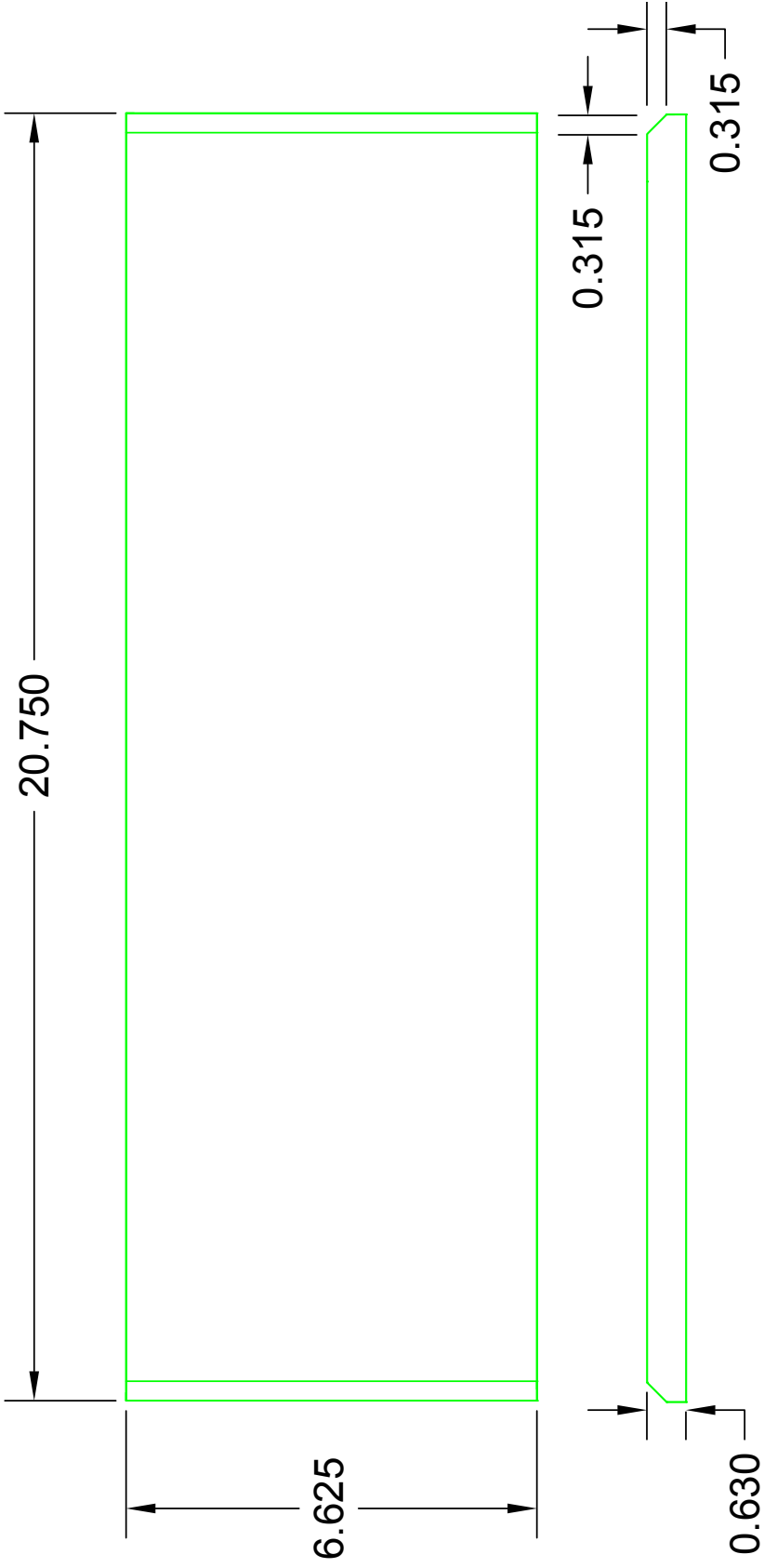
TOLERANCES:
 X.XX ±0.020
 X.XXX ±0.010
DRAWING SCALE: 0.2500
DIMENSIONS IN INCHES



DRAWN BY: Katrina Leaprot
 DATE DRAWN: 03/28/2013
 MATERIAL: Stainless Steel
 QUANTITY: 1
 TITLE: Chamber 1 Back Flange

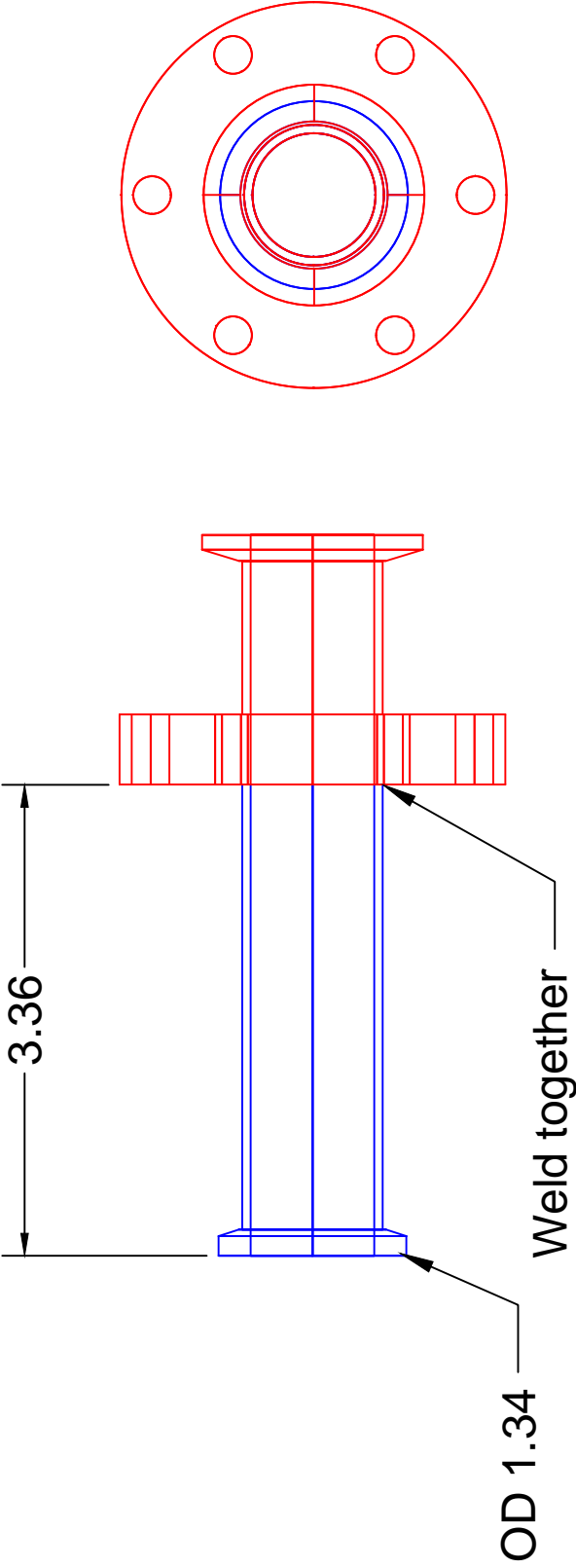
TOLERANCES:
 X.XX ±0.020
 X.XXX ±0.010
 Fractions ±1/32

DRAWING SCALE: 0.2500
 DIMENSIONS IN INCHES



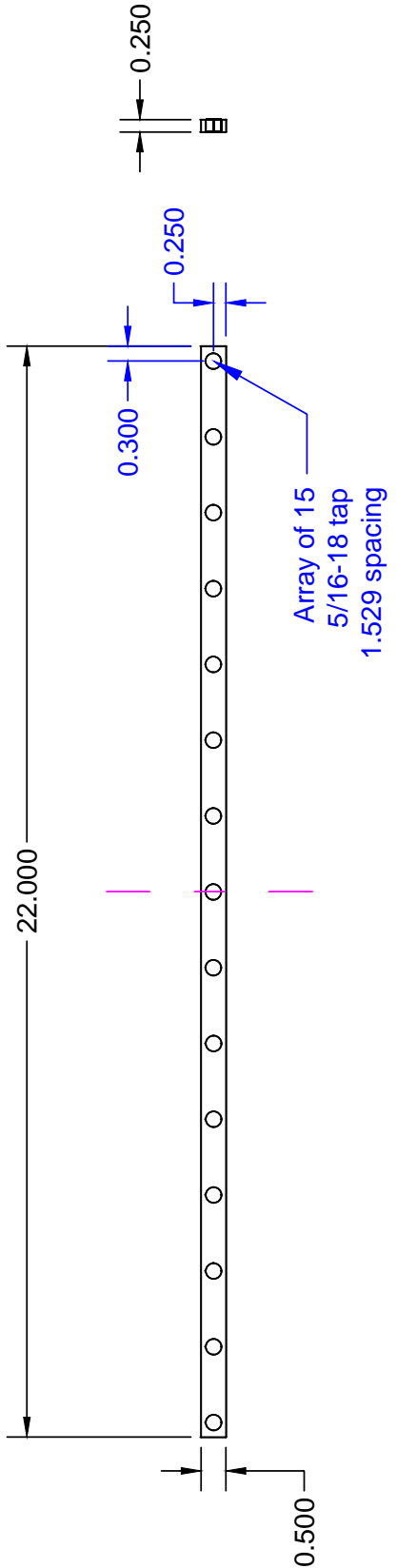
DRAWN BY: Katrina Leaprot
DATE DRAWN: 03/28/12
MATERIAL: 16mm thick Borofloat
QUANTITY: 2
TITLE: Chamber 1 Glass Top

DRAWING SCALE: 0.3800
DIMENSIONS IN INCHES



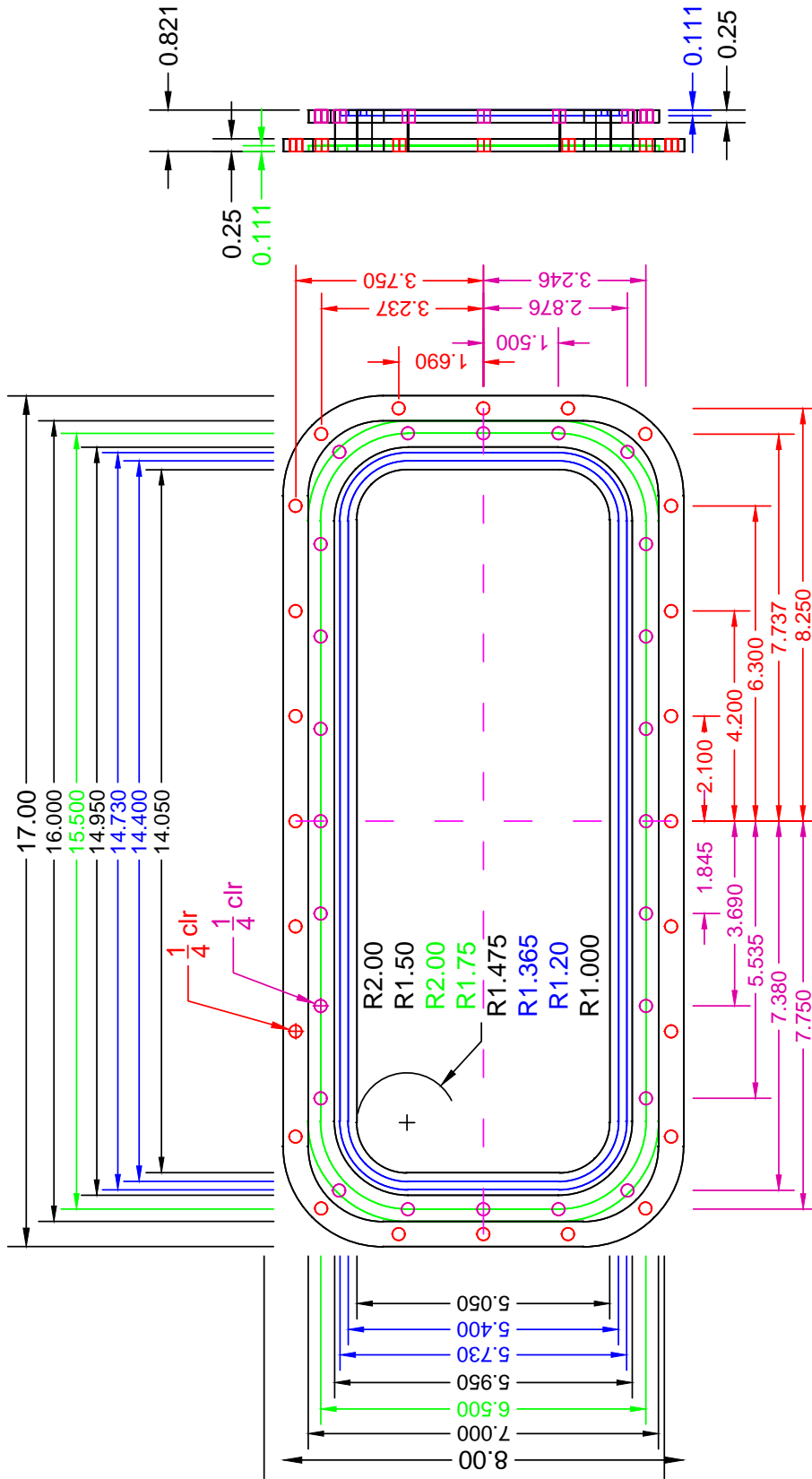
Tolerances:
 X.XX ±0.040
 DRAWING SCALE: 0.7500
 DIMENSIONS IN INCHES

DRAWN BY: Katrina Leaprot
DATE DRAWN: 10/05/12
MATERIAL: Modify existing 2 3/4 CF to KF-25 adapter and KF-25 full nipple
QUANTITY: 1
TITLE: Inner Chamber Pumpout Flange



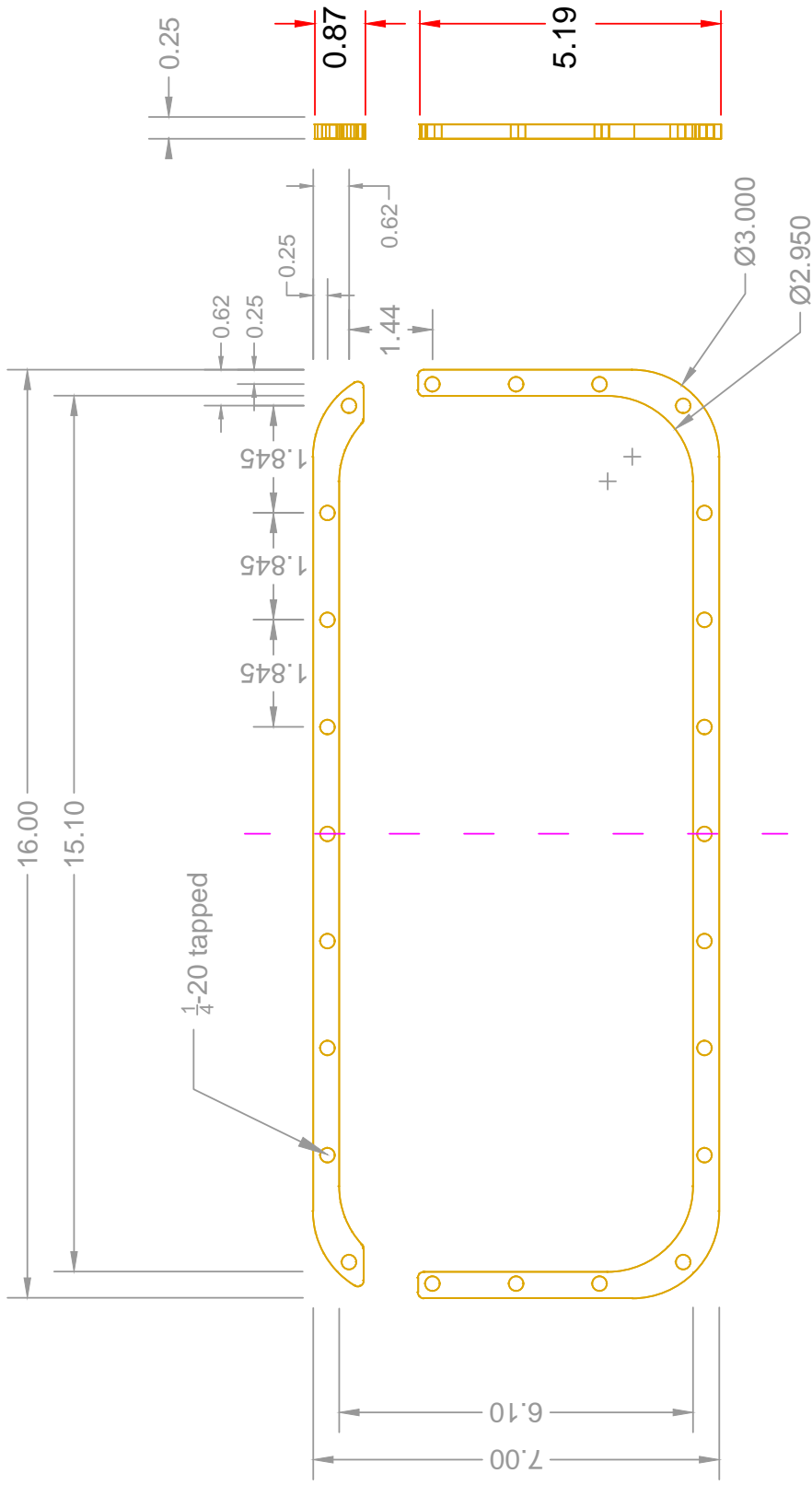
DRAWN BY: Katie Leaptrot
DATE DRAWN: 10/31/12
MATERIAL: Brass
QUANTITY: 3
TITLE: Chamber-Joining Floating Nut

TOLERANCES:
 X.XXX ±0.015
DRAWING SCALE: 0.3000
DIMENSIONS IN INCHES



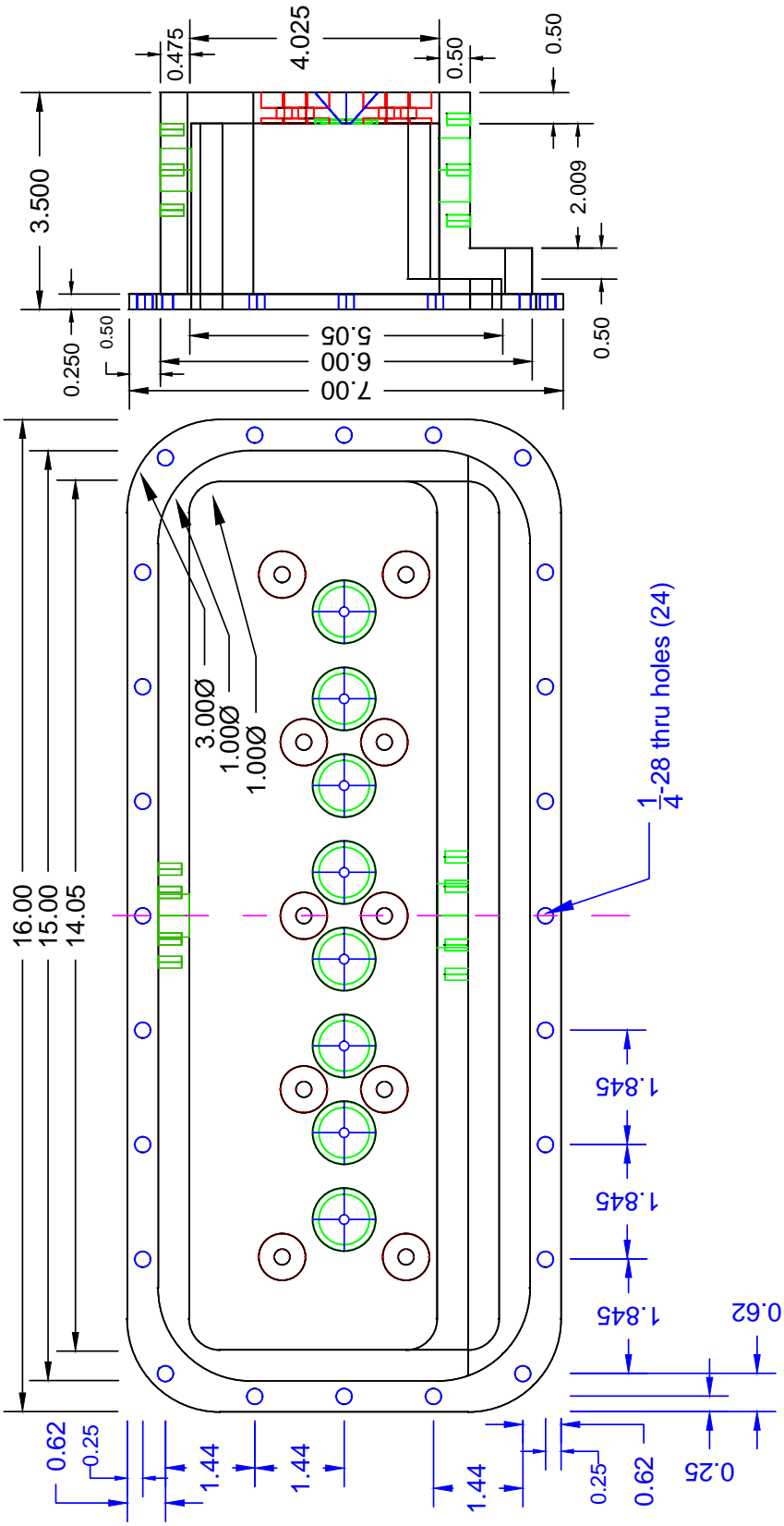
Tolerances:
 X.XX ±0.020
 X.XXX ±0.010
 DRAWING SCALE: 0.3500
 DIMENSIONS IN INCHES

DRAWN BY: Katrina Leaptrot
 DATE DRAWN: 02/21/13
 MATERIAL: Delrin
 QUANTITY: 1
 TITLE: Inner Chamber Smaller; Face Seal



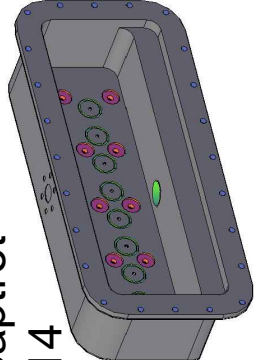
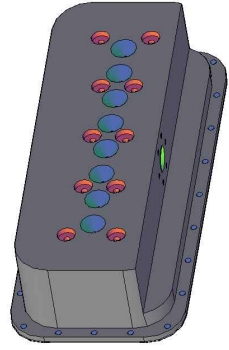
DRAWN BY: Katrina Leaptrot
DATE DRAWN: 02/21/13
MATERIAL: Brass
QUANTITY: 2, Modify existing
TITLE: Floating Nut, Cut

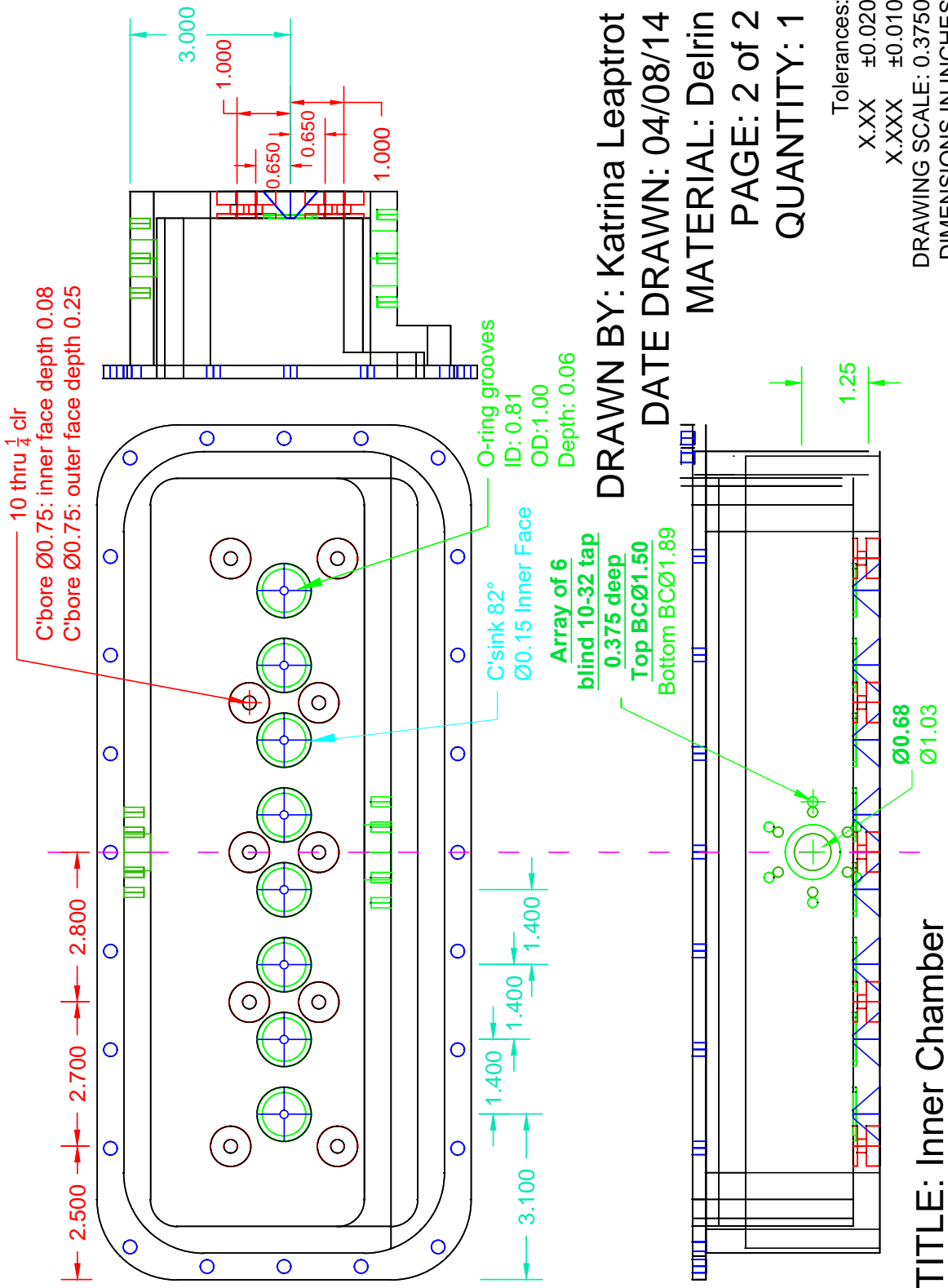
Tolerances:
 X.XX ±0.020
 X.XXX ±0.010
DRAWING SCALE: 0.3500
DIMENSIONS IN: INCHES



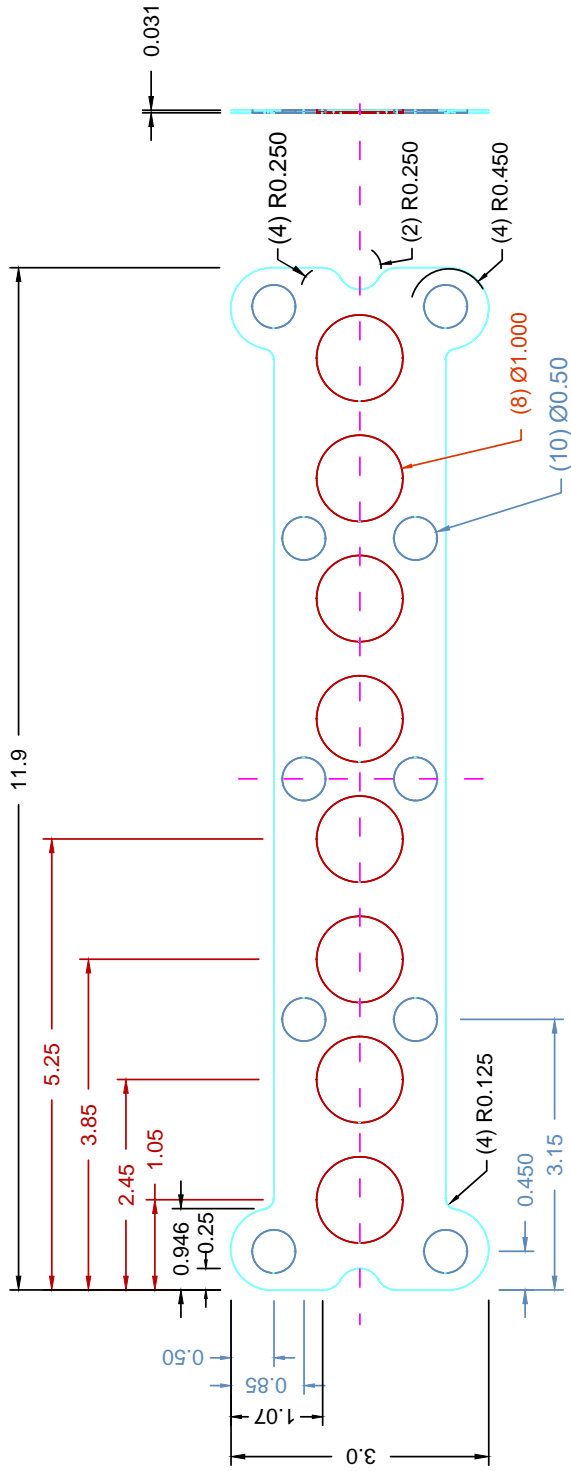
Tolerances:
 X.XX ±0.020
 X.XXX ±0.010
 DRAWING SCALE: 0.3750
 DIMENSIONS IN INCHES

DRAWN BY: Katrina Leaptrot
DATE DRAWN: 04/08/14
MATERIAL: Delrin
PAGE: 1 of 2
QUANTITY: Modify 1
TITLE: Inner Chamber





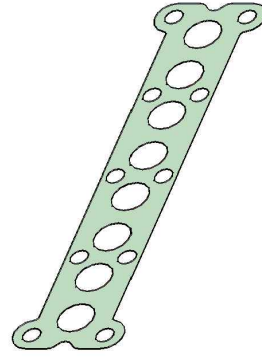
DRAWN BY: Katrina Leaprot
 DATE DRAWN: 04/08/14
 MATERIAL: Delrin
 PAGE: 2 of 2
 QUANTITY: 1

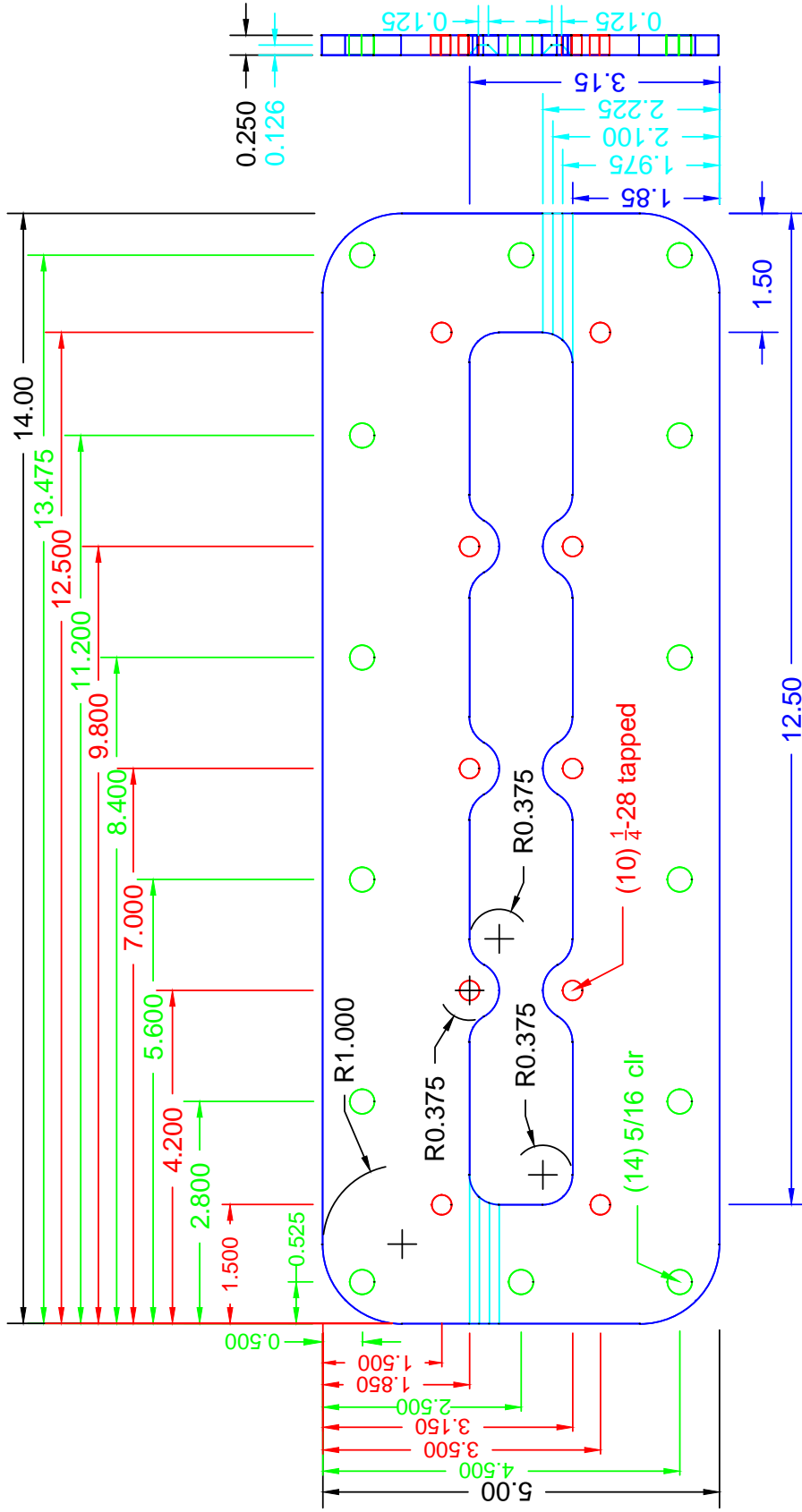


DRAWN BY: Katrina Leaptrot
DATE DRAWN: 12/05/2017
MATERIAL: Delrin
QUANTITY: 1
TITLE: Inner Chamber Exit Spacer

TOLERANCES:
 X.X ±0.040
 X.XX ±0.020
 X.XXX ±0.010

DRAWING SCALE: 0.5000
DIMENSIONS IN INCHES

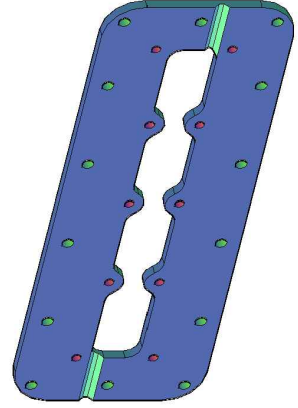


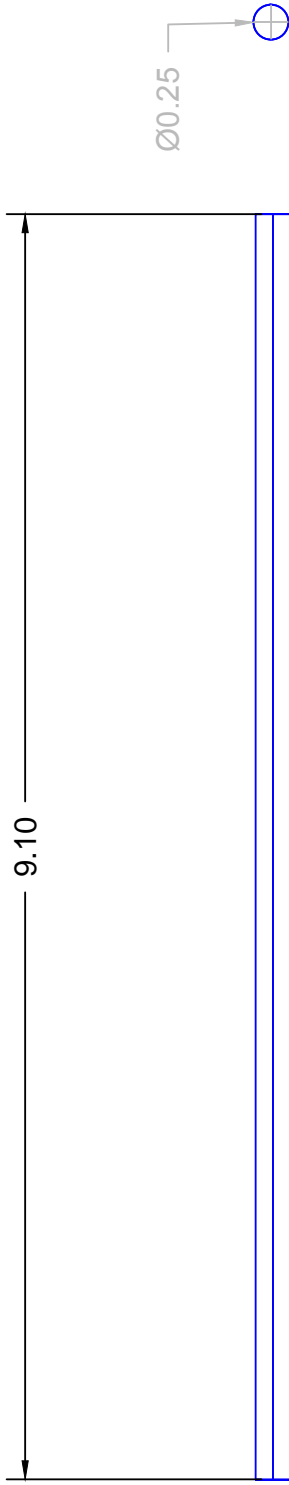


DRAWN BY: Katrina Leaptrot
DATE DRAWN: 01/09/15
MATERIAL: Aluminum
QUANTITY: 1
TITLE: Funnel 1 Mount Block (R2)

TOLERANCES:
 X.XX ±0.030
 X.XXX ±0.020
 Fractions ±1/32

DRAWING SCALE: 0.500
DIMENSIONS IN INCHES





DRAWN BY: Katrina Leaptrot

DATE DRAWN: 01/09/15

MATERIAL: 1/4-28 Stainless Steel Threaded Rod

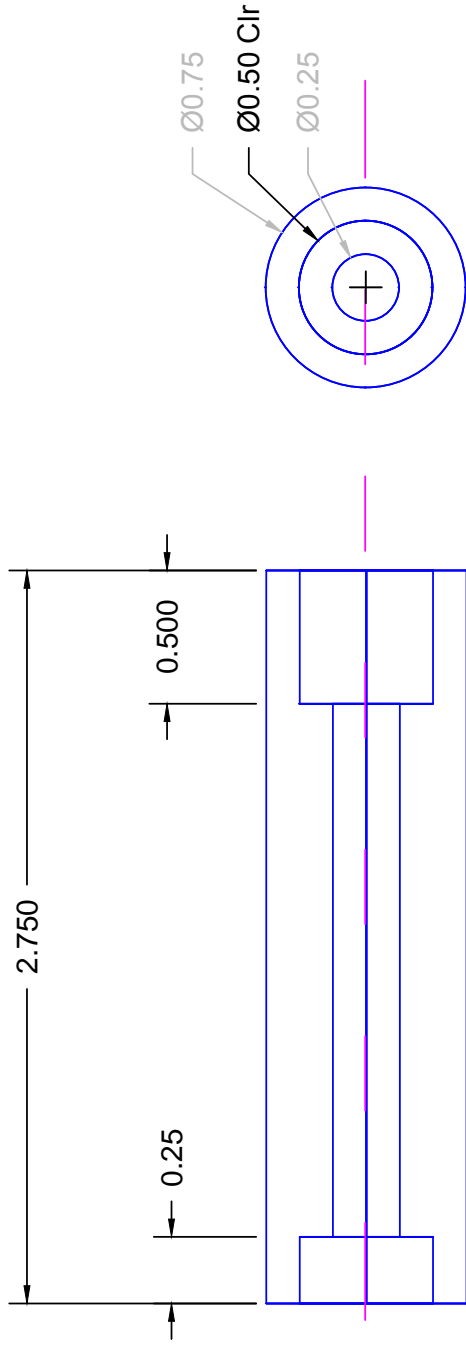
QUANTITY: 10

TITLE: Funnel Mount Rods (R2)

TOLERANCES:

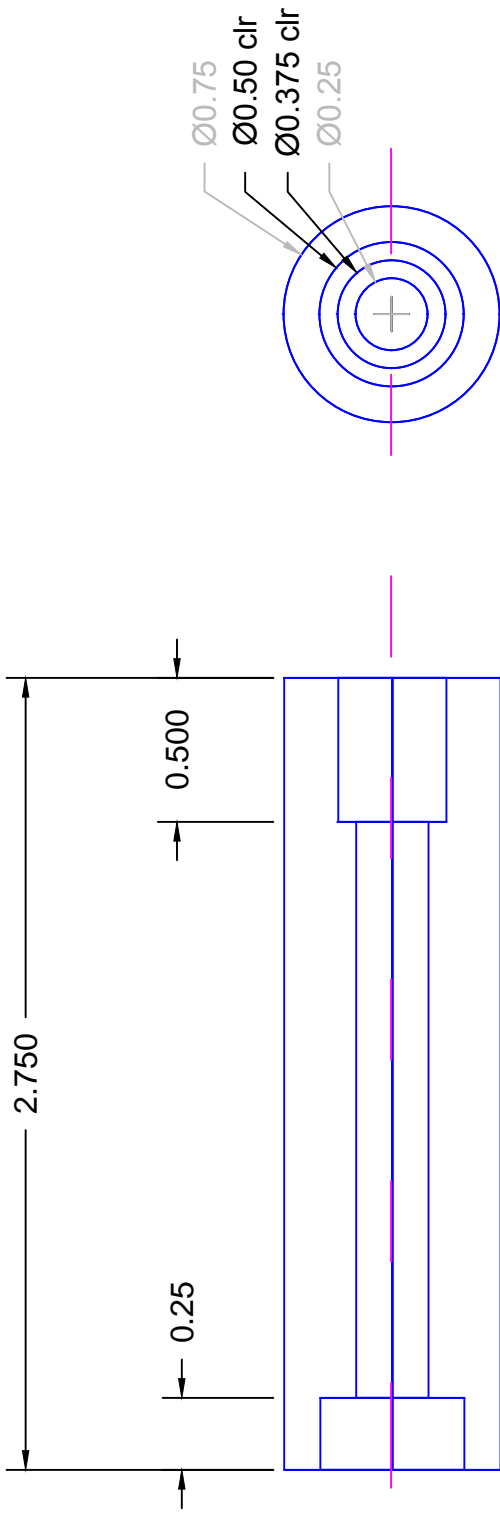
X.XX ±0.030

**DRAWING SCALE: 0.7500
DIMENSIONS IN INCHES**



DRAWN BY: Katrina Leaptrot
 DATE DRAWN: 01/09/15
 MATERIAL: Delrin Tube ($\frac{3}{4}$ OD, $\frac{1}{4}$ ID)
 QUANTITY: 4
 TITLE: Funnel 1 Delrin Standoff Type 1 (R2)

TOLERANCES:
 X.XX ±0.030
 X.XXX ±0.010
 Fractions ±1/32
 DRAWING SCALE: 1.500
 DIMENSIONS IN INCHES



DRAWN BY: Katrina Leaprot

DATE DRAWN: 01/09/15

MATERIAL: Delrin Tube ($\frac{3}{4}$ OD, $\frac{1}{4}$ ID)

QUANTITY: 6

TITLE: Funnel 1 Delrin Standoff Type 2 (R2)

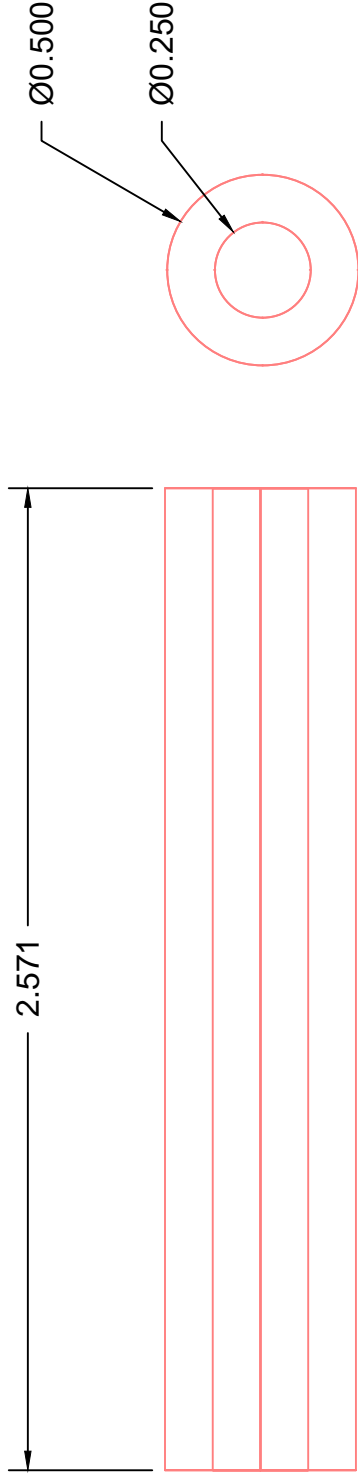
TOLERANCES:

X.XX ± 0.030

X.XXX ± 0.010

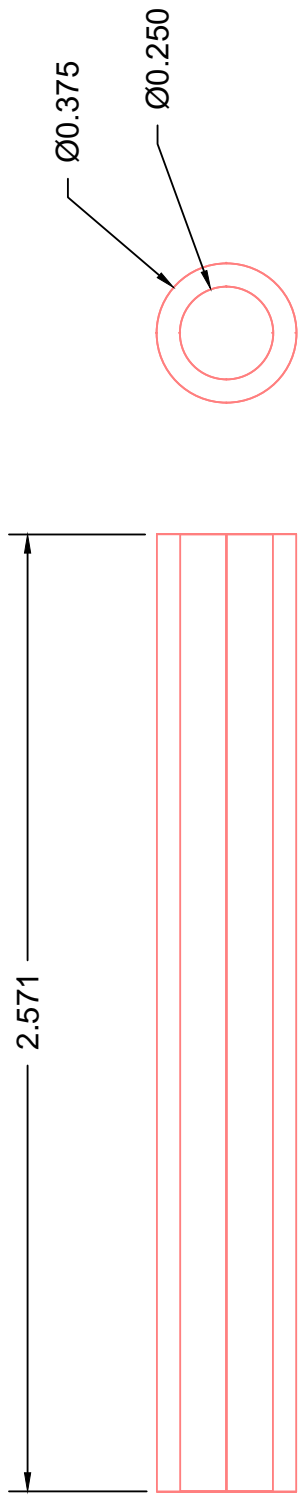
Fractions $\pm 1/32$

DRAWING SCALE: 1.500
DIMENSIONS IN INCHES



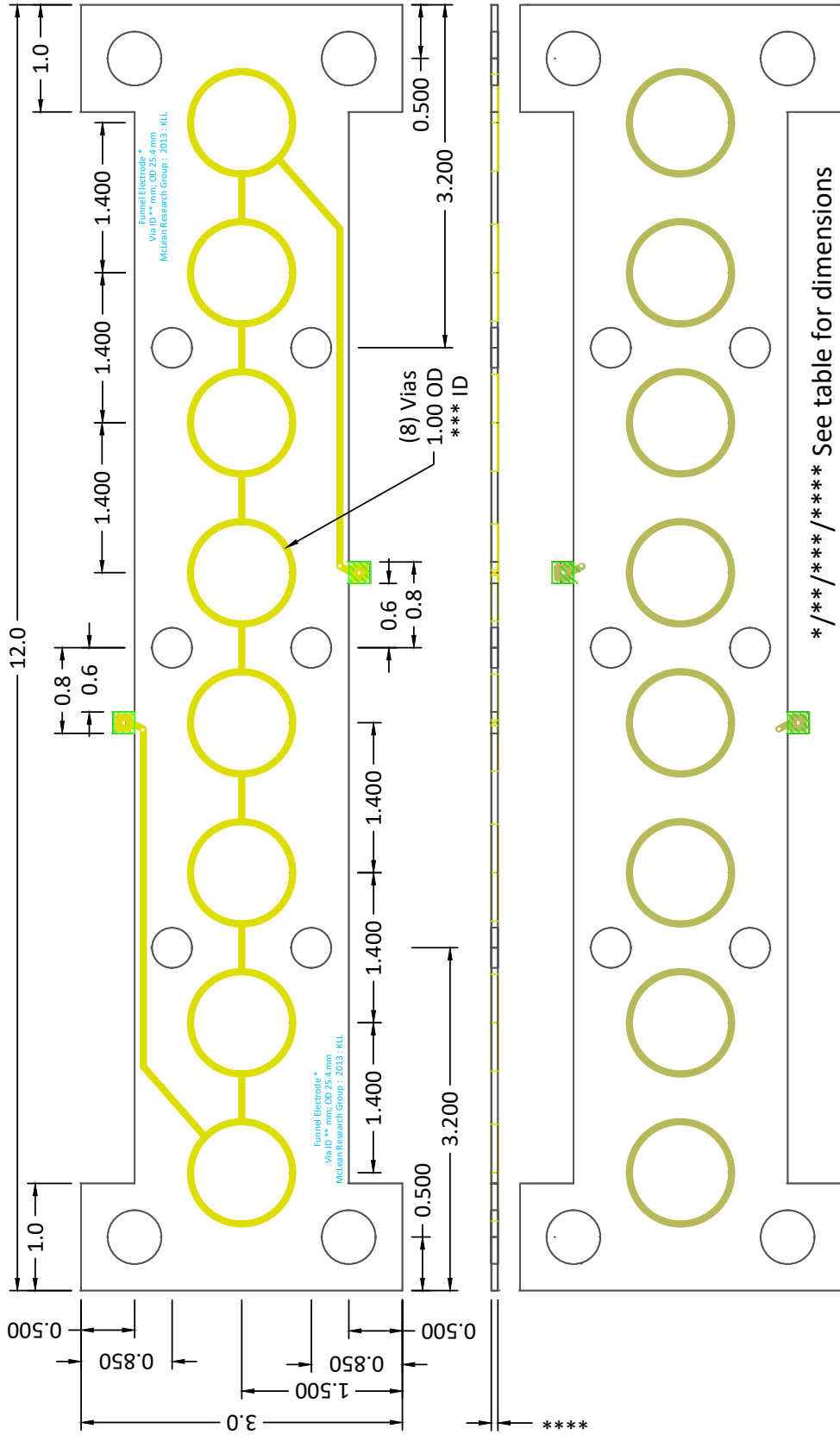
DRAWN BY: Katrina Leaptrot
DATE DRAWN: 11/30/2017
MATERIAL: >95% Alumina Ceramic
QUANTITY: 4
TITLE: Funnel 1 Ceramic Tubes Type 1

TOLERANCES:
X.XXX ±0.010
DRAWING SCALE: 2.0000
DIMENSIONS IN INCHES



DRAWN BY: Katrina Leaptrot
DATE DRAWN: 11/30/2017
MATERIAL: >95% Alumina Ceramic
QUANTITY: 6
TITLE: Funnel 1 Ceramic Tubes Type 2

TOLERANCES:
X.XXX ±0.010
DRAWING SCALE: 2.0000
DIMENSIONS IN INCHES



DRAWN BY: Katrina Leaprot

DATE DRAWN: 12/06/2017

MATERIAL: PCB

QUANTITY: 36

TITLE: Funnel Electrode Template

TOLERANCES:

X.X	±0.040
X.XX	±0.030
X.XXX	±0.020

KEY:

- EDGE CUTS
- FRONT COPPER
- FRONT SILKSCREEN
- FRONT SOLDER MASK
- BACK COPPER
- BACK SOLDER MASK

DRAWING SCALE: 0.7000

DIMENSIONS IN INCHES

NONESSENTIALS OMITTED, FOR SIMPLICITY

*/**/**/**** See table for dimensions

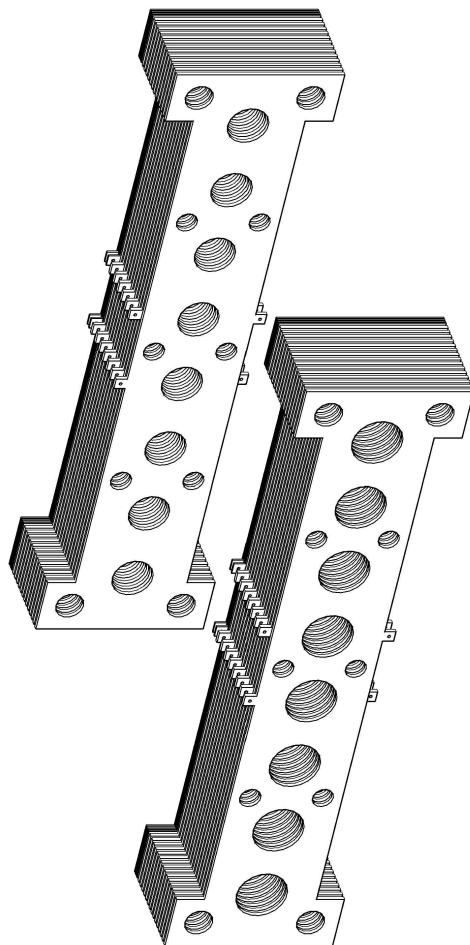
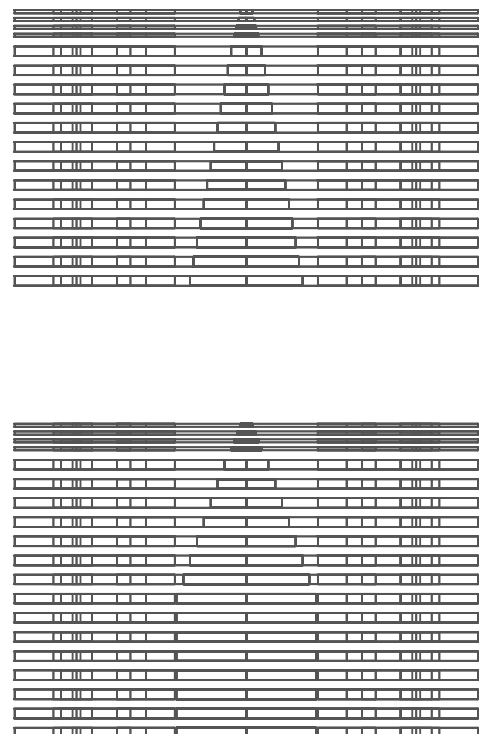
Funnel 1

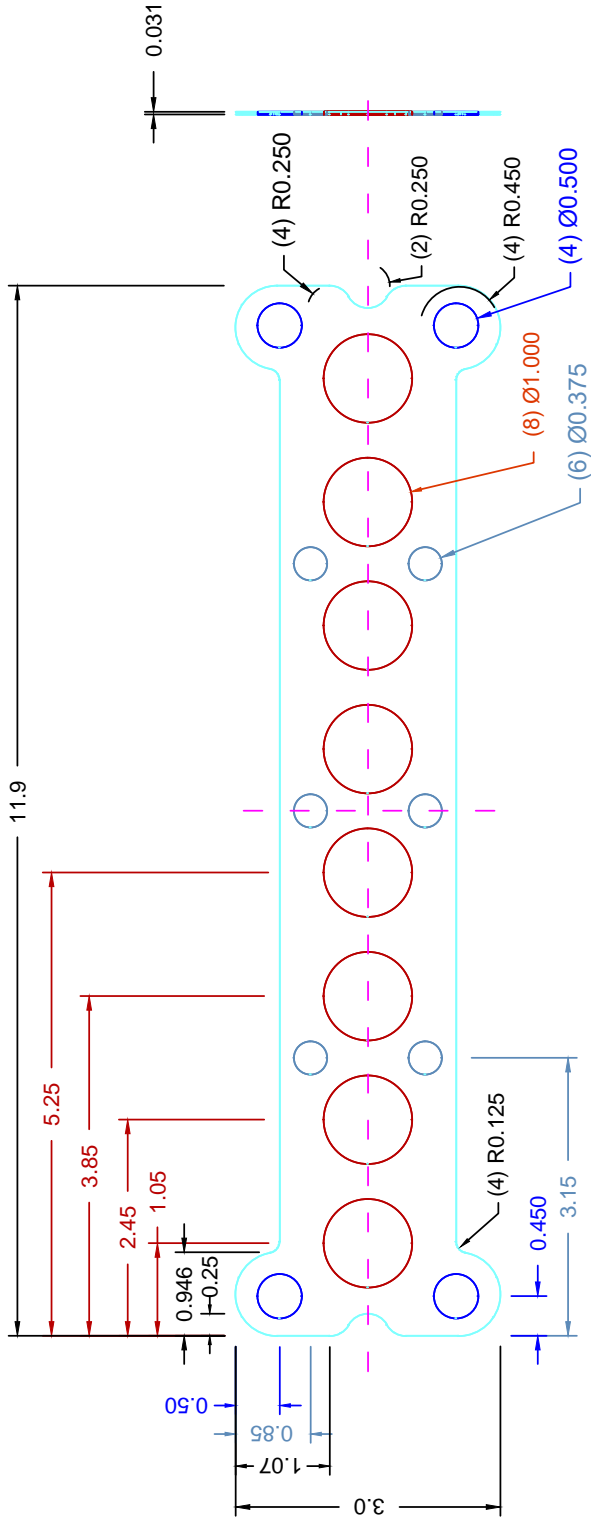
Electrode Number, *	Via ID, ** (mm)	Via ID, *** (in)	PCB Thickness, **** (in)
1	23	0.9055	0.0625
2	23	0.9055	0.0625
3	23	0.9055	0.0625
4	23	0.9055	0.0625
5	23	0.9055	0.0625
6	23	0.9055	0.0625
7	23	0.9055	0.0625
8	23	0.9055	0.0625
9	20.75	0.8169	0.0625
10	18.5	0.7283	0.0625
11	16.25	0.6398	0.0625
12	14	0.5512	0.0625
13	11.75	0.4626	0.0625
14	9.5	0.3740	0.0625
15	7.25	0.2854	0.0625
16	5	0.1969	0.02
17	4	0.1575	0.02
18	3	0.1181	0.02
19	2	0.0787	0.02

Funnel 2

Electrode Number, *	Via ID, ** (mm)	Via ID, *** (in)	PCB Thickness, **** (in)
20	18.5	0.7283	0.0625
21	17.375	0.6841	0.0625
22	16.25	0.6398	0.0625
23	15.125	0.5955	0.0625
24	14	0.5512	0.0625
25	12.875	0.5069	0.0625
26	11.75	0.4626	0.0625
27	10.625	0.4183	0.0625
28	9.5	0.3740	0.0625
29	8.375	0.3297	0.0625
30	7.25	0.2854	0.0625
31	6.125	0.2411	0.0625
32	5	0.1969	0.0625
33	3.875	0.1526	0.02
34	3.25	0.1280	0.02
35	2.625	0.1033	0.02
36	2	0.0787	0.02

*/**/***/**** Varying dimensions for Funnel Electrode Template.

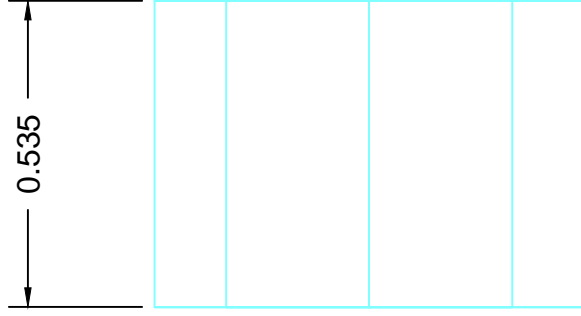
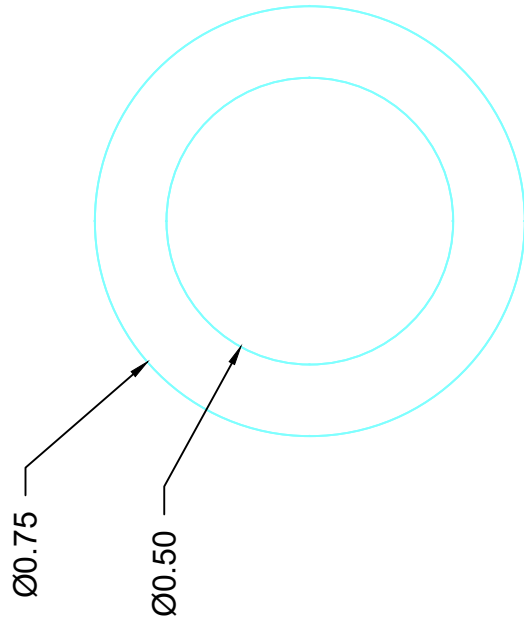




DRAWN BY: Katrina Leaprot
 DATE DRAWN: 12/05/2017
 MATERIAL: Delrin
 QUANTITY: 1
 TITLE: Funnel Spacer

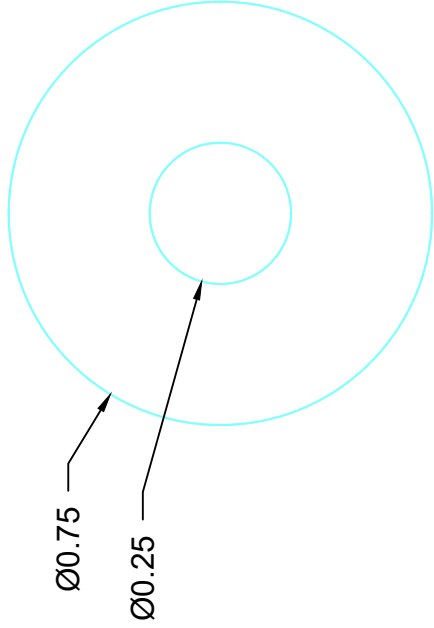
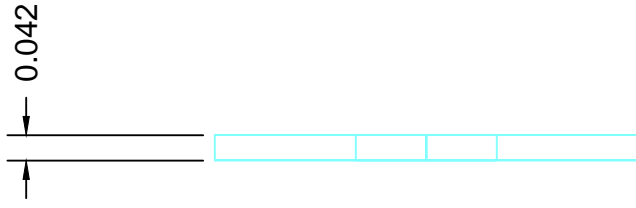
TOLERANCES:
 X.X ±0.040
 X.XX ±0.020
 X.XXX ±0.010

DRAWING SCALE: 0.5000
 DIMENSIONS IN INCHES



DRAWN BY: Katrina Leaptrot
DATE DRAWN: 12/05/2017
MATERIAL: Delrin
QUANTITY: 20
TITLE: Funnel 2 Standoff

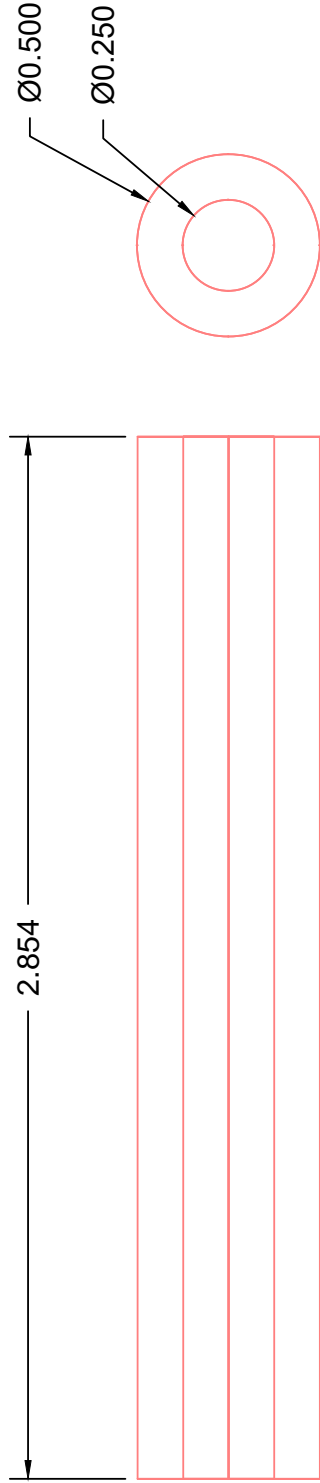
TOLERANCES:
 X.XX ±0.030
 X.XXX ±0.010
DRAWING SCALE: 3.0000
DIMENSIONS IN INCHES



TOLERANCES:
 X.XX ±0.030
 X.XXX ±0.010

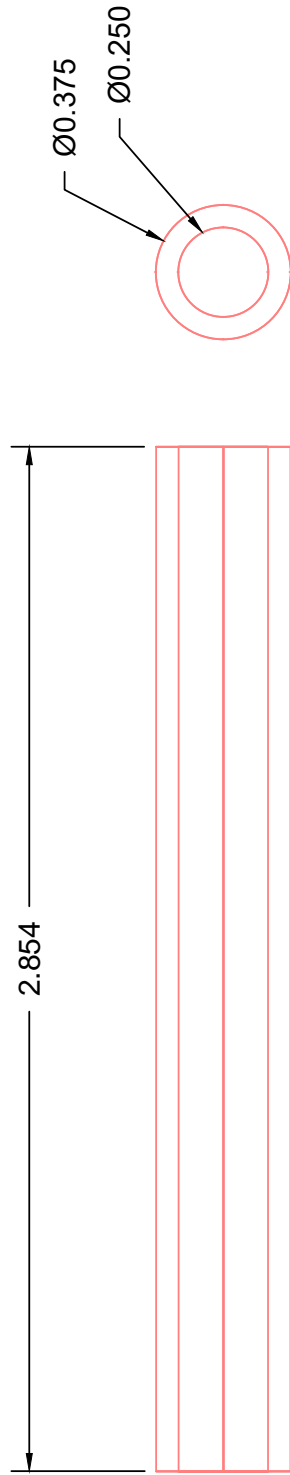
DRAWING SCALE: 3.0000
 DIMENSIONS IN INCHES

DRAWN BY: Katrina Leaprot
DATE DRAWN: 12/05/2017
MATERIAL: Delrin
QUANTITY: 10
TITLE: Funnel 2 Finishing Washer for Standoffs



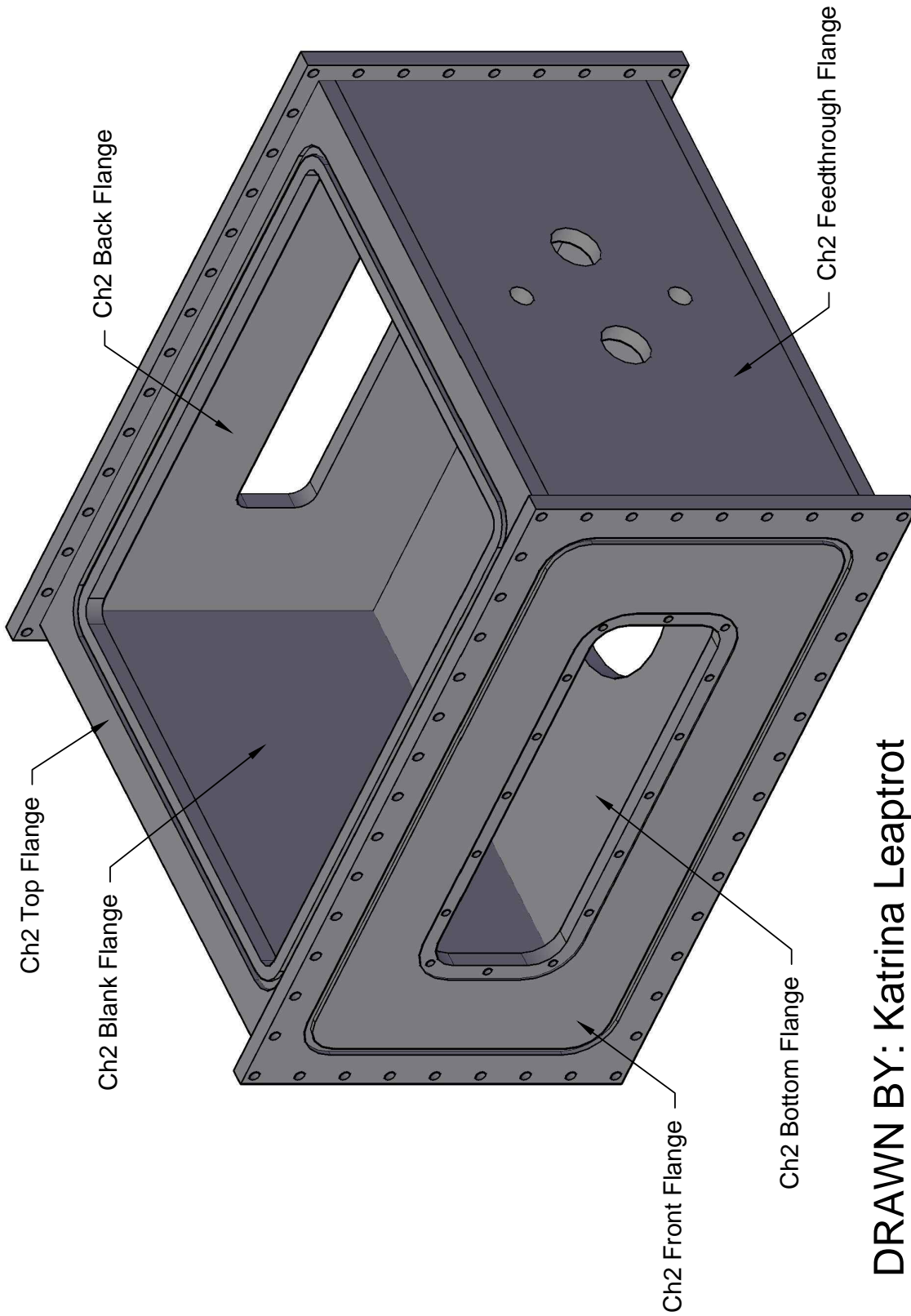
DRAWN BY: Katrina Leaprot
DATE DRAWN: 11/30/2017
MATERIAL: >95% Alumina Ceramic
QUANTITY: 4
TITLE: Funnel 2 Ceramic Tubes Type 1

TOLERANCES:
X.XXX ±0.010
DRAWING SCALE: 2.0000
DIMENSIONS IN INCHES



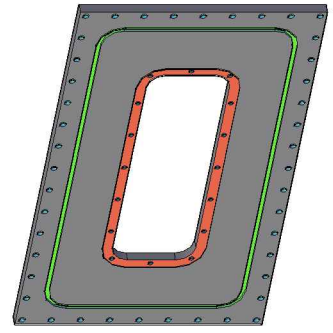
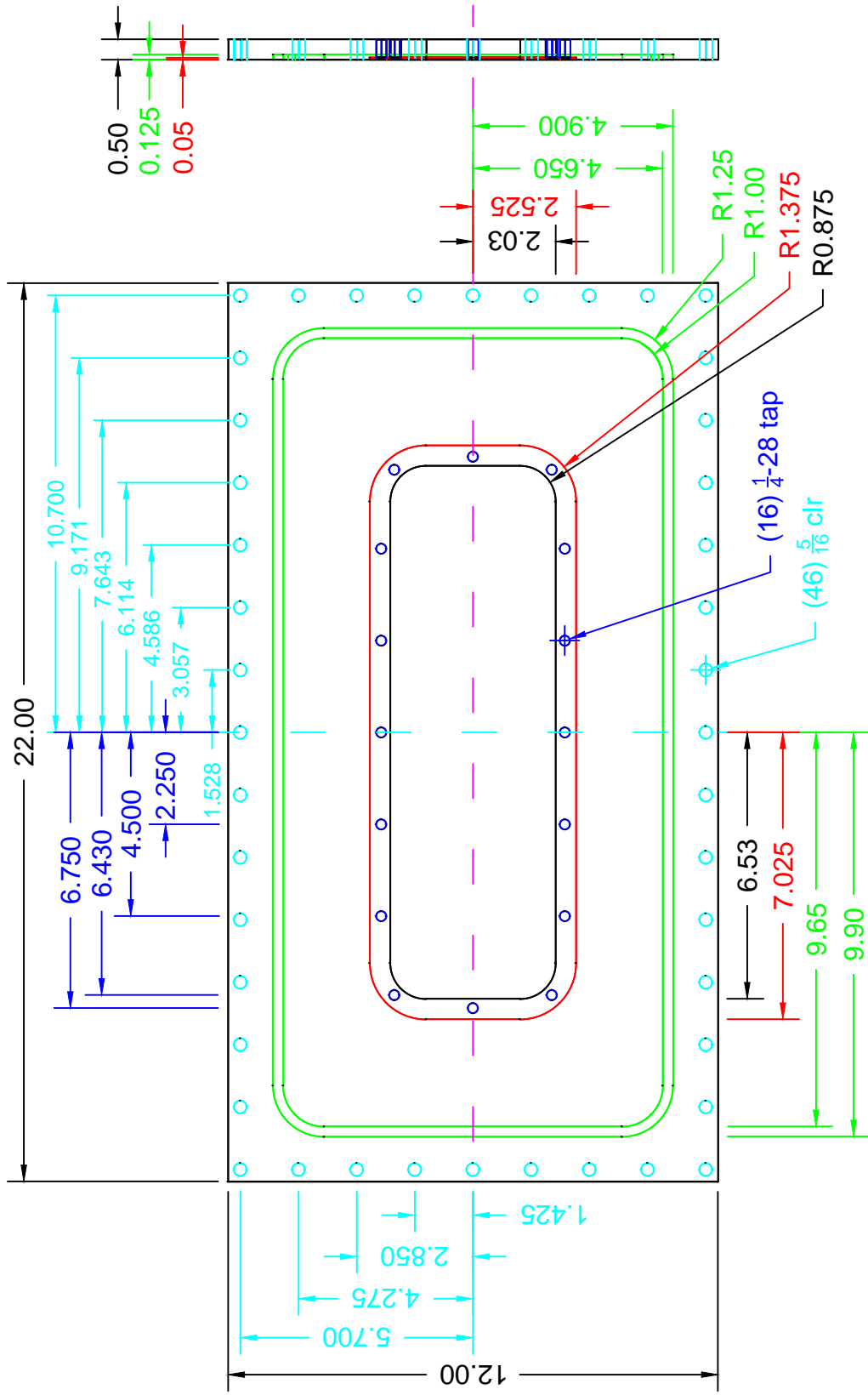
DRAWN BY: Katrina Leaptrot
DATE DRAWN: 11/30/2017
MATERIAL: >95% Alumina Ceramic
QUANTITY: 6
TITLE: Funnel 2 Ceramic Tubes Type 2

TOLERANCES:
X.XXX ±0.010
DRAWING SCALE: 2.0000
DIMENSIONS IN INCHES



DRAWING SCALE: 0.2500

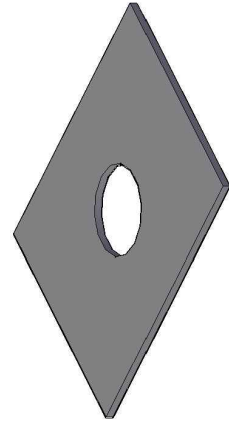
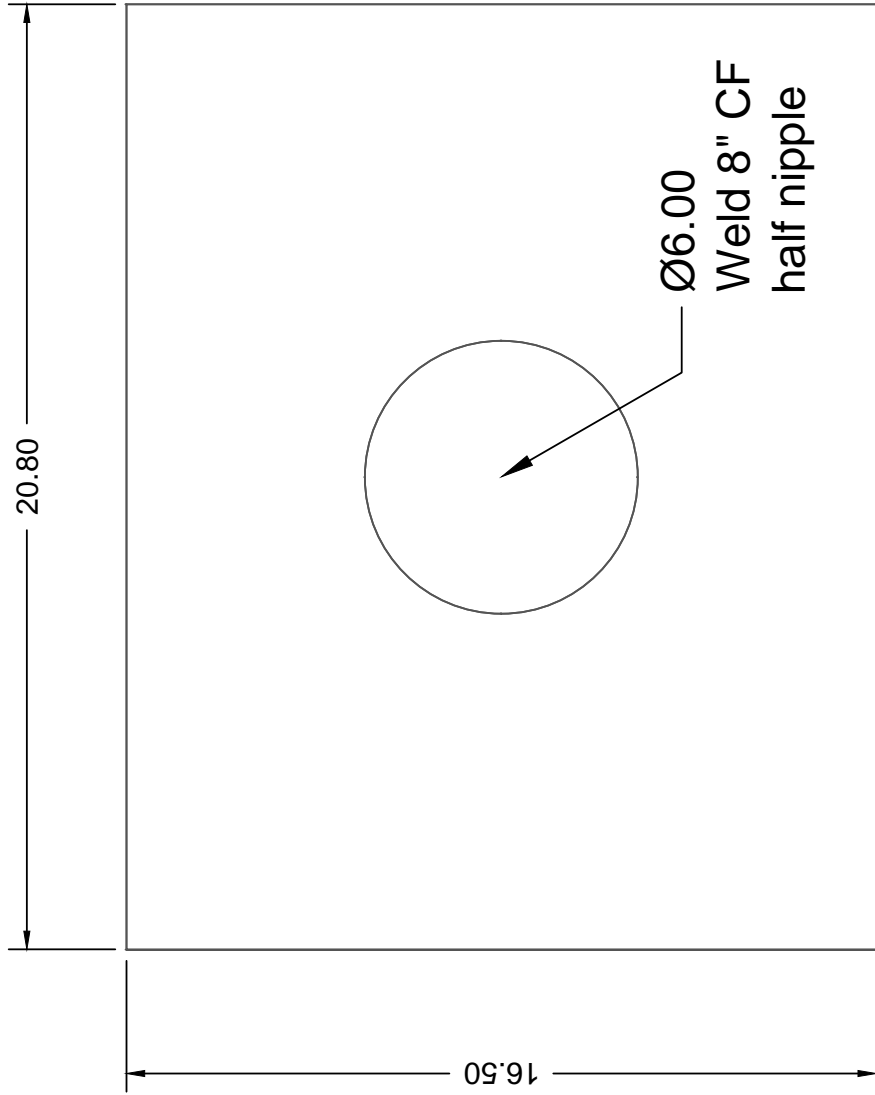
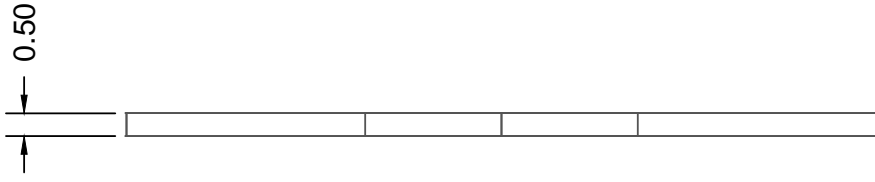
DRAWN BY: Katrina Leaptrot
DATE DRAWN: 11/27/2017
MATERIAL: Weld Existing
TITLE: Chamber 2 Assembly



TOLERANCES:
 X.XX ±0.020
 X.XXX ±0.010
 Fractions ±1/32

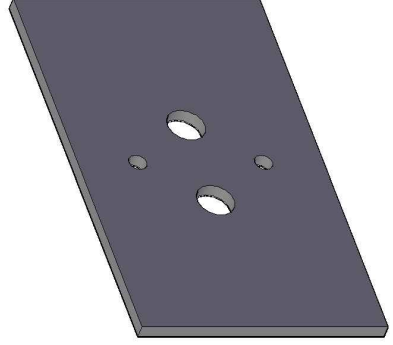
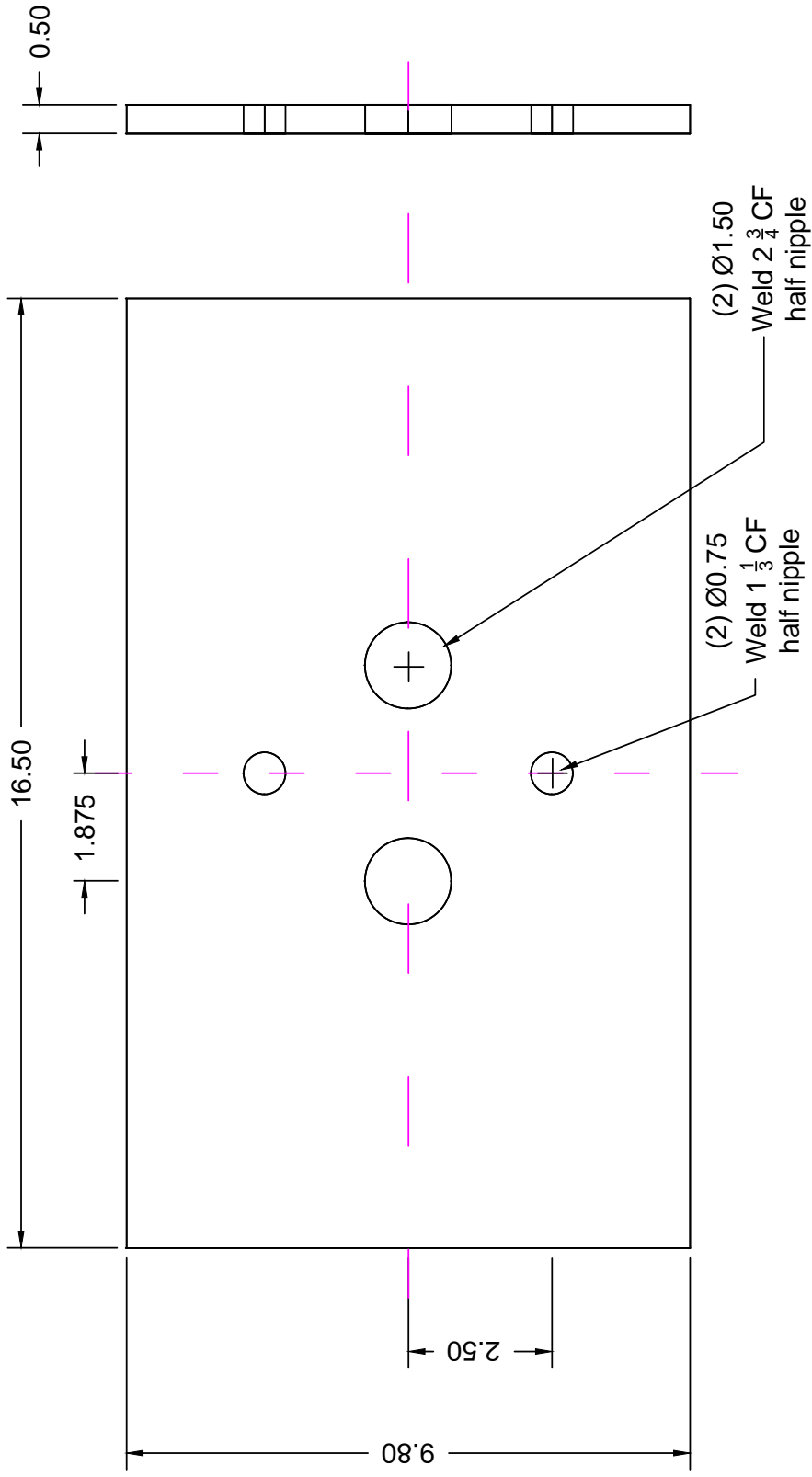
DRAWING SCALE: 0.2500
 DIMENSIONS IN INCHES

DRAWN BY: Katrina Leaprot
 DATE DRAWN: 11/21/2017
 MATERIAL: Stainless Steel
 QUANTITY: 1
 TITLE: Chamber 2 Front Flange



TOLERANCES:
X.XX ±0.020
DRAWING SCALE: 0.2500
DIMENSIONS IN INCHES

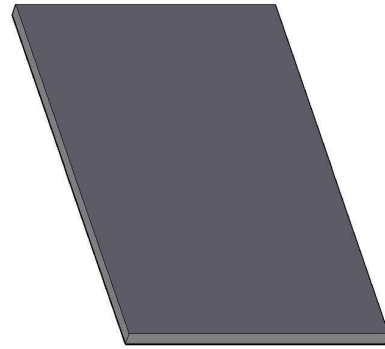
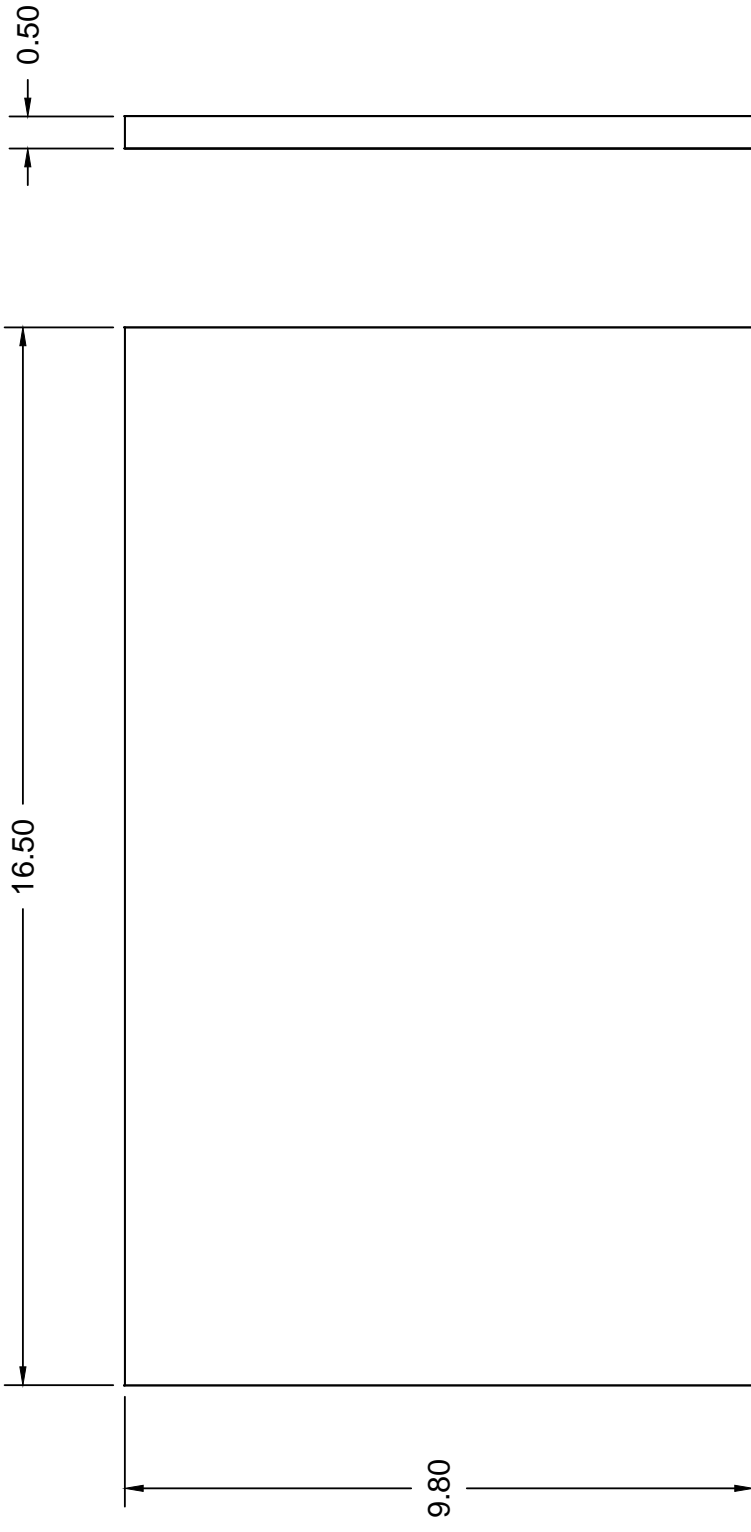
DRAWN BY: Katrina Leaptrot
DATE DRAWN: 11/21/2017
MATERIAL: Stainless Steel
QUANTITY: 1
TITLE: Chamber 2 Bottom Flange



TOLERANCES:
 X.XX ±0.020
 X.XXX ±0.020

DRAWING SCALE: 0.3500
 DIMENSIONS IN INCHES

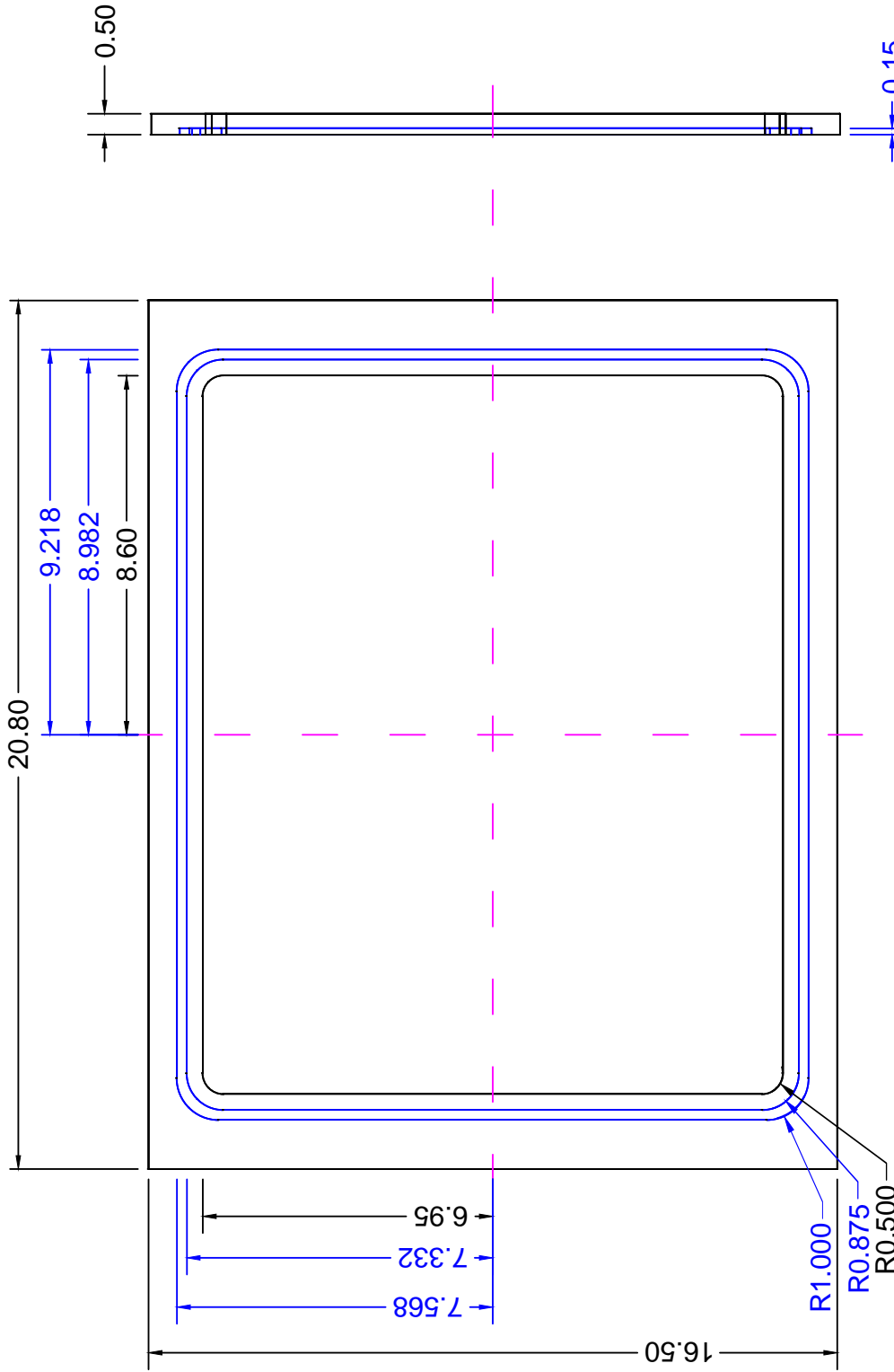
DRAWN BY: Katrina Leaptrot
DATE DRAWN: 11/21/2017
MATERIAL: Stainless Steel
QUANTITY: 1
TITLE: Chamber 2 Feedthrough Flange



TOLERANCES:
X.XX ±0.020

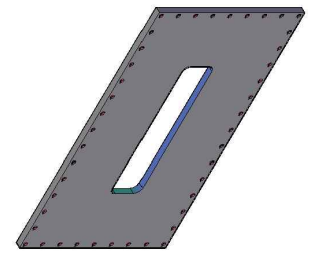
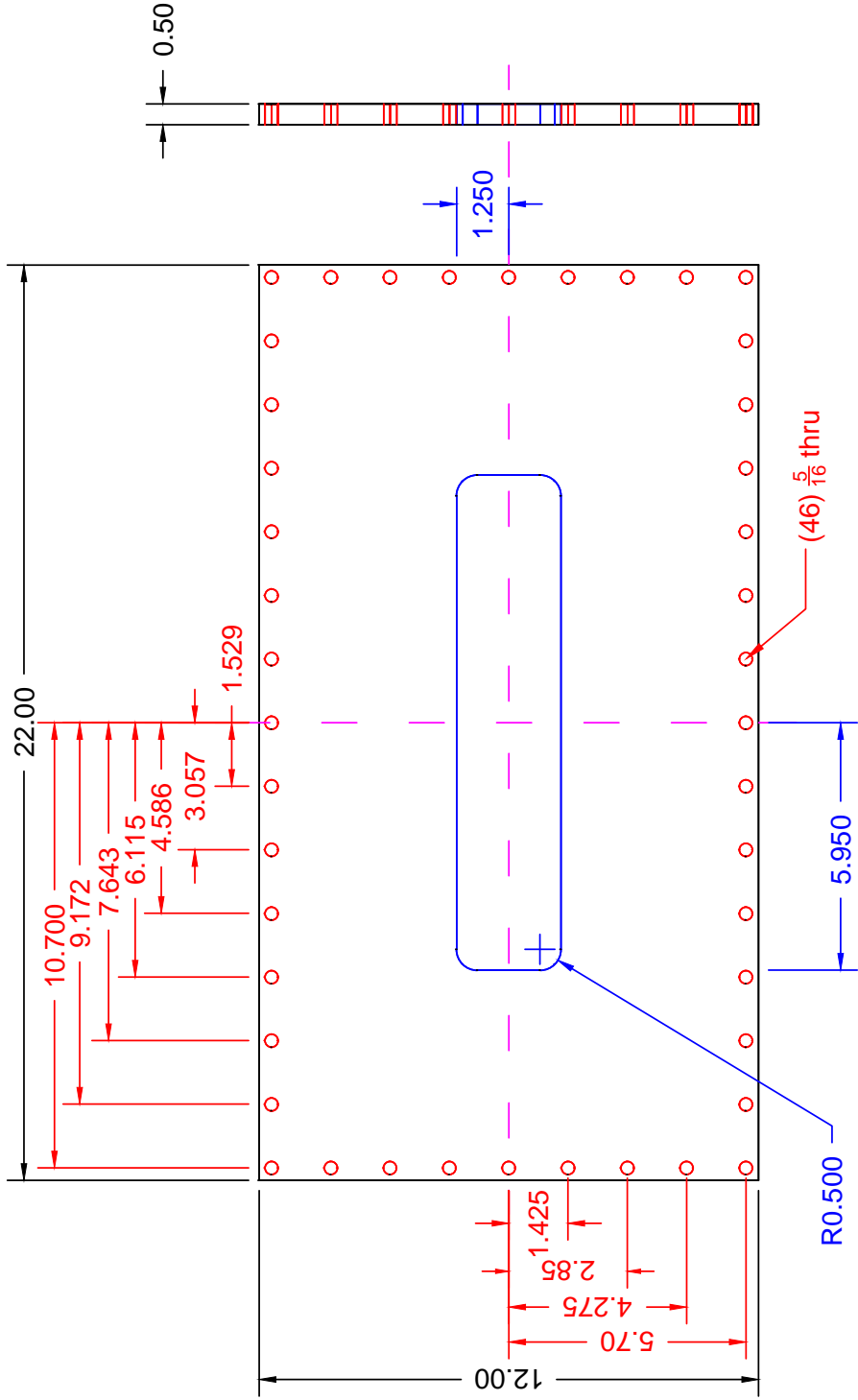
DRAWING SCALE: 0.3500
DIMENSIONS IN INCHES

DRAWN BY: Katrina Leaptrot
DATE DRAWN: 11/21/2017
MATERIAL: Stainless Steel
QUANTITY: 1
TITLE: Chamber 2 Blank Flange



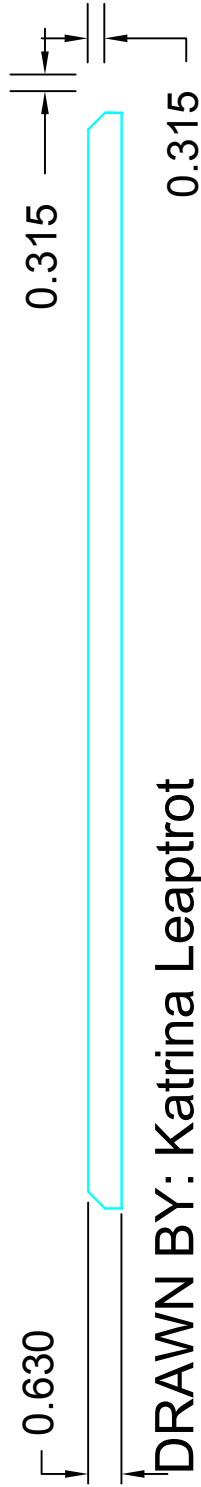
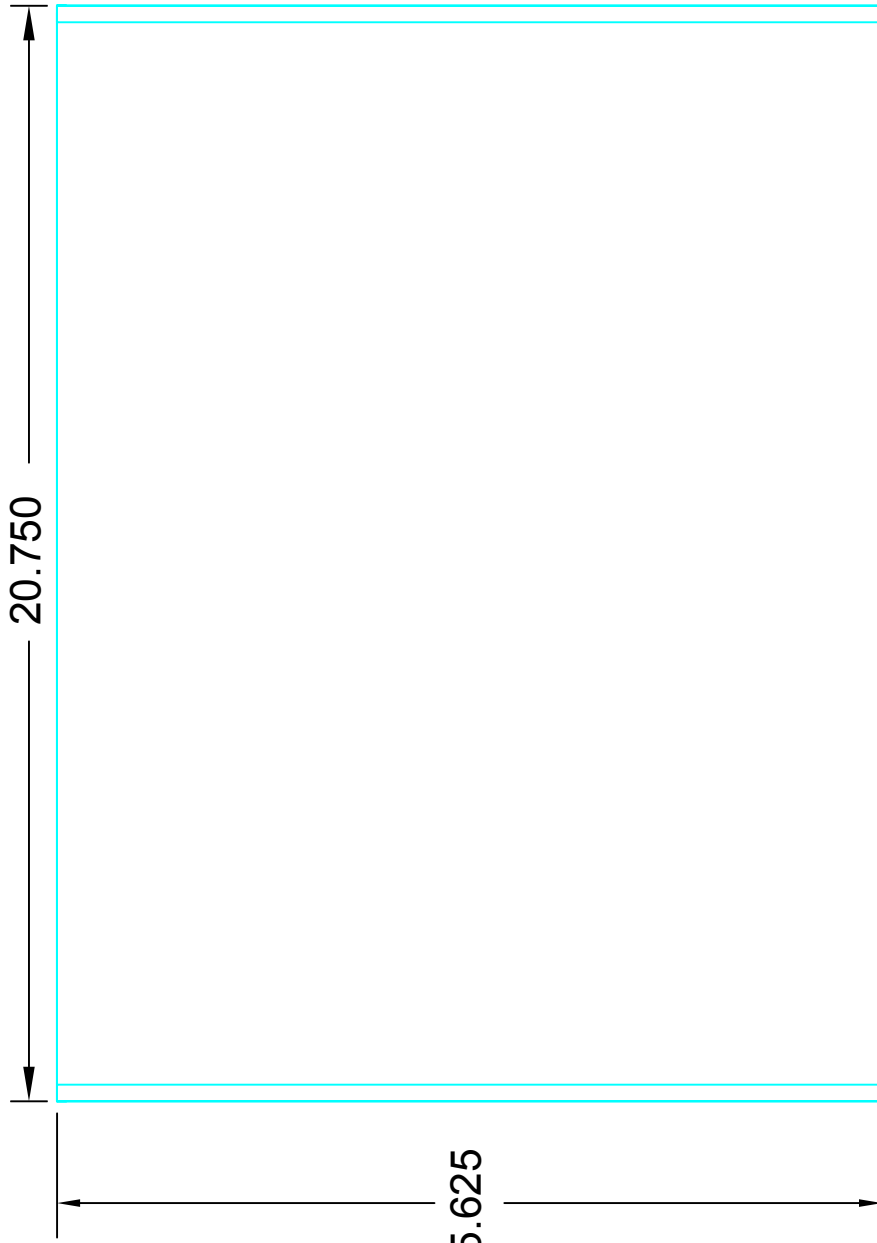
TOLERANCES:
 X.XX ±0.020
 X.XXX ±0.010
 DRAWING SCALE: 0.2500
 DIMENSIONS IN INCHES

DRAWN BY: Katrina Leaptrot
DATE DRAWN: 11/27/2017
MATERIAL: Stainless Steel
QUANTITY: 1
TITLE: Chamber 2 Top Flange



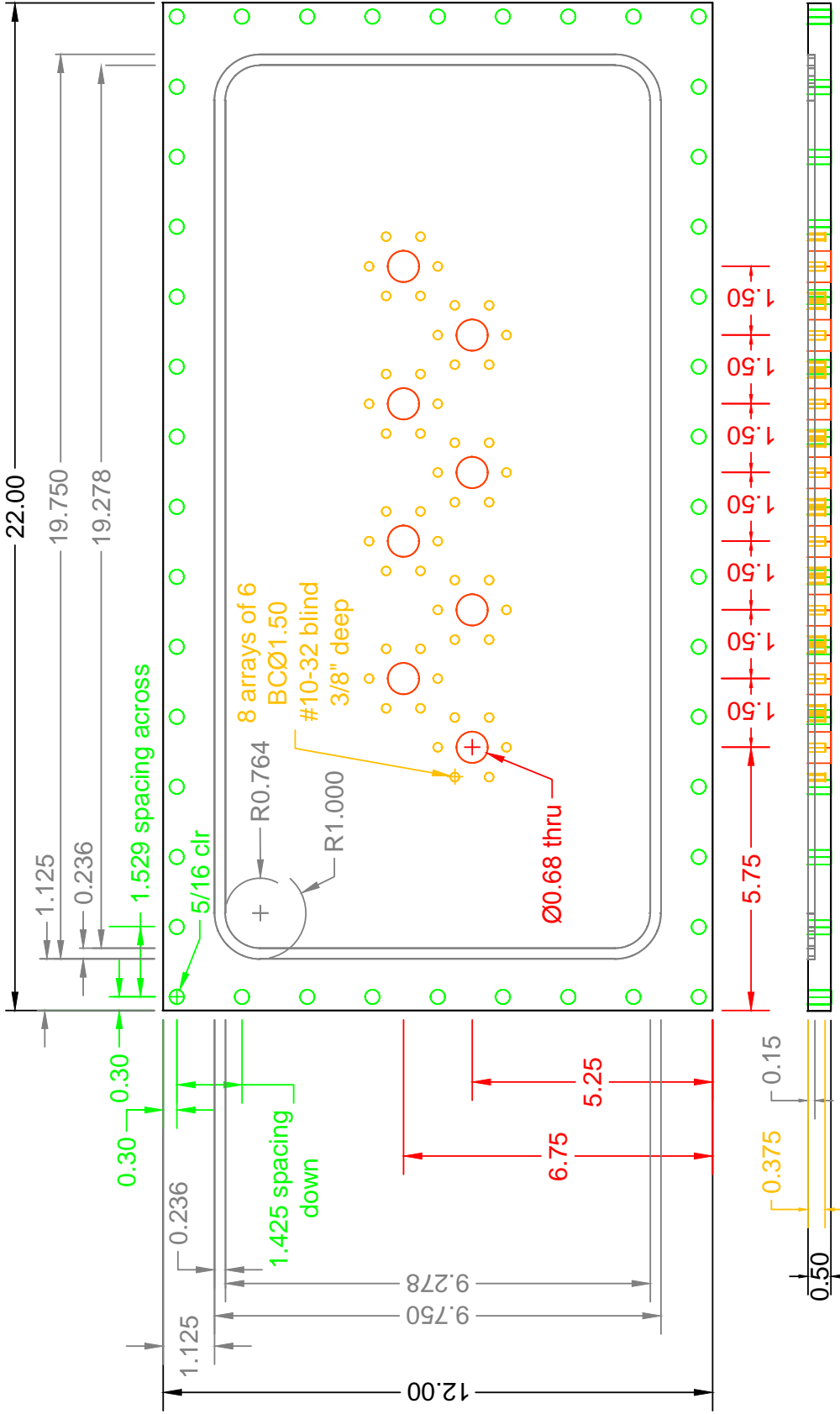
TOLERANCES:
 X.XX ±0.020
 X.XXX ±0.010
 Fractions ±1/32
 DRAWING SCALE: 0.2500
 DIMENSIONS IN INCHES

DRAWN BY: Katrina Leaprot
 DATE DRAWN: 11/27/2017
 MATERIAL: Stainless Steel
 QUANTITY: 1
 TITLE: Chamber 2 Back Flange

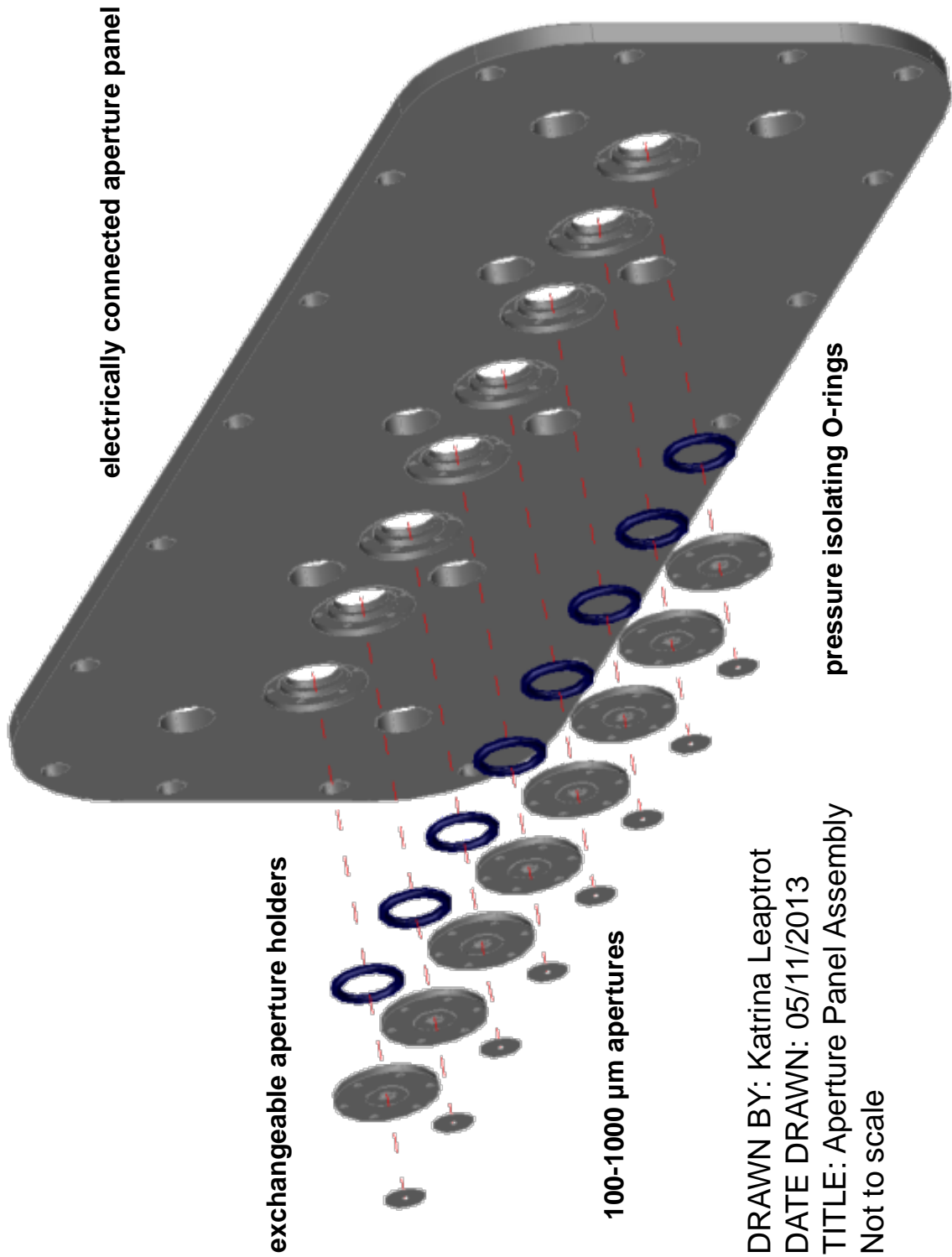


DRAWN BY: Katrina Leaprot
DATE DRAWN: 03/28/12
MATERIAL: 16mm thick Borofloat
QUANTITY: 1
TITLE: Chamber 2 Glass Top

DRAWING SCALE: 0.2750
DIMENSIONS IN INCHES



DRAWN BY: Katrina Leaptrot
DATE DRAWN: 05/01/14
MATERIAL: Aluminum
QUANTITY: 1
TITLE: Faraday Feedthrough Flange (R1)



electrically connected aperture panel

exchangeable aperture holders

100-1000 μm apertures

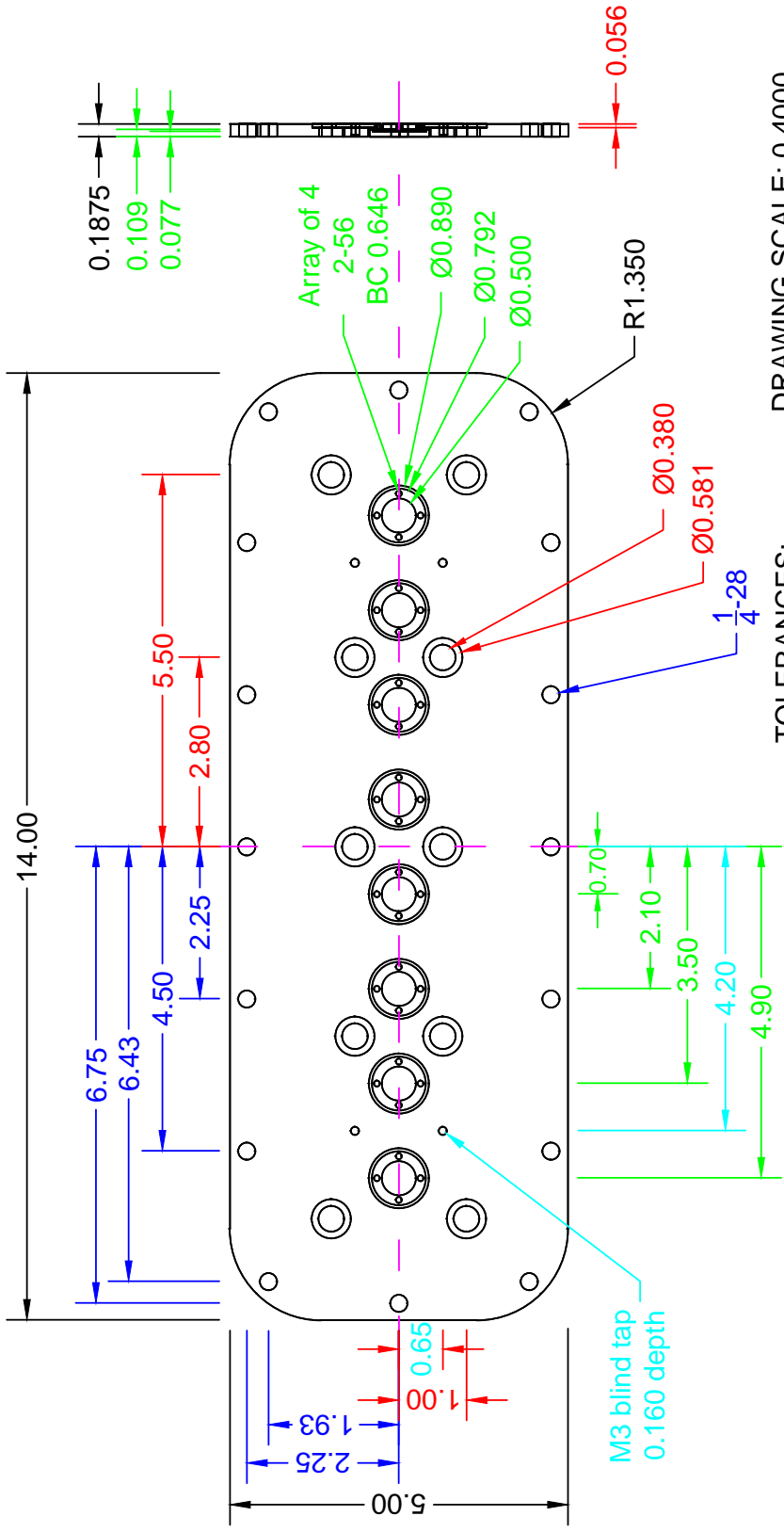
pressure isolating O-rings

DRAWN BY: Katrina Leaptrot

DATE DRAWN: 05/11/2013

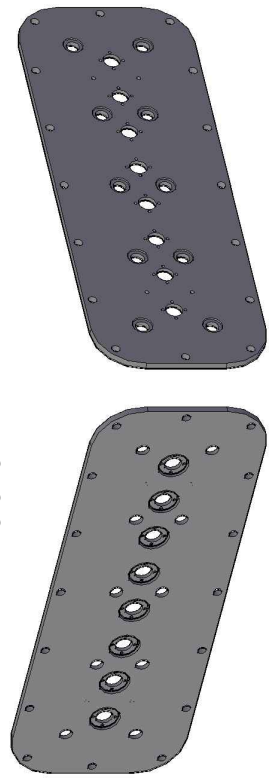
TITLE: Aperture Panel Assembly

Not to scale

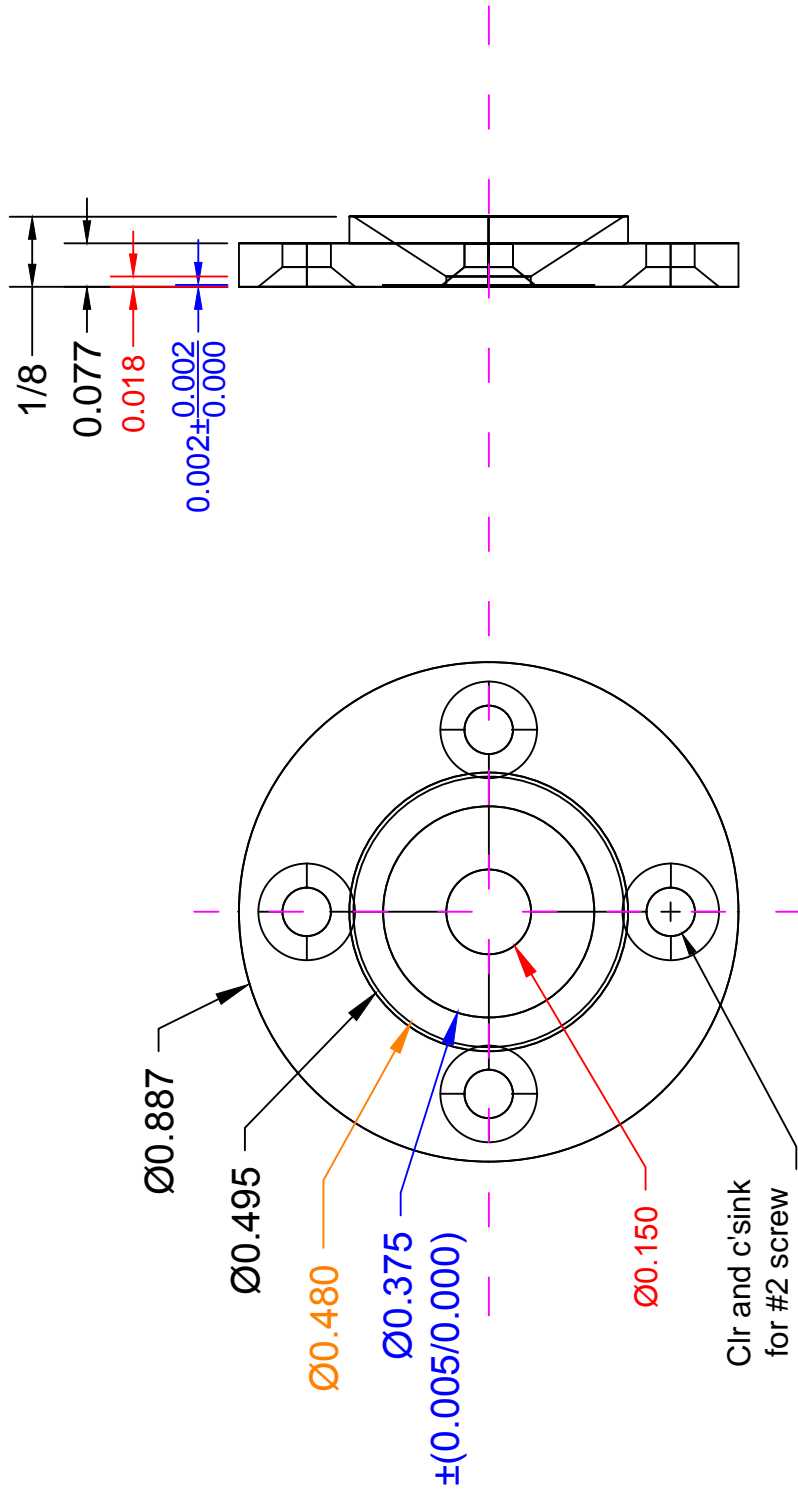


DRAWING SCALE: 0.4000
DIMENSIONS IN INCHES

TOLERANCES:
X.XX ±0.030
X.XXX ±0.015
X.XXXX ±0.010



DRAWN BY: Katrina Leaptrot
DATE DRAWN: 03/28/13
MATERIAL: Stainless Steel
QUANTITY: 1
TITLE: Aperture Panel (r2)



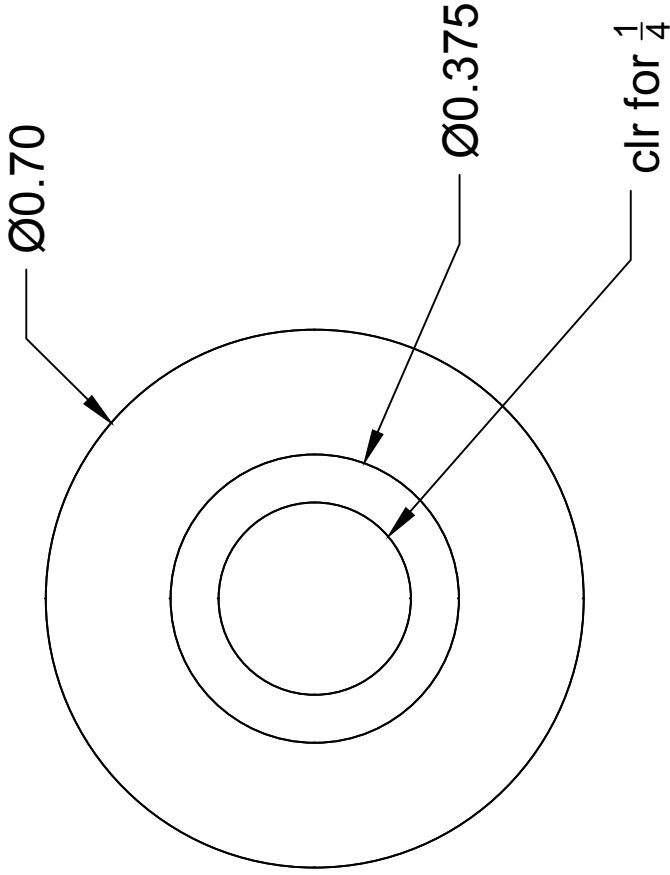
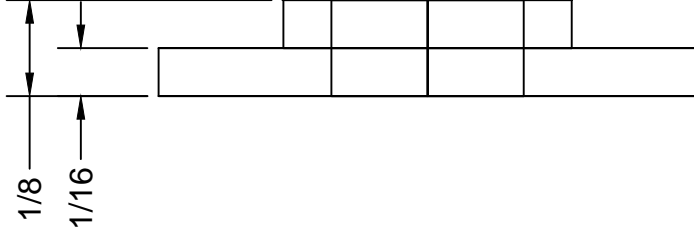
TOLERANCES:

X.XXX ±0.010

Fractions ±1/32

DRAWING SCALE: 3.000
DIMENSIONS IN INCHES

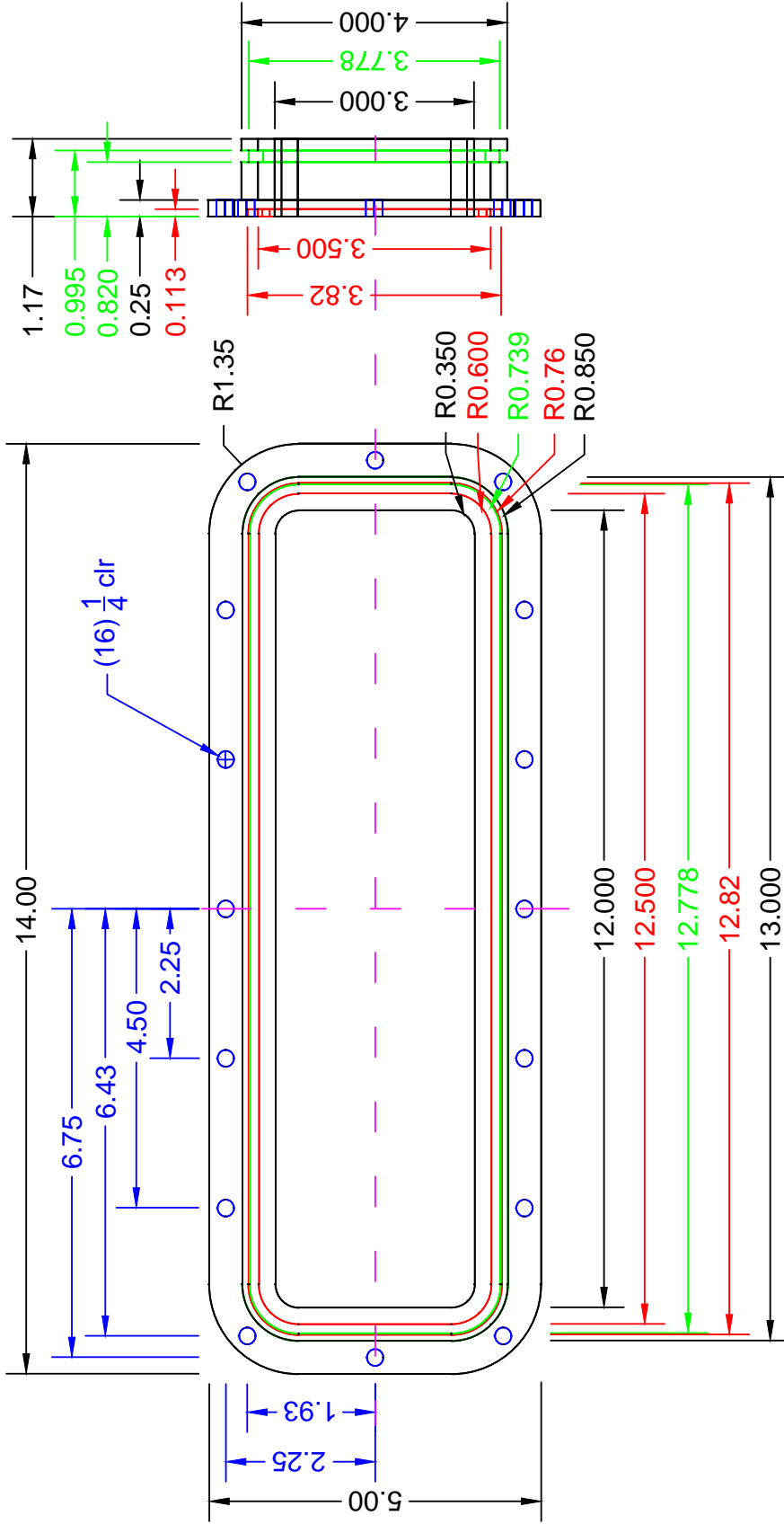
DRAWN BY: Katrina Leaptrot
DATE DRAWN: 03/28/13
MATERIAL: Stainless Steel
QUANTITY: 8
TITLE: Aperture Holder (r2)



TOLERANCES:
 X.XX ±0.020
 X.XXX ±0.010
 FRACTIONS ± $\frac{1}{32}$

DRAWING SCALE: 4.000
 DIMENSIONS IN INCHES

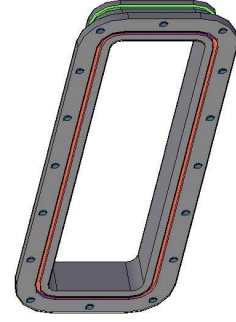
DRAWN BY: Katrina Leaprot
 DATE DRAWN: 03/28/13
 MATERIAL: Delrin
 QUANTITY: 10
 TITLE: Insulating Washers (r2)

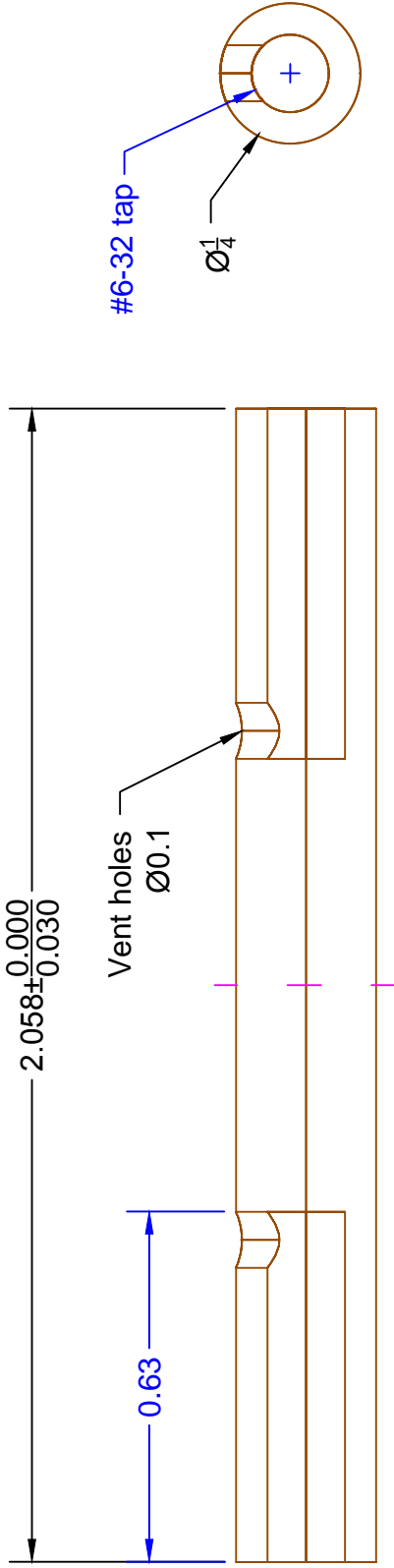


TOLERANCES:
 X.XX ±0.030
 X.XXX ±0.015
 FRACTIONS $\pm\frac{1}{32}$

DRAWING SCALE: 0.4000
 DIMENSIONS IN INCHES

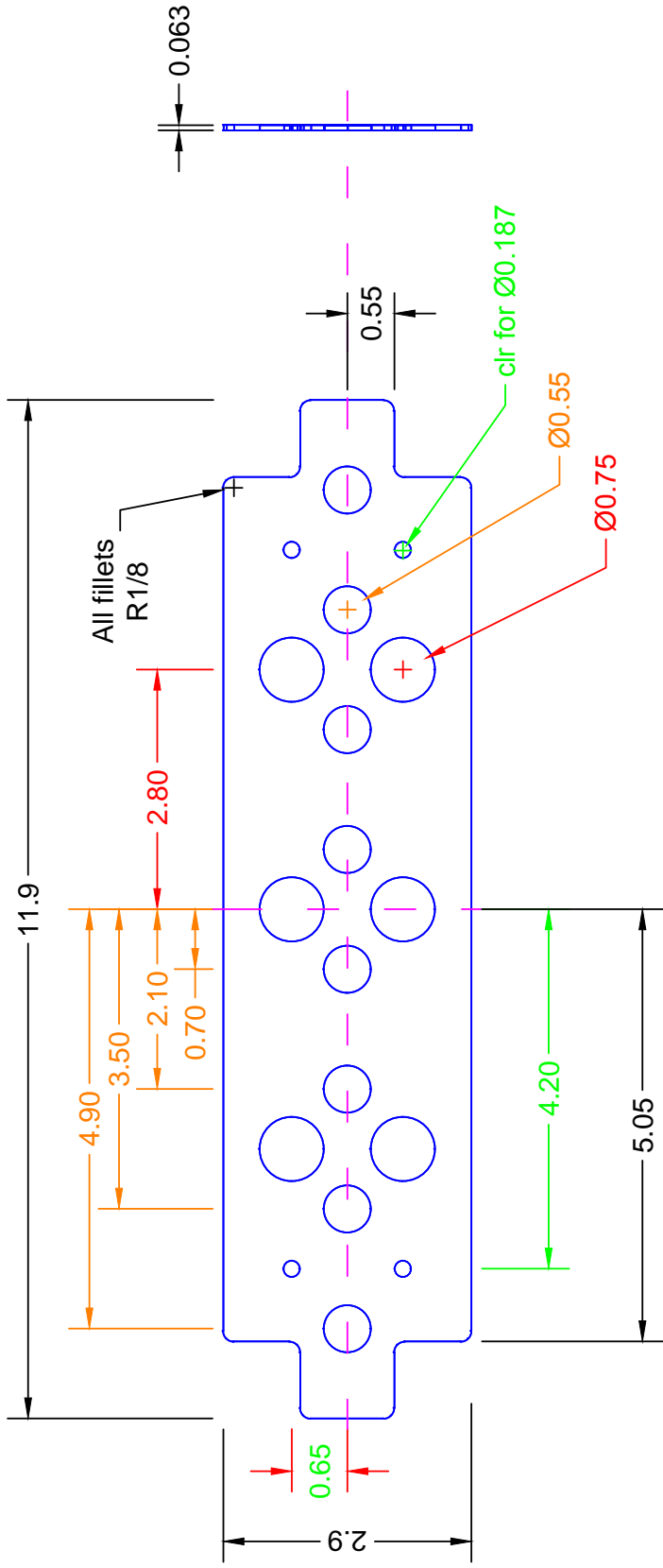
DRAWN BY: Katrina Leaptrot
 DATE DRAWN: 07/10/14
 MATERIAL: Delrin
 QUANTITY: 1
 TITLE: Aperture Panel Piston Seal (r3)





DRAWN BY: Katrina Leaprot
 DATE DRAWN: 03/28/13
 MATERIAL: PEEK
 QUANTITY: 5
 TITLE: PEEK Column (r2)

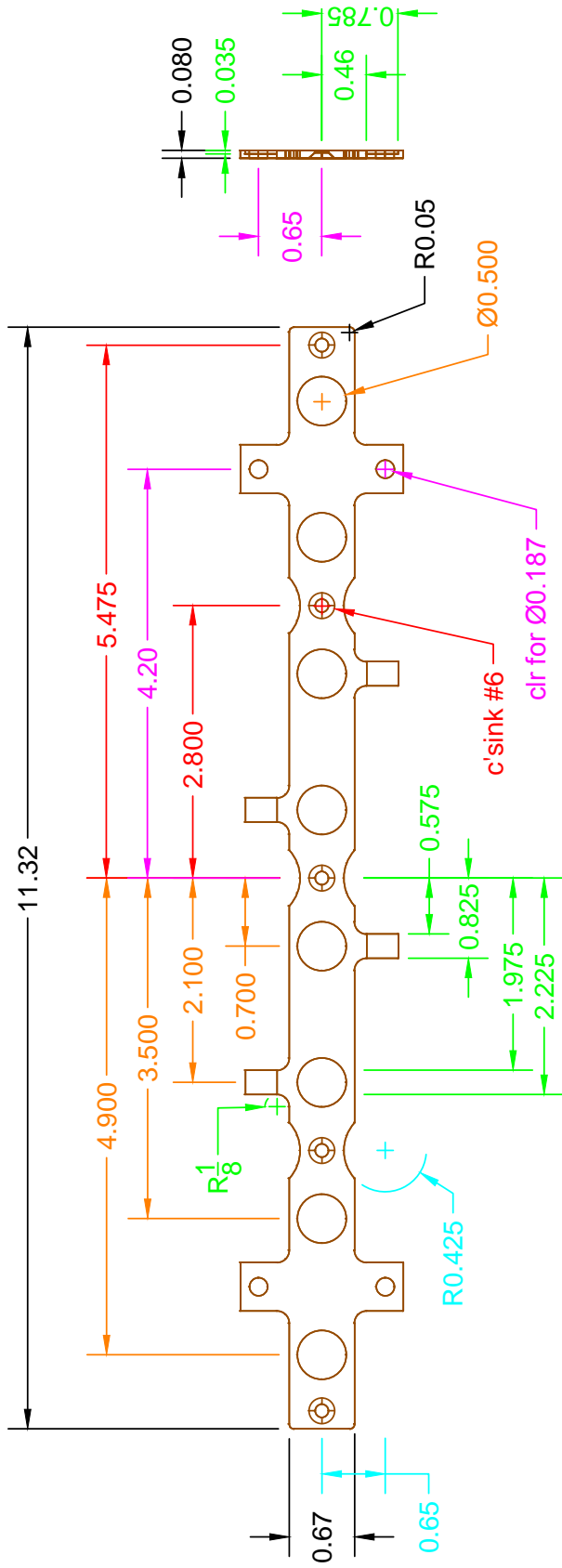
TOLERANCES:
 X.X ± 0.060
 X.XX ± 0.030
 FRACTIONS $\pm \frac{1}{32}$
 DRAWING SCALE: 3.0000
 DIMENSIONS IN INCHES



TOLERANCES:
 X.X ±0.050
 X.XX ±0.030
 X.XXX ±0.015
 FRACTIONS $\pm\frac{1}{32}$

DRAWING SCALE: 0.5000
 DIMENSIONS IN INCHES

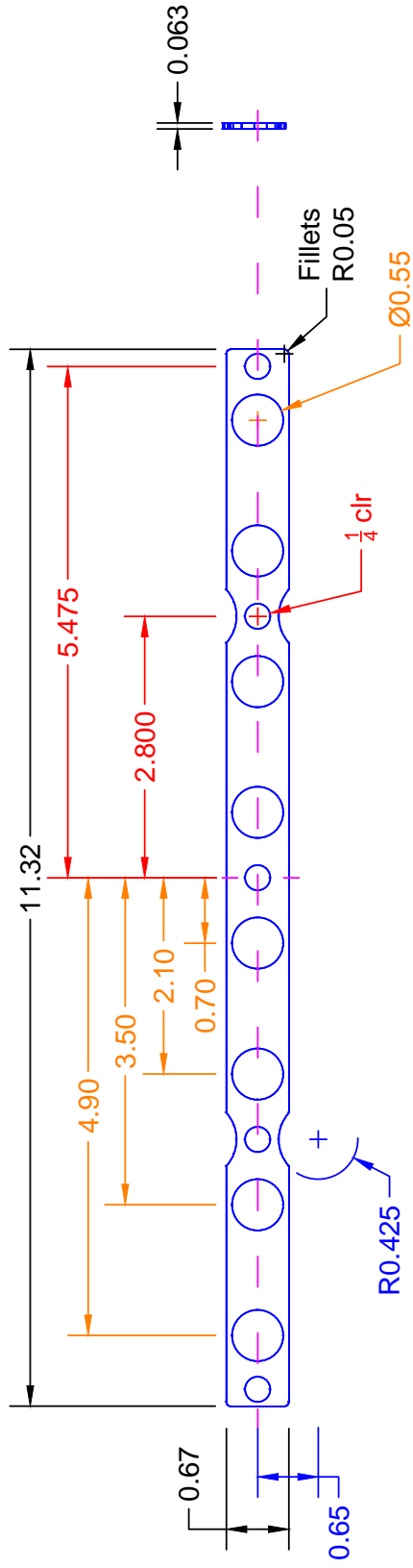
DRAWN BY: Katrina Leaprot
 DATE DRAWN: 03/28/13
 MATERIAL: Delrin
 QUANTITY: 1
 TITLE: Narrow DT Spacer Large (r2)



DRAWN BY: Katrina Leaptrot
 DATE DRAWN: 03/28/13
 MATERIAL: Brass
 QUANTITY: 1
 TITLE: Narrow DT Tabbed Electrode (r2)

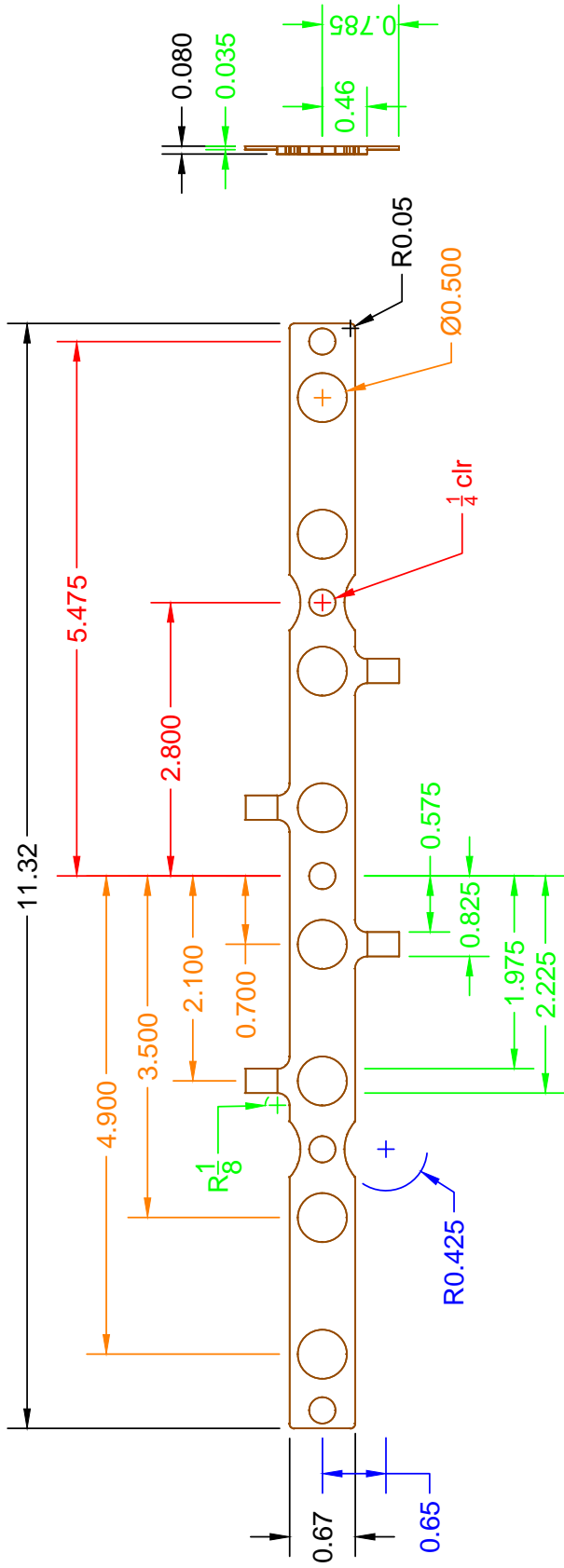
TOLERANCES:
 X.XX ± 0.030
 X.XXX ± 0.015
 FRACTIONS $\pm \frac{1}{32}$

DRAWING SCALE: 0.6000
 DIMENSIONS IN INCHES



DRAWN BY: Katrina Leaptrot
 DATE DRAWN: 03/28/13
 MATERIAL: Delrin
 QUANTITY: 15
 TITLE: Narrow DT Spacer (r2)

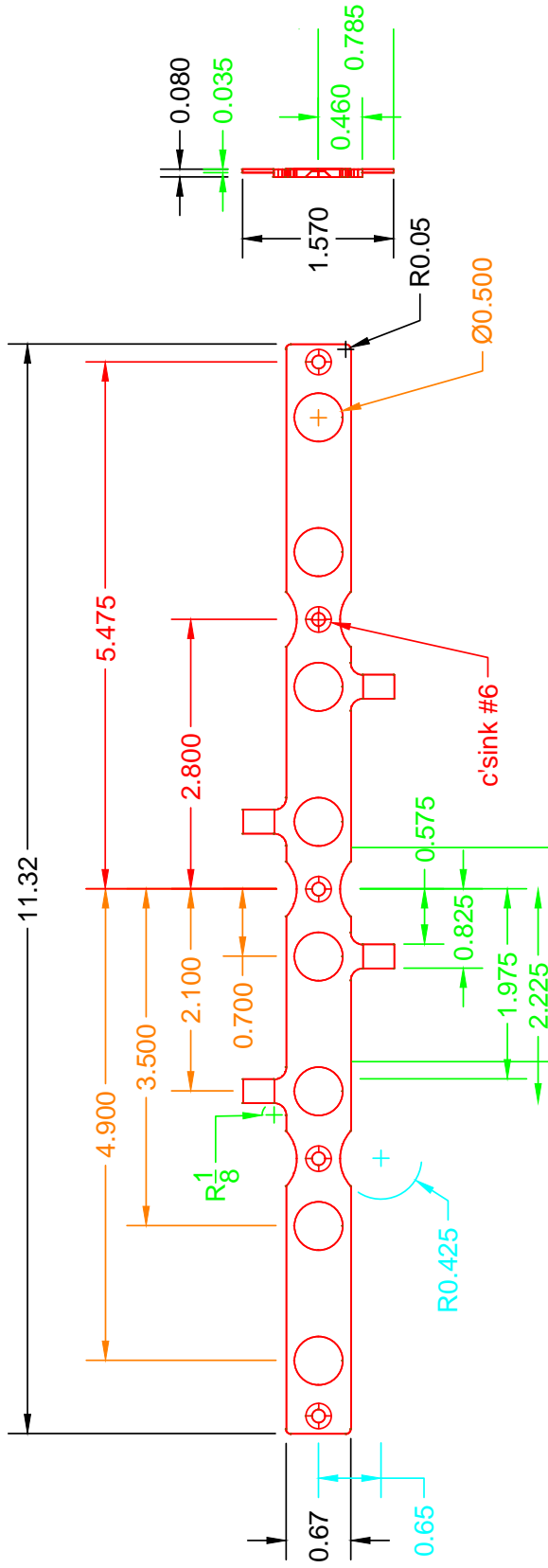
TOLERANCES:
 X.XX ± 0.030
 X.XXX ± 0.015
 DRAWING SCALE: 0.5500
 DIMENSIONS IN INCHES



TOLERANCES:
 X.XX ±0.030
 X.XXX ±0.015
 FRACTIONS ±₃₂¹

DRAWING SCALE: 0.6000
 DIMENSIONS IN INCHES

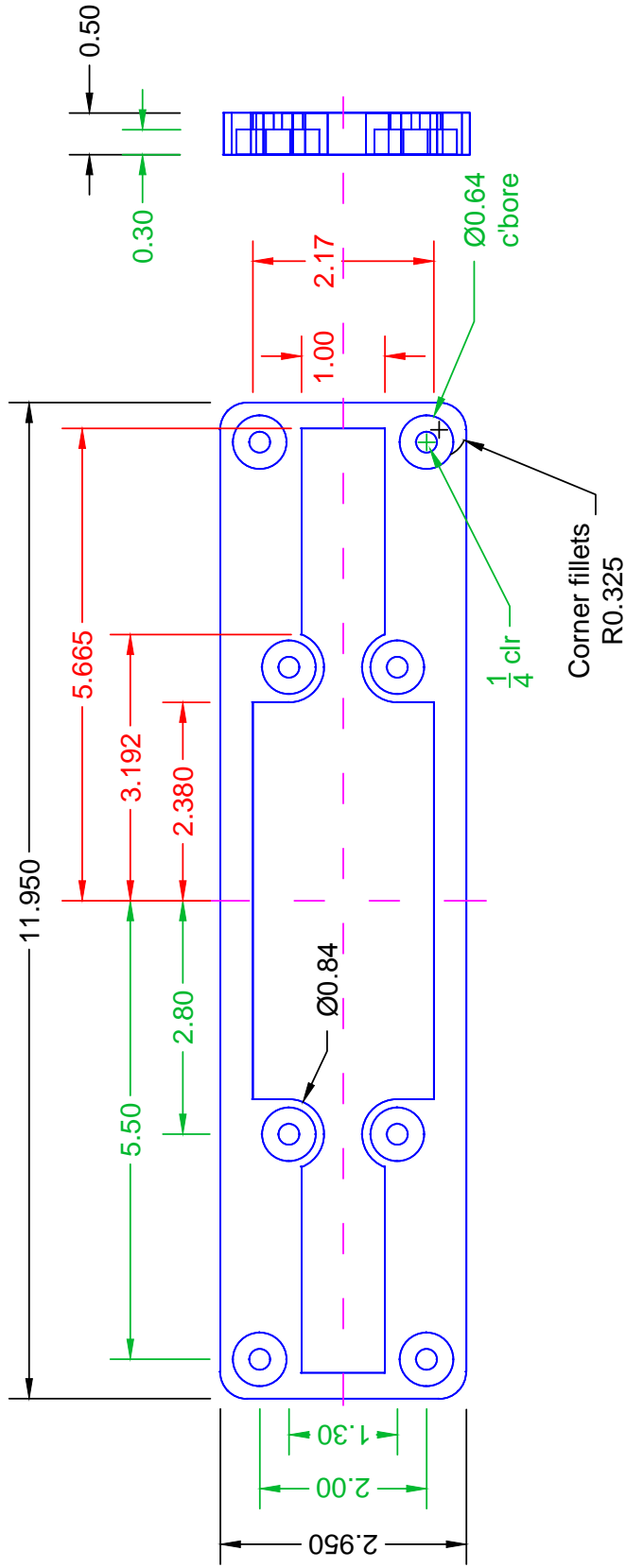
DRAWN BY: Katrina Leaptrot
 DATE DRAWN: 03/28/13
 MATERIAL: Brass
 QUANTITY: 14
 TITLE: Narrow DT Middle Electrode (r2)



DRAWN BY: Katrina Leaprot
 DATE DRAWN: 08/06/14
 MATERIAL: Brass
 QUANTITY: 1
 TITLE: Narrow DT Electrode

TOLERANCES:
 X.XX ±0.030
 X.XXX ±0.015
 FRACTIONS $\pm\frac{1}{32}$

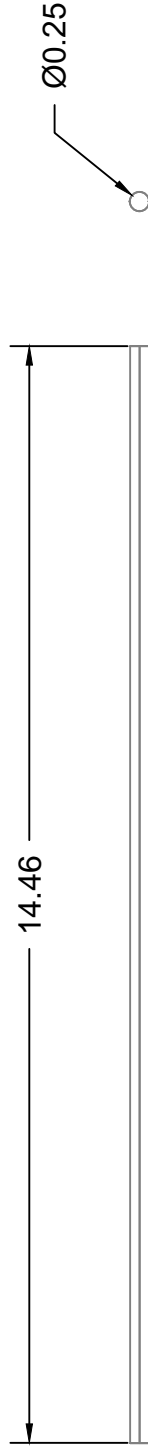
DRAWING SCALE: 0.6000
 DIMENSIONS IN INCHES



TOLERANCES:
 X.XX ± 0.030
 X.XXX ± 0.015
 FRACTIONS $\pm \frac{1}{32}$

DRAWING SCALE: 0.5000
 DIMENSIONS IN INCHES

DRAWN BY: Katrina Leaptrot
 DATE DRAWN: 03/28/13
 MATERIAL: Delrin
 QUANTITY: 1
 TITLE: DT Mount Block Front (r2)



DRAWN BY: Katrina Leaprot

DATE DRAWN: 12/01/2017

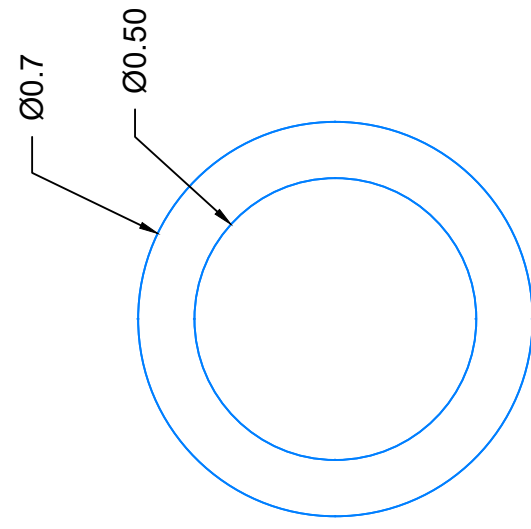
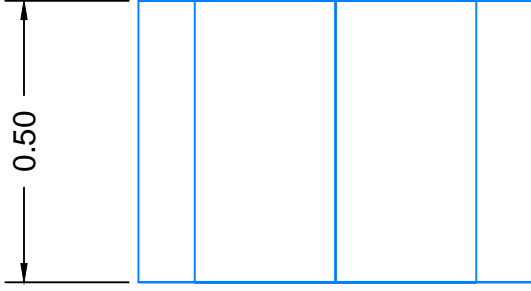
MATERIAL: 1/4-28 Stainless Steel Threaded Rod

QUANTITY: 10

TITLE: Drift Tube Threaded Rods

**TOLERANCES:
X.XX ±0.030**

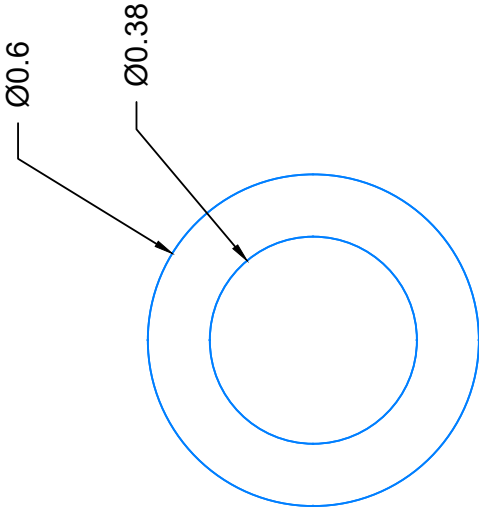
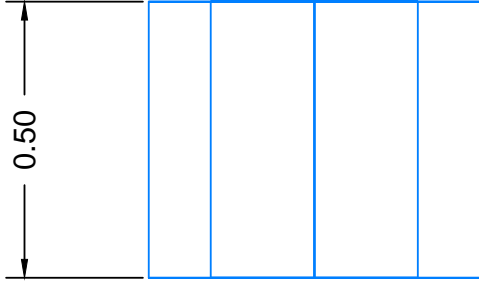
**DRAWING SCALE: 0.4000
DIMENSIONS IN INCHES**



DRAWN BY: Katrina Leaptrot
DATE DRAWN: 12/01/2017
MATERIAL: Delrin
QUANTITY: 8
TITLE: Drift Tube Standoffs Type 1

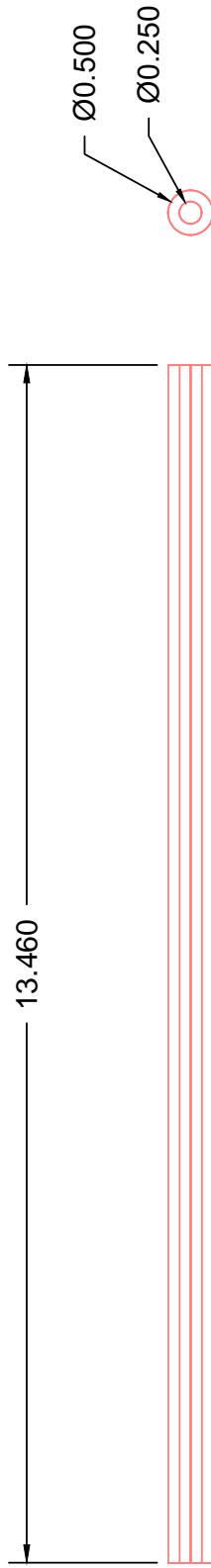
TOLERANCES:
X.X ±0.030
X.XX ±0.010

DRAWING SCALE: 3.0000
DIMENSIONS IN INCHES



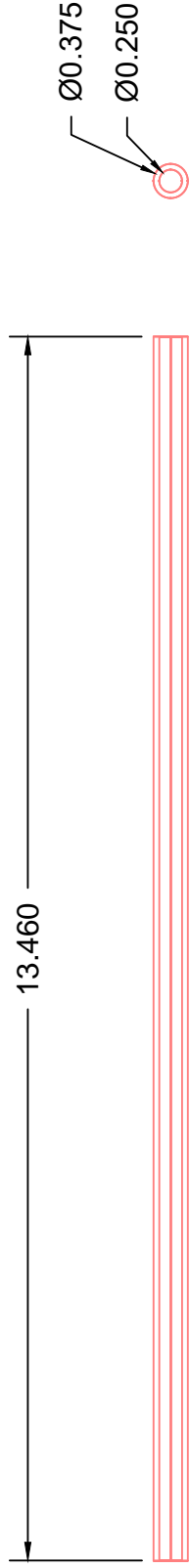
DRAWN BY: Katrina Leaprot
DATE DRAWN: 12/01/2017
MATERIAL: Delrin
QUANTITY: 12
TITLE: Drift Tube Standoffs Type 2

TOLERANCES:
X.XX ± 0.030
X.XXX ± 0.010
DRAWING SCALE: 3.0000
DIMENSIONS IN INCHES



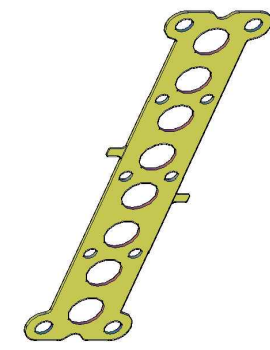
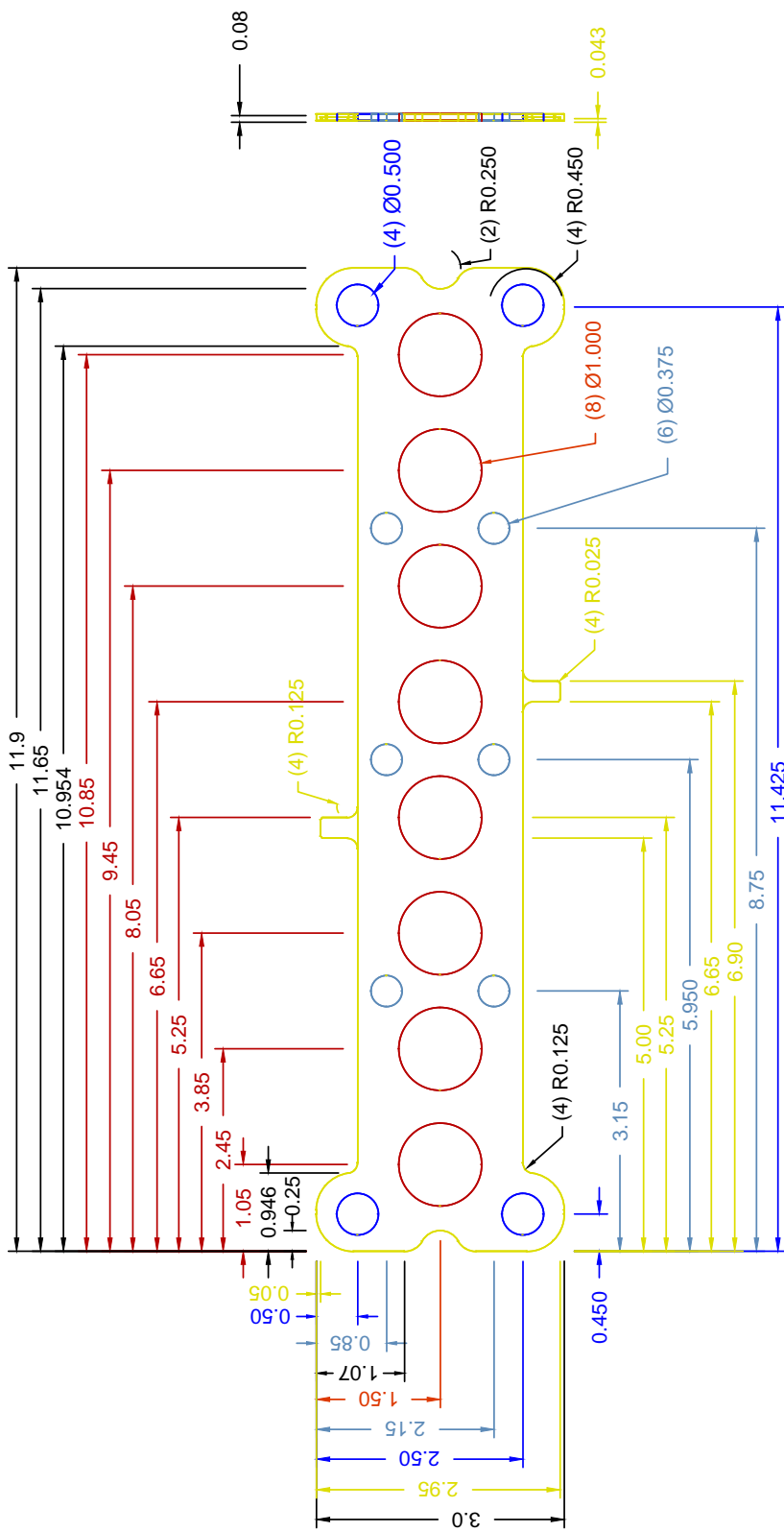
DRAWN BY: Katrina Leaprot
DATE DRAWN: 11/30/2017
MATERIAL: >95% Alumina Ceramic
QUANTITY: 4
TITLE: Drift Tube Ceramic Tubes Type 1

TOLERANCES:
X.XXX ±0.010
DRAWING SCALE: 0.5000
DIMENSIONS IN INCHES



DRAWN BY: Katrina Leaptrot
DATE DRAWN: 11/30/2017
MATERIAL: >95% Alumina Ceramic
QUANTITY: 6
TITLE: Drift Tube Ceramic Tubes Type 2

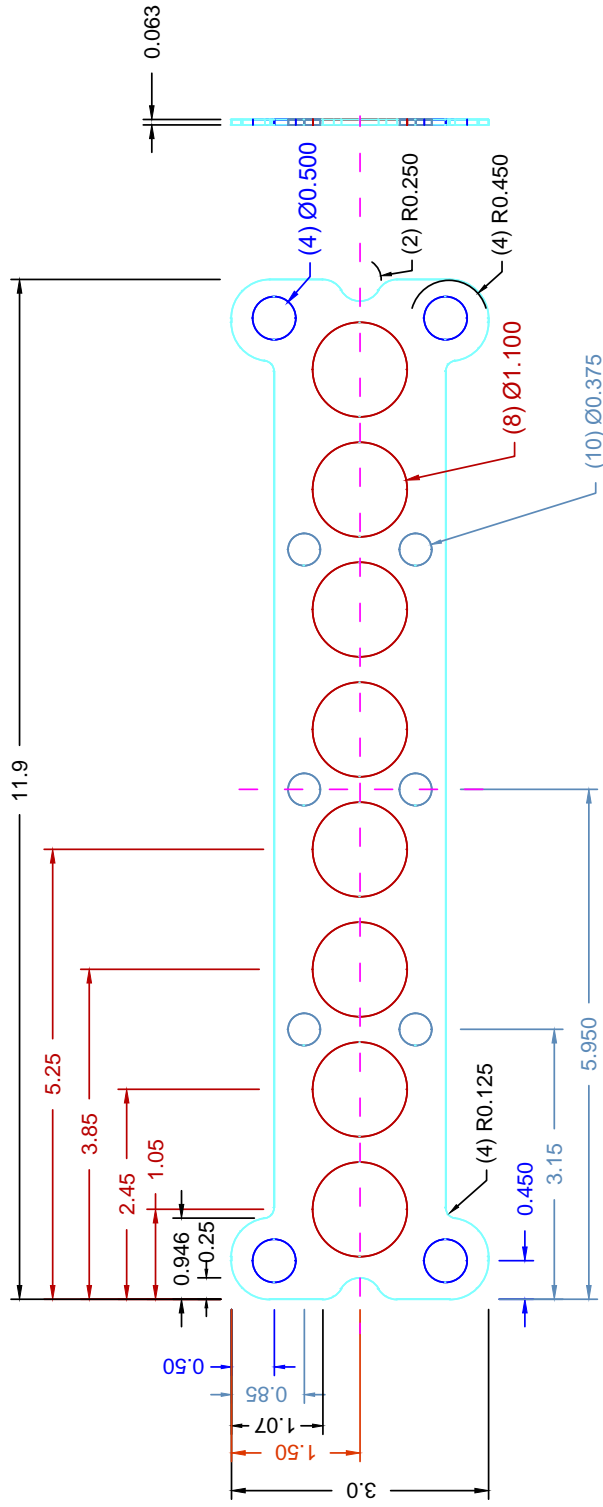
TOLERANCES:
X.XXX ±0.010
DRAWING SCALE: 0.5000
DIMENSIONS IN INCHES



TOLERANCES:
 X.X ±0.040
 X.XX ±0.020
 X.XXX ±0.010

DRAWING SCALE: 0.5000
 DIMENSIONS IN INCHES

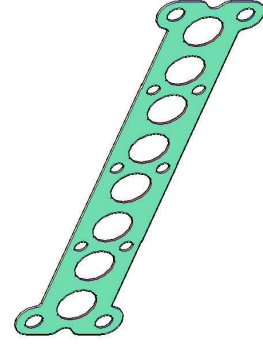
DRAWN BY: Katrina Leaprot
DATE DRAWN: 12/04/2017
MATERIAL: Brass
QUANTITY: 87
TITLE: Drift Tube Electrode

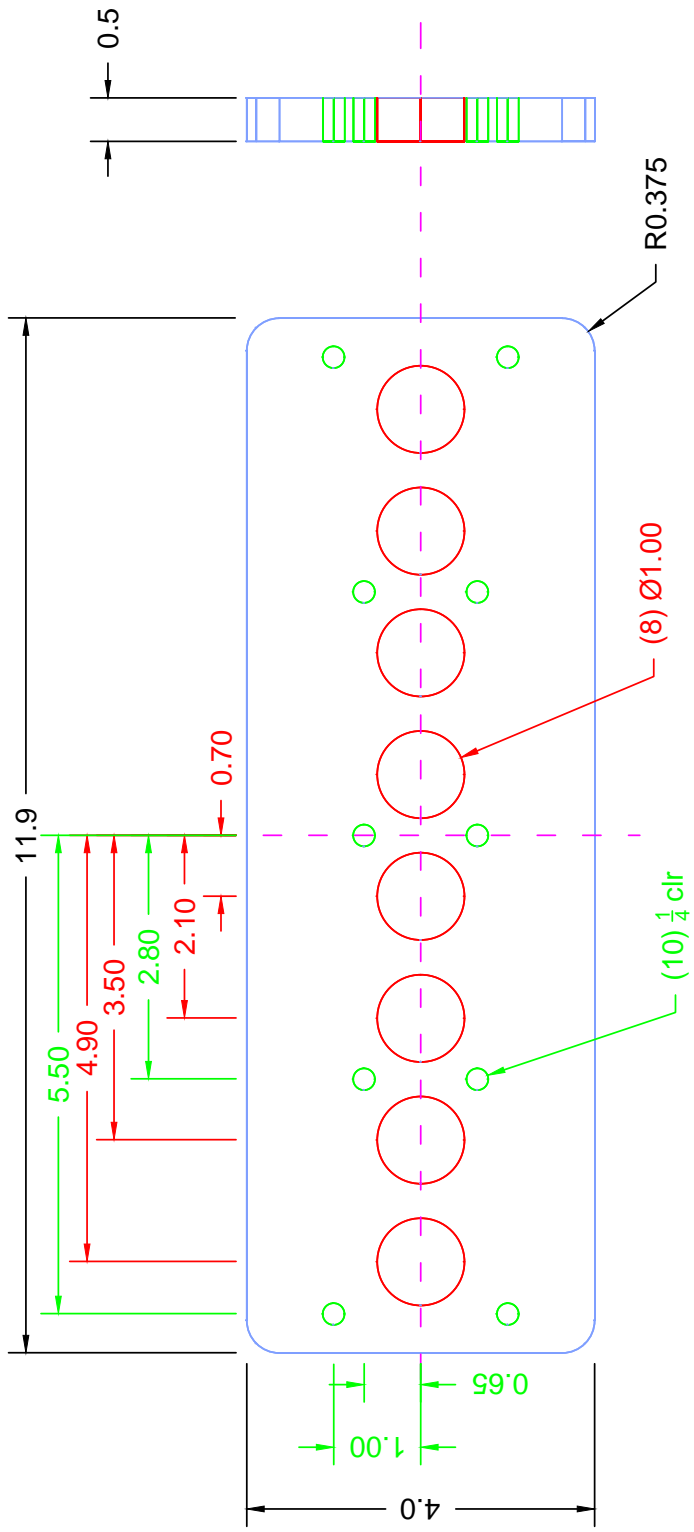


DRAWN BY: Katrina Leaptrot
 DATE DRAWN: 12/04/2017
 MATERIAL: Delrin
 QUANTITY: 88
 TITLE: Drift Tube Spacer

TOLERANCES:
 X.X ±0.040
 X.XX ±0.020
 X.XXX ±0.010

DRAWING SCALE: 0.5000
 DIMENSIONS IN INCHES



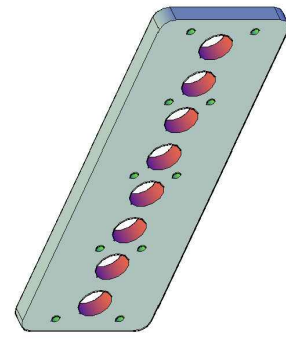


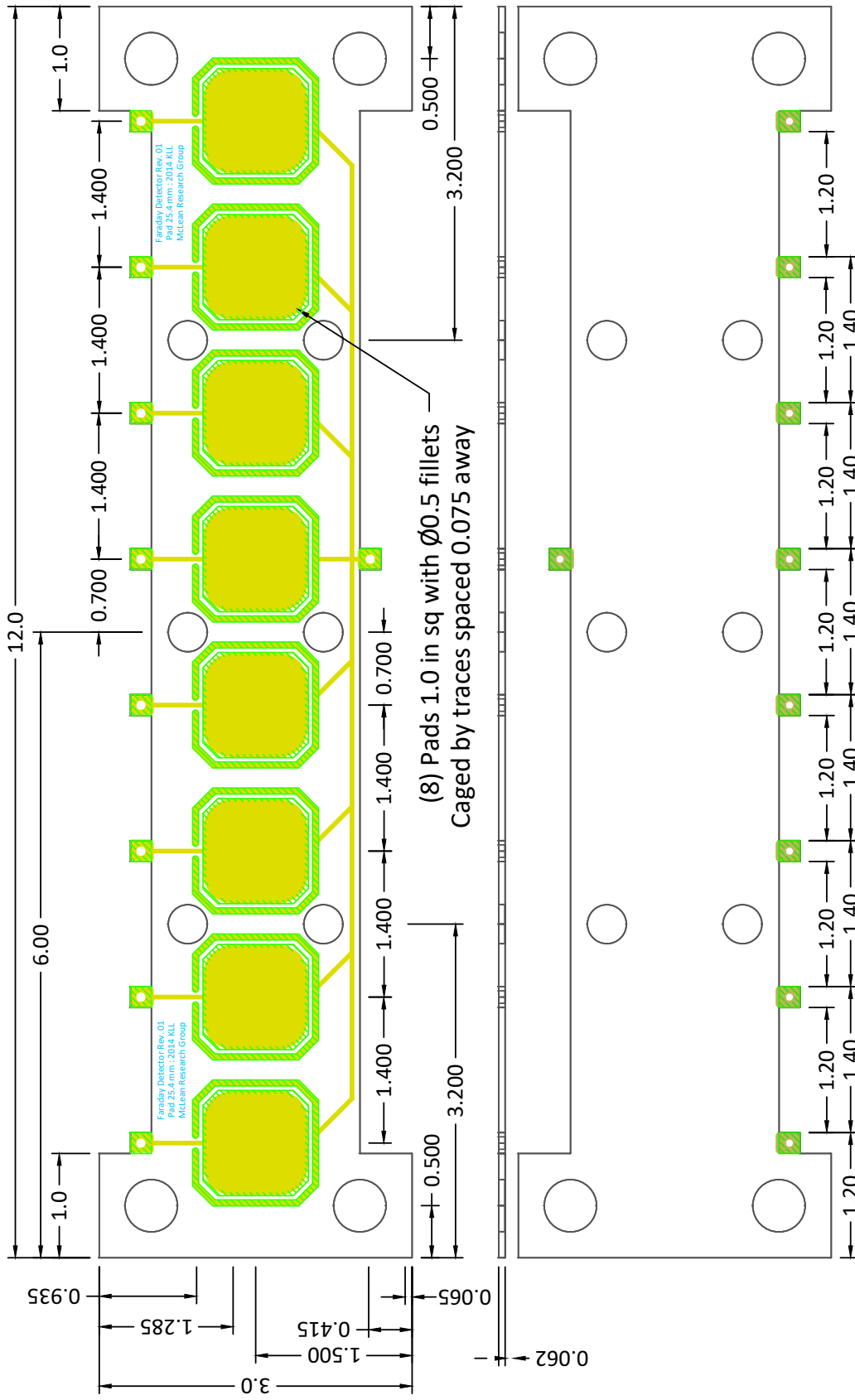
DRAWN BY: Katrina Leaprot
DATE DRAWN: 12/01/2017
MATERIAL: Delrin
QUANTITY: 1
TITLE: Drift Tube Mount Block Back

TOLERANCES:

X.X	±0.030
X.XX	±0.020
X.XXX	±0.020
Fractions	±1/32

DRAWING SCALE: 0.5000
DIMENSIONS IN INCHES





Faraday Detector Rev. 01
 Pad 25.4 mm; 2014 KLL
 McLean Research Group

Faraday Detector Rev. 01
 Pad 25.4 mm; 2014 KLL
 McLean Research Group

(8) Pads 1.0 in sq with $\varnothing 0.5$ fillets
 Caged by traces spaced 0.075 away

KEY:

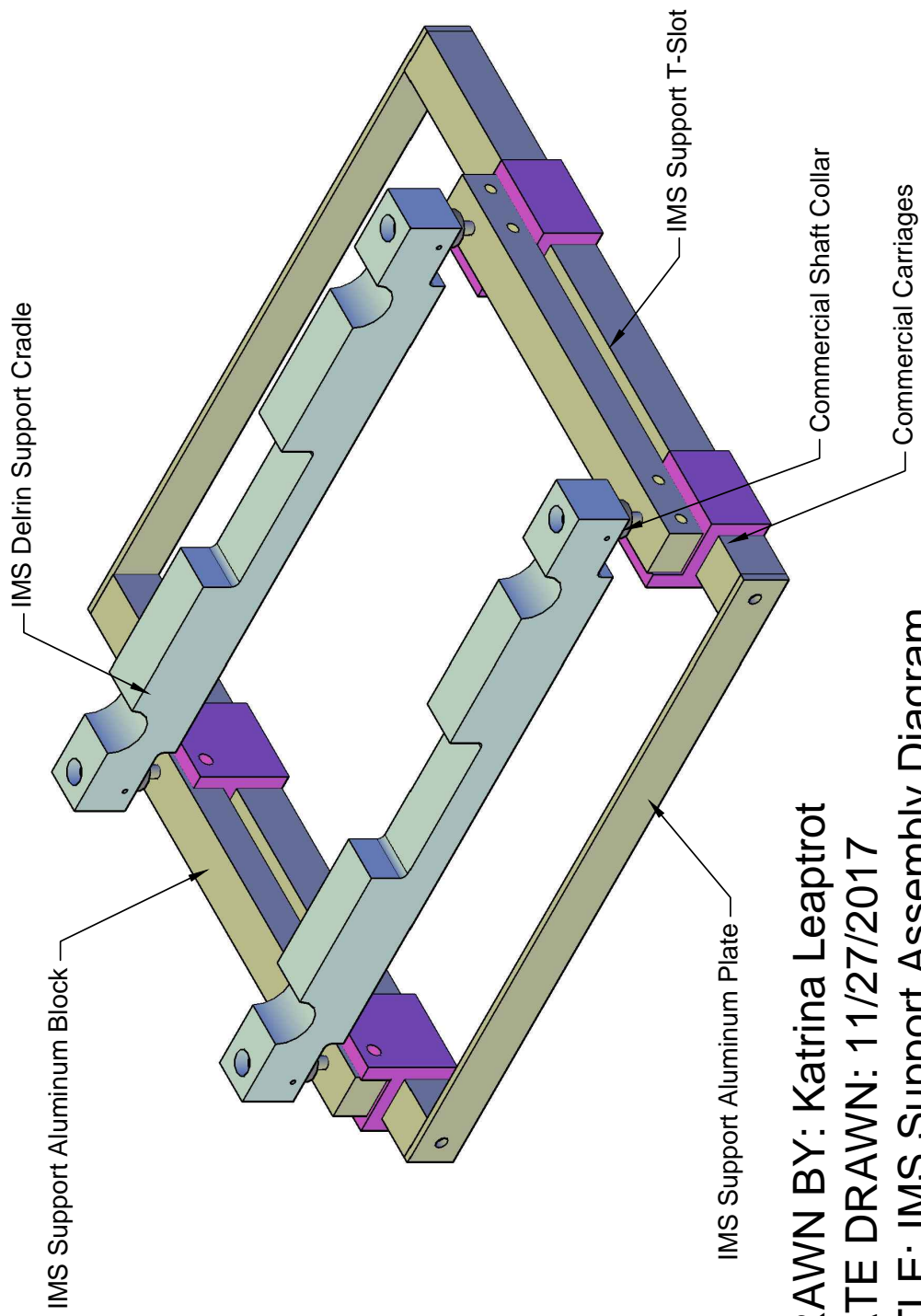
- EDGE CUTS
- FRONT COPPER
- FRONT SILKSREEN
- FRONT SOLDER MASK
- BACK COPPER
- BACK SOLDER MASK

TOLERANCES:

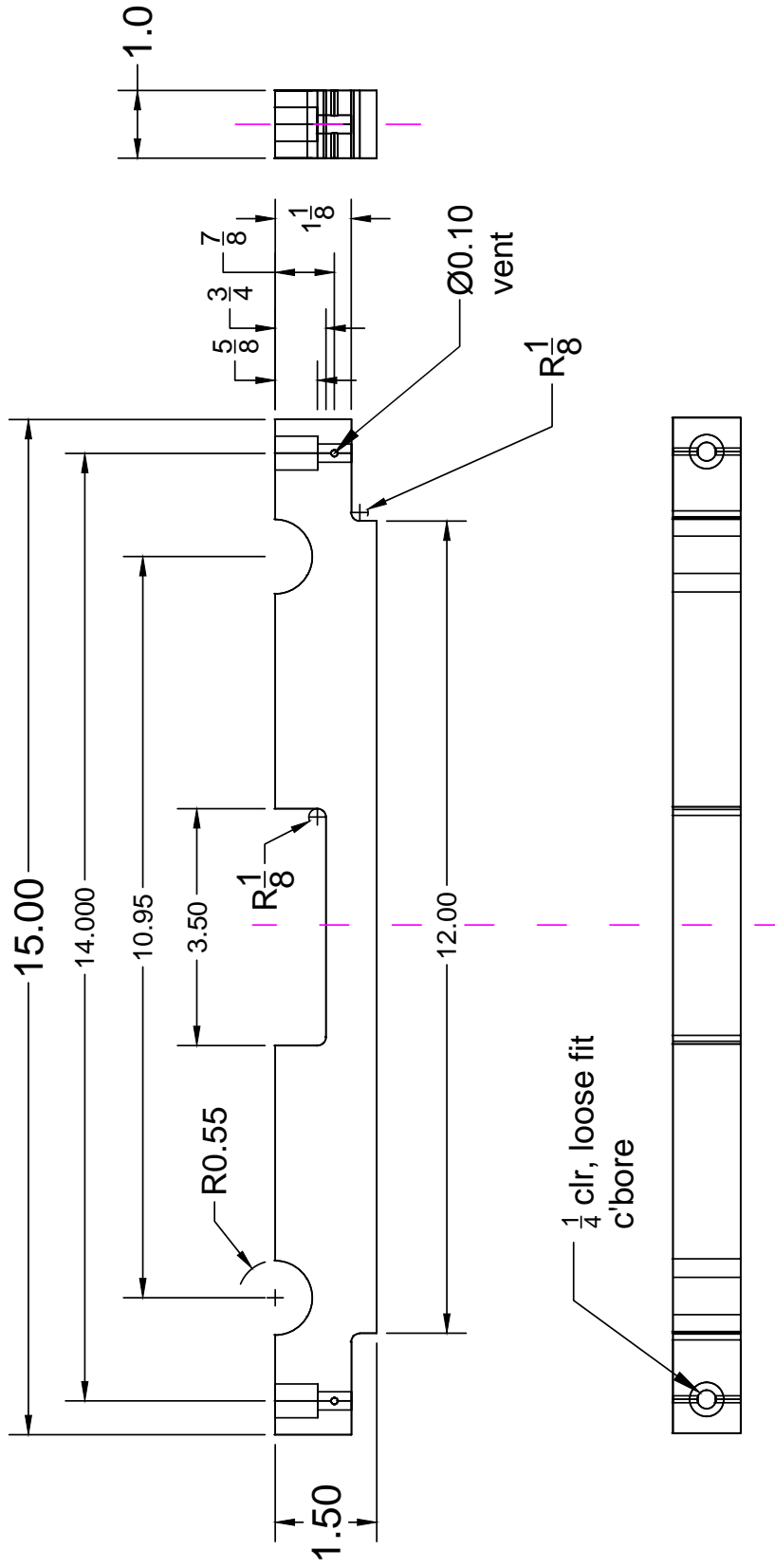
- X.X ±0.040
- X.XX ±0.030
- X.XXX ±0.020

DRAWING SCALE: 0.7000
 DIMENSIONS IN INCHES
 NONESSENTIALS OMITTED, FOR SIMPLICITY

DRAWN BY: Katrina Leaptrot
 DATE DRAWN: 12/11/2017
 MATERIAL: PCB
 QUANTITY: 1
 TITLE: Faraday Detector



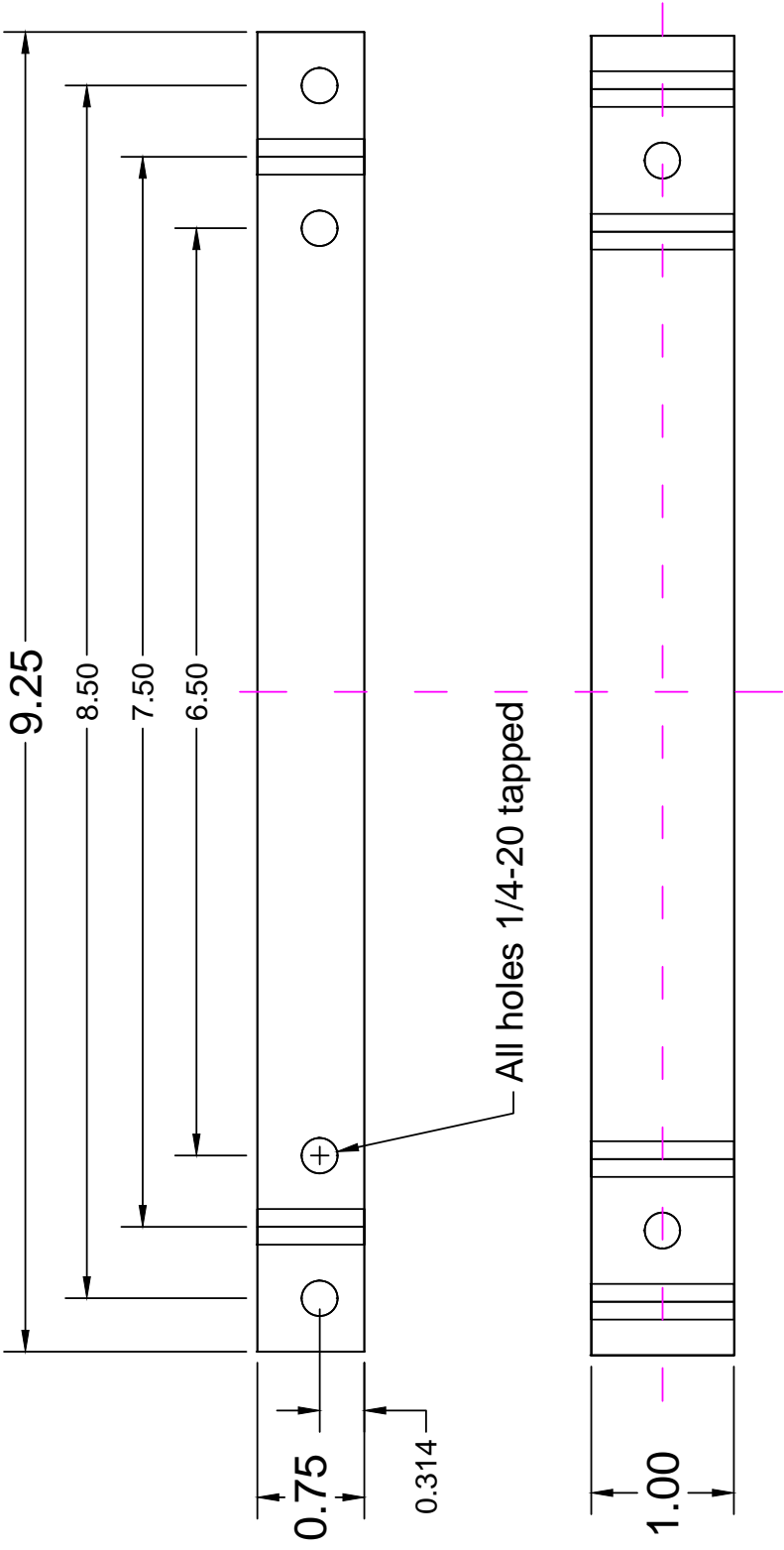
DRAWN BY: Katrina Leaptrot
DATE DRAWN: 11/27/2017
TITLE: IMS Support Assembly Diagram



TOLERANCES:
 X.X ±0.060
 X.XX ±0.030
 X.XXX ±0.015
 FRACTIONS ± $\frac{1}{32}$

DRAWING SCALE: 0.4200
 DIMENSIONS IN INCHES

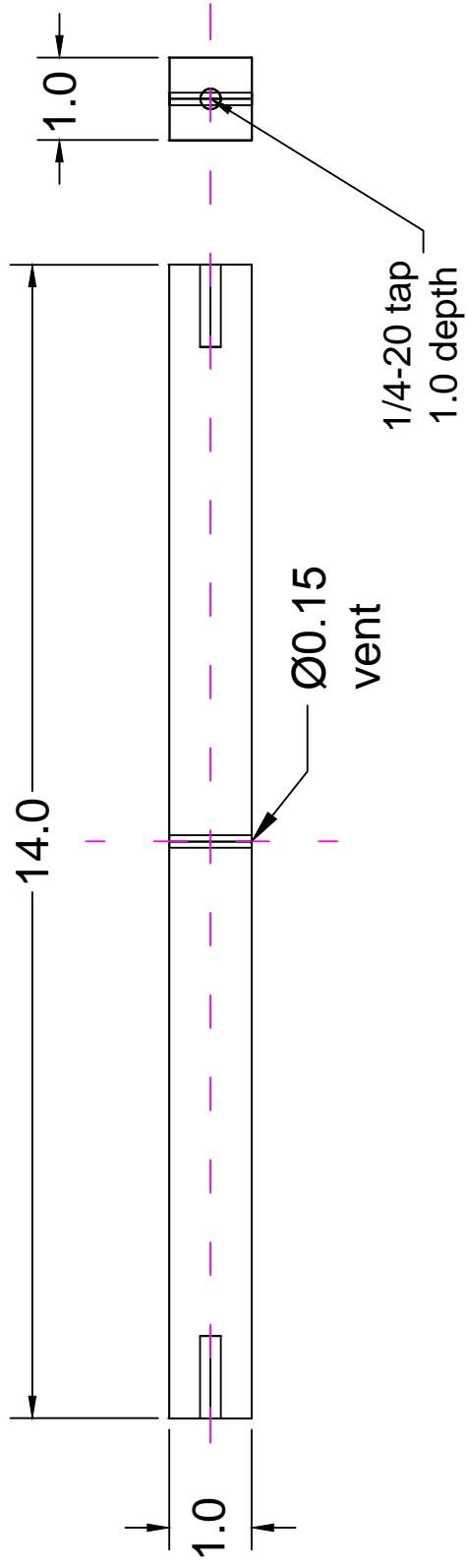
DRAWN BY: Katrina Leaptrot
 DATE DRAWN: 03/14/13
 MATERIAL: Delrin
 QUANTITY: 2
 TITLE: IMS Delrin Support Cradle



DRAWN BY: Katrina Leaptrot
 DATE DRAWN: 03/14/13
 MATERIAL: Aluminum
 QUANTITY: 2
 TITLE: IMS Support Aluminum Block

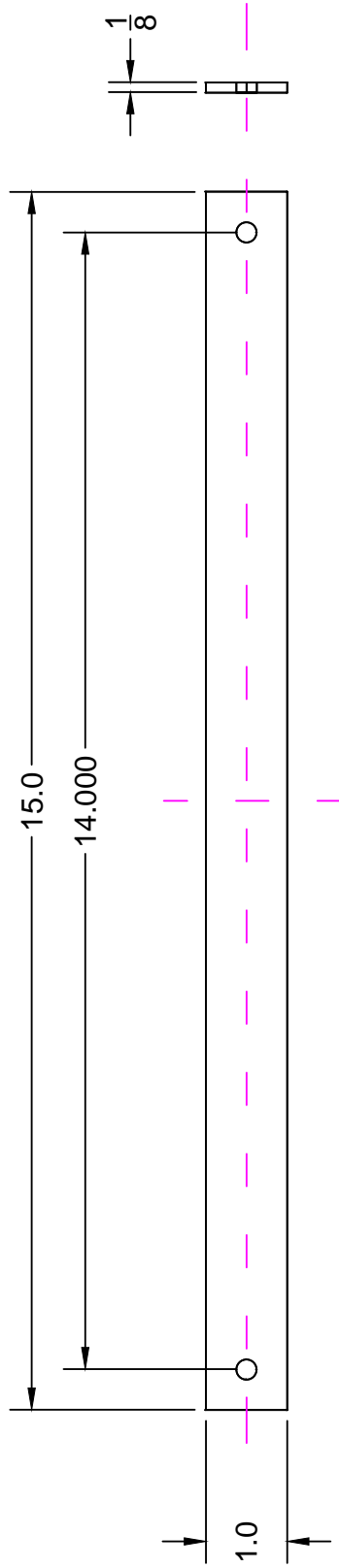
TOLERANCES:
 X.XX ±0.030
 X.XXX ±0.015
 FRACTIONS $\pm\frac{1}{32}$

DRAWING SCALE: 0.8000
 DIMENSIONS IN INCHES



DRAWN BY: Katrina Leaptrot
 DATE DRAWN: 03/14/13
 MATERIAL: T-Slot
 QUANTITY: 2
 TITLE: IMS Support T-Slot

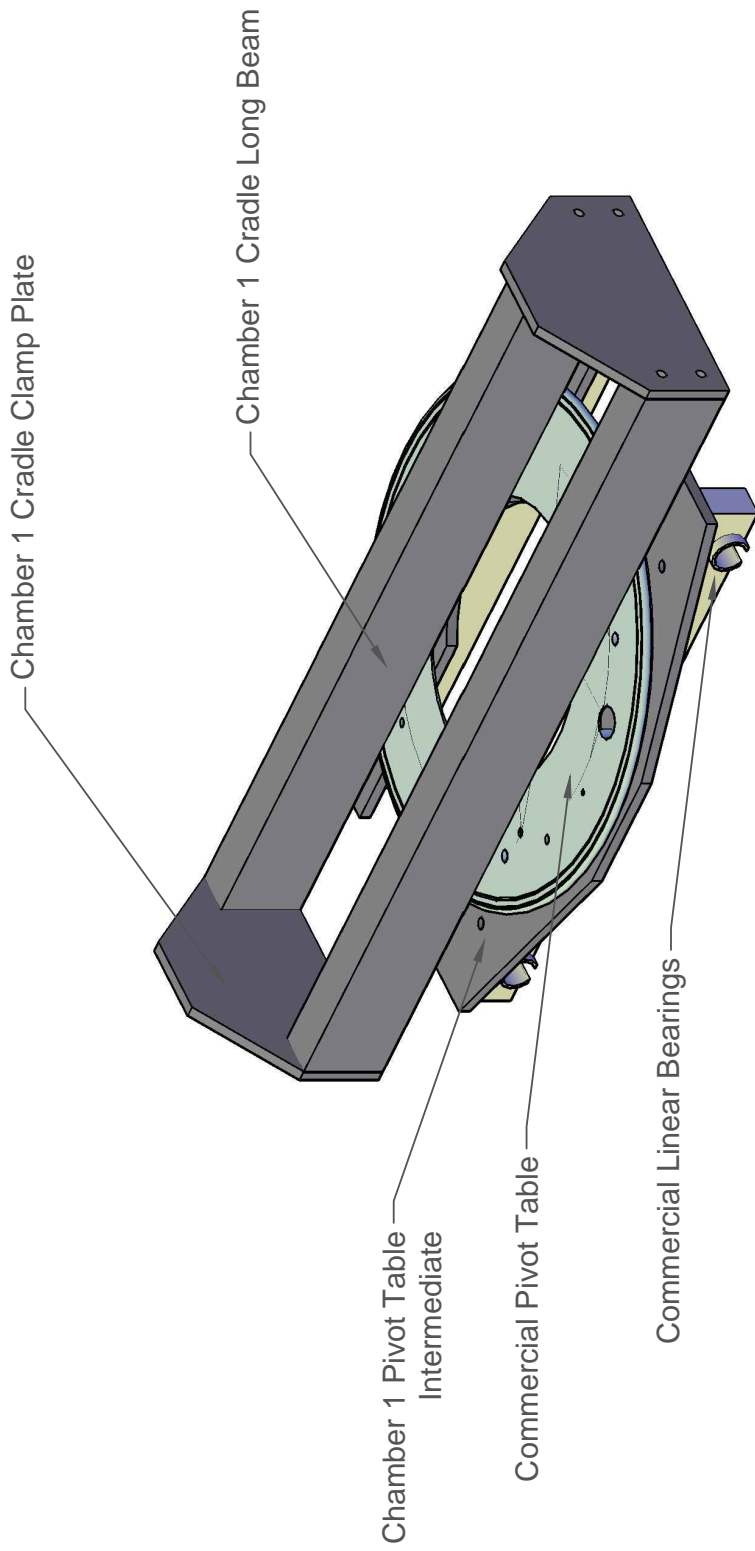
TOLERANCES:
 X.X ±0.060
 X.XXX ±0.015
 FRACTIONS ± $\frac{1}{32}$
 DRAWING SCALE: 0.4500
 DIMENSIONS IN INCHES



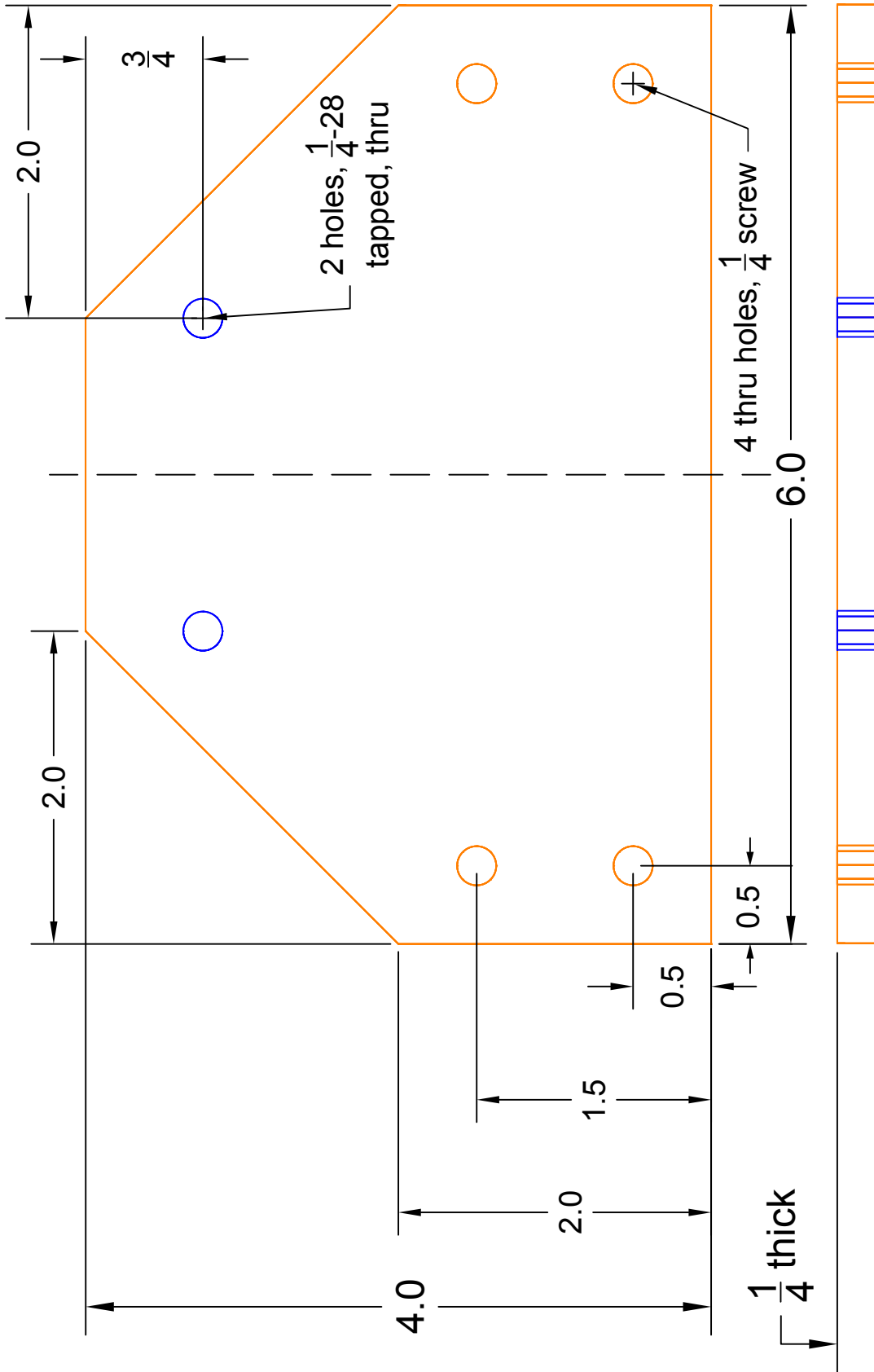
DRAWN BY: Katrina Leaptrot
DATE DRAWN: 03/14/13
MATERIAL: Aluminum
QUANTITY: 2
TITLE: IMS Support Aluminum Plate

TOLERANCES:
 X.X ±0.060
 X.XXX ±0.015
 FRACTIONS ± $\frac{1}{32}$

DRAWING SCALE: 0.4500
DIMENSIONS IN INCHES



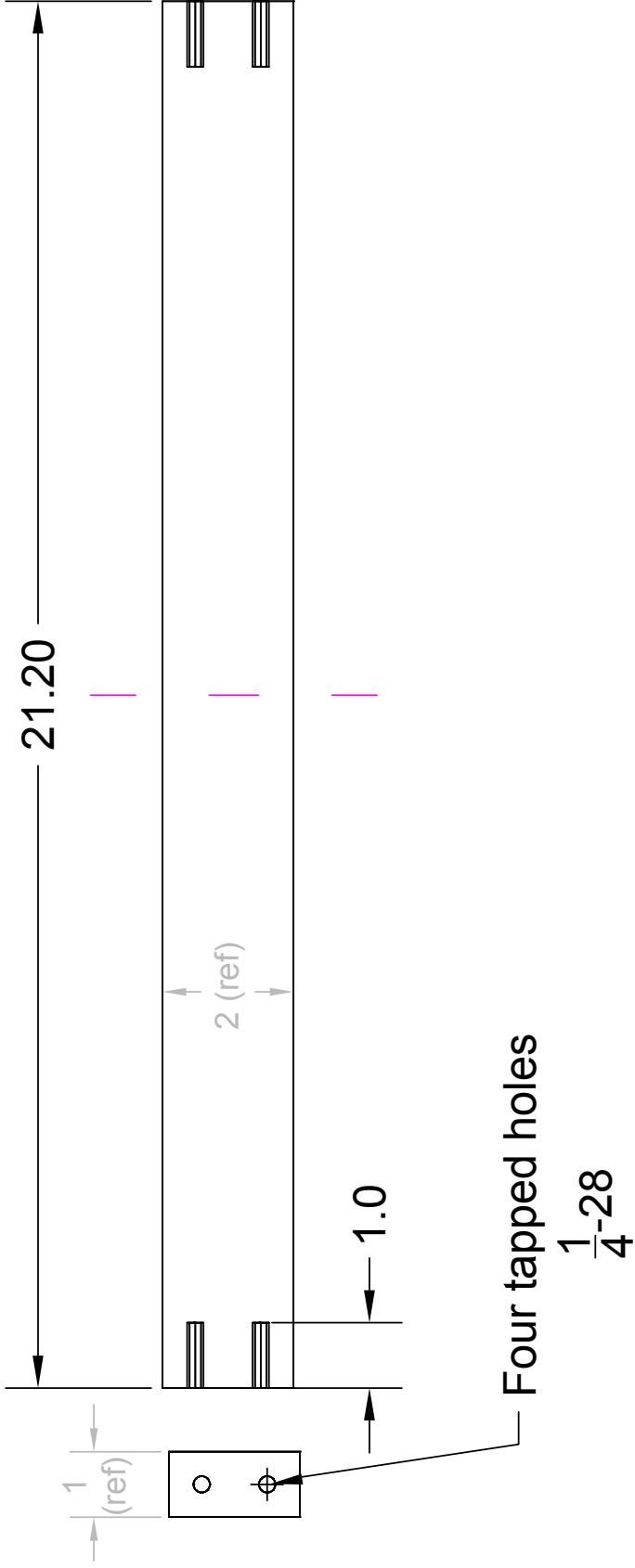
DRAWN BY: Katrina Leaptrot
DATE DRAWN: 11/27/2017
TITLE: Chamber 1 Support Assembly Diagram



TOLERANCES:
 X.X ±0.020
 Fractions $\pm\frac{1}{32}$

DRAWING SCALE: 1
 DIMENSIONS IN INCHES

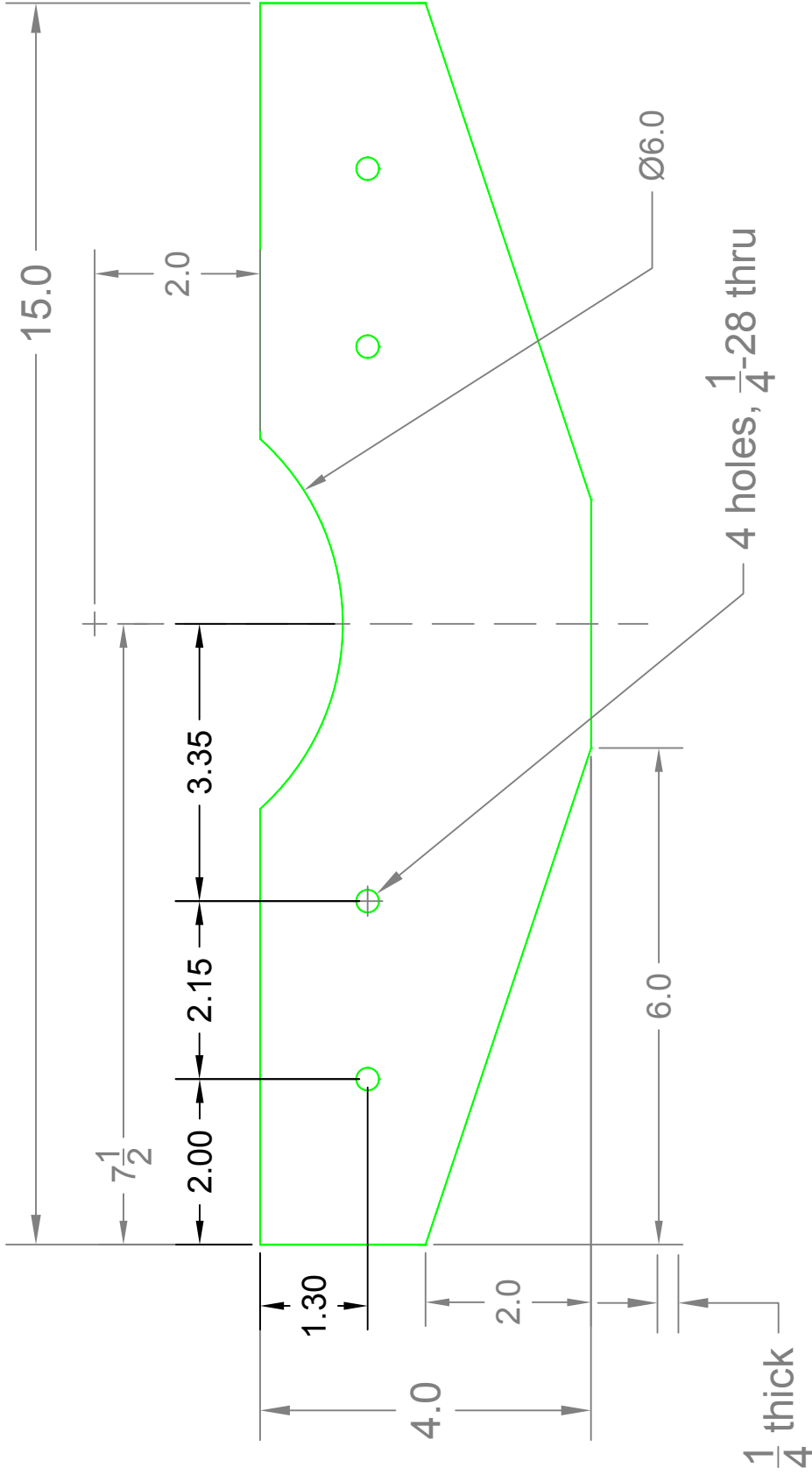
DRAWN BY: Katrina Leaptrot
 DATE DRAWN: 02/16/12
 MATERIAL: Aluminum
 QUANTITY: 2
 TITLE: Chamber 1 Cradle Clamp Plate



DRAWN BY: Katrina Leaptrot
DATE DRAWN: 02/16/12
MATERIAL: T-Slot 1"X2" Extrusion
QUANTITY: 2
TITLE: Chamber 1 Cradle Long Beam

TOLERANCES:
 X.X ±0.050
 X.XX ±0.010
 Fractions ± $\frac{1}{16}$

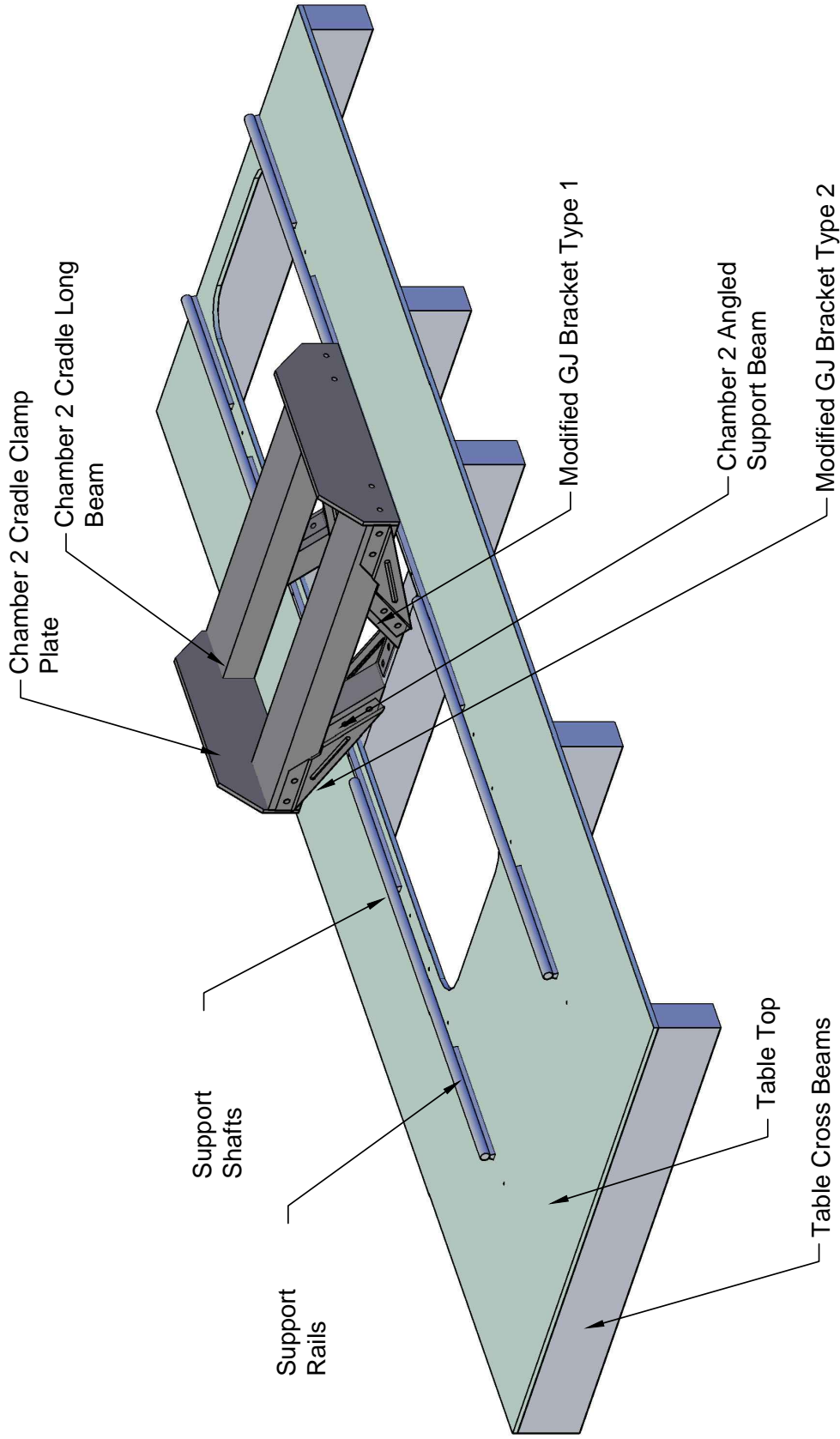
DRAWING SCALE: 0.4000
DIMENSIONS IN INCHES



TOLERANCES:
 X.X ± 0.020
 X.XX ± 0.010
 X.XXX ± 0.005
 fractions ± $\frac{1}{32}$

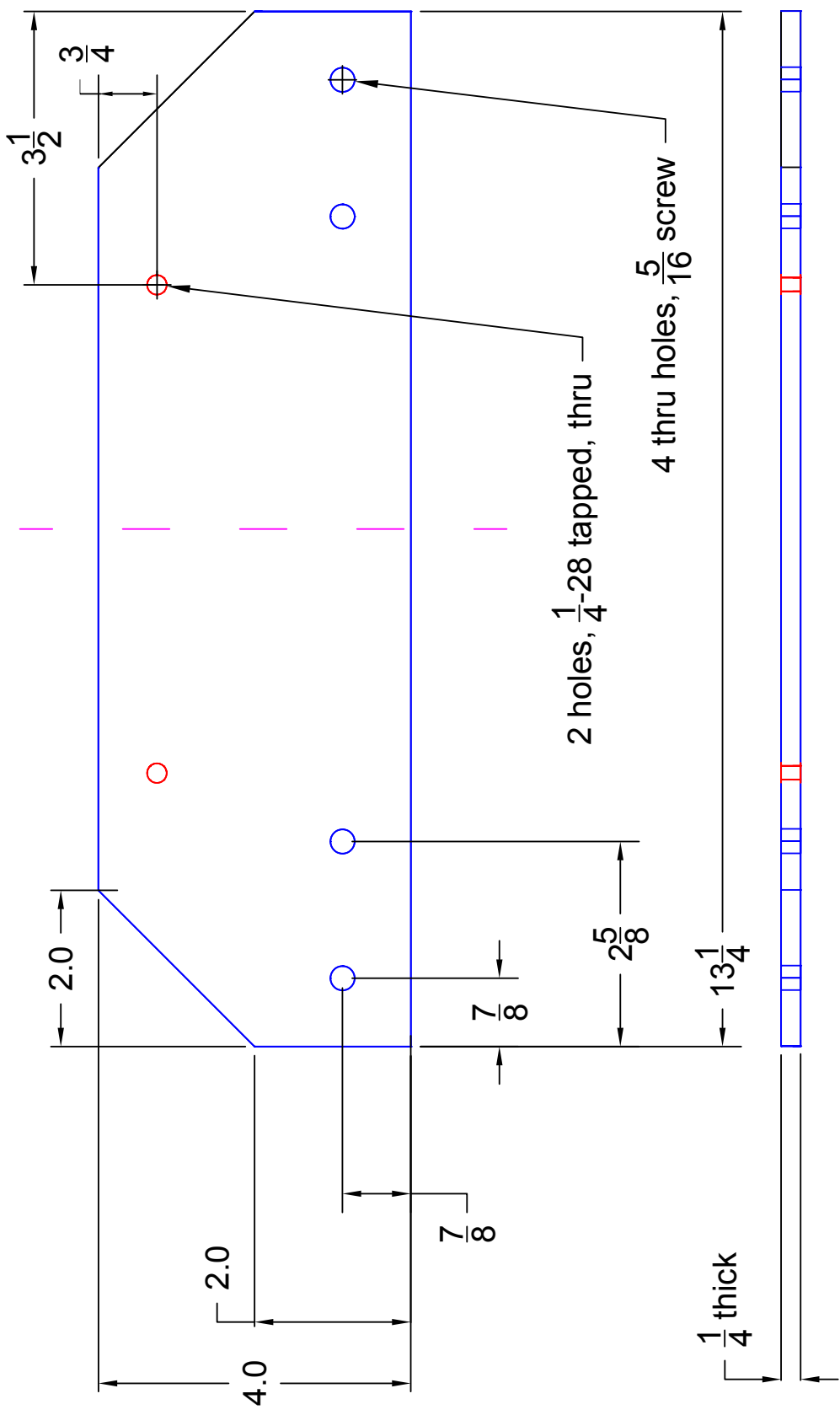
DRAWING SCALE: 0.5
 DIMENSIONS ARE IN INCHES

DRAWN BY: Katrina Leaptrot
DATE DRAWN: 10/10/11
MATERIAL: Aluminum
QUANTITY: 2
TITLE: Chamber 1 Pivot Table Intermediate



DRAWN BY: Katrina Leaptrot
 DATE DRAWN: 11/27/2017

TITLE: Chamber 2 and Rail Support Assembly Diagram



DRAWN BY: Katie Leaptrot

DATE DRAWN: 02/01/12

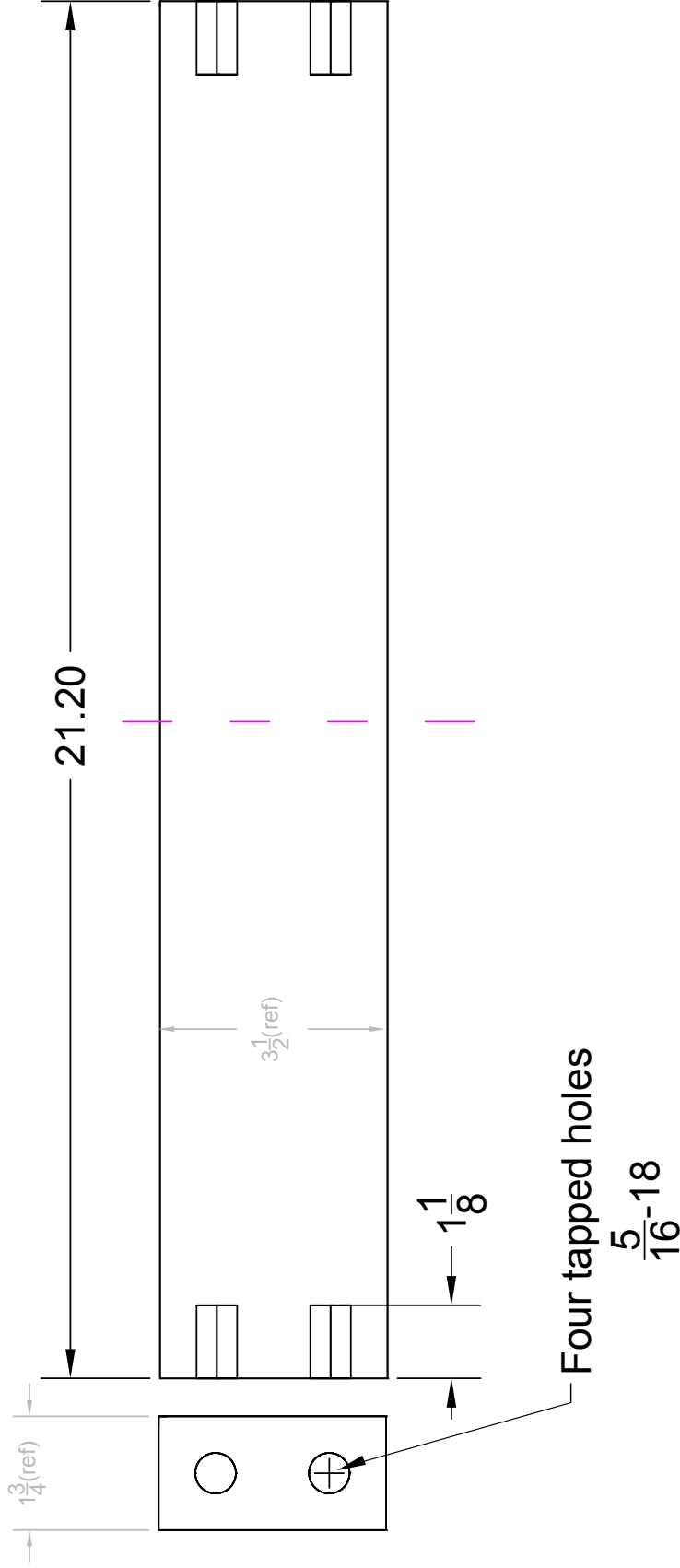
MATERIAL: Aluminum

QUANTITY: 2

TITLE: Chamber 2 Cradle Clamp Plate

TOLERANCES:
 X.X ±0.020
 Fractions ± $\frac{1}{32}$

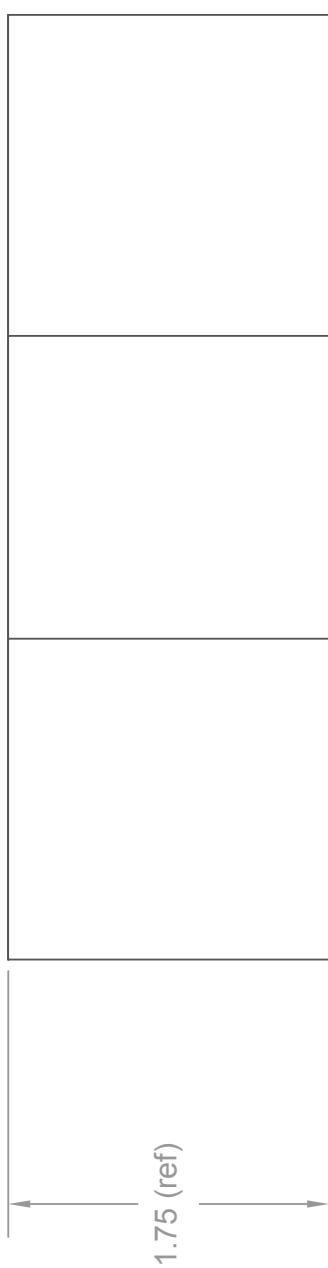
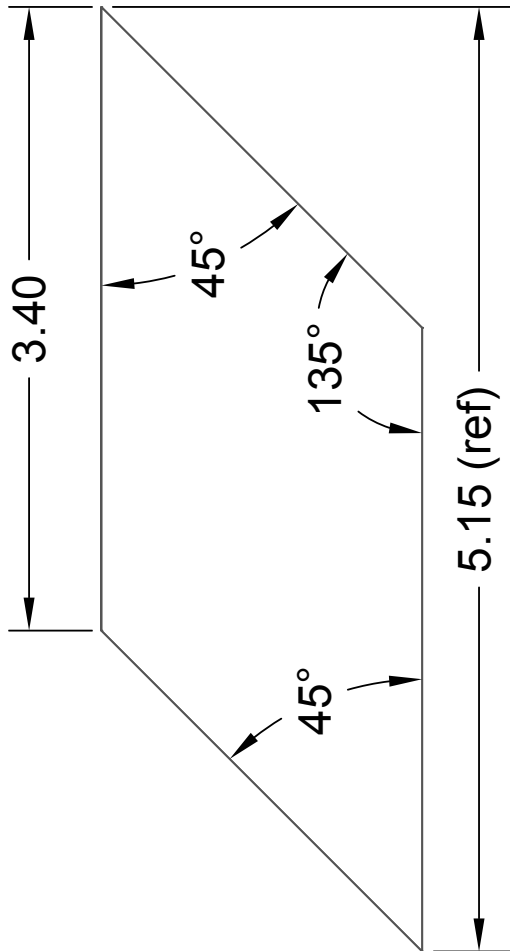
DRAWING SCALE: 0.5000
DIMENSIONS IN INCHES



DRAWN BY: Katrina Leaprot
 DATE DRAWN: 02/01/12
 MATERIAL: GatorJaw GJX350
 QUANTITY: 2
 TITLE: Chamber 2 Cradle Long Beam

TOLERANCES:
 X.XX ± 0.010
 Fractions $\pm \frac{1}{16}$

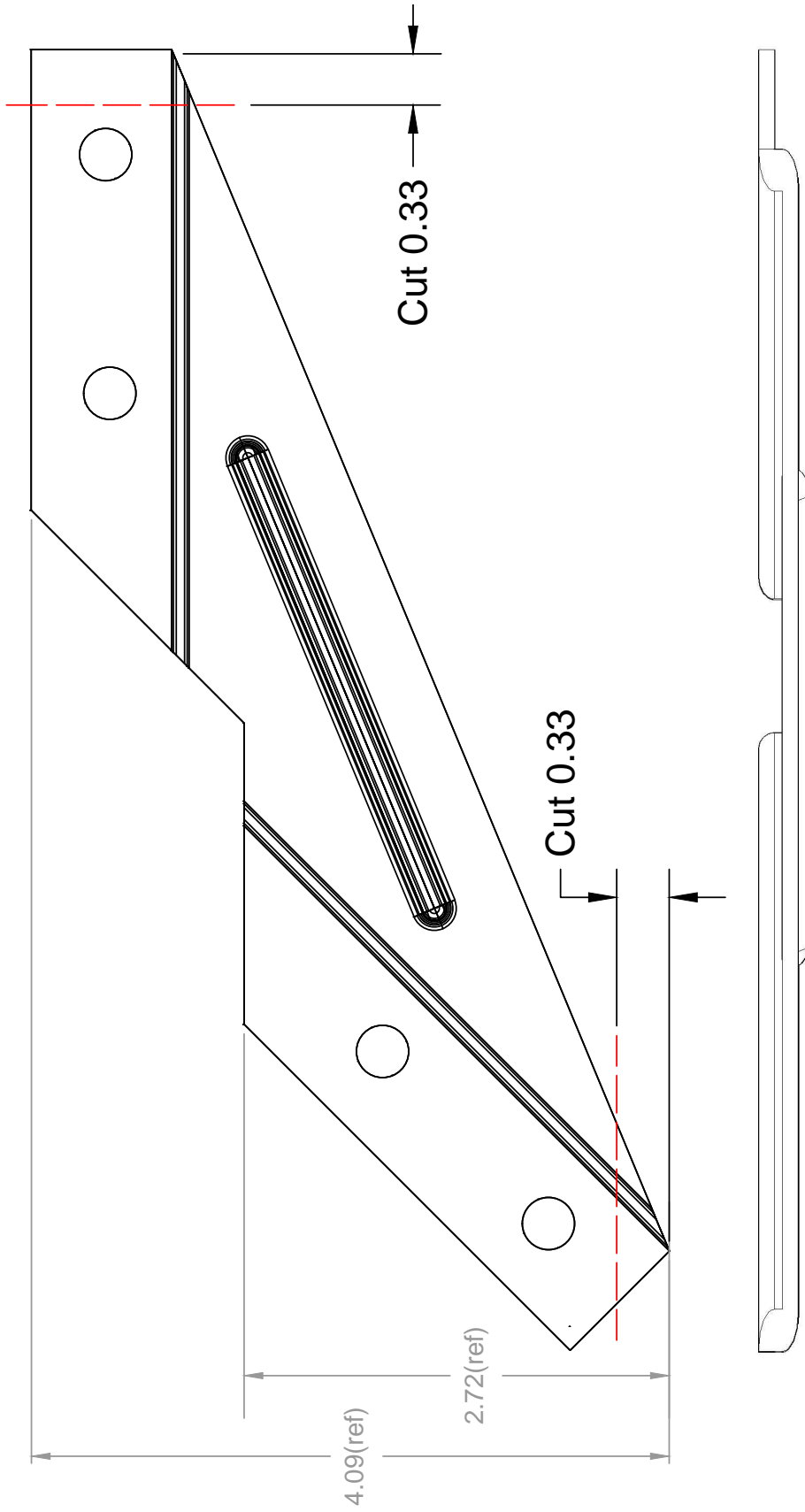
DRAWING SCALE: 0.4000
 DIMENSIONS IN INCHES



DRAWN BY: Katrina Leaptrot
DATE DRAWN: 02/01/12
MATERIAL: GatorJaw GJX175
QUANTITY: 4
TITLE: Chamber 2 Angled Support Beam

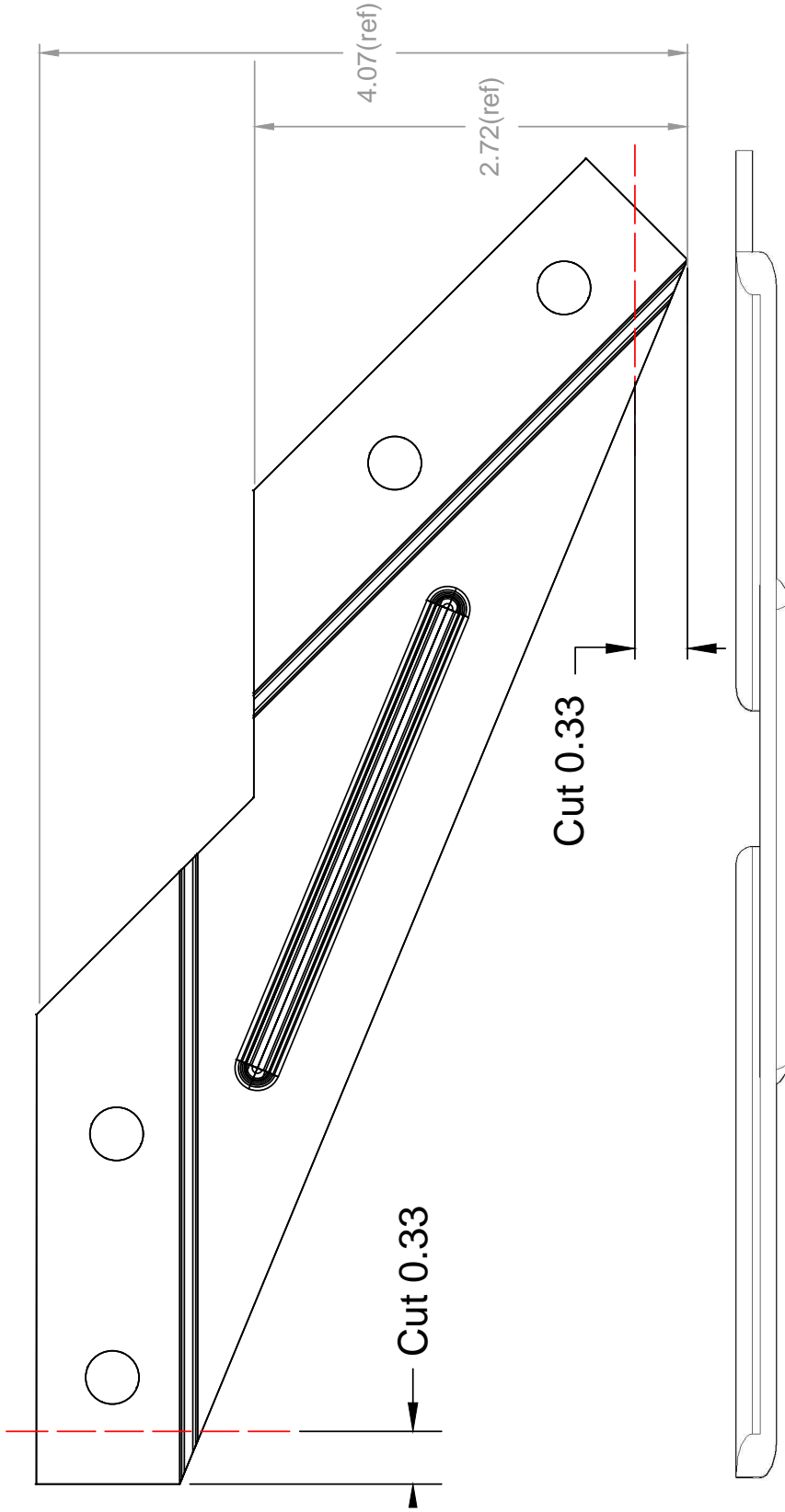
TOLERANCES:
 X.XX ±0.010
 Angles ±0.5°

DRAWING SCALE: 1.000
DIMENSIONS ARE IN INCHES



DRAWN BY: Katrina Leaprot
DATE DRAWN: 02/01/12
MATERIAL: GatorJaw Outer 45° Brackets
QUANTITY: Modify 4 Existing Parts
TITLE: Modified GJ Bracket Type 1

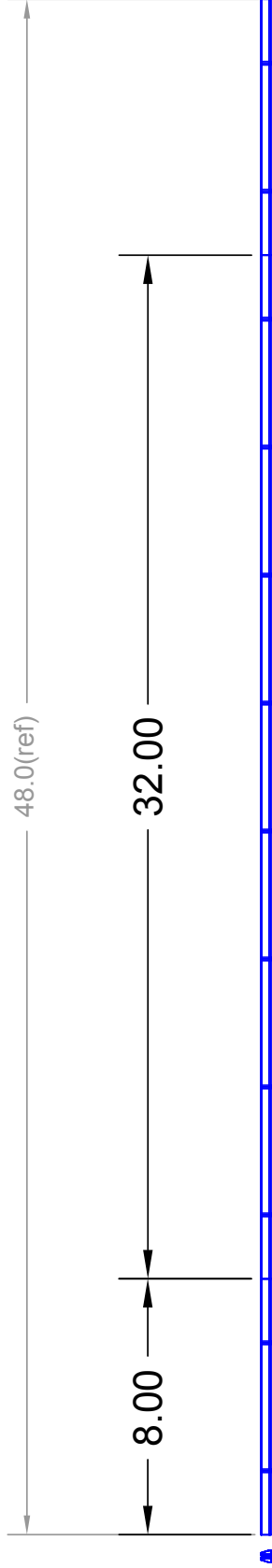
TOLERANCES:
 X.XX ±0.050
DRAWING SCALE: 1.000
DIMENSIONS IN INCHES



TOLERANCES:
 X.XX ±0.050
 DRAWING SCALE: 1.000
 DIMENSIONS IN INCHES

DRAWN BY: Katirina Leaptrot
DATE DRAWN: 02/01/12
MATERIAL: GatorJaw Outer 45° Brackets
QUANTITY: Modify 2 Existing Parts
TITLE: Modified GJ Bracket Type 2

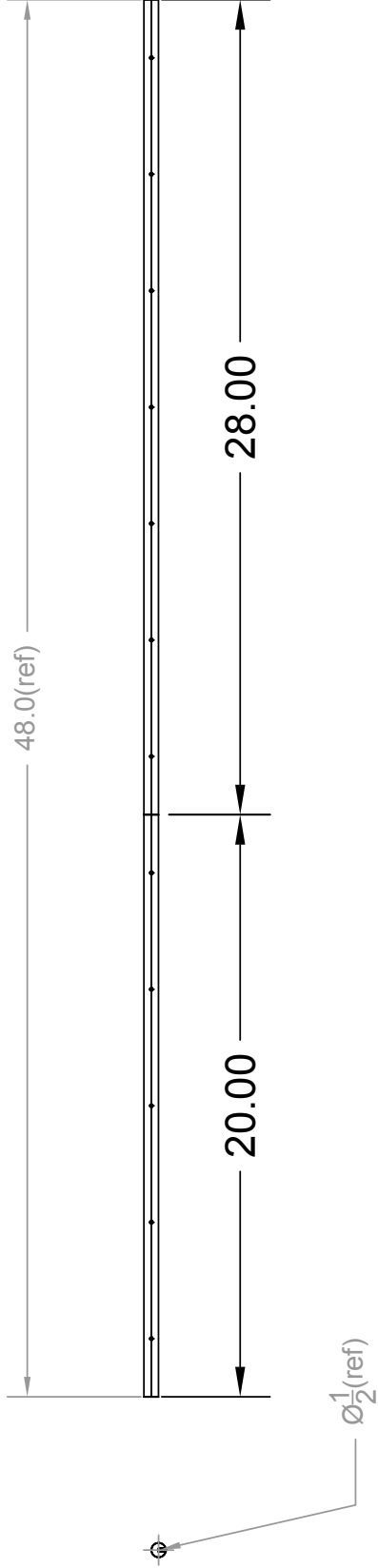
Cut into three pieces as shown



DRAWN BY: Katrina Leaptrot
DATE DRAWN: 02/01/12
MATERIAL: Aluminum Low-Profile Support Rails
QUANTITY: Modify 2 Existing Parts
TITLE: Vacuum Chamber Support Rails

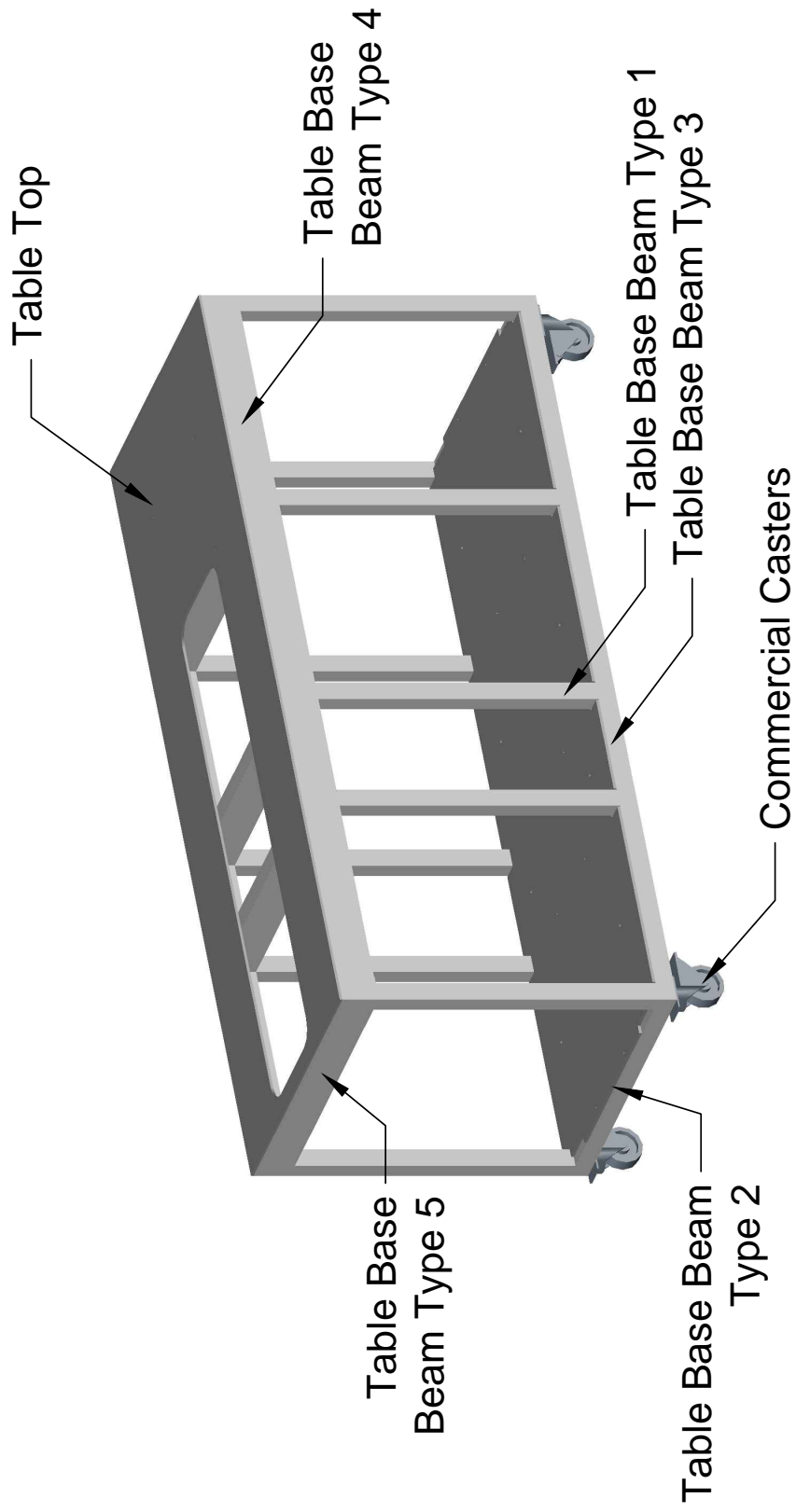
TOLERANCES:
X.XX ±0.050
DRAWING SCALE: 0.200
DIMENSIONS IN INCHES

Cut into two pieces as shown

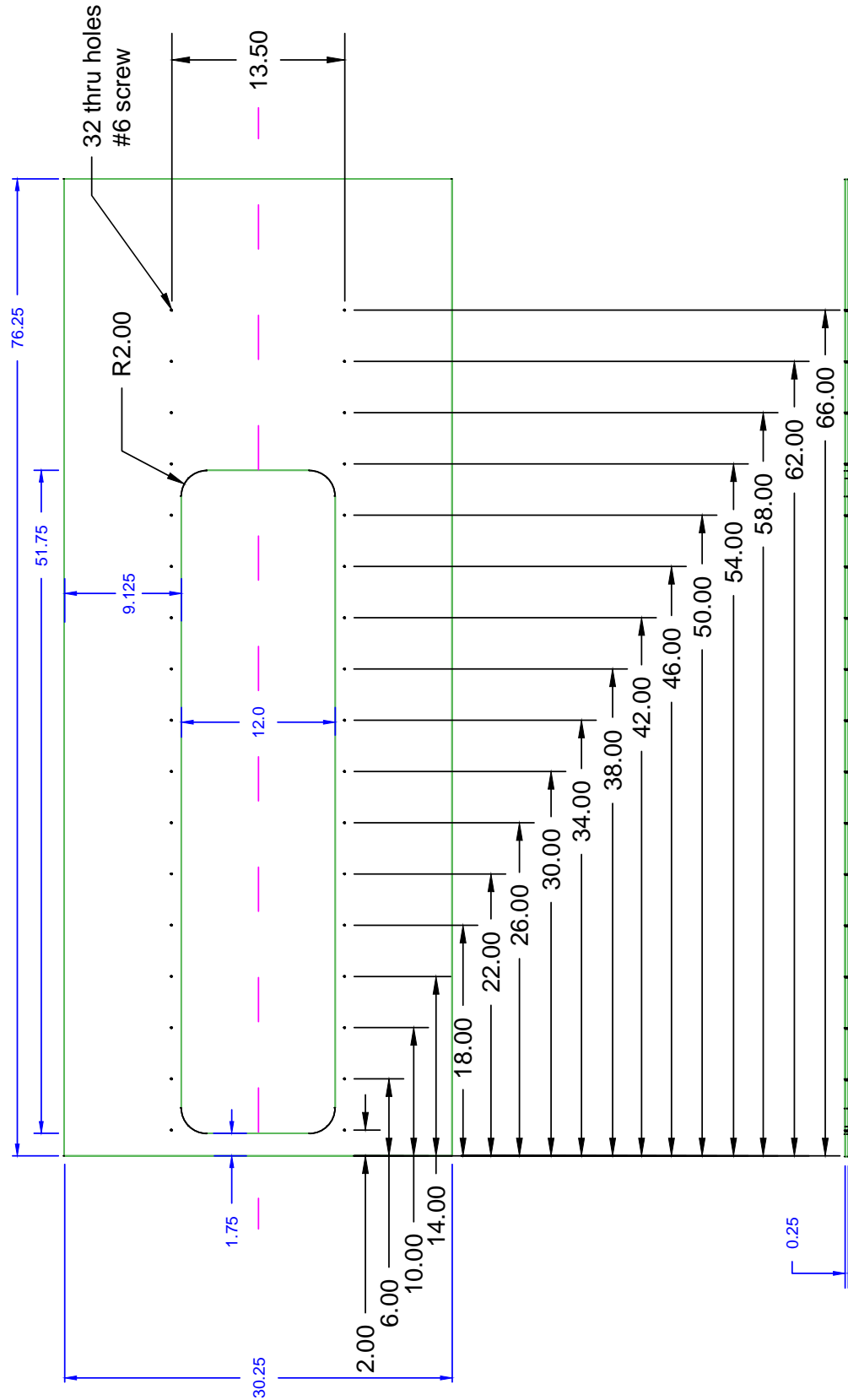


DRAWN BY: Katrina Leaptrot
DATE DRAWN: 02/01/12
MATERIAL: Steel Shafts (Case Hardened)
QUANTITY: Modify 2 Existing Parts
TITLE: Vacuum Chamber Support Shafts

TOLERANCES:
X.XX ±0.050
DRAWING SCALE: 0.175
DIMENSIONS IN INCHES



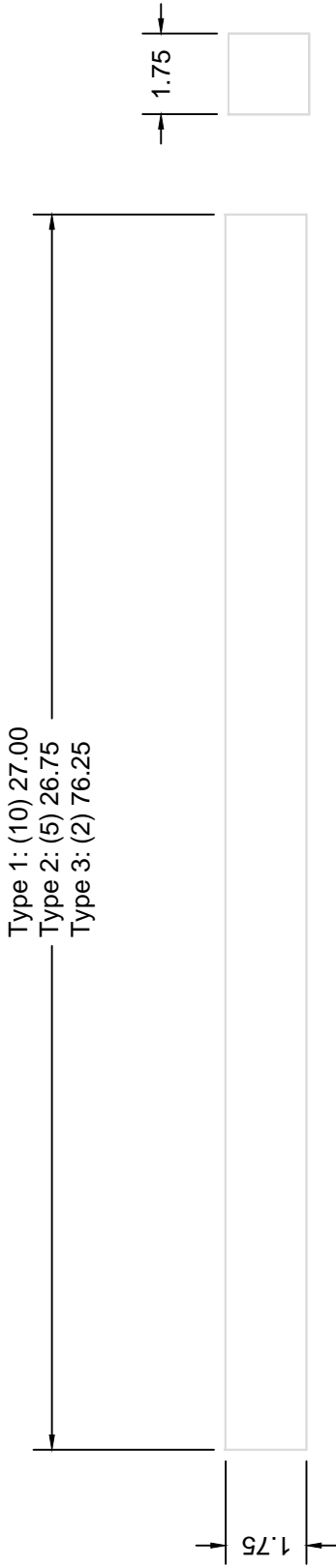
DRAWN BY: Katrina Leaprot
 DATE DRAWN: 11/28/2017
 TITLE: Table Assembly Diagram



DRAWN BY: Katrina Leaptrot
 DATE DRAWN: 01/25/12
 MATERIAL: Aluminum
 QUANTITY: 1
 TITLE: Table Top

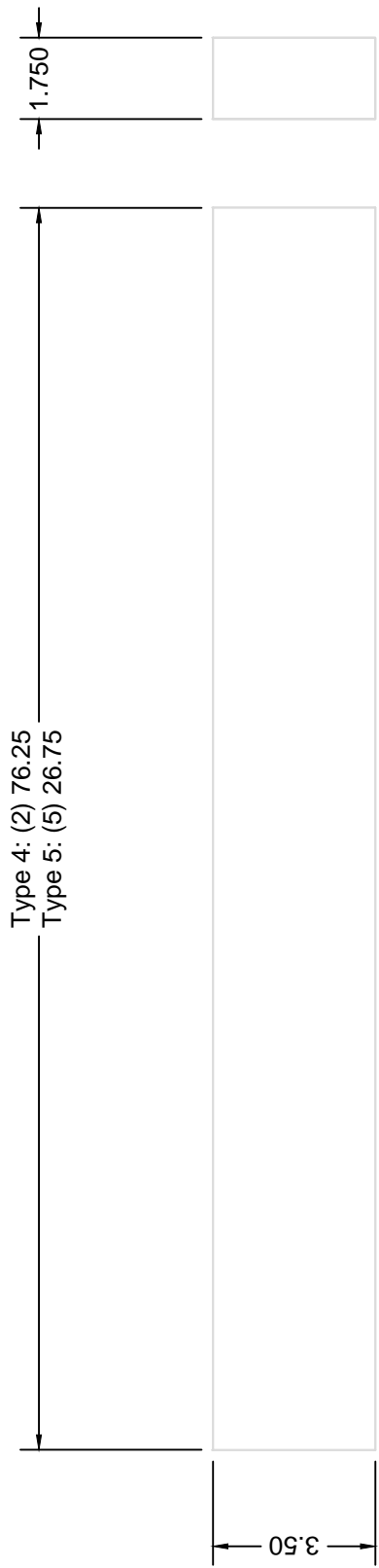
TOLERANCES:
 X.X ±0.030
 X.XX ±0.015
 X.XXX ±0.015

DRAWING SCALE: 0.0871
 DIMENSIONS ARE IN INCHES



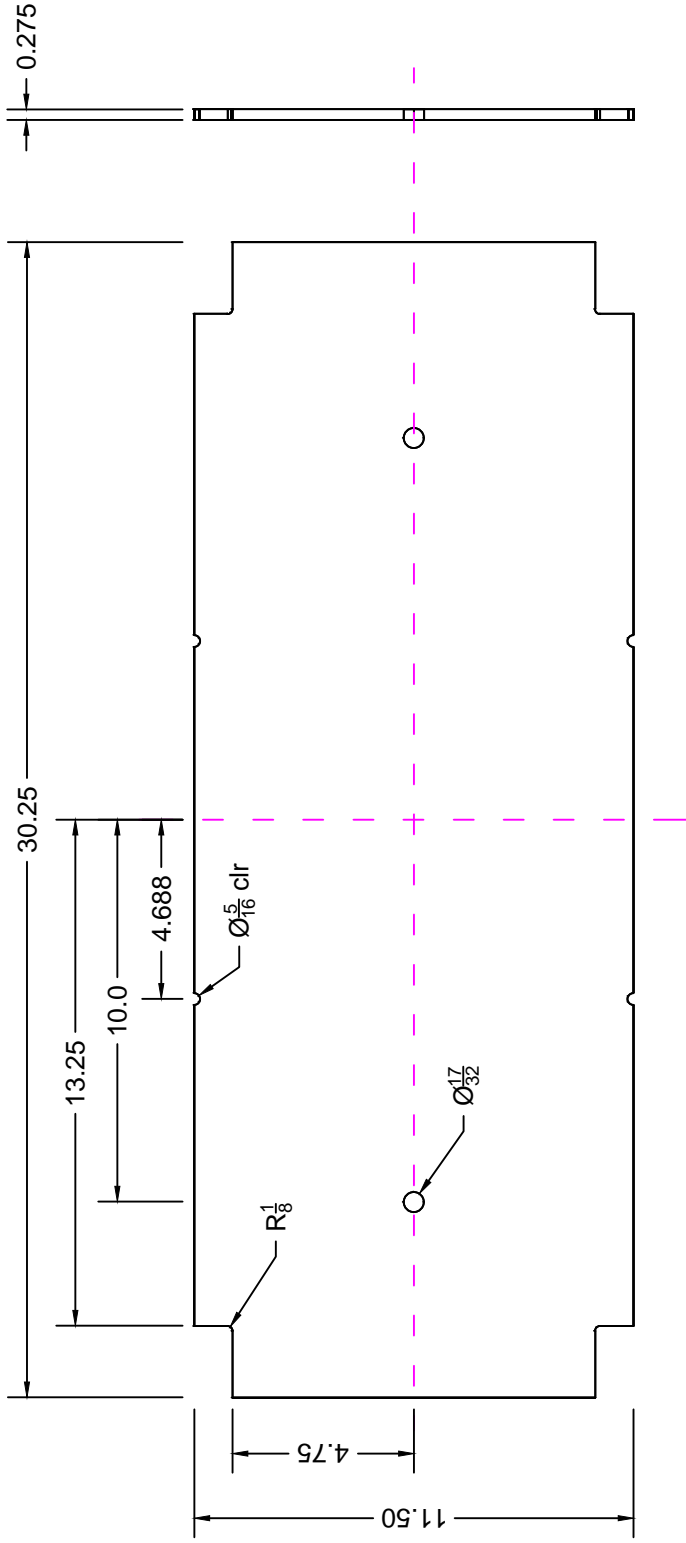
DRAWN BY: Katrina Leaptrot
DATE DRAWN: 12/12/2017
MATERIAL: Gatorjaw Aluminum Extrusion
QUANTITY: 17, of 3 lengths
TITLE: Table Base Beam Type 1, 2, & 3

TOLERANCES:
X.XX ±0.030
DRAWING SCALE: 0.2500
DIMENSIONS IN INCHES



DRAWN BY: Katrina Leaptrot
DATE DRAWN: 12/12/2017
MATERIAL: Gatorjaw Aluminum Extrusion
QUANTITY: 15, of 2 lengths
TITLE: Table Base Beam Type 4 & 5

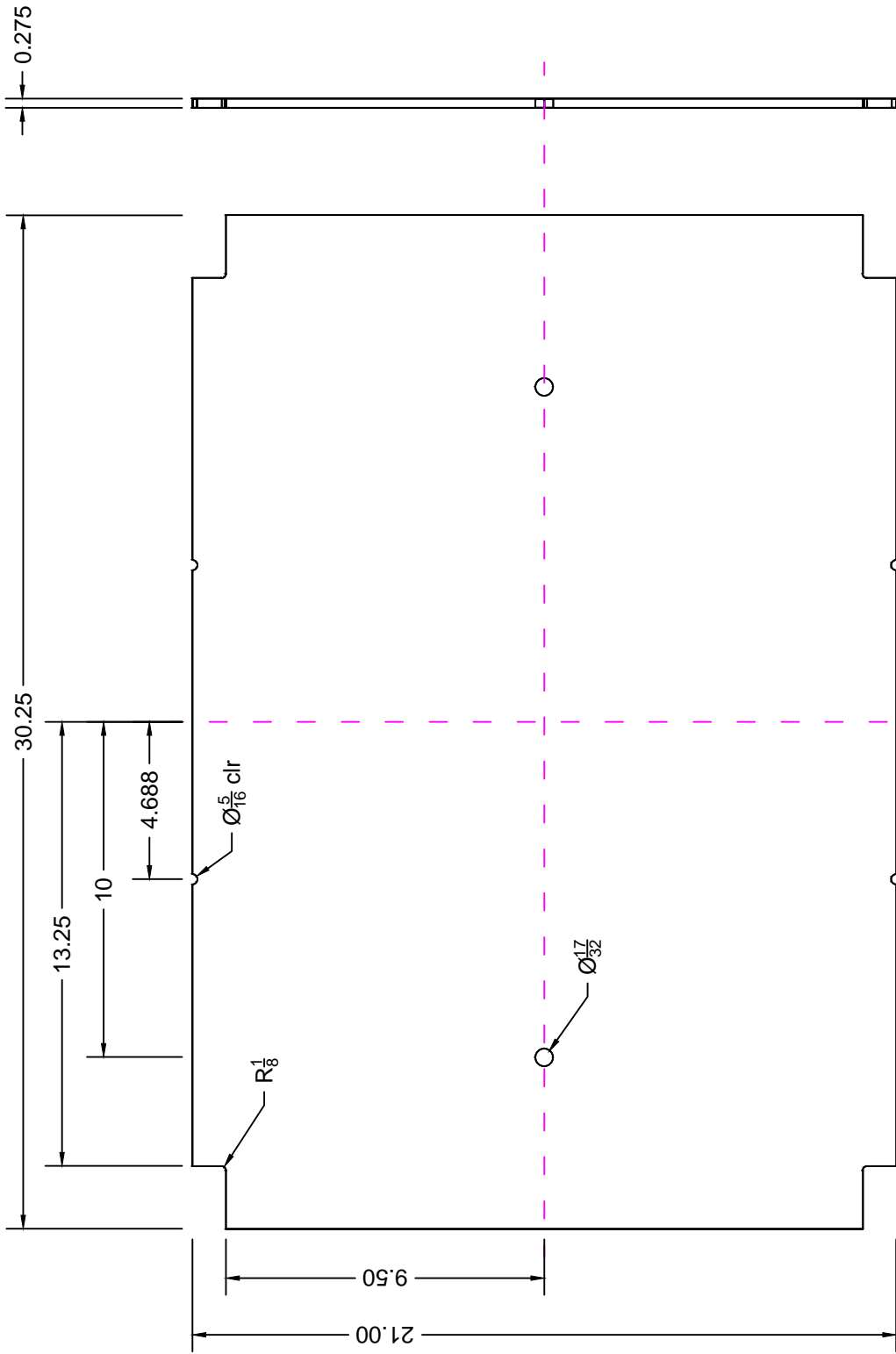
TOLERANCES:
X.XX ±0.030
DRAWING SCALE: 0.2500
DIMENSIONS IN INCHES



DRAWN BY: Katrina Leaptrot
DATE DRAWN: 12/12/2017
MATERIAL: Aluminum
QUANTITY: 1
TITLE: Table Base Panel Type 1

TOLERANCES:
 X.X ±0.040
 X.XX ±0.030
 X.XXX ±0.020
 Fractions ±1/32

DRAWING SCALE: 0.2000
DIMENSIONS IN INCHES



DRAWN BY: Katrina Leaptrot

DATE DRAWN: 12/12/2017

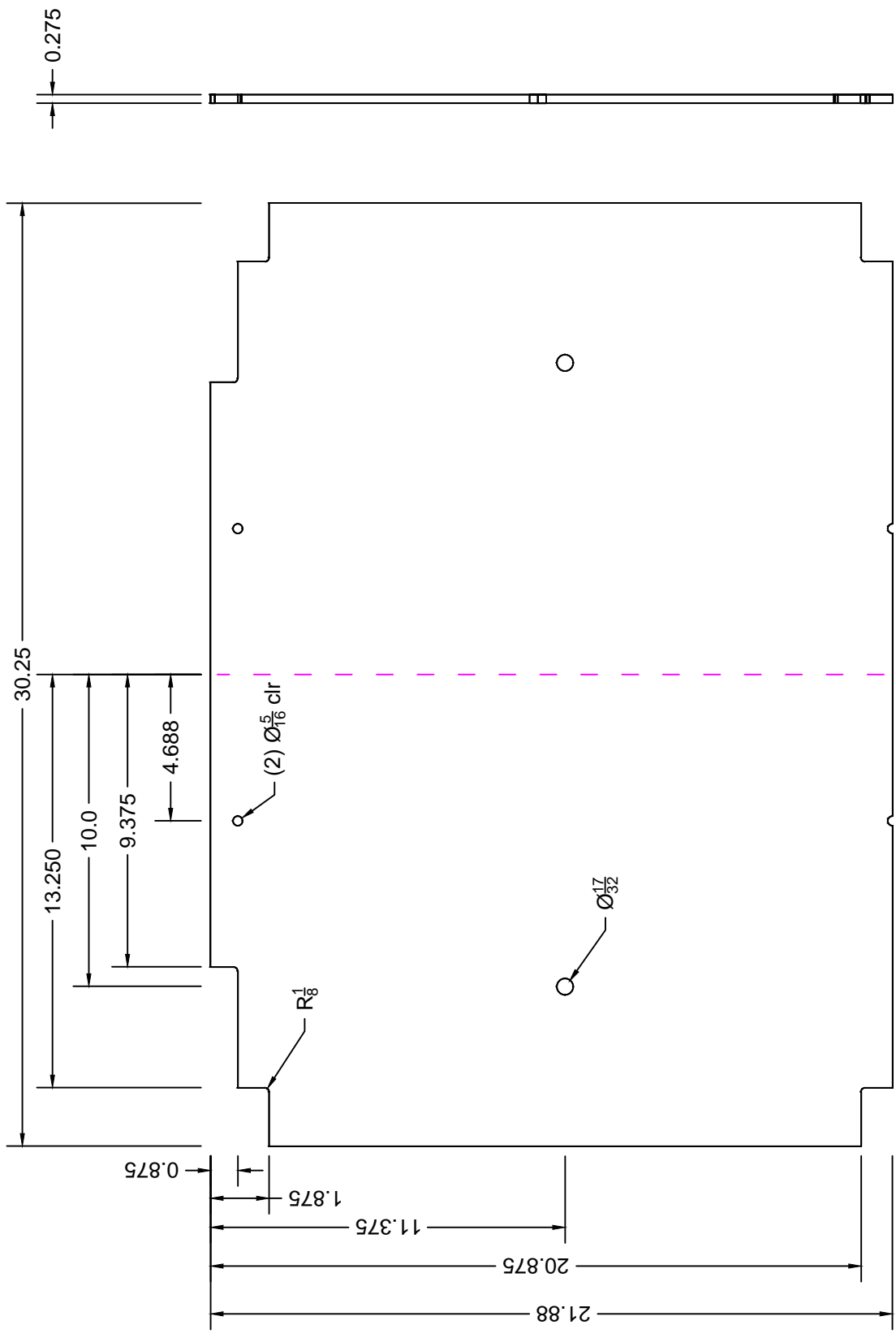
MATERIAL: Aluminum

QUANTITY: 1

TITLE: Table Base Panel Type 2

TOLERANCES:
 X.X ±0.040
 X.XX ±0.030
 X.XXX ±0.020
 Fractions ±1/32

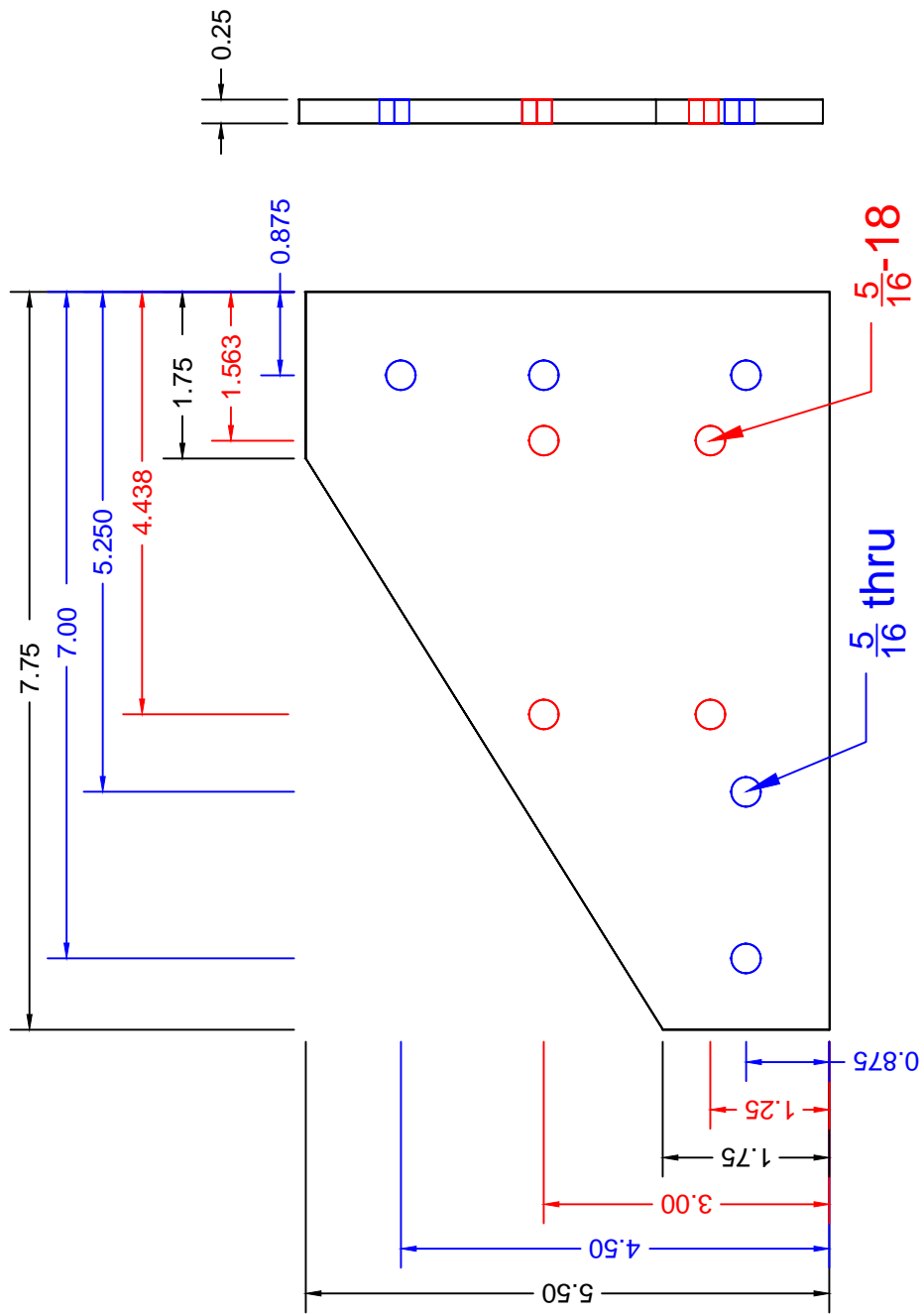
DRAWING SCALE: 0.2000
DIMENSIONS IN INCHES



DRAWN BY: Katrina Leaptrot
 DATE DRAWN: 12/12/2017
 MATERIAL: Aluminum
 QUANTITY: 2
 TITLE: Table Base Panel Type 3

TOLERANCES:
 X.X ±0.040
 X.XX ±0.030
 X.XXX ±0.020
 Fractions ±1/32

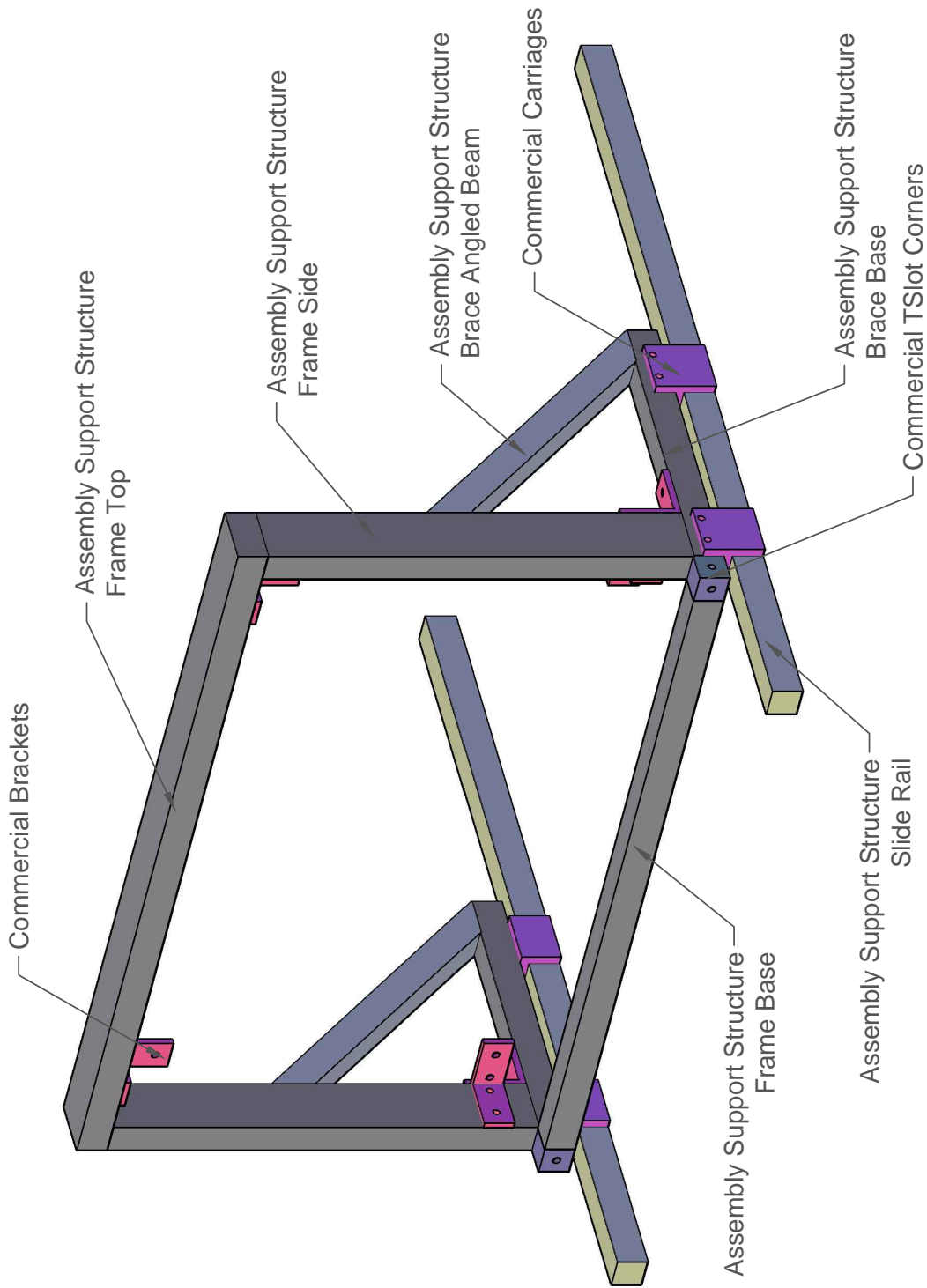
DRAWING SCALE: 0.2000
 DIMENSIONS IN INCHES



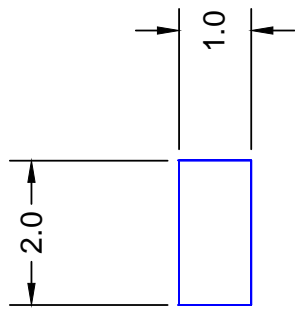
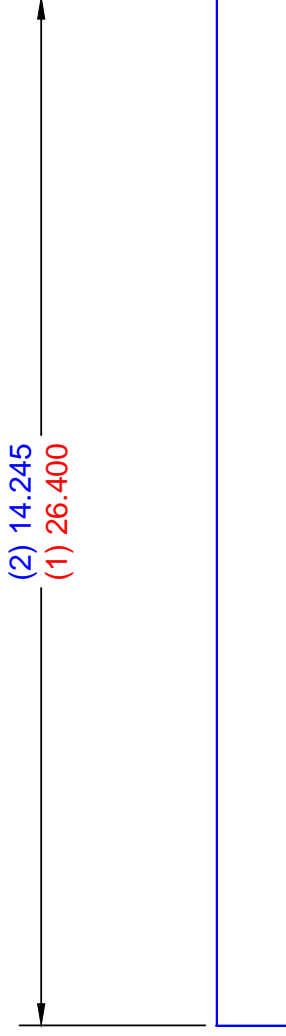
TOLERANCES:
 X.XX ±0.020
 X.XXX ±0.020
 Fractions ±1/32

DRAWN BY: Katrina Leaptrot
DATE DRAWN: 01/05/2017
MATERIAL: Aluminum
QUANTITY: 4
TITLE: Caster Adapter Plate

DRAWING SCALE: 0.5000
 DIMENSIONS IN INCHES

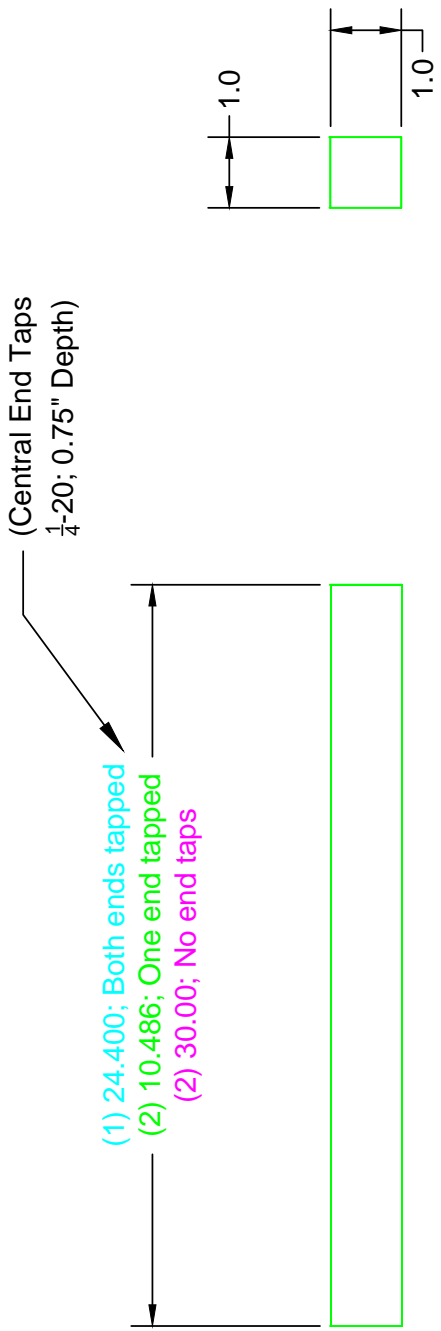


DRAWN BY: Katrina Leaptrot
DATE DRAWN: 11/28/2017
TITLE: Assembly Support Structure Assembly Diagram



DRAWN BY: Katrina Leaprot
DATE DRAWN: 10/31/12
MATERIAL: T-Slot 1"x2"x72" Extrusion
QUANTITY: 3 pieces of 2 designated lengths
TITLE: Assembly Support Structure- Frame
 Sides and Frame Top

TOLERANCES:
 X.X Reference Dimension
 X.XXX ±0.020
DRAWING SCALE: 0.4000
DIMENSIONS IN INCHES



DRAWN BY: Katrina Leaptrot

DATE DRAWN: 10/31/12

MATERIAL: T-Slot 1"X1" Extrusion

QUANTITY: 5 pieces of 3 designated lengths

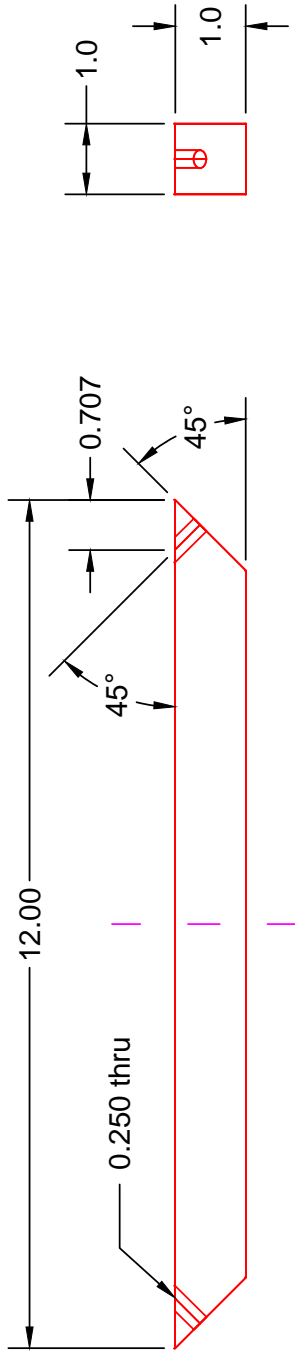
TITLE: Assembly Support Structure- Frame

Base, Brace Base, and Slide Rails

TOLERANCES:

X.X	Reference Dimension
X.XX	±0.050
X.XXX	±0.020

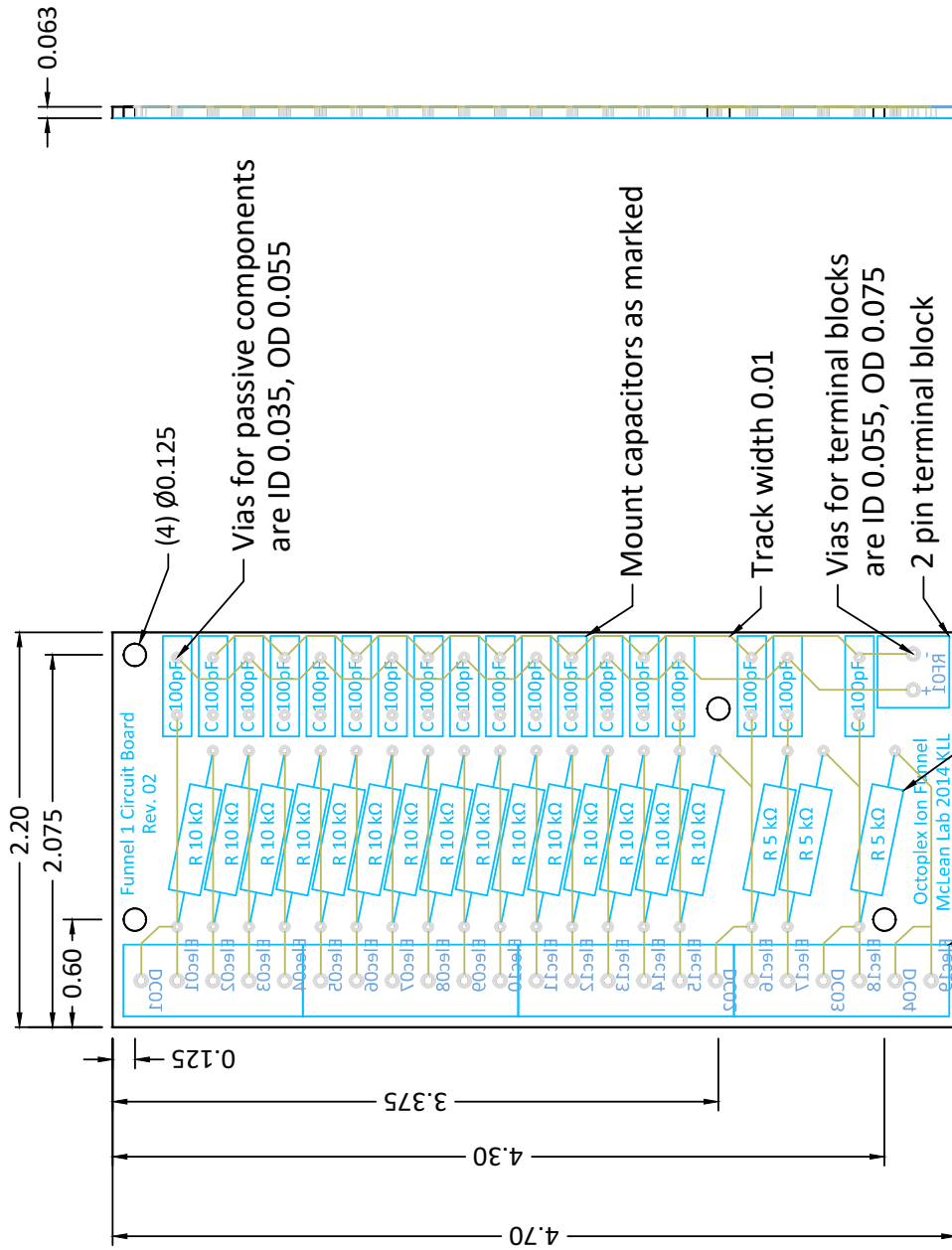
DRAWING SCALE: 0.4000
DIMENSIONS IN INCHES



DRAWN BY: Katie Leaptrot
DATE DRAWN: 10/31/12
MATERIAL: T-Slot 1"X1" Extrusion
QUANTITY: 2
TITLE: Assembly Support Structure- Brace
Angled Beam

TOLERANCES:
 X.X Reference Dimension
 X.XX ±0.050
 X.XXX ±0.015
 Degrees ±1°

DRAWING SCALE: 0.4000
DIMENSIONS IN INCHES



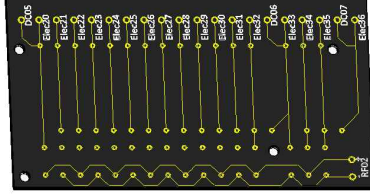
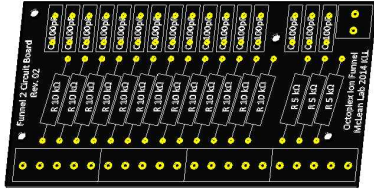
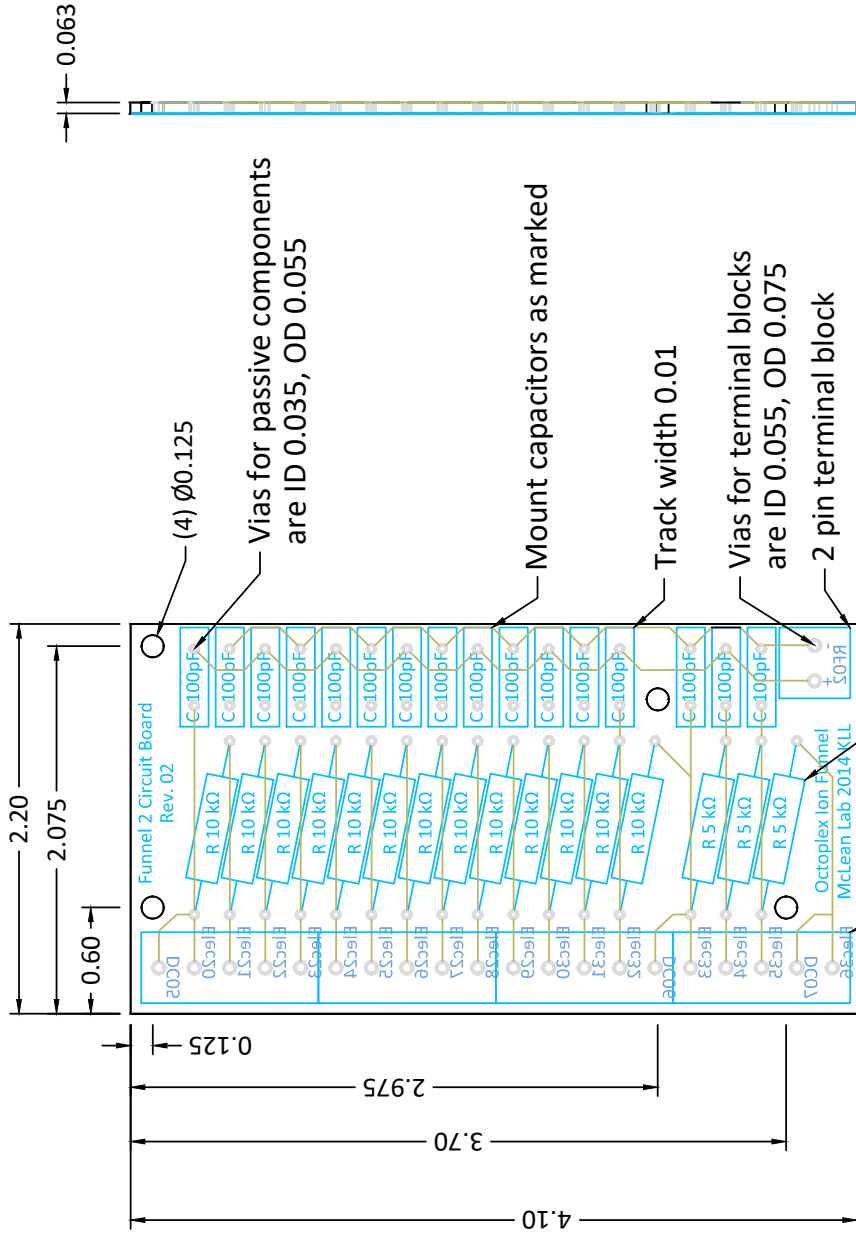
KEY:
EDGE CUTS

VIAS
FRONT SILKSCREEN
BACK SILKSCREEN
BACK COPPER

TOLERANCES:
X.XX ±0.030
X.XXX ±0.020
DRAWING SCALE: 1:0000
DIMENSIONS IN INCHES

DRAWN BY: Katrina Leaptrot
DATE DRAWN: 12/12/2017
MATERIAL: PCB
QUANTITY: 1
TITLE: Funnel 1 RC Circuit Board

COMPONENTS POSITIONED ON A 0.100 GRID
NONESENTIALS OMITTED, FOR SIMPLICITY

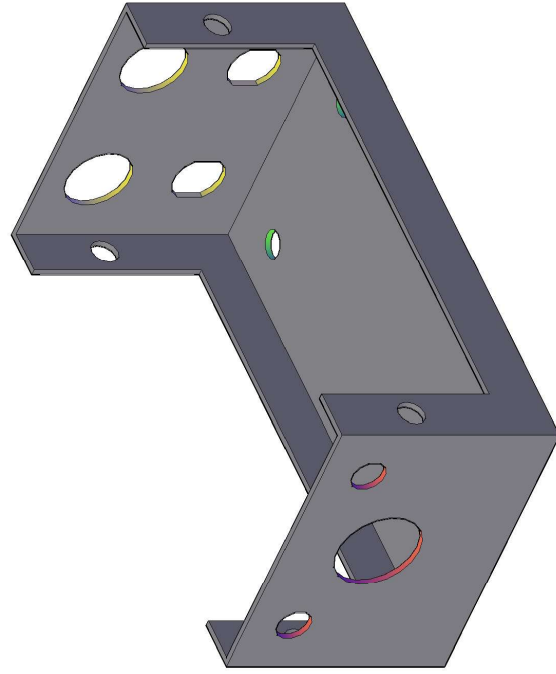
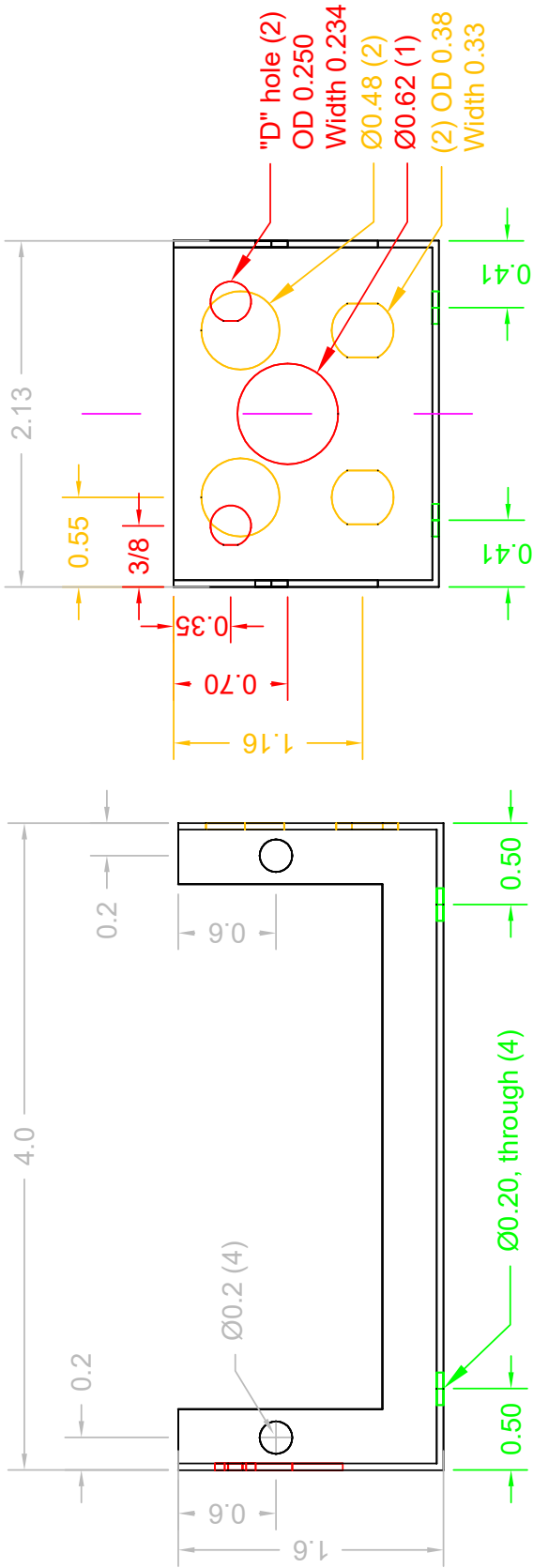


KEY:
 EDGE CUTS
 VIAS
 FRONT SILKSCREEN
 BACK SILKSCREEN
 BACK COPPER

TOLERANCES:
 X.XX ±0.030
 X.XXX ±0.020

DRAWING SCALE: 1.0000
 DIMENSIONS IN INCHES
 COMPONENTS POSITIONED ON A 0.100 GRID
 NONESSENTIALS OMITTED, FOR SIMPLICITY

DRAWN BY: Katrina Leaprot
 DATE DRAWN: 12/12/2017
 MATERIAL: PCB
 QUANTITY: 1
 TITLE: Funnel 2 RC Circuit Board

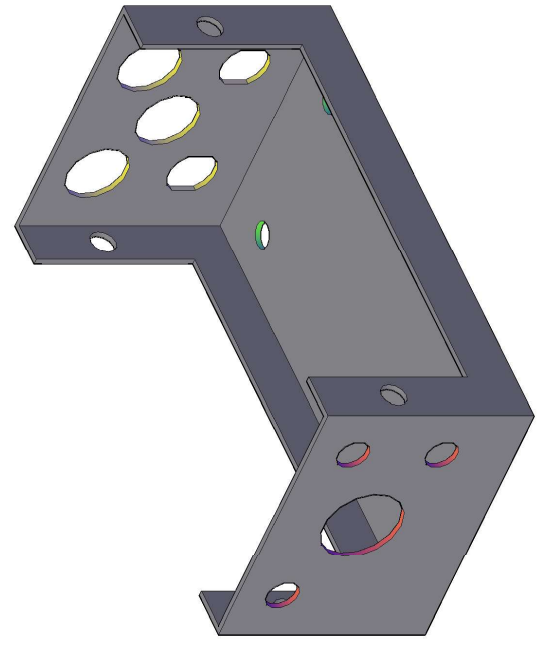
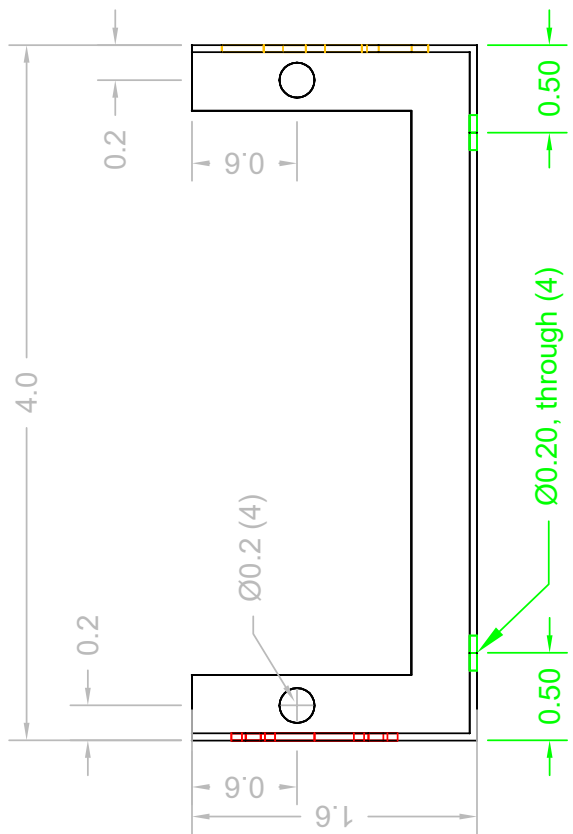
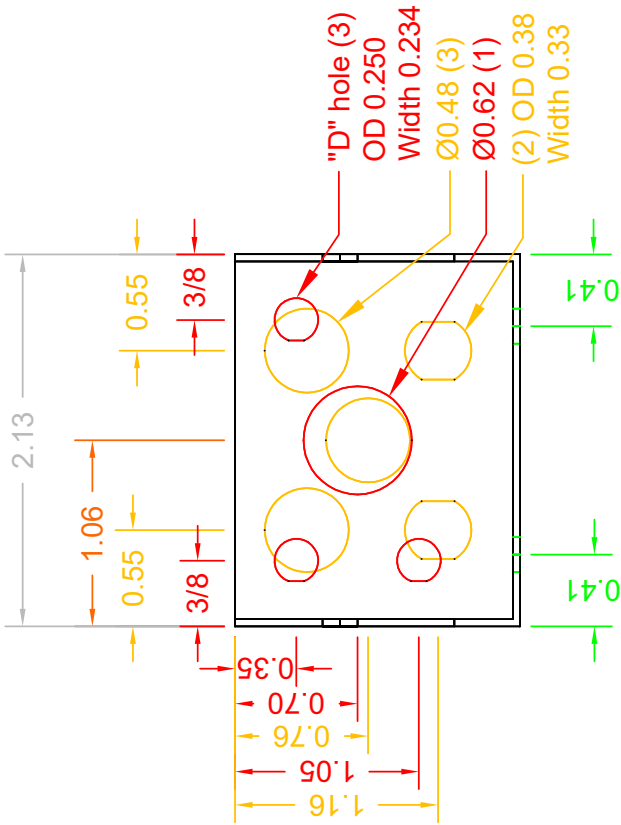


DRAWN BY: Katrina Leaptrot
DATE DRAWN: 10/05/2016
MATERIAL: Bud Aluminum Enclosure
QUANTITY: 1, Modify Existing
TITLE: Funnel 1 Breakout Box

TOLERANCES:

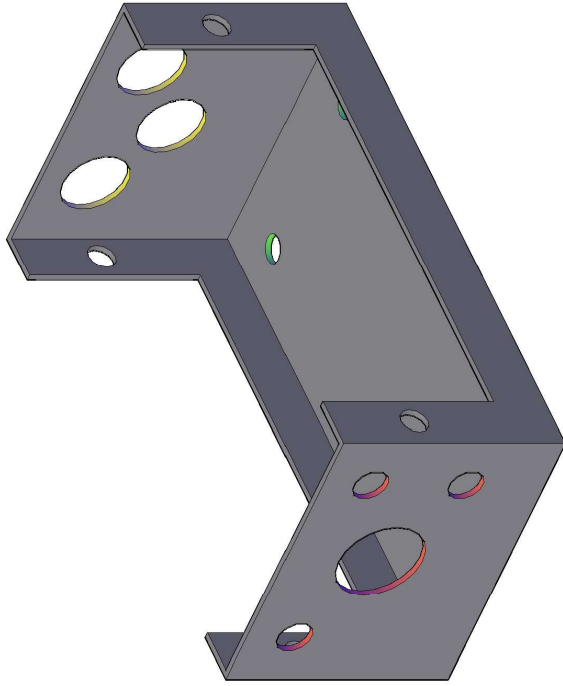
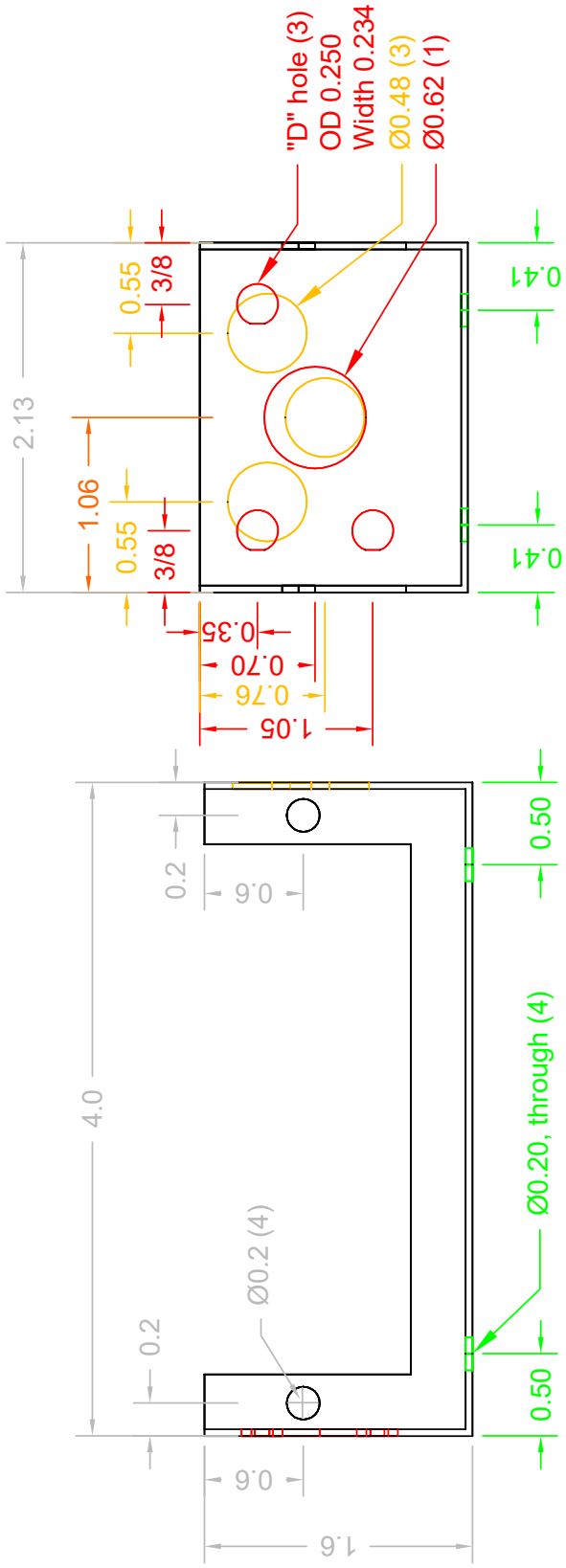
X.X	±0.040
X.XX	±0.030
X.XXX	±0.020
Fractions	±1/32

DRAWING SCALE: 1.0000
DIMENSIONS IN INCHES



DRAWN BY: Katrina Leaprot
DATE DRAWN: 10/05/2016
MATERIAL: Bud Aluminum Enclosure
QUANTITY: 1, Modify Existing
TITLE: Funnel 2 Breakout Box

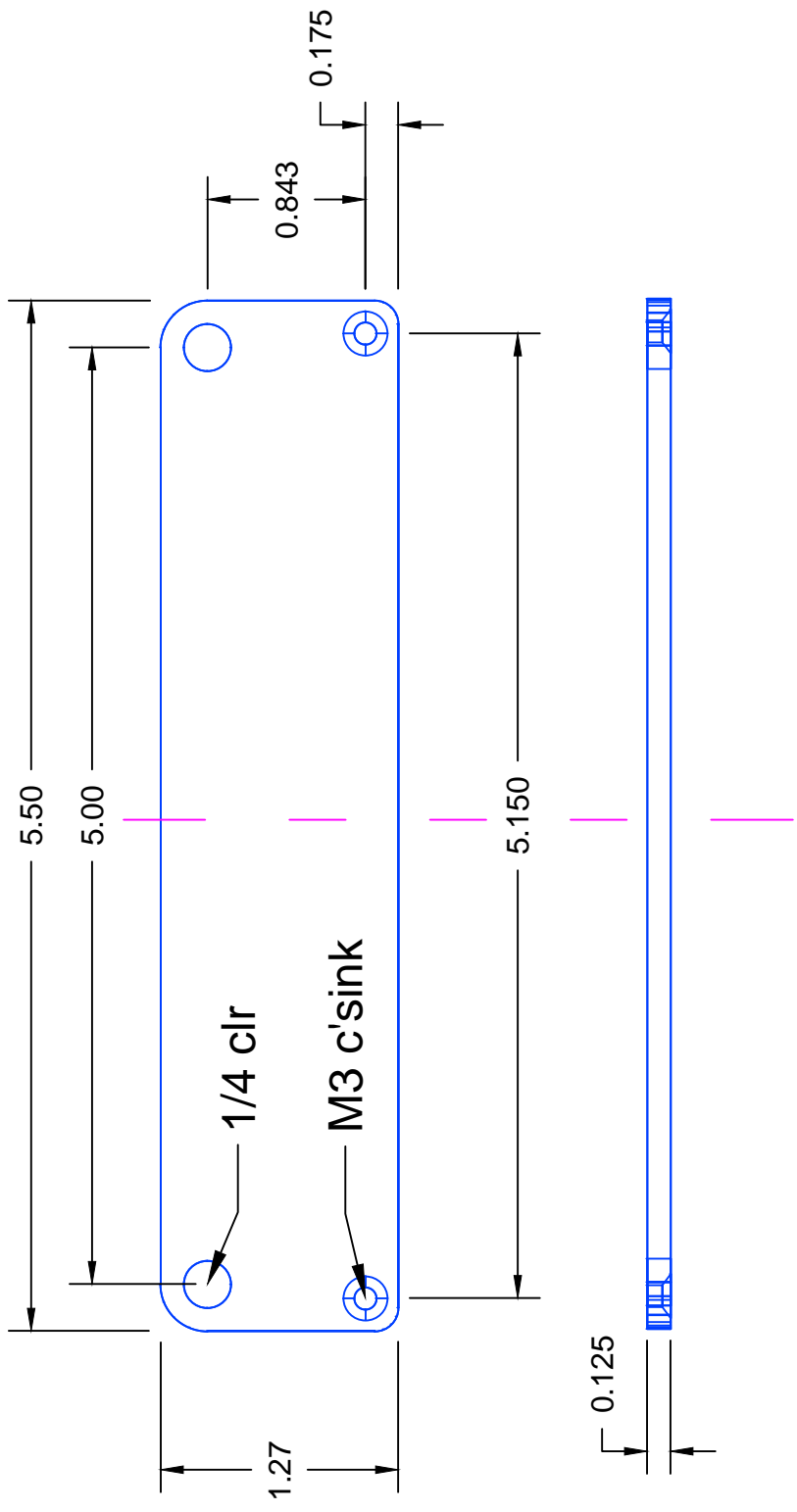
TOLERANCES:
 X.X ±0.040
 X.XX ±0.030
 X.XXX ±0.020
 Fractions ±1/32
DRAWING SCALE: 1.0000
DIMENSIONS IN INCHES



DRAWN BY: Katrina Leaptrot
DATE DRAWN: 10/05/2016
MATERIAL: Bud Aluminum Enclosure
QUANTITY: 1, Modify Existing
TITLE: Drift Tube Breakout Box

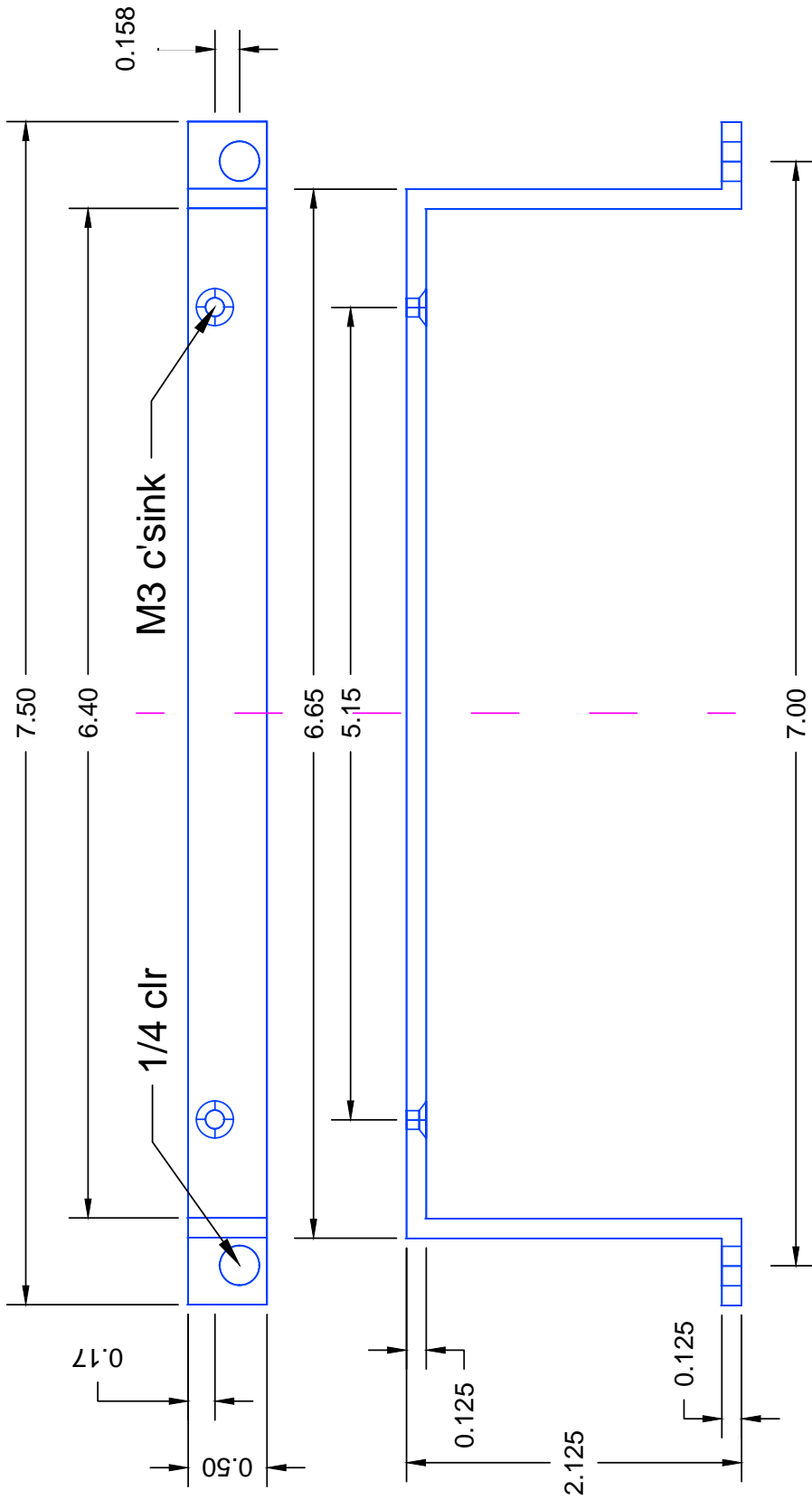
TOLERANCES:
 X.X ±0.040
 X.XX ±0.030
 X.XXX ±0.020
 Fractions ±1/32

DRAWING SCALE: 1.0000
DIMENSIONS IN INCHES



DRAWN BY: Katrina Leaptrot
DATE DRAWN: 10/20/14
MATERIAL: Aluminum
QUANTITY: 12
TITLE: Flat Power Supply Mounting Bracket

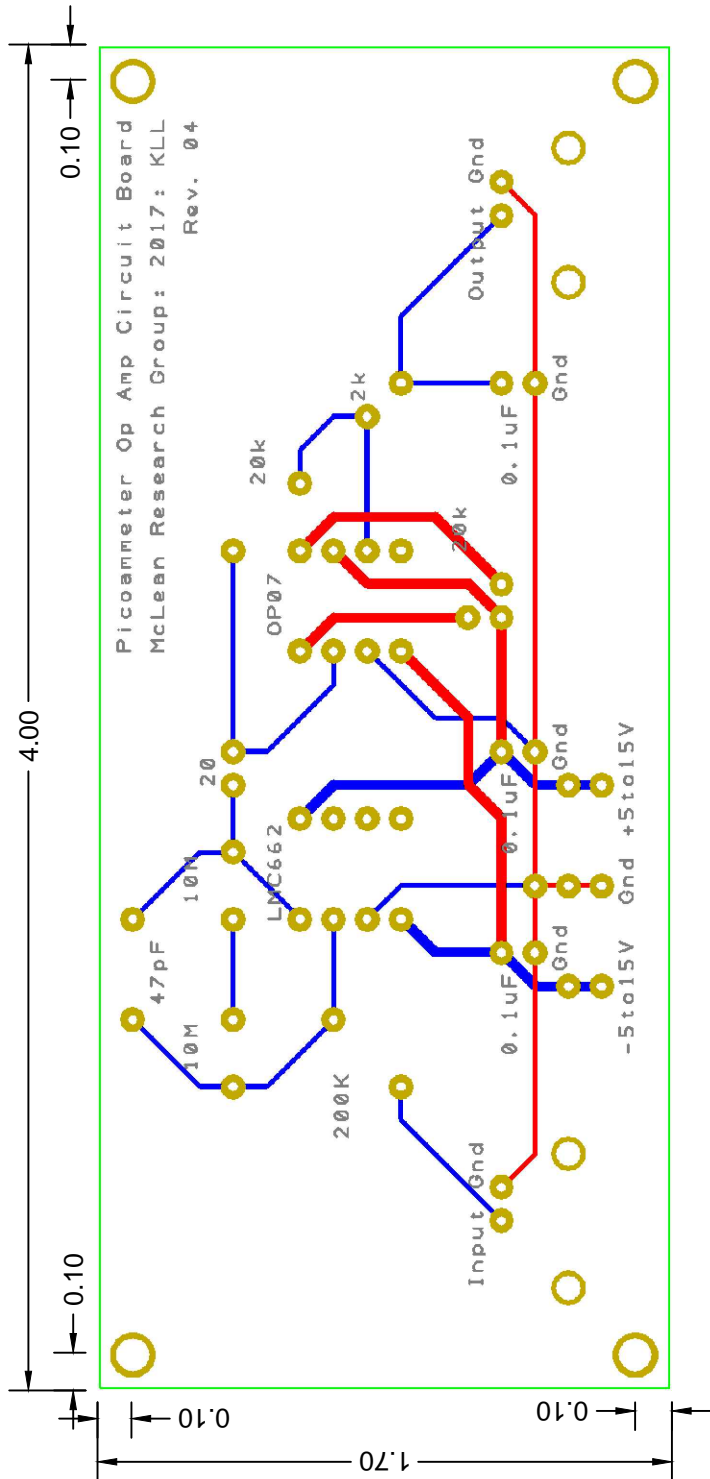
TOLERANCES:
 X.XX ±0.020
 X.XXX ±0.010
DRAWING SCALE: 1.0000
DIMENSIONS IN INCHES



TOLERANCES:
 X.XX ±0.020
 X.XXX ±0.010

DRAWING SCALE: 1.0000
 DIMENSIONS IN INCHES

DRAWN BY: Katrina Leaptrot
DATE DRAWN: 10/20/14
MATERIAL: Brass
QUANTITY: 8
TITLE: Lofted Power Supply Mounting Bracket



DRAWN BY: Katrina Leaptrot
DATE DRAWN: 10/06/2018
MATERIAL: 0.0625" PCB
QUANTITY: 1
TITLE: Op Amp Circuit Board

TOLERANCES:
 X.XX ±0.030
DRAWING SCALE: 0.05714
DIMENSIONS IN INCHES

KEY:
 EDGE CUTS
 FRONT COPPER
 FRONT SILKSCREEN
 BACK COPPER
 VIAS

COMPONENTS POSITIONED ON A 0.100 GRID
 NONESSENTIALS OMITTED, FOR SIMPLICITY

Commercial Components

Associated Component	Description	Qty	Dimensions/Values	Details (Material, Part Number, etc.)	Supplier or Manufacturer
HARDWARE					
Electrospray Ionization Source					
	Single-Syringe Infusion Pump	8	8.33 mL/min max	SK-74900-00	Cole-Parmer
	Fused Silica Capillary Tubing	x	220 µm ID, 360 µm OD	Methyl Deactivated, 0624469	SGE
	Monochrome CCD DSP Camera	1	0.33", 12 VDC	IV-BWCAM3EX	RMA Elec.
	C-Mount Coupler	1	0.69" length	1-6010	Navitar
	Adapter 2X	1	6.25" length	1-6030	Navitar
	Monochrome Monitor	1	12" display	HMM12	Honeywell
ESI Base Plate					
	Mounted Linear Sleeve Bearings	4	0.5" ID, 1.5" length	AI/PTFE, 8649T13	McMaster
	Bolt	16	#6 - 32 x 0.5"	SHC, SST	McMaster
	Flat Washer	16	#6	SST	McMaster
ESI Brass Floating Nut					
	Bolt	4	1/4 - 28 x 0.75"	Pan Head, SST	McMaster
ESI XYZ to Goniometer Adapter					
	RollerBlock/Micrometer (XYZ)	1	13 mm XYZ travel	RB13M	ThorLabs
	Bolt for Adapter to XYZ	4	M4 x 14	SHC, SST, 92290A150	McMaster
	Goniometer	1	20°, 100 mm center	123-2840	OptoSigma
	Bolt for Goniometer to Adapter	4	1/4 - 20 x 0.75"	SHC, SST	McMaster
ESI Holster Base					
	Bolt to Goniometer	4	1/4 - 20 x 5/8"	SHC, SST	McMaster
ESI Holster Wedge					
	Bolt	12	#4 - 40 x 0.375"	SHC, SST	McMaster
ESI Spring-Loaded Floating Nut					
	Bolt	32	#4 - 40 x 0.75"	SHC, SST	McMaster
	Flat Washer	32	#4	SST	McMaster
ESI Spring-Loaded Top					
	Spring	8	0.75" length, 0.18" OD	Music Wire Steel, 9044K128	McMaster
	Bolt for Spring	16	#2 - 56 x 0.375"	Pan Head, SST	McMaster

Commercial Components

Associated Component	Description	Qty	Dimensions/Values	Details (Material, Part Number, etc.)	Supplier or Manufacturer
	Bolt for Positioning	8	#4 - 40 x 1.25"	SHC, SST	McMaster
	Flat Washer	8	#4	SST	McMaster
	Tee Assembly	8	0.020" thru, mountable	PEEK, P-727	IDEX
	Finger Tight Fitting Coned	24	1/16" ID, #10 - 32	PEEK, F-120	IDEX
	MicroTight Sleeve Green	24	1/16" OD, 0.033" ID	PEEK, F-247	IDEX
	Bolt to PEEK Tee	16	#4 - 40 x 0.625"	SHC, SST	McMaster
	Flat Washer	16	#4	SST	McMaster
	Platinum Wire	8	99.95%, 0.010" OD, 1'	1972	SurePure
	ESI Capillary	8	0.005"ID, 0.01" OD	316 St. Steel, 89875K93	McMaster
Atmospheric Inlet and Desolvation					
Heated Desolvation Block					
	Resistive Glass Capillary	8	180 mm, 500 µm ID	Fieldmaster Ion Guide	Photonis
	Spring	8	0.5" length, 0.3" OD	Music Wire Steel, 9001T16	McMaster
	O-ring	8	011	Viton, 9464K16	McMaster
	Insulated Wire	1	4'	Kapton Coated	Accu-Glass
	Autotune Temperature Controller	2	0.1 steps to 200°C	C9000A	Omega
	Bolt thru Insulator Flange to Top Hat	10	1/4 - 28 x 0.875", SHC	WS ₂ Coated, C-2814-NW	UC Comp.
Insulator Flange for Desolvation Block					
	O-ring	2	263	Viton, 9464K562	McMaster
Chamber 1 Top Hat Flange					
	O-ring	1	383	Viton, 9464K647	McMaster
	Bolt thru Top Hat/Extension to 3/4"	20	5/16 - 18 x 2.5"	SHC, SST	McMaster
Extension Collar					
	O-ring	1	383	Viton, 9464K647	McMaster
	Bolt	4	5/16 - 18 x 1.75"	SHC, SST	McMaster
RGC Electrical Feedthrough Piston Seal					
	O-ring	2	112	Viton, 9464K25	McMaster
	Bolt	6	#8-32 x 0.25"	SHC, SST	McMaster
	Single Pin Feedthrough	1	5 kV, 1 A	SST, Ceramic, EFT0512051	K. J. Lesker

Commercial Components

Associated Component	Description	Qty	Dimensions/Values	Details (Material, Part Number, etc.)	Supplier or Manufacturer
	Sealing Compound	1	Compound Q	Apiezon, APQL	K. J. Lesker
	Connector Pin	1	0.050" ID, #4 - 40 set	Beryllium-Copper, 9924001	MDC Vacuum
Chamber 1, 3/4" Flange					
	Bolt to Chamber 1 Front Flange	46	5/16 -18 x 1.75"	SHC, SST	McMaster
	Hex Nut	31	5/16 -18	WS ₂ Coated, N-3118-W	UC Comp.
	Flat Washer Narrow	46	5/16, 0.688" OD	SST	McMaster
First Vacuum Chamber					
Chamber 1 Front Flange					
	O-ring	1	386	Viton, 9464K651	McMaster
Chamber 1 Bottom Flange					
	CF Half Nipple	1	6" CF	304 St. Steel, HN-0600RT	K. J. Lesker
	Bolt	16	5/16 - 24 x 1.25"	SHC, SST	McMaster
	Flat Washer	16	5/16	SST	McMaster
	Gasket	2	For 6" CF	Cu	Duniway
	CF Zero Length Reducer	1	6" CF to 2.75" CF	304 St. Steel, RF600X275	K. J. Lesker
	Bolt	6	1/4 - 28 x 0.875"	SHC, SST	McMaster
	Flat Washer	6	1/4	SST	McMaster
	Gasket	2	For 2.75" CF	Cu	Duniway
	CF to KF Adapter	1	2.75" CF to KF-40	304 St. Steel, F0275XQF40	K. J. Lesker
Chamber 1 Feedthrough Flange					
	CF Half Nipple	2	2.75" CF	304 St. Steel, HN-0275SSRT	K. J. Lesker
	Bolt	12	1/4 - 28 x 0.875"	SHC, SST	McMaster
	Flat Washer	12	1/4	SST	McMaster
	Gasket	2	For 2.75" CF	Cu	Duniway
	CF Half Nipple	2	1.33" CF	304 St. Steel, HN-0133RT	K. J. Lesker
	Bolt	12	#8 - 32 x 0.5"	SHC, SST	McMaster
	Flat Washer	12	#8	SST	McMaster
	Gasket	2	For 1.33" CF	Cu	Duniway
	Blank CF	2	1.33" CF	304 St. Steel, F0133X000N	K. J. Lesker

Commercial Components

Associated Component	Description	Qty	Dimensions/Values	Details (Material, Part Number, etc.)	Supplier or Manufacturer
Chamber 1 Top Flange					
	O-ring	1	384	Viton, 9464K848	McMaster
Chamber 1 Back Flange					
	Bolt to Chamber 2 Front Flange	46	5/16 -18 x 1.5"	SHC, SST	McMaster
	Hex Nut	31	5/16 -18	WS ₂ Coated, N-3118-W	UC Comp.
	Flat Washer Narrow	46	5/16, 0.688" OD	SST	McMaster
Inner Vacuum Chamber					
Inner Chamber Smaller; Face Seal					
	Vented Bolt to 3/4" Flange	24	1/4 - 20 x 0.75"	SHC, SST, C-2012	UC Comp.
	Flat Washer Narrow	24	1/4, 0.625" OD	SST	McMaster
	O-ring	2	278	Viton, 9464K154	McMaster
Floating Nut, Cut					
	Bolt to secure Inner Chamber halves	24	1/4 - 20 x 0.75"	SHC, SST	McMaster
Inner Chamber					
	9 Pin C-Type Feedthrough	1	On KF-16 flange	1000011	Accu-Glass
	Bulkhead Clamp	1	KF-16	Al, QF16-075-BC	K. J. Lesker
	Centering Ring	1	KF-16	Al, Viton, QF16-075-ARV	K. J. Lesker
	90° Radius Elbow	1	KF-25	316 St. Steel, QF25-100-E90	K. J. Lesker
	Bulkhead Clamp	1	KF-25	Al, QF25-10-BC	K. J. Lesker
	Vented Bolt for Bulkhead Clamp	12	#10 - 24 x 0.625"	SST	McMaster
	Flat Washer Narrow	12	#10, 0.5" OD	SST	McMaster
	Flanged Unbraided Bellows	1	KF-25, 12" length	300 St. Steel, MH-QF-B12	K. J. Lesker
	Lever Clamp	2	0.5 lb	Al, QF25-100-CHA	K. J. Lesker
	Centering Ring	3	KF-25	Al, Viton, QF25-100-ARV	K. J. Lesker
	O-ring	8	0.18	Viton, 9464K72	McMaster
	Flat Washer	10	1/4	SST, Corona Dope Coated	McMaster
	Super Corona Dope	1	4100 V/mil	70125548	Allied
	Self-Sealing Hex Nut	10	1/4 - 20	SST, Silicone, 91339A130	McMaster

Commercial Components

Associated Component	Description	Qty	Dimensions/Values	Details (Material, Part Number, etc.)	Supplier or Manufacturer
Ion Funnel					
Funnel 1 Mount Block					
	Hex Nut	10	1/4 - 28, 5/32" high	SST	McMaster
	Vented Bolt to Top Hat Flange	14	5/16 - 24 x 1"	SHC, SST	UC Comp.
	Flat Washer Narrow	14	5/16, 0.688" OD	SST	McMaster
Second Vacuum Chamber					
	Chamber 2 Front Flange				
	O-ring	1	386	Viton, 9464K651	McMaster
Chamber 2 Bottom Flange					
	CF Half Nipple	1	8" CF	304 St. Steel, HN-0800RT	K. J. Lesker
	Bolt	20	5/16 - 24 x 1.75"	SHC, SST	McMaster
	Flat Washer	20	5/16	SST	McMaster
	Gasket	2	For 8" CF	Cu	Duniway
	Blank Flange	1	8" CF	304 St. Steel, F0800X000NT	K. J. Lesker
Chamber 2 Feedthrough Flange					
	CF Half Nipple	2	2.75" CF	304 St. Steel, HN-0275SSRT	K. J. Lesker
	Bolt	12	1/4 - 28 x 0.875"	SHC, SST	McMaster
	Flat Washer	12	1/4	SST	McMaster
	Gasket	2	For 2.75" CF	Cu	Duniway
	CF to KF Adapter	1	2.75" CF to KF-40	304 St. Steel, F0275XQF40	K. J. Lesker
	CF to KF Adapter	1	2.75" CF to KF-16	304 St. Steel, F0275XQF16	K. J. Lesker
	CF Half Nipple	2	1.33" CF	304 St. Steel, HN-0133RT	K. J. Lesker
	Bolt	12	#8 - 32 x 0.5"	SHC, SST	McMaster
	Flat Washer	12	#8	SST	McMaster
	Gasket	2	For 1.33" CF	Cu	Duniway
	CF to Swagelok Adapter	1	1.33" CF, 1/4" fitting	304 St. Steel, F0133X4SWG	K. J. Lesker
Chamber 2 Top Flange					
	O-ring	1	390	Viton, 9464K655	McMaster
Chamber 2 Back Flange					
	Bolt to Faraday Feedthrough Flange	46	5/16 - 18 x 1.75"	SHC, SST	McMaster

Commercial Components

Associated Component	Description	Qty	Dimensions/Values	Details (Material, Part Number, etc.)	Supplier or Manufacturer
	Hex Nut	31	5/16 -18	WS ₂ Coated, N-3118-W	UC Comp.
	Flat Washer Narrow	46	5/16, 0.688" OD	SST	McMaster
Faraday Feedthrough Flange					
	O-ring	1	386	Viton, 9464K651	McMaster
	Bulkhead Clamp	8	KF-16	Al, QF16-075-BC	K. J. Lesker
	Centering Ring	8	KF-16	Al, Viton, QF16-075-ARV	K. J. Lesker
	Bolt	48	#10 - 32 x 0.625"	SST	McMaster
	Flat Washer Narrow	48	#10, 0.5" OD	SST	McMaster
Apertures					
Aperture Panel					
	Bolt	16	1/4 - 28 x 0.375"	SST	McMaster
	Flat Washer Narrow	16	1/4, 0.625"	SST	McMaster
Aperture Holder					
	Stainless Steel Aperture	8	500 µm ID, 0.375" OD	Unmounted, SS-3/8-DISC-500	Lenox LASER
	Conductive Silver Epoxy	1	76%	Epo-Teck, 16014	Ted Pella
	Bolt	32	#2 - 56 x 5/32"	SST, Phillips Flat Head	McMaster
	O-ring	8	018	Viton, 9464K72	McMaster
Insulating Washers					
	O-ring	10	012	Viton, 9464K17	McMaster
	Self-Sealing Hex Nut	10	1/4 - 20	SST, Silicone, 91339A130	McMaster
Aperture Panel Piston Seal					
	O-ring to Aperture Panel	1	273	Viton, 9464K571	McMaster
	O-ring to Chamber 1 Back Flange	1	274	Viton, 9464K572	McMaster
Narrow Drift Tube					
Narrow DT Tabbed Electrode					
	Spacer	4	0.125" ID, 0.425" thick	Ceramic, 0.185" OD	Cer. Gr. Co.
	Bolt to Aperture Panel	4	M3 x 6	SHC, SST	McMaster
	Bolt to PEEK Column	5	#6 - 32 x 0.375"	Phillips Flat Head, SST	McMaster

Commercial Components

Associated Component	Description	Qty	Dimensions/Values	Details (Material, Part Number, etc.)	Supplier or Manufacturer
Narrow DT Electrode					
	Bolt	5	#6 - 32 x 0.375"	Phillips Flat Head, SST	McMaster
Full Size Drift Tube					
DT Mount Threaded Rods					
	Hex Nut	20	1/4 - 28, 5/32" high	SST	McMaster
Drift Tube Infrastructure					
	Threaded Shaft Collar	4	1/4 - 20, 11/16" OD	6438K14	McMaster
	Sleeve Bearing Carriage	4	1" inner, 1.875" length	Al, UHMW, 60585K18	McMaster
	Bolt through Shaft Collar	4	1/4 - 20 x 2.25"	SST	McMaster
	Bolt to Carriage	8	1/4 - 20 x 0.75"	SST	McMaster
	Bolt to T-Slot through Aluminum Plate	4	1/4 - 20 x 0.625"	SST	McMaster
Vacuum Chamber Infrastructure					
Chamber 1 Support Assembly					
	Bolt through Clamp Plate	8	1/4 - 28 x 0.75"	Hex Head, SST	McMaster
	Flat Washer	8	1/4	SST	McMaster
	Bolt to Intermediate through Pivot	4	1/4 - 28 x 0.25"	Pan Head, SST	McMaster
	Bolt to Bearings through Intermediate	4	1/4 - 28 x 0.5"	Pan Head, SST	McMaster
	Pivot Table	1	1000 lb capacity	Galvanized Steel, 1797K12	McMaster
	Linear Bearings	4	1.25' length for 1/2" shaft	6630K49	McMaster
Chamber 2 Support Assembly					
	Bolt through Clamp Plate	8	1/4 - 28 x 0.75"	Hex Head, SST	McMaster
	Flat Washer	8	1/4	SST	McMaster
	Bolt through Bracket to GatorJaw	32	5/16 - 18 x 0.5"	BHHD, Zn Plated Steel	GatorJaw
Rail Support					
	Bolt	16	#6 - 32 x 0.875"	Phillips Flat Head, SST	McMaster
	Low-Profile Support Rails	2	For 1/2" shaft, 4' length	Al, 8154T11	McMaster
	Shafts for Support Rails	2	1/2" OD, 4' length	Carbon Steel, 6499K73	McMaster
Instrument Infrastructure					
GatorJaw Table					
	90 Degree Inside Gusset Bracket	36	4 x 4 x 1, 12 gauge	Zn Plated Steel, GJB-90-IG-ZS	GatorJaw

Commercial Components

Associated Component	Description	Qty	Dimensions/Values	Details (Material, Part Number, etc.)	Supplier or Manufacturer
	90 Degree Inside L-Angle Bracket	16	2.5 x 2.5 x 1, 11 gauge	Zn Plated Steel, GJB-90-IL-ZS	GatorJaw
	Bolt through Bracket to GatorJaw	208	5/16 - 18 x 0.5"	BHHD, Zn Plated Steel	GatorJaw
	End Cover Cap for 1.75"	4	1.75 x 1.75 x 1/16	Al, GJM-175-EC	GatorJaw
	End Cover Cap for 3.5"	4	2.75 x 3.5 x 1/16	Al, GJM-350-EC-AL	GatorJaw
	Low-Profile Fastener	8	5/16 - 18 x 1.875"	GJF-1875	GatorJaw
	Bolt through Bottom Panel to GJ	10	5/16 - 18 x 0.75"	BHHD, Zn Plated Steel	GatorJaw
Table Casters					
	Nylon Wheel Locking Caster	4	4" OD	Zn Plated Frame, 23055T47	McMaster
	Bolt through Adapter Plate to GJ	20	5/16 - 18 x 0.75"	BHHD, Zn Plated Steel	GatorJaw
	Bolt through Caster to Adapter Plate	16	5/16 - 18 x 0.5"	SHC, SST	McMaster
	Flat Washer	16	5/16	SST	McMaster
Table Drawers					
	Mounting Hole Drawer for PSU	4	19" rack, 3U	RBX32-BFP	Thorlabs
	Storage Drawer	1	19" rack, 3U	RAU300	Thorlabs
	Cooling Fan Panel	4	4" square	RBX-FAN	Thorlabs
	AC Power Module Panel	4	4" square	RBX-AC	Thorlabs
	Blank Panels	20	Modified as needed	RBX-BLK1F	Thorlabs
	Screw with Washer for Large Panel	32	#12 - 24 x 0.5"	Pilot Pt Pan Head, RK5000	Thorlabs
	Rack Mount Rail	9	21", #10 - 32 tapped	Bud Industries, PMR-9448	Allied
	Bolt to Rack Mount	40	#10 - 32 x 0.5"	SST	McMaster
	Flat Washer Narrow	40	#10, 0.438" OD	SST	McMaster
	Rack Shelf	1	1/16" thick	Painted Sheet Metal, RK4102	Thorlabs
	Nylatch Panel Fastener	40	1/4" length	Black Plastic, Sold with Panels	Thorlabs
Assembly Support Structure for Front End and Chamber 1 Contents					
	Sleeve Bearing Carriage	4	1" inner, 1.875" length	Al, UHMW, 60585K18	McMaster
	T-Slotted Outside Corner	2	1" rail	Al, 47065T242	McMaster
	T-Slotted Corner Bracket	6	1" rail, Extended Corner	Al, 47065T239	McMaster
	T-Slotted Corner Bracket	2	2" rail, Extended Corner	Al, 47065T237	McMaster
	T-Slot Fastener	40	1/4 - 20	Zn Plated Steel, BHHD, 47065T139	McMaster

Commercial Components

Associated Component	Description	Qty	Dimensions/Values	Details (Material, Part Number, etc.)	Supplier or Manufacturer
ELECTRONICS					
Electrospray Ionization Source					
	Source Power Supply	1	6 kV, 20 mA	PS/FC06R20.0-11	Glassman HV
	Alternate Source Power Supply	1	8 kV, 300 μ A	SC008RCV050	Exelis
	Alligator Clip	1	10 A, crimp	Nickel Plated Steel, 70724760	Allied Elec.
Ion Funnel					
	9 Pin C-Type Vacuum Cable	3	19", female end	Kapton, PEEK, 1000040	Accu-Glass
	9 Pin C-Type Air Side Cable	3	96", female end	1000021	Accu-Glass
	9 Pin C-Type Feedthrough	1	On 1.33" CF flange	1000010	Accu-Glass
	9 Pin C-Type Vacuum Cable	1	19", 2 female end	Kapton, PEEK, 100120	Accu-Glass
	Double 9 Pin C-Type Feedthrough	1	On 2.75" CF flange	1000012	Accu-Glass
	Dual RF Power Supply Controller	1	19" rack mount	694301	Ardara
	Linear AC to DC Power Supply	2	24 VDC, 4.8 A	IHD24-4.8	Int. Power
	DC Power Supply	2	2.5 kV, 400 μ A	HP2.5ZIP025	Exelis
	DC Power Supply	7	1 kV, 1 mA	HP001ZIP026	Exelis
	Power Film Resistor	28	10 k Ω , 3 W	MS221-10k-1%	Caddock
	Power Film Resistor	6	10 k Ω , 3 W	MS221-5k-1%	Caddock
	Capacitor	34	100 pF	Vishay, 561R10TCCT10	Mouser
	Barrier Terminal Block	2	2 position	TE Conn., 282857-2	Mouser
	Barrier Terminal Block	5	5 position	TE Conn., 282857-5	Mouser
	Barrier Terminal Block	3	6 position	TE Conn., 282857-6	Mouser
Detector					
	Kapton Coax Cable	8	19" length, 26 AWG	Accufast 500 Connector, 110190	Accu-Glass
	SHV Shielded Feedthrough	8	KF-16	Glass, Ceramic, 112437	Accu-Glass
	Air Side SHV Cable	8	48" length, female ends	112513	Accu-Glass
Linear AC to DC 24 V Power Supply					
	3 Prong Power Cable	2	10 A, 250 VAC, 6'	Prong Male to C13 Female	Allied Elec.
	AC Power Entry	2	120 VAC	Inlet Connector Pinout	Thorlabs
	Fuse	4	2 Amp, 250 VAC, 1/4"	Fast Acting, Glass Tube	McMaster
	Quick Connect Terminal Block	1	8 Position, 600 V	Black Plastic	Mouser

Commercial Components

Associated Component	Description	Qty	Dimensions/Values	Details (Material, Part Number, etc.)	Supplier or Manufacturer
	Flat Blade Terminal	12	1/4", non-insulated	Male	Mouser
	Flat Blade Terminal	34	1/4", non-insulated	Female	Mouser
	Flat Blade Terminal T	12	1/4", non-insulated	1 Female to 2 Male	Mouser
Flat/Lofted Power Supply Mounting Bracket					
	Bolt to PSU	16	M3 x 10	Phillips Flat Head, SST	McMaster
	Bolt to Drawer Mounting Hole	24	1/4 - 20 x 0.625"	SHCS, SST	McMaster
Funnel 1, Funnel 2, and Drift Tube Breakout Boxes					
	BNC Bulkhead Jack	4	500 V, solder cup	70031716	Allied Elec.
	Test Jack	8	2 mm plug, 1.5 kV, 3 A	Pomona Elec., 4773-6	Newark
	Strain Relief	3	5/8 panel hole	Nylon, Abbatron, 823	Allied Elec.
	Strain Relief	8	7/16 panel hole	Nylon, Abbatron, 939	Allied Elec.
Picoammeter Operational Amplifier (Single Channel Quantities Listed)					
	Aluminum Enclosure	1	4.33 x 3.25 x 1.75"	Bud Industries, CU-4471	Mouser
	Right Angle BNC Connector	2	PCB through, female	TE Conn., 5227161-1	Mouser
	SHV Male Connector	2	5 kV, cable plug	Kings Elec., 1705-2	Allied Elec.
	SHV Female to MHV Male Adapter	1	50 Ω	Brass, Nickel, PE9335	Pasternack
	MHV Female to BNC Male Adapter	1	50 Ω	Brass, Nickel, PE9406	Pasternack
	Coax Cable BNC Male to BNC Male	1	500 V, PTFE insulated	Pomona Elec., BNC-C-72	Allied Elec.
	Metal Film Resistor	1	200 kΩ, 1 W	TE Conn., H4P200KFCA	Mouser
	Metal Film Resistor	2	10 MΩ, 1.5 W	Vishay, CMF6510M000FHEK	Mouser
	Metal Film Resistor	1	20 Ω, 1 W	Vishay, CPF120R000FEB14	Mouser
	Metal Film Resistor	1	20 kΩ, 1 W	TE Conn., H4P20KFCA	Mouser
	Metal Film Resistor	1	2 kΩ, 1 W	Vishay, CPF12K0000FKB14	Mouser
	Potentiometer	1	20 kΩ linear	Bourns, PTD901-1015F-B203	Mouser
	Capacitor	1	47 pF, 2 kV	Panasonic, ECC-A3D470JGE	Digi-Key
	Capacitor	3	0.1 μF, 50 V	AVX, CK05BX104K	Newark
	Precision Amplifier Ultra Low Offset	1	PCB through	Analog Devices, OP07EPZ	Mouser
	Operational Amplifier	1	PCB through	TI, LMC662AIN/NOPB	Mouser
	Dual Tracking DC Power Supply	1	0-60 V, 0-3 A	Topward, 6603D	Test Equity

Commercial Components

Associated Component	Description	Qty	Dimensions/Values	Details (Material, Part Number, etc.)	Supplier or Manufacturer
Multiple					
	Coax Cable	x	RG-58, 19 AWG, Duofoil	7806F 010500	Mouser
	Coax Cable	x	75 Ω, 30 AWG	M17194-RG179	Mouser
	Kapton Coated Wire	x	18 AWG, unshielded	112697	Accu-Glass
	2 Conductor Cable	x	26 AWG, shielded	86102CY	AlphaWire
	4 Conductor Cable	x	26 AWG, shielded	86104CY	AlphaWire
	6 Conductor Cable	x	18 AWG, shielded	5304UE 008500	Digi-Key
	Resistor	x	1 MΩ, ±1%	RNF14FTD1M00	Digi-Key
	Heat Shrink Tubing	x	Various dimensions	Polyolefin	Waytek
	Heat Shrink Tubing	x	Various dimensions	FEP Teflon	AlphaWire
	Kapton Polyimide Film	x	0.005" thick	2271K6	McMaster
	Super Corona Dope	1	4100 V/mil	70125548	Allied Elec.
	Solder	x	0.81 mm OD, flux 3 core	63/37 Tin/Lead	Mouser
	Regular Flux Paste	x	1.7 oz	RectorSeal, 14000	Mouser
	Silver Bearing Solder Kit	x	14 g Ag solder, 14 g flux	Stay-Brite, SBSK	Harris
	D-sub 9 Standard Connector	11	Panel mount, female	Solder Cup, 571-5-747905-2	Mouser
	D-Sub 9 Standard Connector	9	Panel mount, male	Solder Cup, 571-5-747904-2	Mouser
	D-Sub Backshell Kit	9	1.39 x 1.22 x 0.63	Gray Plastic, L-com, SDC9G	Newark
	Ring Terminals	10	0.5" ID, 0.75" OD	Sn-Plated Cu, 7113K81	McMaster
	SHV Female Bulkhead Receptacle	10	5 kV, solder cup	Kings Elec., 1704-1	Allied Elec.
	SHV Male Connector	11	5 kV, cable plug	Kings Elec., 1705-2	Allied Elec.
	SHV T Adapter	1	5 kV, 1 male to 2 female	Kings Elec., 1709-3	Allied Elec.
	Strain Relief	13	5/8 panel hole	Nylon, Abbatron, 823	Allied Elec.
	Strain Relief	1	7/16 panel hole	Nylon, Abbatron, 939	Allied Elec.
VACUUM SYSTEM					
	Scroll Pump	2	10 L/s	XDS35i	Edwards
	Silencer	2	For XDS35i	A50597001	Edwards
	Booster Pump	1	26 L/s	XDS100B	Edwards
	KF Bulkhead Flange	x	KF-16	QF16-075-BC	K. J. Lesker
	Pressure Valve	x	KF-25	L6280-602, NW-25-H/O	Varian

Commercial Components

Associated Component	Description	Qty	Dimensions/Values	Details (Material, Part Number, etc.)	Supplier or Manufacturer
358	Micro-Ion Controller	2	50 mTorr to 0.1 nTorr	Granville-Phillips, 358501-010	MKS Inst.
	Convection Pressure Gauge	5	KF-25	Granville-Phillips, 275196	MKS Inst.
	Pressure Gauge Controller Cable	2	Split for 2 gauges	358002	MKS Inst.
	Pressure/Flow Controller	1	Type 640	640A11TS1V12V	MKS Inst.
	Flow Controller Power and Readout	1	2 channel	PR 4000 F	MKS Inst.
	Pressure Gauge	1	100 Torr range	CDG045	Inficon
	Block Valve	2	KF-40, right angle	Al, L6280-603	Varian
	Bellows	4	KF-40, 18"	300&304L St. Steel, MHT-QF-C18	K. J. Lesker
	Standard Tee	5	KF-40, 2.56" length nipple	304L St. Steel, QF40-150-T	K. J. Lesker
	Right Angle	1	KF-40, 2.56" length nipple	316L St. Steel, QF40-150E90M	K. J. Lesker
	Centering Ring	19	KF-40	Al, Viton, QF40-150-ARV	K. J. Lesker
	Lever Clamp	19	KF-40	Al, QF40-150-CHA	K. J. Lesker
	Block Valve	1	KF-25, right angle	Al, L6280-602	Varian
	Standard Tee	1	KF-25, 1.97" length nipple	304L St. Steel, QF25-150-T	K. J. Lesker
	Centering Ring	9	KF-25	Al, Viton, QF25-150-ARV	K. J. Lesker
	Lever Clamp	9	KF-25	Al, QF25-150-CHA	K. J. Lesker
	KF Adapter	4	KF-40 to KF-25, 1.7"	304L St. Steel, QF40XQF25	K. J. Lesker
	Centering Ring	1	KF-16	Al, Viton, QF16-150-ARV	K. J. Lesker
	Lever Clamp	1	KF-16	Al, QF16-150-CHA	K. J. Lesker
CONTROL AND SIGNAL ACQUISITION					
	Connector Block	5	Noise-rejecting, shielded	SCB-68A, 782536-01	NI
	68-D-Type to 68 VHDCI Cable	2	Shielded, 2 m	SHC68-68-EPM, 192061-02	NI
	SH68-68-D1 Cable	1	Shielded, 2 m	183432-02	NI
	SH68-68-RMIO Cable	1	Shielded, 2 m	189588-02	NI
	SH6C68-68-RDIO Cable	1	Shielded, 1 m	191667-01	NI
	M Series Multifunction DAQ	1	32 AI, 48 digital I/O	PXI-6224, 779114-01	NI
	High Resolution AO Board	1	16 Bit, 32 AO, static PXI	PXI-6704, 777796-01	NI
	R Series Multifunction RIO Module	1	8 AI, 8 AO, 96 digital I/O	PXI-7842R, 780338-01	NI
	Integrated MXIe PXIe-1073	1	5 slots, PCI3 port, cable	781161-01	NI
	Power Cord	1	120 VAC, 2.3 m	763000-01	NI

Commercial Components

Associated Component	Description	Qty	Dimensions/Values	Details (Material, Part Number, etc.)	Supplier or Manufacturer
NI MAX		x		Software	NI
NI LabVIEW 2015 SP1		x		Software	NI
Digital Storage Oscilloscope		1	4 channel, 200 MHz	TDS 2024B	Tektronix

Dimensions in inches, unless otherwise marked

ABBREVIATIONS

Al- Aluminum	Inst.- Instruments
Al- Analog Input	Int.- International
AO- Analog Output	KF- Kwik-Flange
BHHD- Button Head Hex Drive	MHV- Miniature High Voltage
BNC- Bayonet Neill-Concelman	NI- National Instruments
CCD- Charge-Coupled Device	OD- Outer Diameter
Cer. Gr. Co.- Ceramics Grinding Company	PEEK- Polyether Ether Ketone
CF- ConFlat	SHC- Socket Head Cap
Comp.- Components	SHV- Safe High Voltage
Conn.- Connectivity	Sn- Tin
Cu- Copper	SST- 18-8 Stainless Steel
DSP- Digital Signal Processing	St.- Stainless
Elec.- Electronics	TI- Texas Instruments
GJ- GatorJaw	UHMW- Ultra High Molecular Weight Polyethylene
HV- High Voltage	Vac.- Vacuum
I/O- Input Output	Zn- Zinc
ID- Inner Diameter	

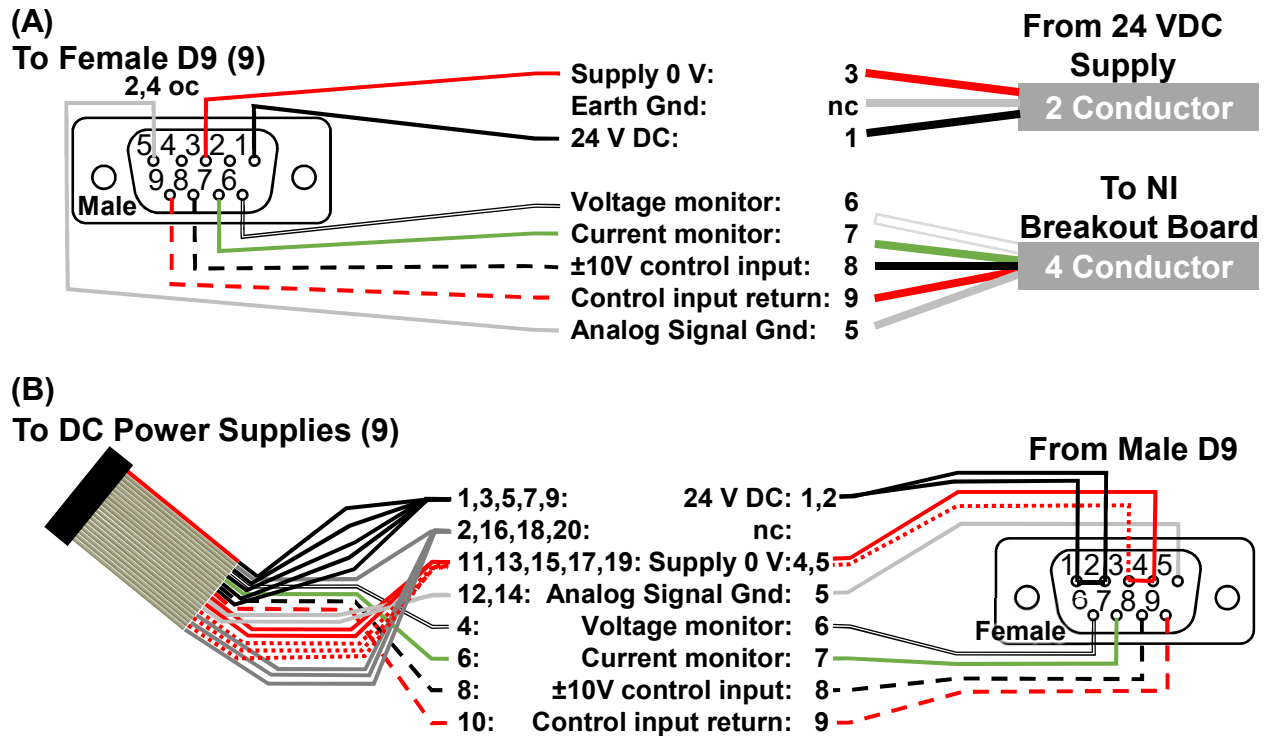


Figure B.17.1: Wiring diagrams for DC power supply inputs with (A) connections for the 20 pin ribbon cables of the nine DC power modules to female 9 pin D-sub connectors and (B) connections for the complementary male 9 pin D-sub connector to the 24 VDC supply and the NI breakout board. Some wires have no connection (nc) and some pins are left open circuit (oc).

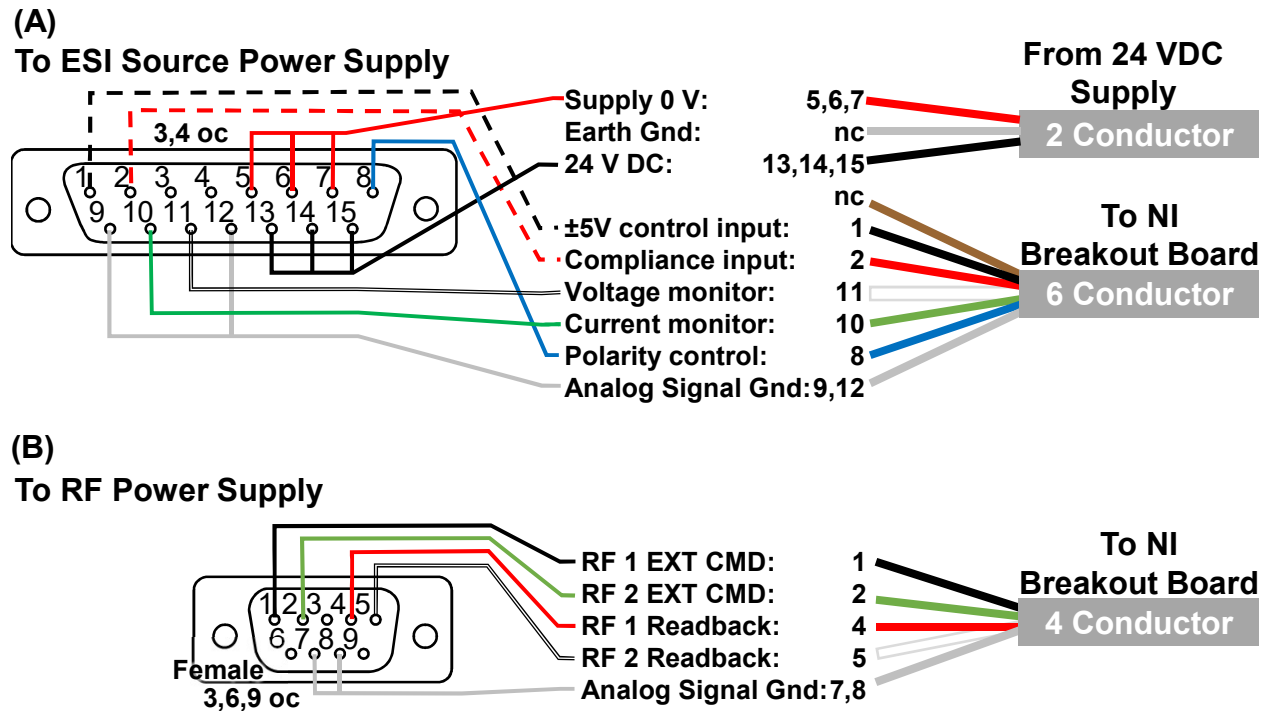


Figure B.17.2: Wiring diagrams for ESI source and RF power supply inputs. Some wires have no connection (nc) and some pins are left open circuit (oc). (A) Wiring for high voltage source power supply (Exelis, SC008RCV050) to a 15 pin D-sub connector using a two-conductor cable to supply 24 VDC, and a six-conductor cable for signal input and output. (B) Wiring for control of RF power supplies external command (EXT CMD) and readback.

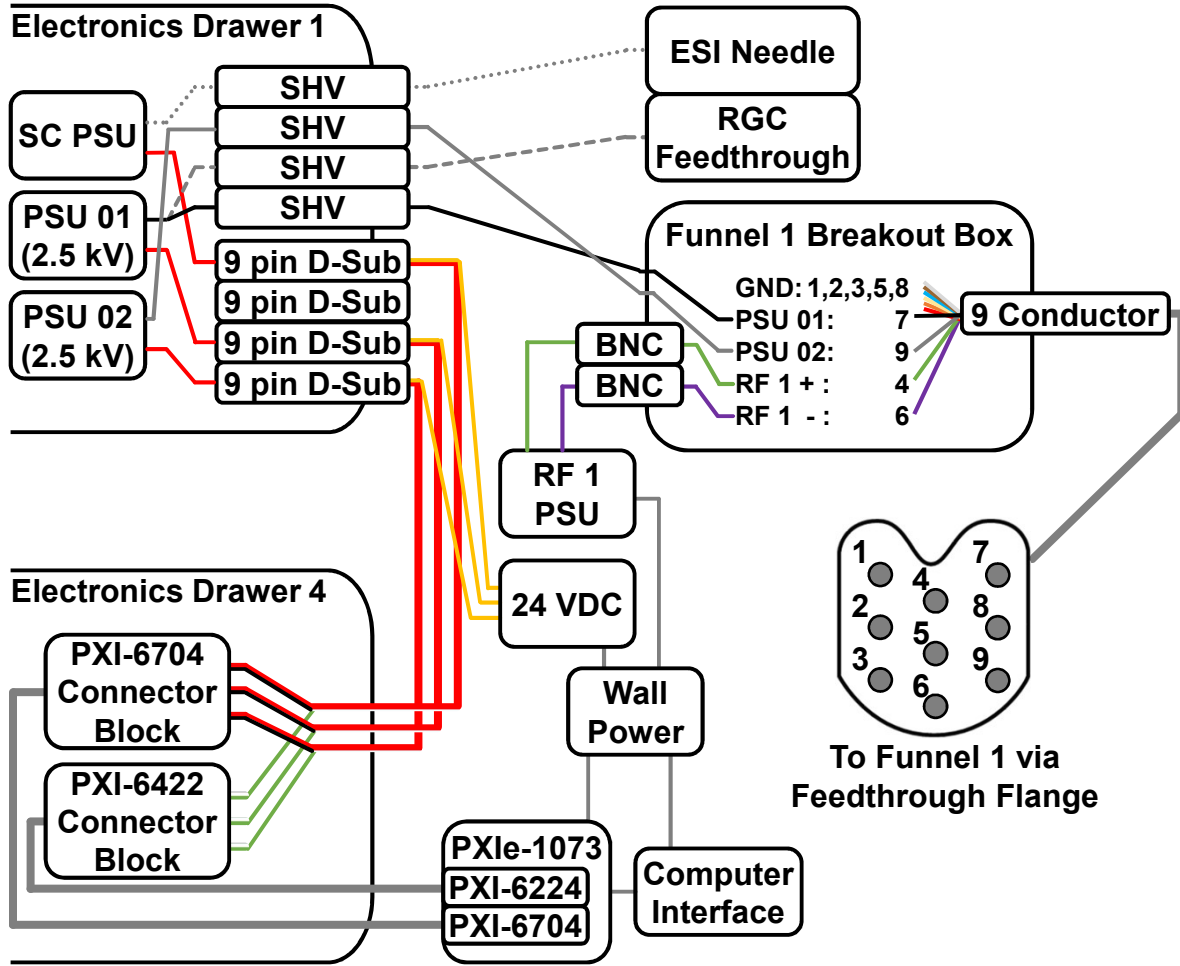


Figure B.17.3: Wiring diagrams for electronic components relating to ESI source, RGC, and the high pressure ion funnel. SHV and 9 pin D-Sub connectors are mounted in panels at the back of the electronics drawer. Cables leading to the fourth electronics drawer pass through strain relief grommets mounted in the panels at the back of the drawer. Connector blocks are connected to respective NI cards with NI-supplied cables. Details for wiring in NI connector blocks are provided in Table B.17.1 and Table B.17.2.

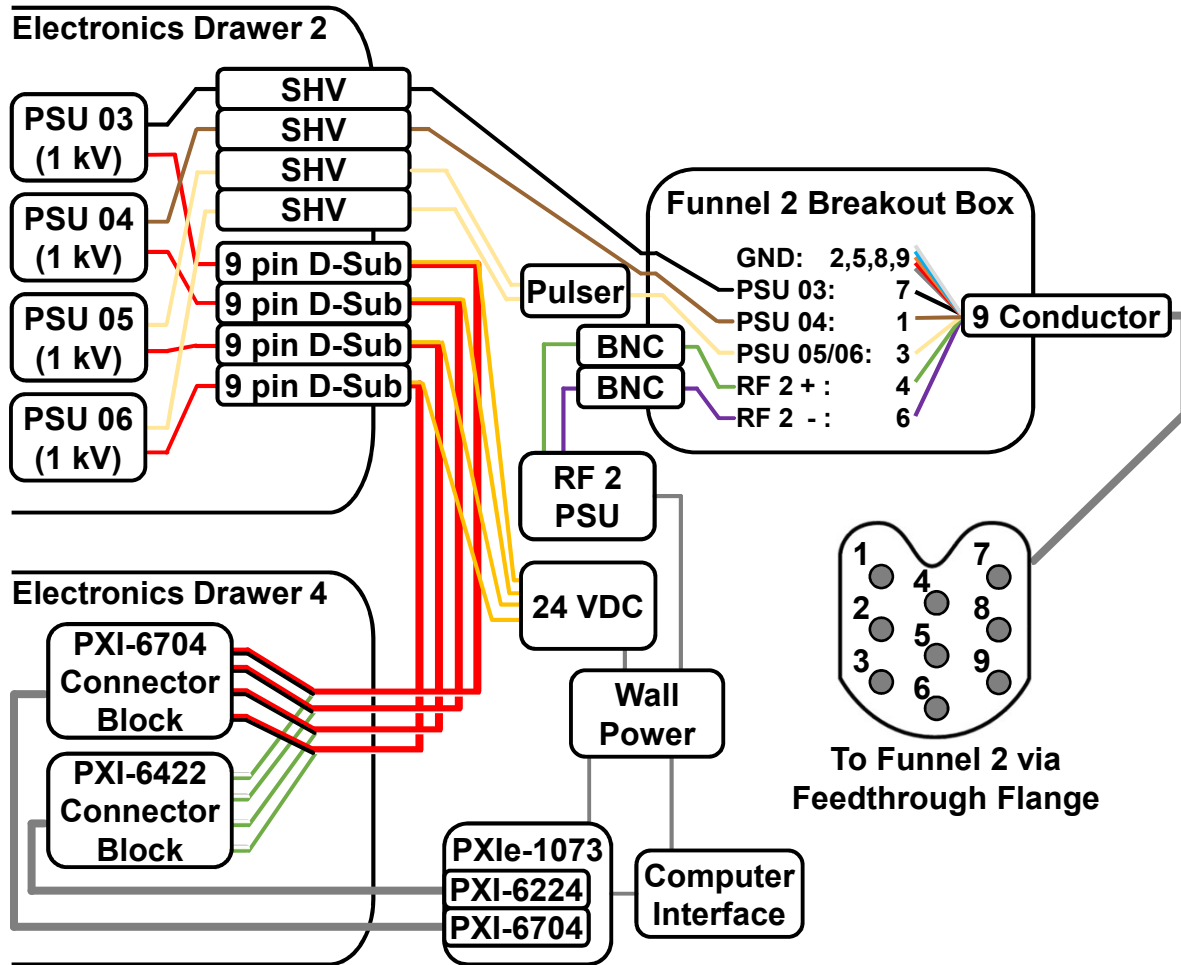


Figure B.17.4: Wiring diagrams for electronic components relating to the low pressure ion funnel. SHV and 9 pin D-Sub connectors are mounted in panels at the back of the electronics drawer. Cables leading to the fourth electronics drawer pass through strain relief grommets mounted in the panels at the back of the drawer. Connector blocks are connected to respective NI cards with NI-supplied cables. Details for wiring in NI connector blocks are provided in Table B.17.1 and Table B.17.2.

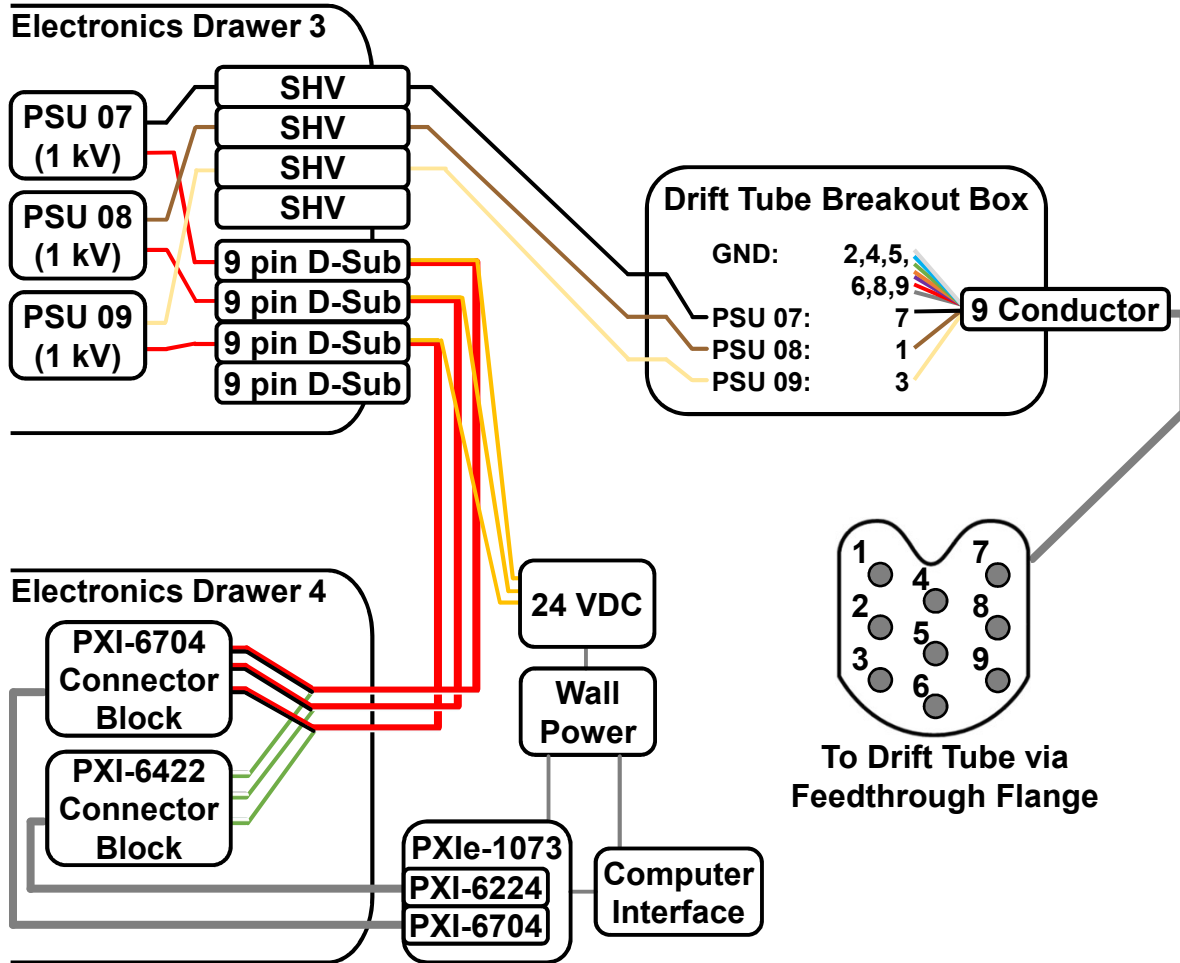
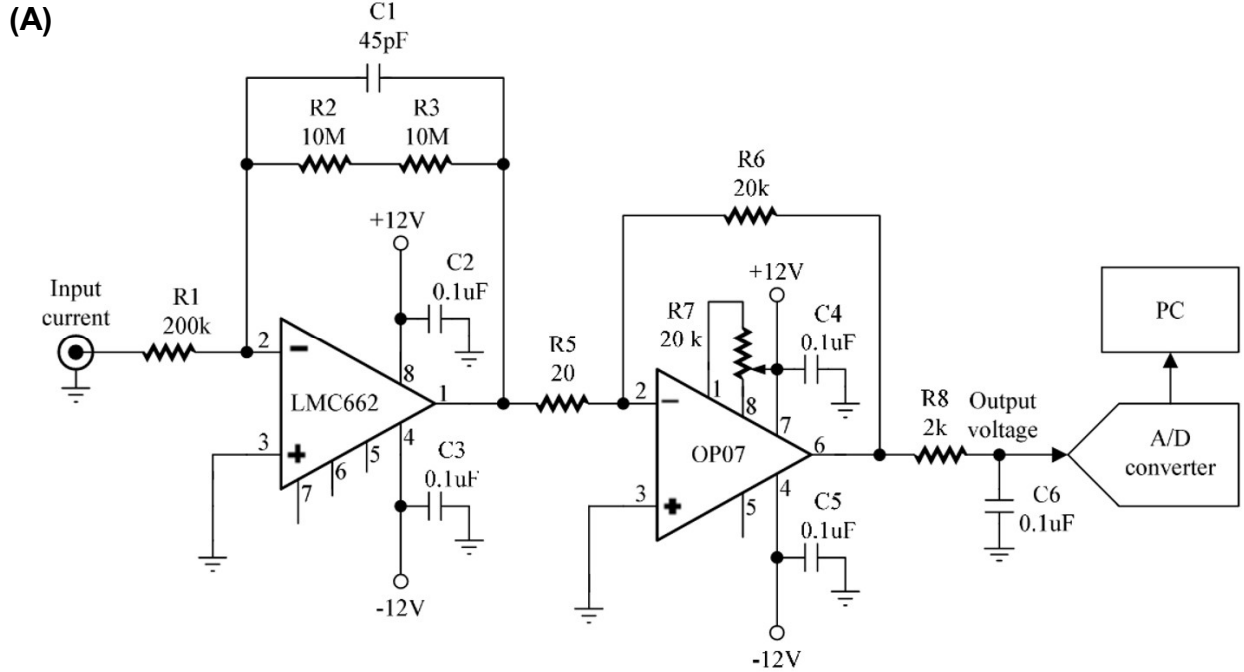


Figure B.17.5: Wiring diagrams for electronic components relating to the drift tube. SHV and 9 pin D-Sub connectors are mounted in panels at the back of the electronics drawer. Cables leading to the fourth electronics drawer pass through strain relief grommets mounted in the panels at the back of the drawer. Connector blocks are connected to respective NI with NI-supplied cables. Details for wiring in NI connector blocks are provided in Table B.17.1 and Table B.17.2.



(B)

Example input current $I_i := 500\text{pA} = 0.5\text{-nA}$

Individual resistor values

$R_1 := 200\text{k}\Omega$ $R_5 := 20\Omega$
 $R_2 := 10\text{M}\Omega$ $R_6 := 20\text{k}\Omega$
 $R_3 := 10\text{M}\Omega$ $R_8 := 2\text{k}\Omega$

Total circuit resistance

$$R_T := R_1 \cdot \left(\frac{R_2 + R_3}{R_1} \cdot \frac{R_6}{R_5} \right) = 2 \times 10^{10} \cdot \Omega$$

Calculated output voltage

$$V_o := I_i \cdot R_1 \cdot \left(\frac{R_2 + R_3}{R_1} \cdot \frac{R_6}{R_5} \right) = 10\text{-V}$$

Detected output voltage $V_{\text{out}} := 5\text{V}$

Calculated input current

$$I_{\text{in}} := \left[\frac{V_{\text{out}}}{R_1 \cdot \left(\frac{R_2 + R_3}{R_1} \cdot \frac{R_6}{R_5} \right)} \right] = 250\text{-pA}$$

(C)

Varied gain with bridge resistor

Bridge resistor $R_{\text{Bridge}} := 1\text{M}\Omega$

Resistance across R2, R3, and RBridge

$$R_{23\text{Bridge}} := \frac{1}{\left(\frac{1}{R_{\text{Bridge}}} + \frac{1}{R_2 + R_3} \right)} = 0.952\text{-M}\Omega$$

Calculated output voltage

$$V_{\text{outBridge}} := I_i \cdot R_1 \cdot \left(\frac{R_{23\text{Bridge}}}{R_1} \cdot \frac{R_6}{R_5} \right) = 0.476\text{-V}$$

Detected output voltage $V_{\text{outBridge}} := 5\text{V}$

Calculated input current

$$I_{\text{inBridge}} := \left[\frac{V_{\text{outBridge}}}{R_1 \cdot \left(\frac{R_{23\text{Bridge}}}{R_1} \cdot \frac{R_6}{R_5} \right)} \right] = 5.25 \times 10^3 \cdot \text{pA}$$

Figure B.17.6: (A) Circuit diagram for picoammeter operational amplifier. Reproduced from Intra, 2009. (B) Calculation for an example input current, showing expected output voltage at the maximum detectable level for the PXI-7842R card and showing the calculation for determining the input current from the measured voltage. (C) Calculations analogous to those in (B) where a bridge resistor is connected across R2 and R3 to vary the gain of the amplifier.

Table B.17.1: PXI-6704 Connector Block Terminals

68	AO GND 0/16	PSU01 Red	59	AO GND 6/22	PSU07 Red	51	AO 26 (I)	1	+5V
34	AO 0 (V)	PSU01 Black	25	AO 6 (V)	PSU07 Black	17	AO 11 (V)	35	D GND
67	AO 16 (I)		58	AO 22 (I)		50	AO GND 11/27	2	P0.0
33	AO GND 1/17	PSU02 Red	24	AO GND 7/23	PSU08 Red	16	AO 27 (I)	36	D GND
66	AO 1 (V)	PSU02 Black	57	AO 7 (V)	PSU08 Black	49	AO GND 12/28	3	P0.1
32	AO 17 (I)		23	AO 23 (I)		15	AO 12 (V)	37	D GND
65	AO GND 2/18	PSU03 Red	56	AO GND		48	AO 28 (I)	4	P0.2
31	AO 2 (V)	PSU03 Black	22	AO 8 (V)	PSU09 Black	14	AO GND 13/29	38	RESERVED
64	AO 18 (I)		55	AO GND 8/24	PSU09 Red	47	AO 13 (V)	5	P0.3
30	AO GND 3/19	PSU04 Red	21	AO 24 (I)		13	AO 29 (I)	39	D GND
63	AO 3 (V)	PSU04 Black	54	AO 9 (V)	RF CMD Black	46	AO GND 14/30	6	P0.4
29	AO 19 (I)		20	AO GND 9/25		12	AO 14 (V)	40	RESERVED
62	AO GND 4/20	PSU05 Red	53	AO 25 (I)		45	AO 30 (I)	7	P0.5
28	AO 4 (V)	PSU05 Black	19	AO GND		11	AO GND 15/31	41	D GND
61	AO 20 (I)		52	AO 10 (V)	RF CMD Green	44	AO 15 (V)	8	P0.6
27	AO GND 5/21	PSU06 Red	18	AO GND 10/26		10	AO 31 (I)	42	D GND
60	AO 5 (V)	PSU06 Black						9	D0.7
26	AO 21 (I)							43	AO GND

Direct Feedthrough: S1 (1,2) left; S2 (1,2,3) down

Table B.17.2: PXI-6224 Connector Block Terminals, Connector 0

68	AI 0 (AI 0+)	PSU 01 White	59	AI GND		51	P0.5	1	PFI 14 / P2.6
34	AI 8 (AI 0-)	PSU 01 Green	25	AI 6 (AI 6+)	PSU 07 White	17	P0.1	35	D GND
67	AI GND		58	AI 14 (AI 6-)	PSU 07 Green	50	D GND	2	PFI 12 / P2.4
33	AI 1 (AI 1+)	PSU 02 White	24	AI GND		16	P0.6	36	D GND
66	AI 9 (AI 1-)	PSU 02 Green	57	AI 7 (AI 7+)	SC White	49	P0.2	3	PFI 9 / P2.1
32	AI GND		23	AI 15 (AI 7-)	SC Green	15	D GND	37	PFI 8 / P2.0
65	AI 2 (AI 2+)	PSU 03 White	56	AI GND		48	P0.7	4	D GND
31	AI 10 (AI 2-)	PSU 03 Green	22	AO 0		14	+5V	38	PFI 7 / P1.7
64	AI GND		55	AO GND		47	P0.3	5	PFI 6 / P1.6
30	AI 3 (AI 3+)	PSU 04 White	21	AO 1		13	D GND	39	PFI 15 / P2.7
63	AI 11 (AI 3-)	PSU 04 Green	54	AO GND		46	PFI 11 / P2.3	6	PFI 5 / P1.5
29	AI GND		20	APFI 0		12	D GND	40	PFI 13 / P2.5
62	AI SENSE		53	D GND		45	PFI 10 / P2.2	7	D GND
28	AI 4 (AI 4+)	PSU 05 White	19	P0.4		11	PFI 0 / P1.0	41	PFI 4 / P1.4
61	AI 12 (AI 4-)	PSU 05 Green	52	P0.0		44	D GND	8	+5V
27	AI GND		18	D GND		10	PFI 1 / P1.1	42	PFI 3 / P1.3
60	AI 5 (AI 5+)	PSU 06 White						9	D GND
26	AI 13 (AI 5-)	PSU 06 Green						43	PFI 2 / P1.2

Direct Feedthrough: S1 (1,2) left; S2 (1,2,3) up

Table B.17.3: PXI-7842R Connector Block Terminals, MIO Connector 0

68	AI 0+	Ion Signal 1	59	AI 6+	51	AO 4	1	+5V
34	AI 0-		25	AI 6-	17	AO GND 4	35	+5V
67	AI GND 0		58	AI GND 6	50	AO 5	2	D GND
33	AI GND 1		24	AI GND 7	16	AO GND 5	36	DIO 0
66	AI 1+		57	AI 7+	49	AO 6	3	D GND
32	AI 1-		23	AI 7-	15	AO GND 6	37	DIO 1
65	AI 2+		56	AI SENSE	48	AO 7	4	D GND
31	AI 2-		22	NC	14	AO GND 7	38	DIO 2
64	AI GND 2		55	AO 0	47	DIO 15	5	D GND
30	AI GND 3		21	AO GND 0	13	DIO 14	39	DIO 3
63	AI 3+		54	AO 1	46	DIO 13	6	D GND
29	AI 3-		20	AO GND 1	12	DIO 12	40	DIO 4
62	AI 4+		53	AO 2	45	DIO 11	7	D GND
28	AI 4-		19	AO GND 2	11	DIO 10	41	DIO 5
61	AI GND 4		52	AO 3	44	DIO 9	8	D GND
27	AI GND 5		18	AO GND 3	10	DIO 8	42	DIO 6
60	AI 5+						9	D GND
26	AI 5-						43	DIO 7

Direct Feedthrough: S1 (1,2) left; S2 (1,2,3) down

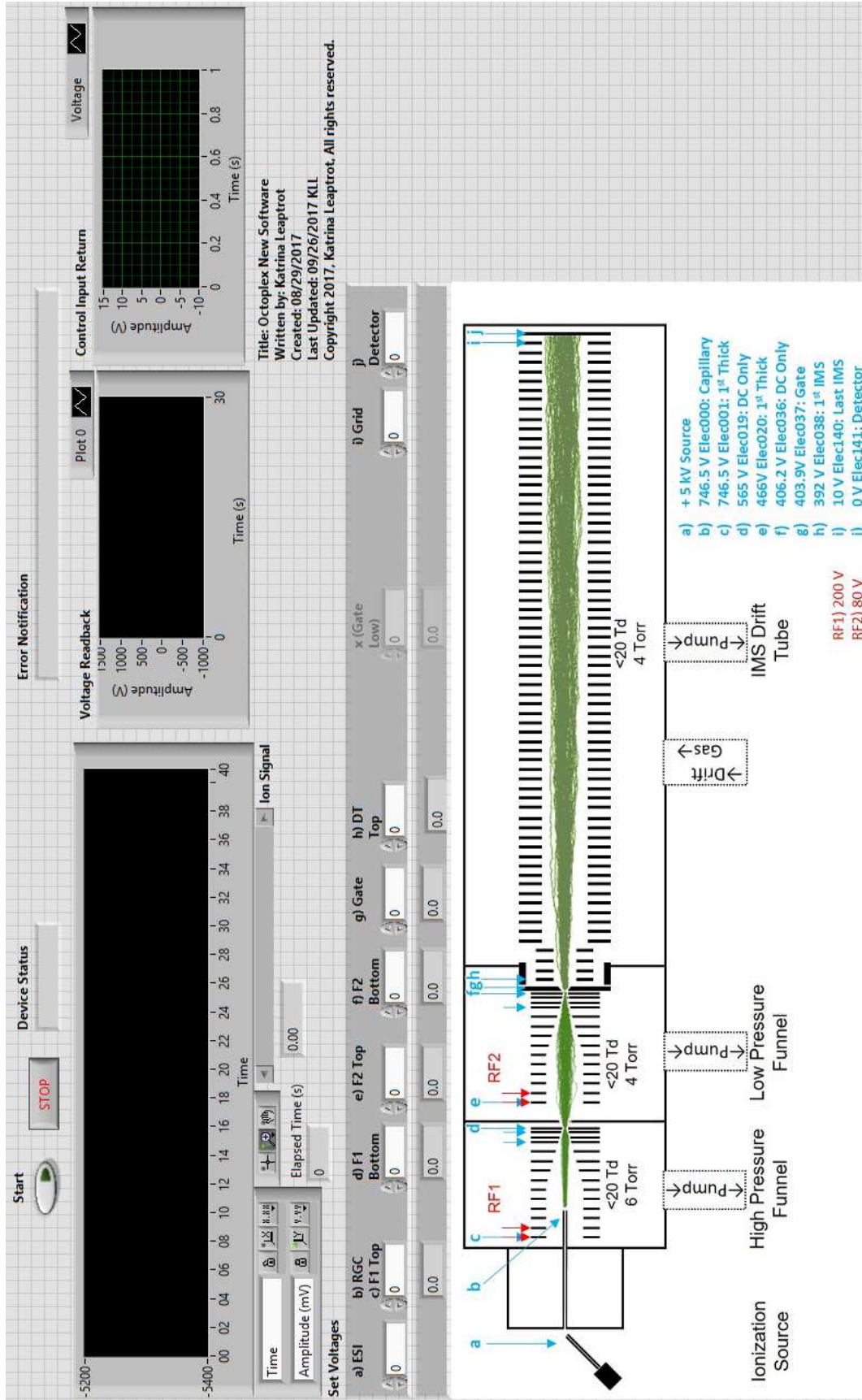


Figure B.18.1: Front panel user interface of control and acquisition software for the spatially multiplexed instrument.

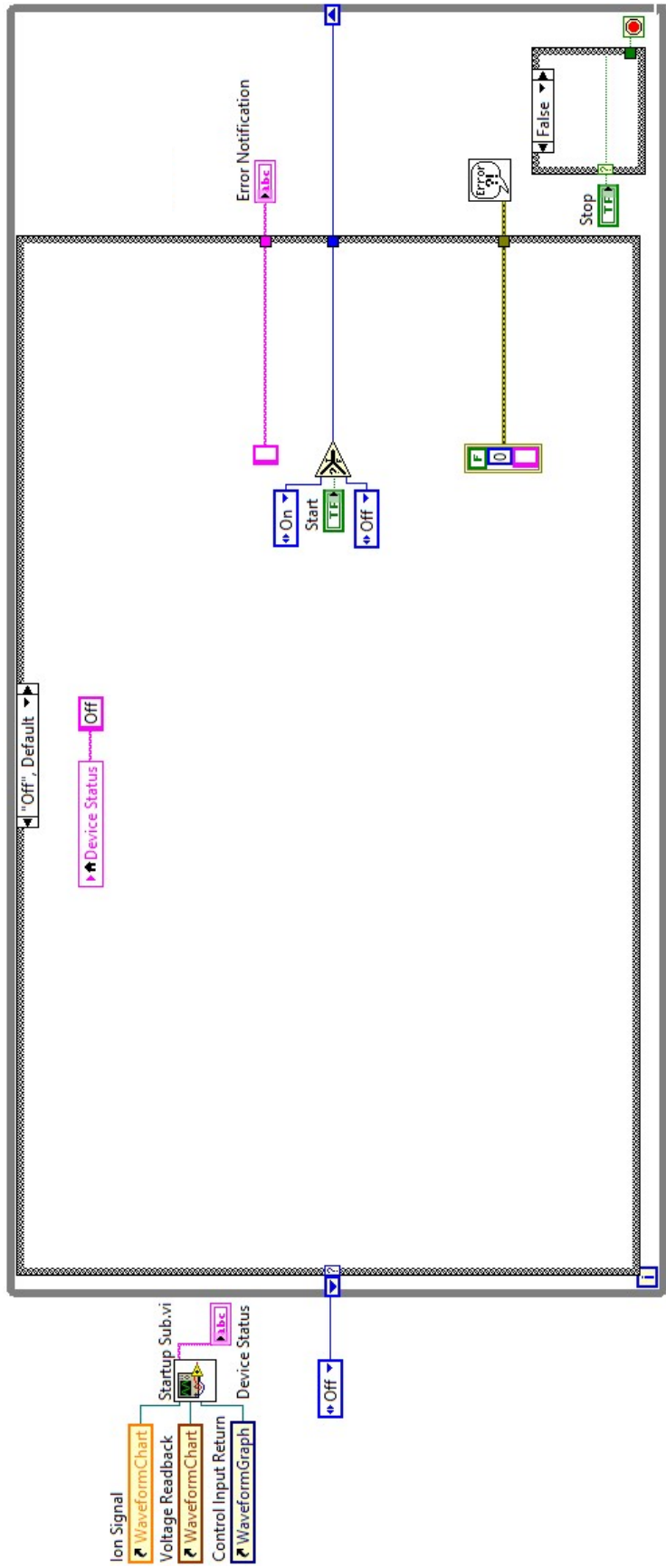


Figure B.18.2: Block diagram of instrument software before initialization. The initial case is off, and the device status stays off until the start button is pressed on the front panel. Case is also shown for pressing the stop button on the front panel, which ends the program execution.

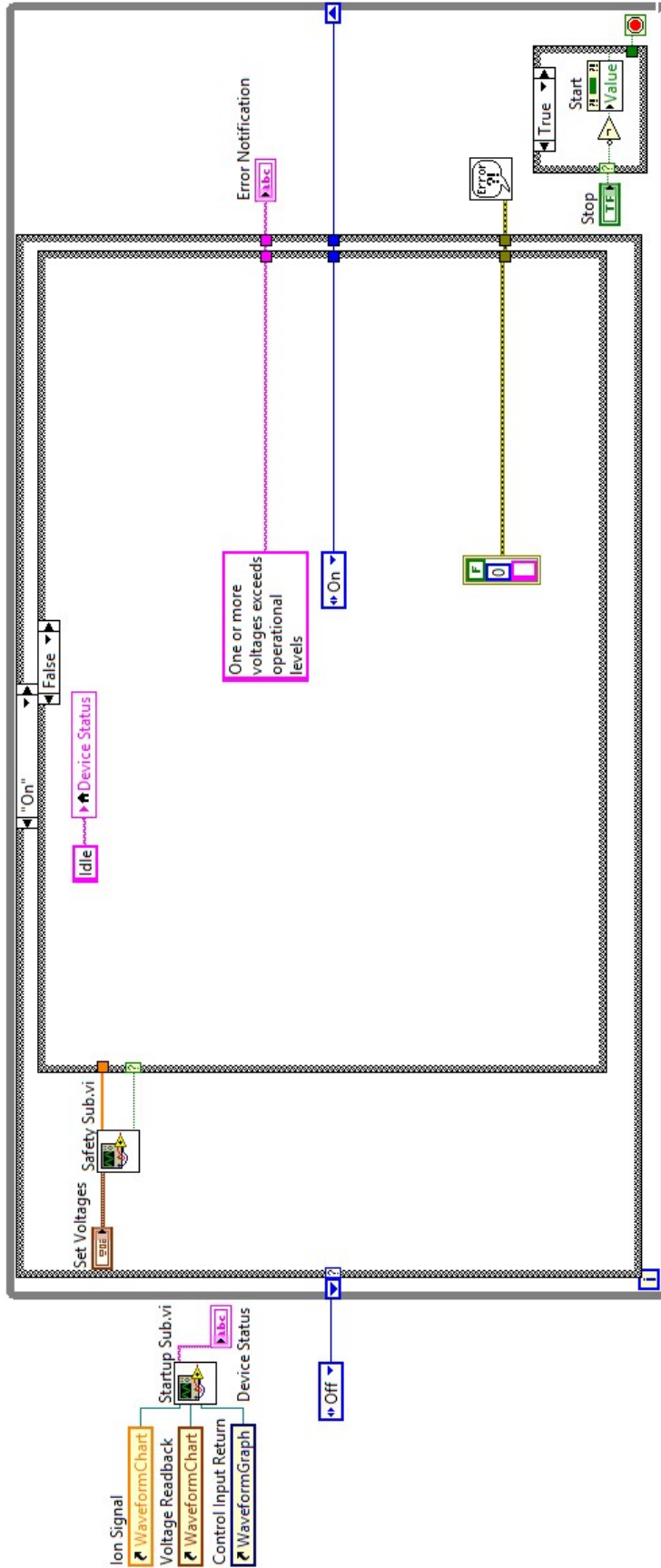


Figure B.18.3: Block diagram of instrument software after the start button is pressed on the front panel, but in the case that the user-input voltages exceed safe values. In this case, the device status is switched to idle and an error message is sent to the user. Correcting the input voltages to save values will allow the program to proceed to the true case for this loop.

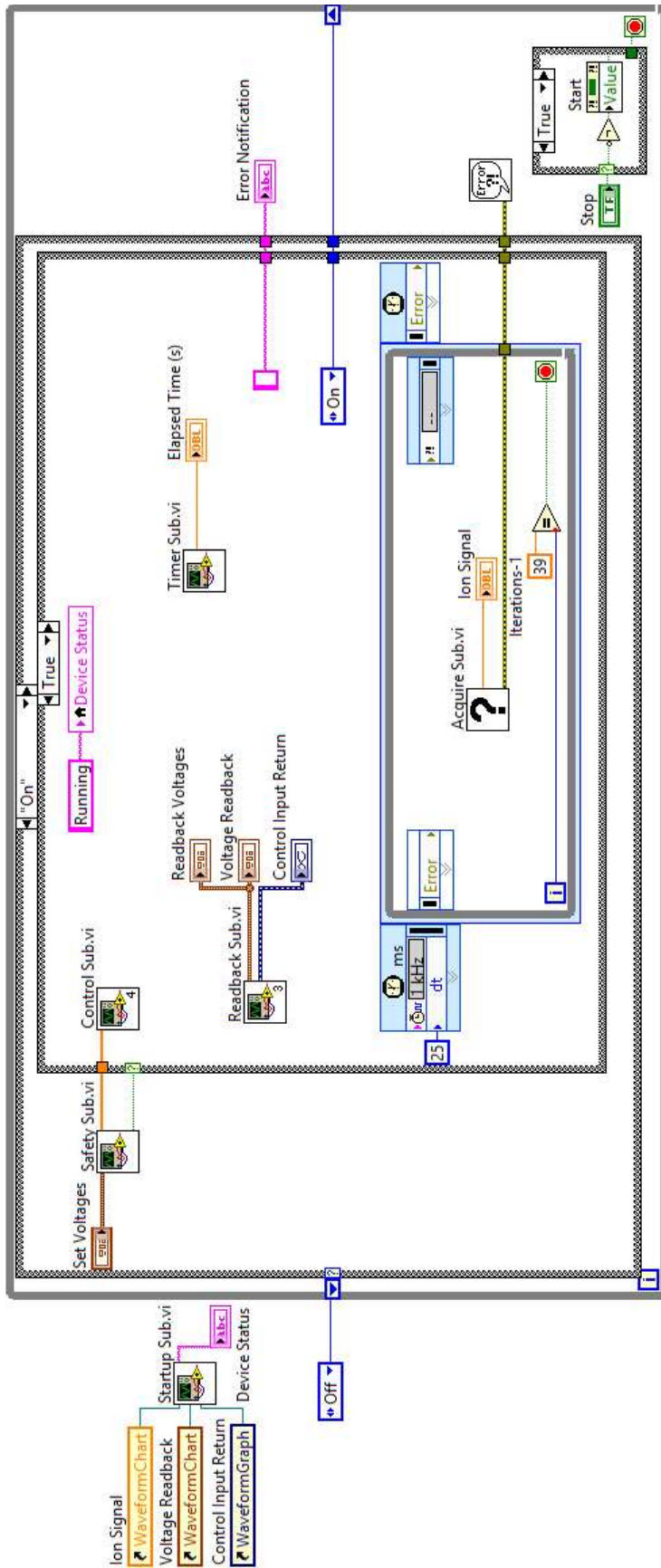


Figure B.18.4: Block diagram of instrument software in the running state. Display plots are initialized, voltage inputs are checked for safety and sent via an analog output card to the power supplies, power supplies monitor the actual output voltage and return the information via an analog input card, and signal is acquired via an analog input card.

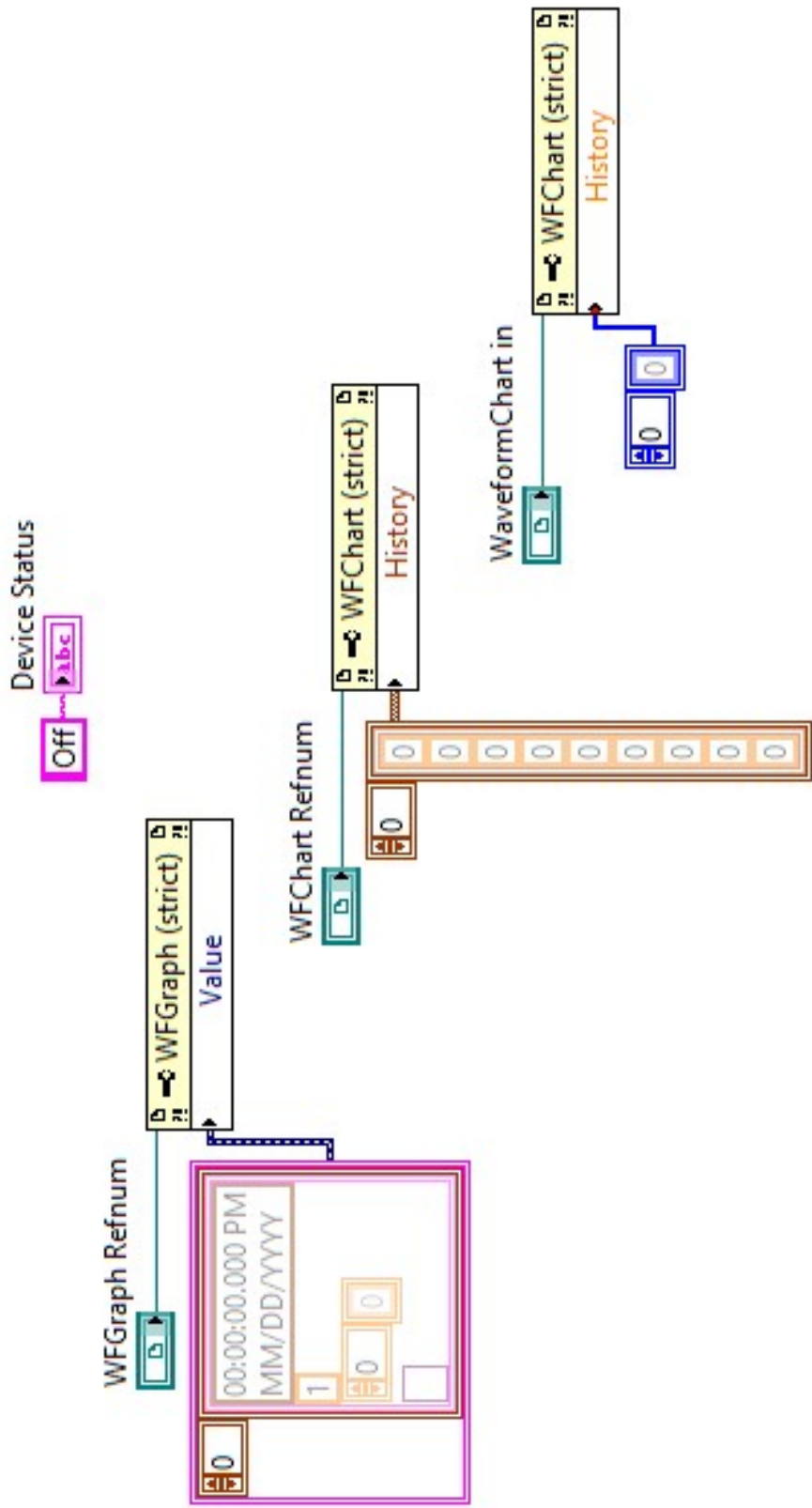


Figure B.18.5: Block diagram of Startup Sub.vi of instrument software showing initialization of plots prior to entering the running state.

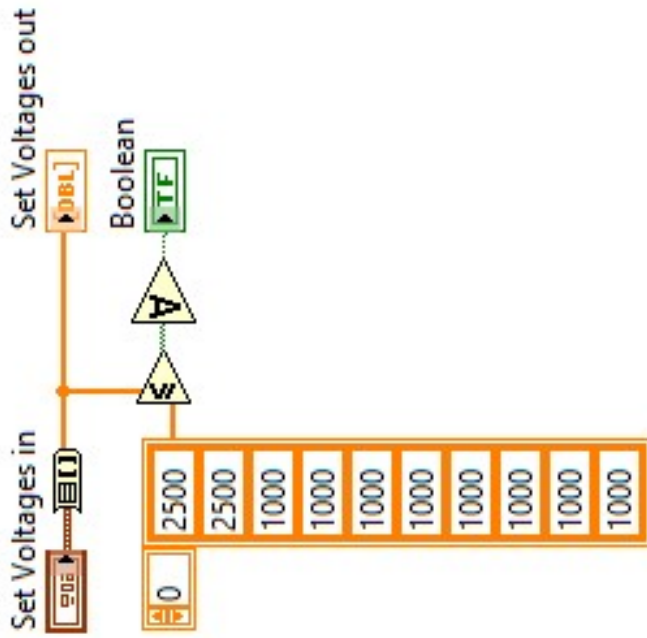


Figure B.18.6: Block diagram of Safety Sub.vi of instrument software showing the check of safe voltage settings for each power supply prior to entering the running state.

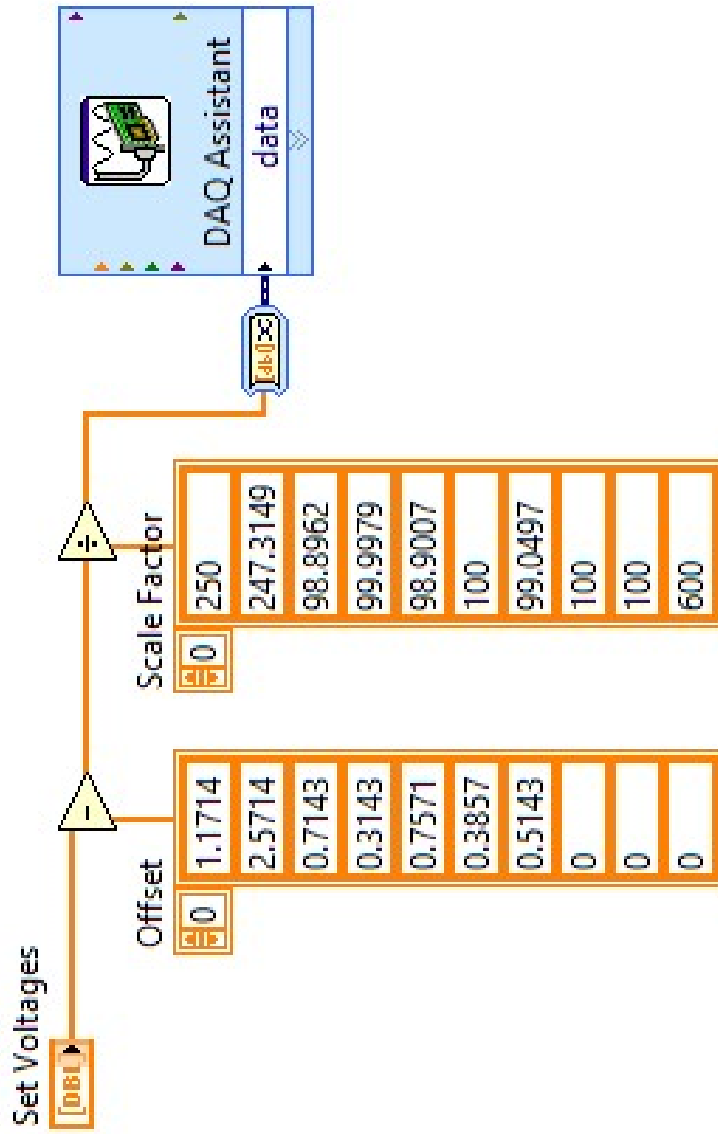


Figure B.18.7: Block diagram of Control Sub.vi of instrument software showing linear offset and scaling of voltages to account for variability in individual power supplies followed by communication of settings to PXI-6704 for delivery to power supply units.

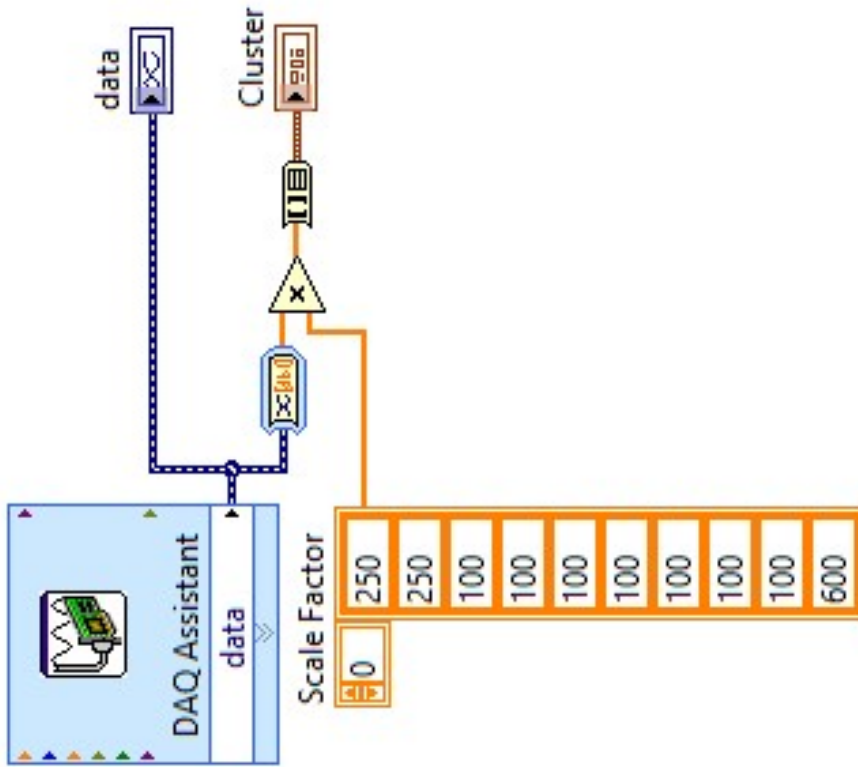


Figure B.18.8: Block diagram of Readback Sub.vi of instrument software showing retrieval of voltage monitors from PXI-6224 with scaling to show the user the actual voltage applied in the instrument.



Figure B.18.9: Block diagram of Timer Sub.vi of instrument software showing elapsed time function which monitors how many seconds the program has been in the run state.

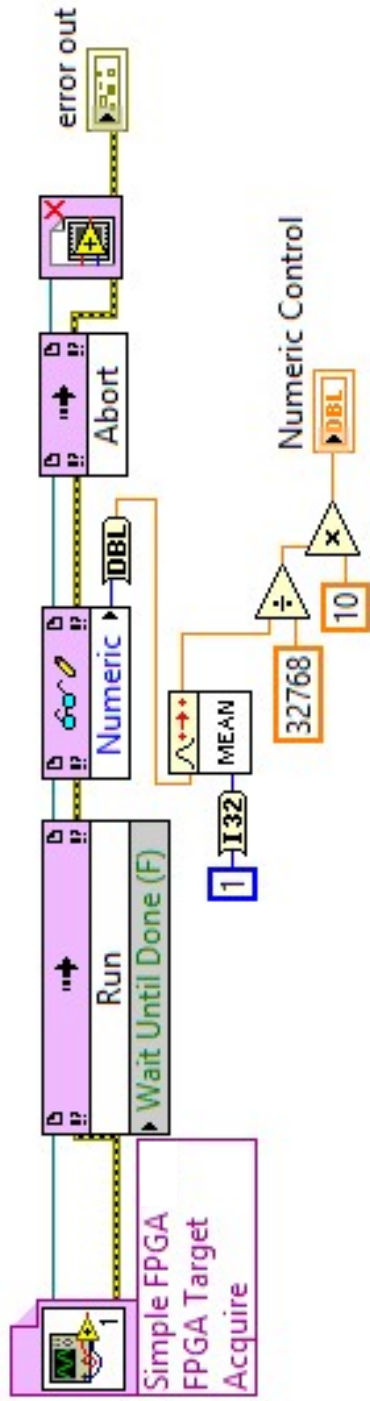


Figure B.18.10: Block diagram of Acquire Sub.vi of instrument software showing collection of ion signal as voltage via Simple FPGA.vi. Signal is averaged and normalized for display on the front panel and that of the Acquire Sub.vi.

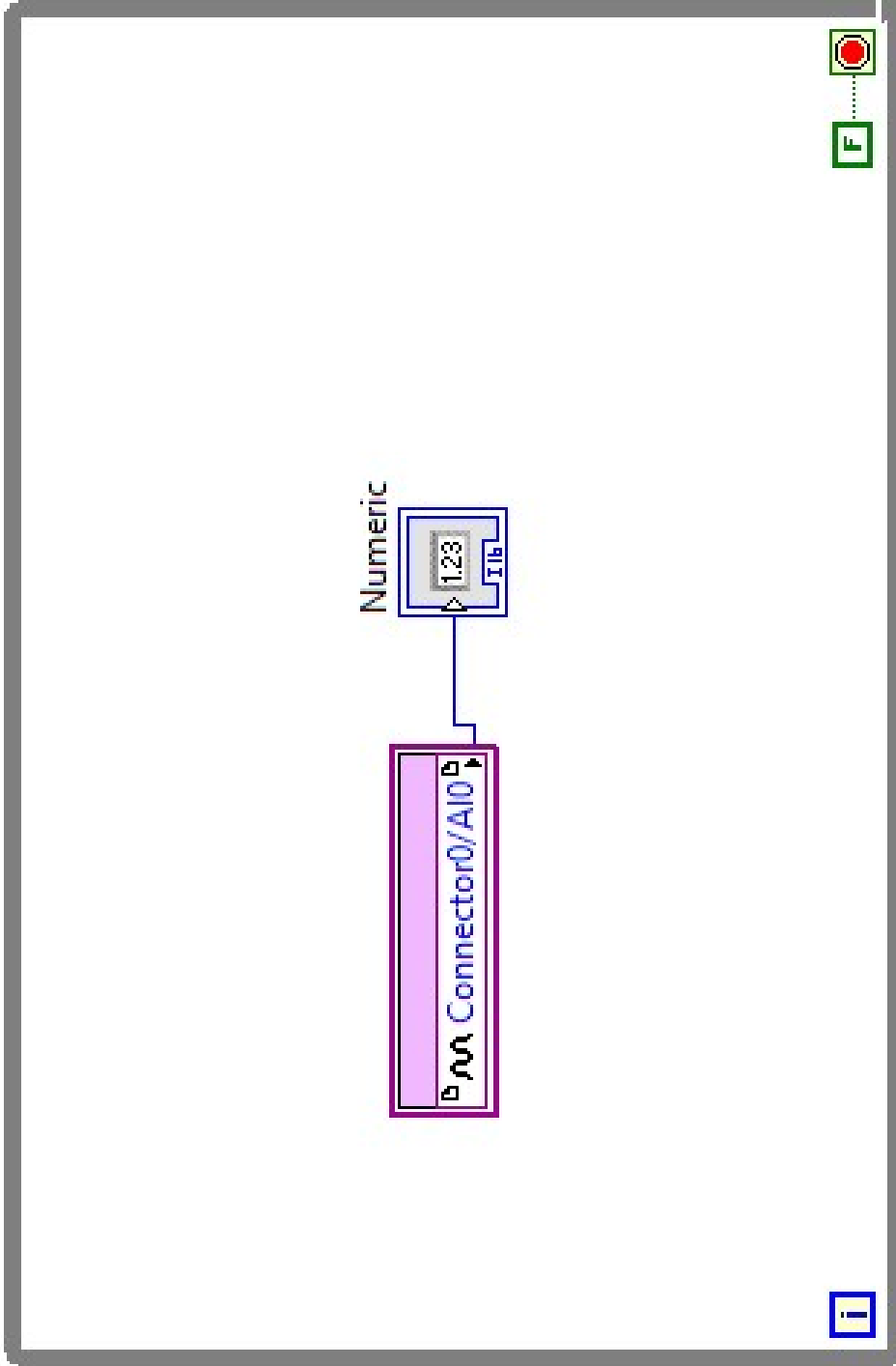


Figure B.18.11: Block diagram of Simple FPGA.vi within Acquire Sub.vi from instrument software showing collection of ion signal as voltage via PXI-7842R, which is connected to the signal amplifier output.

Figure B.19.1: ESI source assembly before and after anodization, without needle

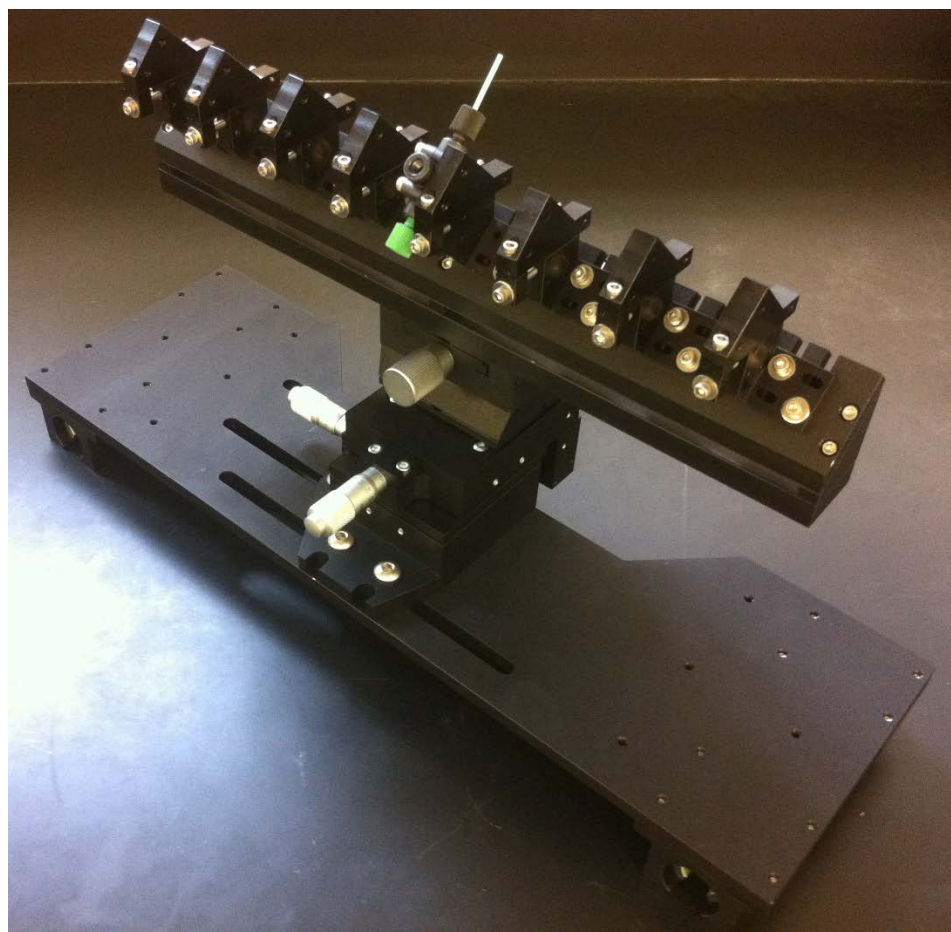
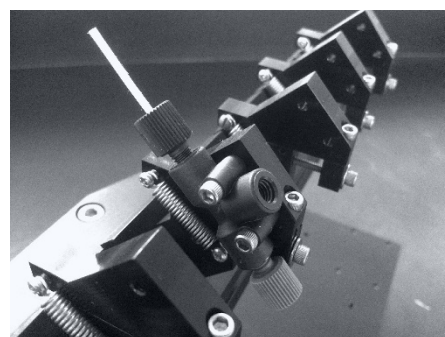


Figure B.19.2: ESI source spray in operation and disassembled fittings

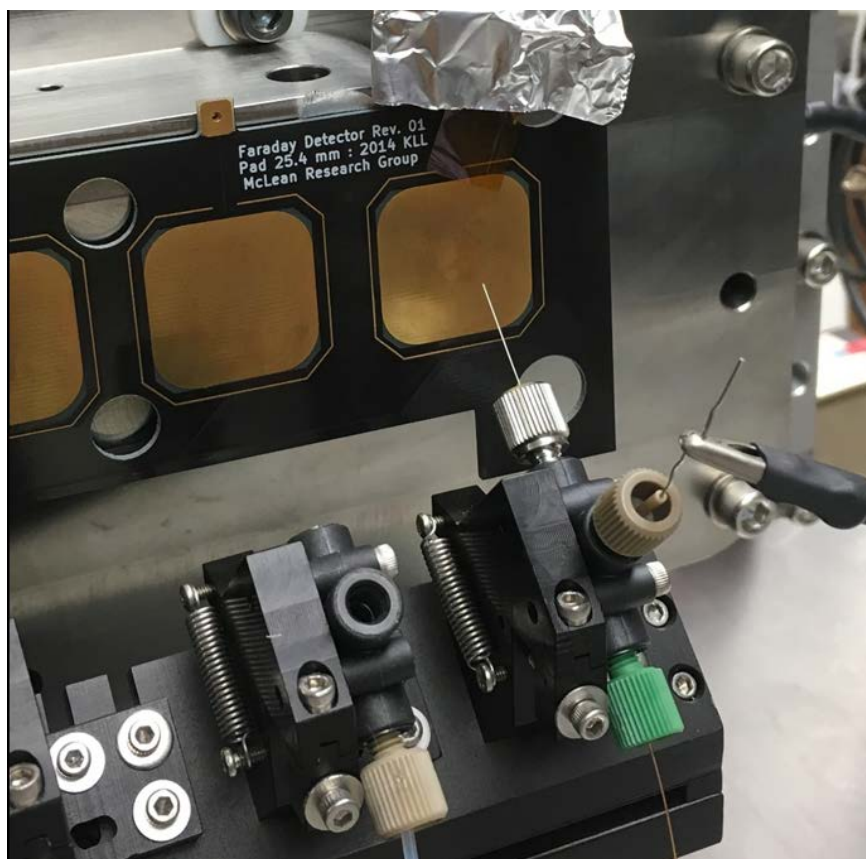
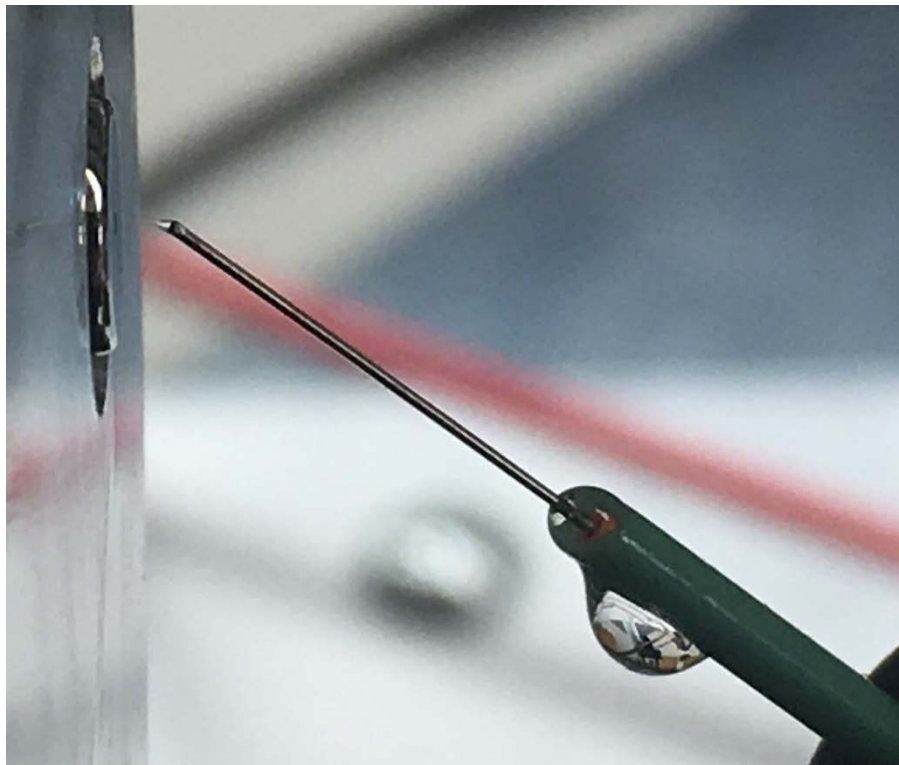


Figure B.19.3: Resistive glass capillary, held up to light and compared to home-built capillary



Figure B.19.4: Heated desolvation block disconnected from top hat flange, insulating flange (later revision made from black Delrin), and early assembly of first chamber

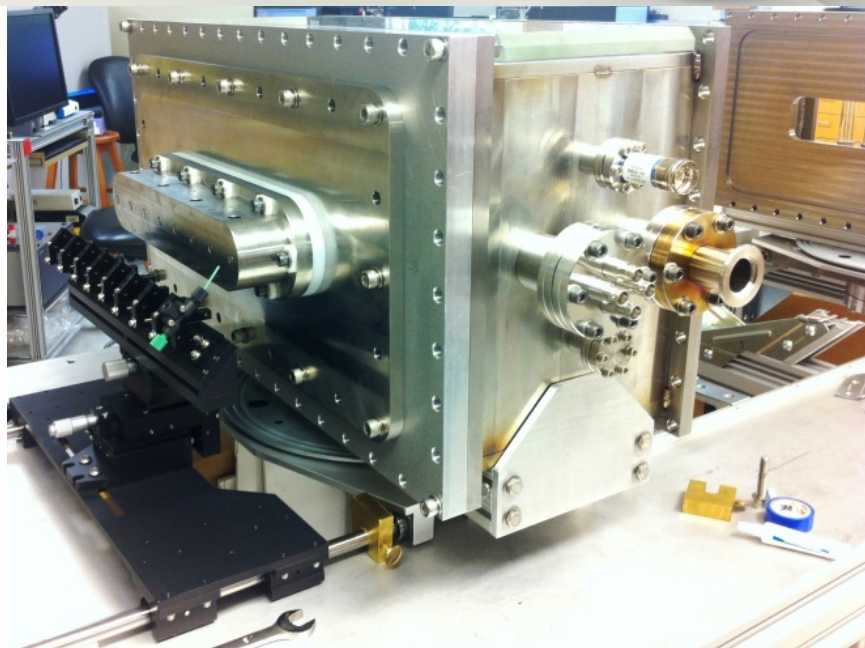
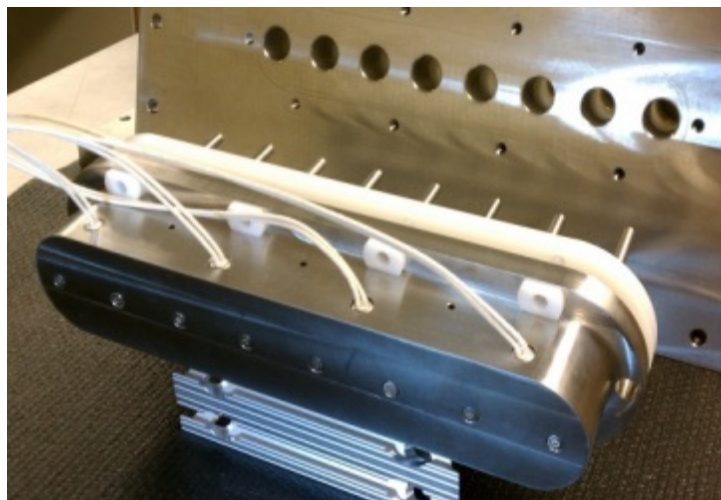


Figure B.19.5: High pressure ion funnel and blown resistor comparison on RC circuit board

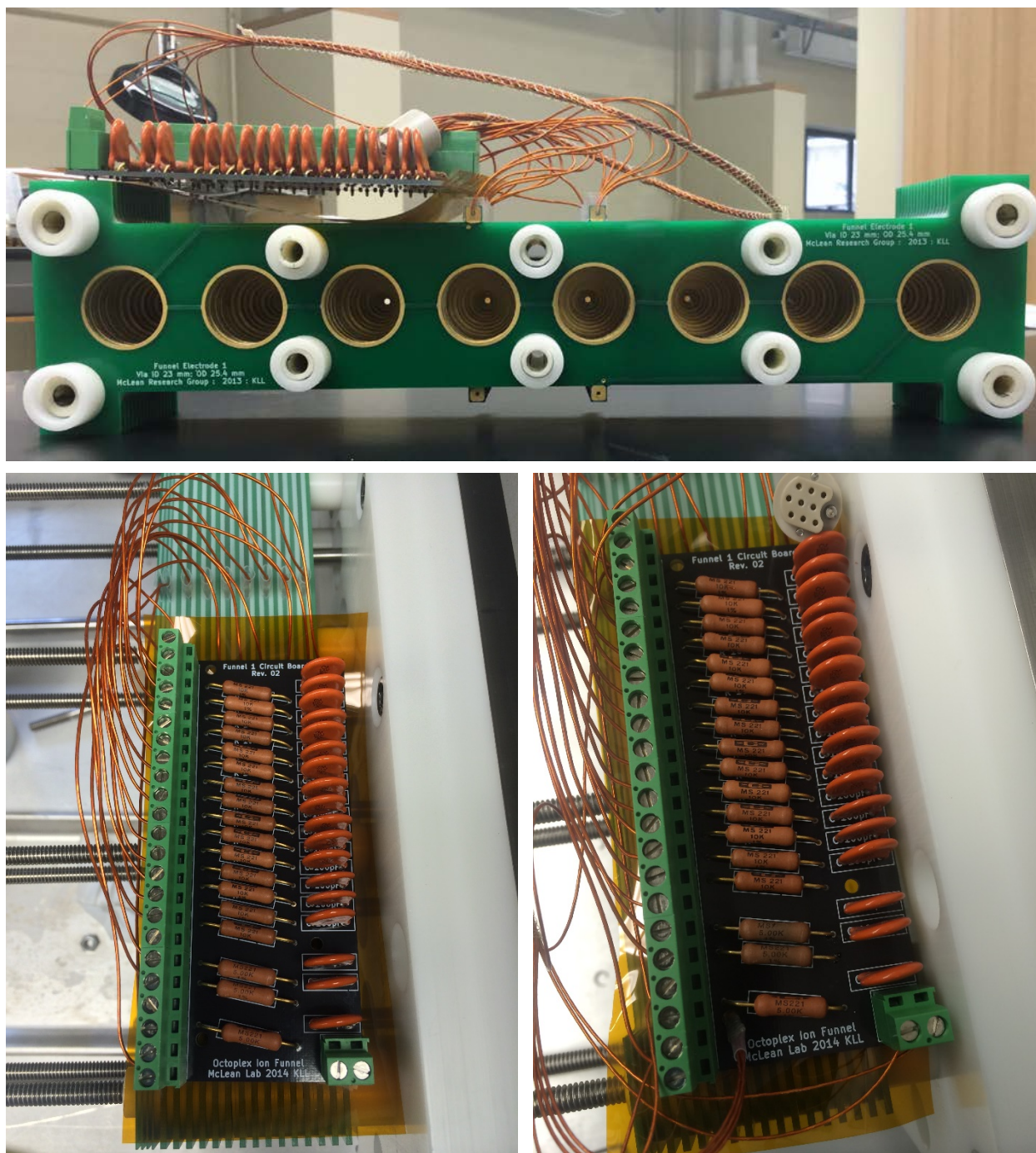


Figure B.19.6: RC circuit for high pressure funnel assembly

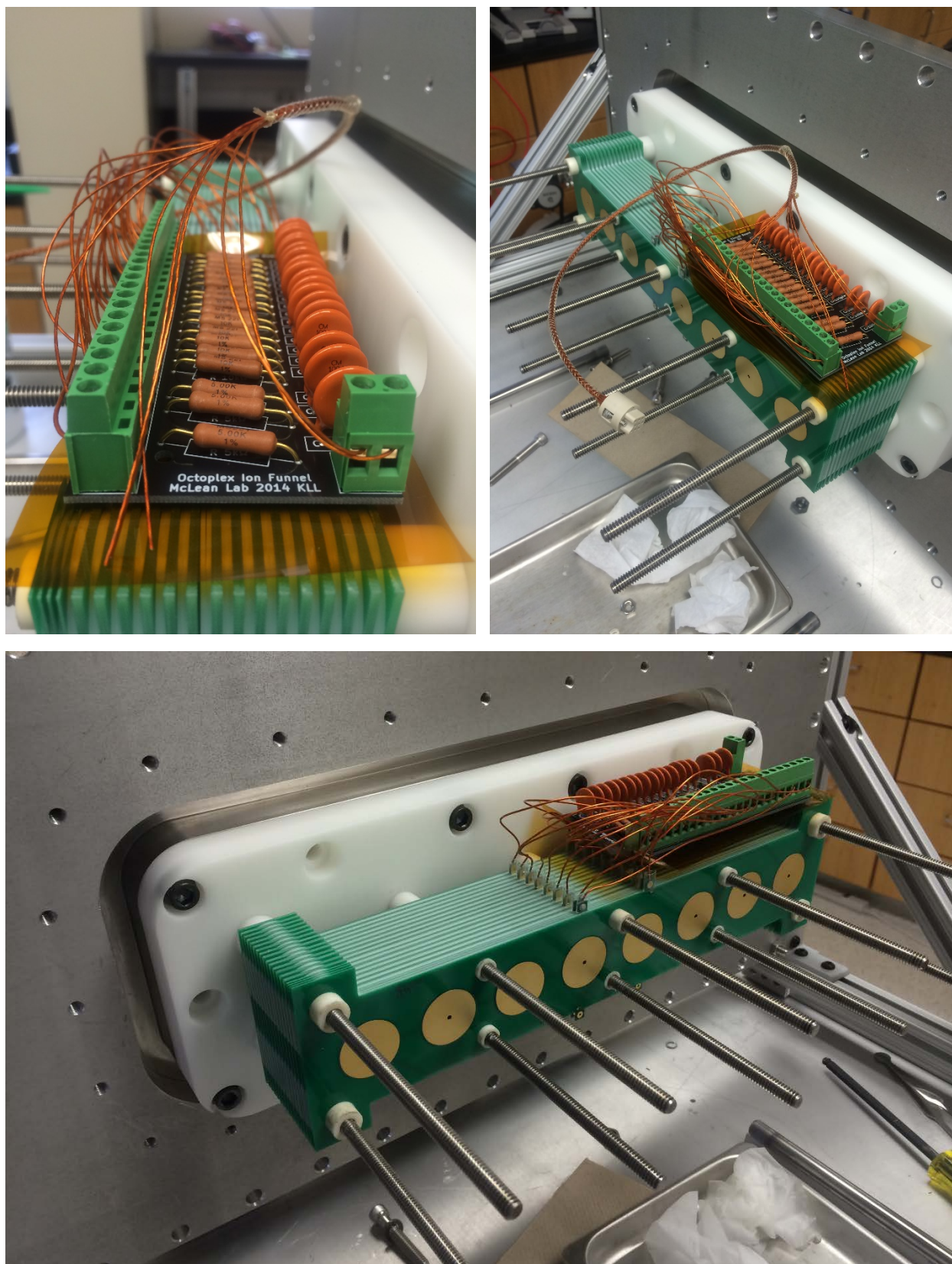


Figure B.19.7: Inner vacuum chamber, smaller Delrin piece pictured is previous revision

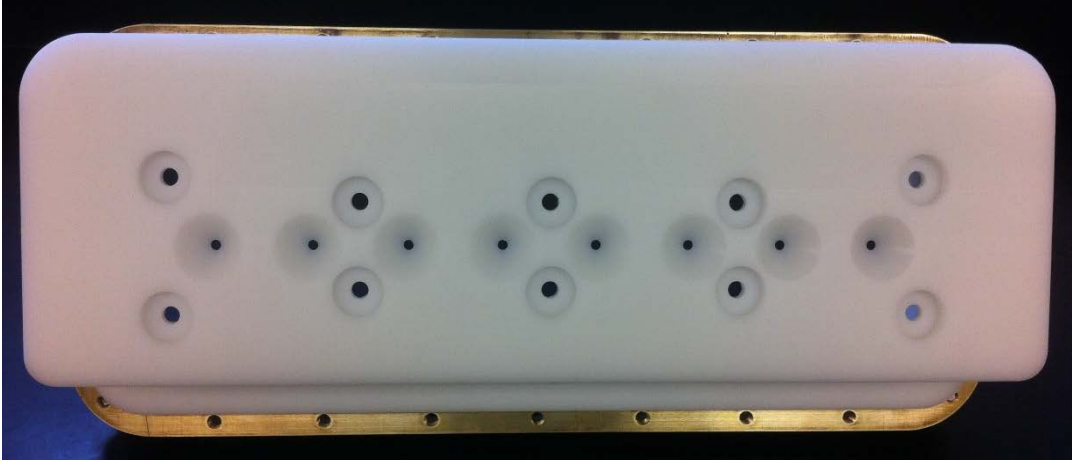
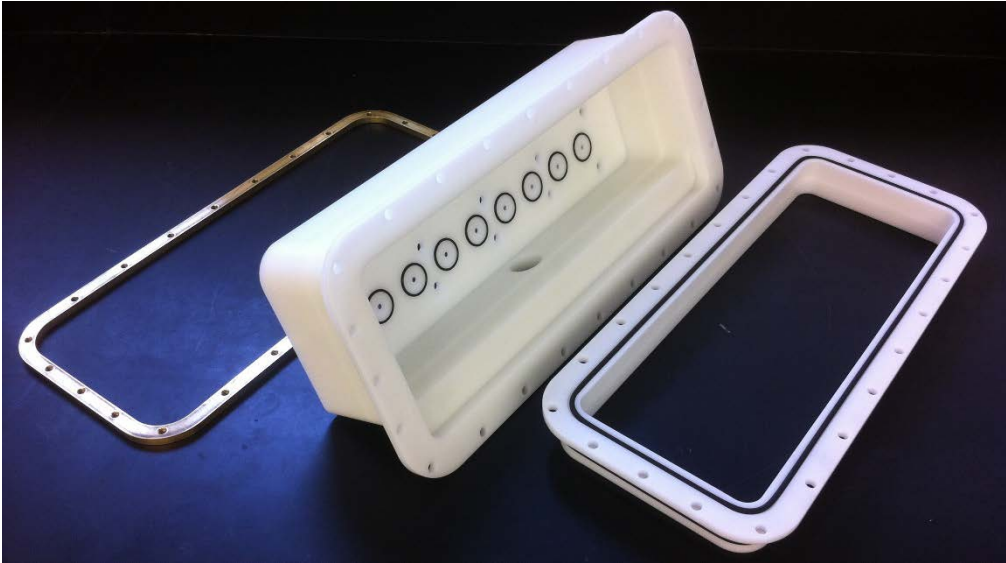


Figure B.19.8: Vacuum connection for inner vacuum chamber pumpout and low pressure funnel RC circuit board

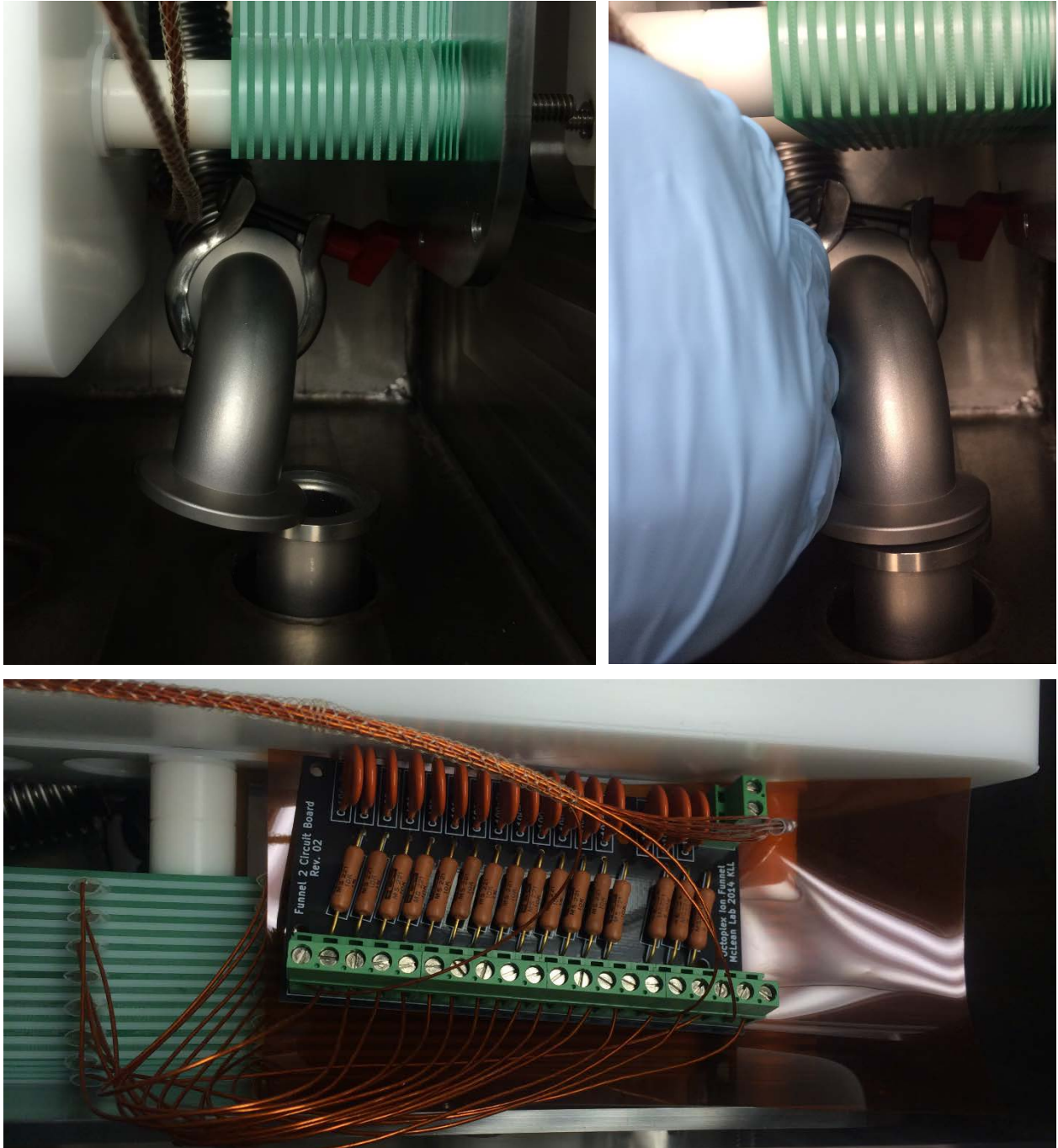


Figure B.19.9: Extension collar and RGC electrical feedthrough piston seal

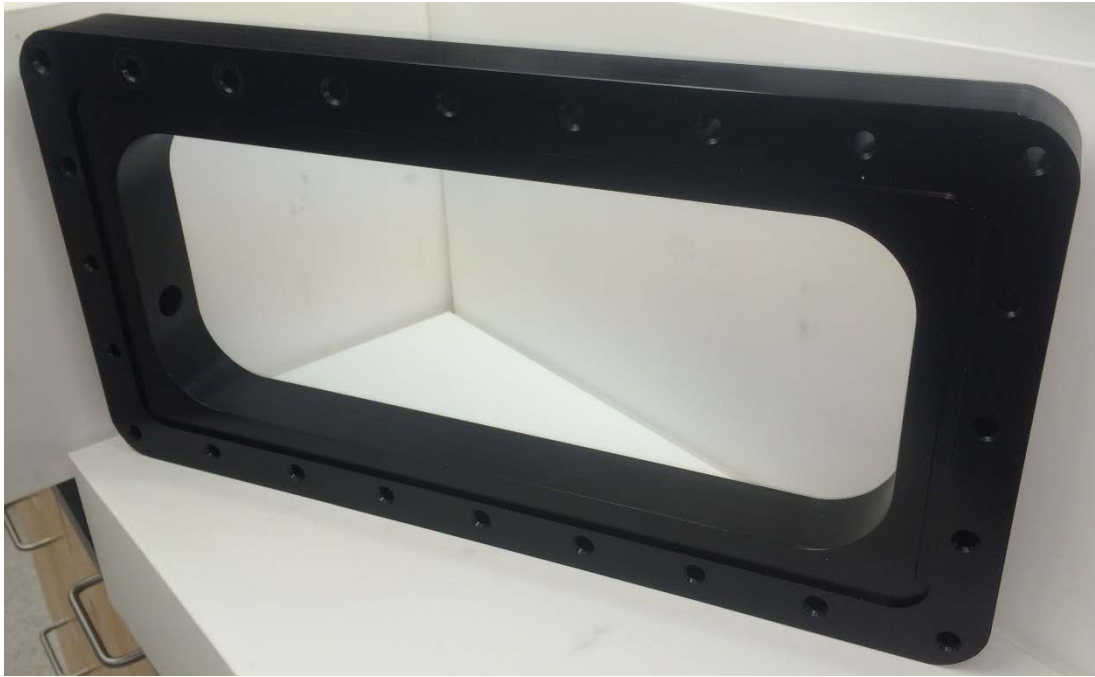


Figure B.19.10: Top hat flange protruding through $\frac{3}{4}$ " flange with seven blank rods and one home-built capillary, used prior to RGC installation, and funnel 1 mount block

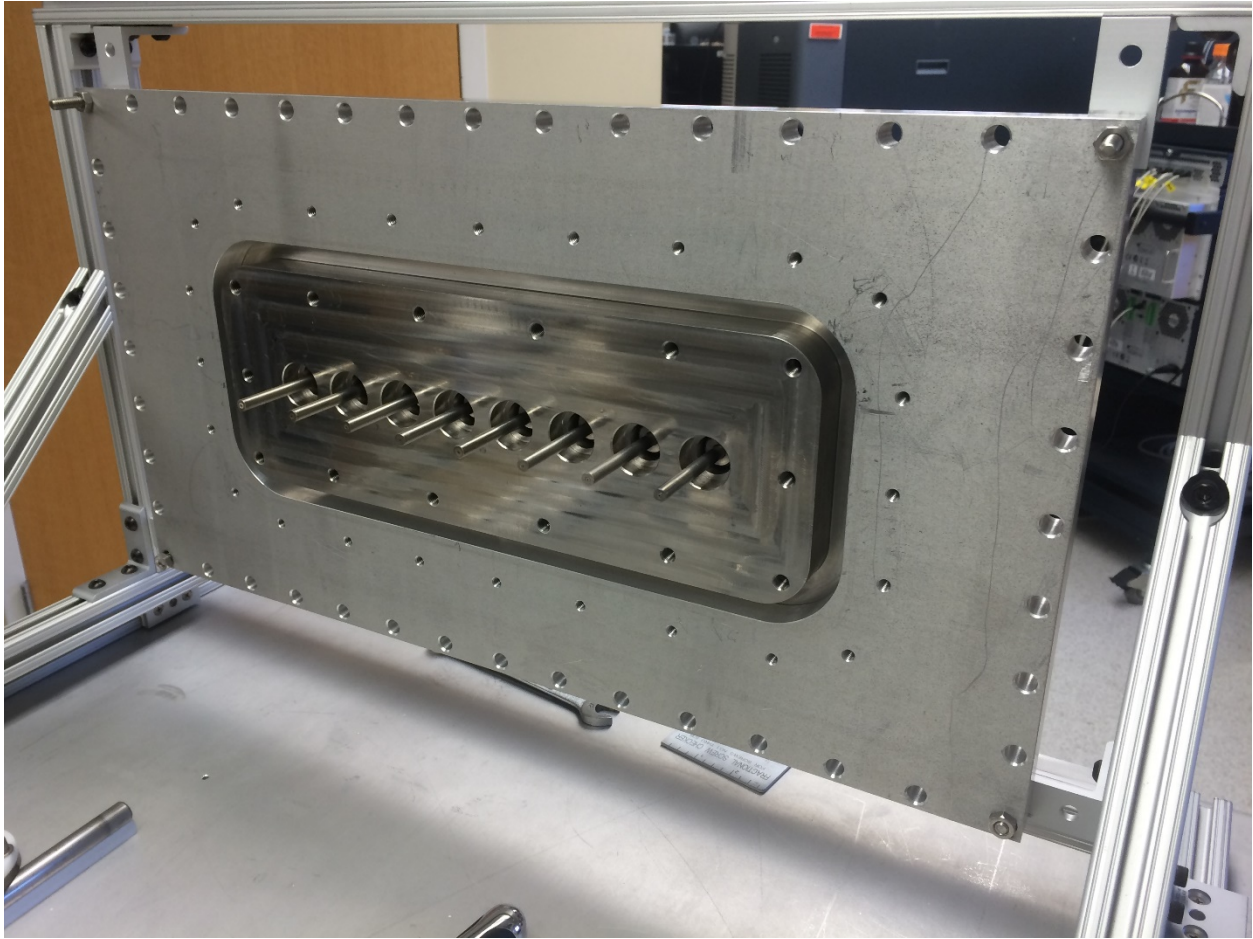


Figure B.19.11: Narrow drift tube mounted on aperture panel, with piston seal Delrin piece installed, and assembled free and resting on table

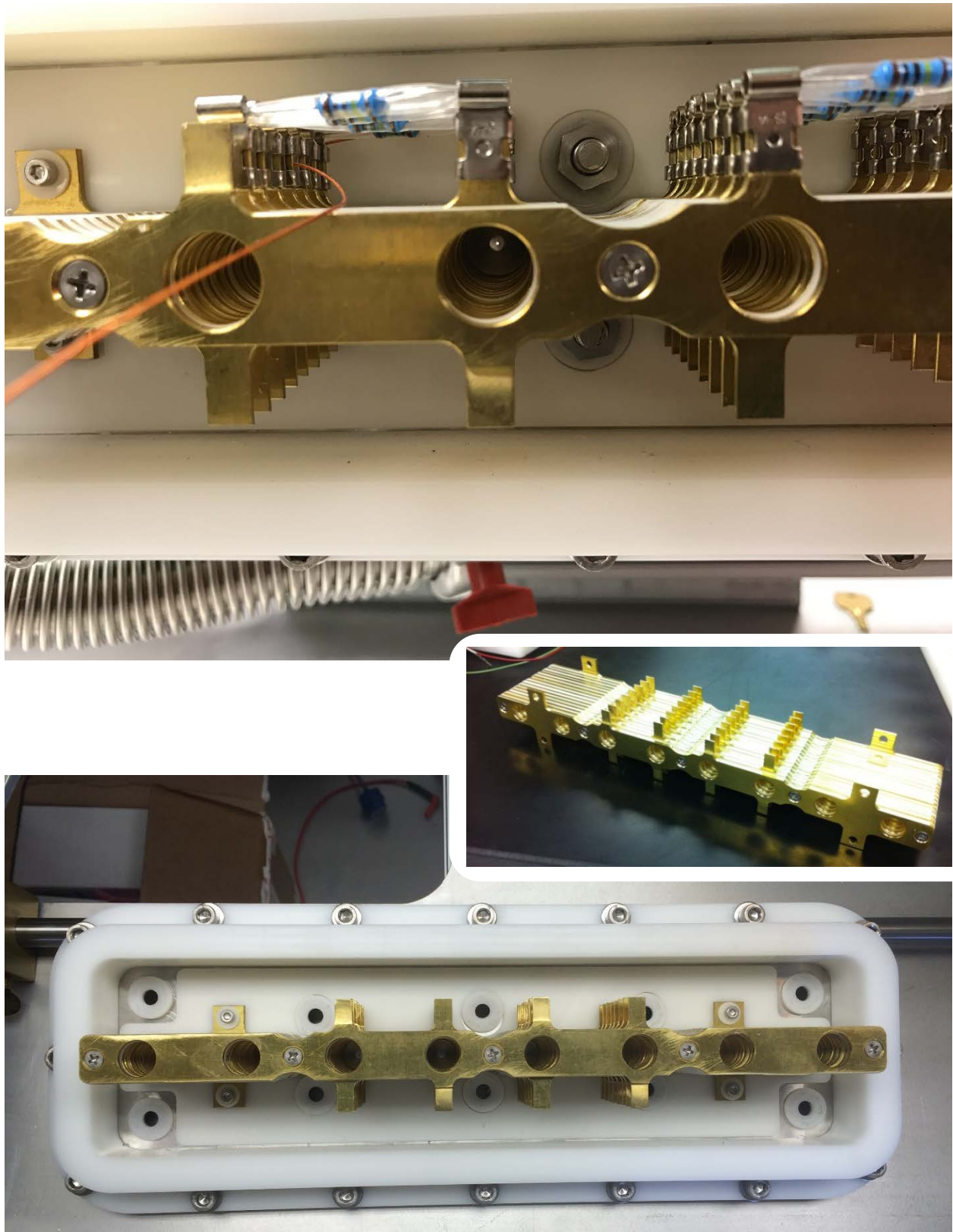


Figure B.19.12: Aperture panel assembly

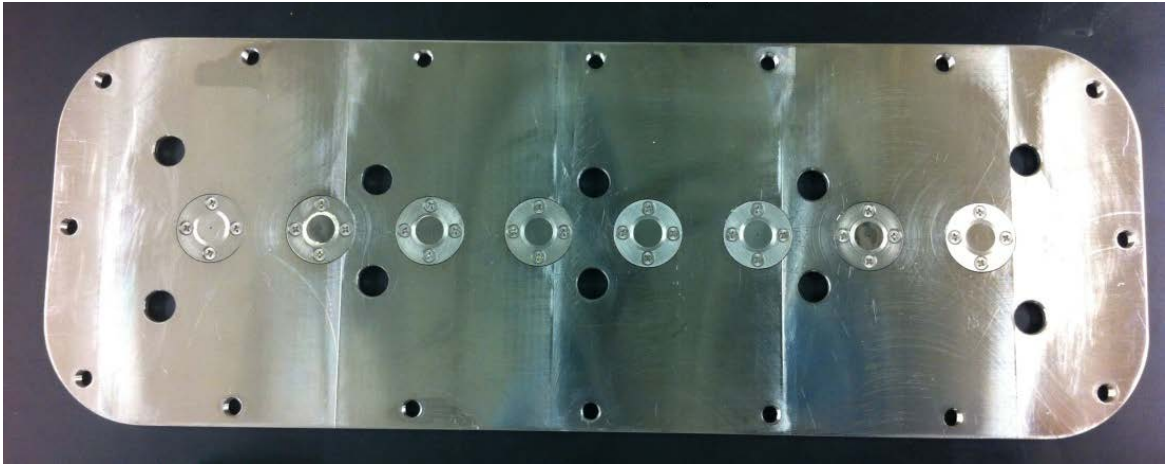


Figure B.19.13: Final drift tube electrode with grid and Faraday plate detector and stacks of drift tube electrodes, disassembled for detector installation

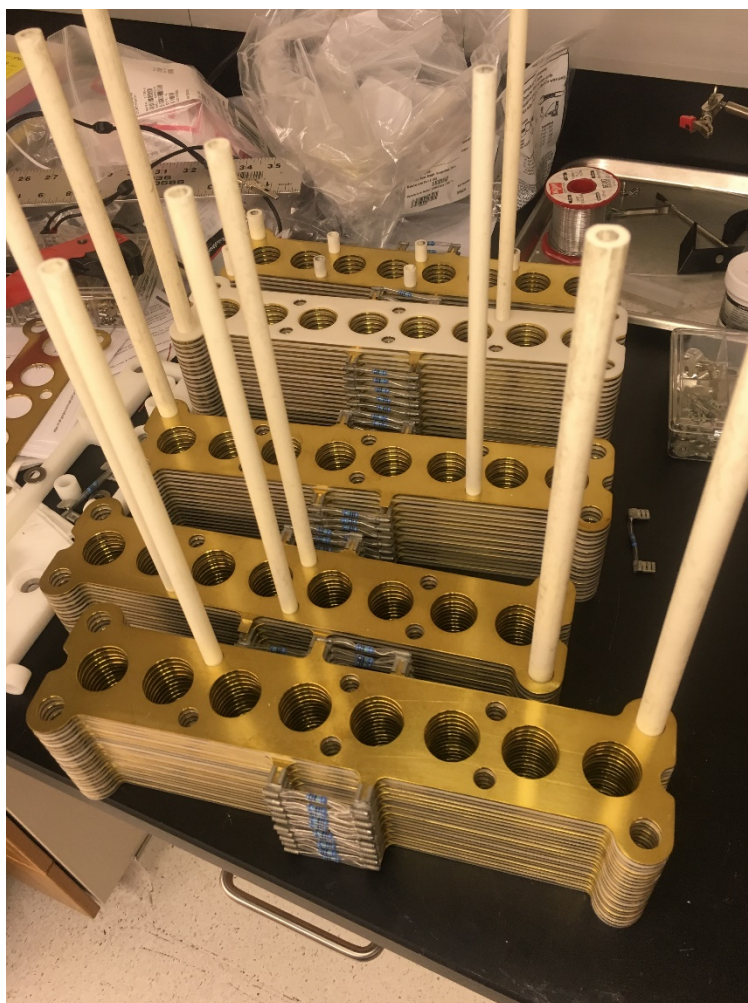
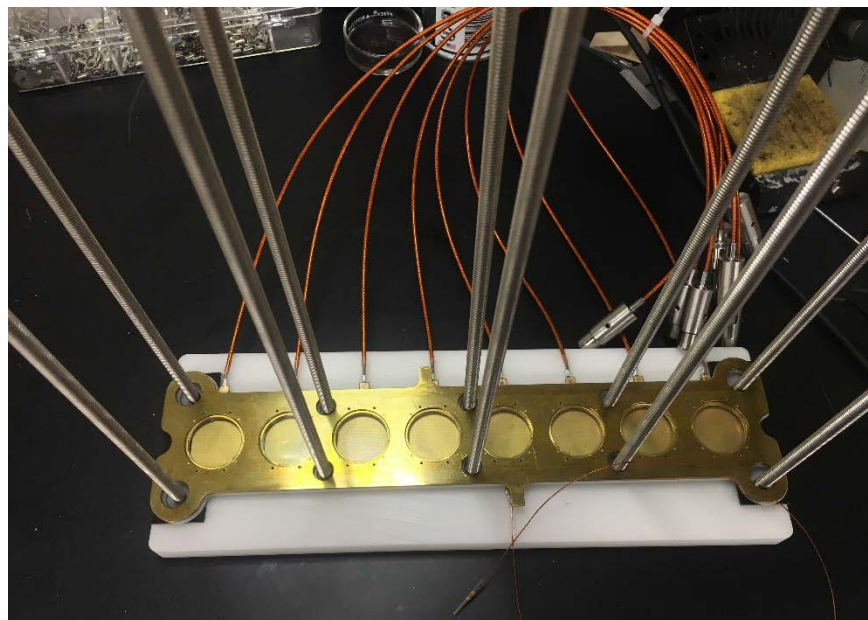


Figure B.19.14: Faraday plate array PCB, close up of pad with collected analyte and same pad after cleaning, temporary foil electrode substituted in troubleshooting

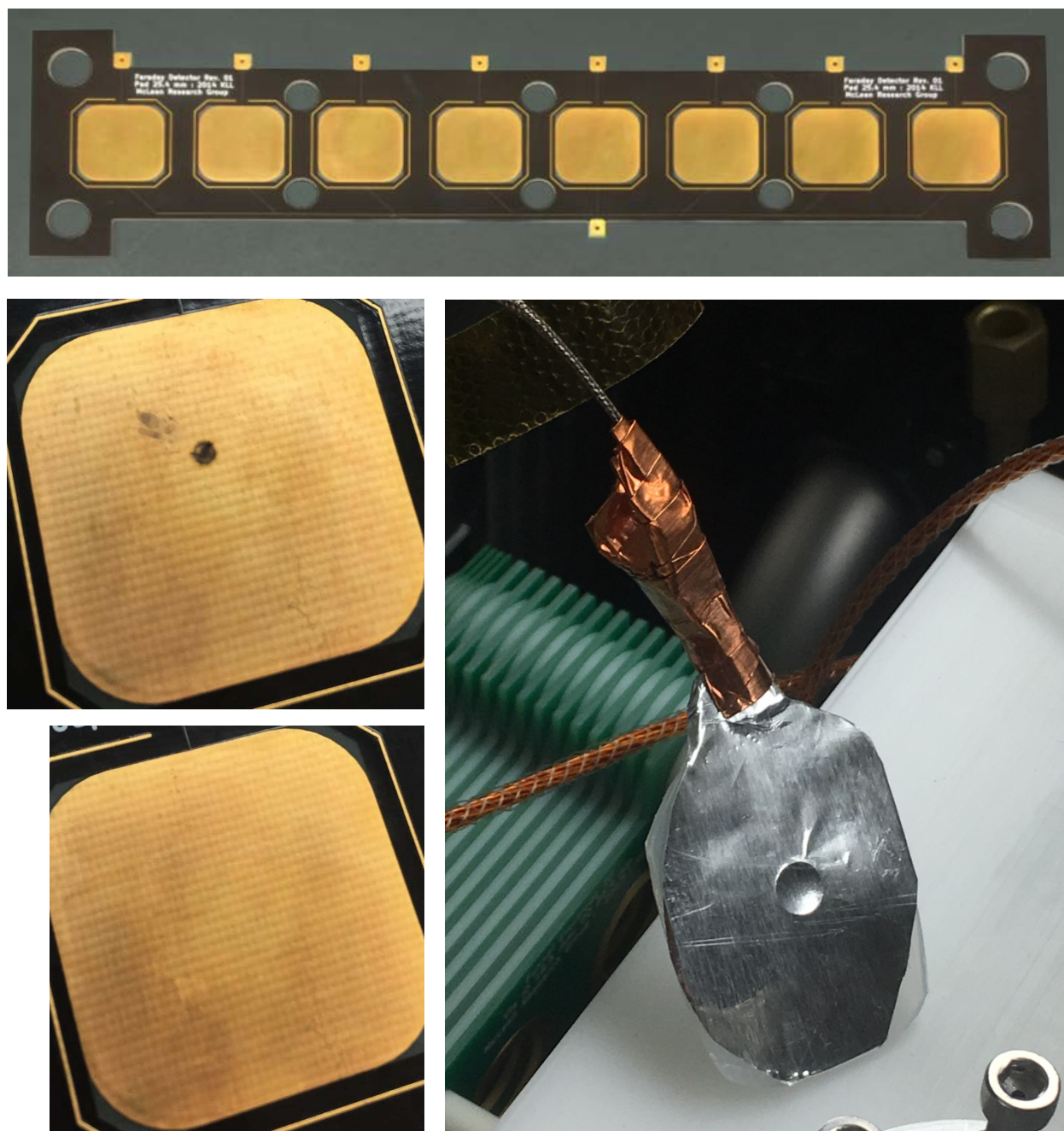


Figure B.19.15: Comparison of previous brass plate ion funnel electrode to current PCB ion funnel electrode

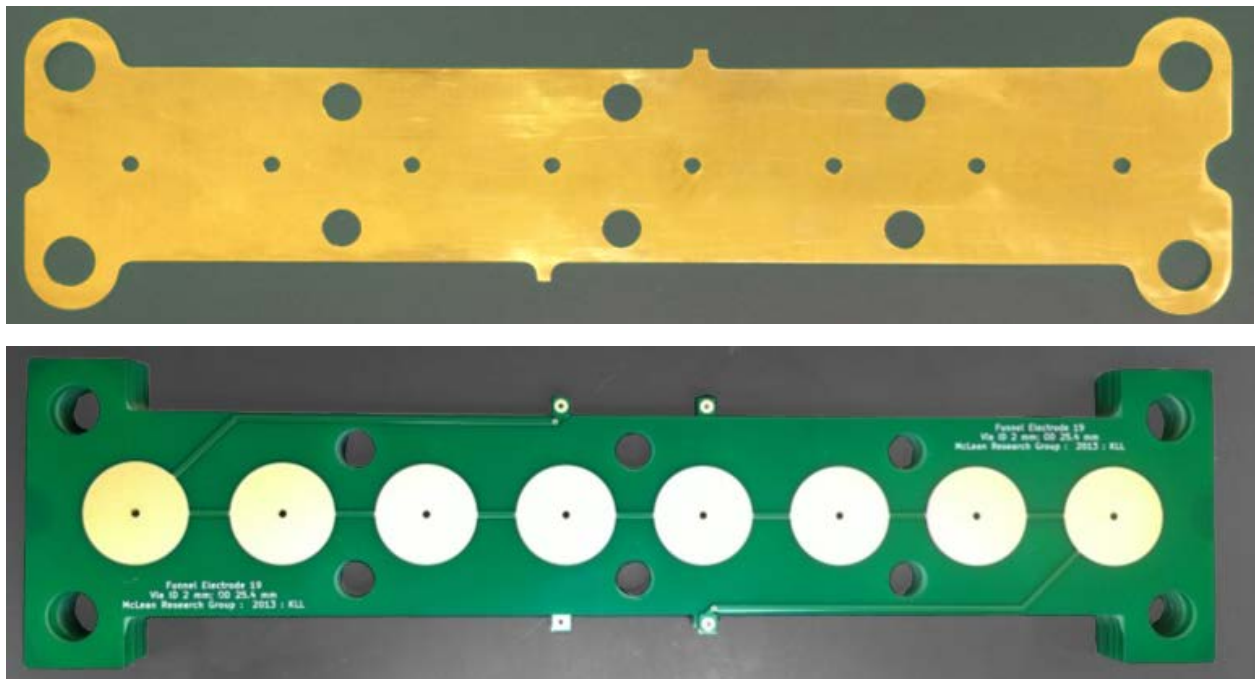


Figure B.19.16: Multiple electrode components resting on table including ion funnel, aperture panel, narrow drift tube, full size drift tube, and grid

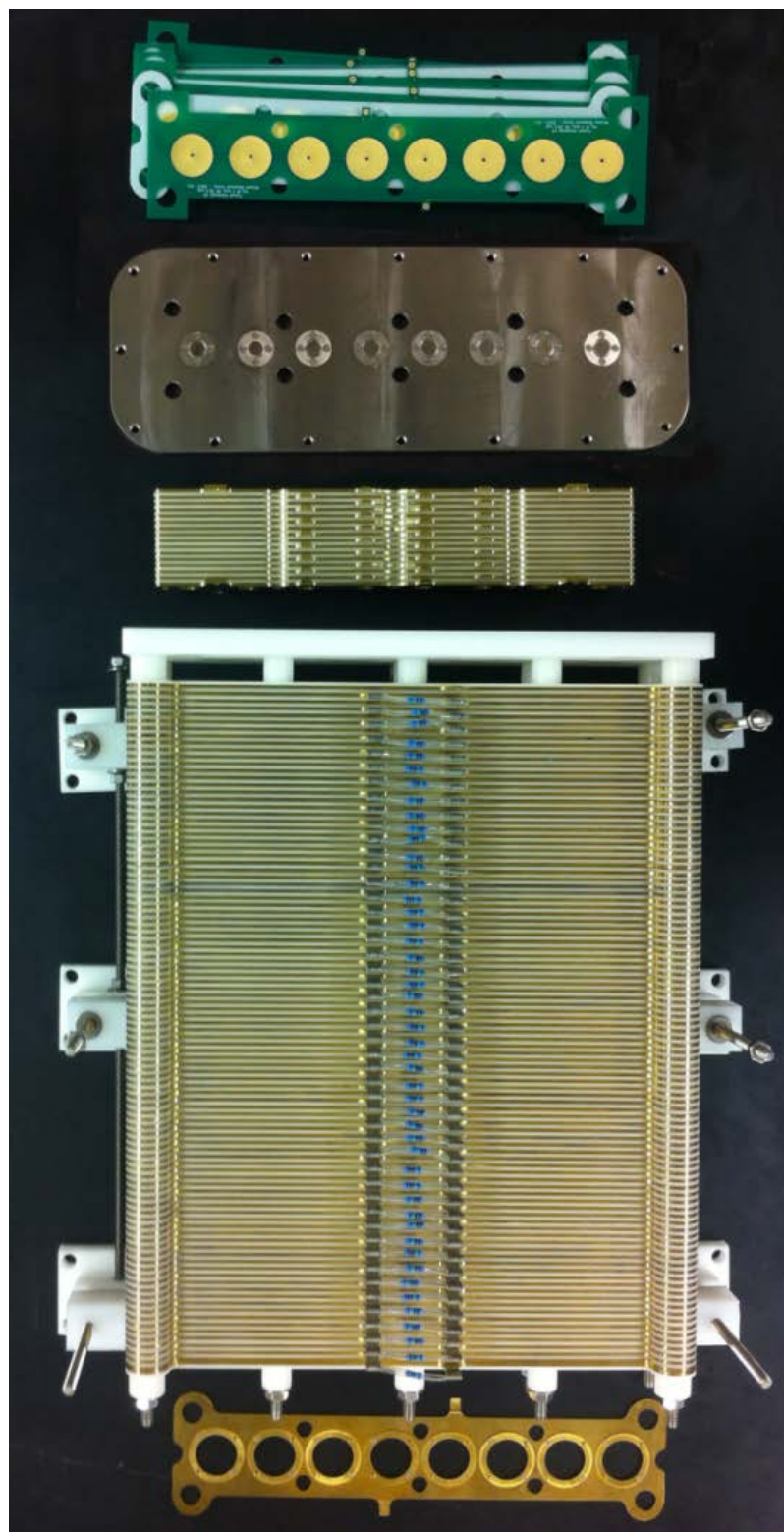


Figure B.19.17: Picoammeter first revision on multipurpose circuit board, amplifier enclosure, and picoammeter fourth revision designed on PCB

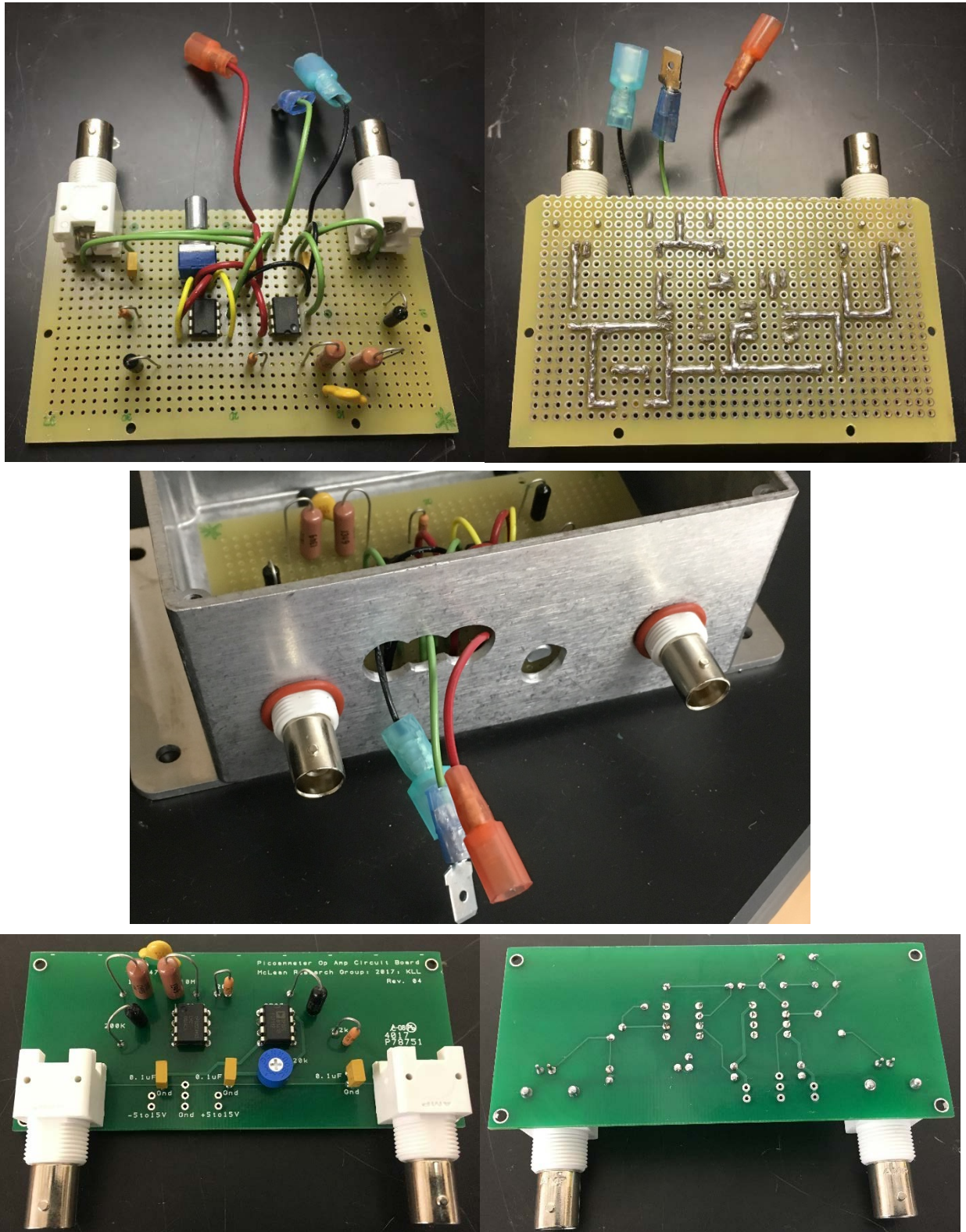


Figure B.19.18: Power supplies, 24 VDC

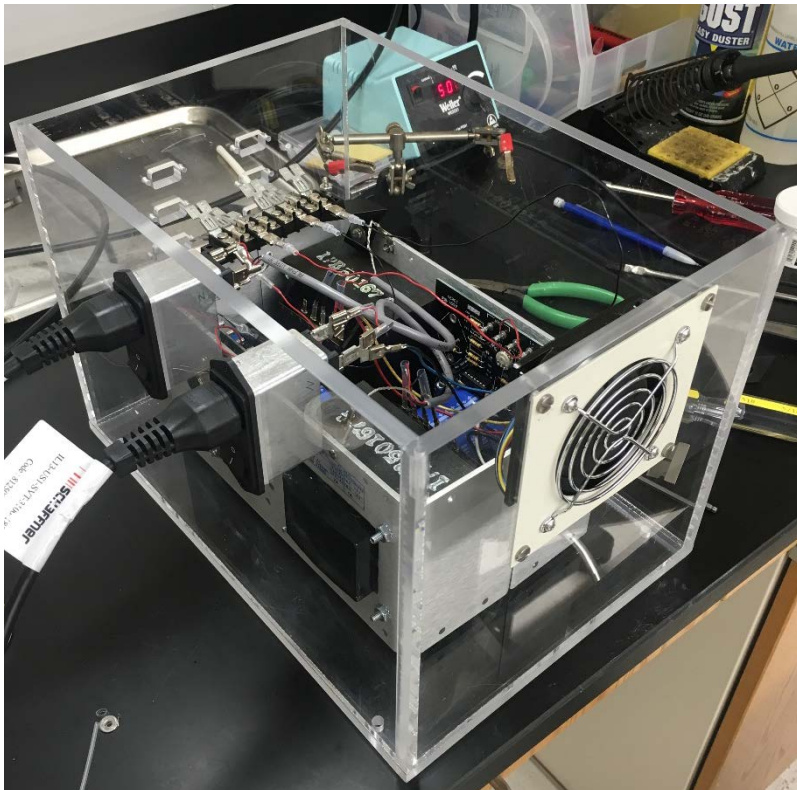
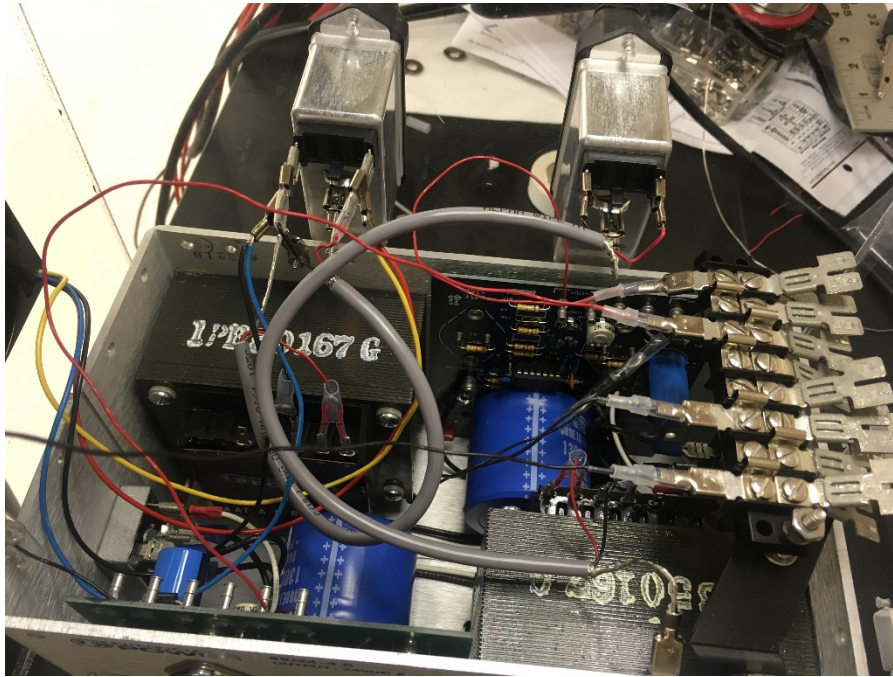


Figure B.19.19: Breakout boxes for high pressure ion funnel (top in each image), low pressure ion funnel (middle in each image), and drift tube (bottom in each image)

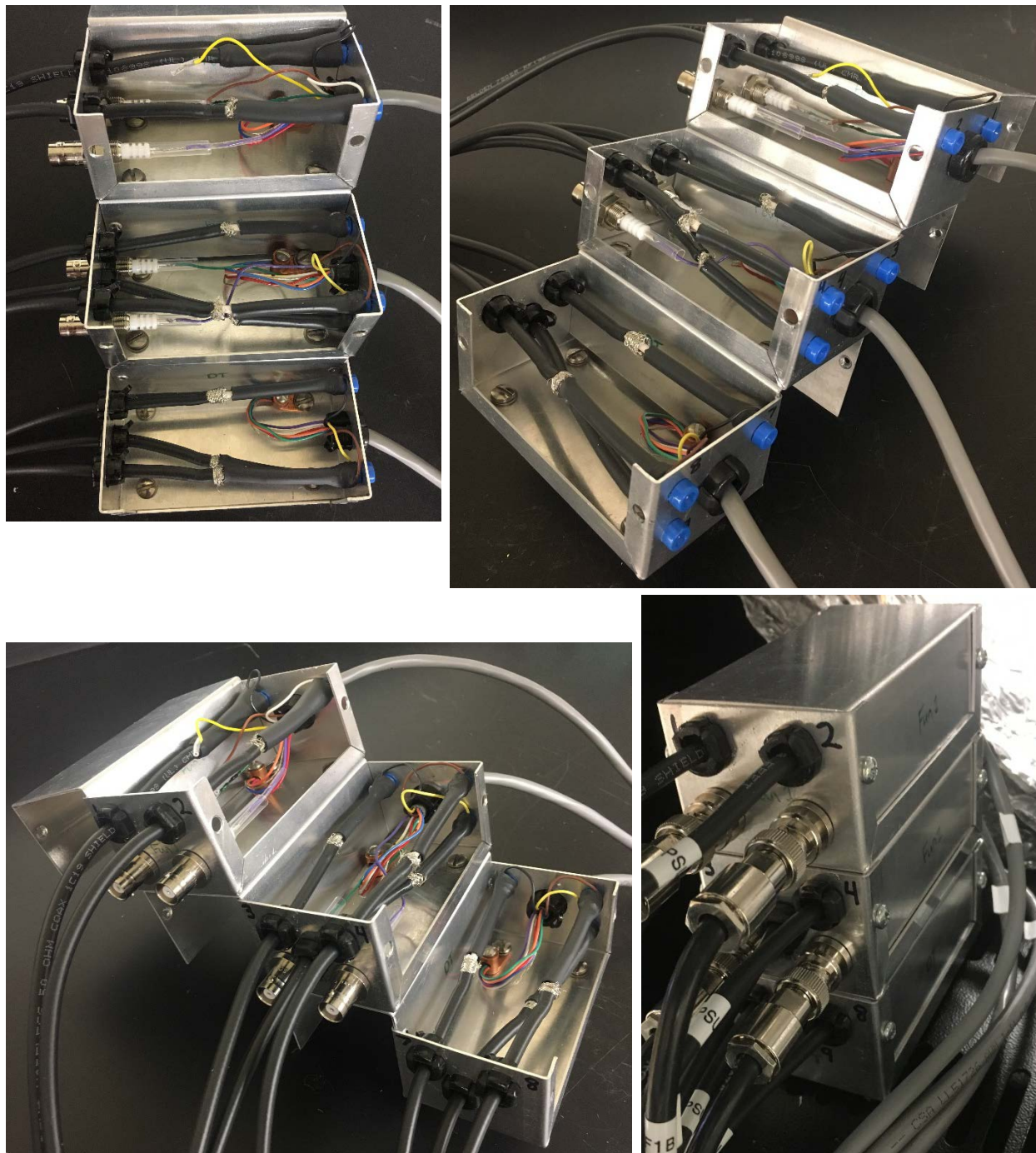


Figure B.19.20: Organization of cables leading from PSUs in drawers to 24 VDC supply, breakout boxes, and NI connector block which connects to NI chassis

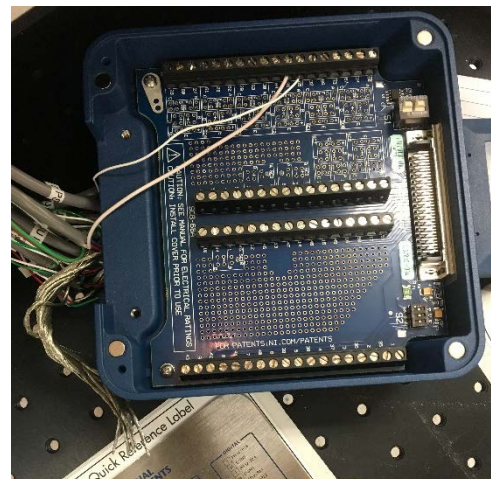


Figure B.19.20: Method using assembly support structure to install components in first vacuum chamber (tilt required to clear chamber edge), and table frame

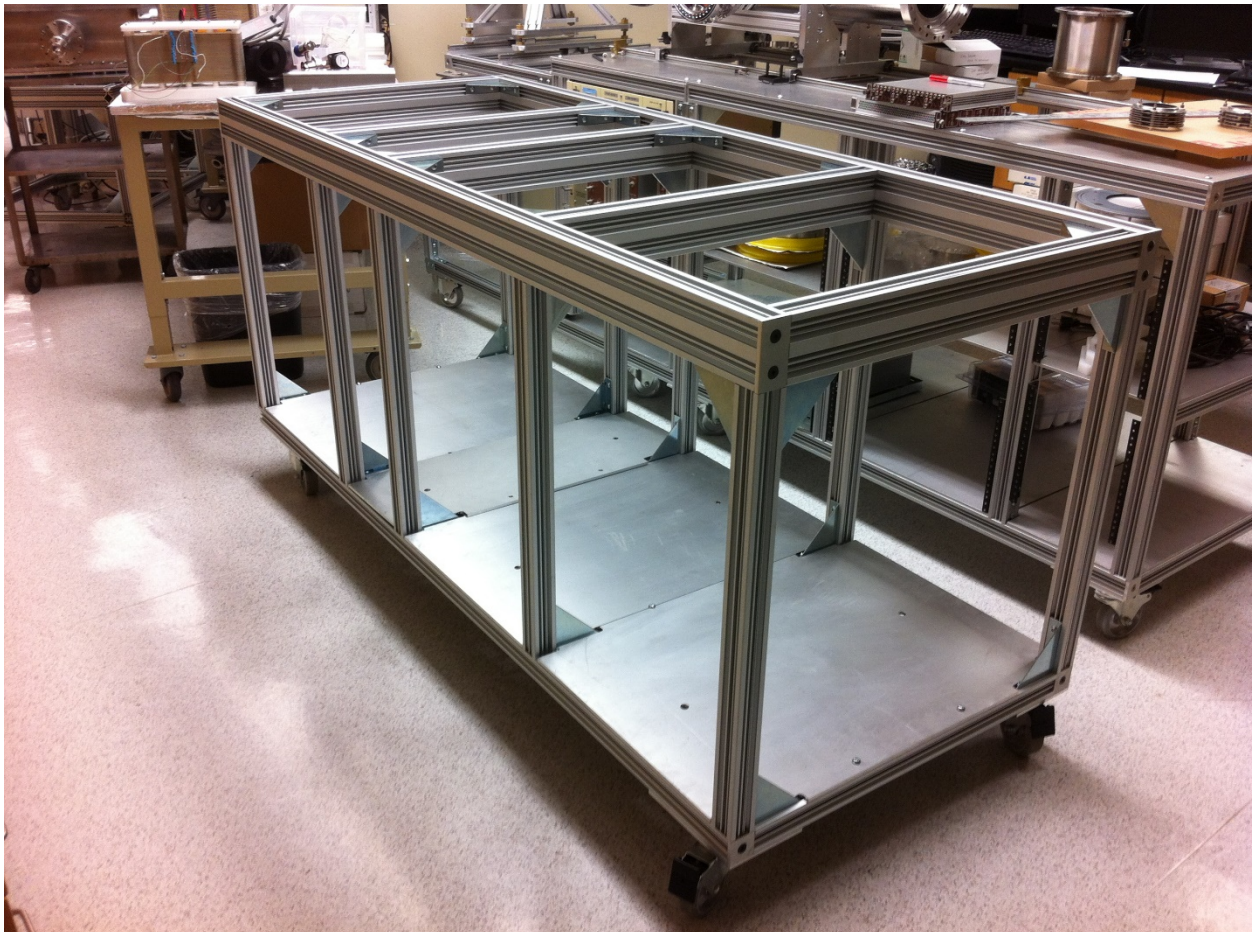
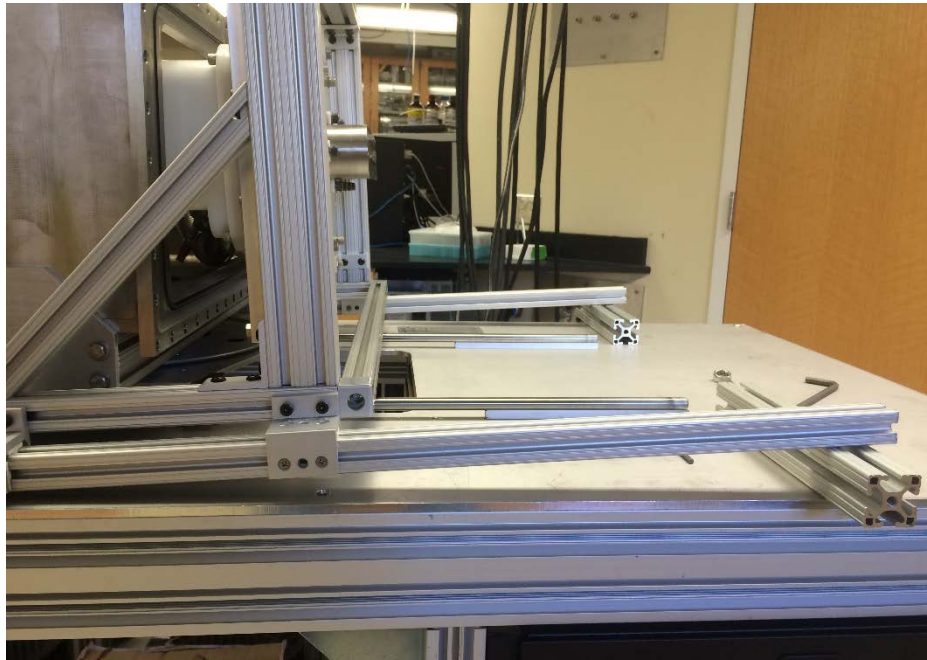


Figure B.19.21: Full instrument assembly prior to electronics wiring

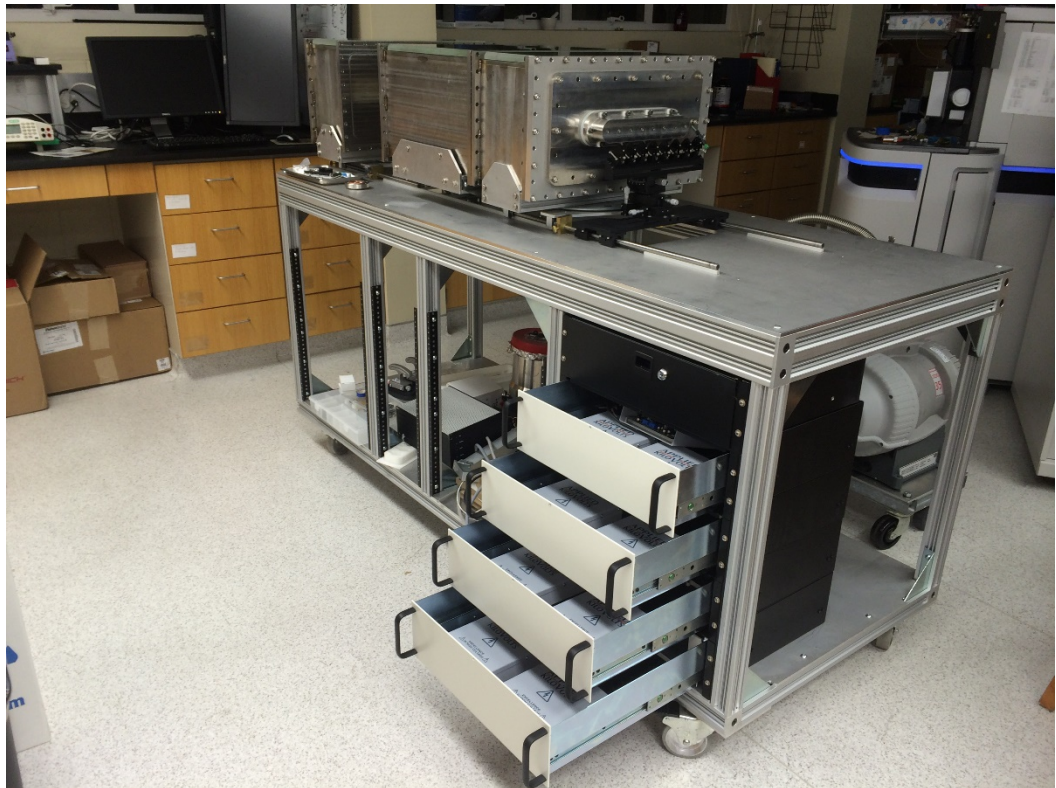
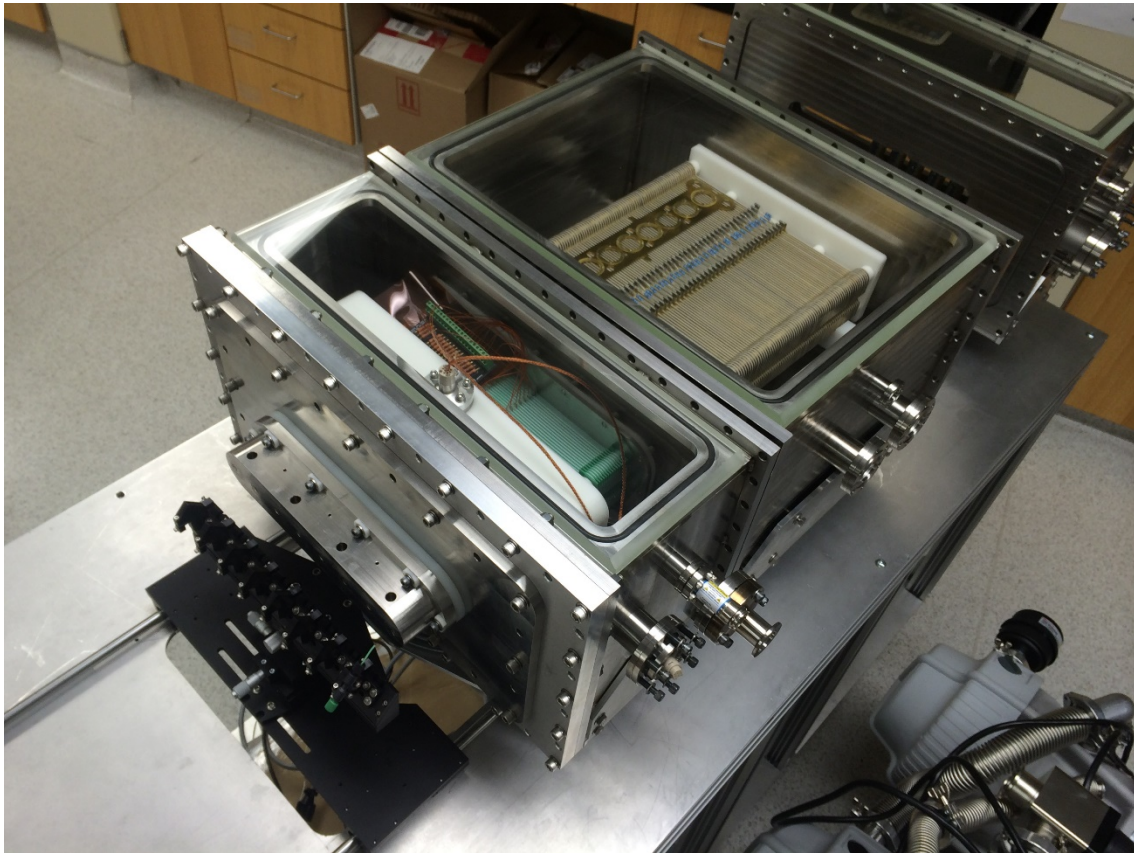


Figure B.19.22: Instrument and user work area during troubleshooting session and bottom pumping port for first vacuum chamber



Figure B.19.24: Back view of instrument during troubleshooting session, showing connections to scroll pumps

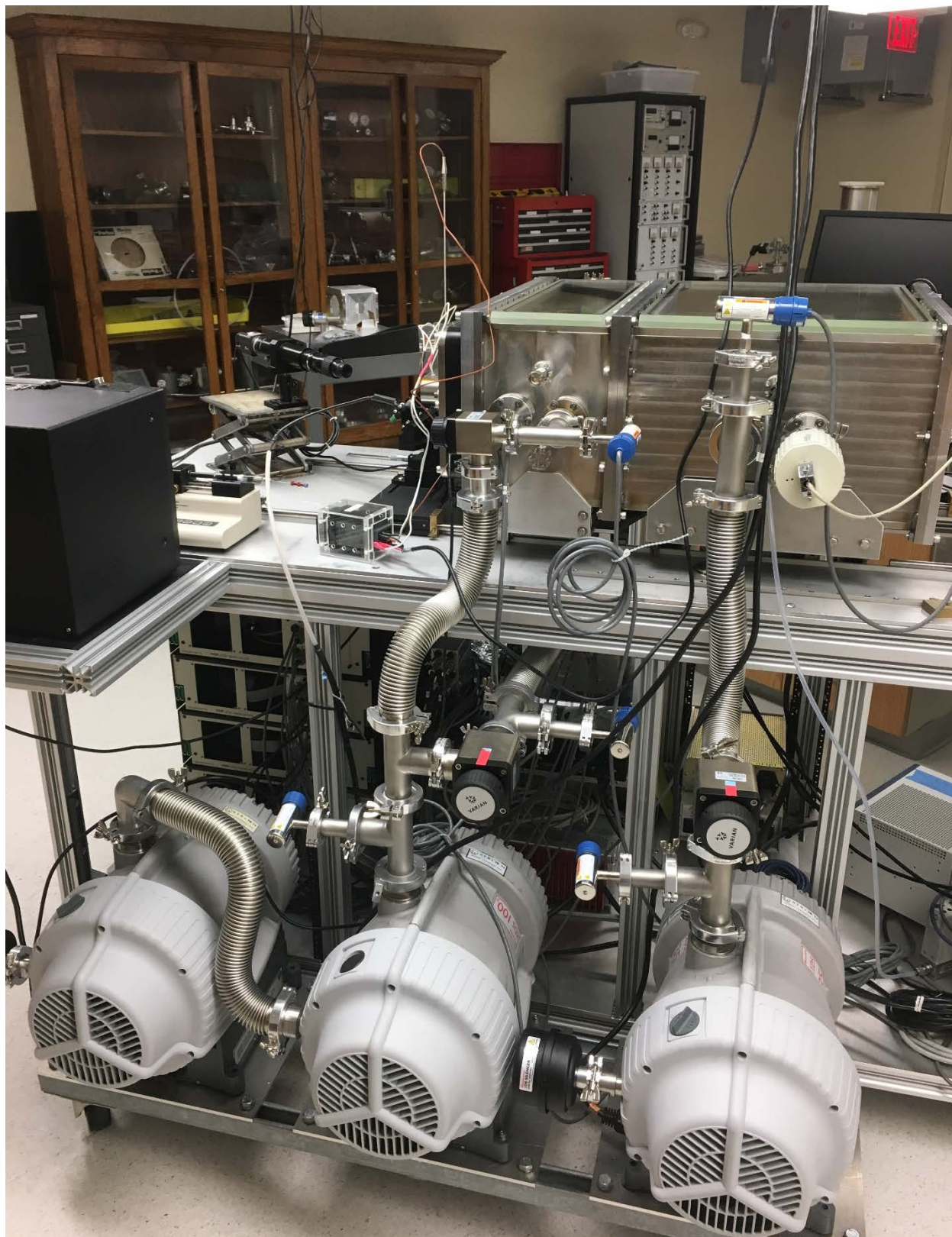


Figure B.19.25: (Counterclockwise from top left) Corona and/or discharge in chamber at aperture panel, drift tube, bottom tab of low pressure funnel, RC circuit board, and outside vacuum between ESI source and RGC



Figure B.19.26: Application of super corona dope to ion funnel RC board to prevent corona and/or discharge



APPENDIX C

SUPPORTING INFORMATION FOR CHAPTER III

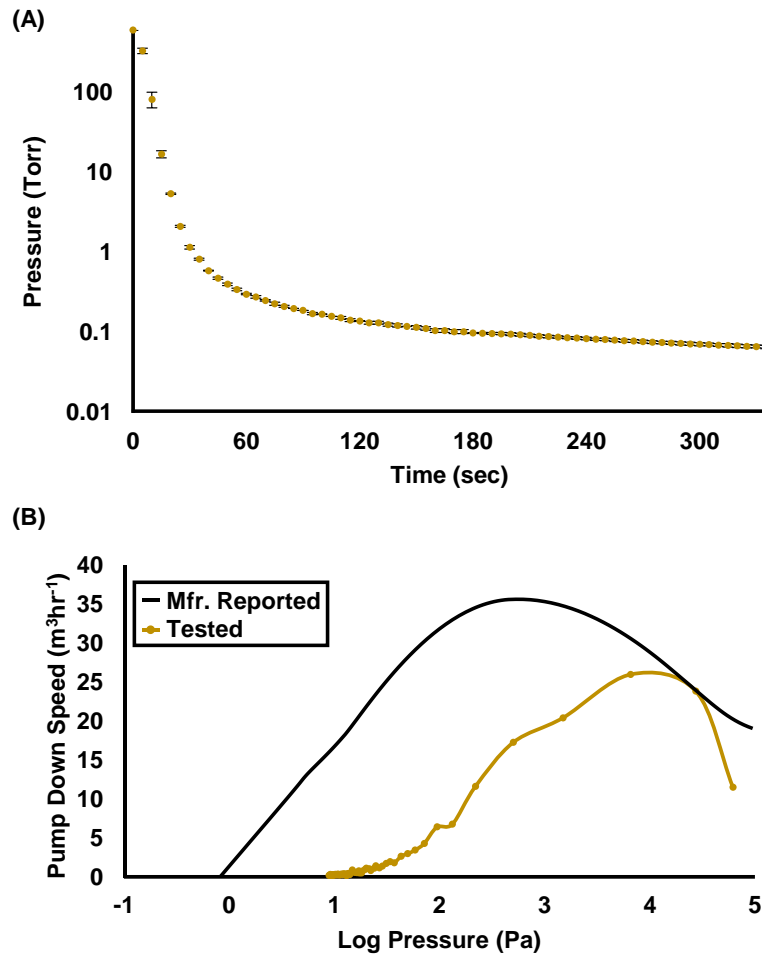


Figure C.1: Evaluation of Edwards XDS35i scroll pump and pump down of first vacuum chamber.

(A) Pump down curve over six minutes to approximately 0.07 Torr for first vacuum chamber with error bars for three replicates. (B) Data comparison of empirical pump down of first vacuum chamber with manufacturer reported pumping speed. Chamber volume was estimated at 25.15 L for calculations.

	Slope ($V_{\text{output}}/V_{\text{input}}$)	Intercept (V_{output})	R²
PSU01	249.541	-0.547	1.000
PSU02	248.481	-0.034	1.000
PSU03	100.419	-0.093	1.000
PSU04	100.462	-0.462	1.000
PSU05	100.550	-0.039	1.000
PSU06	100.292	-0.214	1.000
PSU07	100.546	-0.071	1.000
PSU08	100.610	-0.271	1.000
PSU09	100.346	-0.361	1.000
SC	600.332	-0.754	1.000

Table C.1: Calibration data for DC power supply units. PSU 01 through PSU09 amplify a ± 10 V input control voltage. PSU01 and PSU02 are 2.5 kV supplies. PSU03 through PSU09 are 1 kV supplies. SC is the 6 kV source power supply, which amplifies a ± 5 V input control voltage. The calibration slope and intercept are written into the LabVIEW software for the spatially multiplexed IM to correct for variation of individual power supply modules.

APPENDIX D

SUPPORTING INFORMATION FOR CHAPTER IV

D.1. Comments Regarding Limits of Precision for the CCS Measurements Presented in this Work

The experimental uncertainty is determined from technical replicates representing a minimum of six measurements of CCS, obtained during separate instrument acquisitions. We consider a parsimonious approach essential when compiling a database, and thus individual CCS measurements which contributed to a percent relative standard deviation (RSD) beyond 0.5% were generally found to be indicative of a poor centroid fit (i.e., multiple peak features or low ion counting statistics) and ultimately were not included in the datasets reported in this manuscript. While all CCS values reported are better than 0.5% in experimental uncertainty, the accuracy associated with the result is a sum of this experimental reproducibility and the uncertainty associated with measuring each experimental parameter. The CCS uncertainty for significant experimental parameters is estimated as follows for the lowest CCS value measured in this work (TAA3, 144 Å²): Pressure ± 0.05 Torr ($\pm 1.3\%$), temperature ± 1 K ($\pm 0.3\%$), drift voltage ± 2.5 V ($\pm 0.2\%$), and time centroid extraction ± 0.1 ms ($\pm 0.6\%$), resulting in a total uncertainty of $\pm 1.5\%$, as propagated through the Mason-Schamp equation. There is good reason to believe that the measurement precision is better than what is estimated in the above example. Thus, the accuracy of all values within the database is estimated to be better than 2%.

D.2. Notes on Supplemental Tables

In many cases, lower abundance concomitant species were present in the analytical standards, denoted as derivative signal in the tables. Analyte identities for the derivative signals

are putative and based on the mass measurement. No special considerations were made to optimize for accurate mass data, and so the measured mass and associated accuracies reported in the tables are as obtained from the production prototype instrumentation using an offline calibration. CCS and K_0 measurement precision representing experimental reproducibility error (σ) is reported along with the number of measurements (N). The total accuracy of all transport property values (CCS and K_0) is estimated to be better than 2% (refer to the above discussion).

D.3. Symbol Key, Definitions, and Associated Equations

Mass Accuracy – Mass accuracy (in ppm) is calculated from the following expression:

$$Mass\ Accuracy = \frac{Exact\ Mass - Measured\ Mass}{Exact\ Mass} \cdot 10^6 \quad (1)$$

Reduced Mobility – K_0 , the mobility scaled to standard temperature and pressure, as calculated from the following equation:

$$K_0 = \frac{L^2}{V \cdot t_d} \left(\frac{273.15}{T} \right) \left(\frac{P}{760} \right) \quad (2)$$

where L is the drift length (cm), V is the drift voltage (V), t_d is the corrected drift times (s), T is the drift gas temperature (K), and P is the drift gas pressure (Torr). This gives the units of K_0 in $V \cdot cm^2 \cdot s^{-1}$. Reduced mobility values are classically reported for small mass ions, and provided in the following tables for convenience.

CCS – The first approximation solution of the momentum transfer collision cross-section, as calculated from the following equation (the expanded Mason-Schamp relationship, Mason & Schamp 1958):

$$CCS = \left(\frac{3 \cdot Z \cdot e_c}{16 \cdot N} \right) \cdot \left(\frac{2\pi}{k_B \cdot T} \right)^{\frac{1}{2}} \cdot \left(\frac{m_{ion} + m_{gas}}{m_{ion} \cdot m_{gas}} \right)^{\frac{1}{2}} \cdot \left(\frac{V \cdot t_d}{L^2} \cdot \frac{273.15}{T} \cdot \frac{P}{760} \right) \quad (3)$$

where Z is the integer charge state of the ion (unitless), e_c is the constant for elementary charge ($1.60217657 \times 10^{-19}$ C), N is the gas number density (determined from the kinetic form of the ideal gas law, in units of molecules/m³), k_B is the Boltzmann constant ($1.3806488 \times 10^{-23}$ J·K⁻¹), m_{ion} is the ion mass (Da), and m_{gas} is the neutral drift gas masses (N₂ in this work, Da), respectively.

Note that here and by convention, the CCS is reported in units of Å² (square angstroms). In order to obtain square angstroms directly from the above calculation, it is necessary to multiply the expression (in m²) by 10⁻²⁰, with consideration given for converting the above terms to the proper units: e_c (C), N (molecules/m³), k_B (J·K⁻¹), T (K), m_{ion} and m_{gas} (kg), V (V), td (s), L (m), and P (Torr).

The CCS expression above is considered a first approximation due to the actual dependency on the cross section on the effective ion temperature (two-temperature theory, Mason & McDaniel 1988, Chapter 6-2-C), which is the gas temperature plus the field-induced ion temperature. In the Agilent IM-MS instrument described in this manuscript, for the smallest ion investigated (TAA3, m/z 186) at the highest drift field utilized (20 V·cm⁻¹ at 4 Torr, or *ca.* 15 Td) the field-induced ion temperature is *ca.* 3 K greater than the gas temperature (Wannier 1953). This affects the magnitude of the CCS by less than 0.5% for the ions investigated in this work and so only the drift gas temperature is used for all CCS calculations. For low mass ions where the CCS values are small, incorporating a higher-order (two- or three-temperature) scaling may be significant.

RSD – Relative standard deviation represents the measurement precision (reported as a unitless percentage) and is calculated as follows:

$$RSD = \frac{\sigma}{average} \cdot 100 \quad (4)$$

where σ is the standard deviation from multiple measurements.

Analyte Source – Can be either from a known analytical standard, or as a derivative signal which represents a concomitant ion signal that appears in the samples, often at lower abundances than the standard. For example, the TAA salts were analyzed as received with a reported purity of 98%. The instrument sensitivity was high enough to observe additional ions representing differences of CH_2 (m/z 14), which is suggestive of low abundance impurities possessing various alkyl chain lengths. Note that for the lipid samples, the analyte sources were biological extracts purified into specific lipid classes, thus analyte identifications are putatively based on the mass measurement and the expected mobility-mass correlation trends.

Table D.1: Collision Cross-Section Database of Tetraalkylammonium Salt Cations

Analyte	Z	Molecular Formula	Exact m/z	Measured m/z	Mass Accuracy (ppm)	K ₀	K ₀ σ	CCS σ	CCS σ	RSD (%)	N	Chemical Class	Analyte Source	Vendor Source
TAA2	+	C8H20N	130.16	130.16	-3.6	1.804	0.003	123.3	0.2	0.2%	7	TAA salt	Analytical Standard	Sigma-Aldrich
TAA3 - 2H	+	C12H26N	184.21	184.21	-5.0	1.517	0.007	142.8	0.7	0.5%	14	TAA salt	Derivative Signal	
TAA3	+	C12H28N	186.22	186.22	-1.9	1.506	0.010	144.0	0.7	0.5%	23	TAA salt	Analytical Standard	Acros Organics
TAA4 - CH4	+	C15H32N	226.25	226.25	-0.7	1.306	0.005	163.9	0.6	0.3%	16	TAA salt	Derivative Signal	
TAA4 - (CH2) (peak 1)	+	C15H34N	228.27	228.27	-2.7	1.313	0.005	162.9	0.7	0.4%	15	TAA salt	Derivative Signal	
TAA4 - (CH2) (peak 2)	+	C15H34N	228.27	228.27	-2.7	1.326	0.006	161.3	0.7	0.5%	7	TAA salt	Derivative Signal	
TAA4	+	C16H36N	242.28	242.28	-4.8	1.280	0.007	166.6	0.9	0.5%	16	TAA salt	Analytical Standard	Sigma-Aldrich
TAA5 - (CH2)2 - 2H	+	C18H38N	268.30	268.30	1.8	1.166	0.004	181.9	0.6	0.3%	8	TAA salt	Derivative Signal	
TAA5 - (CH2)2	+	C18H40N	270.32	270.32	1.6	1.163	0.005	182.3	0.7	0.4%	16	TAA salt	Derivative Signal	
TAA5 - (CH2)	+	C19H42N	284.33	284.33	-3.2	1.155	0.006	183.2	0.9	0.5%	15	TAA salt	Derivative Signal	
TAA5	+	C20H44N	298.35	298.35	-0.9	1.116	0.003	190.1	1.0	0.5%	28	TAA salt	Analytical Standard	Acros Organics
TAA6 - (CH2)3 - 2H	+	C21H44N	310.34	310.35	4.3	1.046	0.003	201.5	0.7	0.3%	16	TAA salt	Derivative Signal	
TAA6 - (CH2)3	+	C21H46N	312.36	312.36	0.9	1.074	0.004	196.3	0.7	0.4%	16	TAA salt	Derivative Signal	
TAA6 - (CH2)2	+	C22H48N	326.38	326.38	1.7	1.032	0.004	203.7	0.7	0.4%	16	TAA salt	Derivative Signal	
TAA6 - (CH2) - 2H	+	C23H48N	338.37	338.38	-9.3	1.031	0.004	203.8	0.7	0.4%	15	TAA salt	Derivative Signal	
TAA6 - (CH2)	+	C23H50N	340.39	340.40	3.2	1.008	0.002	208.4	0.4	0.2%	16	TAA salt	Derivative Signal	
TAA6 - 2H	+	C24H50N	352.39	352.39	2.3	0.971	0.002	215.4	0.9	0.4%	31	TAA salt	Derivative Signal	
TAA6	+	C24H52N	354.41	354.41	2.1	0.986	0.003	213.5	1.0	0.5%	31	TAA salt	Analytical Standard	Sigma-Aldrich
TAA7 - (CH2)2	+	C26H56N	382.44	382.44	0.8	0.926	0.003	225.8	0.8	0.4%	16	TAA salt	Derivative Signal	
TAA7 - (CH2) (peak 1)	+	C27H58N	396.46	396.45	4.3	0.913	0.004	228.7	1.1	0.5%	15	TAA salt	Derivative Signal	
TAA7 - (CH2) (peak 2)	+	C27H58N	396.46	396.45	4.3	0.910	0.003	229.4	0.9	0.4%	13	TAA salt	Derivative Signal	
TAA7 - 2H	+	C28H58N	408.46	408.46	-1.7	0.898	0.004	232.3	0.8	0.3%	28	TAA salt	Derivative Signal	
TAA7	+	C28H60N	410.47	410.47	-3.3	0.883	0.001	236.4	0.4	0.2%	31	TAA salt	Analytical Standard	Sigma-Aldrich
TAA8 - (CH2)2 - 2H	+	C30H62N	436.49	436.49	-5.3	0.852	0.002	244.4	0.6	0.3%	31	TAA salt	Derivative Signal	
TAA8 - (CH2)2 (peak 1)	+	C30H64N	438.50	438.50	0.8	0.874	0.002	238.3	0.5	0.2%	16	TAA salt	Derivative Signal	
TAA8 - (CH2)2 (peak 2)	+	C30H64N	438.50	438.50	0.8	0.855	0.002	243.6	0.7	0.3%	16	TAA salt	Derivative Signal	
TAA8 - (CH2)	+	C31H66N	452.52	452.52	-2.4	0.827	0.004	251.6	1.2	0.5%	16	TAA salt	Derivative Signal	
TAA8 - 2H	+	C32H66N	464.52	464.52	-0.4	0.818	0.003	254.3	0.9	0.4%	16	TAA salt	Derivative Signal	
TAA8	+	C32H68N	466.54	466.54	1.4	0.808	0.001	256.6	0.7	0.3%	31	TAA salt	Analytical Standard	Acros Organics
TAA10 - (CH2)7	+	C33H70N	480.55	480.55	-3.9	0.791	0.003	262.5	1.1	0.4%	16	TAA salt	Derivative Signal	

TAA10 - (CH2)6	+	C34H72N	494.57	494.57	1.7	0.779	0.002	266.6	0.6	0.2%	31	TAA salt	Derivative Signal	
TAA10 - (CH2)5	+	C35H74N	508.58	508.58	1.6	0.769	0.002	269.9	0.7	0.3%	31	TAA salt	Derivative Signal	
TAA10 - (CH2)4 - 2H	+	C36H74N	520.58	520.58	-0.6	0.781	0.003	265.4	0.9	0.3%	16	TAA salt	Derivative Signal	
TAA10 - (CH2)4 (peak 1)	+	C36H76N	522.60	522.60	-0.7	0.793	0.003	260.7	1.2	0.5%	31	TAA salt	Derivative Signal	
TAA10 - (CH2)4 (peak 2)	+	C36H76N	522.60	522.60	-0.7	0.754	0.003	275.5	1.0	0.4%	31	TAA salt	Derivative Signal	
TAA10 - (CH2)2	+	C38H80N	550.63	550.63	-0.1	0.729	0.002	284.7	0.9	0.3%	28	TAA salt	Derivative Signal	
TAA10 - (CH2)	+	C39H82N	564.64	564.64	-2.5	0.711	0.002	290.8	0.6	0.2%	28	TAA salt	Derivative Signal	
TAA10	+	C40H84N	578.66	578.66	-8.2	0.702	0.001	293.5	0.7	0.2%	28	TAA salt	Analytical Standard	Sigma-Aldrich
TAA12 - (CH2)7	+	C41H86N	592.68	592.66	-2.9	0.697	0.002	296.0	0.8	0.3%	27	TAA salt	Derivative Signal	
TAA12 - (CH2)6	+	C42H88N	606.69	606.68	-2.2	0.686	0.003	301.5	1.3	0.4%	28	TAA salt	Derivative Signal	
TAA12 - (CH2)4	+	C44H92N	634.72	634.72	-1.0	0.668	0.003	308.6	1.3	0.4%	14	TAA salt	Derivative Signal	
TAA12 - (CH2)3	+	C45H94N	648.74	648.74	-1.7	0.649	0.002	317.6	1.2	0.4%	9	TAA salt	Derivative Signal	
TAA12 - (CH2)2	+	C46H96N	662.75	662.75	-1.9	0.655	0.002	316.3	1.6	0.5%	22	TAA salt	Derivative Signal	
TAA12 - (CH2)	+	C47H98N	676.77	676.77	-0.7	0.641	0.002	320.1	1.5	0.5%	21	TAA salt	Derivative Signal	
TAA12	+	C48H100N	690.79	690.79	-3.4	0.644	0.002	319.0	0.9	0.2%	24	TAA salt	Analytical Standard	Sigma-Aldrich
TAA16 - (CH2)15	+	C49H102N	704.80	704.80	-1.8	0.627	0.000	325.5	1.6	0.5%	18	TAA salt	Derivative Signal	
TAA16 - (CH2)14	+	C50H104N	718.82	718.82	0.1	0.625	0.002	327.2	1.6	0.5%	22	TAA salt	Derivative Signal	
TAA16 - (CH2)12	+	C52H108N	746.85	746.85	-1.0	0.624	0.002	329.6	1.0	0.3%	12	TAA salt	Derivative Signal	
TAA16 - (CH2)11	+	C53H9N	760.86	760.86	-0.8	0.611	0.003	336.3	1.6	0.5%	9	TAA salt	Derivative Signal	
TAA16 - (CH2)10 - 2H	+	C54H9N	772.86	772.87	3.8	0.613	0.002	335.3	1.0	0.3%	11	TAA salt	Derivative Signal	
TAA16 - (CH2)10	+	C54H112N	774.88	774.88	-0.2	0.619	0.001	332.1	0.4	0.1%	12	TAA salt	Derivative Signal	
TAA16 - (CH2)2	+	C62H128N	887.00	887.01	5.2	0.562	0.002	364.6	1.3	0.4%	9	TAA salt	Derivative Signal	
TAA16 - (CH2)	+	C63H11N	901.02	901.03	11.5	0.584	0.002	350.9	1.3	0.4%	8	TAA salt	Derivative Signal	
TAA16	+	C64H132N	915.04	915.04	-0.9	0.569	0.004	360.3	0.9	0.2%	25	TAA salt	Analytical Standard	Sigma-Aldrich
TAA18 - (CH2)7	+	C65H11N	929.05	929.04	-11.4	0.577	0.003	355.1	1.8	0.5%	10	TAA salt	Derivative Signal	
TAA18 - (CH2)6	+	C66H136N	943.07	943.07	-0.6	0.554	0.002	369.7	1.4	0.4%	10	TAA salt	Derivative Signal	
TAA18 - (CH2)4	+	C68H140N	971.10	971.10	-3.8	0.578	0.002	354.5	1.4	0.4%	6	TAA salt	Derivative Signal	
TAA18 - (CH2)2	+	C70H144N	999.13	999.12	-6.6	0.540	0.002	379.2	1.2	0.3%	6	TAA salt	Derivative Signal	
TAA18	+	C72H148N	1027.16	1027.16	-2.0	0.538	0.002	379.0	1.7	0.3%	6	TAA salt	Analytical Standard	Alfa Aesar
TAA (1064)	+	C75H149N	1064.17	1064.15	-16.0	0.521	0.002	392.7	1.3	0.3%	8	TAA salt	Derivative Signal	
TAA (1120)	+	C79H173N	1120.23	1120.22	-9.9	0.495	0.002	412.8	1.9	0.5%	6	TAA salt	Derivative Signal	
TAA (1232)	+	C87H173N	1232.36	1232.34	-10.2	0.476	0.002	428.6	1.9	0.4%	6	TAA salt	Derivative Signal	

Table D.2: Collision Cross-Section Database of Carbohydrates

Analyte	Z	Molecular Formula	Exact m/z	Measured m/z	Mass Accuracy (ppm)	K_0	$K_0 \sigma$	CCS σ	RSD (%)	N	Chemical Class	Analyte Source	Vendor Source
Mannitol	+Li	C6H14O6Li	189.10	189.10	0.8	1.497	0.001	144.5	0.1	14	Carbohydrate	Analytical Standard	Sigma-Aldrich
Sorbitol	+H	C6H15O6	189.10	189.09	-6.6	1.470	0.004	147.2	0.4	8	Carbohydrate	Analytical Standard	Sigma-Aldrich
Mannitol	+Na	C6H14O6Na	205.07	205.07	-3.4	1.531	0.006	140.6	0.5	14	Carbohydrate	Analytical Standard	Sigma-Aldrich
Sorbitol (peak 1)	+Na	C6H14O6Na	205.07	205.07	-6.9	1.544	0.004	139.4	0.3	8	Carbohydrate	Analytical Standard	Sigma-Aldrich
(Hex) ₂ - H ₂ O	+Na	C12H20O10Na	347.10	347.09	-1.9	1.220	0.006	172.0	0.8	14	Carbohydrate	Derivative Signal	
Lactose	+Li	C12H22O11Li	349.13	349.13	-3.2	1.126	0.003	186.3	0.5	7	Carbohydrate	Analytical Standard	Sigma-Aldrich
Lactose/Mannose Mixture	+Na	C12H22O11Na	365.11	365.11	4.2	1.178	0.005	177.8	0.8	15	Carbohydrate	Analytical Standard	Sigma-Aldrich
Lactose	+Na	C12H22O11Na	365.11	365.10	-9.3	1.176	0.002	178.1	0.3	8	Carbohydrate	Analytical Standard	Sigma-Aldrich
Lactose/Mannose Mixture	+K	C12H22O11K	381.08	381.08	-1.9	1.155	0.005	181.1	0.8	16	Carbohydrate	Analytical Standard	Sigma-Aldrich
HexNAC-Hex - H ₂ O	+Na	C14O10N1H23Na	388.12	388.12	-0.2	1.134	0.004	184.3	0.6	16	Carbohydrate	Derivative Signal	
HexNAC-Hex	+Na	C14H25NO11Na	406.13	406.14	6.6	1.097	0.003	190.2	0.5	16	Carbohydrate	Derivative Signal	
HexNAC-Hex	+K	C14H25NO11K	422.11	422.11	2.0	1.091	0.003	191.1	0.6	16	Carbohydrate	Derivative Signal	
Hex-(Fuc) ₂ - H ₂ O (peak 1)	+H	C18H31O13	455.18	455.18	2.1	1.071	0.005	194.2	0.9	13	Carbohydrate	Derivative Signal	
Hex-(Fuc) ₂ - H ₂ O (peak 2)	+H	C18H31O13	455.18	455.18	2.1	1.053	0.004	197.6	0.8	9	Carbohydrate	Derivative Signal	
Maltotriose	+H	C18H33O16	505.18	505.18	-2.7	0.959	0.005	216.3	1.0	14	Carbohydrate	Analytical Standard	Sigma-Aldrich
Melezitose	+H	C18H33O16	505.18	505.18	-0.7	1.023	0.005	202.6	1.0	10	Carbohydrate	Analytical Standard	Sigma-Aldrich
(Hex) ₃ - H ₂ O	+Na	C18H31O15	509.15	509.15	-2.0	1.012	0.003	204.9	0.7	16	Carbohydrate	Derivative Signal	
Melezitose	+Li	C18H32O17	511.19	511.18	-0.8	1.022	0.001	202.9	0.3	14	Carbohydrate	Analytical Standard	Sigma-Aldrich
HexNAC-Fuc-Hex - H ₂ O	+H	C20H34N1O14	512.20	512.20	-2.4	0.996	0.003	208.2	0.5	16	Carbohydrate	Derivative Signal	
Melezitose	+Na	C18H32NaO16	527.16	527.16	-1.7	0.974	0.004	212.8	0.8	16	Carbohydrate	Analytical Standard	Sigma-Aldrich
Maltotriose	+Na	C18H32O16Na	527.16	527.16	1.0	1.022	0.001	202.7	0.2	14	Carbohydrate	Analytical Standard	Sigma-Aldrich
Raffinose	+Na	C18H32O16Na	527.16	527.15	-12.9	0.983	0.001	210.7	0.2	8	Carbohydrate	Analytical Standard	Sigma-Aldrich
HexNAC-Fuc-Hex - H ₂ O	+Na	C20O14NH33Na	534.18	534.17	-11.9	0.969	0.005	213.7	1.1	16	Carbohydrate	Derivative Signal	

Maltotriose	+K	C18H32O16K	543.13	543.13	-2.3	0.955	0.003	216.8	0.7	0.3%	16	Carbohydrate	Analytical Standard	Sigma-Aldrich
melezitose	+K	C18H32KO16	543.13	543.13	-0.8	0.933	0.004	221.9	0.9	0.4%	14	Carbohydrate	Analytical Standard	Sigma-Aldrich
Raffinose	+K	C18H32O16K	543.13	543.13	-13.0	0.973	0.002	212.7	0.3	0.2%	8	Carbohydrate	Analytical Standard	Sigma-Aldrich
HexNAc-(Hex) ₂ - H ₂ O	+Na	C20H33NO15Na	550.17	550.17	-17.4	0.957	0.005	216.3	1.0	0.5%	15	Carbohydrate	Derivative Signal	
HexNAc-Fuc-Hex	+Na	C20O15NH35Na	552.19	552.18	-16.4	0.969	0.005	213.6	1.1	0.5%	13	Carbohydrate	Derivative Signal	
HexNAc-(Hex) ₂	+Na	C20H35NO16Na	568.19	568.18	-5.5	0.940	0.004	220.0	1.0	0.5%	16	Carbohydrate	Derivative Signal	
Melezitose (peak 1)	+Rb	C18H32O16Rb	589.08	589.08	-3.3	1.012	0.001	204.1	0.2	0.1%	13	Carbohydrate	Analytical Standard	Sigma-Aldrich
Melezitose (peak 2)	+Rb	C18H32O16Rb	589.08	589.08	-3.3	0.943	0.004	219.2	0.9	0.4%	13	Carbohydrate	Analytical Standard	Sigma-Aldrich
Raffinose (peak 1)	+Rb	C18H32O16Rb	589.08	589.09	23.0	0.945	0.004	218.7	0.9	0.4%	7	Carbohydrate	Analytical Standard	Sigma-Aldrich
Raffinose (peak 2)	+Rb	C18H32O16Rb	589.08	589.09	23.0	0.900	0.003	229.7	0.9	0.4%	7	Carbohydrate	Analytical Standard	Sigma-Aldrich
Melezitose	+Cs	C18H32CsO16	637.07	637.07	-4.6	1.002	0.001	205.8	0.2	0.1%	14	Carbohydrate	Analytical Standard	Sigma-Aldrich
(Hex) ₄ - H ₂ O	+H	C24H41O20	649.22	649.21	-6.6	0.878	0.004	234.7	1.2	0.5%	15	Carbohydrate	Derivative Signal	
HexNAc-(Fuc) ₂ -Hex - H ₂ O	+H	C26O18NH44	658.26	658.25	-3.5	0.827	0.004	249.3	1.1	0.4%	14	Carbohydrate	Derivative Signal	
Maltotetraose	+H	C24H42O21	667.23	667.23	-5.5	0.865	0.004	238.3	1.2	0.5%	14	Carbohydrate	Analytical Standard	Sigma-Aldrich
(Hex) ₄ - H ₂ O	+Na	C24O20H40Na	671.20	671.20	-3.5	0.877	0.003	234.8	0.8	0.3%	16	Carbohydrate	Derivative Signal	
HexNAc-(Fuc) ₂ -Hex - H ₂ O	+Na	C26O18NH43Na	680.24	680.23	-14.4	0.858	0.004	240.2	1.1	0.5%	16	Carbohydrate	Derivative Signal	
Maltotetraose	+Na	C24H42O21Na	689.21	689.21	-0.2	0.875	0.002	235.3	0.5	0.2%	16	Carbohydrate	Analytical Standard	Sigma-Aldrich
HexNAc-Fuc-(Hex) ₂ - H ₂ O	+Na	C26O19NH43Na	696.23	696.23	-8.2	0.845	0.004	243.8	1.2	0.5%	16	Carbohydrate	Derivative Signal	
(Hex) ₄	+K	C24H42O21K	705.19	705.18	-4.2	0.870	0.003	236.6	0.8	0.3%	16	Carbohydrate	Derivative Signal	
HexNAc-(Hex) ₃ - H ₂ O	+Na	C26H43N1O20Na	712.23	712.22	-4.9	0.840	0.003	244.9	1.0	0.4%	16	Carbohydrate	Derivative Signal	
HexNAc-Fuc-(Hex) ₂	+Na	C26O20NH45Na	714.24	714.24	-6.7	0.822	0.004	250.3	1.2	0.5%	16	Carbohydrate	Derivative Signal	
HexNAc-(Hex) ₃	+Na	C26H45N1O21Na	730.24	730.23	-5.2	0.843	0.002	244.0	0.4	0.2%	16	Carbohydrate	Derivative Signal	
HexNAc-(Hex) ₃	+K	C26H45N1O21K	746.21	746.20	-9.9	0.829	0.004	248.2	1.1	0.5%	16	Carbohydrate	Derivative Signal	
(Hex) ₅ - H ₂ O	+H	C30O25H51	811.27	811.27	-7.9	0.727	0.002	282.3	0.7	0.3%	14	Carbohydrate	Derivative Signal	
(Hex) ₅ - H ₂ O	+Na	C30O25H50Na	833.25	833.25	-7.3	0.780	0.002	263.1	0.8	0.3%	16	Carbohydrate	Derivative Signal	
(Hex) ₅	+Na	C30O26H52Na	851.26	851.26	-4.7	0.791	0.003	259.5	0.8	0.3%	16	Carbohydrate	Derivative Signal	
HexNAc-Fuc-(Hex) ₃ - H ₂ O (peak 1)	+Na	C32O24NH53Na	858.29	858.28	-3.6	0.780	0.004	263.1	1.3	0.5%	14	Carbohydrate	Derivative Signal	

HexNAc-Fuc-(Hex) ₃ - H ₂ O (peak 2)	+Na	C32O24NH53Na	858.29	858.28	-3.6	0.783	0.003	262.0	0.9	0.3%	7	Carbohydrate	Derivative Signal	
HexNAc-(Fuc) ₂ -(Hex) ₂	+Na	C32O24NH55Na	860.30	860.30	-6.0	0.752	0.004	272.8	1.4	0.5%	16	Carbohydrate	Derivative Signal	
Lacto-N-Fucopentaose I	+Li	C32O25NH55Li	860.32	860.32	-3.6	0.761	0.002	269.6	0.6	0.2%	14	Carbohydrate	Analytical Standard	Dextra Laboratories
Lacto-N-Fucopentaose II	+Na	C32O25NH55Na	876.30	876.29	-12.1	0.756	0.001	271.1	0.3	0.1%	8	Carbohydrate	Analytical Standard	Dextra Laboratories
Lacto-N-Fucopentaose I	+Na	C32O25NH55Na	876.30	876.29	-3.4	0.743	0.001	276.1	0.4	0.1%	13	Carbohydrate	Analytical Standard	Dextra Laboratories
Lacto-N-Fucopentaose II	+K	C32O25NH55K	892.27	892.26	-15.6	0.767	0.002	267.2	0.7	0.3%	8	Carbohydrate	Analytical Standard	Dextra Laboratories
Lacto-N-Fucopentaose I	+K	C32O25NH55K	892.27	892.27	-3.5	0.746	0.001	274.7	0.5	0.2%	14	Carbohydrate	Analytical Standard	Dextra Laboratories
HexNAc-(Hex) ₄ (peak 1)	+Na	C32O26NH55Na	892.29	892.27	-27.3	0.751	0.004	272.9	1.3	0.5%	16	Carbohydrate	Derivative Signal	
HexNAc-(Hex) ₄ (peak 2)	+Na	C32O26NH55Na	892.29	892.27	-27.3	0.744	0.002	275.5	0.9	0.3%	16	Carbohydrate	Derivative Signal	
Lacto-N-Fucopentaose II	+Rb	C32O25NH55Rb	938.22	938.21	-11.2	0.736	0.003	278.4	1.0	0.4%	7	Carbohydrate	Analytical Standard	Dextra Laboratories
Lacto-N-Fucopentaose I	+Rb	C32O25NH55Rb	938.22	938.21	-4.5	0.744	0.002	275.2	0.8	0.3%	13	Carbohydrate	Analytical Standard	Dextra Laboratories
Alpha-Cyclodextrin	+H	C36O30H61	973.32	973.32	-3.0	0.718	0.002	285.2	0.8	0.3%	14	Carbohydrate	Analytical Standard	Sigma-Aldrich
Lacto-N-Fucopentaose I	+Cs	C32O25NH55Cs	986.21	986.21	-2.4	0.743	0.003	275.6	0.9	0.3%	14	Carbohydrate	Analytical Standard	Dextra Laboratories
HexNAc-(Fuc) ₄ -Hex (peak 1)	+Na	C38O27NH65Na	990.36	990.35	-17.3	0.728	0.002	281.2	0.7	0.2%	14	Carbohydrate	Derivative Signal	
HexNAc-(Fuc) ₄ -Hex (peak 2)	+Na	C38O27NH65Na	990.36	990.35	-17.3	0.726	0.001	282.1	0.5	0.2%	6	Carbohydrate	Derivative Signal	
Alpha-Cyclodextrin	+Na	C36O30H60Na	995.31	995.31	1.3	0.717	0.001	285.5	0.4	0.1%	14	Carbohydrate	Analytical Standard	Sigma-Aldrich
Lacto-N-Difucohexaose I	+Li	C38H65NO29Li	1006.38	1006.38	-3.4	0.679	0.001	301.4	0.3	0.1%	14	Carbohydrate	Analytical Standard	Dextra Laboratories
Alpha-Cyclodextrin	+K	C36O30H60K	1011.28	1011.28	-3.3	0.711	0.001	287.7	0.6	0.2%	14	Carbohydrate	Analytical Standard	Sigma-Aldrich
Maltohexaose	+Na	C36O31H62Na	1013.32	1013.31	-3.7	0.714	0.002	286.4	0.7	0.2%	14	Carbohydrate	Analytical Standard	Sigma-Aldrich
Lacto-N-Difucohexaose II (peak 1)	+Na	C38H65NO29Na	1022.35	1022.34	-11.9	0.703	0.003	291.2	1.4	0.5%	8	Carbohydrate	Analytical Standard	Dextra Laboratories
Lacto-N-Difucohexaose II (peak 2)	+Na	C38H65NO29Na	1022.35	1022.34	-11.9	0.668	0.001	306.3	0.6	0.2%	8	Carbohydrate	Analytical Standard	Dextra Laboratories
Lacto-N-Difucohexaose I (peak 1)	+Na	C38H65NO29Na	1022.35	1022.35	-2.8	0.704	0.003	290.6	1.3	0.5%	14	Carbohydrate	Analytical Standard	Dextra Laboratories
Lacto-N-Difucohexaose I (peak 2)	+Na	C38H65NO29Na	1022.35	1022.35	-2.8	0.673	0.001	304.2	0.5	0.2%	14	Carbohydrate	Analytical Standard	Dextra Laboratories
Maltohexaose	+K	C36O31H62K	1029.29	1029.29	-4.1	0.698	0.002	293.3	0.6	0.2%	14	Carbohydrate	Analytical Standard	Sigma-Aldrich
Lacto-N-Difucohexaose II	+K	C38H65NO29K	1038.33	1038.31	-13.9	0.669	0.002	305.8	0.8	0.3%	8	Carbohydrate	Analytical Standard	Dextra Laboratories

Lacto-N-Difucohexaose I	+K	C38H65NO29K	1038.33	1038.33	-2.8	0.674	0.001	303.5	0.4	0.1%	14	Carbohydrate	Analytical Standard	Dextra Laboratories
(HexNAc) ₂ -(Hex) ₃ -Fuc (peak 2)	+Na	C40H68N2O30Na	1079.38	1079.37	-3.4	0.692	0.003	295.5	1.4	0.5%	12	Carbohydrate	Derivative Signal	
(HexNAc) ₂ -(Hex) ₃ -Fuc (peak 1)	+Na	C40H68N2O30Na	1079.38	1079.37	-3.4	0.668	0.003	306.0	1.5	0.5%	10	Carbohydrate	Derivative Signal	
Lacto-N-Difucohexaose I	+Rb	C38H65NO29Rb	1084.28	1084.27	-4.4	0.674	0.002	303.2	0.7	0.2%	14	Carbohydrate	Analytical Standard	Dextra Laboratories
Lacto-N-Difucohexaose I	+Cs	C38H65NO29Cs	1132.27	1132.27	-3.5	0.679	0.002	301.2	0.7	0.2%	14	Carbohydrate	Analytical Standard	Dextra Laboratories
Beta-Cyclodextrin (peak 1)	+H	C42O35H71	1135.38	1135.37	-3.9	0.678	0.002	301.3	0.9	0.3%	14	Carbohydrate	Analytical Standard	Sigma-Aldrich
Beta-Cyclodextrin (peak 2)	+H	C42O35H71	1135.38	1135.37	-3.9	0.639	0.002	319.6	1.2	0.4%	12	Carbohydrate	Analytical Standard	Sigma-Aldrich
HexNAc-(Fuc) ₄ -(Hex) ₂	+Na	C44O32NH75Na	1152.42	1152.40	-15.8	0.646	0.002	316.1	0.9	0.3%	12	Carbohydrate	Derivative Signal	
Maltoheptaose	+H	C42O36H73	1153.39	1153.39	0.1	0.674	0.002	303.3	0.7	0.2%	14	Carbohydrate	Analytical Standard	Sigma-Aldrich
Beta-Cyclodextrin	+Na	C42O35H70Na	1157.36	1157.36	-1.9	0.639	0.000	319.7	0.7	0.2%	11	Carbohydrate	Analytical Standard	Sigma-Aldrich
HexNAc-(Fuc) ₃ -(Hex) ₃	+Na	C44O33NH75Na	1168.41	1168.41	-3.6	0.626	0.003	326.3	1.5	0.4%	11	Carbohydrate	Derivative Signal	
Beta-Cyclodextrin	+K	C42O35H70K	1173.33	1173.33	1.2	0.638	0.001	320.3	0.5	0.2%	12	Carbohydrate	Analytical Standard	Sigma-Aldrich
Maltoheptaose	+Na	C42O36H72Na	1175.37	1175.37	-0.9	0.674	0.001	303.1	0.5	0.2%	14	Carbohydrate	Analytical Standard	Sigma-Aldrich
Maltoheptaose	+K	C42O36H72K	1191.34	1191.34	-3.6	0.673	0.001	303.4	0.5	0.2%	14	Carbohydrate	Analytical Standard	Sigma-Aldrich
(Hex) ₈ - H ₂ O	+H	C48H81O40	1297.43	1297.42	-4.5	0.611	0.001	333.8	0.8	0.2%	12	Carbohydrate	Derivative Signal	
Gamma-Cyclodextrin	+H	C48H81O40	1297.43	1297.43	1.2	0.633	0.001	322.6	0.7	0.2%	12	Carbohydrate	Analytical Standard	Sigma-Aldrich
Gamma-Cyclodextrin	+Li	C48H80LiO41	1303.44	1303.44	2.0	0.642	0.001	317.7	0.4	0.1%	12	Carbohydrate	Analytical Standard	Sigma-Aldrich
Gamma-Cyclodextrin	+Na	C48H80NaO42	1319.41	1319.42	2.1	0.633	0.001	322.1	0.5	0.2%	12	Carbohydrate	Analytical Standard	Sigma-Aldrich
Gamma-Cyclodextrin	+K	C48H80KO43	1335.39	1335.39	1.8	0.628	0.001	324.8	0.5	0.2%	12	Carbohydrate	Analytical Standard	Sigma-Aldrich
(Hex) ₈ (peak 1)	+Na	C48O41H82Na	1337.42	1337.42	-2.0	0.636	0.003	320.9	1.3	0.4%	7	Carbohydrate	Derivative Signal	
(Hex) ₈ (peak 2)	+Na	C48O41H82Na	1337.42	1337.42	-2.0	0.602	0.001	338.8	0.7	0.2%	10	Carbohydrate	Derivative Signal	
HexNAc-(Hex) ₇ (peak 1)	+Na	C50H85N1O41Na	1378.45	1378.45	-1.5	0.612	0.003	333.4	1.7	0.5%	11	Carbohydrate	Derivative Signal	
HexNAc-(Hex) ₇ (peak 2)	+Na	C50H85N1O41Na	1378.45	1378.45	-1.5	0.593	0.001	343.7	0.8	0.2%	10	Carbohydrate	Derivative Signal	
Gamma-Cyclodextrin	+Rb	C48H80O44Rb	1381.33	1381.33	-0.3	0.623	0.001	327.3	0.6	0.2%	12	Carbohydrate	Analytical Standard	Sigma-Aldrich
Gamma-Cyclodextrin	+Cs	C48H80CsO45	1429.33	1429.33	-1.3	0.603	0.001	338.2	0.6	0.2%	10	Carbohydrate	Analytical Standard	Sigma-Aldrich
(Hex) ₈ - H ₂ O	+H	C54H91O45	1459.48	1459.48	-0.3	0.577	0.002	353.3	1.2	0.4%	10	Carbohydrate	Derivative Signal	
(Hex) ₈ (peak 1)	+Na	C54H92O46Na	1499.48	1499.48	-0.4	0.598	0.003	340.5	1.6	0.5%	10	Carbohydrate	Derivative Signal	

(Hex) ₉ (peak 2)	+Na	C54H92O46Na	1499.48	1499.48	1499.48	-0.4	0.579	0.002	351.9	1.5	0.4%	10	Carbohydrate	Derivative Signal
HexNAc-(Hex) ₈	+H	C56H96N1O46	1518.52	1518.52	1518.52	-3.4	0.586	0.003	347.8	1.5	0.4%	10	Carbohydrate	Derivative Signal
HexNAc-(Hex) ₈ (peak 1)	+Na	C56H95N1O46Na	1540.50	1540.50	1540.50	-0.5	0.575	0.003	354.2	1.7	0.5%	10	Carbohydrate	Derivative Signal
HexNAc-(Hex) ₈ (peak 2)	+Na	C56H95N1O46Na	1540.50	1540.50	1540.50	-0.5	0.579	0.003	351.6	1.5	0.4%	8	Carbohydrate	Derivative Signal
(Hex) ₁₀ - H ₂ O	+H	C60H101O50	1621.54	1621.54	1621.54	0.8	0.531	0.001	383.4	0.9	0.2%	8	Carbohydrate	Derivative Signal
HexNAc-(Fuc) ₂ -(Hex) ₇ - H ₂ O	+H	C62H104N1O48	1630.57	1630.57	1630.58	6.0	0.556	0.001	366.1	0.8	0.2%	10	Carbohydrate	Derivative Signal
(Hex) ₁₀ (peak 1)	+H	C60H103O51	1639.55	1639.55	1639.55	2.2	0.558	0.002	365.1	1.4	0.4%	9	Carbohydrate	Derivative Signal
(Hex) ₁₀ (peak 2)	+H	C60H103O51	1639.55	1639.55	1639.55	2.2	0.522	0.001	390.3	0.8	0.2%	8	Carbohydrate	Derivative Signal
(Hex) ₁₀ (peak 1)	+Na	C60H102O51Na	1661.53	1661.53	1661.53	3.3	0.558	0.002	365.1	1.3	0.4%	10	Carbohydrate	Derivative Signal
(Hex) ₁₀ (peak 2)	+Na	C60H102O51Na	1661.53	1661.53	1661.53	3.3	0.545	0.002	373.8	1.1	0.3%	8	Carbohydrate	Derivative Signal
(Hex) ₁₁ - H ₂ O	+H	C66H111O55	1783.59	1783.60	1783.60	8.0	0.537	0.002	379.1	1.5	0.4%	6	Carbohydrate	Derivative Signal
(Hex) ₁₁	+Li	C66H112O56Li	1807.61	1807.61	1807.59	-11.4	0.546	0.002	372.4	1.1	0.3%	8	Carbohydrate	Derivative Signal
(Hex) ₁₁	+Na	C66H112O56Na	1823.58	1823.58	1823.60	8.9	0.529	0.002	384.6	1.4	0.4%	8	Carbohydrate	Derivative Signal
(Hex) ₁₁ (peak 1)	+K	C66H112O56K	1839.56	1839.56	1839.53	-12.9	0.554	0.002	367.4	1.6	0.4%	7	Carbohydrate	Derivative Signal
(Hex) ₁₁ (peak 2)	+K	C66H112O56K	1839.56	1839.56	1839.53	-12.9	0.550	0.002	369.7	1.4	0.4%	8	Carbohydrate	Derivative Signal
(Hex) ₁₁ (peak 1)	+Rb	C66H112O56Rb	1885.50	1885.50	1885.48	-13.8	0.556	0.002	365.7	1.3	0.4%	8	Carbohydrate	Derivative Signal
(Hex) ₁₁ (peak 2)	+Rb	C66H112O56Rb	1885.50	1885.50	1885.48	-13.8	0.546	0.002	372.5	1.5	0.4%	6	Carbohydrate	Derivative Signal
(Hex) ₁₂ - H ₂ O (peak 1)	+H	C72H121O60	1945.64	1945.64	1945.65	6.5	0.508	0.001	400.3	0.6	0.1%	8	Carbohydrate	Derivative Signal
(Hex) ₁₂ - H ₂ O (peak 2)	+H	C72H121O60	1945.64	1945.64	1945.65	6.5	0.481	0.001	422.9	1.3	0.3%	6	Carbohydrate	Derivative Signal
(Hex) ₁₂ - H ₂ O (peak 1)	+Na	C72H120O60Na	1967.62	1967.62	1967.63	5.4	0.520	0.001	390.6	0.9	0.2%	8	Carbohydrate	Derivative Signal
(Hex) ₁₂ - H ₂ O (peak 2)	+Na	C72H120O60Na	1967.62	1967.62	1967.63	5.4	0.496	0.002	410.0	1.4	0.4%	6	Carbohydrate	Derivative Signal
(Hex) ₁₃ (peak 1)	+Na	C78H132O66Na	2147.69	2147.69	2147.72	13.6	0.504	0.001	402.7	1.0	0.2%	6	Carbohydrate	Derivative Signal
(Hex) ₁₃ (peak 2)	+Na	C78H132O66Na	2147.69	2147.69	2147.72	13.6	0.494	0.001	411.6	1.1	0.3%	6	Carbohydrate	Derivative Signal

Table D.3: Collision Cross-Section Database of Peptides

Analyte	Z	Molecular Formula	Exact m/z	Measured m/z	Mass Accuracy (ppm)	K_0	$K_0 \sigma$	CCS σ	RSD (%)	N	Chemical Class	Analyte Source	Vendor Source	Source Protein
DGDK	+H	C16H28N5O9	434.19	434.19	12.9	1.064	0.004	195.8	0.7	0.3%	Peptide	Analytical Standard	Waters	ENOLASE_YST
YVR	+H	C20H33N6O5	437.25	437.25	-1.8	1.006	0.002	207.0	0.4	0.2%	Peptide	Analytical Standard	Waters	ADH_YST
DVCK	+H	C18H34N5O7S	464.22	464.22	-2.2	1.016	0.004	204.7	0.7	0.4%	Peptide	Analytical Standard	Waters	ALBUMIN_BOV
WIR	+H	C23H36N7O4	474.28	474.27	-17.3	0.964	0.003	215.4	0.7	0.3%	Peptide	Analytical Standard	Waters	PHOSPH_RAB
GVFR	+H	C22H36N7O5	478.28	478.28	-1.0	0.967	0.001	214.8	0.3	0.1%	Peptide	Analytical Standard	Waters	ENOLASE_YST
SDGRG	+H	C17H31N8O9	491.22	491.22	-1.4	1.015	0.003	204.6	0.5	0.3%	Peptide	Analytical Standard	Sigma-Aldrich	SYNTHETIC
GRGDS	+H	C17H31N8O9	491.22	491.22	-1.4	1.008	0.001	205.9	0.2	0.1%	Peptide	Analytical Standard	Sigma-Aldrich	SYNTHETIC
FGER	+H	C22H34N7O7	508.25	508.24	-13.2	0.955	0.002	217.1	0.4	0.2%	Peptide	Analytical Standard	Waters	ENOLASE_YST
VYAR	+H	C23H38N7O6	508.29	508.29	-0.8	0.912	0.001	227.2	0.3	0.1%	Peptide	Analytical Standard	Waters	PHOSPH_RAB
SDGRG	+Na	C17H30N8O9Na	513.20	513.20	-4.5	1.018	0.002	203.5	0.5	0.2%	Peptide	Analytical Standard	Sigma-Aldrich	SYNTHETIC
GRGDS	+Na	C17H30N8O9Na	513.20	513.20	-4.5	0.996	0.002	208.2	0.3	0.2%	Peptide	Analytical Standard	Sigma-Aldrich	SYNTHETIC
ADLAK	+H	C22H41N6O8	517.30	517.30	5.2	0.908	0.004	228.3	1.1	0.5%	Peptide	Analytical Standard	Waters	ALBUMIN_BOV
QENK	+H	C20H36N7O9	518.26	518.26	-1.0	0.946	0.003	219.0	0.6	0.3%	Peptide	Analytical Standard	Waters	PHOSPH_RAB
MVIR	+H	C22H44N7O5S	518.31	518.31	0.0	0.906	0.001	228.7	0.3	0.1%	Peptide	Analytical Standard	Waters	PHOSPH_RAB
WMGK	+H	C24H37N6O5S	521.25	521.26	8.1	0.941	0.002	220.1	0.5	0.2%	Peptide	Analytical Standard	Waters	ENOLASE_YST
SDGRG	+K	C17H30N8O9K	529.18	529.17	5.2	1.009	0.004	205.4	0.8	0.4%	Peptide	Analytical Standard	Sigma-Aldrich	SYNTHETIC
GRGDS	+K	C17H30N8O9K	529.18	529.18	5.2	0.984	0.001	210.4	0.2	0.1%	Peptide	Analytical Standard	Sigma-Aldrich	SYNTHETIC
FWGK	+H	C28H37N6O5	537.28	537.28	-5.4	0.896	0.003	231.0	0.8	0.3%	Peptide	Analytical Standard	Waters	ALBUMIN_BOV
VASLR	+H	C23H45N8O7	545.34	545.34	-0.9	0.890	0.001	232.5	0.3	0.1%	Peptide	Analytical Standard	Waters	ALBUMIN_BOV
QENK	+H	C25H41N8O6	549.31	549.31	-1.3	0.889	0.001	232.8	0.3	0.1%	Peptide	Analytical Standard	Waters	PHOSPH_RAB
NFNR	+H	C23H36N9O7	550.27	550.27	-1.1	0.920	0.002	225.0	0.6	0.3%	Peptide	Analytical Standard	Waters	PHOSPH_RAB
LEYK	+H	C26H42N5O8	552.30	552.30	-1.6	0.863	0.003	239.6	0.9	0.4%	Peptide	Analytical Standard	Waters	ADH_YST
FQNK	+Na	C24H38N7O7Na	559.27	559.27	-2.1	0.848	0.005	243.9	1.4	0.6%	Peptide	Analytical Standard	Waters	PHOSPH_RAB

FQNK	+Na	C23H44N7O8Na	569.31	569.31	-2.5	0.945	0.002	218.9	0.6	0.3%	7	Peptide	Analytical Standard	Waters	ENOLASE_YST
EWTR	+H	C26H39N8O8	591.29	591.29	-3.2	0.885	0.001	233.4	0.4	0.2%	7	Peptide	Analytical Standard	Waters	PHOSPH_RAB
AMGYR	+H	C25H41N8O7S	597.28	597.28	-2.0	0.843	0.001	245.0	0.3	0.1%	7	Peptide	Analytical Standard	Waters	ADH_YST
QISVR	+H	C25H48N9O8	602.36	602.36	-3.2	0.855	0.001	241.4	0.3	0.1%	7	Peptide	Analytical Standard	Waters	PHOSPH_RAB
LWSAK	+H	C29H46N7O7	604.35	604.34	-1.8	0.865	0.001	238.6	0.3	0.1%	7	Peptide	Analytical Standard	Waters	PHOSPH_RAB
AFDEK	+H	C27H41N6O10	609.29	609.29	-1.1	0.867	0.001	238.3	0.3	0.1%	7	Peptide	Analytical Standard	Waters	ALBUMIN_BOV
FSSDR	+H	C25H39N8O10	611.28	611.28	-2.9	0.870	0.001	237.3	0.3	0.1%	7	Peptide	Analytical Standard	Waters	PHOSPH_RAB
FVVPR (peak 1)	+H	C30H49N8O6	617.38	617.37	-3.6	0.810	0.002	254.7	0.7	0.3%	7	Peptide	Analytical Standard	Waters	PHOSPH_RAB
FVVPR (peak2)	+H	C30H49N8O6	617.38	617.37	-3.6	0.828	0.001	249.3	0.4	0.1%	7	Peptide	Analytical Standard	Waters	PHOSPH_RAB
GQIVGR	+H	C26H49N10O8	629.37	629.37	-2.1	0.840	0.001	245.5	0.3	0.1%	7	Peptide	Analytical Standard	Waters	ADH_YST
VSLAEK	+H	C28H52N7O10	646.38	646.38	-2.6	0.828	0.001	249.0	0.3	0.1%	7	Peptide	Analytical Standard	Waters	PHOSPH_RAB
IETMR or CASIQK	+H	C26H49N8O9S	649.33	649.33	-3.4	0.815	0.001	252.8	0.4	0.2%	7	Peptide	Analytical Standard	Waters	ALBUMIN_BOV
AAGHDGK	+H	C26H43N10O10	655.32	655.32	1.1	0.828	0.002	249.0	0.5	0.2%	7	Peptide	Analytical Standard	Waters	ENOLASE_YST
NVATPR	+H	C27H49N10O9	657.37	657.37	-3.8	0.811	0.001	254.0	0.3	0.1%	7	Peptide	Analytical Standard	Waters	PHOSPH_RAB
ANIDVK	+H	C28H51N8O10	659.37	659.37	-3.2	0.831	0.001	248.1	0.4	0.2%	7	Peptide	Analytical Standard	Waters	ENOLASE_YST
VSALYK (peak 1)	+H	C32H54N7O9	680.40	680.40	-2.1	0.787	0.001	261.8	0.3	0.1%	7	Peptide	Analytical Standard	Waters	PHOSPH_RAB
VSALYK (peak 2)	+H	C32H54N7O9	680.40	680.40	-2.1	0.811	0.001	254.0	0.4	0.2%	7	Peptide	Analytical Standard	Waters	PHOSPH_RAB
IHEYK	+H	C32H49N8O9	689.36	689.37	10.6	0.797	0.001	258.5	0.2	0.1%	7	Peptide	Analytical Standard	Waters	PHOSPH_RAB
NIATSGK	+H	C28H52N9O11	690.38	690.38	-3.3	0.801	0.001	257.2	0.3	0.1%	8	Peptide	Analytical Standard	Waters	PHOSPH_RAB
EELFR	+H	C31H49N8O10	693.36	693.35	-2.6	0.810	0.001	254.1	0.3	0.1%	8	Peptide	Analytical Standard	Waters	ADH_YST
DHLVGR	+H	C29H50N11O9	696.38	696.38	-5.2	0.826	0.002	249.4	0.6	0.2%	8	Peptide	Analytical Standard	Waters	PHOSPH_RAB
TVMIGGK	+H	C30H57N8O9S	705.40	705.40	-1.0	0.785	0.001	262.2	0.4	0.2%	7	Peptide	Analytical Standard	Waters	PHOSPH_RAB
GVLHAVK	+H	C33H59N10O8	723.45	723.45	-1.9	0.762	0.001	269.9	0.4	0.2%	7	Peptide	Analytical Standard	Waters	ENOLASE_YST
SVYDSR	+H	C30H48N9O12	726.34	726.34	-2.1	0.796	0.002	258.4	0.6	0.2%	7	Peptide	Analytical Standard	Waters	ENOLASE_YST
VEDVDR	+H	C29H50N9O13	732.35	732.35	-4.1	0.801	0.001	256.6	0.5	0.2%	8	Peptide	Analytical Standard	Waters	PHOSPH_RAB
NVPLYK	+H	C35H57N8O9	733.42	733.42	-5.5	0.756	0.001	272.2	0.4	0.1%	7	Peptide	Analytical Standard	Waters	ENOLASE_YST
QPDLFK	+H	C33H61N8O11	745.45	745.44	-1.9	0.746	0.001	275.5	0.3	0.1%	7	Peptide	Analytical Standard	Waters	ENOLASE_YST
LNQLLR	+H	C33H62N11O9	756.47	756.47	-2.1	0.746	0.001	275.6	0.4	0.1%	7	Peptide	Analytical Standard	Waters	ENOLASE_YST

TNGITPR (peak 1)	+H	C31H56N11O11	758.42	758.41	-1.8	0.733	0.001	280.4	0.3	0.1%	7	Peptide	Analytical Standard	Waters	PHOSPH_RAB
TNGITPR (peak 2)	+H	C31H56N11O11	758.42	758.41	-1.8	0.762	0.001	269.8	0.5	0.2%	7	Peptide	Analytical Standard	Waters	PHOSPH_RAB
TNGITPR (peak 3)	+H	C31H56N11O11	758.42	758.41	-1.8	0.795	0.001	258.4	0.4	0.1%	7	Peptide	Analytical Standard	Waters	PHOSPH_RAB
HLADLSK	+H	C34H59N10O11	783.44	783.43	-4.6	0.752	0.001	273.3	0.5	0.2%	6	Peptide	Analytical Standard	Waters	ENOLASE_YST
LVTDLTK	+H	C35H65N8O12	789.47	789.47	-2.5	0.743	0.001	276.6	0.5	0.2%	7	Peptide	Analytical Standard	Waters	ALBUMIN_BOV
YDLDFK	+H	C38H54N7O12	800.38	800.38	-3.6	0.754	0.001	272.4	0.5	0.2%	7	Peptide	Analytical Standard	Waters	ENOLASE_YST
TFAEALR	+H	C36H59N10O11	807.44	807.43	-1.6	0.724	0.001	283.5	0.5	0.2%	7	Peptide	Analytical Standard	Waters	ENOLASE_YST
YVVDTSK	+H	C36H59N8O13	811.42	811.42	-1.5	0.746	0.001	275.2	0.3	0.1%	7	Peptide	Analytical Standard	Waters	ADH_YST
AADALLK or DIVGAVLK	+H	C37H68N9O11	814.50	814.50	-0.4	0.704	0.001	291.8	0.4	0.1%	7	Peptide	Analytical Standard	Waters	ENOLASE_YST or ADH_YST
AADALLK or DIVGAVLK	+H	C37H68N9O11	814.50	814.50	-0.4	0.739	0.001	277.8	0.3	0.1%	7	Peptide	Analytical Standard	Waters	ENOLASE_YST or ADH_YST
ATEEQLK	+H	C34H60N9O14	818.43	818.42	-2.3	0.730	0.001	281.3	0.5	0.2%	7	Peptide	Analytical Standard	Waters	ALBUMIN_BOV
TIAQYAR	+H	C36H60N11O11	822.45	822.45	-2.1	0.729	0.001	281.6	0.5	0.2%	7	Peptide	Analytical Standard	Waters	PHOSPH_RAB
AWEVTVK	+H	C39H62N9O11	832.46	832.45	-4.2	0.736	0.000	279.0	0.7	0.2%	7	Peptide	Analytical Standard	Waters	PHOSPH_RAB
IGDYAGIK	+H	C38H62N9O12	836.45	836.45	-0.6	0.718	0.001	285.9	0.3	0.1%	6	Peptide	Analytical Standard	Waters	ADH_YST
VLVDLER	+H	C37H67N10O12	843.49	843.49	-1.1	0.718	0.001	285.7	0.4	0.1%	7	Peptide	Analytical Standard	Waters	PHOSPH_RAB
FAAYLER	+H	C41H61N10O11	869.45	869.45	-1.4	0.694	0.001	295.5	0.4	0.1%	7	Peptide	Analytical Standard	Waters	PHOSPH_RAB
YGNPWEK	+H	C42H57N10O12	893.42	893.41	-4.1	0.722	0.001	283.8	0.6	0.2%	7	Peptide	Analytical Standard	Waters	PHOSPH_RAB
DIPVPKPK	+H	C42H73N10O11	893.55	893.54	-2.4	0.697	0.002	294.2	0.7	0.2%	7	Peptide	Analytical Standard	Waters	ADH_YST
NLAENISR	+H	C37H66N13O14	916.48	916.48	-2.1	0.703	0.001	291.7	0.6	0.2%	7	Peptide	Analytical Standard	Waters	PHOSPH_RAB
APNDFNLK	+H	C41H64N11O13	918.47	918.46	-4.5	0.683	0.001	300.0	0.6	0.2%	7	Peptide	Analytical Standard	Waters	PHOSPH_RAB
AEFVEVTK	+H	C42H68N9O14	922.49	922.49	-2.8	0.693	0.001	295.7	0.5	0.2%	7	Peptide	Analytical Standard	Waters	ALBUMIN_BOV
YLYEJAR	+H	C44H67N10O12	927.49	927.49	-1.7	0.672	0.001	305.0	0.5	0.2%	7	Peptide	Analytical Standard	Waters	ALBUMIN_BOV
VLGIDGEGEK	+H	C40H70N11O15	944.50	944.50	-3.2	0.703	0.000	291.2	0.2	0.1%	7	Peptide	Analytical Standard	Waters	ADH_YST
NNVVTMR	+H	C37H67N14O13S	947.47	947.47	1.1	0.681	0.001	300.7	0.6	0.2%	8	Peptide	Analytical Standard	Waters	PHOSPH_RAB
EALDFFAR	+H	C45H66N11O13	968.48	968.48	-0.7	0.669	0.001	305.9	0.4	0.1%	7	Peptide	Analytical Standard	Waters	ADH_YST
LVVSTQTALA	+H	C44H80N11O15	1002.58	1002.58	0.3	0.649	0.001	315.6	0.3	0.1%	6	Peptide	Analytical Standard	Waters	ALBUMIN_BOV
ANELLINVK	+H	C45H81N12O14	1013.60	1013.60	-1.0	0.626	0.001	326.8	0.3	0.1%	6	Peptide	Analytical Standard	Waters	ADH_YST

VIFLENYR	+H	C50H77N12O13	1053.57	1053.57	-0.7	0.643	0.001	318.3	0.4	0.1%	7	Peptide	Analytical Standard	Waters	PHOSPH_RAB
EIWGVEPSR	+H	C48H74N13O15	1072.54	1072.54	-3.4	0.639	0.001	320.2	0.6	0.2%	7	Peptide	Analytical Standard	Waters	PHOSPH_RAB
VAAAFPGDVDR (peak 1)	+H	C49H77N14O16	1117.56	1117.56	-0.2	0.626	0.001	326.7	0.5	0.2%	5	Peptide	Analytical Standard	Waters	PHOSPH_RAB
VAAAFPGDVDR (peak 2)	+H	C49H77N14O16	1117.56	1117.56	-0.2	0.630	0.001	324.3	0.4	0.1%	6	Peptide	Analytical Standard	Waters	PHOSPH_RAB
GVIFYESHGK	+H	C53H78N13O15	1136.57	1136.57	-0.3	0.614	0.001	332.9	0.5	0.2%	5	Peptide	Analytical Standard	Waters	ADH_YST
IGSEVYHNLK	+H	C52H83N14O16	1159.61	1159.61	-2.1	0.586	0.001	348.4	0.7	0.2%	5	Peptide	Analytical Standard	Waters	ENOLASE_YST
LVNELTEFAK	+H	C53H87N12O17	1163.63	1163.63	0.0	0.593	0.000	344.4	0.2	0.1%	5	Peptide	Analytical Standard	Waters	ALBUMIN_BOV
SIVGSYVGNR	+H	C54H91N16O18	1251.67	1251.67	1.0	0.585	0.001	349.1	0.8	0.2%	6	Peptide	Analytical Standard	Waters	ADH_YST
VFADYEEYVK	+H	C60H84N11O19	1262.59	1262.59	-3.0	0.557	0.002	366.4	1.2	0.3%	6	Peptide	Analytical Standard	Waters	PHOSPH_RAB
VNQIGTLESIK	+H	C55H98N15O20	1288.71	1288.71	0.5	0.569	0.001	358.7	0.5	0.1%	5	Peptide	Analytical Standard	Waters	ENOLASE_YST
SIGGEVFIDFTK	+H	C61H94N13O19	1312.68	1312.68	-0.4	0.534	0.001	382.3	0.9	0.2%	5	Peptide	Analytical Standard	Waters	ADH_YST
TMENFVAFVDK	+H	C64H99N14O19S	1399.69	1399.69	-0.1	0.522	0.003	390.2	1.9	0.5%	5	Peptide	Analytical Standard	Waters	ALBUMIN_BOV
AVDDFLISLDGTANK	+H	C69H112N17O25	1578.80	1578.80	1.2	0.474	0.001	429.7	0.7	0.2%	6	Peptide	Analytical Standard	Waters	ENOLASE_YST
TAGIQIVADDLTVTNPK	+H	C76H131N20O27	1755.95	1755.95	-0.1	0.452	0.000	450.6	0.5	0.1%	4	Peptide	Analytical Standard	Waters	ENOLASE_YST

Table D.4: Collision Cross-Section Database of Lipids

Analyte	Z	Molecular Formula	Exact m/z	Measured m/z	Mass Accuracy (ppm)	K_0	$K_0 \sigma$	CCS σ	RSD (%)	N	Chemical Class	Analyte Source	Vendor Source
GlcCer 34:01	+Na	C40H77NO8Na	722.55	722.55	-7.3	0.742	0.002	277.3	0.8	15	Lipid	Analytical Standard	Avanti Polar Lipids
GlcCer 34:00	+Na	C40H79NO8Na	724.57	724.56	-8.2	0.730	0.002	281.7	0.7	14	Lipid	Analytical Standard	Avanti Polar Lipids
GlcCer 36:02	+Na	C42H79NO8Na	748.57	748.56	-7.2	0.727	0.002	282.6	0.6	14	Lipid	Analytical Standard	Avanti Polar Lipids
GlcCer 36:01	+Na	C42H81NO8Na	750.59	750.58	-2.1	0.717	0.001	286.7	0.4	14	Lipid	Analytical Standard	Avanti Polar Lipids
GlcCer 37:01	+Na	C43H83NO8Na	764.60	764.59	-12.0	0.717	0.002	286.8	0.9	14	Lipid	Analytical Standard	Avanti Polar Lipids
GlcCer 36:01 h	+Na	C42H81NO9Na	766.58	766.58	-4.3	0.705	0.001	291.5	0.4	14	Lipid	Analytical Standard	Avanti Polar Lipids
GlcCer 38:02	+Na	C44H83NO8Na	776.60	776.60	-7.7	0.705	0.002	291.4	1.0	14	Lipid	Analytical Standard	Avanti Polar Lipids
GlcCer 38:01	+Na	C44H85NO8Na	778.62	778.61	-4.6	0.699	0.001	293.8	0.4	14	Lipid	Analytical Standard	Avanti Polar Lipids
GlcCer 38:00	+Na	C44H87NO8Na	780.63	780.63	-7.7	0.695	0.001	295.6	0.5	14	Lipid	Analytical Standard	Avanti Polar Lipids
GlcCer 38:02 h	+Na	C44H83NO9Na	792.60	792.59	-8.5	0.692	0.002	296.6	0.8	14	Lipid	Analytical Standard	Avanti Polar Lipids
GlcCer 38:01 h	+Na	C44H85NO9Na	794.61	794.61	-3.9	0.690	0.001	297.7	0.5	14	Lipid	Analytical Standard	Avanti Polar Lipids
GlcCer 40:03	+Na	C46H85NO7Na	802.62	802.61	-6.8	0.694	0.003	295.8	1.3	14	Lipid	Analytical Standard	Avanti Polar Lipids
GlcCer 40:02	+Na	C46H87NO8Na	804.63	804.63	-4.1	0.691	0.002	297.1	0.6	14	Lipid	Analytical Standard	Avanti Polar Lipids
GlcCer 40:01	+Na	C46H89NO8Na	806.65	806.65	-3.4	0.682	0.001	301.1	0.5	14	Lipid	Analytical Standard	Avanti Polar Lipids
GlcCer 40:00	+Na	C46H91NO8Na	808.66	808.66	-7.4	0.679	0.001	302.3	0.5	14	Lipid	Analytical Standard	Avanti Polar Lipids
GlcCer 41:02	+Na	C47H89NO8Na	818.65	818.64	-5.7	0.685	0.001	299.6	0.6	14	Lipid	Analytical Standard	Avanti Polar Lipids
GlcCer 41:01	+Na	C47H91NO8Na	820.66	820.65	-13.2	0.679	0.001	302.5	0.5	14	Lipid	Analytical Standard	Avanti Polar Lipids
GlcCer 40:01 h	+Na	C46H89NO9Na	822.64	822.64	1.0	0.677	0.001	303.4	0.4	14	Lipid	Analytical Standard	Avanti Polar Lipids
GlcCer 40:00 h	+Na	C46H91NO9Na	824.66	824.65	-6.0	0.671	0.001	306.1	0.6	14	Lipid	Analytical Standard	Avanti Polar Lipids
GlcCer 42:03	+Na	C48H89NO8Na	830.65	830.64	-5.1	0.679	0.001	302.3	0.4	14	Lipid	Analytical Standard	Avanti Polar Lipids
GlcCer 42:02	+Na	C48H91NO9Na	832.66	832.67	3.1	0.672	0.001	305.2	0.5	14	Lipid	Analytical Standard	Avanti Polar Lipids
GlcCer 42:01	+Na	C48H93NO10Na	834.68	834.68	-1.5	0.667	0.001	307.5	0.4	14	Lipid	Analytical Standard	Avanti Polar Lipids
GlcCer 42:00	+Na	C48H95NO8Na	836.70	836.68	-18.3	0.666	0.001	308.2	0.5	14	Lipid	Analytical Standard	Avanti Polar Lipids
GlcCer 43:03	+Na	C49H91NO8Na	844.66	844.65	-19.3	0.670	0.002	306.1	0.7	14	Lipid	Analytical Standard	Avanti Polar Lipids
GlcCer 43:02	+Na	C49H93NO9Na	846.68	846.67	-8.1	0.667	0.002	307.8	1.0	14	Lipid	Analytical Standard	Avanti Polar Lipids
GlcCer 42:02 h	+Na	C48H91NO9Na	848.66	848.66	4.3	0.664	0.001	309.0	0.4	14	Lipid	Analytical Standard	Avanti Polar Lipids
GlcCer 42:01 h	+Na	C48H93NO9Na	850.67	850.68	0.4	0.656	0.001	312.7	0.4	12	Lipid	Analytical Standard	Avanti Polar Lipids
GlcCer 44:03	+Na	C50H93NO8Na	858.68	858.67	-6.3	0.660	0.001	310.7	0.7	12	Lipid	Analytical Standard	Avanti Polar Lipids

GlcCer 44:02	+Na	C50H95NO9Na	860.70	860.69	-4.2	0.651	0.001	315.3	0.4	0.1%	12	Lipid	Analytical Standard	Avanti Polar Lipids
GlcCer 43:02 h	+Na	C49H93NO9Na	862.67	862.69	12.0	0.652	0.001	314.6	0.4	0.1%	12	Lipid	Analytical Standard	Avanti Polar Lipids
GlcCer 43:01 h	+Na	C49H95NO9Na	864.69	864.68	-10.7	0.654	0.001	313.7	0.4	0.1%	12	Lipid	Analytical Standard	Avanti Polar Lipids
GlcCer 44:04 h	+Na	C50H91NO9Na	872.66	872.65	-7.8	0.652	0.001	314.7	0.4	0.1%	12	Lipid	Analytical Standard	Avanti Polar Lipids
GlcCer 44:03 h	+Na	C50H93NO9Na	874.67	874.67	-5.3	0.653	0.001	314.0	0.6	0.2%	12	Lipid	Analytical Standard	Avanti Polar Lipids
GlcCer 44:02 h	+Na	C50H95NO9Na	876.69	876.69	-2.3	0.644	0.001	318.4	0.4	0.1%	12	Lipid	Analytical Standard	Avanti Polar Lipids
GlcCer 44:01 h	+Na	C50H97NO9Na	878.71	878.70	-8.2	0.642	0.001	319.5	0.4	0.1%	12	Lipid	Analytical Standard	Avanti Polar Lipids
GlcCer 44:02 h	+K	C50H95NO9K	892.66	892.68	19.0	0.639	0.001	321.1	0.7	0.2%	12	Lipid	Analytical Standard	Avanti Polar Lipids
GlcCer 47:09	+K	C53H87NO8K	904.61	904.60	-3.1	0.648	0.001	316.4	0.6	0.2%	12	Lipid	Analytical Standard	Avanti Polar Lipids
GlcCer 46:02 h	+Na	C52H99NO9Na	904.72	904.72	-7.1	0.633	0.001	323.8	0.6	0.2%	12	Lipid	Analytical Standard	Avanti Polar Lipids
GlcCer 47:10 h	+K	C53H85NO9K	918.59	918.59	6.5	0.643	0.001	318.6	0.5	0.2%	12	Lipid	Analytical Standard	Avanti Polar Lipids
PC 31:02	+K	C39H74NO8PK	754.48	754.48	6.2	0.725	0.002	283.6	0.8	0.3%	8	Lipid	Analytical Standard	Avanti Polar Lipids
PC 31:01	+K	C39H76NO8PK	756.49	756.50	3.4	0.718	0.002	286.5	0.7	0.2%	8	Lipid	Analytical Standard	Avanti Polar Lipids
PC 32:03	+K	C40H74NO8PK	766.48	766.49	11.1	0.711	0.001	288.9	0.6	0.2%	8	Lipid	Analytical Standard	Avanti Polar Lipids
PC 32:02	+K	C40H76NO8PK	768.49	768.50	5.2	0.711	0.001	289.2	0.5	0.2%	8	Lipid	Analytical Standard	Avanti Polar Lipids
PC 33:04	+K	C41H74NO8PK	778.48	778.48	4.6	0.715	0.002	287.5	0.7	0.3%	10	Lipid	Analytical Standard	Avanti Polar Lipids
PC 33:03	+K	C41H76NO8PK	780.49	780.50	10.5	0.708	0.001	290.1	0.5	0.2%	8	Lipid	Analytical Standard	Avanti Polar Lipids
PC 33:02	+K	C41H78NO8PK	782.51	782.52	11.1	0.705	0.001	291.5	0.6	0.2%	9	Lipid	Analytical Standard	Avanti Polar Lipids
PC 34:04	+K	C42H76NO8PK	792.49	792.50	2.7	0.711	0.002	289.0	1.0	0.3%	10	Lipid	Analytical Standard	Avanti Polar Lipids
PC 34:03	+K	C42H78NO8PK	794.51	794.51	5.1	0.702	0.002	292.4	0.8	0.3%	10	Lipid	Analytical Standard	Avanti Polar Lipids
PC 34:02	+K	C42H80NO8PK	796.53	796.53	2.6	0.705	0.001	291.3	0.6	0.2%	8	Lipid	Analytical Standard	Avanti Polar Lipids
PC 36:07	+Na	C44H74NO8PNa	798.50	798.51	8.6	0.702	0.002	292.5	0.7	0.2%	9	Lipid	Analytical Standard	Avanti Polar Lipids
PC 35:06	+K	C43H74NO8PK	802.48	802.48	2.9	0.704	0.002	291.8	1.0	0.3%	10	Lipid	Analytical Standard	Avanti Polar Lipids
PC 35:05	+K	C43H76NO8PK	804.49	804.50	4.3	0.699	0.001	293.8	0.6	0.2%	9	Lipid	Analytical Standard	Avanti Polar Lipids
PC 35:04	+K	C43H78NO8PK	806.51	806.51	2.5	0.697	0.002	294.5	0.7	0.2%	10	Lipid	Analytical Standard	Avanti Polar Lipids
PC 35:03	+K	C43H80NO8PK	808.53	808.53	5.8	0.693	0.001	296.1	0.6	0.2%	10	Lipid	Analytical Standard	Avanti Polar Lipids
PC 35:02	+K	C43H82NO8PK	810.54	810.54	4.0	0.690	0.001	297.7	0.6	0.2%	10	Lipid	Analytical Standard	Avanti Polar Lipids
PC 38:10	+Na	C46H72NO8PNa	820.49	820.50	17.1	0.694	0.001	295.9	0.6	0.2%	9	Lipid	Analytical Standard	Avanti Polar Lipids
PC 38:09	+Na	C46H74NO8PNa	822.50	822.51	3.8	0.689	0.001	297.8	0.6	0.2%	10	Lipid	Analytical Standard	Avanti Polar Lipids
PC 38:08	+Na	C46H76NO8PNa	824.52	824.52	0.1	0.684	0.002	299.9	0.7	0.2%	10	Lipid	Analytical Standard	Avanti Polar Lipids
PC 37:07	+K	C45H76NO8PK	828.49	828.50	2.3	0.692	0.001	296.6	0.6	0.2%	10	Lipid	Analytical Standard	Avanti Polar Lipids
PC 37:06	+K	C45H78NO8PK	830.51	830.51	0.7	0.688	0.001	298.2	0.5	0.2%	10	Lipid	Analytical Standard	Avanti Polar Lipids
PC 37:05	+K	C45H80NO8PK	832.53	832.53	2.2	0.686	0.001	299.0	0.6	0.2%	8	Lipid	Analytical Standard	Avanti Polar Lipids
PC 40:15	+Na	C48H66NO8PNa	838.44	838.45	7.2	0.699	0.002	293.5	1.0	0.3%	9	Lipid	Analytical Standard	Avanti Polar Lipids

PC 40:14	+Na	C48H68NO8PNa	840.46	840.46	2.4	0.700	0.001	293.3	0.6	0.2%	8	Lipid	Analytical Standard	Avanti Polar Lipids
PC 40:13	+Na	C48H70NO8PNa	842.47	842.47	-2.3	0.692	0.002	296.6	0.8	0.3%	8	Lipid	Analytical Standard	Avanti Polar Lipids
PC 40:12	+Na	C48H72NO8PNa	844.49	844.49	0.4	0.683	0.001	300.6	0.6	0.2%	8	Lipid	Analytical Standard	Avanti Polar Lipids
PC 40:11	+Na	C48H74NO8PNa	846.50	846.50	-0.4	0.682	0.002	300.7	0.7	0.2%	9	Lipid	Analytical Standard	Avanti Polar Lipids
PC 40:10	+Na	C48H76NO8PNa	848.52	848.52	-1.8	0.680	0.001	301.5	0.5	0.2%	8	Lipid	Analytical Standard	Avanti Polar Lipids
PC 40:10	+Na	C48H78NO8PNa	850.54	850.53	-6.3	0.679	0.002	302.2	0.7	0.2%	10	Lipid	Analytical Standard	Avanti Polar Lipids
PC 39:07	+K	C47H80NO8PK	856.53	856.53	-0.4	0.675	0.002	303.8	0.7	0.2%	10	Lipid	Analytical Standard	Avanti Polar Lipids
PC 39:06	+K	C47H82NO8PK	858.54	858.54	-1.4	0.676	0.001	303.4	0.7	0.2%	9	Lipid	Analytical Standard	Avanti Polar Lipids
PC 39:05	+K	C47H84NO8PK	860.56	860.55	-4.7	0.673	0.002	304.7	0.7	0.2%	9	Lipid	Analytical Standard	Avanti Polar Lipids
PC 42:15	+Na	C50H70NO8PNa	866.47	866.47	1.0	0.679	0.003	301.9	1.1	0.4%	10	Lipid	Analytical Standard	Avanti Polar Lipids
PC 42:14	+Na	C50H72NO8PNa	868.49	868.49	-1.4	0.686	0.002	299.0	0.7	0.2%	10	Lipid	Analytical Standard	Avanti Polar Lipids
PC 42:13	+Na	C50H74NO8PNa	870.50	870.50	-5.2	0.673	0.002	304.9	0.7	0.2%	9	Lipid	Analytical Standard	Avanti Polar Lipids
PC 42:12	+Na	C50H76NO8PNa	872.52	872.52	-4.5	0.675	0.002	303.9	0.7	0.2%	9	Lipid	Analytical Standard	Avanti Polar Lipids
PC 43:17	+K	C51H68NO8PK	892.43	892.44	9.5	0.675	0.001	303.5	0.5	0.2%	8	Lipid	Analytical Standard	Avanti Polar Lipids
PC 43:16	+K	C51H70NO8PK	894.45	894.44	-5.8	0.674	0.002	304.1	0.7	0.2%	10	Lipid	Analytical Standard	Avanti Polar Lipids
PE O-18:03/0:00	+Na	C23H42NO7PNa	498.26	498.26	-3.3	0.941	0.003	220.5	0.6	0.3%	11	Lipid	Analytical Standard	Avanti Polar Lipids
PE O-20:05	+Na	C25H42NO7PNa	522.26	522.26	-3.3	0.956	0.004	216.8	0.9	0.4%	11	Lipid	Analytical Standard	Avanti Polar Lipids
PE O-20:04	+Na	C25H44NO7PNa	524.28	524.27	-3.6	0.913	0.002	226.9	0.5	0.2%	11	Lipid	Analytical Standard	Avanti Polar Lipids
PE O-20:03	+Na	C25H46NO7PNa	526.29	526.29	-3.9	0.906	0.002	228.7	0.6	0.3%	11	Lipid	Analytical Standard	Avanti Polar Lipids
PE O-22:07	+Na	C27H42NO7PNa	546.26	546.26	-2.8	0.938	0.007	220.6	1.7	0.8%	11	Lipid	Analytical Standard	Avanti Polar Lipids
PE O-22:06	+Na	C27H44NO7PNa	548.28	548.27	-7.5	0.907	0.003	228.1	0.7	0.3%	8	Lipid	Analytical Standard	Avanti Polar Lipids
PE 21:03	+K	C26H46NO8PK	570.26	570.26	-2.6	0.908	0.003	227.8	0.7	0.3%	8	Lipid	Analytical Standard	Avanti Polar Lipids
PE 21:02	+K	C26H48NO8PK	572.28	572.27	-4.1	0.902	0.001	229.3	0.3	0.2%	8	Lipid	Analytical Standard	Avanti Polar Lipids
PE O-26:05	+K	C31H54NO7PK	622.33	622.31	-25.5	0.851	0.002	242.4	0.4	0.2%	8	Lipid	Analytical Standard	Avanti Polar Lipids
PE 26:06	+K	C31H50NO8PK	634.29	634.27	-35.3	0.854	0.003	241.7	1.0	0.4%	8	Lipid	Analytical Standard	Avanti Polar Lipids
PE 26:05	+K	C31H52NO8PK	636.31	636.29	-33.4	0.850	0.003	242.6	0.8	0.3%	8	Lipid	Analytical Standard	Avanti Polar Lipids
PE 26:04	+K	C31H54NO8PK	638.32	638.30	-39.6	0.841	0.003	245.4	1.0	0.4%	8	Lipid	Analytical Standard	Avanti Polar Lipids
PE 28:07	+K	C33H52NO8PK	660.31	660.29	-32.8	0.843	0.003	244.4	0.8	0.3%	8	Lipid	Analytical Standard	Avanti Polar Lipids
PE 28:06	+K	C33H54NO8PK	662.32	662.30	-32.8	0.829	0.002	248.7	0.7	0.3%	8	Lipid	Analytical Standard	Avanti Polar Lipids
PE 28:05	+K	C33H56NO8PK	664.34	664.32	-31.4	0.821	0.002	250.9	0.5	0.2%	8	Lipid	Analytical Standard	Avanti Polar Lipids
PE O-31:06	+K	C36H62NO7PK	690.39	690.37	-27.2	0.799	0.002	257.8	0.5	0.2%	13	Lipid	Analytical Standard	Avanti Polar Lipids
PE 32:01	+Na	C37H72NO8PNa	712.49	712.49	-2.1	0.751	0.002	274.1	0.7	0.3%	8	Lipid	Analytical Standard	Avanti Polar Lipids
PE O-34:04	+Na	C39H72NO7PNa	720.49	720.49	-7.1	0.746	0.002	275.9	0.7	0.2%	11	Lipid	Analytical Standard	Avanti Polar Lipids
PE O-34:03	+Na	C39H74NO7PNa	722.51	722.51	-3.1	0.740	0.003	278.0	0.9	0.3%	12	Lipid	Analytical Standard	Avanti Polar Lipids

PE O-34:02	+Na	C39H76NO7PNa	724.53	724.52	-6.9	0.735	0.002	279.7	0.8	0.3%	12	Lipid	Analytical Standard	Avanti Polar Lipids
PE 34:04	+Na	C39H70NO8PNa	734.47	734.47	-5.6	0.752	0.003	273.6	1.2	0.5%	8	Lipid	Analytical Standard	Avanti Polar Lipids
PE O-O-36:04	+Na	C41H78NO6PNa	734.55	734.55	0.7	0.736	0.003	279.3	1.2	0.4%	8	Lipid	Analytical Standard	Avanti Polar Lipids
PE 34:03	+Na	C39H72NO8PNa	736.49	736.49	-0.8	0.745	0.003	276.1	1.0	0.4%	10	Lipid	Analytical Standard	Avanti Polar Lipids
PE 34:02	+Na	C39H74NO8PNa	738.50	738.51	2.1	0.739	0.001	278.3	0.6	0.2%	11	Lipid	Analytical Standard	Avanti Polar Lipids
PE 34:01	+Na	C39H76NO8PNa	740.52	740.52	0.9	0.731	0.002	281.3	0.6	0.2%	11	Lipid	Analytical Standard	Avanti Polar Lipids
PE 33:00	+K	C38H76NO8PK	744.49	744.49	-5.3	0.742	0.003	277.2	1.2	0.4%	11	Lipid	Analytical Standard	Avanti Polar Lipids
PE O-36:05	+Na	C41H74NO7PNa	746.51	746.51	-4.9	0.736	0.002	279.2	0.7	0.3%	11	Lipid	Analytical Standard	Avanti Polar Lipids
PE O-36:04	+Na	C41H76NO7PNa	748.53	748.52	-4.4	0.730	0.002	281.6	0.6	0.2%	11	Lipid	Analytical Standard	Avanti Polar Lipids
PE O-36:03	+Na	C41H78NO7PNa	750.54	750.54	-1.5	0.720	0.003	285.4	1.1	0.4%	11	Lipid	Analytical Standard	Avanti Polar Lipids
PE 35:02	+Na	C40H76NO8PNa	752.52	752.52	-2.1	0.731	0.001	281.3	0.3	0.1%	8	Lipid	Analytical Standard	Avanti Polar Lipids
PE O-36:02	+Na	C41H80NO7PNa	752.56	752.55	-6.2	0.716	0.001	287.3	0.6	0.2%	12	Lipid	Analytical Standard	Avanti Polar Lipids
PE 35:01	+Na	C40H78NO8PNa	754.54	754.54	5.4	0.727	0.001	282.9	0.6	0.2%	11	Lipid	Analytical Standard	Avanti Polar Lipids
PE 36:06	+Na	C41H70NO8PNa	758.47	758.47	-3.2	0.744	0.001	276.3	0.5	0.2%	11	Lipid	Analytical Standard	Avanti Polar Lipids
PE 36:05	+Na	C41H72NO8PNa	760.49	760.49	-1.8	0.739	0.001	278.2	0.5	0.2%	11	Lipid	Analytical Standard	Avanti Polar Lipids
PE 36:04	+Na	C41H74NO8PNa	762.50	762.51	0.3	0.732	0.001	280.6	0.5	0.2%	11	Lipid	Analytical Standard	Avanti Polar Lipids
PE 36:02	+Na	C41H78NO8PNa	766.54	766.54	1.5	0.719	0.001	285.7	0.4	0.2%	11	Lipid	Analytical Standard	Avanti Polar Lipids
PE 35:02	+K	C40H76NO8PK	768.49	768.49	-2.3	0.728	0.002	282.5	0.7	0.2%	12	Lipid	Analytical Standard	Avanti Polar Lipids
PE 36:01	+Na	C41H80NO8PNa	768.55	768.55	-0.8	0.712	0.001	288.5	0.6	0.2%	11	Lipid	Analytical Standard	Avanti Polar Lipids
PE 35:01	+K	C40H78NO8PK	770.51	770.51	-0.2	0.725	0.001	283.6	0.6	0.2%	10	Lipid	Analytical Standard	Avanti Polar Lipids
PE 35:00	+K	C40H80NO8PK	772.53	772.53	-0.6	0.718	0.002	286.2	0.7	0.2%	11	Lipid	Analytical Standard	Avanti Polar Lipids
PE O-38:05	+Na	C43H78NO7PNa	774.54	774.54	-3.4	0.714	0.001	287.7	0.3	0.1%	11	Lipid	Analytical Standard	Avanti Polar Lipids
PE O-O-38:05	+K	C43H80NO6PK	776.54	776.53	-4.6	0.720	0.003	285.6	1.0	0.4%	10	Lipid	Analytical Standard	Avanti Polar Lipids
PE 37:03	+Na	C42H78NO8PNa	778.54	778.54	-1.3	0.718	0.002	286.2	0.7	0.2%	12	Lipid	Analytical Standard	Avanti Polar Lipids
PE 37:02	+Na	C42H80NO8PNa	780.55	780.55	-1.3	0.713	0.001	288.2	0.4	0.2%	12	Lipid	Analytical Standard	Avanti Polar Lipids
PE 38:08	+Na	C43H70NO8PNa	782.47	782.46	-11.8	0.729	0.002	281.9	0.7	0.2%	13	Lipid	Analytical Standard	Avanti Polar Lipids
PE 37:01	+Na	C42H82NO8PNa	782.57	782.56	-3.5	0.703	0.002	292.2	0.9	0.3%	12	Lipid	Analytical Standard	Avanti Polar Lipids
PE 38:07	+Na	C43H72NO8PNa	784.49	784.49	-0.9	0.724	0.001	283.7	0.5	0.2%	11	Lipid	Analytical Standard	Avanti Polar Lipids
PE 38:06	+Na	C43H74NO8PNa	786.50	786.50	-0.7	0.721	0.001	285.0	0.5	0.2%	11	Lipid	Analytical Standard	Avanti Polar Lipids
PE 38:05	+Na	C43H76NO8PNa	788.52	788.52	0.3	0.715	0.001	287.2	0.5	0.2%	11	Lipid	Analytical Standard	Avanti Polar Lipids
PE 38:04	+Na	C43H78NO8PNa	790.54	790.54	1.5	0.708	0.001	290.0	0.5	0.2%	12	Lipid	Analytical Standard	Avanti Polar Lipids
PE 37:04	+K	C42H76NO8PK	792.49	792.49	-5.7	0.721	0.002	284.7	0.7	0.2%	11	Lipid	Analytical Standard	Avanti Polar Lipids
PE 38:03	+Na	C43H80NO8PNa	792.55	792.54	-9.7	0.710	0.002	289.3	0.7	0.2%	11	Lipid	Analytical Standard	Avanti Polar Lipids
PE 37:03	+K	C42H78NO8PK	794.51	794.51	-2.6	0.717	0.001	286.5	0.4	0.2%	11	Lipid	Analytical Standard	Avanti Polar Lipids

PE 37:02	+K	C42H80NO8PK	796.53	796.52	-4.8	0.709	0.001	289.8	0.6	0.2%	11	Lipid	Analytical Standard	Avanti Polar Lipids
PE 37:01	+K	C42H82NO8PK	798.54	798.54	-3.0	0.696	0.001	295.0	0.5	0.2%	11	Lipid	Analytical Standard	Avanti Polar Lipids
PE 38:07	+K	C43H72NO8PK	800.46	800.48	19.7	0.716	0.001	287.0	0.5	0.2%	11	Lipid	Analytical Standard	Avanti Polar Lipids
PE 39:06	+Na	C44H76NO8PNa	800.52	800.52	1.1	0.717	0.002	286.4	0.7	0.3%	11	Lipid	Analytical Standard	Avanti Polar Lipids
PE 37:00	+K	C42H84NO8PK	800.56	800.56	1.3	0.690	0.001	297.8	0.5	0.2%	10	Lipid	Analytical Standard	Avanti Polar Lipids
PE 38:06	+K	C43H74NO8PK	802.48	802.48	-0.2	0.711	0.001	288.7	0.5	0.2%	12	Lipid	Analytical Standard	Avanti Polar Lipids
PE O-39:06	+K	C44H78NO7PK	802.52	802.52	5.8	0.706	0.001	290.9	0.5	0.2%	12	Lipid	Analytical Standard	Avanti Polar Lipids
PE O-O-40:06	+K	C45H82NO6PK	802.55	802.55	0.7	0.700	0.000	293.3	0.7	0.2%	11	Lipid	Analytical Standard	Avanti Polar Lipids
PE 39:04	+Na	C44H80NO8PNa	804.55	804.55	1.1	0.701	0.002	292.8	0.8	0.3%	11	Lipid	Analytical Standard	Avanti Polar Lipids
PE 40:09	+Na	C45H72NO8PNa	808.49	808.49	-1.6	0.717	0.001	286.6	0.5	0.2%	10	Lipid	Analytical Standard	Avanti Polar Lipids
PE 40:08	+Na	C45H74NO8PNa	810.50	810.50	-2.3	0.710	0.001	289.2	0.3	0.1%	10	Lipid	Analytical Standard	Avanti Polar Lipids
PE 40:07	+Na	C45H76NO8PNa	812.52	812.52	0.5	0.706	0.001	290.8	0.6	0.2%	11	Lipid	Analytical Standard	Avanti Polar Lipids
PE 40:05	+Na	C45H80NO8PNa	816.55	816.55	-1.8	0.696	0.002	294.8	0.7	0.2%	11	Lipid	Analytical Standard	Avanti Polar Lipids
PE O-O-42:11	+K	C47H74NO6PK	818.49	818.50	11.2	0.708	0.002	289.8	0.9	0.3%	12	Lipid	Analytical Standard	Avanti Polar Lipids
PE O-O-42:10	+K	C47H76NO6PK	820.50	820.51	11.7	0.702	0.001	292.6	0.6	0.2%	11	Lipid	Analytical Standard	Avanti Polar Lipids
PE 39:03	+K	C44H82NO8PK	822.54	822.54	-6.9	0.700	0.002	293.4	0.8	0.3%	11	Lipid	Analytical Standard	Avanti Polar Lipids
PE O-O-44:14	+Na	C49H72NO6PNa	824.50	824.48	-18.2	0.712	0.002	288.2	1.0	0.3%	11	Lipid	Analytical Standard	Avanti Polar Lipids
PE 39:02	+K	C44H84NO8PK	824.56	824.55	-10.2	0.694	0.001	295.9	0.6	0.2%	11	Lipid	Analytical Standard	Avanti Polar Lipids
PE O-O-44:13	+Na	C49H74NO6PNa	826.52	826.50	-21.0	0.709	0.001	289.4	0.6	0.2%	10	Lipid	Analytical Standard	Avanti Polar Lipids
PE O-O-42:08	+K	C47H82NO6PK	826.55	826.56	10.1	0.691	0.002	297.0	0.7	0.2%	11	Lipid	Analytical Standard	Avanti Polar Lipids
PE O-O-44:12	+Na	C49H76NO6PNa	828.53	828.51	-20.8	0.707	0.002	290.4	0.8	0.3%	11	Lipid	Analytical Standard	Avanti Polar Lipids
PE 40:06	+K	C45H78NO8PK	830.51	830.53	20.0	0.696	0.002	294.7	0.8	0.3%	11	Lipid	Analytical Standard	Avanti Polar Lipids
PE 42:10	+Na	C47H74NO8PNa	834.50	834.50	-5.1	0.705	0.002	291.0	0.7	0.2%	12	Lipid	Analytical Standard	Avanti Polar Lipids
PE 42:09	+Na	C47H76NO8PNa	836.52	836.52	-2.9	0.694	0.001	295.6	0.4	0.1%	12	Lipid	Analytical Standard	Avanti Polar Lipids
PE 42:08	+Na	C47H78NO8PNa	838.54	838.53	-3.8	0.690	0.001	297.3	0.5	0.2%	11	Lipid	Analytical Standard	Avanti Polar Lipids
PE O-O-44:14	+K	C49H74NO6PK	842.49	842.49	6.9	0.704	0.002	291.4	0.7	0.3%	11	Lipid	Analytical Standard	Avanti Polar Lipids
PE O-O-44:13	+K	C49H76NO6PK	844.50	844.51	4.4	0.696	0.001	294.7	0.6	0.2%	12	Lipid	Analytical Standard	Avanti Polar Lipids
PE O-O-44:12	+K	C49H78NO6PK	846.52	846.52	3.5	0.691	0.001	297.0	0.6	0.2%	12	Lipid	Analytical Standard	Avanti Polar Lipids
PE 42:10	+K	C47H72NO8PK	848.46	848.48	20.9	0.705	0.001	290.8	0.5	0.2%	11	Lipid	Analytical Standard	Avanti Polar Lipids
PE O-O-44:11	+K	C49H80NO6PK	848.54	848.53	-2.9	0.691	0.002	297.1	0.9	0.3%	11	Lipid	Analytical Standard	Avanti Polar Lipids
PE O-O-46:15	+Na	C51H74NO6PNa	850.52	850.50	-19.2	0.701	0.002	292.7	0.7	0.2%	11	Lipid	Analytical Standard	Avanti Polar Lipids
PE 42:08	+K	C47H76NO8PK	852.49	852.51	18.7	0.693	0.002	296.1	0.8	0.3%	11	Lipid	Analytical Standard	Avanti Polar Lipids
PE O-O-45:14	+K	C50H76NO6PK	856.50	856.51	4.9	0.690	0.002	297.2	1.0	0.3%	11	Lipid	Analytical Standard	Avanti Polar Lipids
PE 44:12	+Na	C49H74NO8PNa	858.50	858.51	4.8	0.685	0.002	299.7	1.0	0.3%	8	Lipid	Analytical Standard	Avanti Polar Lipids

PE 44:11	+Na	C49H76NO8PNa	860.52	860.51	-11.5	0.683	0.002	300.3	1.0	0.3%	8	Lipid	Analytical Standard	Avanti Polar Lipids
PE O-O-46:16	+K	C51H74NO6PK	866.49	866.49	6.7	0.689	0.002	297.7	1.1	0.4%	12	Lipid	Analytical Standard	Avanti Polar Lipids
PE O-O-46:15	+K	C51H76NO6PK	868.50	868.51	5.4	0.682	0.002	300.8	0.7	0.2%	11	Lipid	Analytical Standard	Avanti Polar Lipids
PE O-O-46:14	+K	C51H78NO6PK	870.52	870.52	3.0	0.677	0.001	302.9	0.5	0.2%	10	Lipid	Analytical Standard	Avanti Polar Lipids
PE O-45:12	+K	C50H78NO7PK	874.52	874.51	-11.4	0.685	0.002	299.3	1.0	0.3%	7	Lipid	Analytical Standard	Avanti Polar Lipids
PE 44:11	+K	C49H74NO8PK	876.49	876.50	7.6	0.685	0.001	299.3	0.5	0.2%	10	Lipid	Analytical Standard	Avanti Polar Lipids
PE O-47:16	+Na	C52H74NO7PNa	878.51	878.51	0.8	0.684	0.002	299.7	0.9	0.3%	11	Lipid	Analytical Standard	Avanti Polar Lipids
PE O-O-47:16	+K	C52H76NO6PK	880.50	880.51	4.4	0.681	0.002	301.3	0.8	0.3%	11	Lipid	Analytical Standard	Avanti Polar Lipids
PE O-46:14	+K	C51H76NO7PK	884.50	884.51	7.0	0.684	0.003	299.8	1.4	0.5%	8	Lipid	Analytical Standard	Avanti Polar Lipids
PE O-46:13	+K	C51H78NO7PK	886.52	886.52	9.1	0.670	0.002	306.0	1.1	0.4%	8	Lipid	Analytical Standard	Avanti Polar Lipids
PE O-O-48:16	+K	C53H78NO6PK	894.52	894.52	1.1	0.672	0.001	305.1	0.7	0.2%	11	Lipid	Analytical Standard	Avanti Polar Lipids
PE O-47:14	+K	C52H78NO7PK	898.52	898.52	4.9	0.680	0.001	301.2	0.5	0.2%	11	Lipid	Analytical Standard	Avanti Polar Lipids
PE O-47:13	+K	C52H80NO7PK	900.53	900.53	-1.4	0.684	0.003	299.9	1.2	0.4%	11	Lipid	Analytical Standard	Avanti Polar Lipids
PE 46:11	+K	C51H80NO8PK	904.53	904.51	-17.3	0.678	0.002	302.4	0.9	0.3%	8	Lipid	Analytical Standard	Avanti Polar Lipids
PE O-O-49:17	+K	C54H78NO6PK	906.52	906.52	2.5	0.672	0.002	304.9	0.9	0.3%	9	Lipid	Analytical Standard	Avanti Polar Lipids
PE O-48:16	+K	C53H76NO7PK	908.50	908.49	-7.6	0.675	0.002	303.5	0.9	0.3%	9	Lipid	Analytical Standard	Avanti Polar Lipids
PE O-O-49:15	+K	C54H82NO6PK	910.52	910.52	7.0	0.672	0.001	304.9	0.6	0.2%	9	Lipid	Analytical Standard	Avanti Polar Lipids
PE O-49:17	+K	C54H76NO7PK	920.50	920.50	-2.6	0.670	0.002	306.1	1.0	0.3%	8	Lipid	Analytical Standard	Avanti Polar Lipids
PE O-49:16	+K	C54H78NO7PK	922.52	922.52	1.4	0.682	0.002	300.6	1.1	0.4%	9	Lipid	Analytical Standard	Avanti Polar Lipids
PE O-49:15	+K	C54H80NO7PK	924.53	924.53	-6.4	0.673	0.003	304.7	1.2	0.4%	12	Lipid	Analytical Standard	Avanti Polar Lipids
PE O-49:14	+K	C54H82NO7PK	926.55	926.55	-1.6	0.665	0.002	308.1	1.0	0.3%	10	Lipid	Analytical Standard	Avanti Polar Lipids
PE O-50:17	+K	C55H78NO7PK	934.52	934.51	-6.6	0.658	0.002	311.2	1.0	0.3%	9	Lipid	Analytical Standard	Avanti Polar Lipids
PE O-51:16	+K	C56H82NO7PK	950.55	950.54	-9.4	0.659	0.002	311.0	0.7	0.2%	11	Lipid	Analytical Standard	Avanti Polar Lipids
PE (1008.51)	--	--	1008.51	1008.51	--	0.637	0.002	321.2	0.8	0.3%	11	Lipid	Analytical Standard	Avanti Polar Lipids
PE O-O-62:19	+K	C67H100NO6PK	1084.69	1084.69	0.0	0.600	0.001	340.5	0.8	0.2%	10	Lipid	Analytical Standard	Avanti Polar Lipids
PE O-O-62:18	+K	C67H102NO6PK	1086.71	1086.71	0.7	0.598	0.001	341.8	0.7	0.2%	10	Lipid	Analytical Standard	Avanti Polar Lipids
PE O-O-64:19	+K	C69H104NO6PK	1112.72	1112.72	1.0	0.589	0.002	347.3	1.1	0.3%	10	Lipid	Analytical Standard	Avanti Polar Lipids
PE O-O-66:21	+K	C71H104NO6PK	1136.72	1136.73	3.5	0.586	0.001	348.9	0.7	0.2%	10	Lipid	Analytical Standard	Avanti Polar Lipids
PE Dimer 36:05+36:04	+Na	C82H146N2O16P2Na	1500.00	1500.00	-3.4	0.481	0.001	423.9	0.8	0.2%	10	Lipid	Analytical Standard	Avanti Polar Lipids
PE Dimer 36:04	+Na	C82H148N2O16P2Na	1502.02	1502.02	-1.0	0.477	0.001	426.9	0.8	0.2%	10	Lipid	Analytical Standard	Avanti Polar Lipids
PE Dimer 36:05+38:05	+Na	C84H148N2O16P2Na	1526.02	1526.02	2.7	0.474	0.001	429.9	0.7	0.2%	10	Lipid	Analytical Standard	Avanti Polar Lipids
PE Dimer 36:05+38:04	+Na	C85H154N2O15P2Na	1528.04	1528.04	2.9	0.473	0.001	430.3	0.6	0.1%	10	Lipid	Analytical Standard	Avanti Polar Lipids
PE Dimer 38:06	+Na	C86H148N2O16P2Na	1550.02	1550.03	6.8	0.472	0.001	431.8	0.9	0.2%	10	Lipid	Analytical Standard	Avanti Polar Lipids
PE Dimer 38:06+38:05	+Na	C86H150N2O16P2Na	1552.04	1552.04	4.1	0.470	0.001	433.5	0.6	0.1%	10	Lipid	Analytical Standard	Avanti Polar Lipids

PE Dimer 39:06	+Na	C88H152N2O16P2Na	1578.05	1578.06	3.0	0.460	0.000	443.1	0.3	0.1%	8	Lipid	Analytical Standard	Avanti Polar Lipids
PE Dimer 40:07	+Na	C90H152N2O16P2Na	1602.05	1602.05	1.4	0.460	0.001	442.8	0.8	0.2%	8	Lipid	Analytical Standard	Avanti Polar Lipids
PS O-O-36:03	+Na	C42H80NO8PNa	780.55	780.55	1.4	0.707	0.002	290.6	0.6	0.2%	11	Lipid	Analytical Standard	Avanti Polar Lipids
PS O-O-36:02	+Na	C42H82NO8PNa	782.57	782.57	0.7	0.703	0.002	292.2	0.7	0.3%	10	Lipid	Analytical Standard	Avanti Polar Lipids
PS O-O-36:05	+Na	C42H72NO10PNa	804.52	804.52	2.6	0.708	0.002	290.2	0.9	0.3%	10	Lipid	Analytical Standard	Avanti Polar Lipids
PS 36:04	+Na	C42H74NO10PNa	806.49	806.50	1.8	0.713	0.003	287.8	1.0	0.4%	13	Lipid	Analytical Standard	Avanti Polar Lipids
PS 37:04	+Na	C43H76NO10PNa	820.51	820.51	3.6	0.696	0.002	295.0	1.0	0.3%	11	Lipid	Analytical Standard	Avanti Polar Lipids
PS 38:07	+Na	C44H72NO10PNa	828.48	828.48	-3.3	0.707	0.001	290.2	0.4	0.1%	11	Lipid	Analytical Standard	Avanti Polar Lipids
PS 38:06	+Na	C44H76NO10PNa	832.51	832.51	1.0	0.698	0.001	294.0	0.6	0.2%	10	Lipid	Analytical Standard	Avanti Polar Lipids
PS 38:05	+Na	C44H78NO10PNa	834.53	834.53	1.2	0.698	0.002	294.2	0.8	0.3%	12	Lipid	Analytical Standard	Avanti Polar Lipids
PS 37:02	+K	C43H80NO10PK	840.52	840.51	-3.6	0.700	0.002	293.0	0.9	0.3%	10	Lipid	Analytical Standard	Avanti Polar Lipids
PS 39:07	+Na	C45H74NO10PNa	842.49	842.50	1.5	0.700	0.002	293.1	1.0	0.3%	11	Lipid	Analytical Standard	Avanti Polar Lipids
PS 39:06	+Na	C45H78NO10PNa	846.53	846.52	-2.0	0.689	0.002	297.7	1.0	0.3%	9	Lipid	Analytical Standard	Avanti Polar Lipids
PS 39:05	+Na	C45H80NO10PNa	848.54	848.54	-0.9	0.677	0.002	303.3	0.9	0.3%	11	Lipid	Analytical Standard	Avanti Polar Lipids
PE 38:04	+K	C44H78NO10PK	850.50	850.50	2.0	0.683	0.002	300.5	1.0	0.3%	11	Lipid	Analytical Standard	Avanti Polar Lipids
PS O-O-41:10	+K	C47H76NO8PK	852.49	852.49	-2.6	0.692	0.002	296.6	0.6	0.2%	7	Lipid	Analytical Standard	Avanti Polar Lipids
PS 40:08	+Na	C46H74NO10PNa	854.49	854.49	-0.7	0.699	0.002	293.6	0.8	0.3%	11	Lipid	Analytical Standard	Avanti Polar Lipids
PS 40:07	+Na	C46H76NO10PNa	856.51	856.51	0.4	0.694	0.001	295.6	0.6	0.2%	10	Lipid	Analytical Standard	Avanti Polar Lipids
PS 40:06	+Na	C46H80NO10PNa	860.54	860.54	-1.9	0.684	0.002	299.9	0.9	0.3%	10	Lipid	Analytical Standard	Avanti Polar Lipids
PS 40:05	+Na	C46H82NO10PNa	862.56	862.56	-1.7	0.679	0.002	302.2	0.8	0.3%	10	Lipid	Analytical Standard	Avanti Polar Lipids
PS 41:07	+Na	C47H78NO10PNa	870.53	870.52	-3.0	0.686	0.002	299.2	0.9	0.3%	11	Lipid	Analytical Standard	Avanti Polar Lipids
PS O-O-44:13	+Na	C50H76NO8PNa	872.52	872.51	-16.7	0.687	0.002	298.4	1.0	0.3%	8	Lipid	Analytical Standard	Avanti Polar Lipids
PS 41:06	+Na	C47H80NO10PNa	872.54	872.54	-4.7	0.676	0.002	303.3	1.1	0.4%	11	Lipid	Analytical Standard	Avanti Polar Lipids
PS 42:12	+Na	C48H70NO10PNa	874.46	874.46	0.5	0.698	0.003	293.7	1.1	0.4%	10	Lipid	Analytical Standard	Avanti Polar Lipids
PS 42:11	+Na	C48H72NO10PNa	876.48	876.48	0.1	0.697	0.002	294.2	0.7	0.2%	10	Lipid	Analytical Standard	Avanti Polar Lipids
PS 42:10	+Na	C48H74NO10PNa	878.49	878.49	-1.3	0.690	0.001	297.1	0.6	0.2%	10	Lipid	Analytical Standard	Avanti Polar Lipids
PS 42:09	+Na	C48H76NO10PNa	880.51	880.51	1.2	0.679	0.002	302.0	0.7	0.2%	10	Lipid	Analytical Standard	Avanti Polar Lipids
PS 42:08	+Na	C48H78NO10PNa	882.53	882.53	-0.7	0.681	0.002	301.3	0.9	0.3%	12	Lipid	Analytical Standard	Avanti Polar Lipids
PS 42:07	+Na	C48H80NO10PNa	884.54	884.54	-0.3	0.673	0.001	304.7	0.6	0.2%	10	Lipid	Analytical Standard	Avanti Polar Lipids
PS 42:05	+Na	C48H84NO10PNa	888.57	888.57	-2.6	0.668	0.001	307.0	0.6	0.2%	10	Lipid	Analytical Standard	Avanti Polar Lipids
PS 43:09	+Na	C49H78NO10PNa	894.53	894.52	-3.3	0.676	0.002	303.2	1.0	0.3%	10	Lipid	Analytical Standard	Avanti Polar Lipids
PS 43:08	+Na	C49H80NO10PNa	896.54	896.53	-9.1	0.672	0.001	305.2	0.6	0.2%	10	Lipid	Analytical Standard	Avanti Polar Lipids
PS 44:13	+Na	C50H72NO10PNa	900.48	900.48	6.0	0.695	0.002	294.9	0.8	0.3%	8	Lipid	Analytical Standard	Avanti Polar Lipids
PS 44:12	+Na	C50H74NO10PNa	902.49	902.50	0.9	0.684	0.001	299.7	0.5	0.2%	10	Lipid	Analytical Standard	Avanti Polar Lipids

PS 44:11	+Na	C50H76NO10PNa	904.51	904.51	-2.2	0.679	0.001	302.1	0.6	0.2%	10	Lipid	Analytical Standard	Avanti Polar Lipids
PS 44:10	+Na	C50H78NO10PNa	906.53	906.52	-1.3	0.675	0.001	303.5	0.6	0.2%	10	Lipid	Analytical Standard	Avanti Polar Lipids
PS 44:09	+Na	C50H80NO10PNa	908.54	908.54	-5.0	0.675	0.002	303.7	0.7	0.2%	10	Lipid	Analytical Standard	Avanti Polar Lipids
PS 44:08	+Na	C50H82NO10PNa	910.56	910.56	3.5	0.668	0.001	306.8	0.5	0.2%	10	Lipid	Analytical Standard	Avanti Polar Lipids
PS 45:15	+K	C49H80NO10PK	912.52	912.51	-9.8	0.683	0.002	300.2	0.9	0.3%	8	Lipid	Analytical Standard	Avanti Polar Lipids
PS 44:07	+Na	C50H84NO10PNa	912.57	912.58	3.7	0.657	0.002	311.8	1.0	0.3%	13	Lipid	Analytical Standard	Avanti Polar Lipids
PS 45:14	+K	C50H70NO10PK	914.47	914.47	-3.1	0.677	0.002	302.6	1.0	0.3%	11	Lipid	Analytical Standard	Avanti Polar Lipids
PS 43:07	+K	C49H82NO10PK	914.53	914.53	-3.4	0.675	0.002	303.6	0.7	0.2%	8	Lipid	Analytical Standard	Avanti Polar Lipids
PS 44:05	+Na	C50H88NO10PNa	916.60	916.62	15.5	0.658	0.002	311.5	0.8	0.3%	10	Lipid	Analytical Standard	Avanti Polar Lipids
PS O-45:12	+K	C51H78NO9PK	918.51	918.51	5.2	0.674	0.001	304.0	0.6	0.2%	10	Lipid	Analytical Standard	Avanti Polar Lipids
PS 44:09	+K	C50H80NO10PK	924.52	924.52	0.3	0.667	0.002	307.0	0.7	0.2%	10	Lipid	Analytical Standard	Avanti Polar Lipids
PS 46:12	+Na	C52H78NO10PNa	930.53	930.53	1.2	0.662	0.002	309.5	0.8	0.3%	10	Lipid	Analytical Standard	Avanti Polar Lipids
PS 46:11	+Na	C52H80NO10PNa	932.54	932.54	3.3	0.666	0.002	307.7	0.8	0.3%	10	Lipid	Analytical Standard	Avanti Polar Lipids
PS 46:10	+Na	C52H82NO10PNa	934.56	934.56	3.9	0.663	0.002	309.2	0.8	0.3%	11	Lipid	Analytical Standard	Avanti Polar Lipids
PS 45:10	+K	C51H80NO10PK	936.52	936.52	0.9	0.654	0.002	313.2	0.9	0.3%	10	Lipid	Analytical Standard	Avanti Polar Lipids
PS 45:09	+K	C51H82NO10PK	938.53	938.53	-2.8	0.659	0.002	310.6	1.1	0.4%	12	Lipid	Analytical Standard	Avanti Polar Lipids
PS 46:08	+Na	C52H86NO10PNa	938.59	938.60	15.1	0.654	0.002	313.2	0.8	0.2%	8	Lipid	Analytical Standard	Avanti Polar Lipids
PS O-47:14	+K	C53H78NO9PK	942.51	942.51	4.7	0.670	0.002	305.9	0.7	0.2%	11	Lipid	Analytical Standard	Avanti Polar Lipids
PS O-47:13	+K	C53H80NO9PK	944.52	944.52	-3.4	0.665	0.002	308.1	1.0	0.3%	12	Lipid	Analytical Standard	Avanti Polar Lipids
PS O-47:12	+K	C53H82NO9PK	946.54	946.53	-10.5	0.662	0.002	309.2	1.0	0.3%	11	Lipid	Analytical Standard	Avanti Polar Lipids
PS 46:10	+K	C52H82NO10PK	950.53	950.52	-12.7	0.669	0.002	306.3	1.0	0.3%	12	Lipid	Analytical Standard	Avanti Polar Lipids
PS 48:15	+Na	C54H76NO10PNa	952.51	952.52	13.5	0.666	0.002	307.8	0.8	0.3%	10	Lipid	Analytical Standard	Avanti Polar Lipids
PS 48:14	+Na	C54H78NO10PNa	954.53	954.53	1.2	0.657	0.002	312.0	0.8	0.3%	10	Lipid	Analytical Standard	Avanti Polar Lipids
PS 49:18	+Na	C55H72NO10PNa	960.48	960.47	-12.7	0.665	0.001	307.7	0.5	0.2%	8	Lipid	Analytical Standard	Avanti Polar Lipids
PS 47:12	+K	C53H80NO10PK	960.52	960.52	0.6	0.665	0.002	307.8	0.8	0.3%	11	Lipid	Analytical Standard	Avanti Polar Lipids
PS 47:11	+K	C53H82NO10PK	962.53	962.53	-5.7	0.659	0.000	311.0	0.2	0.1%	9	Lipid	Analytical Standard	Avanti Polar Lipids
PS 49:16	+Na	C55H76NO10PNa	964.51	964.50	-6.8	0.661	0.001	309.6	0.7	0.2%	7	Lipid	Analytical Standard	Avanti Polar Lipids
PS O-50:16	+Na	C56H80NO9PNa	964.55	964.54	-4.6	0.655	0.001	312.4	0.6	0.2%	11	Lipid	Analytical Standard	Avanti Polar Lipids
PS 49:15	+Na	C55H78NO10PNa	966.53	966.52	-3.4	0.656	0.000	312.3	1.2	0.4%	12	Lipid	Analytical Standard	Avanti Polar Lipids
PS 49:14	+Na	C55H80NO10PNa	968.54	968.54	-0.2	0.651	0.002	314.6	0.8	0.3%	10	Lipid	Analytical Standard	Avanti Polar Lipids
PS 48:14	+K	C54H78NO10PK	970.50	970.50	2.6	0.658	0.001	311.0	0.6	0.2%	10	Lipid	Analytical Standard	Avanti Polar Lipids
PS 48:13	+K	C54H80NO10PK	972.52	972.52	2.4	0.654	0.002	313.0	0.9	0.3%	10	Lipid	Analytical Standard	Avanti Polar Lipids
PS 48:12	+K	C54H82NO10PK	974.53	974.53	0.9	0.653	0.002	313.6	0.9	0.3%	10	Lipid	Analytical Standard	Avanti Polar Lipids
PS 51:16	+Na	C57H80NO10PNa	992.54	992.54	-1.0	0.645	0.002	317.3	0.8	0.3%	10	Lipid	Analytical Standard	Avanti Polar Lipids

PS 51:15	+Na	C57H82NO10PNa	994.56	994.56	-2.4	0.634	0.001	322.8	0.8	0.2%	10	Lipid	Analytical Standard	Avanti Polar Lipids
PS 52:19	+Na	C58H76NO10PNa	1000.51	1000.51	2.7	0.646	0.002	316.7	0.9	0.3%	10	Lipid	Analytical Standard	Avanti Polar Lipids
PS 52:18	+Na	C58H78NO10PNa	1002.53	1002.53	3.6	0.641	0.001	319.1	0.7	0.2%	10	Lipid	Analytical Standard	Avanti Polar Lipids
PS 52:17	+Na	C58H80NO10PNa	1004.54	1004.54	1.8	0.637	0.001	321.4	0.6	0.2%	10	Lipid	Analytical Standard	Avanti Polar Lipids
PS 52:16	+Na	C58H82NO10PNa	1006.56	1006.57	9.3	0.635	0.001	322.2	0.4	0.1%	7	Lipid	Analytical Standard	Avanti Polar Lipids
PS O-51:10	+K	C56H90NO10PK	1006.63	1006.63	3.6	0.635	0.002	322.4	0.8	0.3%	9	Lipid	Analytical Standard	Avanti Polar Lipids
PS 51:13	+K	C57H86NO10PK	1014.56	1014.55	-15.8	0.626	0.002	326.8	1.0	0.3%	8	Lipid	Analytical Standard	Avanti Polar Lipids
PS 51:12	+K	C57H88NO10PK	1016.58	1016.56	-18.3	0.637	0.001	321.1	0.5	0.2%	8	Lipid	Analytical Standard	Avanti Polar Lipids
PS 53:17	+Na	C57H90NO10PK	1018.56	1018.56	-1.9	0.633	0.001	323.3	0.5	0.2%	7	Lipid	Analytical Standard	Avanti Polar Lipids
PS 55:18	+Na	C61H84NO10PNa	1044.57	1044.57	-0.3	0.621	0.002	329.3	0.9	0.3%	7	Lipid	Analytical Standard	Avanti Polar Lipids
SM 34:01	+Na	C39H79N2O6PNa	725.56	725.56	-2.6	0.722	0.001	285.1	0.4	0.1%	10	Lipid	Analytical Standard	Avanti Polar Lipids
SM O-36:03	+Na	C41H81N2O5PNa	735.58	735.57	-5.5	0.708	0.001	290.4	0.6	0.2%	11	Lipid	Analytical Standard	Avanti Polar Lipids
SM 35:01	+Na	C40H81N2O6PNa	739.57	739.57	-4.1	0.711	0.002	289.1	0.8	0.3%	11	Lipid	Analytical Standard	Avanti Polar Lipids
SM 36:02	+Na	C41H81N2O6PNa	751.57	751.57	-0.5	0.707	0.001	290.9	0.2	0.1%	11	Lipid	Analytical Standard	Avanti Polar Lipids
SM 36:01	+Na	C41H83N2O6PNa	753.59	753.59	3.4	0.703	0.001	292.4	0.2	0.1%	11	Lipid	Analytical Standard	Avanti Polar Lipids
SM 37:01	+Na	C42H85N2O6PNa	767.60	767.60	-3.5	0.697	0.001	294.8	0.6	0.2%	11	Lipid	Analytical Standard	Avanti Polar Lipids
SM O-38:00	+Na	C43H91N2O5PNa	769.66	769.66	-1.6	0.676	0.002	303.9	1.0	0.3%	11	Lipid	Analytical Standard	Avanti Polar Lipids
SM 771.07	--	--	771.67	771.67	-5.0	0.672	0.002	305.6	0.9	0.3%	10	Lipid	Analytical Standard	Avanti Polar Lipids
SM 38:01	+Na	C43H87N2O6PNa	781.62	781.62	-1.2	0.688	0.001	298.5	0.4	0.1%	10	Lipid	Analytical Standard	Avanti Polar Lipids
SM 39:01	+Na	C44H89N2O6PNa	795.64	795.63	-3.6	0.681	0.002	301.6	0.7	0.2%	11	Lipid	Analytical Standard	Avanti Polar Lipids
SM O-40:00	+Na	C45H95N2O5PNa	797.69	797.69	-0.6	0.670	0.002	306.7	0.7	0.2%	9	Lipid	Analytical Standard	Avanti Polar Lipids
SM 40:03	+Na	C45H87N2O6PNa	805.62	805.62	-0.5	0.685	0.002	299.9	0.9	0.3%	11	Lipid	Analytical Standard	Avanti Polar Lipids
SM 40:02	+Na	C45H89N2O6PNa	807.64	807.63	-1.7	0.681	0.001	301.7	0.3	0.1%	11	Lipid	Analytical Standard	Avanti Polar Lipids
SM 40:01	+Na	C45H91N2O6PNa	809.65	809.65	-2.7	0.676	0.001	303.9	0.5	0.2%	11	Lipid	Analytical Standard	Avanti Polar Lipids
SM 40:00	+Na	C45H93N2O5PK	811.67	811.66	-5.7	0.672	0.001	305.7	0.5	0.1%	10	Lipid	Analytical Standard	Avanti Polar Lipids
SM O-42:04	+Na	C47H91N2O5PNa	817.66	817.65	-3.5	0.659	0.001	311.3	0.5	0.2%	9	Lipid	Analytical Standard	Avanti Polar Lipids
SM 41:02	+Na	C46H91N2O6PNa	821.65	821.65	-2.2	0.675	0.001	303.9	0.5	0.2%	11	Lipid	Analytical Standard	Avanti Polar Lipids
SM 41:01	+Na	C46H93N2O6PNa	823.67	823.66	-3.4	0.670	0.001	306.3	0.3	0.1%	9	Lipid	Analytical Standard	Avanti Polar Lipids
SM 42:03	+Na	C47H91N2O6PNa	833.65	833.65	-2.2	0.672	0.001	305.6	0.4	0.1%	11	Lipid	Analytical Standard	Avanti Polar Lipids
SM 42:02	+Na	C47H93N2O6PNa	835.67	835.67	3.2	0.666	0.001	308.2	0.2	0.1%	10	Lipid	Analytical Standard	Avanti Polar Lipids
SM 42:01	+Na	C47H95N2O6PNa	837.68	837.68	-3.4	0.663	0.001	309.3	0.3	0.1%	9	Lipid	Analytical Standard	Avanti Polar Lipids
SM 43:03	+Na	C48H93N2O6PNa	847.67	847.66	-5.0	0.663	0.001	309.6	0.3	0.1%	10	Lipid	Analytical Standard	Avanti Polar Lipids
SM 43:02	+Na	C48H95N2O6PNa	849.68	849.68	-2.6	0.659	0.001	311.5	0.3	0.1%	8	Lipid	Analytical Standard	Avanti Polar Lipids
SM 43:01	+Na	C48H97N2O6PNa	851.70	851.69	-12.6	0.657	0.001	312.5	0.4	0.1%	9	Lipid	Analytical Standard	Avanti Polar Lipids

SM O-43:01	+K	C48H99N2O5PK	853.69	853.68	-15.7	0.645	0.001	318.0	0.7	0.2%	9	Lipid	Analytical Standard	Avanti Polar Lipids
SM 44:03	+Na	C49H95N2O6PNa	861.68	861.68	-4.4	0.657	0.001	312.0	0.5	0.2%	8	Lipid	Analytical Standard	Avanti Polar Lipids
SM 44:02	+Na	C49H97N2O6PNa	863.70	863.70	-2.2	0.654	0.001	313.5	0.4	0.1%	10	Lipid	Analytical Standard	Avanti Polar Lipids
SM 44:01	+Na	C49H99N2O6PNa	865.71	865.71	-7.2	0.651	0.001	315.1	0.3	0.1%	9	Lipid	Analytical Standard	Avanti Polar Lipids
SM dimer 35:01	+Na	C80H162N4O12P2Na	1456.16	1456.17	6.6	0.459	0.001	444.2	0.8	0.2%	4	Lipid	Analytical Standard	Avanti Polar Lipids
SM dimer 36:01+36:02	+Na	C82H164N4O12P2Na	1482.17	1482.18	5.3	0.457	0.000	445.6	0.3	0.1%	4	Lipid	Analytical Standard	Avanti Polar Lipids
SM dimer 36:01	+Na	C82H166N4O12P2Na	1484.19	1484.20	9.3	0.465	0.000	438.1	0.1	0.0%	4	Lipid	Analytical Standard	Avanti Polar Lipids
SM dimer 37:01	+Na	C84H170N4O12P2Na	1512.22	1512.23	8.2	0.458	0.000	444.8	0.3	0.1%	4	Lipid	Analytical Standard	Avanti Polar Lipids
SM dimer 38:01+38:02	+Na	C86H172N4O12P2Na	1538.23	1538.25	8.5	0.469	0.000	433.9	0.3	0.1%	4	Lipid	Analytical Standard	Avanti Polar Lipids
SM dimer 38:01	+Na	C86H174N4O12P2Na	1540.25	1540.26	8.3	0.464	0.000	439.4	0.1	0.0%	4	Lipid	Analytical Standard	Avanti Polar Lipids
SM dimer 38:01+39:02	+Na	C87H174N4O12P2Na	1552.25	1552.26	9.4	0.441	0.001	461.7	0.8	0.2%	4	Lipid	Analytical Standard	Avanti Polar Lipids
SM dimer 38:01+39:01	+Na	C87H176N4O12P2Na	1554.27	1554.28	7.9	0.452	0.000	450.2	0.3	0.1%	4	Lipid	Analytical Standard	Avanti Polar Lipids
SM dimer 39:02	+Na	C88H174N4O12P2Na	1564.25	1564.27	13.2	0.464	0.001	438.5	0.6	0.1%	4	Lipid	Analytical Standard	Avanti Polar Lipids
SM dimer 39:01 + 39:02	+Na	C88H176N4O12P2Na	1566.27	1566.28	10.2	0.451	0.000	451.5	0.2	0.1%	4	Lipid	Analytical Standard	Avanti Polar Lipids

Table D.5: CCS Values Measured in Both Helium and Nitrogen Drift Gas

Quaternary Ammonium Salts (N=8) - (Refer to Table 2 in Manuscript)						
Analyte	Exact m/z	Nitrogen CCS (This Work) [\AA^2]	Helium CCS (Literature) [\AA^2]	Difference in CCS [\AA^2]	Absolute Difference [%]	Literature Reference for Helium CCS Values
Carbohydrates (N=24)						
Lactose + Na	342.30	178.1	121.1	57.0	38%	1
Maltotetraose + Na	689.21	235.3	159.0	76.3	39%	1
Lacto-N-fucopentaose I + Li	860.32	269.6	203.1	66.5	28%	1
Lacto-N-fucopentaose I + Na	876.30	276.1	204.4	71.7	30%	1
Lacto-N-fucopentaose II + Na	876.30	271.1	201.3	69.8	30%	1
Lacto-N-fucopentaose I + K	892.27	274.7	205.0	69.7	29%	1
Lacto-N-fucopentaose II + K	892.27	267.2	202.6	64.6	28%	1
Lacto-N-fucopentaose I + Rb	938.22	275.2	198.4	76.8	32%	1
Lacto-N-fucopentaose II + Rb	938.22	278.4	197.5	80.9	34%	1
Lacto-N-fucopentaose I + Cs	986.21	275.6	204.0	71.6	30%	1
α -cyclodextrin + Na	995.31	285.5	200.7	84.8	35%	1
Lacto-N-difucohexaose I + Li	1006.38	301.4	225.9	75.5	29%	5
Maltohexaose + Na	1013.32	286.4	206.0	80.4	33%	1
Lacto-N-difucohexaose I + Na	1022.35	290.6	225.6	65.0	25%	1
Lacto-N-difucohexaose I + Na	1022.35	304.2	225.6	78.6	30%	1
Lacto-N-difucohexaose II + Na	1022.35	291.2	220.6	70.6	28%	1
Lacto-N-difucohexaose II + Na	1022.35	306.3	220.6	85.7	33%	1
Lacto-N-difucohexaose I + K	1038.33	303.5	229.8	73.8	28%	5
Lacto-N-difucohexaose II + K	1038.33	305.8	225.3	80.5	30%	5
Lacto-N-difucohexaose I + Rb	1084.28	303.2	230.0	73.2	27%	5
Lacto-N-difucohexaose I + Cs	1132.27	301.2	232.3	68.9	26%	5
β -cyclodextrin + Na	1157.36	319.7	231.4	88.3	32%	1

Maltoheptaose + Na	1175.37	303.1	236.4	66.7	25%	5
Maltoheptaose + K	1191.34	303.4	236.7	66.7	25%	5
Tryptic Peptides (N=39)						
YVR + H	437.3	207.0	140.2	66.8	38%	2
GVFR + H	478.3	214.8	146.8	68.1	38%	2
SDGRG + H	491.2	204.6	130.0	74.6	45%	3
GRGDS + H	491.2	205.9	132.0	73.9	44%	3
VYAR + H	508.3	217.1	157.1	60.1	32%	2
ADLAK + H	517.3	228.3	159.3	69.0	36%	2
WMGK + H	521.3	220.1	152.9	67.2	36%	2
FWGK + H	537.3	231.0	160.5	70.5	36%	2
VASLR + H	545.3	232.5	163.7	68.8	35%	2
AFDEK + H	609.3	238.3	168.4	69.9	34%	2
GQIVGR + H	629.4	245.5	173.6	71.9	34%	2
IETMR + H	649.3	252.8	181.3	71.5	33%	2
AAGHDGK + H	655.3	249.0	170.2	78.8	38%	2
ANIDVK + H	659.4	248.1	176.8	71.3	34%	2
GVLHAVK + H	723.5	269.9	199.2	70.7	30%	2
SVYDSR + H	726.3	258.4	184.2	74.3	34%	2
NVPLYK + H	733.4	272.2	195.3	76.9	33%	2
IATAIEK + H	745.4	275.5	202.9	72.6	30%	2
LNQLLR + H	756.5	275.6	205.0	70.6	29%	2
HLADLSK + H	783.4	273.3	201.8	71.6	30%	2
LVTDLTK + H	789.5	276.6	205.8	70.8	29%	2
YDLDFK + H	800.4	272.4	201.0	71.4	30%	2
TFAEALR + H	807.4	283.5	210.0	73.5	30%	2
AADALLK + H	814.5	291.8	223.9	68.0	26%	2
DIVGAVLK + H	814.5	277.8	206.1	71.7	30%	2
ATEEQLK + H	818.4	281.3	206.4	74.9	31%	2

IGDYAGIK + H	836.5	285.9	210.4	75.5	30%	2
DIPVPPKPK + H	893.5	294.2	219.2	75.0	29%	2
AEFVEVTK + H	922.5	295.7	223.4	72.3	28%	2
YLYEJAR + H	927.5	305.0	228.0	76.9	29%	2
EALDFFAR + H	968.5	305.9	231.1	74.9	28%	2
LVVSTQTALA + H	1002.6	315.6	239.3	76.3	28%	2
ANELLINVK + H	1013.6	326.8	249.7	77.1	27%	2
GVIFYESHGK + H	1136.6	332.9	254.9	78.0	27%	2
IGSEVYHNLK + H	1159.6	348.4	269.7	78.7	25%	2
LVNELTEFAK + H	1163.6	344.4	267.5	76.9	25%	2
SISIVGSYVGNR + H	1251.7	349.1	267.8	81.3	26%	2
VNQIGTLESSEIK + H	1288.7	358.7	278.8	80.0	25%	2
Lipids (N=49)						
PE 34:02 + Na	738.5	278.3	213.5	64.8	26%	1
PE 34:01 + Na	740.5	281.3	214.7	66.6	27%	1
SM (36:01) + Na	753.6	292.4	221.3	71.1	28%	1
PC 32:01 + Na [†]	754.5	283.6	217.6	66.0	26%	4
PC 32:00 + Na	756.6	286.5	217.4	69.1	27%	4
PE 36:04 + Na	762.5	280.6	214.4	66.2	27%	1
PE 36:02 + Na	766.5	285.7	220.9	64.8	26%	1
PE 35:02 + K [†]	768.6	282.5	221.7	60.8	24%	1
SM O-(38:00) + Na [†]	769.6	303.9	222.7	81.2	31%	1
PC 34:02 + Na	780.6	290.1	218.9	71.2	28%	1
SM (38:01) + Na	781.6	298.5	231.3	67.2	25%	1
PC 34:01 + Na	782.6	291.5	221.7	69.8	27%	1
PE 38:05 + Na	788.5	287.2	220.6	66.6	26%	1
PE 38:04 + Na	790.5	290.0	228.1	61.9	24%	1
SM O-(40:00) + Na [†]	797.6	306.7	227.9	78.8	29%	4
PC 34:01 + K	798.5	292.5	222.0	70.5	27%	4

PC 36:04 + Na	804.6	293.8	221.3	72.5	28%	4
PC 36:03 + Na [†]	806.6	294.5	220.6	73.9	29%	4
GlcCer 40:01 + Na	806.6	301.1	232.9	68.2	26%	1
PC 36:02 + Na	808.6	296.1	226.7	69.4	27%	1
GlcCer 40:00 + Na [†]	808.6	302.3	236.6	65.7	24%	1
SM (40:01) + Na [†]	809.7	303.9	225.4	78.5	30%	4
PC 36:01 + Na	810.6	297.7	228.1	69.6	26%	1
GlcCer 41:01 + Na [†]	820.6	302.5	236.2	66.3	25%	1
PC 36:03 + K	822.5	297.8	222.9	74.9	29%	4
GlcCer 40:01 h + Na	822.6	303.4	234.6	68.8	26%	1
PC 36:02 + K	824.6	299.9	226.2	73.7	28%	1
GlcCer 40:00 h + Na [†]	824.6	306.1	237.9	68.2	25%	1
PC 38:05 + Na	830.6	298.2	222.2	76.0	29%	1
PC 38:04 + Na	832.6	299.0	228.5	70.5	27%	1
GlcCer 42:02 + Na	832.7	305.2	238.8	66.4	24%	1
PS 38:05 + Na [†]	834.5	294.2	225.5	68.7	26%	1
GlcCer 42:01 + Na	834.7	307.5	239.3	68.2	25%	1
SM (42:02) + Na	835.7	308.2	239.4	68.8	25%	1
GlcCer 42:00 + Na [†]	836.7	308.2	240.2	68.0	25%	1
SM (42:01) + Na	837.7	309.3	239.3	70.0	26%	1
PS 37:02 + K [†]	840.6	293.0	222.6	70.4	27%	1
PC 38:06 + K	844.5	300.6	224.6	76.0	29%	4
GlcCer 43:02 + Na [†]	846.6	307.8	238.8	69.0	25%	1
PC 38:04 + K	848.6	301.5	230.0	71.5	27%	4
GlcCer 42:02 h + Na	848.7	309.0	240.3	68.7	25%	1
GlcCer 42:01 h + Na [†]	850.6	312.7	242.8	69.9	25%	4
SM O-(43:01) + K [†]	853.7	318.0	241.2	76.8	27%	4
GlcCer 44:02 + Na	860.7	315.3	245.9	69.4	25%	4
GlcCer 43:02 h + Na [†]	862.7	314.6	244.3	70.3	25%	4

GlcCer 43:01 h + Na [†]	864.6	313.7	245.2	68.5	25%	1
GlcCer 44:02 h + Na	876.7	318.4	246.7	71.7	25%	4
PS 42:09 + Na	880.5	302.0	238.0	64.0	24%	1
PS 42:08 + Na	882.5	301.3	230.8	70.5	26%	1

* Absolute difference is calculated as the difference between the two CCS values divided by their average value.

[†] Denotes lipid identifications which are different than originally reported in literature, due to the higher mass accuracy measurements obtained in this study.

References:

1. L.S. Fenn, M. Kliman, A. Mahsut, S. Zhao, J.A. McLean, *Analytical and Bioanalytical Chemistry* **2009**, 394, 235-244.
2. S.J. Valentine, A.E. Counterman, D.E. Clemmer, *Journal of the American Society for Mass Spectrometry* **1999**, 10, 1188-1211.
3. M.F. Bush, Z. Hall, K. Giles, J. Hoyes, C.V. Robinson, B.T. Ruotolo, *Analytical Chemistry* **2010**, 82(22), 9557-9565.
4. W.B. Ridenour, M. Kliman, J.A. McLean, R.M. Caprioli, *Analytical Chemistry* **2010**, 82(5), 1881-1889.
5. Unpublished values measured in helium on a uniform field IM-MS instrument (Vanderbilt drift tube). For instrumentation details, see: S. Sundarapandian, J.C. May, J.A. McLean, *Analytical Chemistry* **2010**, 82, 3247-3254.

D.4. Carbohydrate Abbreviations Not Previously Listed

Lacto-N-fucopentaose I	Fuc α 1-2Gal β 1-3GlcNAc β 1-3Gal β 1-4Glc
Lacto-N-fucopentaose II	Gal β 1-3[Fuc α 1-4]GlcNAc β 1-3Gal β 1-4Glc
Lacto-N-difucohexaose I	Fuc α 1-2Gal β 1-3[Fuc α 1-4]GlcNAc β 1-3Gal β 1-4Glc
Lacto-N-difucohexaose II	Gal β 1-3[Fuc α 1-4]GlcNAc β 1-3Gal β 1-4[Fuc α 1-3]Glc
α -cyclodextrin	cyclomaltohexaose
β -cyclodextrin	cyclomaltoheptaose

D.5. Carbohydrate Nomenclature

Hex – Hexose (Hexose assignments in the database are based on exact mass measurement.

The exact type of hexose is uncertain)

Fuc – Fucose (All pentose identifications are assigned as fucose in the database as this is the only pentose present in the samples)

HexNAc – N-acetylated hexosamine (the exact type of hexose is uncertain).

Gal – Galactose

Glc – Glucose

GlcNAc – N-acetylglucosamine

D.6. Lipid Nomenclature

Glycerophospholipids (ex. PC x:y):

PC, PE, PS = abbreviated names for phosphatidylcholine, phosphatidylethanolamine, phosphatidylserine respectively

x = total number of carbons in fatty acid chains

y = total number of double bonds in fatty acid chains

Sphingolipids (ex. SM x:y):

SM, GlcCer = abbreviated names for sphingomyelin and cerebroside respectively

x = total number of carbons in the amide linked fatty acid of the ceramide plus eighteen carbons from the sphingosine backbone

y = total number of double bonds, one trans double bond in the sphingosine backbone plus the number of double bonds in the amide linked fatty acid of the ceramide

Hydroxylation on Cerebrosides (ex. GlcCer x:y h):

h = denotes hydroxylation on the number two carbon (from the carbonyl) of the amide linked fatty acid

Alkyl Ether Linkage (ex. PS O-x:y):

x = total number of carbons in fatty acid chains

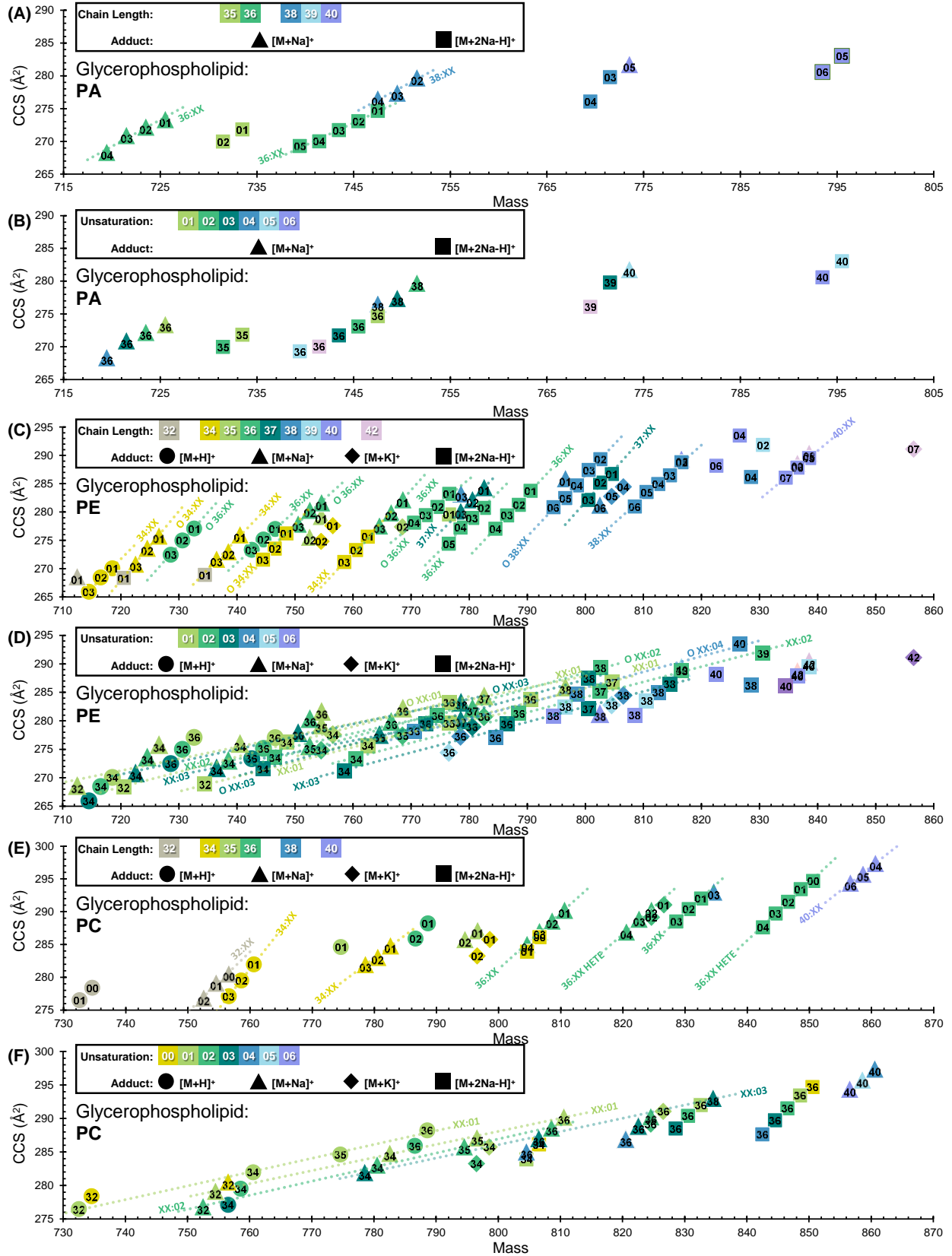
y = total number of double bonds in fatty acid chains

O = alkyl ether substituent

O-O = alkyl ether substituent occurs on both chains

APPENDIX E

SUPPORTING INFORMATION FOR CHAPTER V



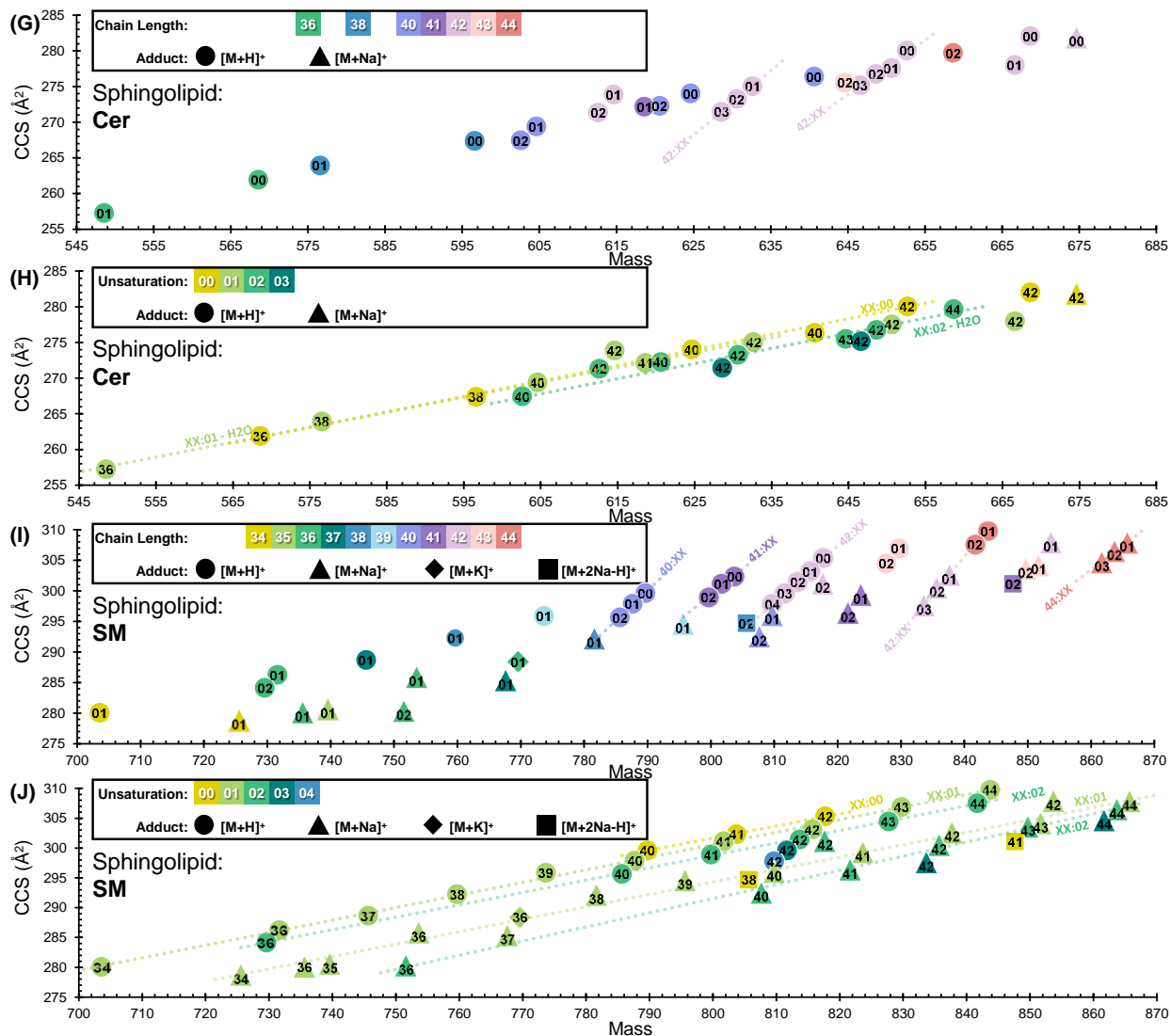


Figure E.1: Plots of quantitative correlations occurring within lipid classes. Colors correspond to either summed chain length or degree of unsaturation and shapes correspond to cation type, as specified in the legend. Numbers within the symbols correspond to either the degree of unsaturation, or the number of acyl chain carbons. Error bars are within the size of the markers. (A) Glycerophosphatidic acid (PA) chain length trends, and (B) PA trends in sites of unsaturation. (C) Glycerophosphoethanolamine (PE) chain length trends, and (D) PE trends in sites of unsaturation. (E) Glycerophosphotidylserine (PS) chain length trends, and (F) PS trends in sites of

unsaturation. (G) Ceramide (GlcCer) chain length trends, and (H) GlcCer trends in sites of unsaturation. (I) Sphingomyelin (SM) chain length trends, and (J) SM trends in sites of unsaturation.

Lipids in Trend Share Number of Carbons

(A)

	$Slope \left(\frac{\text{\AA}^2}{m/z} \right)$		R^2		Number	
	Avg	%RSD	Avg	Min	Trendlines	Points/line
PA	0.87	13%	0.992	0.980	3	4.0
PE	1.10	17%	0.988	0.953	17	3.4
PC	0.87	17%	0.993	0.981	8	3.4
PS	0.92	18%	0.978	0.897	12	4.6
SM	0.88	8%	0.989	0.968	5	3.4
GlcCer	0.93	18%	0.966	0.886	9	3.4
Cer	0.83	11%	0.979	0.958	2	3.5
Average	0.97	19%	0.962	0.962	56	3.7

Lipids in Trend Share Degree of Unsaturation

(B)

	$Slope \left(\frac{\text{\AA}^2}{m/z} \right)$		R^2		Number	
	Avg	%RSD	Avg	Min	Trendlines	Points/line
PA	-	-	-	-	0	-
PE	0.26	13%	0.991	0.957	12	3.8
PC	0.20	3%	0.998	0.996	4	3.8
PS	0.24	7%	0.984	0.941	10	4.1
SM	0.21	6%	0.995	0.990	5	7.2
GlcCer	0.21	6%	0.998	0.994	11	5.3
Cer	0.21	2%	0.996	0.990	3	4.3
Average	0.23	13%	0.992	0.941	44	4.7

Table E.1. Tables summarizing statistics for linear fits to CCS vs. mass data. (A) Statistics relating to lipids common in modification, adduct, and alkyl chain length, but differing in degree of unsaturation, arranged by head group. (B) Statistics relating to lipids common in modification, adduct, and degree of unsaturation, but differing in length of alkyl chains, arranged by head group.

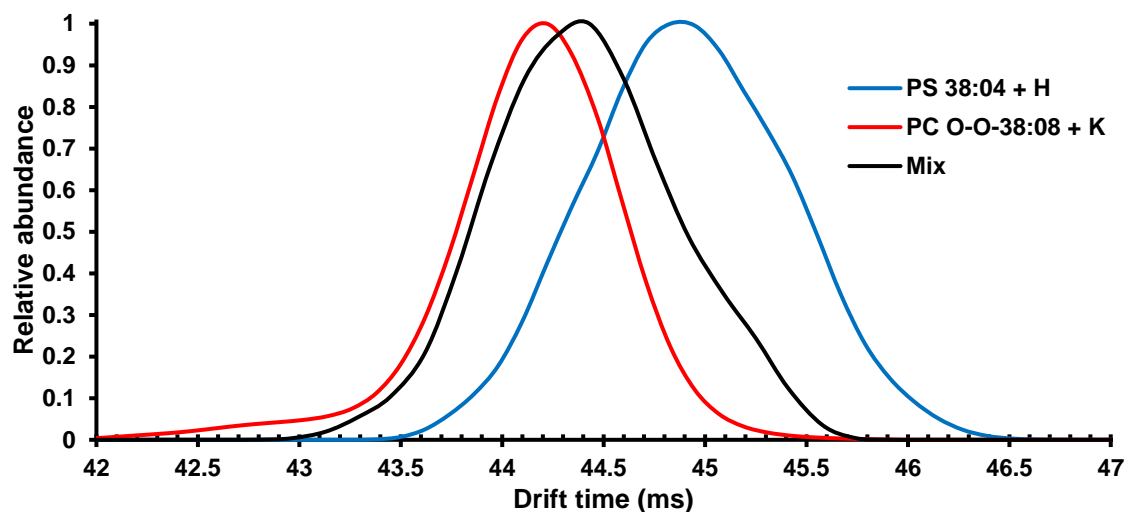


Figure E.2: Plot of individual drift times for lipid features found at 812.54 Da, with 99,980 ppm mass resolution needed for mass separation. PS 38:04 + H and PC 38:08 + K traces are obtained from the IM-MS analysis of individual standards, whereas the plot of mixed drift times was obtained from a mixture of the PS and PC standards. Though the mixed trace is broader than the individual traces, indicating the presence of multiple features, the limitations of IM-MS for lipid analysis are displayed here, as separation was not achieved in the mixture.

Table E.2: Collision Cross Section Data for All Lipids Investigated

ID	Mod	Cation	Molecular Formula	Exact m/z	Measured m/z	Mass Accuracy (ppm)	K0	K0 SD	CCS	CCS SD	RSD	N
PA 36:04	-	+Na	C39H69O8PNa	719.46	719.46	-2.43	0.728	0.001	268.4	0.4	0.1%	16
PA 36:03	-	+Na	C39H71O8PNa	721.48	721.48	0.79	0.722	0.001	271.0	0.4	0.1%	8
PA 36:02	-	+Na	C39H73O8PNa	723.49	723.49	-4.68	0.716	0.001	272.2	0.4	0.1%	16
PA 36:01	-	+Na	C39H75O8PNa	725.51	725.51	-0.53	0.711	0.000	273.4	0.2	0.1%	8
PA 38:04	-	+Na	C41H73O8PNa	747.49	747.50	2.93	0.702	0.002	276.5	0.6	0.2%	8
PA 38:03	-	+Na	C41H75O8PNa	749.51	749.51	-1.79	0.701	0.001	277.4	0.2	0.1%	8
PA 38:02	-	+Na	C41H77O8PNa	751.53	751.53	-0.33	0.694	0.001	279.7	0.5	0.2%	8
PA 40:05	-	+Na	C43H75O8PNa	773.51	773.51	-0.59	0.687	0.001	281.8	0.5	0.2%	8
PA 35:02	-	+2Na-H	C38H70O8PNa2	731.46	731.46	-0.73	0.725	0.001	270.0	0.4	0.1%	8
PA 35:01	-	+2Na-H	C38H72O8PNa2	733.48	733.48	0.09	0.719	0.001	271.8	0.5	0.2%	8
PA 36:05	-	+2Na-H	C39H66O8PNa2	739.43	739.42	-6.01	0.727	0.000	269.3	0.1	0.1%	8
PA 36:04	-	+2Na-H	C39H68O8PNa2	741.44	741.44	-5.45	0.725	0.001	270.0	0.6	0.2%	8
PA 36:03	-	+2Na-H	C39H70O8PNa2	743.46	743.46	-0.86	0.717	0.002	271.7	0.7	0.2%	16
PA 36:02	-	+2Na-H	C39H70O8PNa2	745.48	745.48	0.52	0.724	0.001	273.1	0.3	0.1%	16
PA 36:01	-	+2Na-H	C39H72O8PNa2	747.49	747.49	-3.48	0.720	0.001	274.7	0.4	0.2%	16
PA 38:04	-	+2Na-H	C41H72O8PNa2	769.48	769.47	-2.23	0.715	0.002	276.1	0.6	0.2%	16
PA 38:03	-	+2Na-H	C41H74O8PNa2	771.49	771.49	2.14	0.693	0.002	279.8	0.6	0.2%	8
PA 40:06	-	+2Na-H	C43H72O8PNa2	793.48	793.48	0.29	0.715	0.002	280.6	0.6	0.2%	8
PA 40:05	-	+2Na-H	C43H74O8PNa2	795.49	795.49	1.62	0.709	0.003	283.1	1.1	0.4%	8
PE 34:03	-	+H	C39H73NO8P	714.51	714.51	2.64	0.760	0.001	265.9	0.5	0.2%	8
PE 34:02	-	+H	C39H75NO8P	716.52	716.53	2.87	0.752	0.001	268.4	0.4	0.1%	8
PE 34:01	-	+H	C39H77NO8P	718.54	718.54	1.97	0.748	0.001	270.1	0.3	0.1%	8
PE 36:03	-	+H	C41H77NO8P	742.54	742.53	-5.67	0.739	0.001	273.3	0.4	0.2%	8
PE 36:02	-	+H	C41H79NO8P	744.55	744.55	0.87	0.734	0.001	275.1	0.4	0.1%	8
PE 36:01	-	+H	C41H81NO8P	746.57	746.57	-0.92	0.729	0.001	277.0	0.4	0.1%	8
PE 36:03	O	+H	C41H79NO7P	728.56	728.56	4.74	0.741	0.001	272.5	0.4	0.2%	8
PE 36:02	O	+H	C41H81NO7P	730.58	730.57	-3.54	0.734	0.001	275.0	0.3	0.1%	8

PE 36:01	O	+H	C41H83NO7P	732.59	732.59	-3.03	0.729	0.002	277.1	0.7	0.2%	8
PE 32:01	-	+Na	C37H72NO8PNa	712.49	712.49	0.75	0.752	0.001	268.6	0.4	0.2%	8
PE 34:03	-	+Na	C39H72NO8PNa	736.49	736.49	-2.39	0.729	0.002	271.7	0.6	0.1%	16
PE 34:02	-	+Na	C39H74NO8PNa	738.50	738.50	-0.47	0.726	0.001	273.1	0.3	0.1%	16
PE 34:01	-	+Na	C39H76NO8PNa	740.52	740.52	-0.86	0.717	0.001	276.0	0.3	0.1%	16
PE 35:02	-	+Na	C40H76NO8PNa	752.52	752.52	-4.43	0.705	0.001	275.6	0.3	0.1%	8
PE 35:01	-	+Na	C40H78NO8PNa	754.54	754.53	-5.13	0.695	0.001	279.3	0.3	0.1%	8
PE 36:03	-	+Na	C41H76NO8PNa	764.52	764.52	-2.58	0.699	0.001	277.6	0.3	0.1%	8
PE 36:02	-	+Na	C41H78NO8PNa	766.54	766.54	-0.68	0.707	0.001	279.9	0.3	0.1%	16
PE 36:01	-	+Na	C41H80NO8PNa	768.55	768.55	-3.44	0.687	0.001	282.2	0.3	0.1%	8
PE 37:03	-	+Na	C42H78NO8PNa	778.54	778.53	-5.06	0.692	0.001	280.2	0.3	0.1%	8
PE 37:02	-	+Na	C42H80NO8PNa	780.55	780.55	-2.66	0.687	0.001	282.2	0.4	0.2%	8
PE 37:01	-	+Na	C42H82NO8PNa	782.57	782.56	-3.73	0.682	0.001	284.3	0.4	0.1%	8
PE 38:01	-	+Na	C43H84NaO8P	796.58	796.58	-6.75	0.705	0.001	285.9	0.4	0.2%	8
PE 40:05	-	+Na	C45H80NO8PNa	816.55	816.55	-4.14	0.669	0.001	289.4	0.4	0.1%	8
PE 42:09	-	+Na	C47H76NO8PNa	836.52	836.52	-3.80	0.670	0.001	288.6	0.4	0.1%	8
PE 42:08	-	+Na	C47H78NO8PNa	838.54	838.53	-4.55	0.666	0.001	290.4	0.4	0.1%	8
PE 38:06	HETE	+Na	C43H74NO9PNa	802.50	802.50	-4.51	0.689	0.001	281.2	0.4	0.1%	8
PE 34:03	O	+Na	C39H74NO7PNa	722.51	722.51	-4.47	0.718	0.001	270.8	0.4	0.1%	8
PE 34:02	O	+Na	C39H76NO7PNa	724.53	724.52	-4.24	0.710	0.003	273.6	1.2	0.4%	8
PE 34:01	O	+Na	C39H78NaO7P	726.54	726.54	-2.76	0.732	0.001	275.8	0.5	0.2%	8
PE 36:03	O	+Na	C41H78NO7PNa	750.54	750.54	-2.54	0.712	0.001	277.9	0.3	0.1%	16
PE 36:02	O	+Na	C41H80NO7PNa	752.56	752.55	-3.18	0.706	0.001	280.4	0.4	0.2%	16
PE 36:01	O	+Na	C41H82NO7PNa	754.57	754.57	-4.91	0.716	0.001	281.7	0.4	0.1%	8
PE 38:03	O	+Na	C43H82NaO7P	778.57	778.57	-4.93	0.712	0.001	283.2	0.3	0.1%	8
PE 34:02	-	+K	C39H74KNO8P	754.48	754.48	-1.14	0.734	0.001	274.8	0.3	0.1%	8
PE 34:01	-	+K	C39H76KNO8P	756.49	756.49	-0.66	0.727	0.001	277.6	0.3	0.1%	8
PE 35:02	-	+K	C40H76NO8PK	768.49	768.49	-1.79	0.700	0.001	277.4	0.5	0.2%	8
PE 36:05	-	+K	C41H72KNO8P	776.46	776.46	-2.65	0.735	0.001	274.4	0.4	0.2%	8
PE 36:04	-	+K	C41H74KNO8P	778.48	778.48	-2.05	0.728	0.001	277.2	0.3	0.1%	8
PE 36:03	-	+K	C41H76KNO8P	780.49	780.49	0.22	0.723	0.001	278.9	0.4	0.1%	8

PE 36:02	-	+K	C41H78KNO8P	782.51	782.51	-2.25	0.718	0.001	280.7	0.3	0.1%	8
PE 38:05	-	+K	C43H76KNO8P	804.49	804.49	-1.44	0.713	0.001	282.8	0.4	0.1%	8
PE 38:04	-	+K	C43H78KNO8P	806.51	806.51	-4.46	0.709	0.001	284.4	0.3	0.1%	8
PE 42:07	-	+K	C47H80NO8PK	856.53	856.52	-7.47	0.692	0.001	291.1	0.5	0.2%	8
PE 32:01	-	+2Na-H	C37H71NO8PNa2	734.47	734.47	-2.42	0.723	0.002	268.9	0.6	0.2%	8
PE 34:03	-	+2Na-H	C39H71NO8PNa2	758.47	758.47	-2.03	0.717	0.001	271.2	0.5	0.2%	8
PE 34:02	-	+2Na-H	C39H73NO8PNa2	760.49	760.49	-0.40	0.725	0.001	273.3	0.3	0.1%	16
PE 34:01	-	+2Na-H	C39H75NO8PNa2	762.50	762.50	0.93	0.718	0.001	275.6	0.3	0.2%	16
PE 35:01	-	+2Na-H	C40H77NO8PNa2	776.52	776.52	-1.15	0.694	0.001	279.6	0.3	0.1%	8
PE 36:04	-	+2Na-H	C41H73NO8PNa2	784.49	784.49	0.00	0.714	0.001	277.1	0.4	0.1%	16
PE 36:03	-	+2Na-H	C41H75NO8PNa2	786.50	786.50	1.09	0.708	0.001	279.4	0.3	0.1%	16
PE 36:02	-	+2Na-H	C41H77NO8PNa2	788.52	788.52	0.72	0.703	0.001	281.3	0.3	0.1%	16
PE 36:01	-	+2Na-H	C41H79NO8PNa2	790.53	790.54	1.81	0.697	0.001	283.7	0.3	0.2%	16
PE 37:03	-	+2Na-H	C42H77NO8PNa2	800.52	800.52	2.92	0.687	0.001	282.1	0.5	0.2%	8
PE 37:02	-	+2Na-H	C42H79NO8PNa2	802.53	802.53	-3.62	0.679	0.000	285.2	0.2	0.1%	8
PE 37:01	-	+2Na-H	C42H81NO8PNa2	804.55	804.55	1.69	0.675	0.001	286.7	0.4	0.1%	8
PE 38:06	-	+2Na-H	C43H73NO8PNa2	808.49	808.49	-1.24	0.703	0.001	281.0	0.3	0.1%	16
PE 38:05	-	+2Na-H	C43H75NO8PNa2	810.50	810.50	-0.24	0.697	0.001	283.6	0.3	0.4%	16
PE 38:04	-	+2Na-H	C43H77NO8PNa2	812.52	812.52	1.01	0.693	0.001	285.0	0.3	0.1%	16
PE 38:03	-	+2Na-H	C43H79NO8PNa2	814.53	814.53	0.29	0.690	0.001	286.5	0.3	0.1%	16
PE 38:02	-	+2Na-H	C43H81NO8PNa2	816.55	816.55	-2.37	0.698	0.001	288.8	0.5	0.2%	8
PE 39:02	-	+2Na-H	C44H83NO8PNa2	830.57	830.56	-1.02	0.663	0.001	291.8	0.5	0.2%	8
PE 40:07	-	+2Na-H	C45H75NO8PNa2	834.50	834.50	-2.67	0.677	0.001	286.1	0.2	0.1%	8
PE 40:06	-	+2Na-H	C45H77NO8PNa2	836.52	836.51	-4.29	0.700	0.001	287.9	0.4	0.1%	8
PE 40:05	-	+2Na-H	C45H79NO8PNa2	838.53	838.53	-3.85	0.696	0.001	289.5	0.4	0.1%	8
PE 38:04	HETE	+2Na-H	C43H77NO9PNa2	828.51	828.51	-0.88	0.676	0.001	286.2	0.4	0.1%	8
PE 32:01	O	+2Na-H	C37H73NO7PNa2	720.49	720.49	-2.21	0.725	0.001	268.4	0.3	0.1%	8
PE 34:03	O	+2Na-H	C39H73NO7PNa2	744.49	744.49	-3.30	0.716	0.001	271.6	0.5	0.2%	8
PE 34:02	O	+2Na-H	C39H75NO7PNa2	746.51	746.50	-3.61	0.710	0.001	273.5	0.2	0.1%	8
PE 34:01	O	+2Na-H	C39H77NO7PNa2	748.52	748.52	-3.12	0.703	0.001	276.2	0.2	0.1%	8
PE 36:04	O	+2Na-H	C41H75NO7PNa2	770.51	770.51	0.70	0.698	0.001	278.1	0.4	0.1%	8

PE 36:03	O	+2Na-H	C41H77NO7PNa2	772.52	772.52	0.76	0.708	0.001	279.5	0.5	0.1%	16
PE 36:02	O	+2Na-H	C41H79NO7PNa2	774.54	774.54	-2.07	0.704	0.001	280.9	0.3	0.2%	16
PE 36:01	O	+2Na-H	C41H81NO7PNa2	776.55	776.55	-2.55	0.684	0.001	283.2	0.3	0.1%	8
PE 38:06	O	+2Na-H	C43H75NO7PNa2	794.51	794.51	-0.29	0.690	0.001	280.9	0.4	0.1%	8
PE 38:05	O	+2Na-H	C43H77NO7PNa2	796.52	796.52	-2.22	0.686	0.001	282.5	0.4	0.1%	8
PE 38:04	O	+2Na-H	C43H79NO7PNa2	798.54	798.54	-0.94	0.694	0.001	284.7	0.3	0.2%	16
PE 38:03	O	+2Na-H	C43H81NO7PNa2	800.55	800.55	-1.79	0.688	0.001	287.4	0.6	0.1%	16
PE 38:02	O	+2Na-H	C43H83NO7PNa2	802.57	802.57	0.79	0.697	0.001	289.3	0.4	0.1%	8
PE 40:06	O	+2Na-H	C45H79NO7PNa2	822.54	822.54	-3.87	0.672	0.001	288.2	0.3	0.1%	8
PE 40:04	O	+2Na-H	C45H83NO7PNa2	826.57	826.57	-3.33	0.659	0.001	293.5	0.6	0.2%	8
PC 32:01	-	+H	C40H79NO8P	732.55	732.55	-1.91	0.729	0.001	276.5	0.4	0.1%	8
PC 32:00	-	+H	C40H81NO8P	734.57	734.57	-5.65	0.724	0.001	278.4	0.4	0.2%	8
PC 34:03	-	+H	C42H79NO8P	756.55	756.55	-3.30	0.727	0.003	277.1	1.0	0.4%	8
PC 34:02	-	+H	C42H81NO8P	758.57	758.57	-2.31	0.721	0.001	279.5	0.4	0.1%	8
PC 34:01	-	+H	C42H83NO8P	760.59	760.58	-1.31	0.714	0.001	282.0	0.4	0.1%	8
PC 35:01	-	+H	C43H85NO8P	774.60	774.60	-2.90	0.708	0.001	284.6	0.4	0.1%	8
PC 36:02	-	+H	C44H85NO8P	786.60	786.60	-2.98	0.704	0.001	285.9	0.4	0.1%	8
PC 36:01	-	+H	C44H87NO8P	788.62	788.61	-3.93	0.698	0.001	288.2	0.4	0.1%	8
PC 32:02	-	+Na	C40H76NaNO8P	752.52	752.52	1.76	0.703	0.003	276.9	1.3	0.5%	8
PC 32:01	-	+Na	C40H78NaNO8P	754.54	754.53	-3.32	0.709	0.001	279.2	0.3	0.1%	16
PC 32:00	-	+Na	C40H80NaNO8P	756.55	756.55	-4.67	0.705	0.002	280.6	1.0	0.3%	16
PC 34:03	-	+Na	C42H78NO8PNa	778.54	778.53	-3.20	0.687	0.001	282.0	0.4	0.1%	8
PC 34:02	-	+Na	C42H80NaNO8P	780.55	780.55	-1.46	0.697	0.001	283.1	0.4	0.2%	16
PC 34:01	-	+Na	C42H82NaNO8P	782.57	782.56	-1.17	0.693	0.001	284.8	0.4	0.1%	16
PC 35:02	-	+Na	C43H82NaNO8P	794.57	794.56	-2.63	0.675	0.001	285.8	0.6	0.2%	8
PC 35:01	-	+Na	C43H84NaNO8P	796.58	796.58	3.28	0.672	0.001	287.1	0.6	0.2%	8
PC 36:04	-	+Na	C44H80NaNO8P	804.55	804.55	-0.31	0.692	0.001	285.0	0.6	0.2%	16
PC 36:03	-	+Na	C44H82NaNO8P	806.57	806.56	-3.62	0.687	0.001	287.0	0.5	0.2%	16
PC 36:02	-	+Na	C44H84NaNO8P	808.58	808.58	-1.66	0.682	0.001	288.6	0.4	0.2%	16
PC 36:01	-	+Na	C44H86NaNO8P	810.60	810.59	-3.17	0.678	0.001	290.3	0.4	0.2%	16
PC 38:03	-	+Na	C46H86NaNO8P	834.60	834.60	-4.01	0.686	0.001	293.1	0.5	0.2%	8

PC 40:06	-	+Na	C48H84NaO8P	856.58	856.58	3.12	0.651	0.001	294.4	0.3	0.1%	8
PC 40:05	-	+Na	C48H86NaO8P	858.60	858.59	2.18	0.647	0.001	295.8	0.7	0.2%	8
PC 40:04	-	+Na	C48H88NaO8P	860.61	860.61	-0.15	0.643	0.001	297.4	0.5	0.2%	8
PC 36:04	HETE	+Na	C44H80NO9PNa	820.55	820.54	1.43	0.672	0.001	286.9	0.4	0.2%	8
PC 36:03	HETE	+Na	C44H82NO9PNa	822.56	822.56	0.34	0.666	0.001	288.9	0.6	0.2%	8
PC 36:02	HETE	+Na	C44H84NO9PNa	824.58	824.57	-2.21	0.663	0.001	290.3	0.6	0.2%	8
PC 34:02	-	+K	C42H80KNO8P	796.53	796.53	4.23	0.711	0.001	283.3	0.4	0.1%	8
PC 34:01	-	+K	C42H82KNO8P	798.54	798.54	-0.73	0.704	0.001	285.8	0.4	0.1%	8
PC 36:02	-	+K	C44H84KNO8P	824.56	824.56	-1.25	0.696	0.001	289.2	0.4	0.1%	8
PC 36:01	-	+K	C44H86KNO8P	826.57	826.57	-6.15	0.691	0.001	291.1	0.5	0.2%	8
PC 34:01	-	+2Na-H	C42H81NO8PNa2	804.55	804.55	-1.85	0.709	0.002	283.9	0.9	0.3%	8
PC 34:00	-	+2Na-H	C42H83NO8PNa2	806.57	806.56	-0.92	0.703	0.001	286.1	0.5	0.2%	8
PC 36:03	-	+2Na-H	C44H81NO8PNa2	828.55	828.55	1.15	0.682	0.001	288.5	0.5	0.2%	16
PC 36:02	-	+2Na-H	C44H83NO8PNa2	830.57	830.56	-1.41	0.677	0.001	290.4	0.5	0.2%	16
PC 36:01	-	+2Na-H	C44H85NO8PNa2	832.58	832.58	0.36	0.673	0.001	292.0	0.4	0.1%	16
PC 36:04	HETE	+2Na-H	C44H79NO9PNa2	842.53	842.52	1.86	0.670	0.001	287.6	0.4	0.1%	8
PC 36:03	HETE	+2Na-H	C44H81NO9PNa2	844.54	844.54	-0.99	0.664	0.001	289.7	0.6	0.2%	8
PC 36:02	HETE	+2Na-H	C44H83NO9PNa2	846.56	846.55	-0.87	0.659	0.001	291.5	0.5	0.2%	8
PC 36:01	HETE	+2Na-H	C44H85NO9PNa2	848.58	848.57	-0.04	0.654	0.001	293.4	0.4	0.1%	8
PC 36:00	HETE	+2Na-H	C44H87NO9PNa2	850.59	850.59	0.90	0.650	0.001	294.7	0.6	0.2%	8
PS 36:02	-	+H	C42H79NO10P	788.54	788.54	0.73	0.714	0.001	280.9	0.3	0.1%	8
PS 36:01	-	+H	C42H81NO10P	790.56	790.56	1.56	0.708	0.001	283.4	0.4	0.2%	8
PS 38:05	-	+H	C44H77NO10P	810.53	810.53	-1.03	0.712	0.001	281.7	0.4	0.1%	8
PS 38:04	-	+H	C44H79NO10P	812.54	812.54	-0.96	0.705	0.001	284.4	0.3	0.1%	8
PS 38:02	-	+H	C44H83NO10P	816.58	816.57	-0.70	0.697	0.001	287.7	0.4	0.1%	8
PS 38:01	-	+H	C44H85NO10P	818.59	818.59	-0.99	0.693	0.001	289.6	0.4	0.2%	8
PS 40:06	-	+H	C46H79NO10P	836.54	836.55	1.51	0.697	0.001	287.7	0.4	0.1%	8
PS 40:05	-	+H	C46H81NO10P	838.56	838.56	-1.52	0.692	0.001	289.6	0.4	0.1%	8
PS 40:04	-	+H	C46H83NO10P	840.58	840.57	-0.98	0.689	0.001	291.1	0.4	0.1%	8
PS 40:03	-	+H	C46H85NO10P	842.59	842.59	-3.64	0.685	0.001	292.6	0.4	0.1%	8
PS 40:02	-	+H	C46H87NO10P	844.61	844.61	-0.85	0.682	0.001	294.0	0.4	0.1%	8

PS 40:01	-	+H	C46H89NO10P	846.62	846.62	-3.14	0.677	0.001	295.9	0.4	0.1%	8
PS 42:05	-	+H	C48H85NO10P	866.59	866.59	-1.64	0.679	0.001	295.2	0.3	0.1%	8
PS 42:04	-	+H	C48H87NO10P	868.61	868.61	-1.69	0.676	0.001	296.4	0.5	0.2%	8
PS 42:03	-	+H	C48H89NO10P	870.62	870.62	-3.69	0.672	0.001	298.0	0.4	0.1%	8
PS 42:02	-	+H	C48H91NO10P	872.64	872.64	-0.64	0.669	0.001	299.5	0.5	0.2%	8
PS 42:01	-	+H	C48H93NO10P	874.65	874.65	-3.21	0.664	0.001	301.9	0.6	0.2%	8
PS 40:07	-	+Na	C46H76NaO10P	856.51	856.51	-2.09	0.692	0.001	289.7	0.5	0.2%	8
PS 40:06	-	+Na	C46H78NaO10P	858.53	858.53	1.24	0.687	0.001	291.7	0.4	0.1%	8
PS 40:05	-	+Na	C46H80NaO10P	860.54	860.54	-1.26	0.682	0.001	293.8	0.4	0.1%	8
PS 40:04	-	+Na	C46H82NO10PNa	862.56	862.56	-1.08	0.679	0.001	295.2	0.4	0.1%	8
PS 40:03	-	+Na	C46H84NO10PNa	864.57	864.57	-3.32	0.676	0.001	296.3	0.5	0.2%	8
PS 42:05	-	+Na	C48H84NO10PNa	888.57	888.57	-1.72	0.673	0.001	297.7	0.6	0.2%	8
PS 42:04	-	+Na	C48H86NO10PNa	890.59	890.59	-1.65	0.670	0.001	298.9	0.4	0.1%	8
PS 42:02	-	+Na	C48H90NO10PNa	894.62	894.62	-3.98	0.663	0.001	302.0	0.4	0.1%	8
PS 42:01	-	+Na	C48H92NO10PNa	896.64	896.63	-3.13	0.661	0.001	303.2	0.4	0.1%	8
PS 44:010	-	+Na	C50H78NO10PNa	906.53	906.53	-1.16	0.675	0.001	296.9	0.6	0.2%	8
PS 36:02	-	+K	C42H78NO10PK	826.50	826.50	-0.28	0.703	0.001	285.2	0.4	0.1%	8
PS 36:01	-	+K	C42H80NO10PK	828.52	828.51	-3.36	0.698	0.001	287.5	0.4	0.1%	8
PS 38:05	-	+K	C44H76NO10PK	848.48	848.48	-2.29	0.699	0.002	286.6	0.8	0.3%	8
PS 38:04	-	+K	C44H78NO10PK	850.50	850.50	-3.28	0.693	0.001	289.4	0.3	0.1%	8
PS 40:06	-	+K	C46H78NO10PK	874.50	874.50	-1.20	0.684	0.001	292.8	0.4	0.1%	8
PS 40:05	-	+K	C46H80NO10PK	876.52	876.51	-4.78	0.681	0.001	294.2	0.5	0.2%	8
PS 40:04	-	+K	C46H82NO10PK	878.53	878.53	-5.16	0.678	0.001	295.4	0.6	0.2%	8
PS 42:09	-	+K	C48H76NO10PK	896.48	896.48	-5.08	0.680	0.001	294.6	0.4	0.1%	8
PS 34:01	-	+2Na-H	C40H75NO10PNa2	806.49	806.49	-0.96	0.714	0.002	280.8	0.7	0.2%	8
PS 36:04	-	+2Na-H	C42H73NO10PNa2	828.48	828.47	-3.39	0.712	0.001	281.5	0.4	0.1%	8
PS 36:02	-	+2Na-H	C42H77NO10PNa2	832.51	832.51	-0.25	0.701	0.001	286.0	0.4	0.1%	16
PS 36:01	-	+2Na-H	C42H79NO10PNa2	834.52	834.52	1.08	0.697	0.001	287.9	0.4	0.1%	16
PS 37:04	-	+2Na-H	C43H75NO10PNa2	842.49	842.49	-0.33	0.702	0.002	285.9	1.0	0.3%	8
PS 37:02	-	+2Na-H	C43H79NO10PNa2	846.52	846.52	0.88	0.694	0.002	289.3	0.7	0.2%	8
PS 37:01	-	+2Na-H	C43H81NO10PNa2	848.54	848.54	-1.17	0.685	0.002	293.5	0.6	0.2%	8

PS 38:05	-	+2Na-H	C44H75NO10PNa2	854.49	854.49	-2.24	0.702	0.001	285.7	0.5	0.2%	8
PS 38:04	-	+2Na-H	C44H77NO10PNa2	856.51	856.51	-0.64	0.695	0.001	288.7	0.5	0.2%	8
PS 38:02	-	+2Na-H	C44H81NO10PNa2	860.54	860.54	-1.43	0.687	0.002	292.5	0.8	0.3%	8
PS 38:01	-	+2Na-H	C44H83NO10PNa2	862.55	862.55	-1.59	0.680	0.001	295.4	0.6	0.2%	8
PS 39:04	-	+2Na-H	C45H79NO10PNa2	870.52	870.52	-1.41	0.688	0.001	291.9	0.6	0.2%	8
PS 40:09	-	+2Na-H	C46H71NO10PNa2	874.46	874.46	-0.35	0.704	0.003	284.8	1.3	0.5%	8
PS 40:08	-	+2Na-H	C46H73NO10PNa2	876.48	876.48	-1.42	0.697	0.001	288.0	0.4	0.1%	8
PS 40:07	-	+2Na-H	C46H75NO10PNa2	878.49	878.49	-1.91	0.692	0.001	290.2	0.6	0.2%	8
PS 40:06	-	+2Na-H	C46H77NO10PNa2	880.51	880.51	0.36	0.679	0.001	295.6	0.5	0.2%	16
PS 40:05	-	+2Na-H	C46H79NO10PNa2	882.52	882.52	-0.71	0.675	0.001	297.2	0.5	0.2%	16
PS 40:04	-	+2Na-H	C46H81NO10PNa2	884.54	884.54	-0.56	0.674	0.001	298.3	0.6	0.2%	8
PS 40:02	-	+2Na-H	C46H85NO10PNa2	888.57	888.57	-2.56	0.671	0.001	299.4	0.4	0.1%	8
PS 40:01	-	+2Na-H	C46H87NO10PNa2	890.59	890.58	-4.96	0.668	0.001	301.1	0.6	0.2%	8
PS 41:06	-	+2Na-H	C47H79NO10PNa2	894.52	894.52	-0.33	0.678	0.002	296.2	0.8	0.3%	8
PS 41:05	-	+2Na-H	C47H81NO10PNa2	896.54	896.54	-2.60	0.673	0.001	298.4	0.5	0.2%	8
PS 42:09	-	+2Na-H	C48H75NO10PNa2	902.49	902.49	0.06	0.685	0.001	292.6	0.4	0.2%	16
PS 42:08	-	+2Na-H	C48H77NO10PNa2	904.51	904.51	-1.76	0.680	0.001	295.3	0.5	0.2%	8
PS 42:07	-	+2Na-H	C48H79NO10PNa2	906.52	906.52	-1.24	0.678	0.001	296.4	0.5	0.2%	8
PS 42:06	-	+2Na-H	C48H81NO10PNa2	908.54	908.54	-4.37	0.675	0.001	297.5	0.6	0.2%	8
PS 42:05	-	+2Na-H	C48H83NO10PNa2	910.55	910.55	-2.09	0.669	0.001	300.1	0.5	0.2%	8
PS 42:04	-	+2Na-H	C48H85NO10PNa2	912.57	912.57	-2.35	0.661	0.001	304.2	0.6	0.2%	8
PS 42:02	-	+2Na-H	C48H89NO10PNa2	916.60	916.60	0.52	0.657	0.001	306.1	0.6	0.2%	8
PS 44:08	-	+2Na-H	C50H81NO10PNa2	932.54	932.54	-3.36	0.667	0.002	301.2	0.7	0.2%	8
PS 44:07	-	+2Na-H	C50H83NO10PNa2	934.55	934.55	-2.33	0.663	0.002	303.1	0.8	0.3%	8
PS 44:05	-	+2Na-H	C50H87NO10PNa2	938.59	938.58	-2.19	0.655	0.002	306.9	0.8	0.3%	8
PS 35:02	O	+2Na-H	C41H77NO9PNa2	804.51	804.51	-2.14	0.710	0.002	282.4	0.7	0.2%	8
SM 34:01	-	+H	C39H80N2O6P	703.58	703.58	0.82	0.724	0.001	280.1	0.4	0.2%	8
SM 36:02	-	+H	C41H82N2O6P	729.59	729.59	0.79	0.713	0.001	284.1	0.6	0.2%	8
SM 36:01	-	+H	C41H84N2O6P	731.61	731.61	3.32	0.708	0.001	286.2	0.4	0.1%	8
SM 37:01	-	+H	C42H86N2O6P	745.62	745.62	1.88	0.702	0.002	288.7	0.7	0.2%	8
SM 38:01	-	+H	C43H88N2O6P	759.64	759.64	1.03	0.693	0.001	292.3	0.4	0.1%	8

SM 39:01	-	+H	C44H90N2O6P	773.65	773.66	2.79	0.684	0.001	295.9	0.5	0.2%	8
SM 40:02	-	+H	C45H90N2O6P	785.65	785.65	1.38	0.684	0.001	295.7	0.4	0.1%	8
SM 40:01	-	+H	C45H92N2O6P	787.67	787.67	0.93	0.679	0.001	297.9	0.4	0.1%	8
SM 40:00	-	+H	C45H94N2O6P	789.68	789.68	-1.28	0.675	0.001	299.6	0.3	0.1%	8
SM 41:02	-	+H	C46H92N2O6P	799.67	799.67	0.07	0.677	0.001	298.9	0.5	0.2%	8
SM 41:01	-	+H	C46H94N2O6P	801.68	801.69	0.52	0.672	0.001	301.1	0.3	0.1%	8
SM 41:00	-	+H	C46H96N2O6P	803.70	803.70	-3.52	0.669	0.000	302.3	0.2	0.1%	8
SM 42:04	-	+H	C47H90N2O6P	809.65	809.65	-2.31	0.679	0.002	297.8	0.7	0.2%	8
SM 42:03	-	+H	C47H92N2O6P	811.67	811.67	-0.89	0.675	0.001	299.6	0.3	0.1%	8
SM 42:02	-	+H	C47H94N2O6P	813.68	813.69	1.64	0.671	0.001	301.4	0.4	0.1%	8
SM 42:01	-	+H	C47H96N2O6P	815.70	815.70	-0.62	0.667	0.001	303.2	0.4	0.1%	8
SM 42:00	-	+H	C47H98N2O6P	817.72	817.72	-0.07	0.662	0.001	305.3	0.4	0.1%	8
SM 43:02	-	+H	C48H96N2O6P	827.70	827.70	0.50	0.664	0.001	304.5	0.6	0.2%	8
SM 43:01	-	+H	C48H98N2O6P	829.72	829.72	-1.24	0.659	0.001	306.9	0.5	0.2%	8
SM 44:02	-	+H	C49H98N2O6P	841.72	841.72	3.55	0.657	0.001	307.5	0.6	0.2%	8
SM 44:01	-	+H	C49H100N2O6P	843.73	843.73	-3.03	0.652	0.001	309.8	0.5	0.2%	8
SM 36:01	-	+Na-H2O	C41H81N2NaO5P	735.58	735.58	-1.35	0.694	0.002	280.1	0.7	0.2%	8
SM 42:02	-	+Na-H2O	C47H91N2NaO5P	817.66	817.66	-1.25	0.650	0.001	301.2	0.5	0.2%	8
SM 34:01	-	+Na	C39H79N2O6PNa	725.56	725.56	-2.22	0.712	0.001	278.8	0.5	0.1%	16
SM 35:01	-	+Na	C40H81N2O6PNa	739.57	739.57	-2.49	0.693	0.001	280.6	0.4	0.1%	8
SM 36:02	-	+Na	C41H81N2O6PNa	751.57	751.57	2.10	0.694	0.001	280.3	0.6	0.2%	8
SM 36:01	-	+Na	C41H83N2O6PNa	753.59	753.59	3.01	0.695	0.001	285.9	0.4	0.1%	16
SM 37:01	-	+Na	C42H85N2O6PNa	767.60	767.60	-1.48	0.683	0.001	285.4	0.6	0.2%	8
SM 38:01	-	+Na	C43H87N2O6PNa	781.62	781.62	-0.19	0.680	0.001	292.2	0.5	0.1%	16
SM 39:01	-	+Na	C44H89N2O6PNa	795.64	795.64	1.97	0.663	0.001	294.6	0.4	0.1%	8
SM 40:02	-	+Na	C45H89N2O6PNa	807.64	807.64	-0.39	0.667	0.001	292.5	0.5	0.2%	8
SM 40:01	-	+Na	C45H91N2O6PNa	809.65	809.65	-0.84	0.660	0.001	296.0	0.6	0.2%	8
SM 41:02	-	+Na	C46H91N2O6PNa	821.65	821.65	-1.54	0.659	0.001	296.4	0.6	0.2%	8
SM 41:01	-	+Na	C46H93N2O6PNa	823.67	823.67	-1.97	0.654	0.001	299.3	0.6	0.2%	8
SM 42:03	-	+Na	C47H91N2O6PNa	833.65	833.65	0.54	0.657	0.001	297.6	0.6	0.2%	8
SM 42:02	-	+Na	C47H93N2O6PNa	835.67	835.67	1.39	0.662	0.001	300.5	0.5	0.2%	16

SM 42:01	-	+Na	C47H95N2O6PNa	837.68	837.68	-3.81	0.657	0.001	302.6	0.5	0.1%	16
SM 43:02	-	+Na	C48H95N2O6PNa	849.68	849.68	-1.48	0.645	0.001	303.6	0.5	0.2%	8
SM 43:01	-	+Na	C48H97N2O6PNa	851.70	851.69	-5.66	0.644	0.001	304.2	0.5	0.2%	8
SM 44:03	-	+Na	C49H95N2NaO6P	861.68	861.68	-0.28	0.643	0.001	304.7	0.6	0.2%	8
SM 44:02	-	+Na	C49H97N2O6PNa	863.70	863.70	-1.51	0.639	0.001	306.5	0.6	0.2%	8
SM 44:01	-	+Na	C49H99N2O6PNa	865.71	865.71	-5.16	0.637	0.001	307.9	0.6	0.2%	8
SM 42:01	h	+Na	C47H95N2NaO7P	853.68	853.68	-2.46	0.637	0.001	307.9	0.5	0.2%	8
SM 36:01	-	+K	C41H83N2O6PK	769.56	769.56	1.32	0.702	0.001	288.4	0.5	0.2%	8
SM 38:00	-	+2Na-H	C43H88N2O6PNa2	805.62	805.62	3.54	0.663	0.002	294.7	0.8	0.3%	8
SM 41:00	-	+2Na-H	C46H94N2Na2O6P	847.66	847.66	-1.64	0.650	0.001	301.1	0.7	0.2%	8
GlcCer 47:03	-	+H-2H2O	C53H96NO6	842.72	842.72	-3.15	0.658	0.001	307.7	0.4	0.1%	8
GlcCer 50:04	-	+H-2H2O	C56H100NO6	882.76	882.75	-0.32	0.644	0.001	314.3	0.5	0.2%	8
GlcCer 36:01	-	+H-H2O	C42H80NO7	710.59	710.59	1.48	0.725	0.001	279.9	0.4	0.2%	8
GlcCer 38:01	-	+H-H2O	C44H84NO7	738.62	738.63	0.91	0.708	0.001	286.6	0.5	0.2%	8
GlcCer 40:02	-	+H-H2O	C46H86NO7	764.64	764.64	-0.48	0.698	0.001	290.4	0.4	0.2%	8
GlcCer 40:01	-	+H-H2O	C46H88NO7	766.66	766.66	0.78	0.692	0.001	292.8	0.4	0.1%	8
GlcCer 41:01	-	+H-H2O	C47H90NO7	780.67	780.67	1.42	0.688	0.001	294.6	0.5	0.2%	8
GlcCer 42:02	-	+H-H2O	C48H90NO7	792.67	792.67	1.59	0.684	0.001	296.4	0.4	0.1%	8
GlcCer 42:01	-	+H-H2O	C48H92NO7	794.69	794.69	-0.86	0.679	0.001	298.4	0.4	0.1%	8
GlcCer 44:02	-	+H-H2O	C50H94NO7	820.70	820.70	-1.73	0.672	0.001	301.5	0.4	0.1%	8
GlcCer 46:02	-	+H-H2O	C55H98NO7	884.73	884.73	0.07	0.644	0.001	314.3	0.6	0.2%	8
GlcCer 46:01	-	+H-H2O	C55H100NO7	886.75	886.75	-0.76	0.640	0.001	316.2	0.5	0.1%	8
GlcCer 47:00	-	+Na-2H2O	C53H101NNaO6	870.75	870.75	-2.56	0.645	0.001	313.6	0.4	0.1%	8
GlcCer 49:01	-	+Na-2H2O	C55H103NNaO6	896.77	896.77	-0.96	0.637	0.001	317.5	0.4	0.1%	8
GlcCer 49:00	-	+Na-2H2O	C55H105NNaO6	898.78	898.78	-5.57	0.634	0.001	318.7	0.4	0.1%	8
GlcCer 36:02	-	+H	C42H80NO8	726.59	726.59	0.56	0.721	0.001	281.4	0.4	0.2%	8
GlcCer 36:01	-	+H	C42H82NO8	728.60	728.61	2.56	0.718	0.001	282.4	0.4	0.1%	8
GlcCer 36:00	-	+H	C42H84NO8	730.62	730.62	-0.65	0.713	0.001	284.6	0.4	0.1%	8
GlcCer 38:03	-	+H	C44H82NO8	752.60	752.60	-0.83	0.713	0.001	284.4	0.3	0.1%	8
GlcCer 38:02	-	+H	C44H84NO8	754.62	754.62	0.30	0.704	0.001	287.9	0.5	0.2%	8
GlcCer 38:01	-	+H	C44H86NO8	756.64	756.64	0.25	0.704	0.001	288.1	0.3	0.1%	8

GlcCer 38:00	-	+H	C44H88NO8	758.65	758.65	-1.65	0.699	0.001	290.2	0.5	0.2%	8
GlcCer 40:02	-	+H	C46H88NO8	782.65	782.65	2.75	0.689	0.001	294.0	0.5	0.2%	8
GlcCer 40:01	-	+H	C46H90NO8	784.67	784.67	0.39	0.690	0.001	293.9	0.4	0.1%	8
GlcCer 40:00	-	+H	C46H92NO8	786.68	786.68	-0.29	0.684	0.001	296.2	0.4	0.1%	8
GlcCer 41:01	-	+H	C47H92NO8	798.68	798.68	-0.22	0.682	0.001	297.1	0.4	0.2%	8
GlcCer 42:02	-	+H	C48H92NO8	810.68	810.68	3.05	0.677	0.001	299.3	0.4	0.1%	8
GlcCer 42:01	-	+H	C48H94NO8	812.70	812.70	0.78	0.674	0.001	300.6	0.4	0.1%	8
GlcCer 42:00	-	+H	C48H96NO8	814.71	814.71	-2.34	0.670	0.001	302.3	0.4	0.1%	8
GlcCer 43:02	-	+H	C49H94NO8	824.70	824.70	-1.47	0.670	0.001	302.0	0.4	0.1%	8
GlcCer 44:02	-	+H	C50H96NO8	838.71	838.71	-0.12	0.663	0.001	305.1	0.4	0.1%	8
GlcCer 44:01	-	+H	C50H98NO8	840.73	840.73	-4.93	0.661	0.001	306.4	0.4	0.1%	8
GlcCer 40:00	h	+H	C46H92NO9	802.68	802.68	2.27	0.675	0.001	300.2	0.4	0.1%	8
GlcCer 42:04	h	+H	C48H88NO9	822.65	822.65	3.63	0.656	0.001	299.0	0.4	0.1%	8
GlcCer 42:03	h	+H	C48H90NO9	824.66	824.66	-2.63	0.652	0.001	300.4	0.4	0.2%	8
GlcCer 42:01	h	+H	C48H94NO9	828.69	828.69	-3.51	0.664	0.001	304.7	0.4	0.1%	8
GlcCer 42:00	h	+H	C48H96NO9	830.71	830.71	-1.99	0.662	0.001	306.1	0.5	0.2%	8
GlcCer 44:02	h	+H	C50H96NO9	854.71	854.71	-1.11	0.655	0.001	309.0	0.4	0.1%	8
GlcCer 44:01	h	+H	C50H98NO9	856.72	856.73	3.28	0.652	0.001	310.6	0.5	0.2%	8
GlcCer 44:00	h	+H	C50H100NO9	858.74	858.74	1.48	0.649	0.001	311.9	0.5	0.2%	8
GlcCer 45:00	h	+H	C51H102NO9	872.76	872.76	4.45	0.642	0.001	315.0	0.5	0.2%	8
GlcCer 46:05	h	+H	C52H94NO9	876.69	876.69	-1.67	0.643	0.001	308.7	0.5	0.1%	16
GlcCer 46:04	h	+H	C52H96NO9	878.71	878.70	-4.06	0.641	0.001	309.5	0.5	0.2%	16
GlcCer 34:01	-	+Na	C40H77NNaO8	722.55	722.56	2.94	0.715	0.001	279.0	0.5	0.2%	8
GlcCer 34:00	-	+Na	C40H79NNaO8	724.57	724.57	1.48	0.708	0.001	280.9	0.4	0.2%	8
GlcCer 36:02	-	+Na	C42H79NNaO8	748.57	748.57	-0.28	0.706	0.001	281.5	0.3	0.1%	8
GlcCer 36:01	-	+Na	C42H81NNaO8	750.59	750.59	3.63	0.706	0.001	284.0	0.4	0.1%	16
GlcCer 37:01	-	+Na	C43H83NNaO8	764.60	764.60	-0.86	0.688	0.001	287.4	0.4	0.1%	8
GlcCer 38:02	-	+Na	C44H83NNaO8	776.60	776.60	-0.38	0.688	0.001	287.3	0.5	0.2%	8
GlcCer 38:01	-	+Na	C44H85NNaO8	778.62	778.62	1.60	0.689	0.008	290.5	3.3	1.1%	16
GlcCer 38:00	-	+Na	C44H87NNaO8	780.63	780.63	-1.29	0.677	0.001	291.3	0.4	0.1%	8
GlcCer 39:01	-	+Na	C45H87NNaO8	792.63	792.63	-2.71	0.675	0.001	292.0	0.6	0.2%	8

GlcCer 40:03	-	+Na	C46H85NNaO8	802.62	802.62	-2.03	0.680	0.002	290.3	0.8	0.3%	8
GlcCer 40:02	-	+Na	C46H87NNaO8	804.63	804.63	1.38	0.684	0.001	292.1	0.4	0.2%	16
GlcCer 40:01	-	+Na	C46H89NNaO8	806.65	806.65	0.69	0.674	0.001	296.1	0.4	0.1%	16
GlcCer 40:00	-	+Na	C46H91NNaO8	808.66	808.67	1.56	0.670	0.001	297.7	0.4	0.1%	16
GlcCer 41:02	-	+Na	C47H89NNaO8	818.65	818.65	0.64	0.663	0.001	296.1	0.5	0.2%	8
GlcCer 41:01	-	+Na	C47H91NNaO8	820.66	820.66	-1.62	0.660	0.001	297.4	0.4	0.1%	8
GlcCer 42:03	-	+Na	C48H89NNaO8	830.65	830.65	0.21	0.671	0.001	297.3	0.5	0.2%	16
GlcCer 42:02	-	+Na	C48H91NNaO8	832.66	832.67	5.20	0.665	0.001	299.5	0.4	0.1%	16
GlcCer 42:01	-	+Na	C48H93NNaO8	834.68	834.68	1.41	0.660	0.001	301.8	0.4	0.1%	16
GlcCer 42:00	-	+Na	C48H95NNaO8	836.70	836.69	-1.34	0.656	0.001	303.1	0.4	0.1%	16
GlcCer 43:03	-	+Na	C49H91NNaO8	844.66	844.66	-2.14	0.651	0.001	300.7	0.5	0.2%	8
GlcCer 43:02	-	+Na	C49H93NNaO8	846.68	846.68	-0.79	0.658	0.001	302.4	0.5	0.1%	16
GlcCer 44:03	-	+Na	C50H93NNaO8	858.68	858.68	-1.05	0.643	0.001	303.9	0.6	0.2%	8
GlcCer 44:02	-	+Na	C50H95NNaO8	860.70	860.70	1.21	0.649	0.001	306.3	0.4	0.1%	16
GlcCer 44:01	-	+Na	C50H97NNaO8	862.71	862.71	-0.57	0.657	0.001	307.9	0.4	0.1%	8
GlcCer 36:01	h	+Na	C42H81NNaO9	766.58	766.58	2.96	0.688	0.001	287.5	0.5	0.2%	8
GlcCer 38:01	h	+Na	C44H85NNaO9	794.61	794.61	2.12	0.672	0.001	293.1	0.4	0.1%	8
GlcCer 42:02	h	+Na	C48H91NNaO9	848.66	848.66	1.32	0.659	0.001	301.9	0.4	0.1%	16
GlcCer 42:01	h	+Na	C48H93NNaO9	850.67	850.67	-1.15	0.654	0.001	304.2	0.4	0.1%	16
GlcCer 42:00	h	+Na	C48H95NNaO9	852.69	852.69	-3.87	0.662	0.001	305.5	0.4	0.1%	8
GlcCer 43:02	h	+Na	C49H93NNaO9	862.67	862.68	0.89	0.637	0.001	306.1	0.5	0.2%	8
GlcCer 43:01	h	+Na	C49H95NNaO9	864.69	864.69	1.25	0.648	0.001	306.6	0.5	0.2%	16
GlcCer 44:04	h	+Na	C50H91NNaO9	872.66	872.66	-3.46	0.640	0.001	304.8	0.6	0.2%	8
GlcCer 44:03	h	+Na	C50H93NNaO9	874.67	874.67	-0.08	0.636	0.001	306.6	0.5	0.2%	8
Cer 42:02	-	+H-2H2O	C42H78NO	612.61	612.61	0.43	0.750	0.001	271.3	0.4	0.1%	8
Cer 42:01	-	+H-2H2O	C42H80NO	614.62	614.62	-3.54	0.743	0.002	273.9	0.9	0.3%	8
Cer 36:01	-	+H-H2O	C36H70NO2	548.54	548.54	-0.79	0.794	0.001	257.2	0.4	0.1%	8
Cer 38:01	-	+H-H2O	C38H74NO2	576.57	576.57	-0.71	0.773	0.001	263.9	0.4	0.1%	8
Cer 40:02	-	+H-H2O	C40H76NO2	602.59	602.59	2.08	0.762	0.001	267.5	0.4	0.2%	8
Cer 40:01	-	+H-H2O	C40H78NO2	604.60	604.60	0.02	0.756	0.001	269.4	0.5	0.2%	8
Cer 41:01	-	+H-H2O	C41H80NO2	618.62	618.62	-3.03	0.748	0.001	272.2	0.5	0.2%	8

Cer 42:03	-	+H-H2O	C42H78NO2	628.60	628.60	0.34	0.750	0.000	271.4	0.1	0.0%	8
Cer 42:02	-	+H-H2O	C42H80NO2	630.62	630.62	1.71	0.745	0.001	273.3	0.4	0.1%	8
Cer 42:01	-	+H-H2O	C42H82NO2	632.63	632.63	-2.00	0.740	0.001	275.1	0.5	0.2%	8
Cer 43:02	-	+H-H2O	C43H82NO2	644.63	644.63	0.45	0.738	0.001	275.5	0.4	0.2%	8
Cer 44:02	-	+H-H2O	C44H84NO2	658.65	658.65	-1.97	0.727	0.001	279.7	0.4	0.1%	8
Cer 36:00	-	+H	C36H74NO3	568.57	568.57	0.77	0.779	0.001	261.9	0.4	0.1%	8
Cer 38:00	-	+H	C38H78NO3	596.60	596.60	-1.91	0.762	0.001	267.4	0.5	0.2%	8
Cer 40:02	-	+H	C40H78NO3	620.60	620.60	2.85	0.748	0.001	272.3	0.3	0.1%	8
Cer 40:00	-	+H	C40H82NO3	624.63	624.63	-0.02	0.743	0.001	274.0	0.4	0.2%	8
Cer 42:03	-	+H	C42H80NO3	646.61	646.62	1.90	0.739	0.001	275.2	0.4	0.1%	8
Cer 42:02	-	+H	C42H82NO3	648.63	648.63	-0.79	0.735	0.001	276.8	0.4	0.1%	8
Cer 42:01	-	+H	C42H84NO3	650.65	650.65	0.08	0.733	0.001	277.6	0.4	0.1%	8
Cer 42:00	-	+H	C42H86NO3	652.66	652.66	-1.52	0.726	0.001	280.1	0.4	0.2%	8
Cer 40:00	h	+H	C40H82NO4	640.62	640.62	1.00	0.736	0.001	276.4	0.5	0.2%	8
Cer 42:01	h	+H	C42H84NO4	666.64	666.64	3.16	0.731	0.001	278.0	0.3	0.1%	8
Cer 42:00	h	+H	C42H86NO4	668.66	668.65	-2.00	0.721	0.001	282.1	0.4	0.1%	8
Cer 42:00	-	+Na	C42H85NNaO3	674.64	674.65	4.54	0.721	0.001	281.8	0.5	0.2%	8

* All features came from analytical standard total extracts from Avanti Polar Lipids.

APPENDIX F

Katrina L. Leaptrot

3401 Anderson Road Unit 18
Antioch, TN 37013

Cell: (304) 552-4914
katrina.l.leaptrot@gmail.com

EDUCATION

Ph.D. in Chemistry

Vanderbilt University, Nashville, TN

Expected May 2018

Dissertation: Development of a Spatially Multiplexed Ion Mobility Spectrometer and Utilization of Ion Mobility-Mass Spectrometry for Conformational Analyses of Lipids and Other Biomolecules

Advisor: Prof. John A. McLean

B.S. in Biology and Chemistry

University of Charleston, Charleston, West Virginia

May 2011

RESEARCH EXPERIENCE

Graduate Research Assistant

Aug 2011-May 2018

Vanderbilt University, Nashville, TN

Advisor: Prof. John A. McLean

Development of a spatially multiplexed ion mobility spectrometer including simulation, vacuum system, electronics, hardware, and infrastructure.

Design and development of a device for isoelectric focusing and trapping.

Conformational analyses of lipids with ion mobility-mass spectrometry.

Independent Undergraduate Research

Aug 2009-May 2011

University of Charleston, Charleston, WV

Advisors: Prof. Xiaoping Sun and Prof. David Haas

Spectroscopic studies of uranyl cation in various aqueous media with ultraviolet-visible spectroscopy.

Investigation of electrophilic aromatic substitution reactions of thionyl chloride and selenyl chloride.

Restoration of thermogravimetric-differential thermal analyzer and production of laboratory procedure on function and data acquisition.

Intern

Each May-Aug, 2008-2011

Watershed Assessment Branch, West Virginia Department of Environmental Protection

Assessment of habitat, organisms, and water chemistry of lakes and wadeable streams.

Collection, entry, and processing of stream assessment data.

TECHNICAL SKILLS AND EXPERTISE

Instrumentation: Ion Mobility Time-of-Flight Mass Spectrometry, Ion Mobility Spectrometry, UV-Vis Spectroscopy, Thermogravimetric-Differential Thermal Analysis, Fluorescence Spectroscopy

Software: Adobe Acrobat, Adobe Photoshop, AutoCAD, Autodesk Simulation CFD, ChemDraw, COMSOL Multiphysics, CorelDraw, EndNote, KiCad, NI LabVIEW, Mathcad, Microsoft Excel, Microsoft PowerPoint, Microsoft Word, Microsoft Visual Studio, Notepad++, SIMION

Coding Languages: C++, Python, Lua, Visual Basic

SELECTED HONORS

2015	63 rd Annual ASMS Conference Student Travel Stipend
2013	61 st Annual ASMS Conference Student Travel Stipend
2013	National Science Foundation Graduate Research Fellowship Program Honorable Mention
2013	Award for Top Presentation, 29 th International Symposium on MicroScale Bioseparations, University of Virginia
2012-2013	Mitchum Warren Graduate Fellowship, Vanderbilt University
2011-2012	Vanderbilt Institute of Chemical Biology Graduate Fellowship, Vanderbilt University
2011	President's Award for Outstanding Senior of the Year, University of Charleston
2011	Outstanding Science Student of the Year, University of Charleston
2007	State Advanced Placement Female Scholar, West Virginia
2007-2011	National Merit Bayer Academic Scholarship

PUBLICATIONS

1. **Leaptrot, K. L.**; Khayamian, T.; Jafari, M. T.; McLean, J. A., Ion Mobility Spectrometry and Ion Mobility-Mass Spectrometry, Invited chapter in *Mass Spectrometry with Inductively Coupled Plasmas*, A. Montaser, Ed., John Wiley & Sons, 2018.
2. May, J. C.; Goodwin, C.; Lareau, N.; **Leaptrot, K. L.**; Morris, C. B.; Kurulugama, R.; Mordehai, A.; Klein, C.; William, B.; Darland, E.; Overney, G.; Imatani, K.; Stafford, G.; Fjeldsted, J.; McLean, J. A., Conformational Ordering of Biomolecules in the Gas Phase: Nitrogen Collision Cross-Sections Measured on a Prototype High Resolution Drift Tube Ion Mobility-Mass Spectrometer, *Anal. Chem. (Washington, DC, U.S.)* 2014, 86 (4), 2107-2116.
3. Sun, X.; Haas, D.; McWilliams, S.; Smith, B.; **Leaptrot K. L.**, Investigations on the Lewis-acids-catalysed electrophilic aromatic substitution reactions of thionyl chloride and selenyl chloride, the substituent effects, and the reaction mechanisms, *J. Chem. Res.* 2013, 37 (12), 736-744.
4. Sun, X.; **Leaptrot K. L.**, Effects of various ligands on spectroscopic properties of the uranyl ion, *J. Undergrad. Chem. Res.* 2011, 10 (4), 162-165.

WORKS IN PROGRESS

1. **Leaprot, K.L.**; May, J. C.; Dodds, J. N.; McLean, J. A., Structural Conformation Atlas for High Confidence Lipidomics, in preparation for submission in 2018.

PRESENTATIONS

1. May, J. C.; Sherrod, S. D.; **Leaprot, K. L.**; Nichols, C. M., McLean, J. A., “*Structural Specificity of Ion Mobility Collision Cross Section for Characterization of Lipids*,” 65th American Society for Mass Spectrometry Conference on Mass Spectrometry and Allied Topics, Indianapolis, IN, 2017. **Poster**.
2. **Leaprot, K. L.**; May, J. C.; Dodds, J. N.; McLean, J. A., “*Conformational Atlas of 7 Classes of Sphingolipids and Glycerophospholipids Mapped by Ion Mobility-Mass Spectrometry*,” 64th American Society for Mass Spectrometry Conference on Mass Spectrometry and Allied Topics, San Antonio, TX, 2016. **Poster**.
3. Bello, B. H.; **Leaprot, K. L.**; May, J. C.; McLean, J. A., “*Control Software for a Spatially Multiplexed Ion Mobility-Mass Spectrometer*,” 64th American Society for Mass Spectrometry Conference on Mass Spectrometry and Allied Topics, San Antonio, TX, 2016. **Poster**.
4. **Leaprot, K. L.**; May, J. C.; McLean, J. A., “*Development of a Spatially Multiplexed Ion Mobility-Mass Spectrometer Based on Eight Discrete Ion Beam Paths*,” International Society for Ion Mobility Spectrometry Conference, Cordoba, Spain, 2015. **Oral**.
5. **Leaprot, K. L.**; Morris, C. B., May, J. C.; McLean, J. A., “*Considerations in the Scalability of a Spatially Multiplexed Ion Mobility-Mass Spectrometer to Higher Channel Numbers*,” 63rd American Society for Mass Spectrometry Conference on Mass Spectrometry and Allied Topics, St. Louis, MO, 2015. **Poster**.
6. Dodds, J. N.; **Leaprot, K. L.**; May, J. C.; McLean, J. A., “*Exploring the Separation Capabilities of Ion Mobility-Mass Spectrometers: Resolution and Resolving Power Performance*,” 63rd American Society for Mass Spectrometry Conference on Mass Spectrometry and Allied Topics, St. Louis, MO, 2015. **Poster**.
7. **Leaprot, K. L.**; May, J. C.; McLean, J. A., “*Theoretical performance assessment and development of a spatially multiplexed ion mobility-mass spectrometer*,” Southeastern Regional Meeting ACS, Nashville, TN, 2014. **Oral**.
8. **Leaprot, K. L.**; May, J. C.; McLean, J. A., “*Theoretical Performance Assessment and Development of a Spatially Multiplexed Ion Mobility-Mass Spectrometer*,” VICB Student Symposium, Nashville, TN, 2014. **Poster**.
9. **Leaprot, K. L.**; May, J. C.; McLean, J. A., “*Technical Advances and Theoretical Performance Assessment of a Spatially Multiplexed Ion Mobility-Mass Spectrometer*,” 62nd American Society for Mass Spectrometry Conference on Mass Spectrometry and Allied Topics, Baltimore, MD, 2014. **Poster**.
10. May, J. C.; **Leaprot, K. L.**; Lareau, N. M.; Kurulugama, R. T.; Stafford, G. C.; Mordehai, A.; Fjeldsted, J. C.; McLean, J. A., “*Understanding Global Ion Mobility Separation*”

Differences of Biomolecules in Alternative Drift Gases, " 62nd American Society for Mass Spectrometry Conference on Mass Spectrometry and Allied Topics, Baltimore, MD, 2014. **Poster.**

11. **Leaptrot, K. L.;** May, J. C.; McLean, J. A., "*Development and Theoretical Evaluation of a Spatially Multiplexed Ion Mobility Spectrometer,*" VICB Student Symposium, Nashville, TN, 2013. **Poster.**
12. **Leaptrot, K. L.;** May, J. C.; McLean, J. A., "*Development of a Spatially Multiplexed 8-Channel Ion Mobility-Mass Spectrometer: Vacuum System, Ion Source, and Interfacing Ion Funnel Arrays,*" 61st American Society for Mass Spectrometry Conference on Mass Spectrometry and Allied Topics, Minneapolis, MN, 2013. **Poster.**
13. May, J. C.; **Leaptrot, K. L.;** Sundarapandian, S.; McLean, J. A., "*Theoretical Evaluation and Performance Characterization of a Spatially Multiplexed 8-Channel Ion Mobility Spectrometer,*" 29th International Symposium on MicroScale Bioseparations, Charlottesville, VA, 2013. **Poster.**
14. **Leaptrot, K. L.;** May, J. C.; McLean, J. A., "*Design of a Spatially Multiplexed 8-Channel Electrospray Ionization Ion Mobility Spectrometer,*" VICB 10th Anniversary Symposium, Nashville, TN, 2013. **Poster.**
15. May, J. C.; **Leaptrot, K. L.;** Sundarapandian, S.; McLean, J. A., "*Theoretical Evaluation and Performance Characterization of a Spatially Multiplexed 8-Channel Ion Mobility Spectrometer,*" 60th American Society for Mass Spectrometry Conference on Mass Spectrometry and Allied Topics, Vancouver, Canada, 2012. **Poster.**
16. **Leaptrot, K. L.,** "*Spectroscopic Characterization of the Dissociative Excited State of the Uranyl Ion in Various Aqueous Media,*" Undergraduate Research Day at the Capitol, Charleston, WV, 2011. **Poster.**
17. **Leaptrot, K. L.,** "*Spectroscopic Characterization of the Dissociative Excited State of the Uranyl Ion in Various Aqueous Media,*" Student Assessment Day, University of Charleston, 2011. **Oral.**
18. **Leaptrot, K. L.,** "*Spectroscopic Characterization of the Dissociative Excited State of the Uranyl Ion in Various Media,*" Chi Beta Phi Science Honorary National Conference, Charleston, WV, 2010. **Oral.**
19. **Leaptrot, K. L.,** "*Spectroscopic Characterization of the Dissociative Excited State of the Uranyl Ion in Various Media,*" Robert C. Nunley Conference, Charleston, WV, 2010. **Oral.**

TEACHING EXPERIENCE

Student Scientific Advisor

2016-May 2018

SyBBURE Searle Undergraduate Research Program, Vanderbilt University

Mentorship of undergraduates in scientific research and professional development

Head Teaching Assistant

Fall 2015

Teaching Assistant

Fall 2013, Spring 2014

Department of Chemistry, Vanderbilt University
Laboratory instruction of undergraduates in analytical chemistry and general chemistry

Teaching Assistant

Aug 2008-May 2011

Department of Chemistry, University of Charleston
Laboratory instruction of undergraduates in organic chemistry

UNIVERSITY AND COMMUNITY SERVICE

- 2014 Chemical Biology Association of Students Demonstrations at Nashville
 Adventure Science Center
 Constructed a hyperbolic paraboloid (rotating saddle) mechanical
 representation of a quadrupole mass spectrometer
 Constructed hands-on representation of ion mobility drift tube
- 2014 Vanderbilt Women in Science and Engineering and Vanderbilt Chemical Biology
 Association of Students Graphic Design Award for the Promotion of Science
- 2014 Vanderbilt Graduate Student Council Pen Pal with a Purpose Vanderbilt Campus
 Visit, Wright Middle School
- 2013 Vanderbilt Student Volunteers for Science Team Leader
 Four interactive science lessons, Meigs Magnet Middle School.
 Annual After-School Science Carnival, Head Magnet Middle School
- 2013-2015 Vanderbilt Graduate Student Council Pen Pal with a Purpose, Wright Middle
 School
- 2010-2011 University of Charleston Chi Beta Phi National Science Honorary Science
 Demonstrations
 Clendenin Middle School site visit
 Home-school group visit to University of Charleston campus
 Elkview Elementary School site visit